Journal of Engineering for Gas Turbines and Power

Published Quarterly by ASME

VOLUME 127 • NUMBER 1 • JANUARY 2005

TECHNICAL PAPERS

Transactions of the ASME, Journal of Engineering for Gas Turbines and Power (ISSN 0742-4795) is published quarterly (Jan., April, July, Oct.) by The American Society of Mechanical Engineers, Three Park Avenue, New York, NY 10016. Periodicals postage paid at New York, NY and additional mailing offices. POSTMASTER: Send address changes to Transactions of the ASME, Journal of Engineering for Gas Turbines and Power, c/o THE AMERICAN SOCIETY OF MECHANICAL ENGINEERS, 22 Law Drive, Box 2300, Fairfield, NJ 07007-2300.
CHANGES OF ADDRESS must be received at Society headquarters seven weeks before they are to be effective. Please send old label and new address.
STATEMENT from By-Laws. The Society shall not be responsible for statements or opinions advanced in papers or ... printed in its publications (B7.1, par. 3).

INDEXED by Applied Mechanics Reviews and Engineering Information, Inc. Canadian Goods & Services Tax Registration #126148048

(**Contents continued**)

Journal of Engineering for Gas Turbines and Power **JANUARY 2005**

Volume 127, Number 1

ANNOUNCEMENTS AND SPECIAL NOTES

(**Contents continued**)

Journal of Engineering for Gas Turbines and Power **JANUARY 2005**

Volume 127, Number 1

The ASME Journal of Engineering for Gas Turbines and Power is abstracted and indexed in the following:

AESIS (Australia's Geoscience, Minerals, & Petroleum Database), Applied Science & Technology Index, Aquatic Sciences and Fisheries Abstracts, Civil Engineering Abstracts, Compendex (The electronic equivalent of Engineering Index), Computer & Information Systems Abstracts, Corrosion Abstracts, Current Contents, Engineered Materials Abstracts, Engineering Index, Enviroline (The electronic equivalent of Environment Abstracts), Environment Abstracts, Environmental Science and Pollution Management, Fluidex, INSPEC, Mechanical & Transportation Engineering Abstracts, Mechanical Engineering Abstracts, METADEX (The electronic equivalent of Metals Abstracts and Alloys Index), Pollution Abstracts, Referativnyi Zhurnal, Science Citation Index, SciSearch (The electronic equivalent of Science Citation Index), Shock and Vibration Digest

Johannes C. Kloppers

Detlev G. Kröger[1]
e-mail: dgk@sun.ac.za

Department of Mechanical Engineering,
University of Stellenbosch,
Stellenbosch 7600, South Africa

Cooling Tower Performance Evaluation: Merkel, Poppe, and *e*-NTU Methods of Analysis

*The heat rejected and water evaporated in mechanical and natural draft cooling towers are critically evaluated by employing the Merkel, Poppe, and e–number-of-transfer-units (e-*NTU*) methods of analysis, respectively, at different operating and ambient conditions. The importance of using a particular method of analysis when evaluating the performance characteristics of a certain fill material and subsequently employing the same analytical approach to predict cooling tower performance is stressed. The effect of ambient humidity and temperature on the performance of cooling towers employing the Merkel, e-NTU, and Poppe methods of analysis are evaluated.* [DOI: 10.1115/1.1787504]

Introduction

The art of evaporative cooling is quite ancient, although it is only relatively recently that it has been studied scientifically [1]. Merkel [2] developed the theory for the thermal evaluation of cooling towers in 1925. This work was largely neglected until 1941 when the paper was translated into English. Since then, the model has been widely applied [3].

The Merkel theory relies on several critical assumptions to reduce the solution to a simple hand calculation. Because of these assumptions, however, the Merkel method does not accurately represent the physics of heat and mass transfer process in the cooling tower fill.

The critical simplifying assumptions of the Merkel theory are

- the Lewis factor, Le_f, relating heat and mass transfer is equal to 1;
- the air exiting the tower is saturated with water vapor and it is characterized only by its enthalpy;
- the reduction of water flow rate by evaporation is neglected in the energy balance.

Jaber and Webb [4] developed the equations necessary to apply the *e*-NTU method directly to counterflow or crossflow cooling towers. This approach is particularly useful in the latter case and simplifies the method of solution when compared to a more conventional numerical procedure. The *e*-NTU method is based the same simplifying assumptions as the Merkel method.

The Poppe model was developed by Poppe and Rögener [5] in the early 1970s. The method of Poppe does not make the simplifying assumptions made by Merkel. The critical differences between the Merkel and Poppe methods are investigated by Kloppers and Kröger [6]. The objective of this investigation is to include the *e*-NTU method in the investigation.

Fills or packing are employed in cooling towers to increase the contact area and contact time between the water that needs to be cooled and the cooling air. There are basically three different types of fill designs, i.e., film, splash, and trickle type fills. A thin film of water runs down the film fill surface while the splash fill breaks the water stream into smaller droplets. The trickle film is basically a combination of film and splash type fill. Figures 1 and 2 show an idealized model of the interface between the water and the air for all types of counterflow cooling tower fill materials. The results of this study, i.e., the differences between the Merkel, Poppe, and *e*-NTU approaches, are independent of the type of fill considered.

Merkel Theory

Equations (1) and (2) are obtained from mass and energy balances of the control volumes shown in Figs. 1 and 2 where air is in counterflow with a downwards flowing water stream. For the Merkel theory it is assumed that the change in water mass flow rate due to evaporation is negligible, i.e., $dm_w = 0$,

$$\frac{di_{ma}}{dz} = \frac{h_d a_{fi} A_{fr}}{m_a}(i_{masw} - i_{ma}), \tag{1}$$

$$\frac{dT_w}{dz} = \frac{m_a}{m_w}\frac{1}{c_{pw}}\frac{di_{ma}}{dz}. \tag{2}$$

Equations (1) and (2) describe, respectively, the change in the enthalpy of the air-water vapor mixture and the change in water temperature as the air travel distance changes. Equations (1) and (2) can be combined to yield upon integration the Merkel equation,

$$\mathrm{Me}_M = \frac{h_d a_{\mathrm{fi}} A_{\mathrm{fr}} L_{\mathrm{fi}}}{m_w} = \frac{h_d a_{\mathrm{fi}} L_{\mathrm{fi}}}{G_w} = \int_{T_{wo}}^{T_{wi}} \frac{c_{pw} dT_w}{(i_{masw} - i_{ma})}, \tag{3}$$

where Me_M is the transfer coefficient or Merkel number according to the Merkel approach, a_{fi} is the surface area of the fill per unit volume of fill, and h_d is the mass transfer coefficient. It is often difficult to evaluate the surface area per unit volume of fill due to the complex nature of the two-phase flow in fills. It is, however, not necessary to explicitly specify the surface area per unit volume or the mass transfer coefficient as these are contained in the Merkel number which can be obtained from the right-hand side of Eq. (3).

It is not possible to calculate the true state of the air leaving the fill according to Eq. (3). Merkel assumed that the air leaving the fill is saturated with water vapor. This assumption enables the air temperature leaving the fill to be calculated.

Poppe Theory

Without the simplifying assumptions of Merkel, the mass and energy balances from Figs. 1 and 2 yield after manipulation for unsaturated air

$$dw/dT_w = c_{pw}(w_{sw} - w)m_w/m_a/[i_{masw} - i_{ma} + (\mathrm{Le}_f - 1)\{i_{masw} - i_{ma} - (w_{sw} - w)i_v\} - (w_{sw} - w)c_{pw}T_w], \tag{4}$$

[1]Author to whom correspondence should be addressed.

Contributed by the Advanced Energy Systems Division of THE AMERICAN SOCIETY OF MECHANICAL ENGINEERS for publication in the ASME JOURNAL OF ENGINEERING FOR GAS TURBINES AND POWER. Manuscript received by the AES Division December 4, 2002; final revision received October 20, 2003. Associate Editor: G. Reistad.

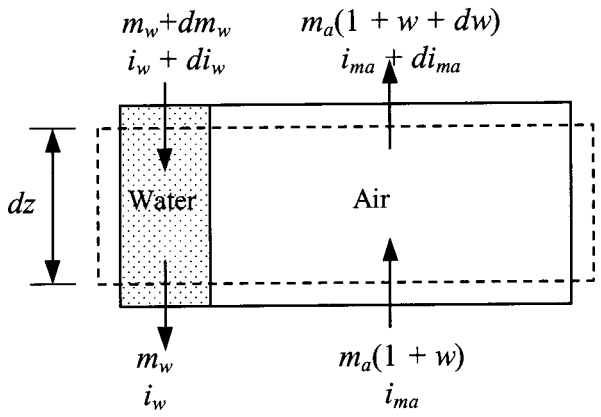

Fig. 1 Control volume of counterflow fill

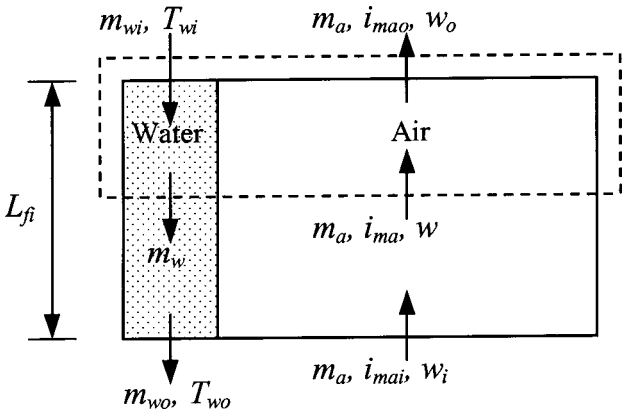

Fig. 3 Control volume of the fill

$$di_{ma}/dT_w = c_{pw}(m_w/m_a)[1+(w_{sw}-w)c_{pw}T_w/[i_{masw}-i_{ma} + (\mathrm{Le}_f-1)\{i_{masw}-i_{ma}-(w_{sw}-w)i_v\}-(w_{sw} - w)c_{pw}T_w]], \quad (5)$$

where the Lewis factor, which is an indication of the relative rates of heat and mass transfer in an evaporative process, is defined as $\mathrm{Le}_f = h/h_d c_{pa}$. Bosnjakovic [7] proposed the following relation to express the Lewis factor for air-water vapor systems:

$$\mathrm{Le}_f = 0.865^{2/3}\left(\frac{w_{sw}+0.622}{w+0.622}-1\right) \Big/ \ln\left(\frac{w_{sw}+0.622}{w+0.622}\right). \quad (6)$$

The transfer coefficient or Merkel number according to the Poppe approach is given by

$$d\mathrm{Me}_P/dT_w = c_{pw}/[i_{masw}-i_{ma}+(\mathrm{Le}_f-1)\{i_{masw}-i_{ma}-(w_{sw} - w)i_v\}-(w_{sw}-w)c_{pw}T_w]. \quad (7)$$

The varying mass flow rate ratio in Eqs. (4) and (5) can be determined by considering the control volume in the fill of Fig. 3. A mass balance of the control volume yields

$$\frac{m_w}{m_a} = \frac{m_{wi}}{m_a}\left(1-\frac{m_a}{m_{wi}}(w_o-w)\right). \quad (8)$$

Equations (4)–(7) are only valid if the air is unsaturated. If the air is supersaturated, the governing equations are

$$dw/dT_w = c_{pw}(w_{sw}-w_{sa})m_w/m_a/[i_{masw}-i_{ss}+(\mathrm{Le}_f-1) \times\{i_{masw}-i_{ss}-(w_{sw}-w_{sa})i_v+(w-w_{sa})c_{pw}T_w\}+(w - w_{sw})c_{pw}T_w] \quad (9)$$

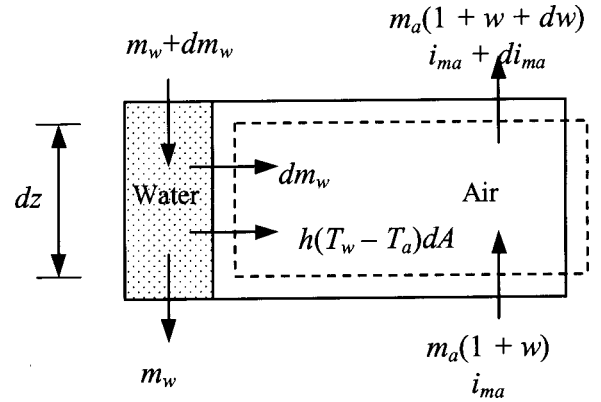

Fig. 2 Air-side control volume of fill

$$di_{ma}/dT_w = c_{pw}(m_w/m_a)[1+(w_{sw}-w_{sa})c_{pw}T_w/[i_{masw}-i_{ss} + (\mathrm{Le}_f-1)\{i_{masw}-i_{ss}-(w_{sw}-w_{sa})i_v+(w - w_{sa})c_{pw}T_w\}+(w-w_{sa})c_{pw}T_w]], \quad (10)$$

where the Lewis factor for supersaturated air is given by

$$\mathrm{Le}_f = 0.865^{2/3}\left(\frac{w_{sw}+0.622}{w_{sa}+0.622}-1\right) \Big/ \ln\left(\frac{w_{sw}+0.622}{w_{sa}+0.622}\right). \quad (11)$$

The Merkel number according to the Poppe approach is given by

$$d\mathrm{Me}_P/dT_w = c_{pw}/[i_{masw}-i_{ss}+(\mathrm{Le}_f-1)\{i_{masw}-i_{ss}-(w_{sw} - w_{sa})i_v+(w-w_{sa})c_{pw}T_w\}+(w-w_{sw})c_{pw}T_w]. \quad (12)$$

The equations of the Poppe method must be solved by an iterative procedure because the humidity ratio at the air outlet side of the fill, w_o in Eq. (8), is not known a priori. Refer to Poppe and Rögener [5], Bourillot [8], and Baard [9] for more detailed information on the derivation of these equations.

e-NTU Method

It can be shown according to Jaber and Webb [4] that

$$\frac{d(i_{masw}-i_{ma})}{(i_{masw}-i_{ma})} = h_d\left(\frac{di_{masw}/dT_w}{m_w c_{pw}}-\frac{1}{m_a}\right)dA. \quad (13)$$

Equation (13) corresponds to the heat exchanger *e*-NTU equation

$$\frac{d(T_h-T_c)}{(T_h-T_c)} = -U\left(\frac{1}{m_h c_{ph}}+\frac{1}{m_c c_{pc}}\right)dA. \quad (14)$$

Two possible cases of Eq. (13) can be considered where m_a is greater or less than $m_w c_{pw}/(di_{masw}/dT_w)$. The maximum of the dry air mass flow rate m_a and $m_w c_{pw}/(di_{masw}/dT_w)$ is called the maximum fluid capacity rate, denoted by $C_{\max}$ and the minimum by $C_{\min}$. The gradient of the saturated air enthalpy-temperature curve is

$$\frac{di_{masw}}{dT_w} = \frac{i_{maswi}-i_{maswo}}{T_{wi}-T_{wo}}. \quad (15)$$

The fluid capacity rate ratio is defined as

$$C = C_{\min}/C_{\max}. \quad (16)$$

The effectiveness is given by

$$e = \frac{Q}{Q_{\max}} = \frac{m_w c_{pw}(T_{wi}-T_{wo})}{C_{\min}(i_{maswi}-f-i_{mai})}, \quad (17)$$

where f is a correction factor, according to Berman [10], to improve the approximation of the i_{masw} versus T_w curve as a straight line. The correction factor f is given by

$$f=(i_{maswo}+i_{maswi}-2i_{maswm})/4, \tag{18}$$

where i_{maswm} denotes the enthalpy of saturated air at the mean water temperature. The number of transfer units for counterflow cooling towers is given by

$$\mathrm{NTU}=\frac{1}{1-C}\ln\frac{1-eC}{1-e}. \tag{19}$$

If the dry air mass flow rate m_a is greater than $m_w c_{pw}/(di_{masw}/dT_w)$ the Merkel number according to the e-NTU approach is given by

$$\mathrm{Me}_e=\frac{c_{pw}}{di_{masw}/dT_w}\mathrm{NTU}. \tag{20}$$

If m_a is less than $m_w c_{pw}/(di_{masw}/dT_w)$ the Merkel number according to the e-NTU approach is given by

$$\mathrm{Me}_e=m_a\mathrm{NTU}/m_w. \tag{21}$$

Comparison Between Merkel, e-NTU, and Poppe Approaches

Performance calculation examples of the natural draft wet-cooling tower in Kröger [11] and the mechanical draft tower in Baard [9] are taken as reference towers in these analyses. The performance of these towers are determined by the Merkel approach with detailed consideration of the transfer characteristics in the fill, rain, and spray zones as well as the various flow resistances that affect tower draft.

The differences between the Merkel, Poppe, and e-NTU approaches are investigated at various operating conditions for natural draft and mechanical draft cooling tower performance calculations. Ambient air temperatures of 280, 290, 300, and 310 K are considered. The humidity of the air is varied from completely dry to saturated conditions. The effect of inlet temperature and humidity on cooling tower performance can therefore be determined over a wide range of atmospheric conditions.

Two cases for the natural draft cooling tower, where the ambient temperatures are 280 and 300 K, respectively, are illustrated in Figs. 4(a)–(j). Figures 4(a)–(e) show selected solution variables for the case where the ambient temperature is 280 K. The case where the ambient temperature is 300 K is shown in Figs. 4(f)–(j). The selected solution variables are the heat-transfer rate (Q), water outlet temperature (T_{wo}), air outlet temperature (T_{ao}), air-water vapor mass flow rate (m_{av}), and the water evaporation rate ($m_{w(\mathrm{evap})}$).

Air Outlet Temperature. The outlet air temperature can be measured in fill performance tests. However, this temperature is not used in either the Merkel, e-NTU, or Poppe theories to calculate the Merkel number for a particular fill test. The approximate air outlet temperature can be predicted by the Merkel and e-NTU methods in fill performance tests, by assuming that the air is saturated. The outlet air temperature is calculated by the Poppe approach. These temperatures, according to the different approaches, can be used to test the accuracy of the models by comparing them to measured data.

Figure 5 shows the measured air outlet drybulb temperatures measured in the fill test facility at the University of Stellenbosch. Tests are conducted with fixed air and water mass flow rates with variable inlet water temperatures. Cyclone separators are used to separate the water droplets from the outlet air before measurement. There are water droplets in the outlet air due to condensation, supersaturation, and drift. The outlet air temperatures predicted by the Merkel, e-NTU, and Poppe approaches are also shown in Fig. 5 for a 2-m-thick counterflow trickle grid fill for each test. It can be seen that the Poppe approach predicts the air outlet temperature very accurately compared to the Merkel and e-NTU methods of analysis, as the Poppe method is the more rigorous approach.

The draft through natural draft cooling towers is a function of the density of the air above the fill. It is thus very important to predict the air temperature above the fill accurately. The Merkel and e-NTU methods are unable to predict the temperature of the outlet air without the assumption that the outlet air is saturated with water vapor. The Poppe method therefore predicts more accurately the draft through natural draft cooling towers.

Cooling tower air outlet temperatures generally increase when air inlet temperatures and humidity increase, as can be seen in Figs. 4(c) and (h). In very hot very dry conditions the air outlet temperature can be less than the air inlet temperature. This case is not shown in Fig. 4. Thus both the air and the water are cooled. Is this possible?

The potential for enthalpy transfer between the hot water and the cooling air provides a qualitative indication of the direction of nett heat flow in the cooling tower fill. Air at condition x (refer to Figs. 6 and 7) is in contact with water at temperature T_w. Figures 6 and 7 represent two different cases that can occur inside a cooling tower fill. Consider the case in Fig. 6 where $w_{sw}>w$, thus the latent heat transfer is from the water to the air and $T_w>T_a$, where the sensible heat transfer is from the water to the air. The total enthalpy transfer is from the water to the air since $i_{masw}>i_{ma}$ and since both the latent and sensible heat transfer are from the water to the air. The air is heated and the water cooled.

The fact that both the air and the water are cooled can be described as follows: Consider the case in Fig. 7, where $w_{sw}>w$, thus the latent heat transfer is from the water to the air and $T_a>T_w$, where the sensible heat transfer is from the air to the water. The nett enthalpy transfer is from the water to the air since $i_{masw}>i_{ma}$.

Notwithstanding the fact that the air outlet temperature is colder than the ambient temperature, there is still a draft through the tower. Draft through the natural draft tower is still possible, because the molar mass of vapor is less than that of air at the same temperature. Thus a potential for draft still exists because the density of the air-vapor mixture inside the tower is less than that of the hotter less humid air on the outside of the tower.

Water Inlet and Outlet Temperatures. The water outlet temperatures predicted by the Merkel, e-NTU, and Poppe approaches are practically identical where the draft through the tower is approximately the same as can be seen in Figs. 4(b) and (g).

The Merkel numbers, determined by the Poppe and e-NTU approaches for the expanded metal fill employed in this natural draft cooling tower analysis, are respectively approximately 9% higher and 1% lower than the Merkel number determined by the Merkel approach. Notwithstanding these differences, the subsequent application of the Merkel method employing the smaller value for the Merkel number obtained during fill tests, will predict nearly the same cooling tower water outlet temperature as obtained by the more rigorous Poppe method. A very small difference in water outlet temperature is due to the fact that the Merkel and Poppe methods predict different air outlet conditions causing the draft to be different in the two cases.

It is expected that the results of the Merkel and e-NTU approaches must be identical since the same simplifying assumptions are used in these methods. However, it can be seen from Fig. 4 that there are differences in the predicted performance by the Merkel and e-NTU approaches. The reason why the predicted performance is not the same for both approaches is because the cooling tower fill was originally tested at different ambient and operating conditions than where it was subsequently applied in this investigation.

As mentioned above, there is approximately a 1% difference in the Merkel numbers predicted by the Merkel and e-NTU ap

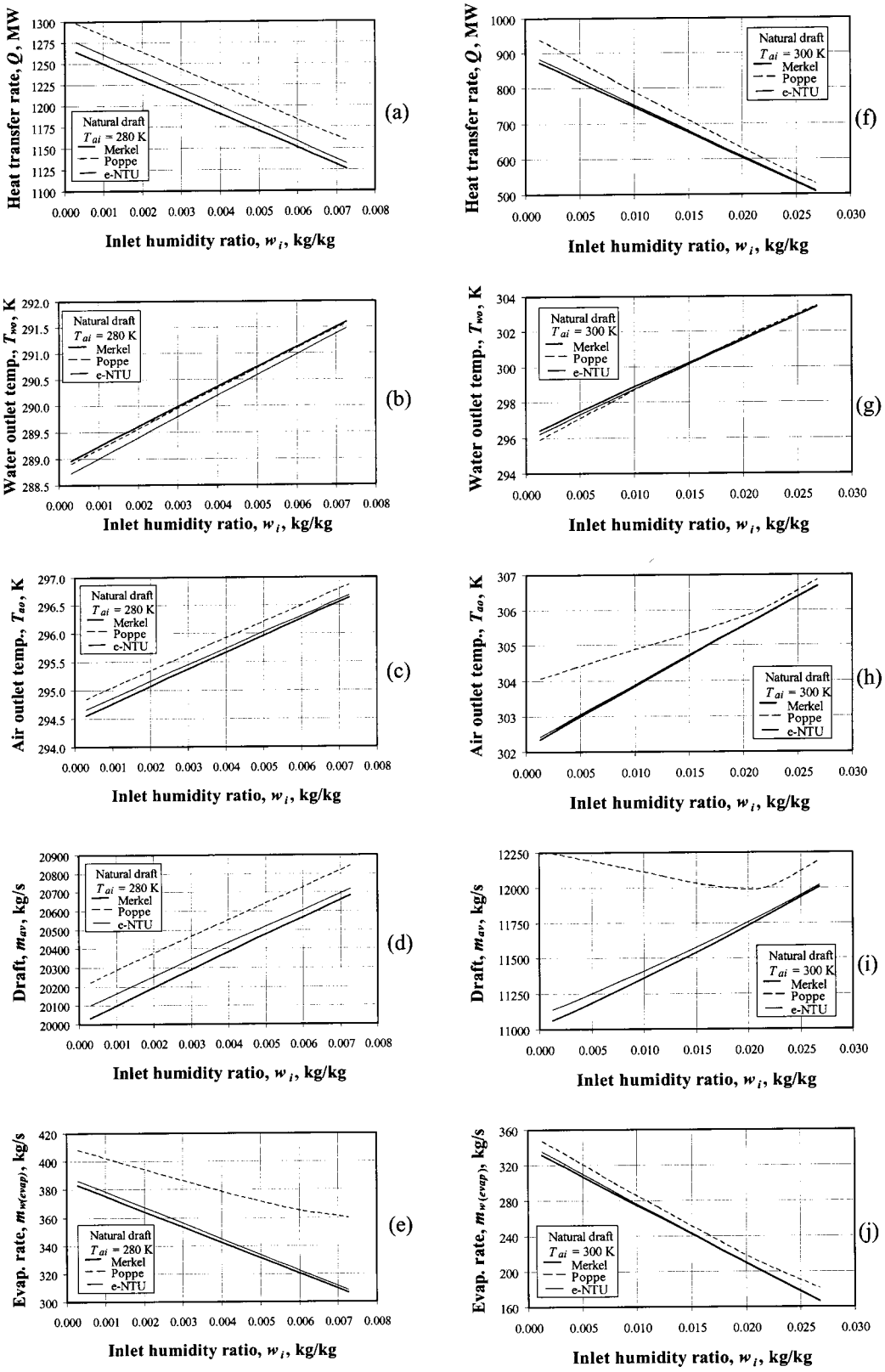

Fig. 4 Heat rejected, Q; water outlet temperature, T_{wo}; air outlet temperature T_{ao}; mean air-vapor mass flow rate, m_{av}; and mass flow rate of evaporated water, $m_{w(evap)}$ for T_{ai}=280 and 300 K

proaches during the fill test phase for the fill employed in this investigation. However, at other inlet water temperatures this difference can reach 4%, therefore the differences in Fig. 4.

Figure 8 shows the Merkel numbers according to the Merkel, *e*-NTU, and Poppe approaches as a function of the water inlet temperature that are obtained during a fill test where only the water temperature is not constant. The relative differences between the Merkel numbers according to the Merkel and Poppe

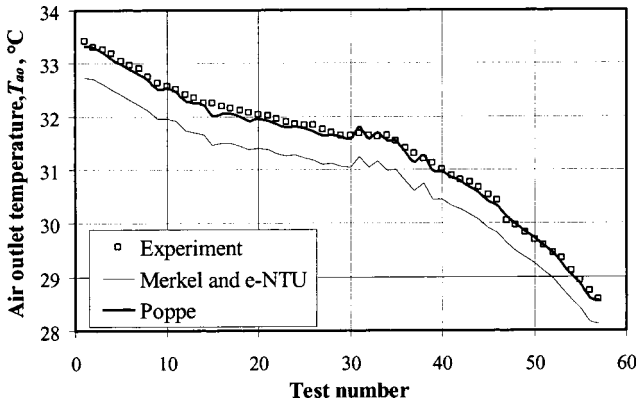

Fig. 5 Measured outlet air temperature versus Merkel, *e*-NTU and Poppe predictions

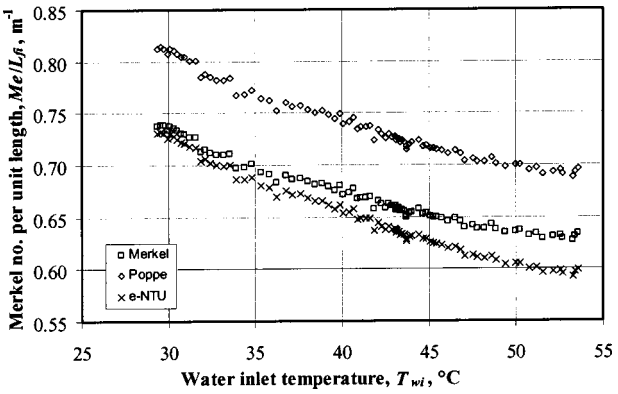

Fig. 8 Merkel number versus water inlet temperature

approaches are not as strongly influenced by the water temperatures as those with the Merkel and *e*-NTU approaches as can be seen in Fig. 8.

It is thus recommended that the fill performance characteristics are determined at conditions close to cooling tower operating and ambient conditions, or the empirical relation expressing the Merkel number must also be expressed as a function of water inlet temperature.

Heat Rejected. The Poppe approach predicts higher heat rejection rates (Q) than the Merkel approach as can be seen in Figs. 4(*a*) and (*f*). This is because the Merkel approach ignores the loss in water mass flow rate in the energy equation. In cooling tower analyses, employing the Merkel or *e*-NTU approach, the heat-transfer rate is given by

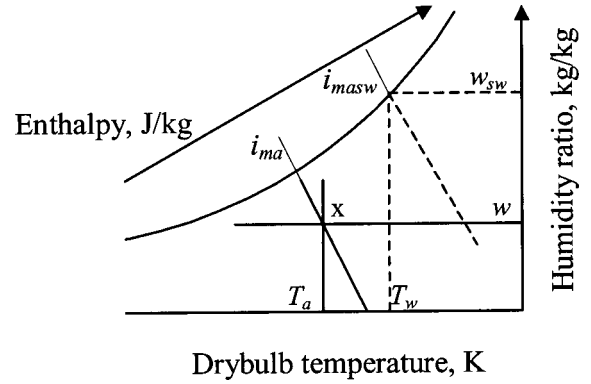

Fig. 6 Psychrometric chart

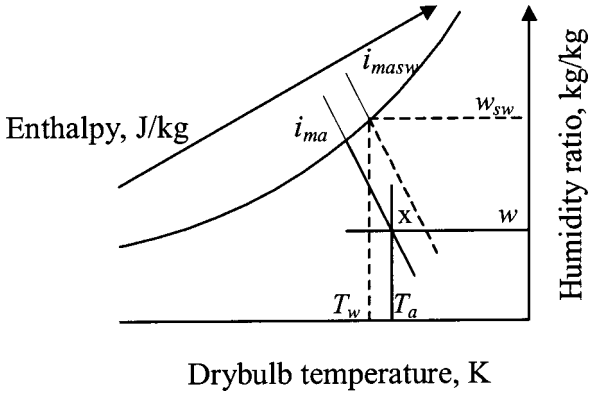

Fig. 7 Psychrometric chart

$$Q = m_w c_{pwm}(T_{wi} - T_{wo}), \tag{22}$$

where the effect of the change in water mass flow rate is not included in the energy balance. If it is assumed that the air is saturated at the outlet of the fill then the mass flow rate of the evaporated water can be determined, i.e.,

$$m_{w(\text{evap})} = m_a(w_o - w_i). \tag{23}$$

A new improved equation for the heat rejection rate, according to the Merkel or *e*-NTU approach, is proposed where the water loss, due to evaporation, is included in the energy equation, i.e.,

$$Q = m_{wi} c_{pwm} T_{wi} - (m_{wi} - m_{w(\text{evap})}) c_{pwm} T_{wo}. \tag{24}$$

When this equation for the heat-transfer rate is included in the cooling tower analyses of the Merkel and *e*-NTU approaches, the predictions for the rejected heat and water outlet temperature are in general within close tolerance of the results of the Poppe model.

Air Outlet Humidity and Evaporation. It was found by Bourillot [8,12] that predictions from the Poppe formulation resulted in values of evaporated water flow rate that were in good agreement with full scale cooling tower test results. Grange [13] shows in a comparative study that the Merkel method tends to underestimate the amount of water that evaporates when compared to the Poppe approach but that the discrepancy decreases with increasing ambient temperatures.

The results of Grange [13] are verified in this investigation. It can be seen from Figs. 4(*e*) and (*j*) that the discrepancy between the Merkel and Poppe approaches for the water evaporation rate is smaller where the temperature is greater. The predicted water rate that evaporates is underestimated by the Merkel method, compared to the Poppe approach for the natural draft tower considered. However, it is found for mechanical draft towers operating during very hot dry conditions that the Merkel approach predicts higher evaporation rates than the Poppe approach. This is because the Poppe approach predicts unsaturated outlet air under these extreme conditions.

The water content of the outlet air is an important consideration for the design of hybrid cooling towers. The Poppe method is thus the preferred method of analysis during the design of hybrid cooling towers [14].

Tower Draft. If applied to mechanical draft towers, the Merkel approach generally produces water outlet temperatures that are essentially the same as those produced by the Poppe approach. For natural draft towers, however, the discrepancy between the Merkel and Poppe approaches increases as the air gets warmer and drier. This is because the air outlet temperature (T_{ao}) and tower draft or air-water vapor mass flow rate (m_{av}) are strongly coupled for natural draft towers, which is not the case with mechanical draft towers. Figures 4(*c*) and (*d*) show, respectively, the

air outlet temperature and the mean air-water vapor mass flow rate (m_{av}) where the ambient temperature is 280 K. When compared to the case where the ambient temperature is 300 K (Figs. 4(*h*) and (*i*)) it can be seen that the discrepancy is large between the Merkel and Poppe approaches for the draft and air outlet temperatures. Because of the higher draft of the Poppe method at higher air temperatures with lower humidity, more cooling is taking place. This can be seen in Fig. 4(*g*) where the water temperature according to the Poppe approach is less than that predicted by the Merkel approach.

Lewis Factor Influence

Merkel [2] assumed that the Lewis factor is equal to 1. Poppe and Rögener [5] used Eq. (6) that was proposed by Bosnjakovic [7] to express the Lewis factor in the Poppe cooling tower theory. The derivation of this equation can be seen in Bourillot [8] and Grange [13]. Hässler [15] cited that other researchers showed that the assumption of Merkel is not correct and that most of the researchers find Lewis factors in the range from 0.6 to 1.3. One researcher even found a Lewis factor as high as 4. An analysis of both splash and film packings by Feltzin and Benton [16], indicates that for counterflow towers, a Lewis factor of 1.25 is more appropriate. According to Feltzin and Benton [16], the Lewis number does not appear to be dependent on whether the packing is splash type or film type, but only on the configuration (i.e., counterflow or crossflow). Sutherland [17] used a Lewis factor of 0.9 in his tower performance analysis. Osterle [3] developed a wet-cooling tower model that corrected the Merkel [2] assumption so that the mass of water lost by evaporation is accounted for. However, he still assumes that the Lewis factor is equal to unity. Hässler [15] stated that the discrepancy in published results for the Lewis factor is because the Lewis factor is a function of the humidity of the air in the boundary layer at the air-water interface.

The cooling tower analysis in this study was repeated for the different atmospheric temperatures with dry to saturation conditions. Different Lewis factors were specified. The minimum Lewis factor specified was 0.5 and the maximum 1.5. Bosnjakovic's [7] equation was also employed in the analysis. The value of his equation is approximately 0.92. It was found that the higher the Lewis factor, the more heat is rejected from the tower, with a corresponding increase in outlet air temperature and a decrease in the outlet water temperature. Less water is evaporated with increasing Lewis factors. However, as the inlet air temperature increases, the discrepancy in the results with the different Lewis factors decreases. The Lewis factor is thus only of importance when the ambient temperature is less than approximately 26°C.

Again it is stressed that the same specification of the Lewis factor must be used when evaluating the performance characteristics of a certain fill material and subsequently employing the same Lewis factor specification to predict cooling tower performance. At higher temperatures (>26°C) it does not matter as much if the Lewis factor specification is applied inconsistently.

If working consistently, as mentioned above, the water temperature and heat rejected are within close tolerance for different Lewis factors. However, the evaporated water and air outlet temperature do not follow the same trend. More water is evaporated for lower Lewis factors. This is because the Lewis factor is an indication of the relative rates of heat and mass transfer in an evaporative process.

Conclusion

If only the water outlet temperature is of importance to the designer, the less accurate Merkel and *e*-NTU approaches can be used, as all the approaches predict practically identical water outlet temperatures for mechanical and natural draft towers. Care must be taken with natural draft towers where the Poppe approach can predict lower water outlet temperatures under warm dry ambient conditions. The Merkel and *e*-NTU approaches give heat-transfer rates that are lower than that predicted the Poppe approach. The heat rejected by the cooling tower while employing the Merkel approach can usually be determined more accurately by employing the Eq. (24) instead of Eq. (22).

It is recommended that the fill performance characteristics be determined close to tower operational conditions. The particular method of analysis when evaluating the performance characteristics of a certain fill material must subsequently be employed in the analytical approach to predict cooling tower performance. The same Lewis factor must also be used in the Poppe approach.

Acknowledgment

The authors gratefully acknowledge Sasol Ltd. for their financial support.

Nomenclature

A = Area, m^2
a = Surface area per unit volume, m^{-1}
C = Fluid capacity rate, kg/s, or C_{min}/C_{max}
c_p = Specific heat at constant pressure, J/kg K
e = Effectiveness
f = Enthalpy correction factor, J/kg
G = Mass velocity, $kg/m^2 s$
h = Heat-transfer coefficient, $W/m^2 K$
h_d = Mass transfer coefficient, $kg/m^2 s$
i = Enthalpy, J/kg
i_{masw} = Enthalpy of saturated air at the local bulk water temperature, J/kg
L = Length, m
Le_f = Dimensionless Lewis factor
m = Mass flow rate, kg/s
Me = Merkel number
NTU = Number of transfer units
Q = Heat transfer rate, W
T = Temperature, °C or K
U = Overall heat-transfer coefficient, $W/m^2 K$
w = Humidity ratio, kg water vapor/kg dry air
w_{sa} = Humidity ratio of saturated air at T_a, kg/kg
w_{sw} = Saturation humidity ratio of air evaluated at the local bulk water temperature, kg/kg
z = Elevation, m

Subscripts

a = Air
c = Cold
e = *e*-NTU approach
fi = Fill
fr = Frontal
h = Hot
i = Inlet
M = Merkel approach
m = Mean
max = Maximum
min = Minimum
o = Outlet
P = Poppe approach
s = Saturation
ss = Supersaturated
v = Vapor
w = Water

References

[1] McKelvey, K. K., and Brooke, M., 1959, *The Industrial Cooling Tower*, Elsevier, Amsterdam.
[2] Merkel, F., "Verdunstungskühlung," 1925, *VDI-Zeitchrift*, Vol. 70, pp. 123–128.
[3] Osterle, F., 1991, "On the Analysis of Counter-Flow Cooling Towers," Int. J. Heat Mass Transfer, **34**(4/5), pp. 1313–1316.
[4] Jaber, H., and Webb, R. L., 1989, "Design of Cooling Towers by the Effectiveness-NTU Method," ASME J. Heat Transfer, **111**, pp. 837–843.

[5] Poppe, M., and Rögener, H., 1991, ''Berechnung von Rückkühlwerken,'' *VDI-Wärmeatlas*, pp. Mi 1–Mi 15.
[6] Kloppers, J. C., and Kröger, D. G., 2001, ''A Critical Cooling Tower Performance Evaluation,'' 12th IAHR Symposium in Cooling Towers and Heat Exchangers, UTS, Sydney, Australia.
[7] Bosnjacovic, F., 1965, ''Technische Thermodinmik,'' Theodor Steinkopf, Dresden.
[8] Bourillot, C., 1983, ''TEFERI, Numerical Model for Calculating the Performance of an Evaporative Cooling Tower,'' EPRI Report CS-3212-SR, Electric Power Research Institute, Palo Alto.
[9] Baard, T. W., 1998, ''Performance Characteristics of Expanded Metal Cooling Tower Fill,'' M. Eng. thesis, University of Stellenbosch, Stellenbosch, South Africa.
[10] Berman, L. D., 1961, *Evaporative Cooling of Circulating Water*, 2nd Edition, Chap. 2, pp. 94–99, edited by H. Sawistowski, translated from Russian by R. Hardbottle, Pergamon, New York.
[11] Kröger, D. G., 1998, *Air-Cooled Heat Exchangers and Cooling Towers Thermal-Flow Performance, Evaluation and Design*, PennWell Corp., Tulsa, OK.
[12] Bourillot, C., 1983, ''On the Hypothesis of Calculating the Water Flowrate Evaporated in a Wet Cooling Tower,'' EPRI Report CS-3144-SR, Electric Power Research Institute, Palo Alto.
[13] Grange, J. L., 1994, ''Calculating the Evaporated Water Flow in a Wet Cooling Tower,'' paper presented at the 9th IAHR Cooling Tower and Spraying Pond Symposium, von Karman Institute, Brussels, Belgium.
[14] Roth, M., 2001, ''Fundamentals of Heat and Mass Transfer in Wet Cooling Towers. All Well Known or are Further Developments Necessary?'' 12th IAHR Symposium in Cooling Towers and Heat Exchangers, UTS, Sydney, Australia.
[15] Hässler, R., 1999, ''Einfluss von Kondensation in der Grenzschicht auf die Wärme-und Stoffübertragung an einem Rieselfilm,'' Fortschritt-Berichte VDI, Reihe 3, Nr. 615.
[16] Feltzin, A. E., and Benton, D., 1991, ''A More Exact Representation of Cooling Tower Theory,'' CTI J., **12**(2), pp. 8–26.
[17] Sutherland, J. W., 1983, ''Analysis of Mechanical-Draught Counterflow Air/Water Cooling Towers,'' ASME J. Heat Transfer, **105**, pp. 576–583.

A Flight Simulation Vision for Aeropropulsion Altitude Ground Test Facilities

Milt Davis

Peter Montgomery

Aerospace Testing Alliance, ATA,
Arnold Engineering Development Center,
Arnold Air Force Base, TN 37389-9013

Testing of a gas turbine engine for aircraft propulsion applications may be conducted in the actual aircraft or in a ground-test environment. Ground test facilities simulate flight conditions by providing airflow at pressures and temperatures experienced during flight. Flight-testing of the full aircraft system provides the best means of obtaining the exact environment that the propulsion system must operate in but must deal with limitations in the amount and type of instrumentation that can be put on-board the aircraft. Due to this limitation, engine performance may not be fully characterized. On the other hand, ground-test simulation provides the ability to enhance the instrumentation set such that engine performance can be fully quantified. However, the current ground-test methodology only simulates the flight environment thus placing limitations on obtaining system performance in the real environment. Generally, a combination of ground and flight tests is necessary to quantify the propulsion system performance over the entire envelop of aircraft operation. To alleviate some of the dependence on flight-testing to obtain engine performance during maneuvers or transients that are not currently done during ground testing, a planned enhancement to ground-test facilities was investigated and reported in this paper that will allow certain categories of flight maneuvers to be conducted. Ground-test facility performance is simulated via a numerical model that duplicates the current facility capabilities and with proper modifications represents planned improvements that allow certain aircraft maneuvers. The vision presented in this paper includes using an aircraft simulator that uses pilot inputs to maneuver the aircraft engine. The aircraft simulator then drives the facility to provide the correct engine environmental conditions represented by the flight maneuver. [DOI: 10.1115/1.1806452]

1 Introduction

The Arnold Engineering Development Center (AEDC) has within its assets, ground facility infrastructure for the testing of gas turbine engines at sea level and altitude conditions [1]. These facilities have been built-up over the last 50 years based upon a ground-testing philosophy and methodology that simulates engine conditions that would be present during steady state flight conditions. These methodologies have served the gas turbine propulsion community well as it has developed gas turbine engines for military and civilian transport aircraft. The major advantage of ground-testing is that systematic investigations can be conducted and repeated with certainty using current established methodologies. However, there are limitations that prohibit testing of certain types of transient phenomena and thus the engine's performance during flight maneuvers. These types of maneuvers have been relegated to flight-testing. Flying the aircraft with its propulsion system puts the gas turbine engine in the environment it is to operate within. However, because of limitations with instrumentation, measurements of engine performance are limited. Flight-testing can only provide the answer when the investigator knows exactly what to look for and how to obtain the information with the correct instrumentation. In addition to the performance measurement limitation, flight-testing can be expensive as compared to ground-testing and has a higher risk of loss of the aircraft as well as the pilot if something should go wrong. Thus, it has always been the wise course-of-action to conduct investigations and qualification of the propulsion system in ground-test facilities prior to any flight-testing and ultimate implementation within a fleet of aircraft.

To understand the limitations within the ground test methodology, a brief review of the current ground test practice is in order. As an aircraft flies through the atmosphere, whether it is subsonic or supersonic, the velocity and quality of the airflow must be presented to the compression system at conditions that will allow it to do its job (i.e., raise the pressure of the air to a higher level). Today's compression systems cannot accept supersonic flow at the engine face. In the case of high subsonic or supersonic flight, the engine inlet velocity must be slowed down to a point where the Mach number is on-the-order-of 0.5. In the case of low subsonic flow, the compression system will pull (suck) the airflow it requires. In both instances, the flight velocity and the atmospheric conditions (pressure and temperature) define the engine airflow conditions, which can be quantified by the specification of engine airflow, total pressure and total temperature (W, P_T, T_T). By providing airflow to an engine at the pressure and temperature conditions that represent the flight condition, engine performance can be simulated as if the engine were actually flying at those conditions. To obtain engine thrust, the effect of the difference in engine nozzle exhaust pressure and atmospheric pressure can be accounted for by testing the engine in an environment such that the nozzle exhausts to a pressure associated with the altitude condition of flight. When both of these conditions are met, a ground simulation of engine flight is obtained. This concept is illustrated in Fig. 1.

The air-side plant supplies the engine with the required airflow at the total pressure (P_T) and temperature (T_T) desired to simulate the flight condition (altitude and Mach number). The engine is situated in an isolated test cell that has a bellmouth attached to the engine inlet that is used to capture the airflow supplied by the plant as illustrated in Fig. 2. The cell pressure is maintained by the

Contributed by the International Gas Turbine Institute (IGTI) of THE AMERICAN SOCIETY OF MECHANICAL ENGINEERS for publication in the ASME JOURNAL OF ENGINEERING FOR GAS TURBINES AND POWER. Paper presented at the International Gas Turbine and Aeroengine Congress and Exhibition, Amsterdam, The Netherlands, June 3–6, 2002; Paper No. 2002-GT-30003. Manuscript received by IGTI, December 2001, final revision, March 2002. Associate Editor: E. Benvenuti.

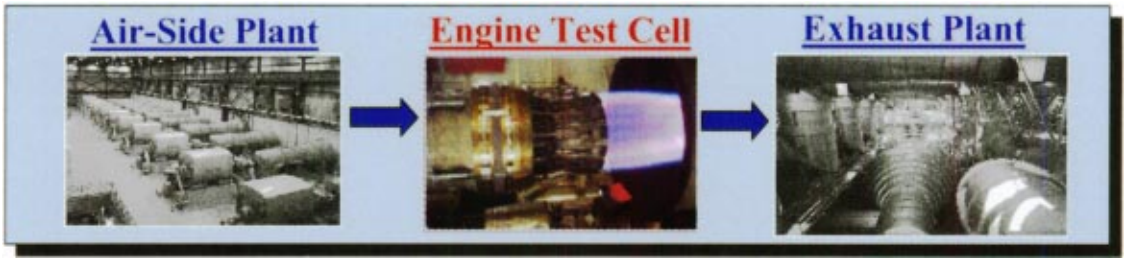

Fig. 1 Typical ground test facility/engine configuration

exhaust plant that sets the altitude pressure and exhausts the combustion products ultimately to atmosphere after they have been properly cleaned and cooled. These facilities were designed to operate the engine in a steady manner. The airside plant, as originally designed, did not have the capability to change the engine inlet temperature in a rapid manner. Some transient capability has been obtained with the original cell design (circa 1950) by small modifications such as removing airflow-measuring venturis and using atmospheric inbleed. However, these transient capabilities were very limited and did not produce true conditions as needed to simulate flight [2].

In a internal AEDC study, engine test cell requirements for the next 25 years have been established in order to support anticipated propulsion needs. To meet these future requirements, facility design modifications have been proposed and are currently being implemented as part of the Propulsion Consolidation and Streamlining (PCS) Program. A part of the study also addressed the need of changing conditions required for future transient testing. These requirements are driven by the anticipated mission profiles which can be categorized into three main areas.

1. *Zoom climbs (altitude climbs at constant Mach number)*;
2. *Mach dashes (accelerations and decelerations at constant altitude)*;
3. *Complex profiles (variations in both altitude and Mach number, such as wind-up-turns, spins, etc.)*.

The required maximum rates of change of conditions for a typical test facility are:

a. 1.75 psia/s for inlet pressure;
b. −0.4 psia/s for cell pressure;
c. +15°F/s or −10°F/s for inlet temperature, depending upon the maneuver.

Airflow during these maneuvers will scale with the particular engine size being tested. In addition, flow varies with throttle setting and flight condition. The range considered in the study was 140–500 lbm/s at sea level conditions.

Before the PCS program began, many of these mission profile rates were unattainable. As part of this program, new designs and concepts are being investigated via facility numerical modeling before implementation. Upon completion of this program it is expected that the facility will be able to achieve these desired transient rates. Better simulation of gas turbine engine operation will then be possible in a ground test facility. Reference [2] discusses the changes implemented by the PCS program so far as well as those proposed for the future.

2 The Plant Flight Simulation Vision

During the last several years, AEDC has been in the process of modernizing and improving its plant facilities [3]. Many of these modifications have been investigated and made possible using a numerical plant model. The goal of the PCS program has been to improve the efficiency of the test facilities while increasing test capabilities. An additional capability that could be provided is the ability to ''fly'' the engine through flight maneuvers while in a ground-test facility. To do so requires simulation of an aircraft system to provide aerodynamic input to the propulsion system. This effort will support an ultimate capability for ''flight-testing'' an engine in an altitude test cell. Engine data along with aircraft maneuvers would be used to determine settings for the plant conditions, inlet distortion, and engine services to simulate transient flight conditions during ground-testing.

Modeling and simulation capabilities will be acquired and/or developed for simulation of aircraft maneuvers and the environment presented to the propulsion device. The ultimate vision is to have a simulation of the aircraft providing input into the settings for the facility. In this way, the engine may be effectively ''flight-tested'' while in a ground test facility. This vision will be presented in two phases. A pictorial of this vision in its simplest form, *Non-Distorted Inlet Flow*, is presented in Fig. 3.

For nondistorted inlet airflow, an aircraft simulator is used to provide the plant set conditions for either steady or transient maneuvers. It is envisioned that a cockpit simulator is positioned in the control room for an operator to effectively provide inputs as if he were the pilot. The plant provides the conditions based on the aircraft simulator for the inlet pressure, temperature, airflow rate, and altitude pressure. The actual engine is then ''flown'' at the conditions of the aircraft. The engine performance is fed back into the aircraft simulator to provide propulsion performance to the aircraft. Maneuvers such as zoom climbs and Mach dashes can be effectively simulated in this sort of test configuration. More complex flight profiles such as wind-up turns and gas ingestion require

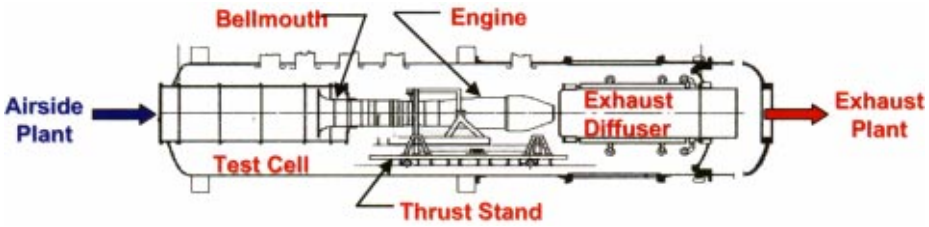

Fig. 2 Typical test cell configuration

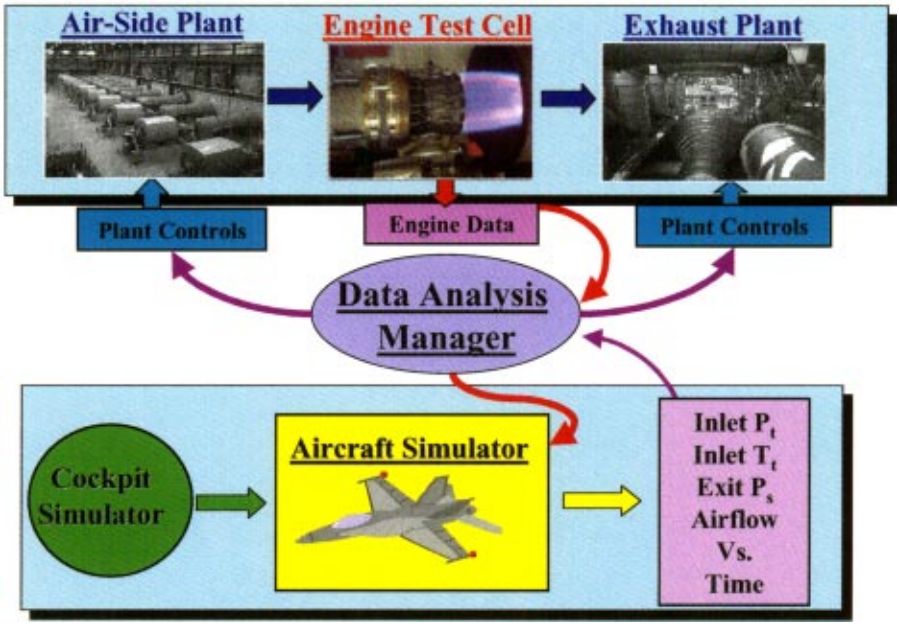

Fig. 3 Nondistorted inlet flow plant flight simulation vision

simulation of complex inlet flow distortions. The vision must be modified for the inclusion of inlet flow distortion and will be discussed later in the paper.

3 Technical Approach: Nondistorted Inlet Flow

As ambitious as this vision appears, there is a very logical and inexpensive way to accomplish feasibility studies to see what is possible with the current and future modifications to AEDC's ground test facilities. As a major part of the facility upgrade project, numerical models of the existing AEDC facilities are being developed. These models are being developed in a modular manner, which allows for proposed modifications to be easily incorporated into the simulation. Thus, where today's facilities may not support the Plant Flight Simulation Vision, modifications may be postulated and verified using the numerical simulation without the cost of implementing the idea via hardware. The Nondistorted Inlet Airflow portion of the vision can thus be implemented via the numerical simulation as illustrated in Fig. 4. To implement this simulation, it is necessary to characterize the major subsimulations: the Facility Simulation, the Aircraft Simulator, the Cockpit Simulator, the Engine Model, and the Data Analysis Manager. The subsimulations described in the next several paragraphs are typical simulations but may not necessarily be the ones used in any implementation of the vision.

3.1 The Facility Simulation. At the heart of the described system is the real-time mathematical model and simulation developed through the use of the MathWorks, Inc. Matlab/Simulink® software. Under this software, system models may be created

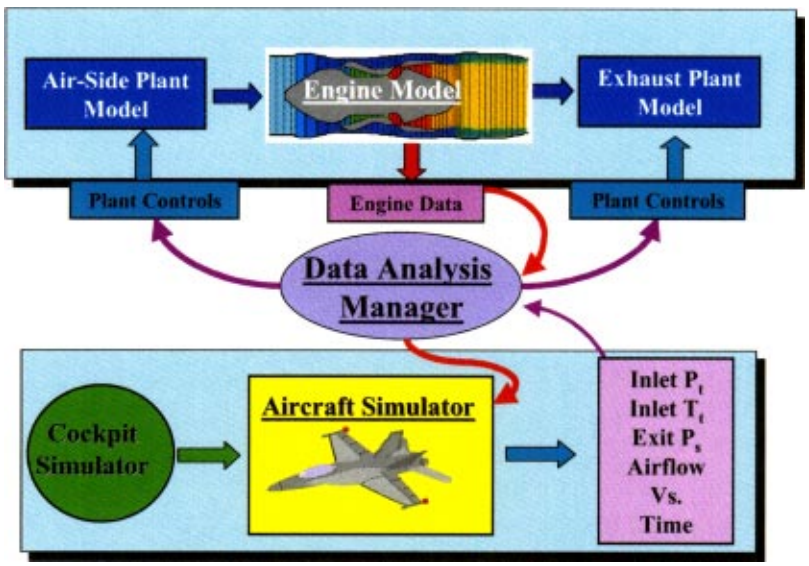

Fig. 4 Numerical simulation of the nondistorted inlet airflow plant simulation vision

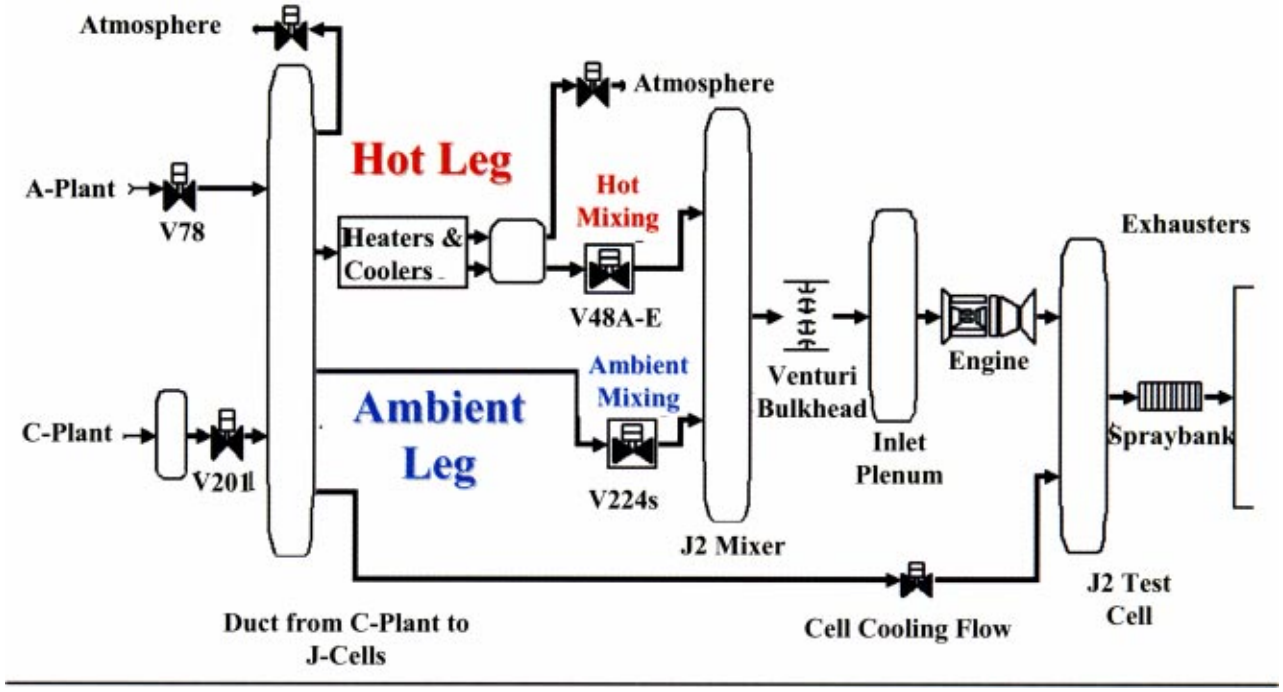

Fig. 5 Diagram for the J-turbine engine test facility as it currently exists

through the use of block diagrams. Once the model is operating in the desired manner, optimized C code may be generated directly from these diagrams using the Real-Time Workshop® option of the Matlab/Simulink® software package. The facility interfaces are modeled at the graphical user interface (GUI) level using a library of standard objects. Using the GUI, development of a real-time model becomes a one-step process that includes: code generation; compilation and dynamic download. This allows the model to be executed as a real-time task.

Figure 5 shows the top level of the current facility configuration and its simulation in the Matlab/Simulink® software environment [3]. Each rectangular box, elliptical duct or control volume, and valve represents a masked subsystem of varying level of complexity. From this advantage point, however, the general layout of the system is clearly seen. Moving from left to right, the A-plant and/or C-plant passes air through its ducting and then through valves into the J1 or J2 test facilities. Upon leaving the test facilities, the exhaust gases pass through the exhaust ducting, valves, and finally into the exhausters.

A proposed modification is presented in Fig. 6 that includes a cooling leg in order to provide rapid changes in inlet temperature. The temperature changes represent extremes that the current configuration may only be able to achieve by being on condition for a long period of time. In the future upgrade to the facility, air passing through turbo expanders for additional cooling can be mixed

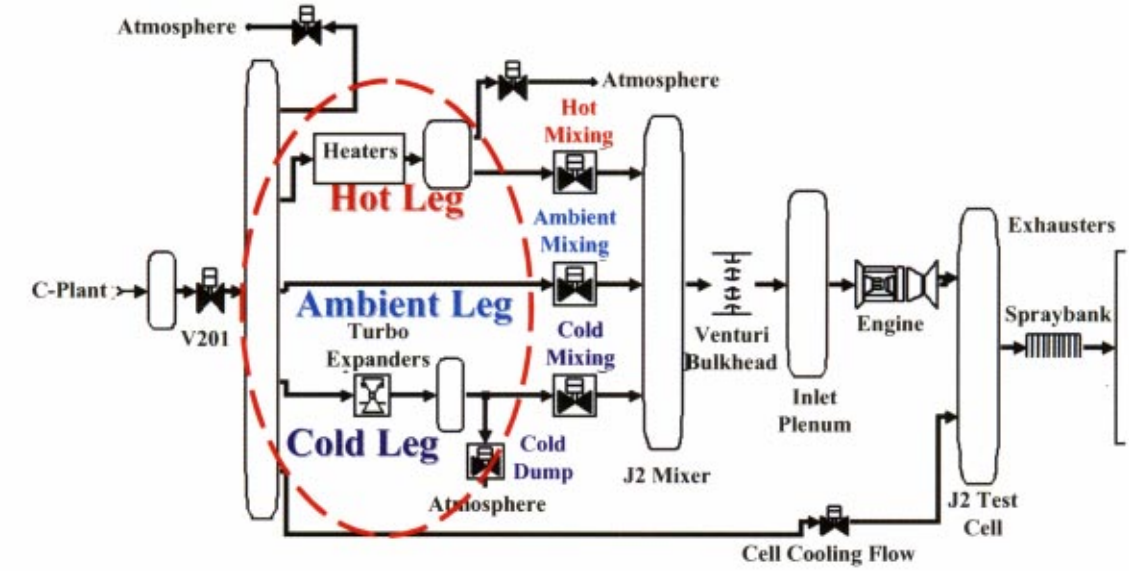

Fig. 6 Proposed future modification to the J-cells facility to allow additional cooling

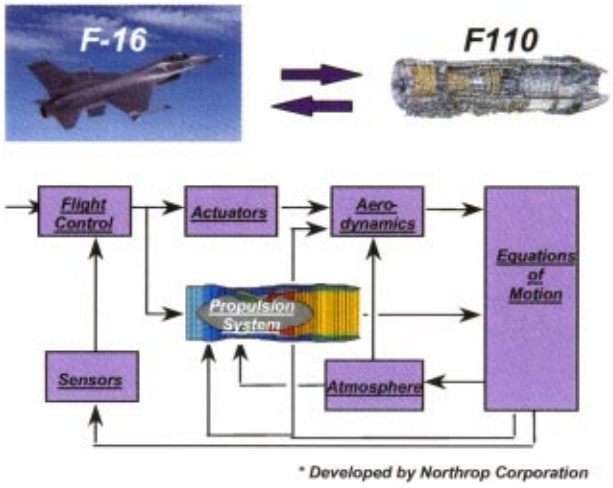

Fig. 7 The aircraft simulator, GENESIS

with ambient and hot air for greater temperature range capability. The major modifications are circled in Fig. 6 for easy identification.

3.2 The Aircraft Simulator. An aircraft simulator known as GENESIS [4,5] has been identified and is in use at AEDC. GENESIS is a simulation tool that can be used for the analysis of any time varying system. While GENESIS evolved over many years of aircraft applications, its use has become increasingly diversified. GENESIS comes with a large library of utility functions, which represent the common elements comprising any dynamic system. All dynamic utilities are self-initializing and possess the necessary logic to handle linear model generation. The GENESIS simulation provides the user with the capability to produce time responses, to generate linear models, and to debug the model of a nonlinear dynamic system. GENESIS is modular and a typical example of an aircraft simulator is illustrated in Fig. 7. GENESIS has been configured for the F-16 aircraft with an F110 turbofan engine ATEST simulation. It is proposed to use this aircraft simulation and the F110 engine as a demonstration of the concept.

3.3 The Cockpit Simulator. The cockpit simulator can be obtained from commercial aircraft simulator companies. One such example is AIRFOX [6]. AIRFOX has developed a product known as Flightlab (illustrated in Fig. 8), which is a high performance, reconfigurable desktop flight simulator that optimally fulfills the client's individual requirements, providing an expandable cost-effective solution. Based on Matlab/Simulink® software tools, aircraft models can be created by block diagrams. An aircraft block library provides a selection of elements (e.g., engines,

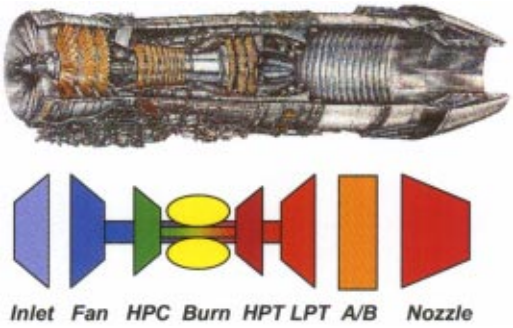

Fig. 9 Component-level engine model representation

gear, wind, motivators, etc.) as well as ready-for-use aircraft models. Real-time simulation is implemented including:

1. Generic cockpit instrumentation;
2. Visual system: photo realistic out-of-window view;
3. Primary controls: control stick, pedals, throttle levers;
4. Control panel: software configurable push buttons with LCD-display on button for secondary and user-defined controls.

AIRFOX® Flightlab provides real-time flight simulation with a generic aircraft cockpit and allows mathematical aircraft models to be modified using Matlab/Simulink® block diagrams.

3.4 The Engine Model. The engine model should be of the type that will provide engine performance. The most likely candidate for this sub-system is a cycle code or component-level code as illustrated in Fig. 9.

Any cycle code can be used. What has currently been implemented is the AEDC generated ATEST(AEDC Turbine Engine Simulation Technique) code [7]. To be complementary to the F-16 aircraft simulation with GENESIS, a simulation of the F110-GE-129 engine has been implemented within the facility simulation as well as GENESIS.

3.5 The Data Analysis Manager. As envisioned, this part of the approach is basically a data handler. This may be easily implemented with the Matlab/Simulink® environment, as part of the plant model, or it may be a separate routine that passes data to-and-from each of the other components. As we move on to the more complex vision, Distorted Inlet Airflow, the Manager may have to become more complex to be able to handle the information from databases.

4 Nondistorted Inlet Airflow Simulation Demo

The initial portion of this vision allows for a simulation of aircraft maneuvers without distortion present. Aircraft altitude and

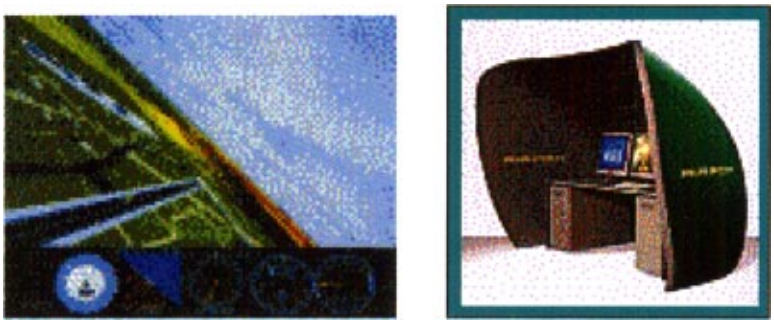

Fig. 8 AIRFOX's FlightLab simulator

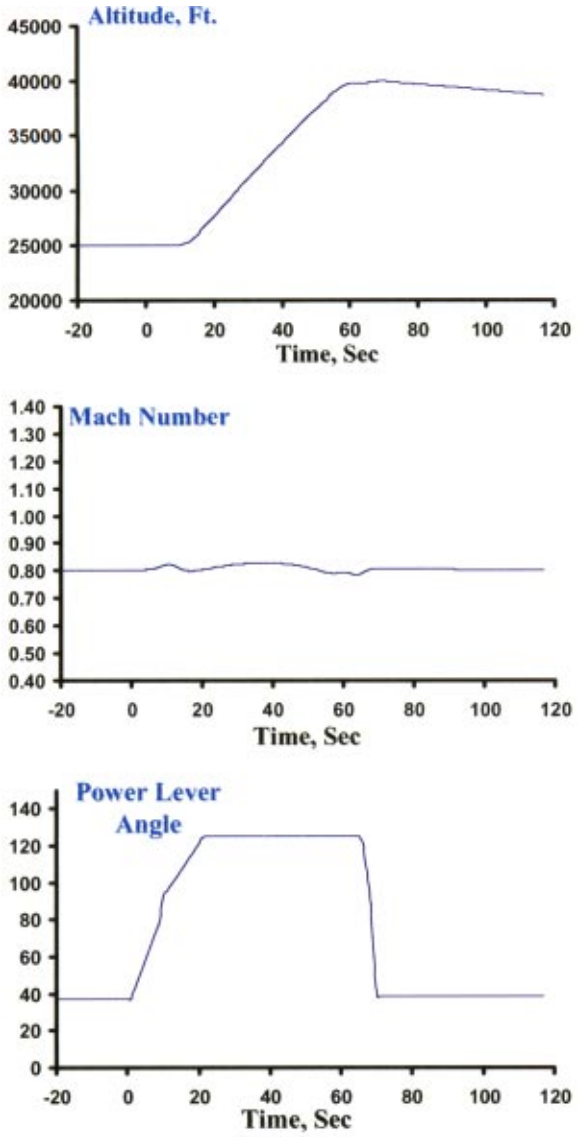

Fig. 10 Altitude and Mach number conditions for zoom-climb from 25 000 ft to 40 000 ft at Mach number of 0.8. Conditions obtained with GENESIS flight simulator.

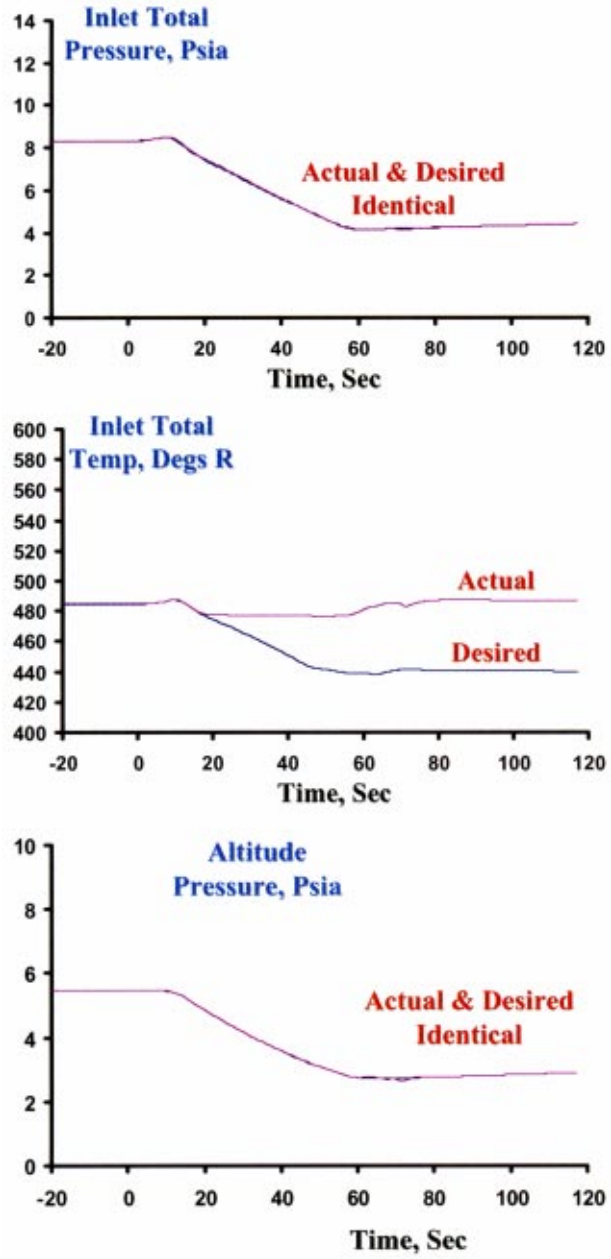

Fig. 11 Facility conditions for zoom climb from 25 000 ft to 40 000 ft altitude with current facility configuration

speed changes can be accomplished by carefully simulating inlet and altitude conditions (P_T, T_T, and P_0), respectively. With simulations of certain AEDC turbine engine test facilities, a demonstration of the vision was accomplished and is presented within this section. Two aircraft maneuvers have been chosen to be presented. The first is commonly known as a ''Zoom-Climb.'' In this maneuver, the aircraft climbs in altitude with the goal of having the final Mach Number the same as the initial condition. A Zoom-Climb from an altitude of 25 000 ft to 40 000 ft at a constant Mach Number of 0.8 was chosen and is presented in Fig. 10.

The climb was started with the aircraft flying at 25 000 ft altitude Mach 0.8 level steady flight. Initially the aircraft was given a ramp to full throttle command and then the stick was pulled back to establish a rapid climb rate. When the aircraft reached a climb angle of 30° relative to the ground the stick was pushed forward to maintain a constant climb angle. At 38 000 ft altitude the aircraft was rolled over 180° using the ailerons. The stick was then pulled back to obtain a nearly level inverted flying condition at 40 000 ft altitude. The aircraft was then rolled over another 180° to an upright condition and the nose pushed down using the stick. Adjustments were then made to the stick and power level angle to establish a trim flying condition at 40 000 ft altitude Mach 0.8.

Note: The roll sequence was performed for 2 reasons:

1. Pilots do not like to experience the large negative *g*'s that would occur if the aircraft were pushed over in an upright attitude.
2. Large negative angles of attack would be experienced by a nonrolled maneuver severely degrading inlet performance.

Using engine inlet total pressure and temperature as well as altitude pressure from this maneuver, the ground facility model can be executed to determine if the aircraft maneuver can be simulated in the real facility. The maneuver was first executed in a model of the facility as it exists today [3]. Associated with this configuration is the ability to mix ambient air with the conditioned inlet air prior to the engine test cell plenum to obtain a better temperature simulation. Prior to this configuration, inlet tempera-

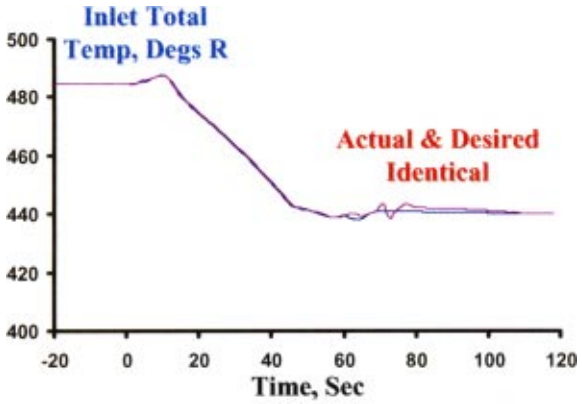

Fig. 12 Inlet temperature conditions for zoom-climb using the future facility configuration

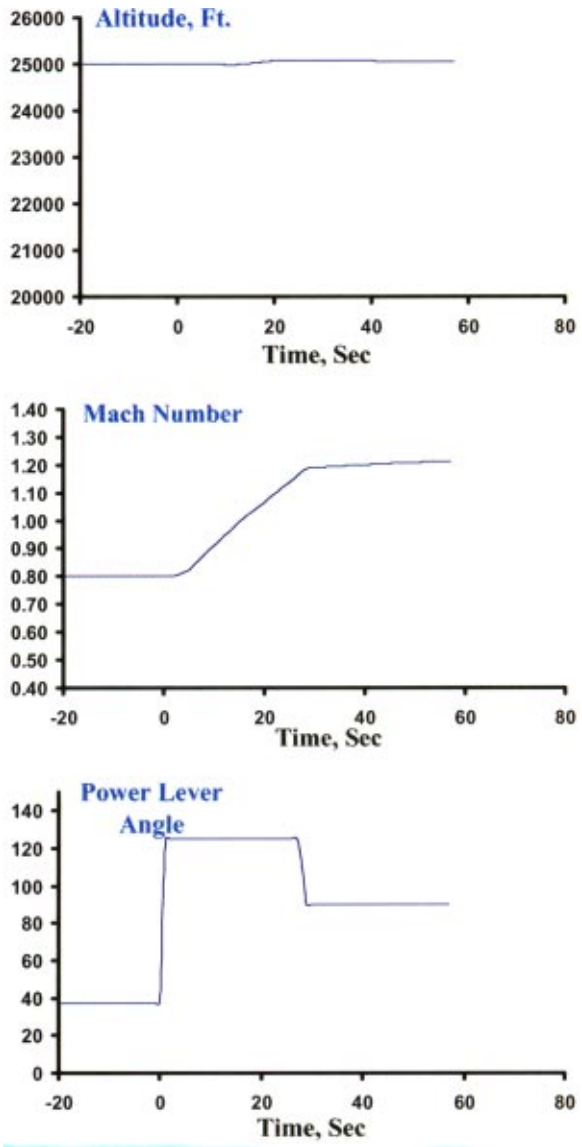

Fig. 13 Altitude and Mach number conditions for Mach dash from 0.8 to 1.2 at 25 000 ft, Altitude. Conditions obtained with GENESIS flight simulator.

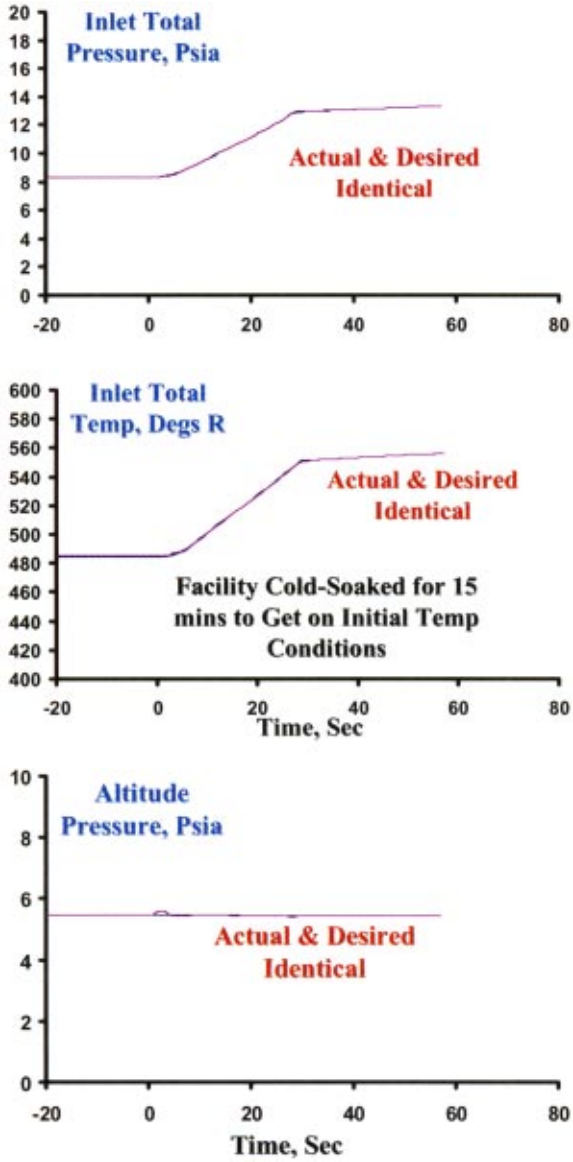

Fig. 14 Facility conditions for Mach dash from 0.8 to 1.2 at 25 000 ft altitude with current facility configuration

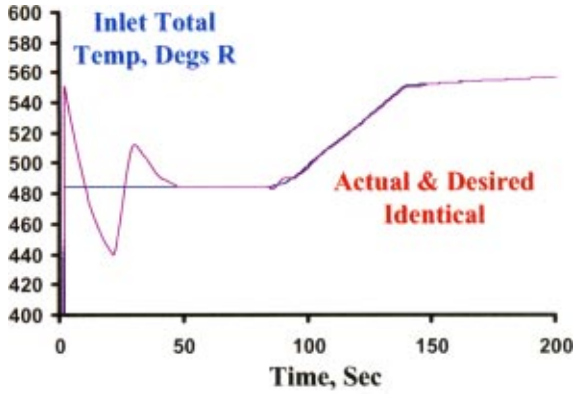

Fig. 15 Inlet temperature conditions for Mach dash using the future facility configuration

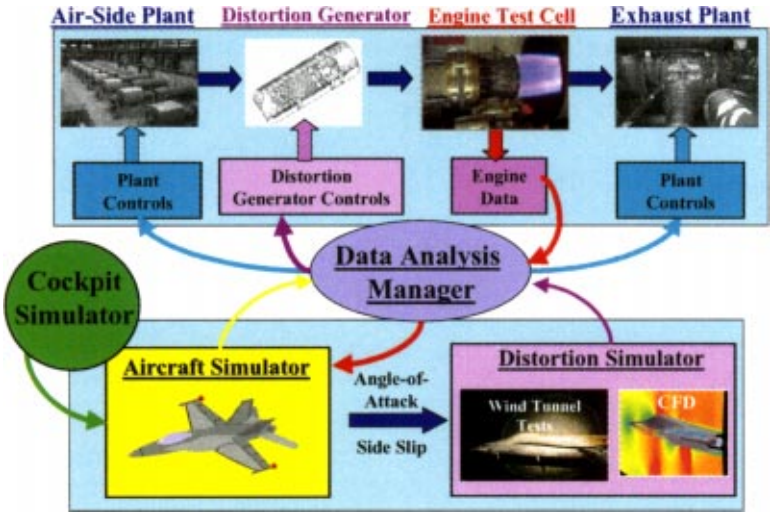

Fig. 16 Distorted inlet flow plant flight simulation vision

ture was controlled only by coolers and heat exchangers. The pertinent simulation parameters are presented in Fig. 11.

As one can see, the inlet total pressure and the altitude pressure provided by the exhaust plant follow the desired conditions, identically. However, the inlet total temperature did not follow the desired conditions, mainly because there was no capacity with this configuration to cool the air to the conditions required. In a proposed upgrade to the facility, cooled air along with ambient air will be able to be mixed with the conditioned air [3]. Using a model of the proposed facility, the same ''Zoom-Climb'' was executed. Again inlet total pressure and altitude pressure followed the desired conditions. The inlet total temperature, was also able to follow the desired condition as illustrated in Fig. 12.

The second maneuver is known as a Mach Dash. The Mach Dash was started with the aircraft flying at 25 000 ft altitude Mach 0.8 level steady flight. Initially the aircraft was given a full throttle command, as illustrated in Fig. 13. The stick was the pushed forward to keep the nose down and maintain a constant altitude. After a short period (5 s) it was necessary to pull the stick back to prevent the nose from rotating too far down and losing altitude. This position was held for another 5 s when it was necessary to rotate the nose back down to compensate for a decreased trim angle because of the increased speed. When the desired speed of Mach 1.2 was reached the power level was pulled back to maintain a constant velocity.

Again, the ground facility model was executed to determine if the aircraft maneuver can be simulated in the facility. The maneuver was first executed in a model of the facility, as it exists today [3]. The pertinent simulation parameters are presented in Fig. 14. As one can see, the inlet total pressure and the altitude pressure provided by the exhaust plant follow the desired conditions, identically. The inlet temperature followed the desired path only after the facility had been held-on condition for approximately 15 min (cold-soaked) in order to allow the facility metal to reach an equilibrium temperature close to that of the air. This negated any heat transfer to the air from the surroundings and allowed the transient to be accomplished with the prescribed temperature. The facility model was executed again, this time with the proposed changes that would provide additional cooling to see if these changes would allow the transient to be performed without cold-soaking the facility. As illustrated in Fig. 15, the inlet temperature gets on-condition within a minute even when started near standard-day conditions.

5 Technical Approach: Distorted Inlet Flow

A second phase of this vision is to look at facility simulation capabilities with inlet distortion as would be produced during any rapid maneuver. In this phase, the plant system will now include a transient distortion generator as illustrated in Fig. 16. Instead of the current method of producing distortion with screens, a device,

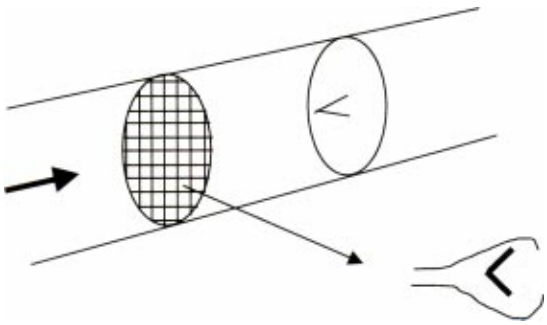

Fig. 17 Transient distortion generator concept. An array of blockage elements distributed over.

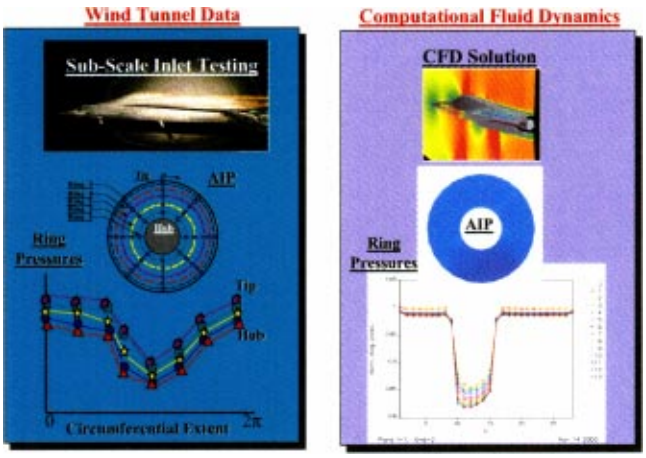

Fig. 18 Inlet data obtained from tests and CFD

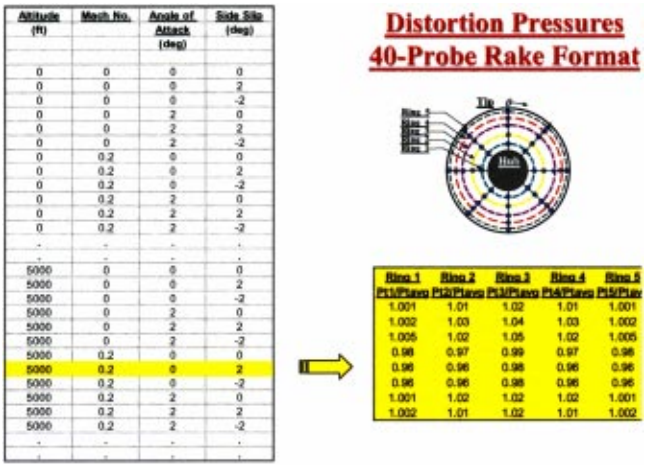

Fig. 19 Distortion simulator database concept

yet to be designed, will be capable of changing the total conditions (both pressure and temperature) in a transient manner such that actual flight maneuvers could be simulated.

5.1 The Distortion Generator. The transient total pressure (P_T) distortion generator focuses on three overall challenges for future engine-airframe compatibility evaluations: (1) advanced inlet systems featuring stealth, (2) supermaneuverability, and (3) test and evaluation (T&E) cost reduction. Meeting these challenges entails simulating new and unique P_T distortion patterns characteristic of evolving inlet configurations. The inlet will have to perform at extremes in flight conditions with time variation of the P_T distortion patterns [8]. The ability to vary distortion without changing screens offers the means to reduce cost of conducting the test portion of the T&E process. The transient P_T distortion generator development approach includes the following steps: (1) simulation requirements definition, (2) concept identification, (3) concept selection, (4) concept development, and (5) prototype validation. The work has progressed into the concept development phase, which includes subscale tests of distortion generator elements.

The selected concept used an aerodynamic blockage method to effect distributions in total pressure. Shown in Fig. 17, the concept uses an array of porous blockage elements that open and close in patterns commensurate with the distortion pattern desired. The opening angle provides the means to vary the magnitude of the total pressure distortion. The generator may use square-shaped elements arranged on a Cartesian grid or trapezoidal-shaped elements on a polar grid (i.e., on rings of different radii). The concept development experiments adopted the polar arrangement. In the future work, analysis of the results will be used to refine the definition of the distortion generator elements. The refinements will include element size, plan-form shape, porosity, and arrangement on the air supply duct cross section. The results will be used in the next phase of the development, assembly and testing of a subscale prototype distortion generator.

5.2 The Distortion Simulator. For inlet flows that are distorted, the Aircraft Simulator not only provides information for plant inlet and exit conditions, but also supplies angle-of-attack and sideslip to a Distortion Simulator for determination of the inlet flow distortion present. The Distortion Simulator is envisioned to be a database of information correlated from both wind tunnel tests of the specific inlet and computational fluid dynamic calculations of that same inlet configuration. This information is fed into a Distortion Generator that will set a distortion pattern (includes both pressure and temperature distortion) that simulates what is expected in flight. The real engine test article feeds back its performance to the Aircraft Simulator and provides the propulsive power for the aircraft.

The Distortion Simulator is envisioned to be information collated from previous wind tunnel tests and Computational Fluid Dynamics (CFD) simulations for the particular aircraft/inlet of interest, Fig. 18 [9]. Since CFD solutions of inlet flow fields take many CPU processors and lots of ''clock'' time to produce, it is envisioned that the distortion simulator will consist of previously obtained test data and CFD solutions implemented in a database as illustrated in Fig. 19. Once the database is populated with AIP information, it can be used to drive the distortion generator to the desired conditions.

5.3 Putting the Pieces Together. Even though distorted Inflow capability of the Vision requires many hardware modifications to become reality, there are, as was the case with the Non-Distorted Inflow Phase, facility simulations which can provide an inexpensive way of determining the feasibility and approach of putting everything together. An overview of the whole Vision us-

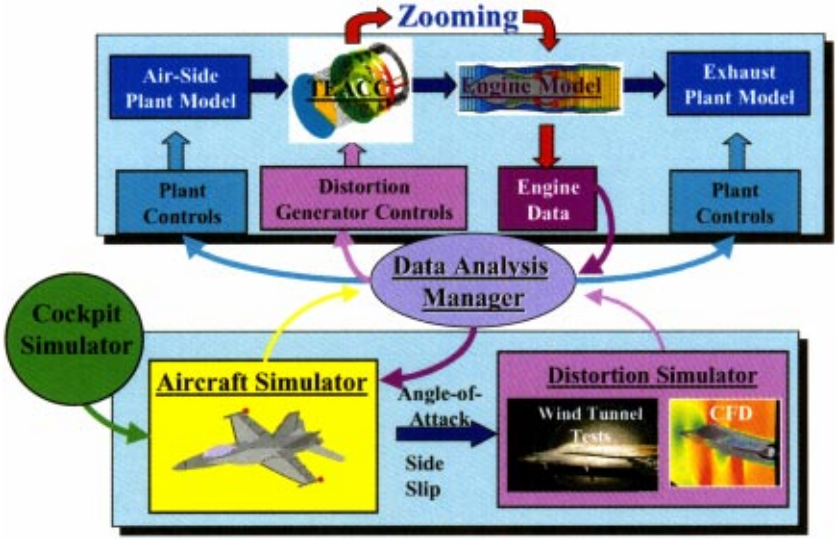

Fig. 20 Plant flight simulation vision. Distorted inlet flow. Numerical simulation.

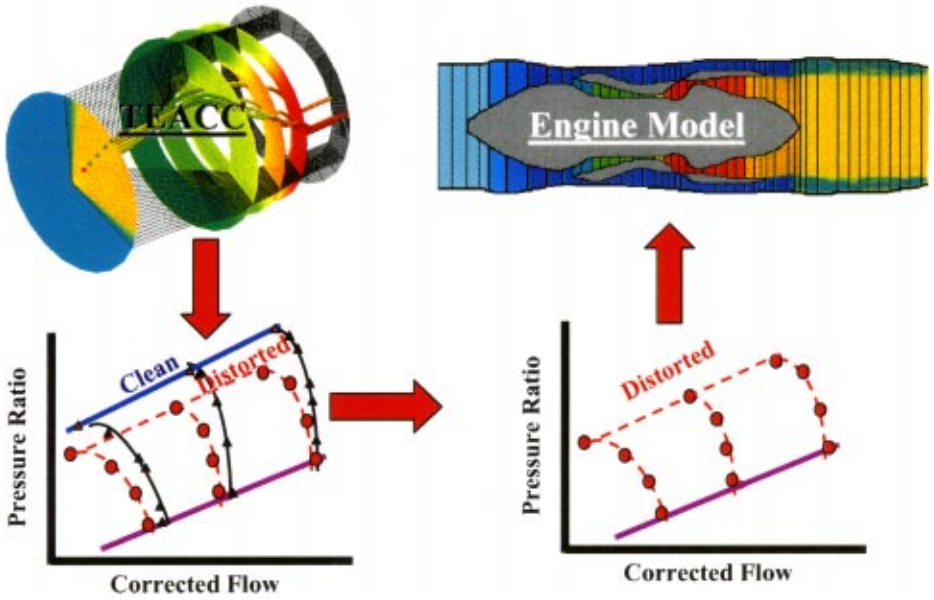

Fig. 21 TEACC zooming to accomplish modifications in compression system maps due to distortion

ing numerical simulations is presented in Fig. 20. The only simulation that has not been discussed is the 3D compressor simulation, TEACC (Turbine Engine Analysis Compressor Code). A complete description of the technology behind the development of TEACC is presented in Ref. [10]. TEACC will be used to modify compression system maps within the engine model when distortion is present. A zooming technique will be used as illustrated in Fig. 21 to accomplish this task.

The initial activities deal with the implementation of GENESIS within the MATLAB environment for execution with the Plant Simulation. Plant Model passes the time-step to GENESIS for the next time of the Aircraft Simulation. Since GENESIS was developed as a FORTRAN ''stand-alone'' program, there are integration issues. MATLAB is its own programming language, and as such, a FORTRAN program must be implemented as a ''wrapped'' executable. Major activities are thus the proper execution of GENESIS and its execution within the MATLAB environment. The latter activities will be directed toward the development of the Distortion Simulator Database using an established aircraft, the F-16. This aircraft's inlet has been extensively tested in AEDC Wind Tunnels, but the data has not been saved from the 40-probe rakes. Much of the data has been reduced to a distortion index that does not quantify the AIP pressure distortion in the right form. Thus, CFD computations will be run to populate the Distortion Simulator for a typical maneuver.

Acknowledgments

The authors would like to acknowledge other SverdrupÅEDC employees for their contributions to the overall effort: Terry Hand for making CFD calculations of the F-16 inlet, Dick Christensen for executing GENESIS, and Chris Davis for implementing the GENESIS output into the facility model. The research reported herein was performed by the Arnold Engineering Development Center (AEDC), Air Force Materiel Command. Work and analysis for this research were done by personnel of Sverdrup Technology, Inc., AEDC Group, technical services contractor. Further reproduction is authorized to satisfy the needs of the U. S. Government.

References

[1] ''Aeropropulsion Systems Test Facility,'' 1998, AEDC Fact Sheet, AEDC Public Web Page, http://www.arnold.af.mil/aedc/factsheets/astf/ASTF.html, April 1998.
[2] Montgomery, P. A., et al., 2002, ''Evolution of a Turbine Engine Test Facility to Meet the Test Needs of Future Aircraft,'' ASME International Gas Turbine Institute 2002 TurboExpo, Paper No. TBD, June 2002.
[3] Montgomery, P. A., et al., 2000, ''A Real-Time Turbine Engine Facility Model and Simulation For Test Operations Modernization and Integration,'' ASME Paper No. 2000-GT-0576, presented at the ASME TurboExpo 2000 in Munich Germany, May 2000.
[4] McKeehen, P. D., 1995, ''GENESIS Simulation of a Modified Vista/F-16,'' AIAA Paper No. 95-3381, presented at Flight Simulation Technologies Conference, Baltimore MD, August 1995.
[5] McKeehen, P. D., 1999, ''Hypervelocity Vehicle Modeling and Simulation Using GENESIS,'' AIAA Paper No. 99-4326, presented at the AIAA Modeling and Simulation Technologies Conference and Exhibit, Portland, OR, August 1999.
[6] ''AIRFOX FlightLab,'' AMST Systemtechnik Web Page, http://www.amst.co.at/products/flitesim.htm
[7] Chappell, M. A., and McLaughlin, P. W., 1993, ''Approach to Modeling Continuous Turbine Engine Operation From Startup to Shutdown,'' J. Propul. Power, **9**, No. 3, pp. 466–471.
[8] Davis, M. W., Jr., Hale, A. A., and Beale, D., 2001, ''An Argument for Enhancement of the Current Inlet Distortion Ground Test Practice for Aircraft Turbine Engines,'' ASME Paper No. 2001-GT-0507, presented at the IGTI TurboExpo in New Orleans, LA, June 2001.
[9] Davis, M. W., Jr., et al., 1999, ''A Proposal for Integration of Wind Tunnel and Engine Test Programs for the Evaluation of Airframe-Propulsion Compatibility Using Numerical Simulations,'' ASME Paper No. 99-GT-345, June 1999.
[10] Hale, A. A., and O'Brien, W. F., 1998, ''A Three-Dimensional Turbine Engine Analysis Compressor Code (TEACC) for Steady-State Inlet Distortion,'' J. Turbomach., **120**, pp. 422–430.

Transfer Function Calculations for Aeroengine Combustion Oscillations

M. Zhu
Department of Thermal Engineering,
Tsinghua University,
Beijing 100084, China
e-mail: zhumin@tsinghua.edu.cn

A. P. Dowling

K. N. C. Bray

Department of Engineering,
University of Cambridge,
Trumpington Street,
Cambridge CB2 1PZ, UK

Combustors with fuel-spray atomizers are particularly susceptible to a low-frequency oscillation at idle and subidle conditions. For aeroengine combustors, the frequency of this oscillation is typically in the range 50–120 Hz and is commonly called "rumble." The mechanism involves interaction between the plenum around the burner and the combustion chamber. Pressure variations in the plenum or the combustor alter the inlet air and fuel spray characteristics, thereby changing the rate of combustion. This in turn leads to local "hot spots" which generate pressure oscillations as they convect through the downstream nozzle. In order to eliminate the combustion oscillations, it is essential to determine which fuel atomizers are particularly likely to lead to instability by quantifying their sensitivity to flow perturbations. This can be done by identifying the system through understanding the transfer function, which represents the relationship between the unsteadiness of combustion and the inlet fuel and air. In the present work, various types of signals are applied to produce a small change in the inlet fuel and air flow rates, the response in the rate of heat release caused downstream was calculated and stored for subsequent analysis. Afterwards, the system transfer function is calculated by determining the coefficients of an IIR filter (Infinite Impulse Response) for which the output signal is the downstream heat release rate and the input signal is the inlet flow rate. The required transfer function then follows from the Fourier transform of this relationship. The resulting transfer functions are compared with those obtained by the forced harmonic oscillations at a fixed given frequency. Suitably chosen input signals accurately recover the results for harmonic forcing at a single frequency, but also give detailed information about the combustor response over a wide frequency range. There are two distinct forms to the low-frequency quasisteady response. In the primary zone, the rate of combustion is influenced by the turbulence and is enhanced when the inlet air velocity is large. Near the edge of combustion zone, the rate of combustion depends on the mixture fraction and is high when the mixture fraction is close to the stoichiometric value. This generates 'hot spots' which convect into the dilution zone. At higher frequencies, the combustion lags this quasi-steady response through simple lag-laws and the relevant time delays have been identified. [DOI: 10.1115/1.1806451]

1 Introduction

The pressure oscillations induced by unsteady combustion are a major technical challenge to the development of high performance propulsion systems. In principle, the combustion oscillations are driven by the resonant interaction between pressure waves and unsteady combustion. For aero-gas turbines, combustors with fuel-spray atomizers are particularly susceptible to a low-frequency oscillation at idle and subidle conditions. The frequency of this oscillation is typically in the range 50–120 Hz and is commonly called ''rumble.'' In a previous study, it was demonstrated that this low frequency oscillation can be established by the interaction between unsteady combustion and pressure, the inlet fuel and air supplies, and a downstream nozzle [1]: the pressure variations in the plenum and combustor alter the inlet air and fuel spray characteristics, thereby changing the rate of combustion. This in turn leads to local ''hot spots'' which generate pressure oscillations as they convect through the downstream nozzle. If the phase relationship is suitable this upstream propagating pressure wave re-inforces the fluctuations in the inlet flow, a combustion oscillation is established.

Contributed by the International Gas Turbine Institute (IGTI) of THE AMERICAN SOCIETY OF MECHANICAL ENGINEERS for publication in the ASME JOURNAL OF ENGINEERING FOR GAS TURBINES AND POWER. Paper presented at the International Gas Turbine and Aeroengine Congress and Exhibition, New Orleans, LA, June 4–7, 2001; Paper 2001-GT-0374. Manuscript received by IGTI, December 2000, final revision, March 2001. Associate Editor: R. Natole.

It is known experimentally that certain atomisers are particularly susceptible to combustion oscillations. In order to eliminate these oscillations, it is important to understand the fundamental mechanisms of the system so that undesirable phenomena can be avoided by either redesigning the atomiser to reduce the sensitivity of the combustion to flow perturbations or by increasing the acoustic damping, or even suppressing the instability by active control techniques. To achieve this aim, it is essential to identify the system through examination of the flame transfer function. In this study, the combustion chamber can be viewed as a dynamical system for analysis. The flow rates of inlet air and fuel are considered ''input variables.'' The observable signals that are of interest, e.g., heat release rate, mixture fraction or temperature, are regarded as output signals.

Here, a linear system is assumed since attention in this study is restricted to the onset of the oscillation modes when their amplitudes and growth rates are small. For continuous time signals, the transfer function in frequency domain can be described as the ratio of the Fourier transform of the output of the system, to the Fourier transform of its input, which is our case represents the relationship between the unsteadiness of combustion at a fixed position $\underline{x}$, and the fluctuations in inlet air flow rate,

$$H(\omega,\underline{x})=\frac{\hat{q}(\omega,\underline{x})}{\hat{m}_a(\omega)}, \tag{1}$$

where ω is the frequency. $\hat{q}(\omega,\underline{x})$ is the Fourier transform of $q(\underline{x},t)$, the heat release rate at $(\underline{x},t)$, and $\hat{m}_a(\omega)$ the Fourier trans-

form of the input air mass flow rate. In ''rumble'' instabilities, the convection of gas containing nonuniform density regions or entropy spots through a nozzle is a significant source of combustion oscillations [2,3]. As the characteristic velocity of the entropy spots is the convective speed of fluid, so for given frequency, its characteristic length is much shorter than that of pressure wave. To identify the instability of system, it is desirable to have the information of ''distributed'' unsteady heat release along the direction of wave propagation. This information can be obtained by integration over the combustor cross section and using $q(x,t)$, the rate of heat release per unit length of combustor, as the output signal.

The performance of the combustor in the time domain must be known before determining the transfer function. A seemingly straightforward approach to obtaining the transfer function is by means of experiments. Considering a swirl burner system as the upstream and downstream ducts, and the flame three separate parts, Lawn [4] investigated the response of flames to the acoustic perturbation. With the measured empirical parameters, a predictive acoustic model for this type of swirl burner can be devised. Lieuwen and Neumeier [5] studied the response of a premixed combustion process to imposed pressure oscillations. The result shows that the nonlinear relationship between pressure and heat-release oscillation plays an important role in limit cycle oscillations. Unfortunately, experimental investigation is not always feasible for the problem we meet in practice. It could be an expensive and time consuming procedure to set up a high pressure, high temperature rig that correctly reproduces the engine conditions. Experimental investigations of potentially unstable system are prone to unwanted, high amplitude oscillations which can break the hardware. Moreover, many of the flow parameters of interest are not easy to measure. Nowadays, CFD provides a flexible, low cost tool as a supplement to direct measurement. A method has been presented by Bohn et al. [6] to predict the dynamic flame behavior by means of unsteady combustion simulation. After a steady-state solution, a sudden change in the mass flow rate at the atomizer is imposed. The frequency response to this disturbance represents the dynamic behavior of the flame [7,8]. With the properties of combustion system described by multiport networks, Polifke et al. [9] suggested that the transfer matrices can be determined from time-dependent numerical simulation of the multiport's response to a perturbation of boundary conditions. Recently, several attempts have been made to study flame response under forcing or flame transfer functions with large eddy simulations (LES) [10,11]. It is demonstrated that this technique has the potential to provide reliable information for fully understanding combustion instability in gas turbines. In our previous work, CFD was used to calculate the unsteady flow in the combustor. Through calculations of the forced unsteady combustion resulting from the specified time-dependent variation in the fuel and air supplies, we were able to identify the main source of the unsteady heat release. Forcing harmonically at a specified frequency gives information on the transfer function between rate of heat release and the air flow rate through the atomizer. However, there are two drawbacks in this method. One is that the flow must be calculated for many cycles after the start of the excitation before the steady-state response to harmonic forcing is obtained. This means that the computations are very time-consuming, and it is not feasible to investigate a wide range of flow conditions. Another is that only the transfer function for one particular frequency can be calculated at a time. This is not convenient if the flame response is to be incorporated into a linear stability analysis to predict the frequencies of self-excited oscillation. Then the flame transfer function is required as a function of (complex) frequency. Thus, it is desirable to develop the new approaches to determine the system transfer function. Afterwards, the flame transfer function can be introduced into a one dimensional linear stability analysis of the flow

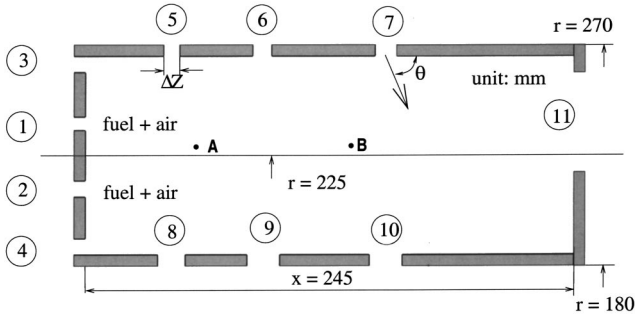

Fig. 1 Schematic diagram of the geometry

in the combustor, to interpret the numerical results, understand the feedback mechanisms, and to investigate the susceptibility to instability.

In the next section, the CFD models and the results of harmonic forcing calculations at a particular frequency will be described. These results are used as a benchmark for the other cases. In Sec. 3, the air supply was modulated by a small amplitude impulse, and the response of downstream flow was recorded for subsequent analysis. The system transfer function is calculated with the use of an IIR filter (Infinite Impulse Response) for which the output signal is the downstream responses and the input signal is the impulse function. In Sec. 4, two other forms of input signals, containing information at a range of frequencies plus noise, are used to calculate the transfer function. These methods give reliable information of the combustion response across a wide frequency bandwidth. Finally, general conclusions and further work are discussed.

2 Harmonic Forcing Calculations

As in previous work, the CFD calculation has been conducted in the idealised 2D axisymmetric annular combustor shown in Fig. 1. Fuel and air are injected through inlets 1 and 2 and dilution air through ports 3–10. The boundary conditions are specified to be representative of an aero-engine at idle. A contour plot of a typical mean temperature distribution is shown in Fig. 2 for cross-referencing in following discussion. More information on the CFD algorithm and boundary conditions can be found in Zhu et al. [12]. Although quite simple models are used here to describe spray, turbulence, and combustion processes, it is worth emphasizing that the same methods can in principle be applied to determine the transfer function from more advanced CFD methods including LES. This system has the very convenient characteristic that when an open-end boundary condition of constant pressure is applied at the combustor exit, the flow is stable and perturbations decay [12]. However, self-excited oscillations occur when the boundary condition is modified to describe the effects of the choked turbine downstream [1]. The mean flow is unaltered and the flame transfer function can be determined by forcing stably combusting flow.

Fluid flows are distributed and so this system is clearly multi-input and multi-output. It is therefore important to choose the input and output variables so that they capture the major dynamics of the system. In our previous study, it was demonstrated that the air mass flow rate through the atomizer has a significant influence on the unsteady combustion. It not only alters the air–fuel ratio in the combustion zone, but also leads to a variation of droplet size distribution. Therefore, the air mass flow rate at inlets 1 and 2 is chosen as the input signal. For the frequency range of interest for the ''rumble'' phenomenon (up to 150 Hz), the atomizer is very small in comparison to the acoustic wavelengths, we therefore assume that its response can be modeled quasisteadily. Hence, in calculations, when the total pressure $p_0(t)$ at the inputs 1 and 2 is varied, the air mass flow rate, $m_a(t)$, is traced according to a

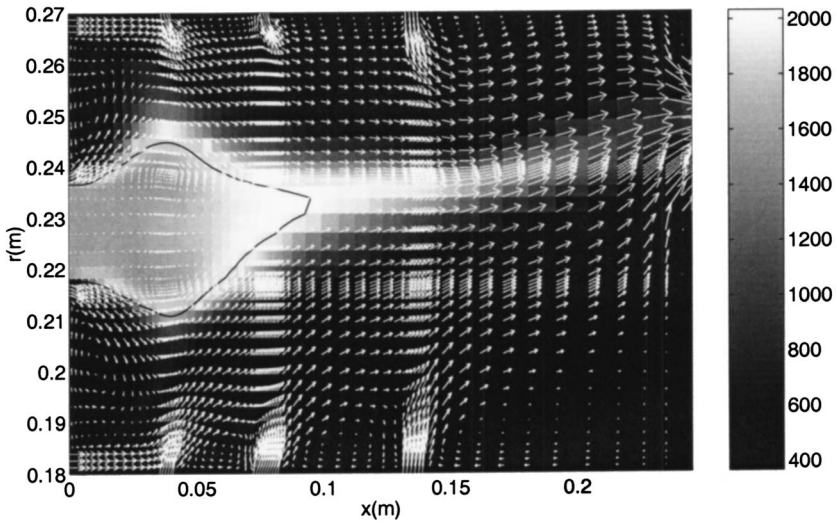

Fig. 2 Contour plot of the mean temperature distribution chamber at idle conditions. The black line indicates the mean position of the stoichiometric curve and arrows denote the direction and magnitude of the mean velocity.

specified discharge relationship. An empirical correlation (Eq. (2) of Ref. [1]) is used to describe the change this causes in the SMD of inlet fuel droplets. Once the Sauter mean diameter $\bar{D}_{32}$ is obtained, the droplet size distribution is assumed to vary with SMD according to the nondimensional expression

$$\frac{dV}{V} = 13.5\left(\frac{D}{\bar{D}_{32}}\right)^3 \exp\left(-3\left(\frac{D}{\bar{D}_{32}}\right)\right) d\left(\frac{D}{\bar{D}_{32}}\right), \tag{2}$$

where dV/V is the volume fraction occupied by droplets within the size range D to $D+dD$. We use Eq. (2) and $\bar{D}_{32}$ to relate the fuel droplet size to the instantaneous air and fuel flow for low frequency fluctuations. Since the unsteady combustion is the driving mechanism, it is appropriate to choose a measure of the heat release rate as the output signals.

The shape of the input signal has a very substantial influence on the observed data. It determines the operating points of the system and which parts and modes of the system are excited. The advantage of CFD is that it is convenient to set up various shapes of input signal for investigation. In general, if the frequency in which we are particularly interested is known, detailed information about the system at this frequency can be obtained from a calculation with sinusoid forcing. Here we know that the frequency of the combustion oscillation at the idle condition is in the range 50–120 Hz. Thus the harmonic forcing of the inlet flow is implemented by the stagnation pressure at inlet to ports 1 and 2 as

$$\frac{p_{0,12}(t)}{\bar{p}_{0,12}} = 1 + a\sin(2\pi f t). \tag{3}$$

Figure 3 gives time traces of mixture fraction, scalar dissipation, and heat release rate for forcing at a frequency f equal to 50 Hz and amplitude a of 0.02. Results are given for two sample points. As shown in Figs. 1 and 2, the point A is within the recirculation zone, while the point B is near the tip of the flame. An increase in $p_0(t)$, the total pressure of the air supply, leads to more air through the atomizer. In these sample results, the peak-to-peak fluctuation amplitude is equivalent to 15% of the mean value of the air mass flow rate. An increase in the atomizer air flow rate leads to a decrease in SMD of the inlet fuel droplets [see Fig. 3(*a*)]. These smaller droplets evaporate quickly, increasing the gaseous mixture fraction in the recirculation zone with a recirculation time delay as shown in Fig. 3(*b*). At point A, the mixture fraction is larger than the stoichiometric value 0.06 and so an increase in the mixture fraction tends to reduce the rate of combustion. Turbulence has the opposite effect: an increase in inlet air velocity, increases the shear and hence the turbulence scalar dissipation rate [Fig. 3(*c*)]. Through the laminar flamelet modelling this tends to increase the rate of combustion. We see in Fig. 3(*d*) that the scalar dissipation has most effect. At point B, the scalar

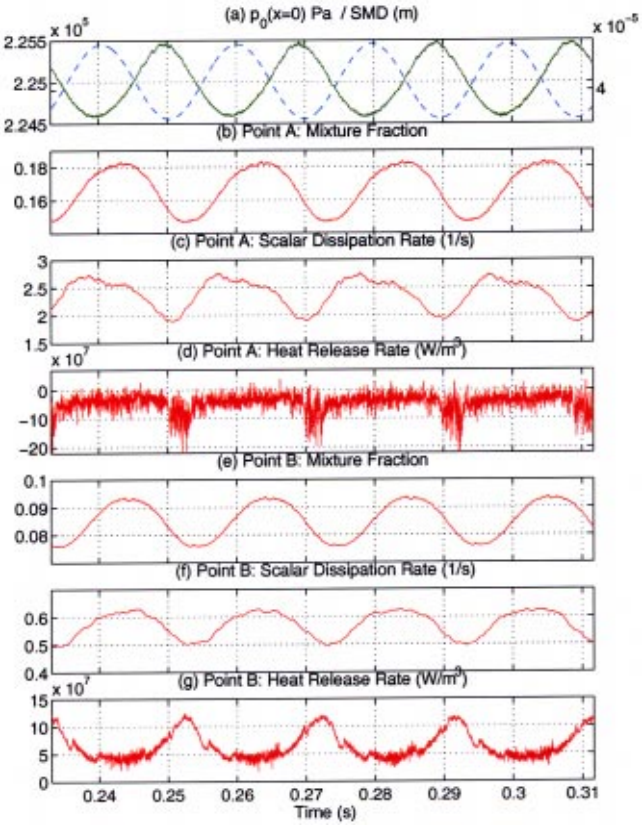

Fig. 3 Sinusoidal changes of the total pressure in the atomiser air inlet lead to oscillations in the mixture fraction, scalar dissipation, and heat release rate at points A and B

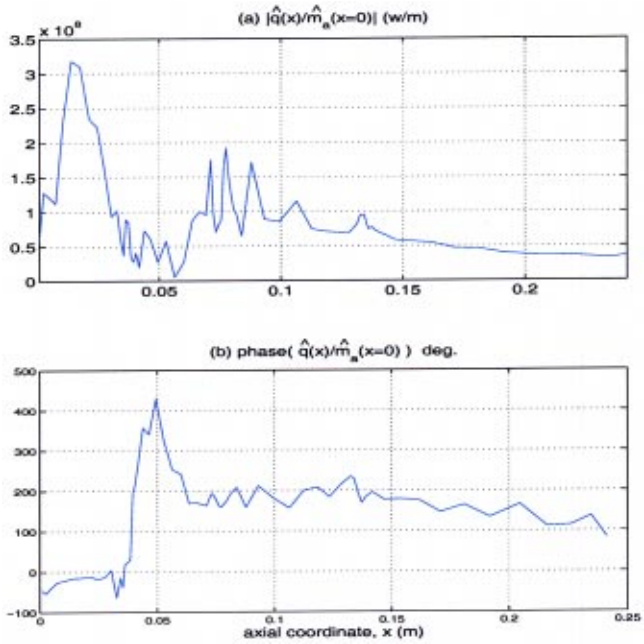

Fig. 4 The transfer function between the heat release rate per unit length and the sinusoidal changes of air flow rate through the atomizer at the forcing frequency of 50 Hz

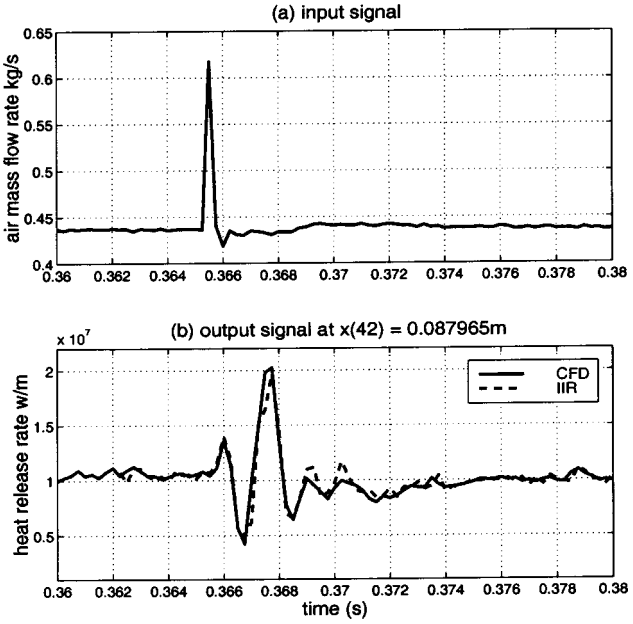

Fig. 5 (*a*) The air mass flow rate at the inlet boundary as the impulse function was applied. (*b*) The downstream response of the heat release rate at the location $x=0.088$ m, where the solid lines indicate the result from the CFD calculation and dashed line indicates that from the IIR filter in time domain.

dissipation is small and the variation in mixture fraction has most effect on the rate of combustion. Since the mixture fraction is richer than stoichiometric, the increase in mixture fraction tends to reduce the rate of combustion.

In the simulation, the input and output signals are obtained by utilizing the sampled signals at discrete times. The values of the variables are evaluated at successive time intervals. It is important to select the sampling period so that the information losses are insignificant. For a sampling frequency f_s of 2 kHz, the Nyquist frequency is 1 kHz. The frequency response can be highlighted by evaluating the Fourier transforms of $q(x,t)$, the rate of heat release/unit length of combustor and the inlet air flow rate, and the input forcing signal

$$H(\omega,x)=\frac{\hat{q}(\omega,x)}{\hat{m}_a(\omega)}=\frac{\sum_{k=1}^{K} q(kT)z^{-k}}{\sum_{k=1}^{K} m_a(kT)z^{-k}}, \tag{4}$$

where $z=e^{i\omega T}$, and T is the sampling period. The magnitude and phase of the transfer function $\hat{q}(\omega,x)/\hat{m}_a(\omega)$ at the forcing frequency are plotted in Fig. 4. Two regions with distinct and different forms of flame response are now evident. The gradual decrease in phase seen clearly throughout the region $x>0.12$ m indicates a convective time delay. The phase shift around 0.05 m indicates that the heat release is controlled by different mechanisms in the primary zone and the dilution zone as we discussed with reference to Fig. 3. This result will be used as the benchmark for comparison with those in Secs. 3 and 4.

3 Infinite Impulse Response

The transfer function between the rate of heat release and the air flow rate through the atomiser has been calculated. However, there are two drawbacks to this method. One is that the computations are very time-consuming, and it is not feasible to investigate a wide range of flow conditions. Another is that only the transfer function for one particular frequency can be calculated at a time. This is not convenient and thus, it is desirable to develop a new approach to determine the system transfer function.

Theoretically, the response of a linear system to an impulsive excitation plays an important role in the study of a linear system. The impulse function or Dirac delta function $\delta(t)$ can be defined as follows:

$$\delta(t)=0 \quad \text{if } t\neq 0, \quad \text{and} \quad \int_{-\infty}^{\infty}\delta(t)dt=1. \tag{5}$$

It is well known that a linear, time-invariant, causal system can be described by its impulse response. Of course we cannot apply such an impulse to a CFD calculation. Instead we use a short duration pulse; the time duration of the pulse is chosen to be short enough to contain the frequencies in which we are interested. The other conditions are the same as for the harmonic forcing calculation. The air mass flow rate at the inlet is shown in Fig. 5(a). The amplitude of the pulse leads to 30% change in inlet air flow rate. The pulse duration is 0.4 ms. The output signal $q(x,t)$ at a sample downstream location is shown by a solid line in Fig. 5(b). The perturbation and its time delay are clearly demonstrated.

Since the response to the pulse is of such short duration, we first process the signals in the time domain before applying the Fourier transform. The linear relationship between an output signal $q(x,t)$ and an input $m_a(t)$ can be expanded in the form of an IIR (Infinite Impulse Response) filter [13] by writing

$$q(x,nT)=\sum_{i=0}^{I-1} a_i(x)m_a[(n-i)T]+\sum_{k=1}^{K} b_k(x)q[x,(n-k)T]. \tag{6}$$

The coefficients $a_i(x)$ and $b_k(x)$ for each x position and the order of the filter (I,K) are found by fitting the right-hand side of Eq. (6) to $q(x,nT)$. The least mean square algorithm is employed for the coefficient optimization. In order to examine the success of the filter, the output signals in time domain, which are obtained from the IIR filter in Eq. (6), are compared with the CFD results. Figure 5(b) shows a sample comparison with $I=8$ $K=8$. It can be seen that they are in good agreement.

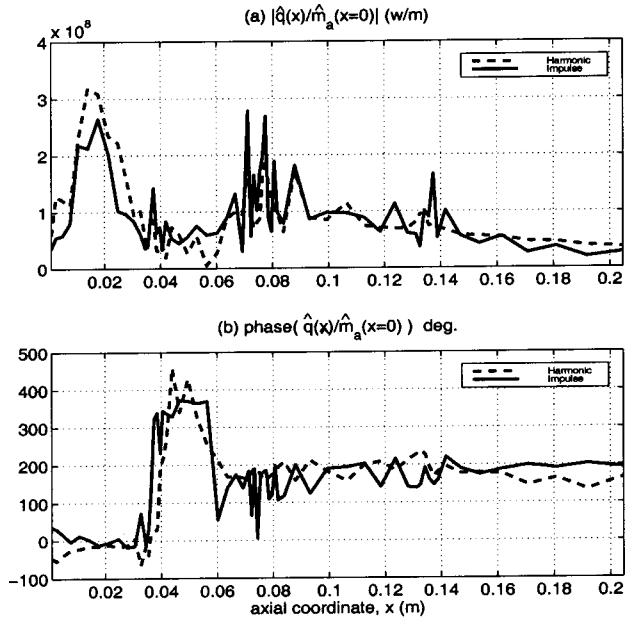

Fig. 6 The transfer function between the heat release rate per unit length and the sinusoidal changes of air flow rate through the atomizer at frequency 50 Hz, where the dashed lines indicate the result from the harmonic forcing calculation and solid lines indicate that from the IIR filter

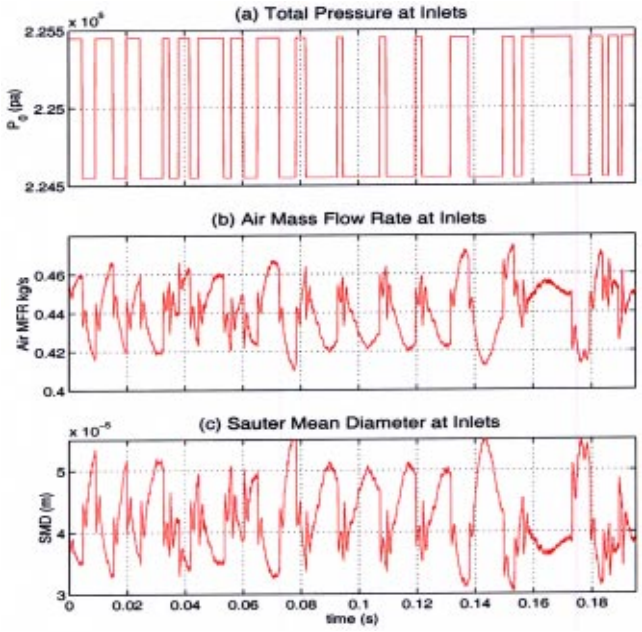

Fig. 7 The variations of the total pressure, air mass flow rate, and the Sauter mean diameter in the atomizer inlet due to the forcing of the random binary signal

Once the coefficients in the IIR filters are known, the transfer functions between the heat release rate and air flow rate through the atomizer can be calculated. By taking the Fourier transform and assuming zero initial conditions, the frequency domain transfer function of the digital system can be written as

$$H(\omega,x)=\frac{\hat{q}(\omega,x)}{\hat{m}_a(\omega)}=\frac{\sum_{i=0}^{I-1} a_i(x)z^{-i}}{1-\sum_{k=1}^{K} b_k(x)z^{-k}}. \tag{7}$$

For the particular frequency of 50 Hz, as used in the harmonically forced calculation, the results are shown in Fig. 6. It can be seen that their main features agree quite well although there is some deviation at a few axial positions. Compared with the calculation for harmonic forcing, the computing time for the case of an impulse is significantly reduced, particularly for the low frequencies oscillation considered here. Furthermore, the transfer function is determined as a general function of frequency ω by Eq. (7) thereby giving broadband information on the flame transfer function.

4 Other Input Signals

In the last section, the impulse response method was found to have the advantage of requiring a short time sequence for the calculation of the transfer function. However, this method does require that the noise level in the system be low. The error caused by the noise is inversely proportional to the amplitude of the pulse [14]. In practice, the input signal amplitude is constrained to be low enough for the physical system to respond in a linear way. This is a basic weakness and many physical processes do not allow pulse inputs of such an amplitude that the error is insignificant compared to the impulse response coefficients.

In order to overcome this difficulty, it is worthwhile to design the input signals carefully so as to generate data that are sufficiently informative. Consider changes to the inlet stagnation pressure of the from

$$\frac{p_{0,12}(t)}{\overline{p}_{0,12}}=1+au(t), \tag{8}$$

where $\overline{p}_{0,12}$ is unperturbed mass flow rate. There are many different design methods for choosing the nondimensional function $u(t)$. Two kinds of input signal shapes have been tried out in the CFD simulations. One is based on the random binary signal, which is written as

$$u(nT)=\tfrac{1}{2}(u_1+u_2)+\tfrac{1}{2}(u_1-u_2)\text{sign}[R(w(nT))],$$

and

$$n=1,\ldots,N, \tag{9}$$

where u_1 and u_2 are two permitted input levels, which are chosen to be zero and unity here, respectively, and $w(nT)$ is the computer-generated sequence of random numbers chosen from a normal distribution with mean zero and variance one, which is filtered by the digital filter R. Different spectral characteristics can be realized by choice of this filter. Here a Butterworth filter with a pass-band frequency range of 0–200 Hz was chosen in the calculation. The input signal is shown in Fig. 7(a). The resulting variations in the inlet air mass flow rate and the Sauter mean diameter of the fuel droplets are shown in Figs. 7(b) and 7(c).

The other input signal we used here is the sum of sinusoidal signals, before normalization it can be written as

$$u(nT)=\sum_{k=1}^{K} \sin(2\pi(n-1)\omega_k T+2\pi w(k)),$$

and

$$n=1,\ldots,N, \tag{10}$$

where K is the number of sinusoids which are equally spread over the passband. ω_1 and ω_2 are the lower and upper limits of the passband, and $\omega_k=\omega_1+k(\omega_2-\omega_1)/K$, $k=1,\ldots,K$. $w(k)$ describes the phase of the kth sinusoid at $t=0$ and is a random number chosen from a uniform distribution on the interval zero and unity. The harmonic forcing signal can be seen as a special case of Eq. (10) with K unity. The random sum of sinusoids signal, $\omega_1=0$ $\omega_2=500$ Hz $K=20$, is shown in Fig. 8(a). The result-

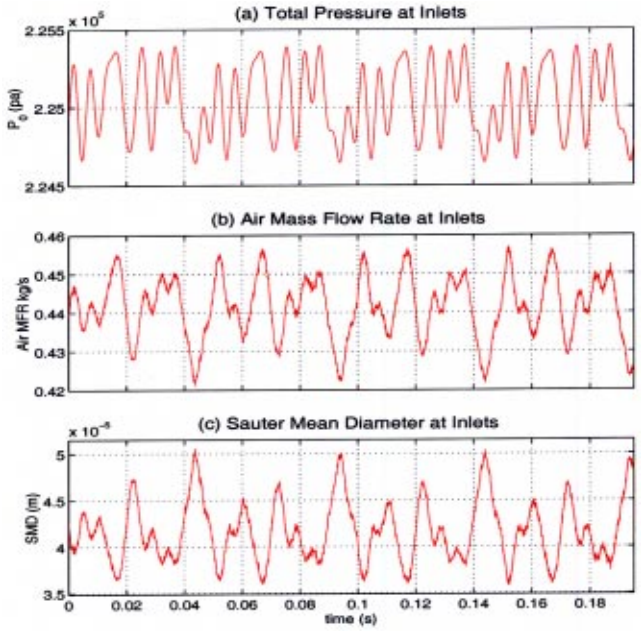

Fig. 8 The variations of the total pressure, air mass flow rate, and the Sauter mean diameter in the atomizer inlet due to the forcing by the sum of the random sinusoids

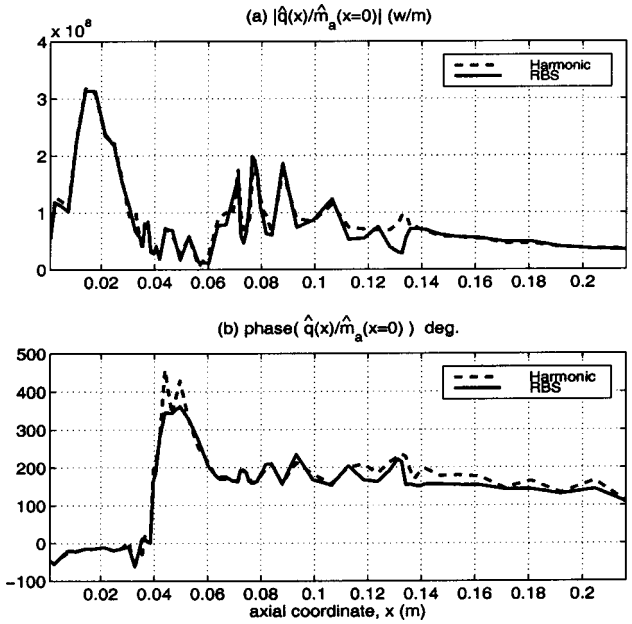

Fig. 9 The transfer function between the heat release rate per unit length and the sinusoidal changes of air flow rate through the atomizer at frequency 50 Hz, where the dashed lines indicate the result from the harmonic forcing calculation and solid lines indicate that from the random binary signal forcing calculation

ing variations of the inlet air mass flow rate and the Sauter mean diameter are shown in Figs. 8(*b*) and 8(*c*). From Figs. 7 and 8, it can be seen that the atomizer is more sensitive to low frequencies, and acts like a low-pass filter. A sudden change of the total pressure in the binary signal case leads to a more gradual rise in amplitude of the air mass flow rate and a reduction in Sauter mean diameter.

The ARX model is used in the transfer function calculation [15]. This means the transfer function is written in the form of an IIR filter, with additional noise, i.e.

$$q(x,nT)=\sum_{i=0}^{I-1} a_i(x)m_a[x,(n-i-N)T] + \sum_{k=1}^{K} b_k(x)q[x,(n-k)T]+e(nT). \quad (11)$$

The error $e(t)$ is assumed to be uncorrelated to $q(x,t)$ and independent of frequency. Here AR refer to the autoregressive part (i.e., the earlier output signals) $\Sigma_{k=1}^{K} b_k(x)q[x,(n-k)T]$, and X to the extra input $\Sigma_{i=0}^{I-1} a_i(x)m_a[x,(n-i-N)T]$. The number N is the number of delays from input to output. The predicted transfer functions at 50 Hz, calculated with the random binary signal and the sum of sinusoid signal inputs, are shown in Figs. 9 and 10, respectively. In order to make a comparison, the result obtained from the harmonic forcing calculation in Sec. 2 is also plotted with a dashed line. In both cases, they are in very good agreement. The harmonic and designed forcing signals take similar computing times and it can be seen that they give comparable results for the flame transfer function at this frequency. However, with designed forcing signals, the transfer function is determined as a function of frequency, such as Eq. (7), and is convenient for system identification.

The main advantage of these more carefully designed forcing signals is that, in a single calculation, they provide broadband frequency information. The frequency variation of the transfer function between the rate of heat release and the inlet air flow rate can be calculated directly from Eq. (7). Figure 11 shows this flame transfer function for point A in Fig. 1, a typical location in the primary zone, derived from the results of forcing by the sum of sinusoidal signals. We see clearly that at low frequencies the rate of heat release is in phase with the inlet air velocity. This is direct confirmation of mechanism we identified at point A in Fig. 3: an increase in inlet air velocity, increases the shear and hence the turbulence scalar dissipation rate, which increases the rate of the

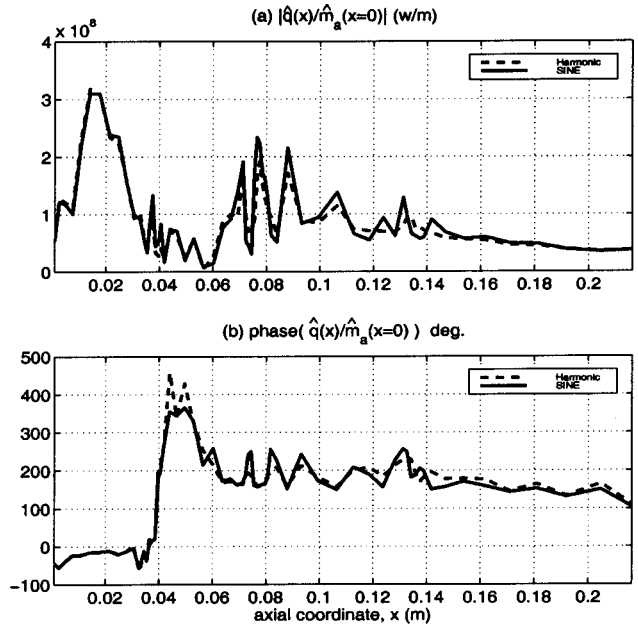

Fig. 10 The transfer function between the heat release rate per unit length and the sinusoidal changes of air flow rate through the atomizer at frequency 50 Hz, where the dashed lines indicate the result from the harmonic forcing calculation and solid lines indicate that from the sum of the random sinusoids forcing calculation

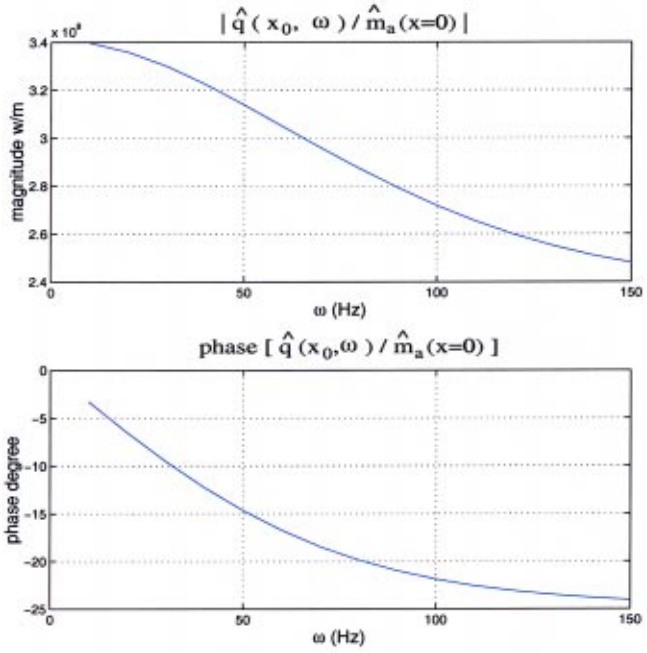

Fig. 11 Magnitude and phase of the transfer function between heat release rate per unit length and air flow rate through the atomizer, for a location $x_0=0.014$ m in the primary zone, calculated by forcing by the sum of random sinusoids

combustion. This can also be demonstrated by the magnitude and phases of the frequency responses of local heat release rate, mixture fraction and scalar dissipation in Fig. 12.

As the frequency increases, the phase of the transfer function tends to decrease linearly, representing a time-delay. Throughout the primary zone, the time delay between the rate of heat release and the inlet air velocity is approximately constant at 1.5 ms a typical recirculation time. At higher frequencies, we see that the

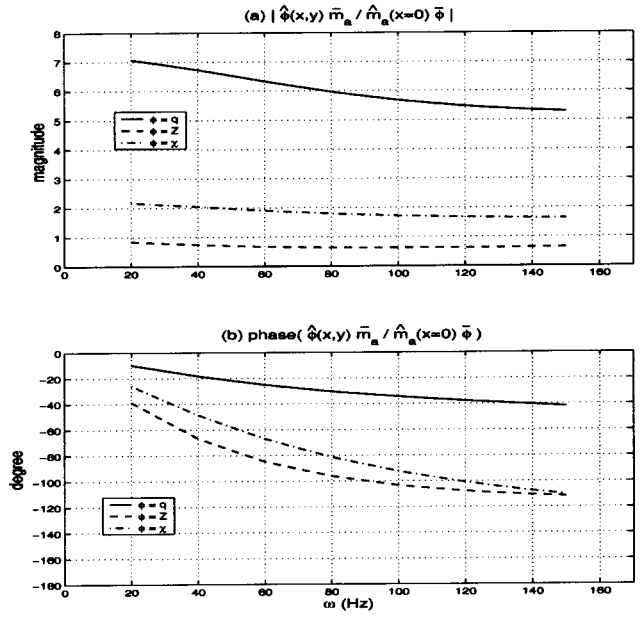

Fig. 12 Magnitudes (*a*) and phases (*b*) of the frequency response of local heat release rate, mixture fraction, and scalar dissipation calculated by forcing by the sum of sinusoids at point A in Fig. 1

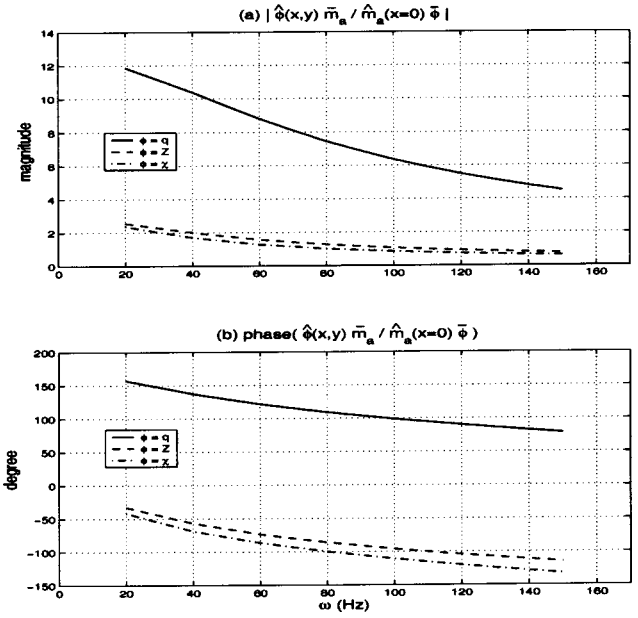

Fig. 13 Magnitudes (*a*) and phases (*b*) of the frequency response of local heat release rate, mixture fraction, and scalar dissipation calculated by forcing by the sum of sinusoids at point B in Fig. 1

magnitude of the transfer function decreases with ω and the phase reduction is less than linear. This structure is typical of a lag-law. For example, a first-order lag-law with system response

$$\tau\frac{dq(t)}{dt}+q(t)=k\dot{m}_a(t), \tag{12}$$

where τ is the time constant and, $k=\overline{q}/\overline{m}_a$, has the frequency response

$$H(\omega,x_i)=\frac{k}{1+i\omega\tau}. \tag{13}$$

The magnitude of this transfer function is $k/(1+\omega^2\tau^2)^{1/2}$; its phase is $-\omega\tau$ for $\omega\tau$ is small and tends to $-90°$ for large $\omega\tau$. Figure 11 shows similar trends, but the amplitude decays somewhat faster with frequency and the phase more slowly.

The magnitude and phase of the frequency response of local heat release rate, mixture fraction and scalar dissipation at point B are shown in Fig. 13. As we noted in the discussion of Fig. 3, at this location, the rate of heat release is mainly influenced by the mixture fraction. From the phase plot we see that at zero frequency the rate of heat release tends to be 180 deg out of phase with the inlet air velocity. Again this reinforces our understanding of the important combustion response. In this region the maximum rate of heat release occurs when the inlet air velocity is low and hence the SMD of fuel droplets is large. When the mixture fraction decreases to the stoichiometric value, the heat release rate is increased due to complete chemical reaction. This generates ''hot spots'' with the opposite phase of that in primary zone propagate to the downstream dilution zone.

The flame transfer function for a downstream location is shown in Fig. 14. As the frequency increases, there is again a linear reduction in phase like a lag-law. At low frequencies, the rate of heat release/unit area again tends to be 180° out of phase with the inlet air velocity: a trend we saw in Fig. 4. The lag-time can be estimated from the phase plot in Fig. 14. It is 3.5 ms at this axial location. In Fig. 15, the variation of the lag-time $\tau(x)$ with the axial coordinate is demonstrated. It increases approximately linearly with x in this downstream region. The propagation velocity can be estimated in terms of its slope $dx/d\tau$. For the current flow

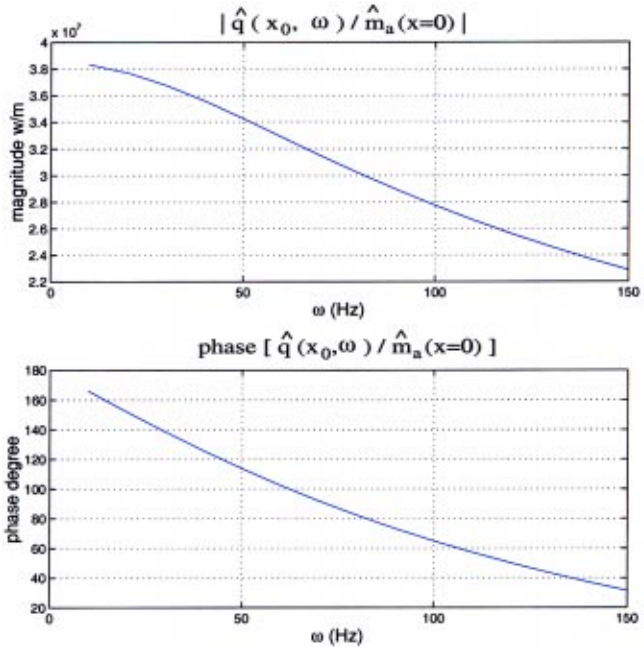

Fig. 14 Magnitude and phase of the transfer function between heat release rate per unit length and air flow rate through the atomiser, for a location $x_0=0.226$ m in the dilution zone, calculated by forcing by the sum of random sinusoids

conditions, it is about 168 m/s, which is in good agreement with CFD results for flow velocities near the combustor center-line. We see that the amplitude of the flame response decreases at higher frequencies and that phase reduction is less than linear, once again, reminiscent of lag-laws.

5 Discussion and Conclusions

In order to understand and eliminate combustion oscillations, it is essential to identify the system through understanding the transfer function, which represents the relationship between the unsteadiness of combustion and the flow rates of inlet fuel and air.

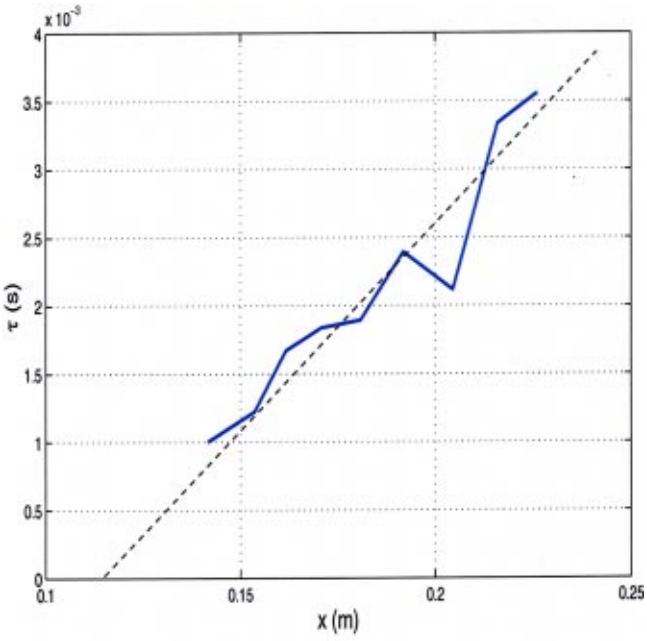

Fig. 15 The lag-time τ against axial coordinate

Table 1 The CPU time and calculation deviation

Case	Forcing*	Impulse	Binary	Sin
t_c hr	96.0	30.0	170.0	170.0
δ	0.0	2.114	0.081	0.101

*at a single frequency.

In current work, the transfer function between the heat release rate per unit length and the air flow rate through the atomizer has been investigated through time-dependent CFD calculations of the combustion processes. Four types of inlet forcing signals were investigated in this study. Each of them has some advantages and disadvantages. First, the transfer function was calculated based on results for harmonic forcing frequency. This gives detailed information about the system at the single forcing frequency. The disadvantage of this method is that the computations are time-consuming and the transfer function for only one particular frequency can be determined at a time. To reduce the computation time, the transfer function is calculated through the use of an IIR filter for which the output signal is the downstream response and the inlet is a short-duration pulse. Although at a single frequency the results are comparable with those obtained by harmonic forcing at same frequency, the influence of noise in the short-duration signal is obvious. Finally, two carefully chosen input signals were studied. These contain the information on the range of interesting frequencies and have a longer time duration. Two kinds of signals were employed: the random binary signal and the sum of the sinusoidal signals. The influence of noise in the CFD calculation was considered in the transfer function calculation. The results show that they are in good agreement with those obtained from the harmonically forced oscillations. The transfer function is determined as a function of frequency. The calculation CPU time and resulting errors in the transfer functions for the four cases are summarized in Table 1. Here the error δ is based on the mean-square error in comparison with the harmonic forcing calculation at 50 Hz, and can be written as

$$\delta=\frac{1}{N}\sum_{i=1}^{N}\left|\frac{H(\omega,x_i)-H_{\text{harmonic}}(\omega,x_i)}{H_{\text{harmonic}}(\omega,x_i)}\right|^2. \tag{14}$$

The advantages and weaknesses of each methods are clearly demonstrated by the numerical information in Table 1.

The transfer function we obtained through this study has helped us to understand the combustion oscillation better. We found that in the primary zone quasisteady response of the rate of heat release is in phase with the inlet air flow rate, higher inlet air velocities resulting in more turbulence and hence an enhanced rate of heat release. At higher frequencies the combustion response displays typical dynamics of a simple lag-law. Near the edge of combustion zone, the unsteady heat release is due to variations in mixture fraction around the stoichiometric value, which is increased by low inlet velocities leading to fuel droplets with large SMD. The important time delays to the ''hot spots'' propagation can be identified from the combustion response at higher frequencies. It is consistent with a convection time delay emanating from CFD calculations.

Several methods for calculating the transfer function have been developed in the present study. In later work, these results will be combined with a one-dimensional linear stability analysis to give predications for instability onset and the frequencies of oscillation. We anticipate that this approach will be particularly useful when the calculation is extended from an axisymmetric geometry to three dimensions. Then it will be very time consuming to use numerical simulations to investigate self-exciting oscillations, but the integration to calculation flame transfer functions using CFD and a linear stability analysis provides a feasible method [16].

Acknowledgments

This work was funded by the Engineering and Physical Sciences Research Council, Rolls-Royce and European Union GROWTH Program, Research project ''ICLEAC: Instability Control of Low Emission Aero Engine Combustors'' Contract No. G4RD-CT2000-0215, whose support are gratefully acknowledged.

Nomenclature

a = coefficient of IIR filter
b = coefficient of IIR filter
D = fuel droplet diameter
$\bar{D}_{32}$ = Sauter mean diameter
f = frequency, Hz
H = flame transfer function
m_a = inlet air mass flow rate
p_0 = inlet total pressure
q = rate of heat release
r = radial coordinate
R = digital filter
t = time
T = sampling period
u = nondimensional forcing signal
V = droplet volume
x = axial coordinate
z = complex number $e^{i\omega T}$
δ = delta function
ω = complex frequency
τ = time lag
σ = error estimate

Subscripts

$\bar{}$ = time average
$\hat{}$ = complex amplitude

References

[1] Zhu, M., Dowling, A. P., and Bray, K. N. C., 2001, ''Self-Excited Oscillations in Combustors With Spray Atomizers,'' Trans. ASME: J. Eng. Gas Turbines Power, **123**, pp. 779–786.

[2] Cumpsty, N. A., and Marble, F. E., 1977, ''The Interaction of Entropy Fluctuations With Turbine Blade Rows: A Mechanism of Turbojet Engine Noise,'' Proc. R. Soc. London, Ser. A, **357**, pp. 323–344.

[3] Marble, F. E., and Candel, S. M., 1977, ''Acoustics Disturbances From Gas Non-Uniformities Convected Through a Nozzle,'' J. Sound Vib., **55**, pp. 225–243.

[4] Lawn, C. J., 2000, ''Thermo-Acoustic Frequency Selection by Swirled Premixed Flames,'' in *Proceedings of the Combustion Institute*, **28**, pp. 823–830, Edinburgh, Scotland.

[5] Lieuwen, T., and Neumeier, Y., 2002, ''Nonlinear Pressure-Heat Release Transfer Function Measurements in a Premixed Combustor,'' in *Proceedings of the Combustion Institute*, **29**, pp. 99–105, Sapporo, Japan.

[6] Bohn, D., Deutsch, G., and Krüger, U., 1998, ''Numerical Prediction of the Dynamic Behavior of Turbulent Diffusion Flames,'' Trans. ASME: J. Eng. Gas Turbines Power, **120**, pp. 713–720.

[7] Hobson, D., Fackrell, J., and Hewitt, G., 1999, ''Combustion Instabilities in Industrial Gas Turbines: Measurements on Operating Plant and Thermoacoustic Modelling,'' ASME Paper No. 99-GT-110, Indianapolis, Indiana, June 1999, ASME International Gas Turbine and Aeroengine Congress and Exhibition.

[8] Krüger, U., Hüren, J., Hoffmann, S., Krebs, W., and Bohn, D., 1999, ''Prediction of Thermoacoustic Instabilities With Focus on the Dynamic Flame Behavior for the 3A-Series Gas Turbine of Siemens KWU,'' ASME Paper No. 99-GT-111, Indianapolis, Indiana, June 1999. ASME International Gas Turbine and Aeroengine Congress and Exhibition.

[9] Polifke, W., Poncet, A., Paschereit, C. O., and Döbbeling, K., 2001, ''Reconstruction of Acoustic Transfer Matrices by Instationary Computational Fluid Dynamics,'' J. Sound Vib., **245**, pp. 483–510.

[10] Kaufmann, A., Nicoud, F., and Poinsot, T., 2002, ''Flow Forcing Techniques for Numerical Simulation of Combustion Instabilities,'' Combust. Flame, **131**, pp. 371–385.

[11] Huang, Y., Sung, H. G., Hsieh, S. Y., and Yang, V., 2003, ''Large-Eddy Simulation of Combustion Dynamics of Lean-Premixed Swirl-Stabilized Combustor,'' J. Propul. Power, **19**, pp. 782–794.

[12] Zhu, M., Dowling, A. P., and Bray, K. N. C., 2002, ''Forced Oscillations in Combustors With Spray Atomizers,'' Trans. ASME: J. Eng. Gas Turbines Power, **124**, pp. 20–30.

[13] Nelson, P. A., and Elliott, S. J., 1992, *Active Control of Sound*, Academic Press, London.

[14] Ljung, L., 1987, *System Identification*, Prentice-Hall, Englewood Cliffs, New Jersey.

[15] Ljung, L., 1991, *System Identification Toolbox User's Guide*, The MathWorks Inc.

[16] Zhu, M., Dowling, A. P., and Bray, K. N. C., 2001, ''Integration of CFD and Low-Order Models for Combustion Oscillations in Aero-Engines,'' ISABE-2001-1088, Bangalore, India, 2–7 September, 2001. XV International Symposium on Air-Breathing Engines.

Lance L. Smith
Hasan Karim
Marco J. Castaldi
Shahrokh Etemad
William C. Pfefferle

Precision Combustion, Inc.,
410 Sackett Point Road,
North Haven, CT 06473

Vivek Khanna
Kenneth O. Smith

Solar Turbines, Inc.,
2200 Pacific Highway,
San Diego, CA 92186

Rich-Catalytic Lean-Burn Combustion for Low-Single-Digit NO_x Gas Turbines

A new rich-catalytic lean-burn combustion concept (trademarked by PCI as RCL) was tested at industrial gas turbine conditions, in Solar Turbines' high-pressure (17 atm) combustion rig and in a modified Solar Turbines engine, demonstrating ultralow emissions of $NO_x<2$ ppm and CO<10 ppm for natural gas fuel. For the single-injector rig tests, an RCL catalytic reactor replaced a single swirler/injector. $NO_x<3$ ppm and CO<10 ppm were achieved over a 110°C operating range in flame temperature, including $NO_x<1$ ppm at about 1350°C flame temperature. Combustion noise was less than 0.15% peak to peak. Four RCL catalytic reactors were then installed in a modified (single can combustor) engine. NO_x emissions averaged 2.1 ppm over the allowable operating range for this modified engine, with CO<10 ppm and without combustion noise (less than 0.15% peak to peak). [DOI: 10.1115/1.1787510]

Introduction

Background. In the last ten years, gas turbine operators have had to comply with increasingly strict exhaust emissions regulations. The exhaust constituents of greatest concern are oxides of nitrogen (NO_x) that can act as smog precursors. To date, improvements in gas turbines have resulted in impressive NO_x emissions reductions to levels below 25 ppm using lean-premixed combustion of natural gas. Despite the large reductions achieved in gas turbine NO_x emissions, there are areas in the U.S. that have even more stringent requirements. Massachusetts and Texas are moving toward NO_x emissions requirements of 9 ppm or less, while areas in California require NO_x emissions as low as 2.5 ppm. In general, NO_x emissions limits have been tightening continuously over the last ten years with California air quality agencies leading the way. This trend is expected to continue.

Catalytic combustion has the potential to provide the needed step change reduction in NO_x emissions down to low single digit levels. The use of a catalytic reactor within the combustion system allows combustor flame temperature (and thus NO_x emissions) to be maintained at levels lower than in today's lean-premixed combustors. Methane and natural gas fuels have been the recent focus of interest, because natural gas is currently the low-emissions fuel of choice for power-generating gas turbines.

For methane oxidation under fuel-lean conditions, however, only Pd-based catalysts are currently practical, because only they offer acceptable activity, lightoff temperature, and resistance to volatilization [1–3]. Unfortunately Pd-PdO catalyst morphology and its reactions with methane are complex, and lead to complex behaviors such as deactivation at high temperature (above about 750°C/1380°F), hysteresis in reaction rate over heating and cooling cycles [4–7], and oscillations in activity and temperature [8–11]. In addition, lightoff and extinction temperatures are well above 300°C (570°F) for fuel-lean reaction on Pd-based catalysts, thus requiring the use of a preburner in many engine applications [12,13].

In addition to these catalyst challenges, commercial acceptance of catalytic combustion by gas turbine manufacturers and by power generators has been slowed by the need for durable substrate materials. Of particular concern is the need for catalyst substrates which are resistant to thermal gradients and thermal shock [12,14,15]. Metal substrates best fill this need, but their temperature must be limited to less than 950°C (1750°F) to assure sufficient material strength and long life. Downstream of the catalyst, combustion temperatures greater than about 1200°C (2200°F) are required for gas-phase reactions to complete the burnout of fuel and CO in a reasonable residence time (on the order of 10 ms). Thus only a portion of the fuel can be reacted on the catalyst.

A major challenge, then, is to limit the extent of reaction within the catalyst bed such that excessive heat does not damage the catalyst or substrate, yet release sufficient heat that downstream gas-phase combustion is stabilized under ultralow emission conditions. For systems which lean-premix fuel and air upstream of the catalyst, the degree of reaction can be limited by chemical reaction rate upon the catalyst, or by channeling within the reactor such that only a limited fraction of the fuel contacts the catalyst. In all cases, however, it is imperative that gas-phase reactions do not occur within the catalyst bed, since this implies a loss of reaction limitation and ultimate overtemperature and failure of the catalyst bed. Preventing such gas-phase reactions is especially challenging in applications to advanced, high-firing temperature turbines, where fuel/air ratios in the catalyst-bed are well within the flammability limits.

Fuel-Rich Catalyst Systems. An alternative means to limiting the extent of reaction is to operate the catalyst fuel rich. In this scenario, there is insufficient oxygen to fully oxidize all fuel in the catalyst bed, and the extent of reaction is therefore limited even if gas-phase reactions occur. To use a fuel-rich catalyst bed in a catalytic combustion system, additional air is introduced downstream of the catalyst so that combustion completion can occur fuel lean. Based on this concept, fuel-rich catalytic reactors were tested by NASA and contractors for liquid fuel applications, and showed good soot-free performance [16,17]. An examination of fuel-rich catalysis on a variety of liquid fuels was also conducted at Yale University under support from NASA [18]. Like the NASA results, this work showed soot-free catalyst performance on a range of fuel types, including a surrogate jet fuel. United Technologies Research Center [19] also investigated fuel-rich

Contributed by the International Gas Turbine Institute (IGTI) of THE AMERICAN SOCIETY OF MECHANICAL ENGINEERS for publication in the ASME JOURNAL OF ENGINEERING FOR GAS TURBINES AND POWER. Paper presented at the International Gas Turbine and Aeroengine Congress and Exhibition, Atlanta, GA, June 16–19, 2003, Paper No. 2003-GT-38129. Manuscript received by IGTI, Oct. 2002, final revision, Mar. 2003. Associate Editor: H. R. Simmons.

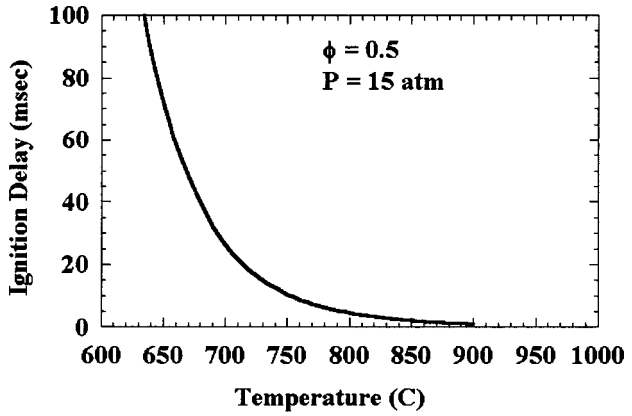

Fig. 1 Autoignition delay time for natural gas, as a function of fuel/air mixture gas temperature

catalytic reaction of liquid fuels, to reduce downstream thermal NO_x generation by removing some heat of reaction prior to gas-phase combustion.

For these liquid fuel applications, ultralow NO_x emissions (<3 ppm) have not been considered feasible because of these fuels' propensity for autoignition during mixing with additional combustion air downstream of the catalyst. Even for natural gas fuel, previous systems have not permitted mixing of raw catalyst effluent with additional combustion air. For example, Acurex tested a two-stage natural gas combustion system having a fuel-rich catalyst stage followed by interstage heat extraction [20]. Additional combustion air was introduced only after heat extraction, and prior to a final fuel-lean catalytic combustion stage.

For natural gas fuels, however, we have found that it is possible to mix catalyst effluent with additional combustion air without incurring autoignition [21]. This is possible because significant improvement in combustion stability is imparted to the downstream fuel-lean combustion even at catalyst effluent temperatures well below the instantaneous autoignition temperature of the effluent. Autoignition delay time is plotted in Fig. 1 for a representative natural gas composition (94.9% CH_4, 3.1% C_2H_6, 0.65% C_3H_8, 0.3% C_4H_{10}, 0.1% C_5H_{12}, 0.1% C_6H_{14}, 0.05% C_7, and higher-order hydrocarbons, and 0.8% diluent) mixed with air at 0.5 equivalence ratio, 15 atm pressure, and varying temperature. The delay times were calculated using the correlation of Spadaccini and Colket [22], and approximately represent the delay time of catalyst effluent after heating by catalytic reaction (vitiation is neglected here). For temperatures below 700°C (1290°F) the autoignition delay time is greater than 25 ms, and for temperatures below 650°C (1200°F) the delay time is greater than 75 ms. These delay times are far greater than the 2–5-ms residence time required to mix catalyst effluent with final combustion air, and are also greater than the typical 10–20 ms residence time of gas turbine combustors.

A simple stirred-reactor combustion model demonstrates that combustion stability is significantly improved when catalytic pre-reaction heats the combustor inlet gases to temperatures in the range of 700°C/1290°F (well below the instantaneous autoignition temperature). A schematic of the stirred-reactor model is shown in Fig. 2. Here, methane and air enter a catalytic reactor at 400°C (752°F) and 15 atm pressure, and are partially reacted to provide an increased inlet temperature to a perfectly stirred reactor (PSR) having 0.5-ms residence time for gas-phase combustion reactions.

The Stanjan equilibrium calculation code [23] and the JANAF thermodynamic data base [24] were used to calculate inlet temperature and composition to the stirred-reactor for varying degrees of reaction over the catalyst, and for varying methane/air equivalence ratios, assuming full oxidation products only (no CO or H_2) and zero heat loss. Stirred-reactor calculations were performed

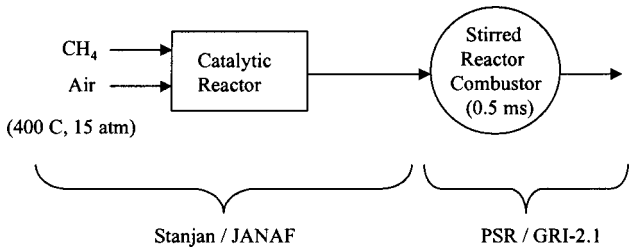

Fig. 2 Schematic of simple stirred-reactor model for calculating effect of catalytic pre-reaction on combustion stability (lean blowout)

using the perfectly stirred reactor (PSR) chemical reaction model from Sandia National Laboratories [25], together with the GRI-2.1 set of gas-phase reaction mechanisms [26].

For each different inlet temperature to the stirred reactor, PSR calculations were initially performed for high equivalence ratio, well above lean blowout. This result was then used as a restart (initial guess) for a PSR calculation at an incrementally lower equivalence ratio, and the process was repeated until the lean blowout point, where reactions in the PSR are extinguished, was found. In this manner, the curve in Fig. 3 was generated, showing the gas temperature (''flame'' temperature) within the PSR reactor at imminent blowout as a function of gas temperature entering the PSR reactor. Note that a 400°C (752°F) inlet temperature to the catalytic reactor is assumed, so that increased inlet temperature to the PSR reactor implies greater catalytic pre-reaction, and greater vitiation of the fuel/air mixture at the PSR inlet.

As seen in Fig. 3, increased inlet temperature improves combustion stability and reduces the lean blowout limit: for example, with catalytic pre-reaction providing 700°C (1290°F) inlet temperature to the PSR, combustion reactions are sustained at a temperature that is 55°C (100°F) lower than the minimum stable combustion temperature without catalytic pre-reaction. At the same time, the 25-ms autoignition delay time at 700°C (1290°F) permits complete mixing of fuel-rich catalytic reaction products with final combustion air, allowing ultralow NO_x emissions from a well-mixed and stable lean combustion zone downstream of the catalyst.

Rich-Catalytic Lean-Burn (RCL) Combustion. In this paper, we present results from full-pressure, full-scale testing of a new rich-catalytic lean-burn (RCL) combustion system based on this concept of stabilizing combustion with catalyst effluent having a temperature below the instantaneous autoignition temperature. The RCL system is shown schematically in Fig. 4. As shown,

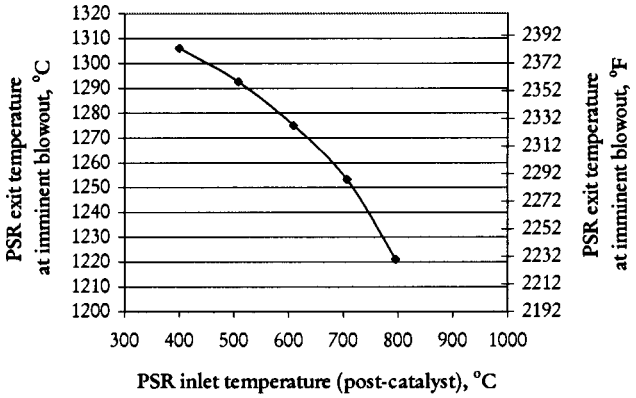

Fig. 3 Gas temperature (''flame'' temperature) within PSR reactor at imminent blowout, as a function of PSR inlet temperature (catalyst exit temperature)

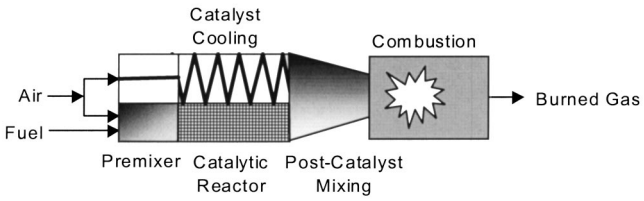

Fig. 4 Schematic of rich-catalytic lean-burn (RCL) system. Catalyst cooling air and fuel-rich catalyst effluent mix prior to lean-premixed gas-phase combustion.

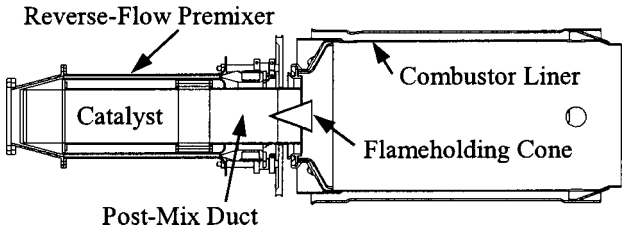

Fig. 5 Assembly of RCL catalytic reactor with 20-cm (8-in.) diameter combustor liner in Solar Turbines' single-injector combustion test facility. Bulk flow is from left to right.

the combustion air stream is split into two parts upstream of the catalyst. One part is mixed with all of the fuel and contacted with the catalyst, while the second part is used to backside cool the catalyst. At the exit of the reactor, the catalyzed fuel/air stream and the cooling air are rapidly mixed to produce a fuel-lean, reactive mixture prior to final combustion. Note that the catalyst is cooled only by primary combustion air, so that no heat is extracted from the system.

With this approach, the fuel-rich mixture contacting the catalyst has insufficient oxygen to completely oxidize all of the fuel, thus limiting the extent of catalyst-stage reaction and enabling limitation of the catalyst-stage operating temperature to a safe value.

Fuel-rich operation of the catalyst provides significant catalyst advantages, including wide choice of catalyst type (non-Pd catalysts are active to methane under fuel-rich conditions), improved catalyst durability (nonoxidizing catalyst environment), and low catalyst lightoff and extinction temperatures. Catalyst extinction temperature is particularly low, and is generally less than 200°C (400°F) for the precious-metal catalysts used in the work reported here (that is, once the catalyst has been lit off, the catalyst remains lit at inlet air temperatures as low as 200°C/400°F). It should also be noted that for catalytic combustion of sulfur-containing fuels, catalyst operating temperatures are sufficiently high that even partially sulfided catalysts are active enough to promote the desired combustion reactions. We also find this to be true during lightoff under fuel-rich conditions, having tested with fuel sulfur levels up to 250 ppm with no increase in catalyst lightoff temperature. A more complete discussion of fuel-rich versus fuel-lean catalyst behavior for methane oxidation is given by Lyubovsky et al. [27].

In this paper, we report two significant experimental milestones in RCL combustion development:

1. Experimental confirmation of the ultralow-NO_x capability of RCL combustion, obtained at full-scale in Solar Turbines' high-pressure (17 atm) single-injector test facility.
2. Demonstration of RCL combustion feasibility for gas turbine engine operation, as shown by ultralow-NO_x operation of a modified (single-can combustor) Solar Turbines Saturn engine.

Single-Injector Tests

Hardware Configuration. A 7.6 cm (3.0 in.) diameter RCL catalytic reactor was fabricated for testing in Solar Turbines' high-pressure single-injector combustion test facility. The catalyst size was chosen to replace a single Solar Taurus 70 (T70) injector, and tests were performed at simulated T70 engine operating conditions as representative of an advanced industrial gas turbine application.

Solar's single-injector test facility is capable of flowing heated air (maximum inlet air temperature of 650°C/1200°F) at a rate of 3.6 kg/s (8 pps) and a pressure of 2.1 MPa (300 psig). Air entering the rig is split into two streams. One stream (primary zone air) flows through the injector and reacts with the fuel while the other stream (dilution air) is used to cool the combustor and is then mixed with combustion products downstream of the primary zone. The percentage of inlet air entering the primary combustion zone is determined by the effective flow area of the combustor liner (including cooling and dilution air holes) versus the effective flow area of the injector.

For the tests reported here, the rig combustor liner was cylindrical, 20 cm (8.0 in.) in diameter, and backside cooled. Four nominally 1.3 cm (0.5 in.) diameter holes were located at the combustor liner's downstream end, to allow the dilution air to enter the combustor after cooling it. The dilution air flow path effective area, including losses during convective cooling along the liner length, was measured at 5.2 cm^2/0.8 $in.^2$ (discharge coefficients included). For comparison, the RCL catalytic reactor effective flow area was approximately 11 cm^2 (1.7 $in.^2$), and there was an additional approximately 1.9 cm^2 (0.3 $in.^2$) effective flow area of leakage. Leakage occurred primarily at the combustor's downstream seal (into the post-combustion flow path), and at the injector insertion seal (grommet seal).

A schematic of the complete RCL combustor assembly, including premixer, catalytic reactor, and downstream combustor liner as tested at Solar is shown in Fig. 5. The catalytic reactor design is described generally in Smith et al. [28], and includes backside cooling of the catalyst. An annular reverse-flow premixer was fitted around the catalytic reactor, to provide a premixed fuel-rich mixture to the catalyst. Note that all fuel entered via this premixer, and all fuel contacted the catalyst. Catalyst cooling air bypassed the premixer, and entered from the left-hand side in Fig. 5. Downstream of the catalyst, but upstream of the combustor, the fuel-rich mixture and the catalyst cooling air were combined in a post-catalyst mixing duct (''post-mix'' duct) to create a partially reacted fuel-lean fuel/air mixture. The premixer, catalytic reactor, and post-mix duct together constitute what we will call the ''RCL injector.'' Conceptually, the RCL injector replaces a conventional dry low-NO_x (DLN) premixer/swirler arrangement, such as Solar's SoLoNO$_x$ injector.

As shown in Fig. 5, the 7.6 cm (3.0 in.) diameter post-mix duct was fitted into a grommet seal at the upstream end of Solar's rig combustor liner, to inject the partially-reacted fuel-lean mixture into the combustor. A flameholding cone (6.5 cm/2.6 in. diameter base, 20 deg half angle) was installed at the exit of the post-mix duct, with the apex of the cone located 4.4 cm (1.7 in.) upstream of the post-mix duct exit plane. Recirculation of hot combustion gases in the cone's wake provided a flame anchor zone in the central part of the combustor (note that the cone remained cool, however, because the shallow 20 deg cone angle prevented recirculating gases from impinging on the cone's interior surface). The expansion (dump) of the combustor liner's dome also served to anchor combustion. In general, the catalyst is intended to improve combustion stability and turndown at the flame anchor point, but is not necessarily intended to provide gas-phase ignition. Solar's torch igniter was used to ignite gas-phase combustion during rig testing.

Test Conditions (Simulated T70). Steady-state combustion tests were performed at single-injector T70 full-load airflow conditions, as listed in Table 1. Fuel flow rate was the primary parameter varied, to measure catalyst and combustor performance as a function of fuel/air ratio (adiabatic flame temperature). In addi-

Table 1 Nominal T70 combustor inlet conditions at full load (before catalytic reaction), for a single injector

Combustor Inlet Temperature	430 C (800 F)
Combustor Inlet Pressure	1.7 MPa (250 psia)
Combustor Air Flow / Injector	1.8 kg/s (4 pps)
Combustor Fuel Flow / Injector	0.04 kg/s (0.09 pps)

tion, inlet temperature was ramped up during catalyst lightoff, and transient data were obtained to capture the lightoff event. It should also be noted that torch ignition of the combustor was performed at partial pressure (based on torch igniter limitations), and the rig was then brought to full pressure and full flow after ignition.

For a single T70 injector (one of 12 in a T70 engine) combustor airflow at full load is about 1.8 kg/s (4 pps), as listed in Table 1. For ultralow-NO_x lean-premixed combustion at full load fuel flow, about 1.2 kg/s (2.7 pps) air should pass through the injector into the combustor primary zone, leaving about 0.6 kg/s (1.3 pps) air for combustor liner cooling (including leakage air). In the single-injector rig, however, the combustor liner dilution holes were sized at nominally 0.5-in. (1.3-cm) diameter, and were not resized to provide this air split for the RCL injector. Instead, rig total airflow was adjusted to give 1.2 kg/s (2.7 pps) air to the RCL injector (combustor primary zone) as desired. The liner was then slightly overcooled. This overcooling is assumed to have minimal effect on RCL combustion performance.

For the tests reported here, the emissions rake was located just upstream of the combustor dilution air holes, or about 38 cm (15 in.) downstream of the post-mix duct exit. This corresponds to about 30 ms combustor residence time at the nominal T70 full load conditions, for 1.2 kg/s (2.7 pps) air to the combustor primary zone. The emissions rake consisted of a water-cooled area-averaging single diametral probe in a fixed position. The probe was considered nonintrusive (no impact on flow, CO quenching, or flameholding) because it was located well downstream of the primary combustion zone.

The emissions rake feeds gas samples to Solar's emissions train, consisting of analyzers for NO_x, CO, UHC, O_2, and CO_2. The UHC sample is not dried, but all other analyzers receive a chiller-dried sample. The NO_x analyzer range is 25 ppm at its most sensitive setting, with an accuracy better than 2% of full scale (0.5 ppm). The analyzers are zeroed and calibrated twice each day, and a linearity check is performed on the NO_x analyzer monthly, using a range of gases including a zero gas and a bottom-end calibration gas of 5 ppm NO.

Test Results (Simulated T70). With San Diego natural gas fuel flowing through the catalyst bed (giving 0.55 equivalence ratio at the RCL injector exit), and with the downstream combustor ignited and providing burnout, the rig inlet air temperature was ramped up from approximately 320 to 420°C (610 to 790°F) at 15 atm pressure. At a temperature just over 320°C (610°F) the catalyst became active, and the catalyst surface temperature increased to a value well above the 320°C (610°F) inlet temperature. This event is shown below in Fig. 6, where catalyst surface temperature is plotted versus rig inlet air temperature. The data points in Fig. 6 were obtained at 1-sec intervals. Catalyst surface temperatures were measured by thermocouples attached to the metal catalyst substrate.

After catalyst lightoff, rig temperature was increased to give a T70 full load condition of about 430°C (810°F) inlet air temperature. At steady airflow conditions, fuel flow was increased to a value above the full load fuel flow condition, and steady-state data were obtained. Fuel flow was then decreased incrementally, and steady-state data were obtained at each increment, until combustion approached lean blowout as indicated by rapidly increasing

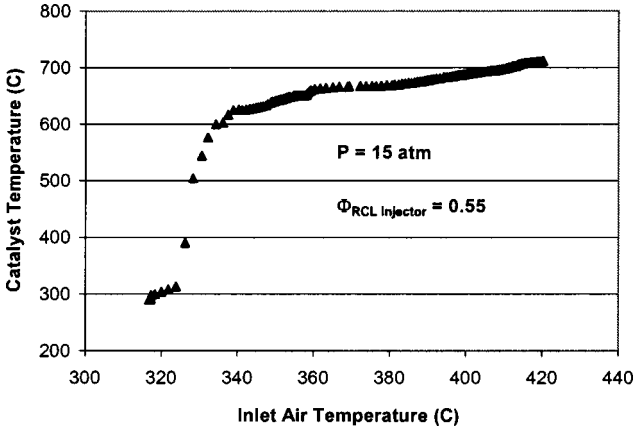

Fig. 6 Catalyst lightoff in Solar's single-injector rig. Lightoff occurs at about 320°C (610 F) inlet air temperature.

and/or fluctuating CO emissions. The rig was not operated with the flame blown off, to prevent unburned fuel from accumulating in the exhaust duct and test area.

Figure 7 shows steady-state catalyst surface temperatures plotted against adiabatic flame temperature at the RCL injector exit, prior to addition of any leakage or cooling air. Adiabatic flame temperature is calculated for San Diego natural gas in air at 432°C (810°F) inlet air temperature and 21°C (70°F) inlet fuel temperature. For this calculation, fuel/air ratio at the injector exit was calculated based on total fuel and air flows together with the injector, liner, and rig leakage effective flow areas. At several steady-state conditions, gas samples were extracted from the RCL injector exit and analyzed by gas chromatograph (GC) to provide independent confirmation of injector fuel/air ratio.

As shown in Fig. 7, catalyst surface temperature increased only slightly as fuel flow was reduced. All catalyst surface temperature measurements remained below 780°C (1430°F) over the complete range of operating conditions tested (1440–1700°C/2620–3090°F range in adiabatic flame temperature).

RCL catalyst temperatures do not vary significantly with fuel/air ratio because reaction rate (heat release) upon the catalyst surface is controlled by oxygen flow (air flow) under fuel-rich conditions, and because heat removal (heat transfer) from the catalyst is also determined primarily by air flow. Fuel flow has little effect on reaction rate and little effect on heat removal rate. These results hold for the case where catalyst selectivity and hence heat of

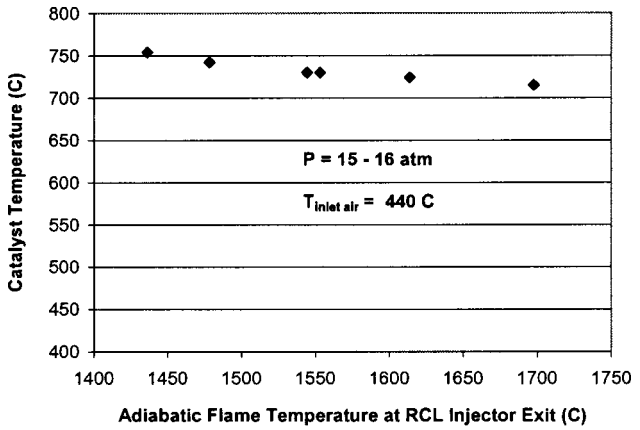

Fig. 7 Catalyst surface temperature as a function of adiabatic flame temperature at RCL injector exit. Data obtained at nominal T70 airflow conditions.

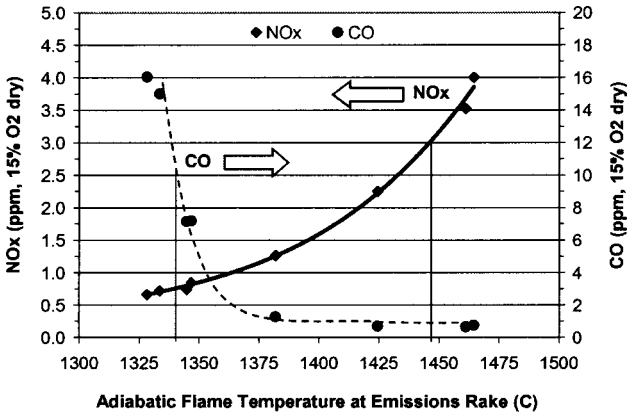

Fig. 8 NO_x and CO emissions, as a function of adiabatic flame temperature at emissions rake. Data obtained at 16 atm pressure, and at nominal T70 airflow conditions.

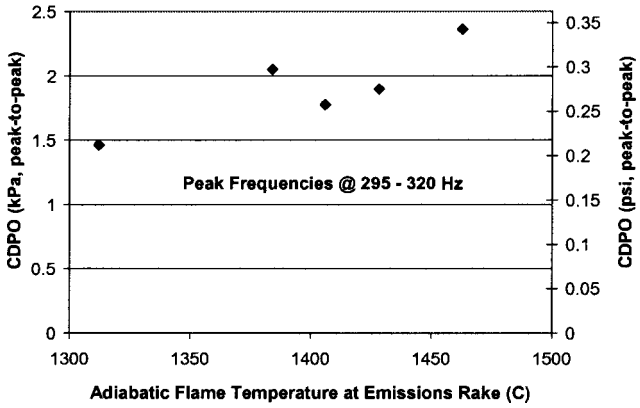

Fig. 9 Combustor-driven pressure oscillations (CDPO) for RCL combustion, at flame temperatures from about 1310 to 1470°C (2390 to 2680 F). Pressure oscillations remained less than 2.4 kPa (0.35 psi) peak to peak for all conditions tested.

reaction do not vary with fuel/air ratio. For the results presented here, the catalyst was primarily selective to full oxidation products (CO_2 and H_2O) over the range of fuel/air ratios tested.

NO_x and CO emissions from RCL combustion testing are plotted in Fig. 8 as a function of adiabatic flame temperature at the emissions rake. Fuel/air ratio at the emissions rake was calculated from measured O_2 and CO_2 concentrations, and the corresponding adiabatic flame temperature was then calculated for San Diego natural gas in air at 432°C (810 F) inlet air temperature and 21°C (70°F) inlet fuel temperature. NO_x and CO emissions are reported after correction to 15% O_2 on a dry basis. UHC emissions are reported on a wet basis, corrected to 15% O_2.

As shown in Fig. 8, the RCL combustion system achieved ultralow emissions over a wide operating window of approximately 110°C (200°F) variation in flame temperature, with CO below 10 ppm and NO_x below 3 ppm (and as low as 1 ppm). Unburned hydrocarbons (UHC) remained less than 2 ppm at all conditions shown in Fig. 8.

As measured at the emissions rake (located just upstream of the combustor dilution holes) the primary zone adiabatic flame temperature varied from about 1340 to 1450°C (2440 to 2640°F) during ultralow-emissions operation, as shown in Fig. 8. Gas samples extracted from the RCL injector exit and analyzed by GC, however, showed that the adiabatic flame temperature exiting the injector was about 130°C (230°F) higher than the primary zone adiabatic flame temperature. The indication is that leakage air entered the primary combustion zone, most likely at the grommet seal between the Solar rig combustor liner and the RCL injector. Imperfect mixing of this leakage air with the injector's fuel/air mixture can increase NO_x emissions to values slightly higher than expected for perfectly premixed combustion at the adiabatic flame temperatures measured at the emissions rake. In fact, the NO_x emissions shown in Fig. 8 are about 1 ppm higher than expected at 1450°C (2650°F) based on perfectly premixed combustion.

For the data shown in Fig. 8, the total combustor pressure drop, from air inlet to combustor exit, was less than 5% of the combustor inlet pressure. Pressure drop will be reduced to about 3% in future work, by enlarging the catalyst cross-sectional area and by using a more open catalyst bed. Combustion-driven pressure oscillations (noise) were also monitored, and remained less than 2.4 kPa (0.35 psi) peak to peak (less than 0.15% peak to peak of mean combustor pressure) at all conditions tested, indicating quiet operation. Low levels of combustion noise were expected, since gas-phase energy release in the combustor (the driving force for combustion noise) is reduced when a portion of the fuel is catalytically reacted prior to gas-phase combustion. For the single-injector rig combustor, peak noise occurred in the 295–320-Hz range; peak noise in this range is plotted in Fig. 9 for RCL combustion at adiabatic flame temperatures from about 1310 to 1470°C/2390 to 2680°F (based on emissions rake O_2 and CO_2 concentrations).

The high-pressure ultralow-emissions results obtained using the RCL combustion system demonstrate that it is possible to mix fuel-rich catalyst effluent with final combustion air, without inducing autoignition, yet imparting significant combustion stability to the downstream combustion process. Thus fuel-rich catalytic reactions can stabilize fuel-lean premixed combustion to provide stable, quiet combustor operation with ultralow NO_x and CO emissions.

Rig Test at Saturn-Engine Conditions. As discussed in more detail below (next section), four RCL injectors were fabricated for engine testing in a modified Solar Saturn engine. Each injector had the same basic design and dimensions as the original single RCL injector tested at T70 conditions described above. One of the four Saturn-bound RCL injectors was tested in Solar's single-injector test rig. The purpose of this test was to evaluate RCL operation at low inlet temperature, prior to actual Saturn engine testing. In particular, it was desired to confirm catalyst activity (maintained lightoff) at low inlet temperature (e.g., Saturn half load combustor inlet temperature of 215°C/420°F), and to also measure achievable combustor emissions at these low inlet temperatures.

Three operating points for the modified Saturn engine were selected for single-injector tests, as listed in Table 2. Based on one-quarter Saturn-engine fuel flow (for one of four injectors), a full load RCL injector airflow of 0.6 kg/s (1.3 pps) was selected to provide ultralow-emissions lean-premixed combustion. For part-load testing, injector airflow was scaled according to combustor inlet pressure.

Table 2 Nominal Saturn-engine combustor inlet conditions for modified (catalytic) Saturn engine

Saturn Combustor Inlet Cond.	57% LOAD	74% LOAD	100% LOAD
Temperature	215C / 415F	225C / 440F	250C / 485F
Pressure	4.85 atm	5.41 atm	6.15 atm
Emissions from Single Injector Rig	<2 ppm NO_x <6 ppm CO	<2 ppm NO_x <5 ppm CO	<2 ppm NO_x <2 ppm CO

Because the Saturn-engine combustor inlet temperature is below the catalyst lightoff temperature (but above the catalyst extinction temperature) the test procedure included a catalyst lightoff transient wherein the rig inlet temperature was increased to about 360°C (680°F) to ensure catalyst lightoff. This catalyst lightoff procedure (rig inlet temperature ramp) was performed at Saturn full-load flows and pressure (Table 2), with the downstream combustor ignited and providing burnout. To confirm the low catalyst extinction temperature, rig inlet air temperature was then decreased to the Saturn combustor inlet temperature (e.g., 250°C/485°F for Saturn full load conditions). After lightoff the catalyst remained lit at all conditions tested, including no-preburner combustor inlet temperatures (catalyst inlet temperatures) as low as 215°C (415°F).

For each Saturn load condition tested, rig airflow conditions (flow rate, pressure, and temperature) were established and then fuel flow was varied to determine optimal emissions. This simulated, approximately, combustor tuning in the modified Saturn-engine via variable airflow valves (discussed in more detail below, next section). At selected points, fuel/air ratio at the RCL injector exit was confirmed by gas sample extraction and GC analysis.

RCL combustor emissions are listed in the bottom row of Table 2, for each airflow load condition tested. In general, NO_x emissions below 2 ppm were achievable with CO below 10 ppm at all inlet temperatures tested, including inlet temperatures as low as 215°C (415°F). UHC emissions were below 2 ppm for all conditions listed in Table 2.

Saturn Engine Operation

Based on the successful single-injector rig tests, a ''cluster'' of four RCL injectors was installed in a modified (single can combustor) Saturn engine, to assess controls compatibility and transient operation in an engine environment, including engine start, acceleration, and load variation. In addition, steady-state operating data were obtained, including NO_x and CO emissions at the engine exhaust. The engine test also provided a basis for evaluating RCL reactor robustness in an engine environment, over a range of operating conditions and demands (including start, acceleration, and load).

Test Engine Specifications and Configuration. The test engine was a modified version of a two-shaft recuperated Saturn T1200 engine, nominally rated at 750 kW (1000 hp) after modification. This engine was selected as a test bed because its external combustor configuration was amenable to modification. For the tests reported here, the recuperator was removed, but the compressor discharge scroll and turbine inlet scroll were retained, allowing a single side-mounted combustor can to be installed.

The overall combustor configuration is shown in Fig. 10. Note that variable airflow butterfly valves were fitted in the combustor primary zone air pipe and the dilution air pipe, to allow combustor air to be varied for best emissions at any given fuel flow (engine load). Also note that a preburner was located in the combustor primary zone air pipe below the butterfly valve, to temporarily increase catalyst inlet air temperature to about 350°C (660°F) to ensure catalyst lightoff. The preburner was turned off after catalyst lightoff, and before engine emissions were measured.

The multiport gas-sampling probe was mounted in the engine exhaust stack and used to gather gas samples for emissions analysis. Gas samples were transported from the probe to the emissions analyzers through heated hoses.

The cluster of four RCL injectors were assembled in the Saturn-engine combustor, parallel to one another in a square array as shown in the photograph in Fig. 11. Each RCL catalytic reactor was 7.6 cm (3 in.) in diameter. A flameholding cone was positioned at the end of each post-mix duct, as in the single-injector rig tests described above. Each RCL injector was also fitted with an annular reverse-flow premixer, located outside the catalytic reactor housing, as in the single-injector rig tests. Note that the perforated duct upstream of the RCL injectors (visible in the photograph of Fig. 11) was for inlet airflow conditioning, since air entered the combustor housing from the top, as shown in Fig. 10. The perforated duct was hollow (except for instrumentation and fuel lines) and did not perform any fuel/air premixing functions.

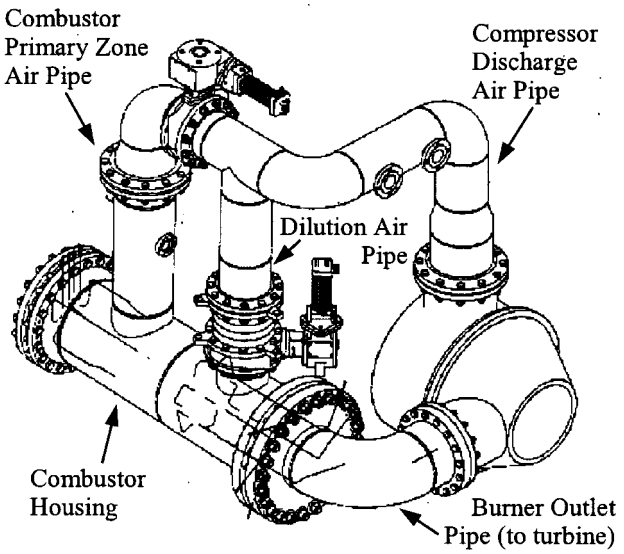

Fig. 10 Side-mounted combustor configuration in modified Saturn engine, showing variable airflow control valves in primary zone air pipe and dilution air pipe

All fuel and air entered the combustor through the four RCL injectors (neglecting leakage air). The combustor liner was backside cooled with dilution air, before the dilution air entered the hot gas path 60 cm (24 in.) downstream of the combustor's upstream end (the round plate through which the post-mix ducts are inserted, visible in Fig. 11, forms the combustor's upstream end). The combustor liner itself was cylindrical and 38 cm (15 in.) in diameter. At full Saturn engine load, and assuming 0.6 kg/s (1.3 pps) airflow through each RCL injector for ultralow-emissions operation, combustor residence time is about 35 ms.

Engine Operating Procedure. Engine start-up data are shown in Fig. 12, with annotations, giving a graphical depiction of the startup procedure. Note that there are three fuel circuits: a preburner fuel stage, which received about 25 kg/h (55 pph) fuel during catalyst lightoff, and two RCL injector fuel stages, which

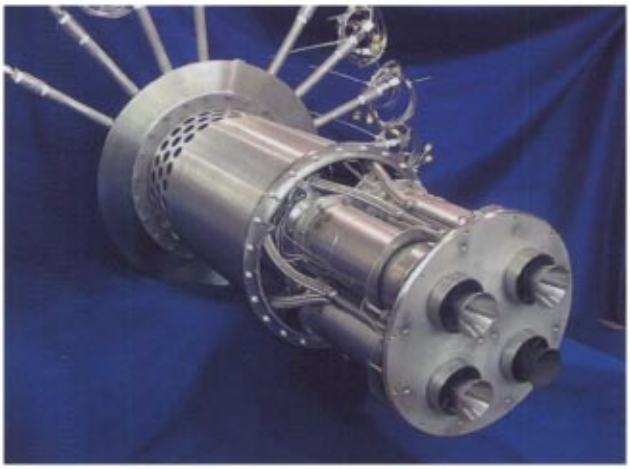

Fig. 11 Photograph of four-RCL-injector assembly, prior to installation in Saturn engine

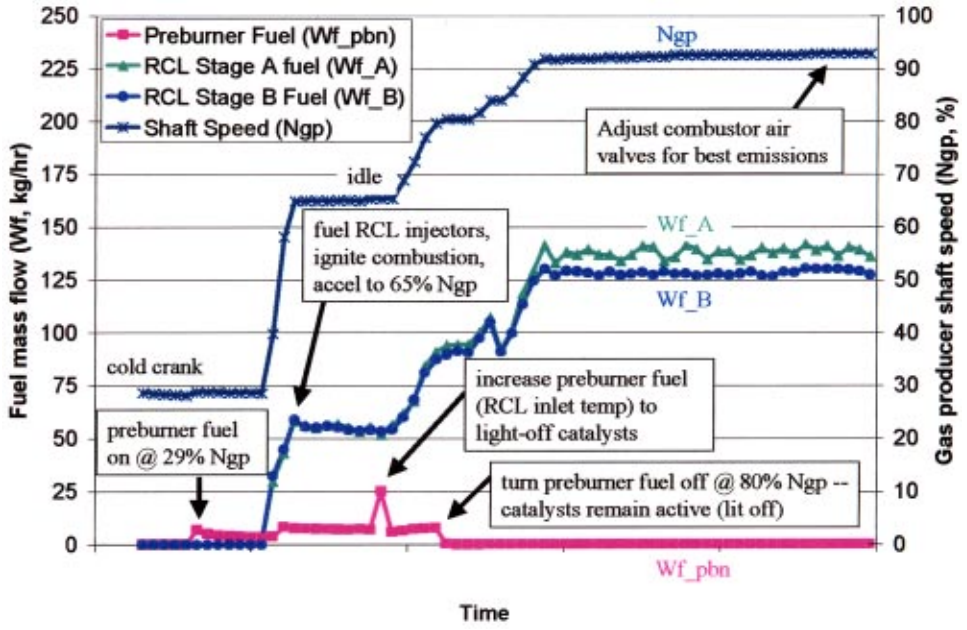

Fig. 12 Saturn engine start-up data, obtained using RCL combustion, showing engine acceleration, catalyst activation by preburner (followed by preburner shutoff with continued catalyst activity), and loading of engine

together received up to about 275 kg/h (600 pph) fuel at load. RCL fuel stage A supplied fuel to the top two injectors, while RCL fuel stage B supplied fuel to the bottom two injectors. Each stage was separately adjustable, so that fuel/air ratio could be equalized for all injectors (for minimum NO_x emissions) even if airflow was asymmetric between the top and bottom injectors. Top-bottom airflow asymmetry was anticipated because primary-zone air entered the combustor casing from the top, as shown in Fig. 10. GC analysis of gas samples from each of the four RCL injector exits, however, showed little airflow asymmetry during engine operation.

At cold crank conditions (29% gas producer shaft speed, Ngp) the preburner was ignited and adjusted to 260°C (500°F) outlet temperature, below the catalyst lightoff temperature. As seen in Fig. 12, the small preburner fuel flow provided little motive power to the engine and negligible increase in engine speed. Next, while still at 29% Ngp, fuel was introduced to the RCL injectors and combustion was ignited by a torch igniter in the main combustor. With the starter motor still engaged, fuel flow was ramped up as the engine accelerated to 65% Ngp. At 65% Ngp the starter motor was disengaged and the engine controller added fuel to maintain a constant idle speed of 65% Ngp (no load). Preburner outlet temperature remained at 260°C (500°F), and the catalysts remained inactive.

Preburner temperature was then increased to about 350°C (660°F) to ensure catalyst lightoff. Engine speed was increased to 80% Ngp, the preburner was turned off, and the catalysts remained active. Engine speed was then increased to 90% and the variable airflow valves were adjusted to obtain optimum emissions. The valves served to vary the airflow to the RCL injectors thus allowing control of NO_x and CO emissions. Emissions data were taken as engine speed was reduced in increments of about 1% Ngp. The airflow valves were adjusted for best emissions at each speed.

Engine controls were based on a Saturn T1202R design and used a state of the art Allen-Bradley microprocessor console to run the logic. For the RCL combustor engine tests, catalyst temperatures were not used in the fuel control algorithm. Instead, fuel control was performed according to standard DLN methods (primarily monitoring engine speed versus set point), with the addition of a preburner fuel control during initial start and catalyst lightoff. This was possible because catalyst temperature is insensitive to fuel/air ratio under fuel-rich conditions, as shown in Fig. 7 for the single-injector rig tests. In addition, the RCL catalyst is air cooled by a large fraction of the total combustion air, and reactions on the catalyst are limited by available oxygen (fuel-rich); thus the catalyst is resistant to flashback, autoignition, and overheating damage, and can operate safely without active temperature control.

Engine Performance With RCL Combustor. With RCL combustion, Saturn engine NO_x emissions averaged 2.1 ppm with less than 10 ppm CO over an achievable engine operating range (82–89% Ngp), as shown in Fig. 13. Over this engine operating range, UHC emissions remained below 3 ppm, and combustion-driven pressure oscillations (CDPO) remained less than 0.7 kPa (0.1 psi) peak to peak (less than 0.15% peak to peak of mean combustor pressure).

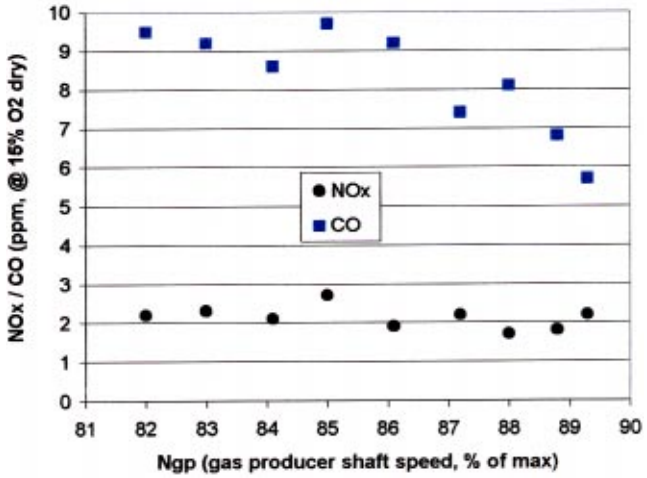

Fig. 13 RCL combustor emissions during Saturn engine operation, showing ultralow NO_x and CO emissions over an achievable engine operating range of 82–89% speed

Table 3 Saturn engine operating data at low-end and high-end of achievable operating range. Note catalyst activity and ultralow emissions achieved at inlet temperatures as low as 191°C (376°F).

Engine Speed	82% Ngp	89% Ngp
NOx Emissions	2.2 ppm	2.2 ppm
CO Emissions	9.5 ppm	5.7 ppm
CDPO (noise)	< 0.7 kPa pk-pk	< 0.7 kPa pk-pk
Power Output	237 kW / 318 hp	453 kW / 607 hp
Nominal Load	32%	61%
Comb. Inlet Pressure	3.9 atm	5.0 atm
Comb. Inlet Temp.	191 C / 376 F	223 C / 434 F

At 89% Ngp, combustor inlet air (compressor discharge air) was at 5.0 atm and 223°C (434°F). At 82% Ngp, combustor inlet air was at 3.9 atm and 191°C (376°F). For all data points shown in Fig. 13 the preburner was turned off, the catalyst remained active at the available compressor discharge temperatures (as low as 191°C/376°F), and NO_x emissions remained below 3 ppm.

Measured power output ranged from 237 kW (318 hp) to 453 kW (607 hp) over the 82–89% Ngp operating range, or about 32–61% load based on a 750-kW (1000-hp) nominal power rating for this modified engine. Engine load was delivered to a water dynamometer.

Engine operation was limited to the 82–89% speed range. At less than 82% Ngp the compressor was at its surge condition, and the compressor bleed valve was opened to prevent surge. This reduced the airflow to the RCL modules thus increasing NO_x emissions. At speeds greater than 89% Ngp operation was limited by locally hot temperatures within the scroll ducting downstream of the combustor. This limitation was not attributable to the RCL combustion technology but to inadequate mixing of combustor dilution air. Improving the test rig dilution mixing was deemed unnecessary to document the controllability of the RCL system.

Table 3 summarizes the Saturn engine operating data at the low-end and high-end of the achievable operating range. In general, the results show good combustor performance (low emissions and low noise) even at very low inlet temperatures. In addition, the Saturn engine operation shows the feasibility of engine startup, acceleration, and operation at load using RCL combustion with simple engine controls. The engine was successfully started, accelerated, and powered at load by fuel injected through the four catalytic reactors, using conventional engine instrumentation and controls without instrumentation input from the catalyst.

Other Engine Applications

In general, implementation of RCL combustion in a gas turbine engine requires consideration for size and pressure drop. Comparing a lean-premixed swirler/injector to an RCL catalytic reactor at equal airflow, one finds that pressure drop is greater through the RCL reactor if the swirler annulus (where the vanes are located) is simply replaced with an RCL reactor, to give equivalent frontal area. However, additional frontal area can be obtained by reducing or eliminating the existing swirler hub, by increasing injector diameter, or by re-design of the injector configuration (size, shape, and/or number of injectors). For example, in the Solar T70 application considered here, pressure drop for the RCL system approached 5% for a 7.6 cm (3.0 in.) diameter RCL (with no hub) designed to replace an approximately 6.5 cm (2.5 in.) diameter swirler (with hub).

While it is often possible to fit the complete RCL combustion system within an existing engine envelope, if insufficient frontal area is available to meet the pressure drop requirements an RCL catalytic pilot approach can be adopted [29], using a combination of RCL catalytic reactors and lean-premixed swirlers/injectors.

Conclusions

A new rich-catalytic lean-burn (RCL) combustion concept was tested at gas turbine conditions, first in a full-scale full-pressure single-injector rig, and second in a modified industrial gas turbine. These constitute two significant experimental milestones:

1. Experimental confirmation of the ultralow-NO_x capability of the RCL combustion concept. In particular, we confirm the ability to mix fuel-rich catalyst effluent with primary combustion air, without inducing autoignition, yet imparting significant stability to the downstream combustion process.
2. Demonstration of RCL combustion feasibility for gas turbine engine operation. In particular, we demonstrate engine startup, acceleration, and operation at load by fuel injected only through RCL injectors (effectively a single fuel stage, with all fuel contacting the catalyst), and with simple engine controls that do not monitor catalyst temperature.

In summary, the data presented here show that fuel-rich catalytic reactions can stabilize fuel-lean premixed combustion to provide stable, quiet combustor operation with ultralow NO_x and CO emissions. In addition, the air-cooled fuel-rich catalyst system can operate safely without active temperature control because its temperature is insensitive to fuel/air ratio.

Acknowledgments

We would like to acknowledge the U.S. Department of Energy Office of Power Technologies, Distributed Energy Resources Program for being instrumental in supporting development of the RCL concept. We appreciate the encouragement and support provided by our contract monitor Mr. Steve Waslo from DOE's Chicago Office.

References

[1] Lee, J. H., and Trim, D. L., 1995, "Catalytic Combustion of Methane," Fuel Process. Technol., **42**, pp. 339–359.
[2] Dalla Betta, R. A., 1997, "Catalytic Combustion Gas Turbine Systems: The Preferred Technology for Low Emissions Electric Power Production and Co-Generation," Catal. Today, **35**, pp. 129–135.
[3] Forzatti, P., and Groppi, G., 1999, "Catalytic Combustion for the Production of Energy," Catal. Today, **54**, pp. 165–180.
[4] Farrauto, R. J., Hobson, M. C., Kennelly, T., and Waterman, E. M., 1992, "Catalytic Chemistry of Supported Palladium for Combustion of Methane," Appl. Catal., A, **81**, pp. 227–237.
[5] Farrauto, R. J., Lampert, J. K., Hobson, M. C., and Waterman, E. M., 1995, "Thermal Decomposition and Reformation of PdO Catalysts; Support Effects," Appl. Catal., B, **6**, pp. 263–270.
[6] McCarty, J. G., 1995, "Kinetics of PdO Combustion Catalysis," Catal. Today, **26**, pp. 283–293.
[7] Rodriguez, N. M., Oh, S. G., Dalla-Betta, R. A., and Baker, R. T. K., 1995, "*In Situ* Electron Microscopy Studies of Palladium Supported on Al_2O_3, SiO_2, and ZrO_2 in Oxygen," J. Catal., **157**, pp. 676–686.
[8] Dalla Betta, R. A., Shoji, T., Tsurumi, K., and Ezawa, N., 1994, "Partial Combustion Process and a Catalyst Structure for Use in the Process," U.S. Patent No. 5,326,253.
[9] Furuya, T., Sasaki, K., Hanakata, Y., Ohhashi, T., Yamada, M., Tsuchiya, T., and Furuse, Y., 1995, "Development of a Hybrid Catalytic Combustor for a 1300°C Class Gas Turbine," Catal. Today, **26**, pp. 345–350.
[10] Ozawa, Y., Tochihara, Y., Mori, N., Yuri, I., Kanazawa, T., and Sagimori, K., 1998, "High Pressure Test Results of a Catalytically Assisted Ceramic Combustor for a Gas Turbine," ASME Paper No. 98-GT-381, Stockholm, Sweden, 2–5 June 1998.
[11] Carroni, R., Schmidt, V., and Griffin, T., 2002, "Catalytic Combustion for Power Generation," Catal. Today, **75**, pp. 287–295.
[12] Kolaczkowski, S. T., 1995, "Catalytic Stationary Gas Turbine Combustors: A Review of the Challenges Faced to Clear the Next Set of Hurdles," Trans. Inst. Chem. Eng., Part A, **73**, pp. 168–190.
[13] Fant, D. B., Jackson, G. S., Karim, H., Newburry, D. M., Dutta, P., Smith, K. O., and Dibble, R. W., 2000, "Status of Catalytic Combustion R&D for the Department of Energy Advanced Turbine Systems Program," ASME J. Eng. Gas Turbines Power, **122**, pp. 293–300.
[14] Hayes, R. E., and Kolaczkowski, S. T., 1997, *Introduction to Catalytic Combustion*, Gordon and Breach, Amsterdam, pp. 33–34.
[15] Johansson, E. M., Papadias, D., Thevenin, P. O., Ersson, A. G., Gabrielsson, R., Menon, P. G., Bjornbom, P. H., and Jaras, S. G., 1999, "Catalytic Com-

bustion for Gas Turbine Applications,'' Catalysis, **14**, pp. 183–235.
[16] Rollbuhler, R. J., 1991, ''Fuel-Rich, Catalytic Reaction Experimental Results,'' *27th Joint Propulsion Conference*, Sacramento, CA, 24–27 June, 1991, NASA Technical Memorandum 104423, AIAA Paper No. 91-2463.
[17] Brabbs, T. A., and Merritt, S. A., 1993, ''Fuel-Rich Catalytic Combustion of a High Density Fuel,'' NASA Technical Paper 3281.
[18] Kraemer, G. O., 1996, ''Fuel-Rich Catalytically Stabilized Combustion for Aircraft Engine Applications,'' Ph.D. thesis, Yale University.
[19] Colket, M. B., Kesten, A. S., Sangiovanni, J. J., Zabielski, M. F., Pandy, D. R., and Seery, D. J., 1993, ''Method and System for Combusting Hydrocarbon Fuels With Low Pollutant Emissions by Controllably Extracting Heat From the Catalytic Oxidation Stage,'' U.S. Patent No. 5,235,804.
[20] Kesselring, J. P., Krill, W. V., Chu, E. K., and Kendall, R. M., 1979, ''Development of Catalytic Combustion Systems,'' *Proc. New Fuels and Advances in Combustion Technologies Symp.*, New Orleans, LA, 26–30 March.
[21] Pfefferle, W. C., Smith, L. L., and Castaldi, M. J., 2002, ''Method and Apparatus for a Fuel-Rich Catalytic Reactor,'' U.S. Patent No. 6,358,040.
[22] Spadaccini, L. J., and Colket, M. B., 1994, ''Ignition Delay Characteristics of Methane Fuels,'' Prog. Energy Combust. Sci., **20**, pp. 431–460.
[23] Reynolds, W. C., 1986, ''The Element Potential Method for Chemical Equilibrium Analysis: Implementation in the Interactive Program STANJAN,'' Version 3, January 1986, Department of Mechanical Engineering, Stanford University.
[24] Chase, M. W., Curnutt, J. L., Downey, J. R., McDonald, R. A., Syverud, A. N., and Valenzuela, E. A., 1982, J. Phys. Chem. Ref. Data, **11**, pp. 695–940.
[25] Glaborg, P., Kee, R. J., GrCar, J. F., and Miller, J. A., 1992, ''PSR: A Fortran Program for Modeling Well-Stirred Reactors,'' Sandia National Laboratories Report, SAND86-8209, reprinted February 1992.
[26] Frenklach, M., Wang, H., Goldenberg, M., Smith, G. P., Golden, D. M., Bowman, C. T., Hanson, R. K., Gardiner, W. C., and Lissianski, V., 1995, ''GRI-Mech—An Optimized Detailed Chemical Reaction Mechanism for Methane Combustion,'' Gas Research Institute Report No. GRI-95/0058.
[27] Lyubovsky, M., Smith, L. L., Castaldi, M., Karim, H., Nentwick, B., Etemad, S., LaPierre, R., and Pfefferle, W. C., 2003, ''Catalytic Combustion Over Platinum Group Catalysts: Fuel-Lean Versus Fuel-Rich Operation,'' Catal. Today, **83**, pp. 71–84.
[28] Smith, L. L., Etemad, S., Castaldi, M. J., Karim, H., and Pfefferle, W. C., 2002, ''Method and Apparatus for a Fuel-Rich Catalytic Reactor,'' U.S. Patent No. 6,394,791.
[29] Karim, H., Lyle, K., Etemad, S., Smith, L. L., Pfefferle, W. C., Dutta, P., and Smith, K., 2003, ''Advanced Catalytic Pilot for Low NO_x Industrial Gas Turbines,'' J. Eng. Gas Turbines Power, **125**, pp. 879–884.

Assessment of Rich-Burn, Quick-Mix, Lean-Burn Trapped Vortex Combustor for Stationary Gas Turbines

Douglas L. Straub
Kent H. Casleton
Robie E. Lewis
Todd G. Sidwell
Daniel J. Maloney
George A. Richards

U.S. Department of Energy,
National Energy Technology Laboratory,
Morgantown, WV 26507

This paper describes the evaluation of an alternative combustion approach to achieve low emissions for a wide range of fuel types. This approach combines the potential advantages of a staged rich-burn, quick-mix, lean-burn (RQL) combustor with the revolutionary trapped vortex combustor (TVC) concept. Although RQL combustors have been proposed for low-Btu fuels, this paper considers the application of an RQL combustor for high-Btu natural gas applications. This paper will describe the RQL/TVC concept and experimental results conducted at 10 atm (1013 kPa or 147 psia) and an inlet-air temperature of 644 K (700°F). The results from a simple network reactor model using detailed kinetics are compared to the experimental observations. Neglecting mixing limitations, the simplified model suggests that NO_x and CO performance below 10 parts per million could be achieved in an RQL approach. The CO levels predicted by the model are reasonably close to the experimental results over a wide range of operating conditions. The predicted NO_x levels are reasonably close for some operating conditions; however, as the rich-stage equivalence ratio increases, the discrepancy between the experiment and the model increases. Mixing limitations are critical in any RQL combustor, and the mixing limitations for this RQL/TVC design are discussed. [DOI: 10.1115/1.1789152]

Introduction

The U.S. Department of Energy is developing technologies for ultraclean, 21st century, energy plants [1] with efficiency and emission goals well beyond the current state-of-the-art gas turbine power plants. Furthermore, recent trends suggest that new energy production is predominantly focusing on natural gas. In fact, 90% of the new power plants are fueled by natural gas [2]. In order to ensure energy security and meet future energy demands, a diversity of fuel sources will be required. Thus, a key feature of these future energy plants is fuel diversity, and gas turbine combustor designs must be capable of operating on a wide range of fuels, including natural gas and fuels derived from gasification processes. Minimizing pollutants such as nitrogen oxides (NO_x), carbon monoxide (CO), and even carbon dioxide is critical for these advanced power plant designs.

In order to achieve ultraclean emission goals with fuel flexibility, revolutionary changes in the gas turbine combustor will be required. One promising concept is the trapped vortex combustor (TVC). The TVC concept was originally conceived at the Air Force Research Laboratory in 1993 [3,4]. A collaborative effort between the Air Force Research Laboratory (AFRL) and the National Energy Technology Laboratory (NETL) began in 1999, and was co-sponsored by the Department of Energy and the Strategic Environmental Research and Development Program (SERDP) to evaluate the TVC concept for stationary power applications.

As a fuel-flexible combustor, the TVC concept can be configured to operate in several different combustion regimes. For example, the TVC can operate as a lean premixed combustor, a conventional diffusion flame combustor, an RQL combustor, or some hybrid approach. This paper will focus on a combustion approach in which the TVC operates as an RQL combustor.

Contributed by the International Gas Turbine Institute (IGTI) of THE AMERICAN SOCIETY OF MECHANICAL ENGINEERS for publication in the ASME JOURNAL OF ENGINEERING FOR GAS TURBINES AND POWER. Paper presented at the International Gas Turbine and Aeroengine Congress and Exhibition, Atlanta, GA, June 16–19; 2003, Paper No. 2003-GT-38569. Manuscript received by IGTI, Oct. 2002, final revision, Mar. 2003. Associate Editor: H. R. Simmons.

Thermal NO_x is an important issue for fuels that have flame temperatures in excess of 1800 K. Although many low-heating value fuels (i.e., air-blown gasification processes) do not have a problem with thermal NO_x, some medium-heating value fuels have higher flame temperatures than natural gas [5,6]. These medium-heating value fuels could be diluted, but fuel-dilution may also reduce the engine surge margin and does not address the problem of fuel-bound nitrogen. Furthermore, existing demonstrations of dilute diffusion flame combustors have produced NO_x levels of 9–25 ppmv, so further improvements are required to meet the goals of coal syn-gas applications [7].

The objective of this study is to investigate the ability of an RQL/TVC to minimize pollutant emissions on a high-heating value fuel like natural gas. It is believed that mixing limitations in a staged RQL approach would govern the potential to achieve ultralow emission levels, particularly for fuels in which thermal NO_x production is an issue. Therefore, in order to investigate the mixing issues in this combustor concept, natural gas is used as a baseline fuel. If low-emission performance can be demonstrated on natural gas, then the RQL/TVC approach may have potential for low-emission performance on other fuels of interest for future power generation.

In the sections that follow, the RQL combustion approach and the TVC concept will be discussed. Additional information will illustrate the differences between the RQL/TVC approach and more conventional RQL combustors. Furthermore, a simple stirred reactor/plug-flow reactor network simulation will be used to show the low emission potential for an RQL combustor operating on methane. Finally, experimental data will be presented to show how this first prototype design performs on natural gas in a pressurized combustion test.

Background

Staged RQL Combustion. Staged combustion approaches have been used primarily to minimize NO_x generated from fuel-bound nitrogen [8–13]. These RQL combustor designs incorporate an axially-staged approach in which the air injection is staged

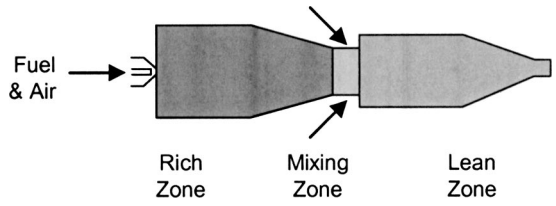

Fig. 1 Conventional axial-staged RQL combustion approach

axially along the axis of the combustor (see Fig. 1). Although fuel-bound nitrogen species are converted to NO_x very efficiently in an oxidizing environment [14], if the nitrogen-bearing fuel is injected into a fuel-rich environment, a significant portion of the fuel-bound nitrogen species will be converted to N_2, instead of NO_x.

Since complete oxidation does not occur in the rich zone of an RQL combustor, additional oxidant is required to complete the combustion at an overall lean condition. The point at which this additional oxidant is injected is often called the quick-mix stage of an RQL combustor. This mixing zone is critical for minimizing thermal, or Zeldovich, NO_x production. In an axially staged combustor, the air injected into the mixing zone should mix quickly, which implies small diameter jets should be used. However, small-diameter jets may not penetrate the main flow enough to distribute the oxidant uniformly across the entire flow area. Therefore, in order to achieve fast mixing and uniformly distribute the oxidant across the mixing zone, a judicious blend of large- and small-diameter jets may be required in an axially staged RQL combustor.

Theoretically speaking, if the mixing between the rich and lean zones occurs at infinitely small time scales (path B in Fig. 2), thermal NO_x levels from an RQL combustor could be very low. If the mixing time scales are too slow and localized high-temperature regions are formed (path A in Fig. 2), significant amounts of thermal NO_x will be produced. As mentioned previously, these mixing issues are common to all fuels in which thermal NO_x is an issue.

Trapped Vortex Combustor. The trapped vortex combustor concept has been under development for several years [3,4,15–18]. In a trapped vortex combustor, a cavity in the combustor wall is used to provide flame stability. If the cavity is designed properly, no vortex shedding occurs [19]. Due to the temporally and spatially stable vortex, it has been proposed that this geometry would produce a very effective means to stabilize a flame [17]. The unique feature of this concept is the fact that the flow in the cavity is nearly independent of the main stream. Therefore, potential upsets in the main airflow do not upset the flame stabilization characteristics. Recent data [20] have shown that this approach leads to significant improvements in ignition, lean blow-out, and relight capability. Furthermore, significant improvements in NO_x emissions for aircraft engine applications have also been demonstrated.

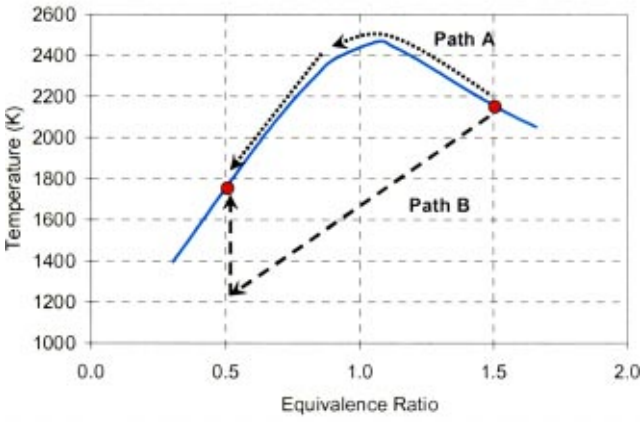

Fig. 2 Illustration of slow (path A) staged-combustion process versus a quick-mix (path B) staged-combustion process

By taking advantage of the TVC geometry and flame-holding characteristics, the combustion approach described in this paper is significantly different from previous axially staged RQL combustor designs. The RQL/TVC is a radially staged design, and all of the fuel is injected into the cavity, or trapped vortex region (see Fig. 3). Therefore, the cavity region of the combustor is fuel-rich, and air is injected through three different paths as shown in Fig. 3. According to computational fluid dynamics (CFD) [21] simulations, the cavity air-injection strategy produces a main vortex that rotates counter to the main flow as shown in Fig. 3(*b*). A second smaller vortex is formed in the shear layer between the cavity and the main airstream. This secondary vortex can either help transport products from the rich zone into the main airstream, or as will be discussed later, this secondary vortex can also entrain air from the main airstream into the rich zone.

Stirred Reactor Network Model

To better understand the details of NO_x formation and CO burnout in an RQL combustor, a simple reactor network has been used so that a detailed chemical mechanism can be employed. This reactor network consists of a perfectly stirred reactor (PSR) representing the fuel-rich region of the combustor. The PSR is followed by a mixing zone and a plug-flow reactor (PFR) [22,23] representing the lean stage where final oxidation occurs. The interstage mixing region is approximated by assuming that the effluent of the PSR is mixed instantaneously and adiabatically with the remaining air before entering the lean stage.

The Chemkin-II [24] package has been used to perform these simulations. Chemkin consists of preprocessor programs, libraries of FORTRAN subroutines, and databases for thermodynamic and transport properties. The subroutine libraries can be used to evaluate equations of state, thermodynamic properties, chemical rate expressions, and transport properties. Coupled with appropriate sets of governing equations, a variety of applications can be investigated, including well-stirred reactors, plug-flow reactors, and premixed flames. Of interest in this investigation are the well-stirred reactor [25] and the PFR.

Chemical kinetic information is supplied in a chemical reaction mechanism provided by the user. In this case, GRI-Mech 3.0 [26] is chosen to describe the methane combustion chemistry. This is a detailed chemical kinetic mechanism optimized to model methane and natural gas combustion, including NO formation and reburn chemistry. It contains 325 elementary chemical reactions and associated rate coefficient expressions and thermochemical parameters for 53 chemical species.

Simulations are performed with this PSR-mix-PFR network structure. All simulations are done assuming a constant air preheat temperature of 644 K (700°F) and an overall equivalence ratio of $\phi=0.5$ for a fuel consisting of methane only. Emissions levels for CO and NO_x are evaluated for cavity residence times from 7.5 to 30 ms and cavity equivalence ratio variations from 1.1 to 2.2. Results from these simulations are compared to experimental results and shown below.

Experimental Results

This work has been conducted at the U.S. Department of Energy's National Energy Technology Laboratory. The Low Emissions Combustor Test and Research (LECTR) facility is a refractory lined pressure vessel designed for operation at a maximum of 3200 kPa (450 psig). The air compression facility is capable of providing 1.45 kg/s (3.2 lb/s) of airflow, and a nonvitiated air preheater is used to control the inlet-air temperature with air pre-

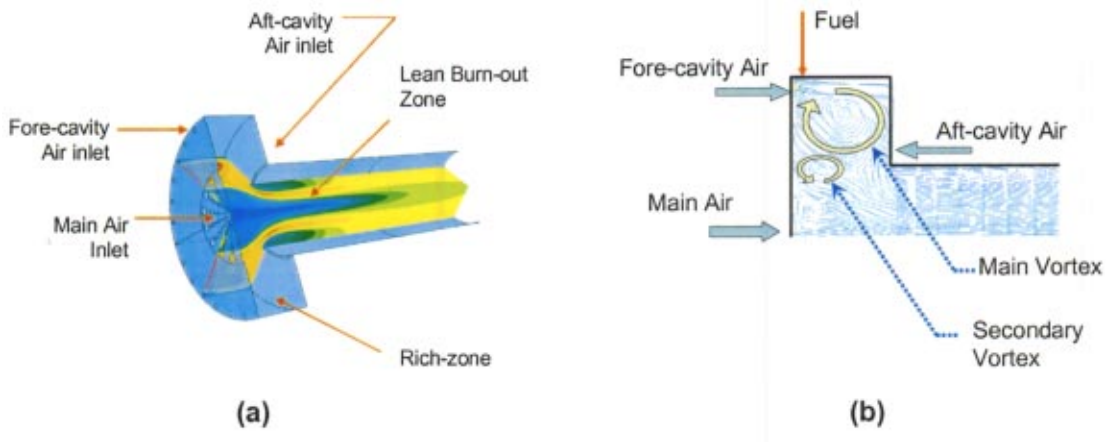

Fig. 3 Schematic of RQL/TVC combustor. Cut-away view (*a*) shows temperature contours predicted by 3D CFD. Cross section (*b*) shows path lines that define vortices in the cavity region.

heat temperatures up to 810 K (1000°F). This facility is capable of controlling the airflow rate, inlet-air temperature, and combustor operating pressure independently.

The RQL/TVC concept described in this paper is designed for a nominal heat rate of 0.7 MWth. Therefore, the fuel and airflow rates in this test program are well below the full capabilities of the facility. Preheated combustion air at 644 K (700°F) is introduced through the main-air distributor plate, the fore-cavity wall, and the aft-cavity wall.

The natural gas composition is analyzed during each day of testing. For the results described in this paper, the average natural gas composition is 94.0% methane, 3.9% ethane, 0.60% propane, 0.85% nitrogen, 0.16% CO_2, and small percentages of higher hydrocarbons. The average higher heating value of the fuel is 55.5 MJ/kg (1046 Btu/scf).

Description of Combustor Prototype. A cutaway schematic and a cross section of the combustor design are shown in Fig. 3, and photos of the combustor are shown in Fig. 4. The combustor walls, with the exception of the aft-cavity wall, are water-cooled. The aft-cavity wall is backside cooled with air that is injected through the annular gap shown in Fig. 4(*c*).

The main air enters the combustor through a distributor plate (see Fig. 4(*a*)). The distributor plate design is critical for good combustor performance, and it should be noted that no swirl is required to stabilize the flame.

The fore-cavity wall air and the aft-cavity wall air drive the main vortex in the direction shown in Fig. 3(*b*). Based on CFD simulations [21], if more of the products from the rich-cavity region exit near the upstream combustor wall, combustor performance is improved.

In addition to driving the main vortex toward the combustor inlet, the aft-cavity wall air jet reduces the amount of spillover that occurs along the downstream wall of the cavity. It has been shown previously [21] that cavity spillover leads to nonuniform temperature and emission profiles at the combustor exit. Therefore, minimizing the cavity spillover is an important consideration in an RQL/TVC design.

Natural gas is injected into the cavity region from the outer cavity wall. The fuel is injected through 28 holes around the circumference of the combustor, so the fuel jets are directed toward the centerline of the combustor. The fuel jets and the fore-cavity air jets intersect at a 90-deg angle.

The sample probe is located roughly 30 cm (12 in.) downstream from the inlet face of the combustor. Depending on the operating condition, the average bulk residence time in the lean-burn zone is on the order of 5–15 ms. The water-cooled sample probe is designed to collect an area-weighted gas sample. The gas sample is transported through heated stainless steel tubing prior to passing through an ice bath to condense the water vapor. The dry gas sample is analyzed for concentrations of NO_x, CO, unburned hydrocarbons, CO_2, and O_2 at each operating point.

Experimental Test Plan. These tests are conducted at a baseline pressure of 1013 kPa (147 psia) and an inlet air temperature of 644 K (700°F). The independent variables that will be de-

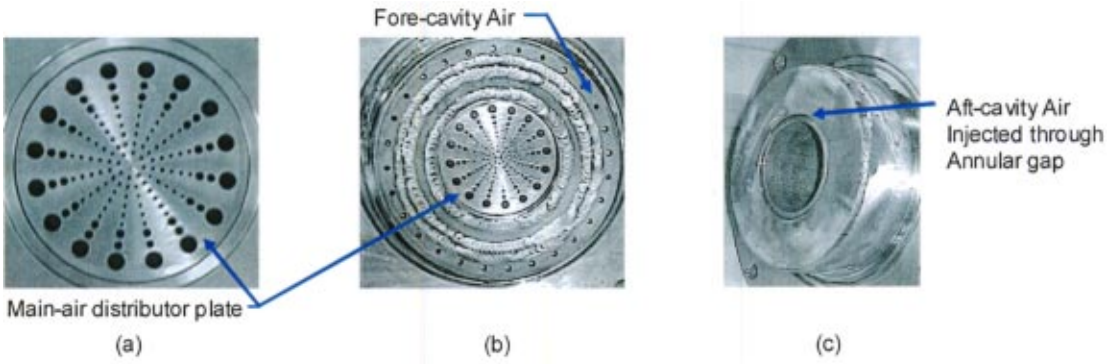

Fig. 4 Photos showing (*a*) the main air distributor plate, (*b*) the upstream combustor wall, and (*c*) the downstream combustor wall and combustor exit

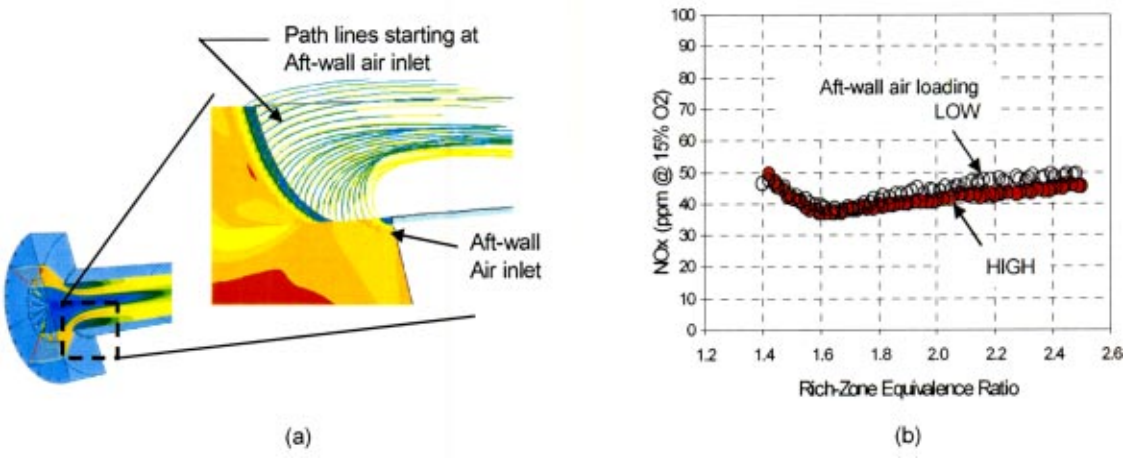

Fig. 5 CFD and experimental data showing aft-wall air effects. Trajectories from the aft-wall air (*a*) immediately turn and exit from the combustor. The experimental NO_x levels are nearly the same (*b*) if the aft-wall air loading is increased by a factor of two. Note that Eq. (1) is used in calculating the rich-zone equivalence ratio in (*b*).

scribed in this paper include the rich-zone residence time and the rich-zone equivalence ratio. The PSR/PFR model results are presented as a benchmark and are also used as a basis for explaining some of the trends observed in the data.

Data Analysis. As previously mentioned, the air-flow rates can be controlled independently and are measured within 2% of calibrated flow standards. This capability allows independent control of the fuel-air mixture in both the rich zone and the lean zone.

In the cavity region, only the fore-cavity air flow is used for calculating the rich-zone equivalence ratio (see Eq. (1)). This definition of cavity equivalence ratio is chosen because CFD simulations have shown that the air from the aft-cavity wall does not mix with the main vortex (see Fig. 5(*a*)). All of the path lines from the aft-cavity wall immediately turn and exit the combustor without mixing with the main vortex. For the boundary conditions used in Fig. 5(*a*), the cavity equivalence ratio using Eq. (1) should be around 1.8.

To further support the approach of ignoring the aft-cavity wall air in the cavity equivalence ratio, Fig. 5(*b*) shows experimental data in which the overall equivalence ratio and the cavity residence time are held constant, but the amount of air injected from the downstream cavity wall is varied by roughly a factor of 2. The effect on the NO_x emissions is small (see Fig. 5(*b*)), which suggests that the effect of the aft-cavity wall air on the cavity stoichiometry is small. Therefore, for the purposes of this paper, Eq. (1) is used to calculate the cavity equivalence ratio:

$$\phi_{\text{rich}} = \frac{(m_{\text{fuel}}/m_{\text{fore cavity}})}{q_{\text{stoich}}}. \tag{1}$$

The overall equivalence ratio can be calculated based on the measured fuel-air flows as shown in Eq. (2), as well as the gas composition in the exhaust. If the overall equivalence ratio based on the flows into the system is compared to the value calculated based on the exhaust emissions, the discrepancy is typically on the order of 2%,

$$\phi_{\text{total}} = \frac{[m_{\text{fuel}}/(m_{\text{fore cavity}} + m_{\text{aft cavity}} + m_{\text{main}})]}{q_{\text{stoich}}}. \tag{2}$$

The residence time in the cavity is difficult to quantify accurately due to uncertainties in the velocity and temperature profiles. However, since all of the flows are measured separately and the dimensions of the combustor are known, an approximation of the average bulk residence time is made using the following expression, where V_{cav} is the volume of the cavity:

$$\tau_{\text{cav}} = \frac{V_{\text{cav}} p \text{MW}}{m_{\text{fore cavity}} RT}. \tag{3}$$

Note that the fuel flow and the aft-cavity wall air flow are not included in the cavity residence time calculations. Furthermore, no gas temperature measurement is available for the cavity region, so the temperature is approximated as the exit temperature calculated from the PSR simulations for the given cavity equivalence ratio.

Discussion of Results

Cavity Residence Time Effects. The cavity residence time can be varied independently in this experiment by changing the amount of air injected into the cavity region. In order for the rich-zone equivalence ratio and the overall equivalence ratio to remain constant, the fuel and air flows must be controlled simultaneously. Figure 6 shows both the experimental and the network model results for a cavity equivalence ratio of 1.50 and an overall equivalence ratio of 0.50. The agreement between the model and the experiment is very good, given the simplicity of the stirred reactor network. Both the model and the experiment show that the NO_x decreases as the residence time in the rich-zone increases.

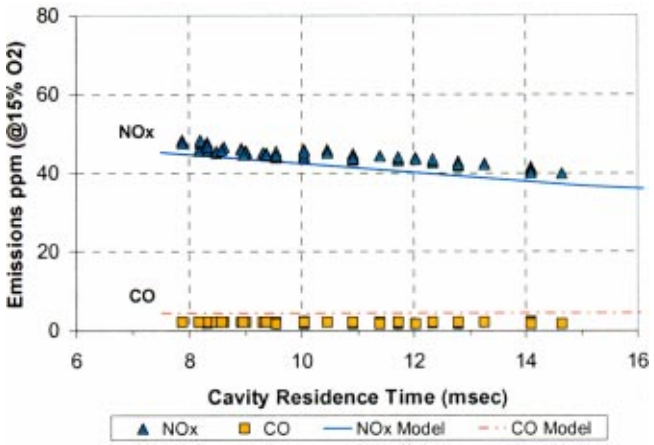

Fig. 6 Comparison of experimental emissions data and PSR-Mix-PFR network model. (Rich-zone equivalence ratio is 1.50, overall equivalence ratio is 0.50.)

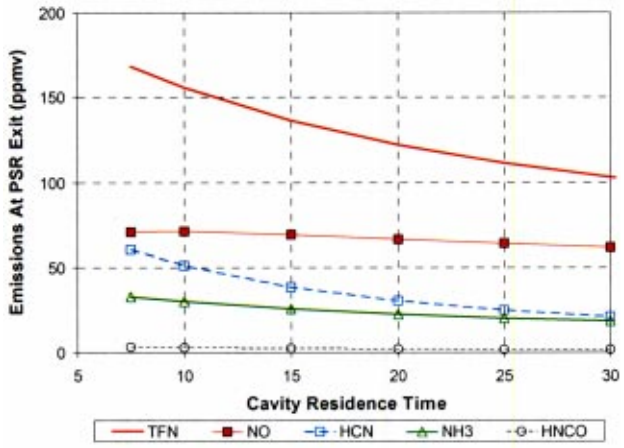

Fig. 7 Predicted fixed-nitrogen species exiting the PSR (rich-zone) as a function of rich-stage residence time

Further investigation of the model shows that the total amount of fixed nitrogen species (i.e., all nitrogen species except N_2) leaving the rich-zone decreases as the residence time is increased (see Fig. 7). However, under these conditions, the reduction in total fixed nitrogen (TFN) species with increasing cavity residence time is primarily due to decreases in HCN. These fixed-nitrogen species (NH_3 and HCN) will produce NO in the lean zone. Therefore, by increasing the residence time in the rich zone, the amount of fixed nitrogen species entering the lean stage of the combustor is reduced. Hence, the amount of NO_x formed in the lean zone from the fixed nitrogen species is reduced as the rich-zone residence time is increased.

Cavity (Rich-Zone) Equivalence Ratio Effect. In order to investigate the effect of cavity equivalence ratio on the NO_x and CO emissions, the cavity equivalence ratio is varied while keeping the cavity residence time and the overall equivalence ratio constant. Figure 8 shows the PSR-Mix-PFR model results plotted on the same graph as the NO_x and CO levels from the experiment.

The experimental CO data shown in Fig. 8 compare reasonably well with the PSR-Mix-PFR model predictions, and the experimental NO_x levels compare reasonably well at low cavity equivalence ratio conditions (i.e., $\phi_{cav}<1.6$). However, at the higher equivalence ratio conditions, the experimental NO_x levels plateau and do not appear to be dependent upon the fuel-air mixture in the

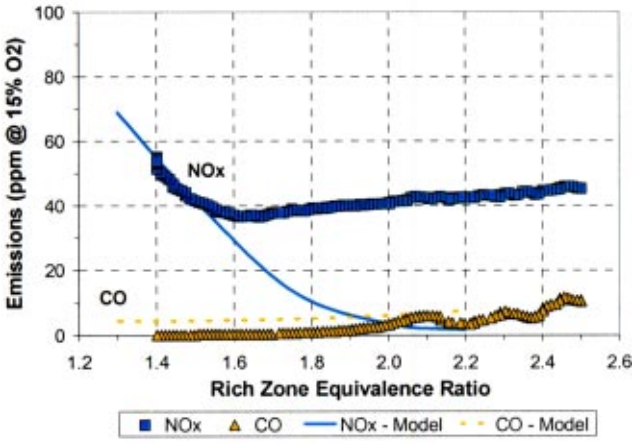

Fig. 8 Comparison of experimental data versus PSR-Mix-PFR model. (Overall equivalence ratio is 0.50.)

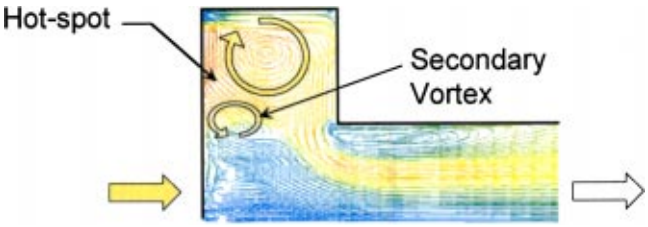

Fig. 9 Path lines computed from 3D CFD simulations of the RQL/TVC. The color scale corresponds to the computed temperature level (red=2400 K). The secondary vortex entrains oxidant into the cavity region.

cavity. It is believed that the primary difference between the experimental results and the model results shown in Fig. 8 are due to imperfect mixing in the experiment.

CFD simulations for a cavity equivalence ratio of 1.8 have been completed (see Fig. 9). For this operating condition, CFD simulations have shown that the secondary vortex transports oxidant from the lean zone into the rich zone. In the rich zone, this entrained oxidant reacts and forms high-temperature regions in the cavity. For the data shown in Fig. 8, the amount of main air injected to maintain an overall equivalence ratio of 0.50 increases as the rich-zone equivalence ratio increases. Early evidence suggests that the behavior of this secondary vortex changes as the amount of main air, relative to the cavity air, is increased. In fact, preliminary CFD simulations [21] suggest that mixing can be enhanced by this secondary vortex motion. In any event, the CFD simulations suggest that a significant portion of the NO_x is formed in the cavity region for a cavity equivalence ratio of 1.80.

It is also interesting to note that under ideal mixing conditions, the PSR model predicts large amounts of NO will be produced in the rich zone, particularly for cavity equivalence ratio conditions less than 1.5. As the rich-zone equivalence ratio is increased, the NO levels decrease rapidly and HCN and NH_3 become the predominant reactive nitrogen species. Although HCN and NH_3 must be considered, Fig. 7 has shown that these species can be reduced by increasing the cavity residence time.

Since the PSR/PFR model neglects mixing limitations, the predicted levels shown in Fig. 8 may reflect a theoretical lower limit. Although the theoretical and experimental results agree for some operating conditions, this does not imply that we achieved perfect mixing in the experiment. There are significant uncertainties in the estimates of some of the experimental variables. For example, the experimental cavity residence time involves assumptions about the distribution of residence times, as well as, the gas temperature in the cavity region. Nevertheless, the detailed kinetic model suggests that ultralow NO_x levels are theoretically possible for an RQL combustor, but single-digit emissions have not been experimentally demonstrated at this time.

Conclusions

This paper describes the design of a nonpremixed, can-style TVC in which all of the fuel is injected into the cavity. In this configuration, the TVC operates as an RQL staged combustor. Contrary to conventional axially-staged RQL combustor approaches, the RQL/TVC concept is radially staged, which is believed to have inherent advantages over a conventional RQL approach.

Detailed kinetic modeling of the RQL/TVC is discussed using a simplified network of a perfectly stirred reactor and a plug-flow reactor. Since these simulations assume perfect mixing, the results represent a lower bound on the emissions from an RQL approach burning methane fuel. These simulation results are useful for identifying variables that are not limited by mixing characteristics, but

still significantly affect the NO_x and CO emissions (i.e., rich-zone residence time and cavity equivalence ratio). These network simulations are compared to the experimental data.

A good comparison between the measured CO levels and the CO levels predicted from the PSR-Mix-PFR model is observed. The measured NO_x levels, however, are somewhat higher than the values predicted from the simulations, particularly for values of the cavity equivalence ratio that are higher than 1.6. These discrepancies are likely a result of practical mixing limitations in the experiment.

3D CFD simulations have been presented to isolate the areas of poor mixing. The 3D CFD simulations show that a secondary vortex is formed in the shear layer between the primary vortex and the main stream. At some operating conditions, this secondary vortex can transport oxidant from the lean-burn zone into the rich zone (see Fig. 9). It is believed that this secondary vortex may have limited the ability to achieve the ultralow NO_x levels that are predicted by the detailed kinetic models.

The PSR/PFR model results predict a strong effect of cavity equivalence ratio on the NO_x emissions. Since the model neglects mixing limitations, the predicted levels may reflect a theoretical lower limit. More work is planned to better understand the sensitivity of these model results to finite mixing times.

Acknowledgments

The authors gratefully acknowledge the support of both past and current Department of Energy Turbine Technology Managers, Ms. Abbie Layne and Mr. Richard Dennis. This work was supported through DOE's Office of Fossil Energy, Turbine program and the Strategic Environmental Research and Development Program (SERDP). R. Lewis acknowledges the support of the Oak Ridge Institute of Science and Engineering (ORISE) Professional Internship program. The authors also acknowledge the special talents and diligent efforts of Mr. Mark Tucker and Mr. T. Mike Dera for their support in the experimental portion of this effort.

Nomenclature

MW = Average molecular weight
R = Ideal gas constant
T = Flame temperature (rich zone)
V_{cav} = Volume of cavity region
m_{fuel} = Mass flow rate of fuel
$m_{fore\ cavity}$ = Mass flow rate of air through fore-cavity
$m_{aft\ cavity}$ = Mass flow rate of air through aft-cavity
m_{main} = Mass flow rate of air through the main air inlet
p = Pressure
q_{stoich} = Stoichiometric fuel-air ratio
τ_{cav} = Cavity, or rich-zone, residence time
ϕ_{rich} = Equivalence ratio in the rich-zone
ϕ_{total} = Overall (total) equivalence ratio

References

[1] U.S. Department Of Energy's Vision 21 Program Plan, "Clean Energy Plants For the 21st Century," http://www.netl.doe.gov/
[2] National Energy Policy, "Reliable, Affordable, and Environmentally Sound Energy for America's Future," Report of the National Energy Policy Development Group, May 2001.
[3] Hsu, K. Y., Goss, L. P., and Roquemore, W. M., 1995, "Performance of a Trapped Vortex Combustor," 33rd AIAA Aerospace Sciences Meeting and Exhibit, Reno, NV, January 1995, AIAA Paper 95-0810.
[4] Katta, V. R., and Roquemore, W. M., 1998, "Numerical Studies on Trapped Vortex Concepts for Stable Combustion," ASME J. Eng. Gas Turbines Power, **120**, pp. 60–68.
[5] Dobbeling, K., Koppel, H. P., Polifke, W., Winkler, D., Steinbach, C., and Sattelmayer, T., 1996, "Low-NOx Premixed Combustion of MBtu Fuels Using the ABB Double Cone Burner (EV Burner)," ASME J. Eng. Gas Turbines Power, **118**, pp. 46–53.
[6] Dobbeling, K., Eroglu, A., Winkler, D., Sattelmayer, T., and Keppel, W., 1997, "Low NOx Premixed Combustion of MBtu Fuels in a Research Burner," ASME J. Eng. Gas Turbines Power, **119**, pp. 553–558.
[7] Todd, D. M., 2000, "Gas Turbine Improvements Enhance IGCC Viability," Presented at the 2000 Gasification Technologies Conference, San Francisco, CA, October 8–11, 2000.
[8] Folsom, B. A., Courtney, C. W., and Heap, M. P., 1980, "The Effects of LBG Composition and Combustor Characteristics on Fuel NOx Formation," ASME J. Eng. Power **102**, pp. 459–467.
[9] Domeracki, W. F., Dowdy, T. E., and Bachovchin, D. M., 1997, "Topping Combustor Status for Second-Generation Pressurized Fluidized Bed Cycle Application," ASME J. Eng. Gas Turbines Power, **119**, pp. 27–33.
[10] Feitelberg, A. S., and Lacey, M. A., 1997, "The GE Rich-Quench-Lean Gas Turbine Combustor," ASME Paper 97-GT-127.
[11] Sato, M., Ninomiya, T. N., Yoshine, T., and Yamada, S. H., 1990, "Coal Gaseous Fueled Low Fuel-NOx Gas Turbine Combustor," ASME Paper 90-GT-381.
[12] Constant, D. R., Bevan, D. M., and Cannon, M. F., 1997, "Development of an LCV Fuel Gas Combustor For an Industrial Gas Turbine," ASME Paper 97-GT-38.
[13] Hasegawa, T., Hisamatsu, T., Katsuki, Y., Sato, M., Yamada, M., Onoda, A., and Utsunomiya, M., 1998, "A Study of Low Nox Combustion In Medium-BTU Fueled 1300°C-Class Gas Turbine Combustor In IGCC," ASME Paper 98-GT-331.
[14] Sarv, H., and Cernansky, N. P., 1989, "NOx Formation From the Combustion of Monodisperse n-Heptane Sprays Doped With Fuel-Nitrogen Additives," Combust. Flame, **76**, pp. 265–283.
[15] Hsu, K. Y., Goss, L. P., and Roquemore, W. M., 1998, "Characteristics of a Trapped Vortex Combustor," J. Propul. Power, **14**, pp. 57–65.
[16] Hsu, K. Y., Carter, C. D., Katta, V. R., and Roquemore, W. M., 1999, "Characteristics of Combustion Instability Associated With Trapped Vortex Burner," AIAA Paper 99-0488.
[17] Roquemore, W. M., Shouse, D. T., and Hsu, K. Y., 1999, U.S. Patent 5,857,339.
[18] Roquemore, W. M., Shouse, D., Burrus, D., Johnson, A., Cooper, C., Duncan, B., Hsu, K. Y., Katta, V. R., Sturgess, G. J., and Vihinen, I., 2001, "Trapped Vortex Combustor Concept For Gas Turbine Engines," AIAA Paper 2001-0483.
[19] Little, Jr., B. H., and Whipkey, R. R., 1979, "Locked Vortex Afterbodies," J. Aircr., **16**, pp. 296–302.
[20] Burrus, D. L., Johnson, A. W., Roquemore, W. M., and Shouse, D. T., 2001, "Performance Assessment of a Prototype Trapped Vortex Combustor Concept For Gas Turbine Application," ASME Paper 2001-GT-0087.
[21] Straub, D. L., Sidwell, T. G., Maloney, D. J., Casleton, K. H., Richards, G. A., Rogers, W. A., and Golden, G. M. 2000, "Simulations of a Rich Quench Lean (RQL) Trapped Vortex Combustor," presented at the 2000 American Flame Research Committee (AFRC) International Symposium, Newport Beach, CA.
[22] Swithenbank, J., Poll, I., Vincent, M. W., and Wright, D. D., 1973, "Combustion Design Fundamentals," *Fourteenth Symposium (International) on Combustion*, The Combustion Institute, Pittsburgh, pp. 627–638.
[23] Turns, S. R., 1996, *An Introduction to Combustion—Concepts and Applications*, McGraw-Hill, New York, p. 173.
[24] Kee, R. J., Rupley, F. M., and Miller, J. A., 1989, "Chemkin-II: A FORTRAN Chemical Kinetics Package for the Analysis of Gas-Phase Chemical Kinetics," Sandia National Laboratory Report SAND89-8009.
[25] Glarborg, P., Kee, R. J., Grcar, J. F., and Miller, J. A., 1990, "PSR: A FORTRAN Program for Modeling Well-Stirred Reactors," Sandia National Laboratory Report SAND86-8209.
[26] Smith, G. P., Golden, D. M., Frenklach, M., Moriarty, N. W., Eiteneer, B., Goldenberg, M., Bowman, C. T., Hanson, R. K., Song, S., Gardiner, W. C., Jr., Lissianski, V. V., and Qin, Z., "GRI-Mech 3.0," http://www.me.berkeley.edu/gri_mech/

Kelly Benson
Woodward Industrial Controls,
Ft. Collins, CO 80525
e-mail: kbenso@woodward.com

Jimmy D. Thornton
e-mail: jthorn@netl.doe.gov

Douglas L. Straub

E. David Huckaby

Geo. A. Richards

U.S. Department of Energy,
National Energy Technology Laboratory,
Morgantown, WV 26507

Flame Ionization Sensor Integrated Into a Gas Turbine Fuel Nozzle

Recent advances in lean premix gas turbine combustion have focused primarily on increasing thermodynamic efficiency, reducing emissions, and minimizing combustion dynamics. The practical limitation on increasing efficiency at lower emissions is the onset of combustion instability, which is known to occur near the lean flammability limit. In a laboratory environment there are many sensors available that provide the combustion engineer with adequate information about flame stability, but those sensors are generally too expensive or unreliable for widespread application in the field. As a consequence, engines must be commissioned in the field with adequate stability margin such that normally expected component wear, fuel quality, and environmental conditions will not cause the turbine to experience unstable combustion. Woodward Industrial Controls, in cooperation with the National Energy Technology Laboratory, is developing a novel combustion sensor that is integrated into the fuel nozzle such that low cost and long life are achieved. The sensor monitors flame ionization, which is indicative of air–fuel ratio and most importantly flame stability. [DOI: 10.1115/1.1788686]

Introduction

There are a variety of methods that have been proposed to both sense combustion conditions and optimize operating conditions. Docquier and Candel [1] provide an excellent review of the subject. These authors note that combustion sensing may be developed for three broad areas of control: operating point control, active combustion enhancement, and active instability control. Among these, operating point control is the most familiar. For example, the fuel flow in a gas turbine is controlled by the load set point, and the combustion conditions will change accordingly with the fuel flow. The need to reduce NO_x emissions has introduced more sophisticated control schemes, which attempt to maintain nearly constant combustion temperatures over the entire engine load range. Laboratory tests have demonstrated the performance advantages of combustion control for reducing emissions [2–4]. For complete gas turbine engines, Corbett and Lines [5] discuss the various control parameters required to produce very low emissions. The absence of a reliable sensor to directly monitor conditions in the combustor requires the addition of numerous indirect sensors for flow rates, inlet humidity, etc. Pandalai and Mongia [6] note the importance of sensing lean blowout and combustion dynamics, and discuss corrective control actions by redirecting fuel flow to various regions of the combustion chamber. In this example, combustion dynamics are monitored using high frequency pressure transducers, but again, there is no direct measure of conditions in the combustion chamber.

Various authors have investigated the use of optical methods to determine fuel–air ratio, and measure fluctuating heat release or fuel–air ratio that drive combustion dynamics [7–9]. Optical sensors have the advantage of avoiding direct contact with the high-temperature combustion products, but are limited to sensing conditions along an available line of sight. In order to incorporate these optical methods in potential gas turbine applications, both the pressure casing and combustion liner must be penetrated. Nevertheless, optical flame sensors detecting flame chemiluminescence are now available [10], and are used as part of the feedback control system in gas turbines.

An alternative to optical sensing is to use flame ionization signals as an indicator of combustion conditions. Flame ionization probes can exhibit high-frequency response characteristics similar to optical techniques. Furthermore, flame ionization probes do not require adding line-of-sight access to the combustion region, and the signal can be collected from a single wire. Ionization sensors have been demonstrated in reciprocating engine applications [11,12], but very little information is available for applications in gas turbines. Earlier papers by some of the present authors [13,14] at the National Energy Technology Laboratory (NETL) demonstrated that the flame ionization signal can be used to detect flame flashback, oscillating combustion, and potentially monitor local fuel–air ratio.

In early 2002 Woodward Industrial Controls and NETL initiated a Cooperative Research and Development Agreement (CRADA) to further develop the ionization sensor as a robust combustion sensor. This paper describes the development and testing of an ionization sensor applied to a fuel injector typical of what is used in heavy-frame gas turbines.

Background

The presence of ions in flames has been known for well over a century. Volumes of literature exist on the subject of flame ionization, including descriptions of the mechanisms for the ion formation and the electrical properties of the flame. Calcote [15] and Fialkov [16] have written thorough review articles on this subject, and it is widely accepted that the key mechanism enabling the flow of electrical current through hydrocarbon flames results from the chemi-ionization of the formyl radical, CHO*:

$$CH + O \rightarrow CHO^* \rightarrow CHO^+ + e^-. \quad (1)$$

The resulting electrical properties of the flame have enabled several practical applications including hydrocarbon analyzers, flame detectors, flame speed detectors [17], flame stabilization [18], and even flame tomography [12]. A typical flame ionization sensing technique consists of at least two electrodes arranged such that a voltage potential can be applied across the flame, or a part of the flame. The electrical properties of the flame facilitate a measurable current that is related to a parameter of interest. For

Contributed by the International Gas Turbine Institute (IGTI) of THE AMERICAN SOCIETY OF MECHANICAL ENGINEERS for publication in the ASME JOURNAL OF ENGINEERING FOR GAS TURBINES AND POWER. Paper presented at the International Gas Turbine and Aeroengine Congress and Exhibition, Atlanta, GA, June 16–19, 2003, Paper No. 2003-GT-38470. Manuscript received by IGTI, October 2002, final revision, March 2003. Associate Editor: H. R. Simmons.

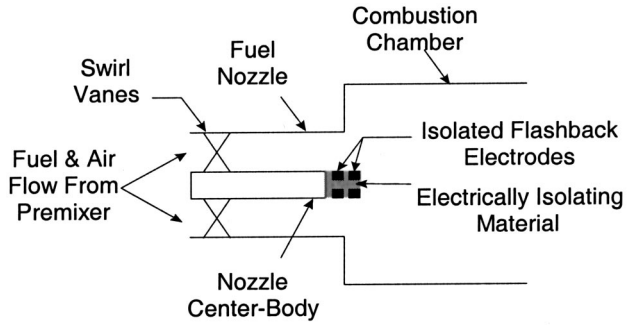

Fig. 1 Lean premix fuel nozzle with CCADS electrode on the fuel injector center-body

example, a typical flame ionization detector (FID) used in a hydrocarbon analyzer has electrodes arranged such that a voltage potential is applied across the entire flame, and the amount of electrical current flow through the flame is linearly proportional to the hydrocarbon concentration [19].

In spite of this successful history, the use of flame ionization sensing for gas turbine applications has only recently been explored. In 2000, Thornton, Richards, and Robey [20] described a flame ionization sensor to detect flashback in premixed combustion systems. Subsequent testing in NETL's atmospheric combustion rig indicated that this novel sensor technique could potentially serve a comprehensive in situ monitoring role as a combustion control (i.e., equivalence ratio) and diagnostic (i.e., autoignition, flashback, flame location, and dynamics detection) sensor. The experimental results [13] show that under certain circumstances the flame ionization current correlates with the OH* chemiluminescence, and the magnitude of the measured current varied linearly with the operating equivalence ratio. Likewise, other researchers have shown that the equivalence ratio can be correlated with ion concentrations for some carefully controlled applications [15,16,1].

The combustion control and diagnostic sensor (CCADS) technique is based on two electrically insulated electrodes installed at the end of the fuel injector's center-body as shown in Fig. 1. The electrode closest to the combustion zone is called the *guard* electrode, and the electrode upstream of the *guard* is called the *sense* electrode. An equal-potential positive voltage is applied to both electrodes, resulting in an electric field at the face of the fuel injector with flux lines equivalent to the illustration in Fig. 2. This novel arrangement of the electrodes facilitates current flow from the *guard* electrode through the flame in the combustion zone to the combustor liner. Due to the electric field imposed by the combination of the guard and *sense* electrodes, a significant ionization current from the *sense* electrode is produced only when the flame enters the premixing region of the fuel injector (i.e., autoignition and flashback).

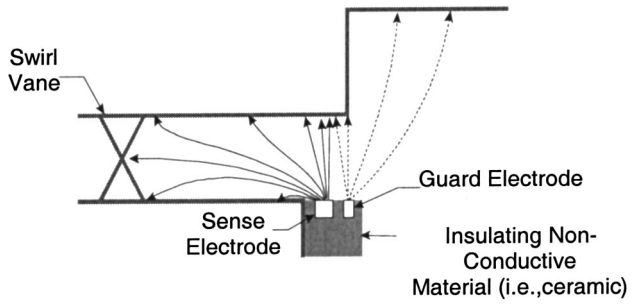

Fig. 2 Illustrates the electric flux lines from the guard and sense electrodes

Recent demonstrations of the CCADS technique for detecting flashback and combustion dynamics at turbine conditions are reported in Straub et al. [14]. Due to hardware failure this prototype CCADS failed to fully demonstrate the sensor capabilities at representative turbine conditions. However, the feasibility of using the CCADS technique to perform multiple sensor functions such as flame detection, flashback detection, and detecting combustion dynamics have all been demonstrated in NETL combustion rigs. The capability to perform multiple functions from a single sensor offers potential cost savings to OEM's and operators of gas turbines. This coupled with potential in situ monitoring for control makes this flame ionization sensing technique very appealing for commercialization. As mentioned in the introduction, NETL and Woodward Industrial Controls are collaboratively addressing the research and development issues in order to commercialize the CCADS concept for gas turbine applications.

Approach

One goal of the collaboration between Woodward and NETL is to produce a durable CCADS prototype, using fuel injector geometry and materials similar to those used in heavy-frame DLN turbines, which can withstand extensive testing to evaluate the sensor performance at turbine conditions. The main objectives of the initial testing reported herein are to demonstrate durability, and evaluate the prototype design for performing three sensor functions:

1. Detect the presence of a flame in the primary combustion zone. This can be used at startup and during operations to indicate incipient blowout conditions usually encountered at the lean flammability limit. The measured current through the *guard* electrode will provide this functionality.
2. Detect the onset of combustion dynamics. This can be used to perform control functions to mitigate combustion instabilities. The measured current through the *guard* electrode will provide this functionality.
3. Detect flashback and *incipient* flashback (i.e., flame ''flicker'' into the premixing region). This can be used to perform corrective action prior to hardware failure to prevent costly repairs and downtime. The measured current through the *sense* electrode will provide this functionality.

Furthermore, the initial data will also be examined for a linear relationship between the measured current through the *guard* electrode and the equivalence ratio of the combustor. Although previous demonstrations of the CCADS technique to measure the equivalence ratio at certain conditions are encouraging, a more thorough understanding of the physics and the effects of the gas turbine environment on the measured current are needed. In a gas turbine environment, operating pressure, flame location, electrode configuration, and combustion oscillations may all affect the relationship between equivalence ratio and the measured flame ionization current. To adequately characterize this relationship, extensive testing at turbine conditions with different rig geometry is required. Therefore, adequately describing the relationship between current and equivalence ratio is not within the scope of this effort. This will be ascertained in a much more extensive long-term development effort.

Woodward's first prototype design is shown schematically in Fig. 3. This design has several advantages over previous prototypes tested at NETL. First, the fuel injector design has features that are similar to many production nozzles used in heavy-frame DLN turbines. The premix gas is admitted through the swirl vanes perpendicular to air flow. The tip is recessed approximately 1 in. upstream of the combustor dump plane, and contains flow passages for either air or diffusion gas (see Fig. 4). Using the entire tip of the center body as the electrode maximizes the *guard* electrode surface area. This design enhances the ability to collect charged species from the combustion region by extending the

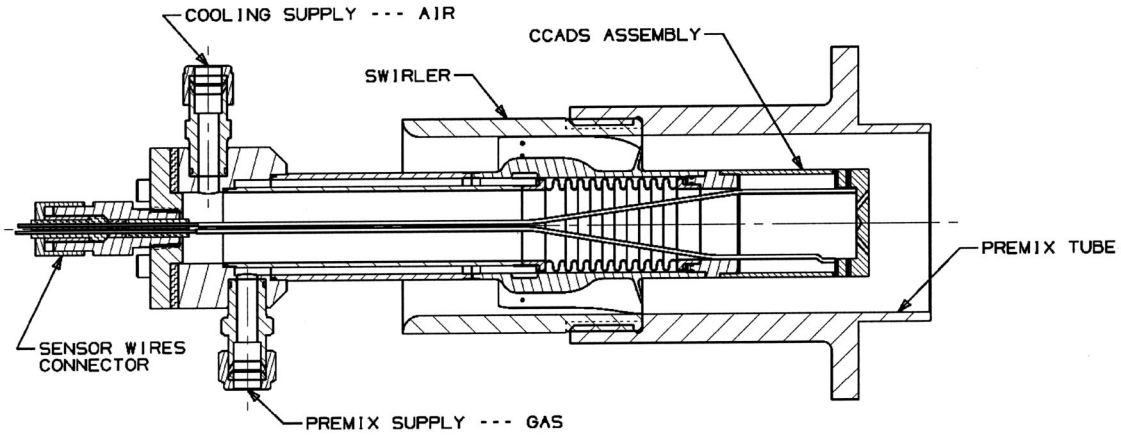

Fig. 3 Schematic of Woodward prototype fuel injector with CCADS

electric field into the combustion region. The added features of the CCADS tip are shown schematically in Fig. 5; these include the following:

- Threaded CCADS tip assembly for convenient replacement during development
- Special design features to tolerate thermal growth
- High-temperature electrode materials
- High-temperature but replaceable insulating materials
- Smooth sensor profile to avoid creating eddy currents for flame holding
- Maximum *guard* electrode surface area to increase sensor performance.

A two-dimensional electrostatic analysis is shown in Fig. 6. These results were calculated using FLUENT [21]. The electrostatic model uses the conductive properties of air in the open premixer and combustion regions. This model does not include the effects of fluid flow and chemical reactions occurring in the combustion region. The model is used to determine suitable center-body electrode configurations, by ensuring maximum electric field extension into the combustion chamber. As shown in Fig. 6, even though the tip is recessed the flux lines extend into the combustion chamber as desired.

The prototype fuel injector shown in Fig. 3 was previously tested with thermocouples installed inside the tip to measure operating temperatures, with diffusion gas, and then with cooling air flowing through the tip. With diffusion gas flowing through the tip, temperatures exceed 1300 K (1880°F) at some operating conditions, particularly conditions in which the bulk flow velocity is less than 60 m/s. With cooling air flowing through the tip, the temperatures remained below 1250 K (1790°F) for all operating conditions. For the tests described in the next section, cooling air flows through the holes on the tip, and the center hole (designed for brazing a thermocouple to tip) is also open to maximize cooling of the tip. Therefore, a significant amount of air cooling is used, and it is believed that this reduces the amount of current measured from the *guard* electrode.

Experimental Setup

Pressurized Combustor. The details of this experimental rig are described elsewhere [22–24]. However, for the purposes of this paper, a brief description of the important details will be given. A schematic of the combustion test rig is shown in Fig. 7. The rig, about 6 m (20 ft) long, is capable of operating at pressures as high as 10 atm with inlet air temperatures as high as 617 K (650°F). The maximum air flow for this rig is about 0.68 kg/s

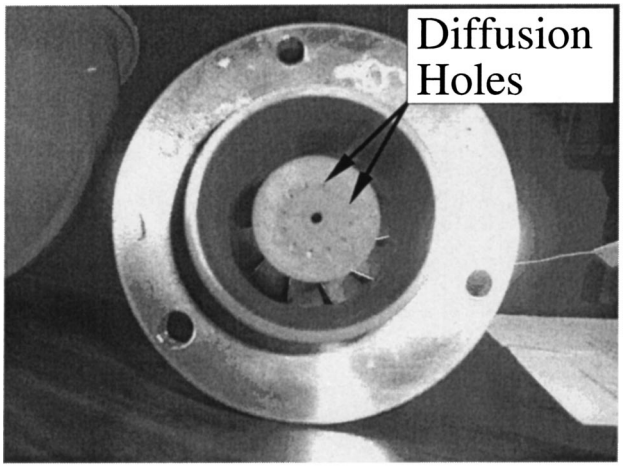

Fig. 4 Front view of Woodward prototype fuel injector

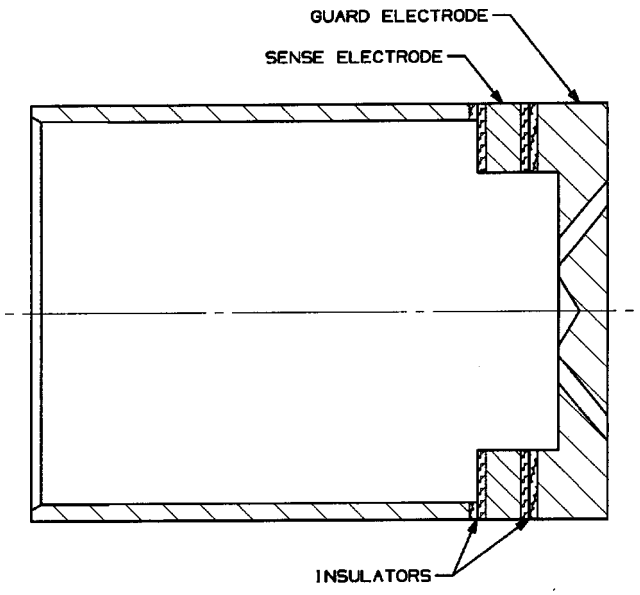

Fig. 5 Schematic of CCADS tip for prototype fuel injector center body

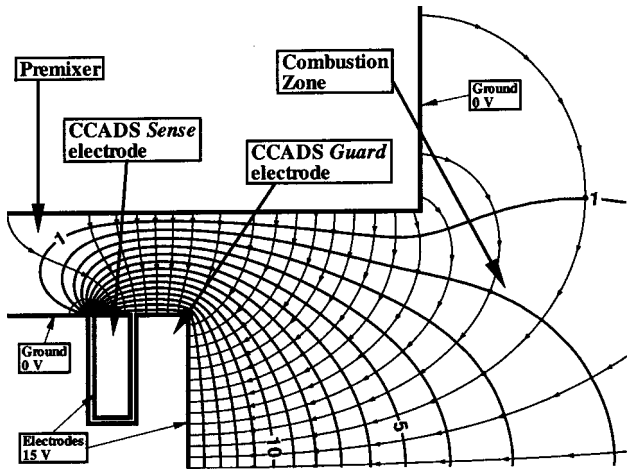

Fig. 6 2D electrostatic simulation potential gradient and flux lines. Flux lines are shown with arrows, potential lines solid. Values from 0 V at ground to 15 V at the electrodes.

(1.5 lb/s), and the rig can operate on natural gas or liquid fuel. Incoming air is heated using a nonvitiated air preheater. This method of preheating the air allows independent control of the inlet-air temperature and the combustor pressure. The preheated air enters a plenum region prior to flowing through the premixing annulus of the Woodward prototype fuel injector.

Fuel is injected into the premixing annulus at the swirl vanes perpendicular to the air flow. In addition to premixed fuel, pilot fuel can be injected into the combustion chamber to provide a diffusion flame pilot. Since cooling air is flowing through the diffusion tip of the center body, the pilot fuel is injected through the dome of the combustor liner, or the step expansion. All of the data described in this paper have been collected using the premix arrangement, with 5% of the fuel being supplied through the pilot.

The test rig is designed specifically to study combustion dynamics. It has no dilution cooling and very strong acoustic feedback. The walls of the combustion chamber are water-cooled, and a flow restriction is located approximately 19.8 cm (7.8 in.) downstream of the combustor dump plane. This area reduction serves to close the recirculation zone in a manner that approximates realistic turbine combustors. This restriction is formed by a cylindrical refractory insert that can be removed or replaced, if necessary (see Fig. 7). It is important to note that the combustor exhaust is not choked, therefore, a wide range of mass flow rates and pressures can be investigated. Furthermore, due to the overall length of the rig, a large number of acoustic modes are readily observed. In an attempt to reduce the acoustic gain, a second flow restriction is installed near a pressure node in the combustor. Although more work is required to understand the effect of this second restriction, for the purposes of this paper, it is mentioned merely as a modification to the existing test rig.

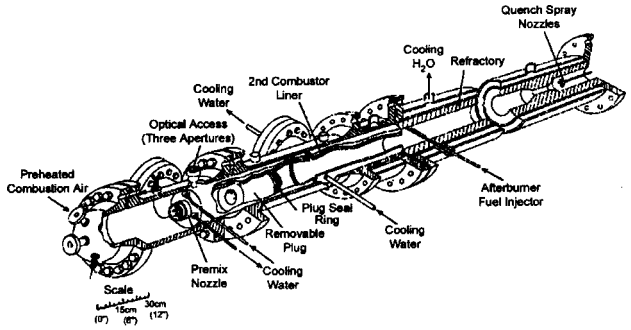

Fig. 7 Schematic of pressurized combustion test rig

Instrumentation. Both real-time and time-averaged data are collected using the flame ionization sensors. For the real-time data, a 15-V (DC) potential is simultaneously applied to both of the electrodes. The current transmitted by the electrons/ions in the combustor is amplified, converted to a voltage signal, and sent to a high-speed data collection system. The high-speed data are stored on digital DAT tapes at a 24,000 samples-per-second rate using a TEAC (Model RD-135T) recorder. The current signal from each of the electrodes is recorded simultaneously along with the combustor pressure.

The dynamic combustor pressure is measured using a Kistler (Model 206) pressure transducer that is located outside the pressure vessel. The pressure transducer is configured in an infinite coil as described by Mahan and Karcher [25] to minimize acoustic reflections in the frequency range of interest. The length of impulse line between the combustor and the pressure transducer is approximately 63.5 cm (25 in.). For these test conditions, the time delay due to the length of the impulse tubing is approximately 1.5 ms.

To collect the time-averaged data, a voltage is applied to both electrodes and the flame ionization current is measured through one electrode at a time. The DC voltage is supplied by a Xantrex (Model XHR-300-2) power supply. The current is measured using an Agilent (Model 34401A) current meter. The voltage is stepped from 0 to 150 to 0 V in 10-V increments. At each voltage setting, the measured flame current is allowed 5 s, to stabilize, then is averaged over 100 power line cycles (1.67 s). Stepping the voltage up and back down helps capture any hysteresis effects that may exist in the measurements.

Test Results

These results have been obtained with a reduced test matrix for initial evaluation of the prototype performance. Table 1 shows the combustor operating conditions for the data that will be discussed in this paper. The inlet-air temperature is constant for all conditions at 577 K (580°F), and the pressure is kept constant at 506.8 kPa (58.8 psig). Other conditions have been tested as part of the randomized test matrix with similar results as those shown for conditions described in Table 1. It is important to note that the test plan focused on varying the pressure, heat rate (fuel flow), and equivalence ratio as independent variables. Therefore, in order to vary the heat rate (fuel flow) and equivalence ratio independently,

Table 1 Summary of test conditions

Test conditions	Pressure [atm (psig)]	Fuel [kg/s (SCFH)]	Air [kg/s (SCFH)]	Equivalence ratio ϕ	Bulk nozzle velocity (m/s)
A	5.0 (58.8)	0.016 (2800)	0.466 (48630)	0.59	75
B	5.0 (58.8)	0.016 (2800)	0.429 (44680)	0.65	69
C	5.0 (58.8)	0.016 (2800)	0.397 (41320)	0.70	64

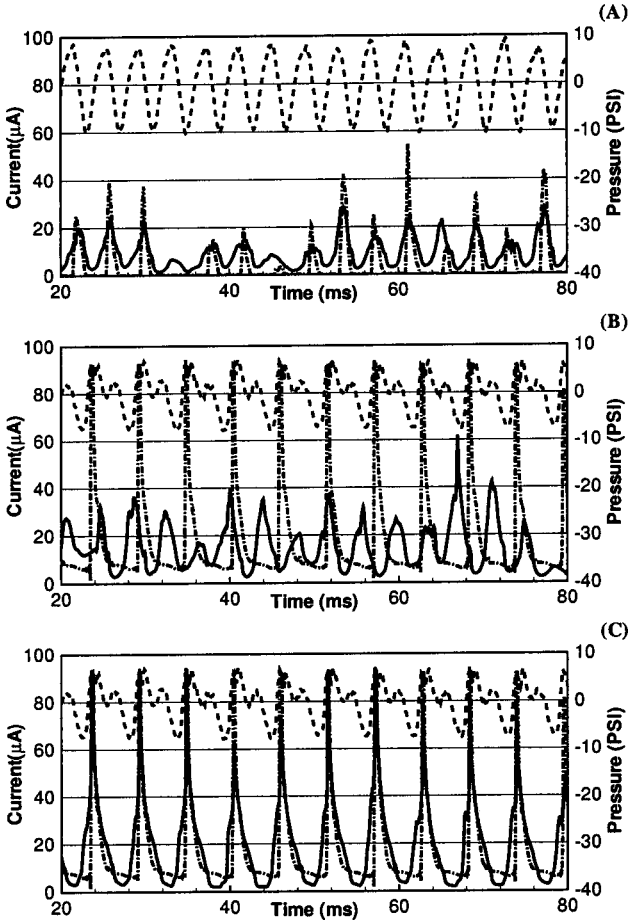

Fig. 8 Time series data showing the dynamic pressure and the measured CCADS current. (*A*) Condition A, ϕ=0.59, (*B*) Condition B, ϕ=0.65, (*C*) Condition C, ϕ=0.7 (see Table 1).

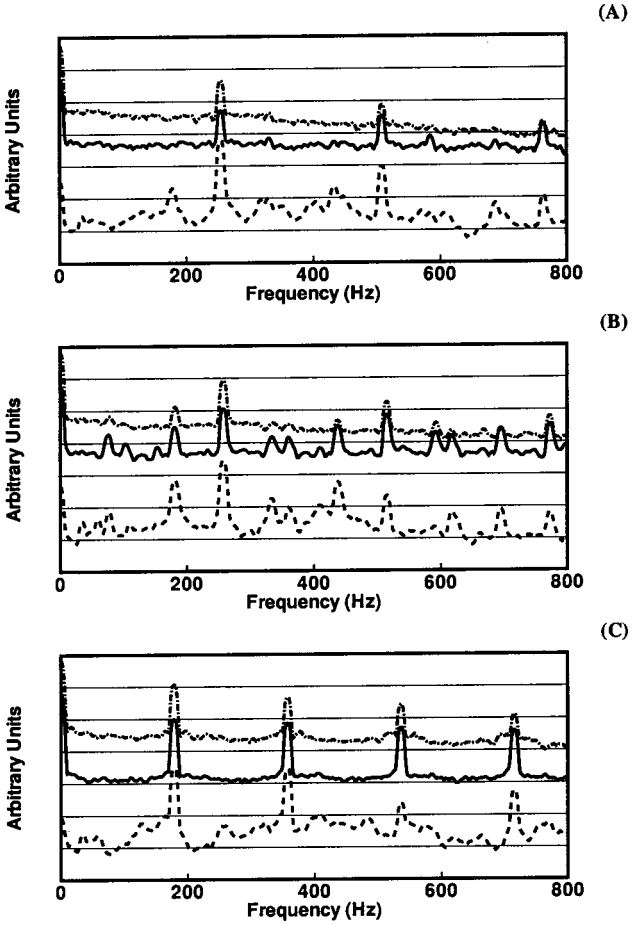

Fig. 9 Frequency spectrum of the dynamic pressure, sense *current* and *guard* current. (*A*) Condition A, ϕ=0.59, (*B*) Condition B, ϕ=0.65, (*C*) Condition C, ϕ=0.7 (see Table 1).

the air flow rate had to change. This has the effect of changing the average bulk flow velocity through the annulus of the premixer. As a result, any effects of the bulk flow velocity on current measurements will be confounded with the equivalence ratio effects.

Figure 8 shows the high-speed pressure and flame ionization current data with 15 V DC applied to both CCADS electrodes. Data from test conditions A, B, and C are shown as Fig. 8*(A)*, 8*(B)*, and 8*(C)*, respectively. One can see that the current measured from the *guard* electrode maintains a small DC offset at all test conditions. This is particularly significant since such a low voltage (15 V DC) is used for these measurements. A higher voltage potential on the *guard* electrode would increase the potential shown in Fig. 6 and produce even larger flame ionization current from the flame in the combustion zone. Therefore, one can conclude that the *guard* electrode could be used to indicate the presence of flame in the combustion zone.

Combustion oscillations are observed at all test conditions shown in Fig. 8, but the frequency and amplitude of the oscillation changes. The power spectra for the CCADS electrodes and the pressure are shown in Fig. 9. The dominant frequency in the pressure signal is also present in the data collected from the electrodes. Therefore, the current measurements from the CCADS electrodes biased at 15 V DC are capable of detecting the frequency of the combustion oscillations. Although a correlation between the amplitude of the electrode signal and the amplitude of the pressure signal is not known at this time, the electrodes can provide additional information about the premixer region that is not available from the pressure signal. This will be described in the next section.

If the *sense* electrode current data in Fig. 8 is examined, the higher flow velocity (lean equivalence ratio) conditions tend to reduce the time-averaged *sense* electrode signal. Furthermore, significant periods of no detectable current exist (see Fig. 8*(A)* and Fig. 8*(B)*). It is believed that these higher velocity (lean equivalence ratio) conditions prevent the flame from anchoring inside the premixer. However, the spikes observed in the *sense* electrode current indicate that the *sense* electrode is collecting electrons, and these peaks in *sense* electrode current correspond with peaks in the combustor pressure. Similar behavior with a different premixer design has been observed in experimental testing [14] and in large eddy simulations (LESs) [26]. Results from the LES simulations indicate that the reaction moves into the premix region during combustion oscillations, and the peaks in the combustor pressure correspond with flow reversal and ''flame flicker'' along the center body. Although it is not clear whether these transient flashback events occur in all straight barrel center-body designs, the CCADS concept is capable of detecting these short duration events that may occur in the premixer. These transient flashback events could not be detected with a pressure transducer or thermocouple.

From the CCADS measurements one can conclude that the flame is not anchored inside the premixer during test conditions A and B because the current measured through the *sense* electrode returns to approximately zero during the oscillation cycle. However, if the bulk flow velocity is further decreased (equivalence ratio is increased) as in condition C, the *sense* electrode signal begins to show a DC offset suggesting that the flame is anchored

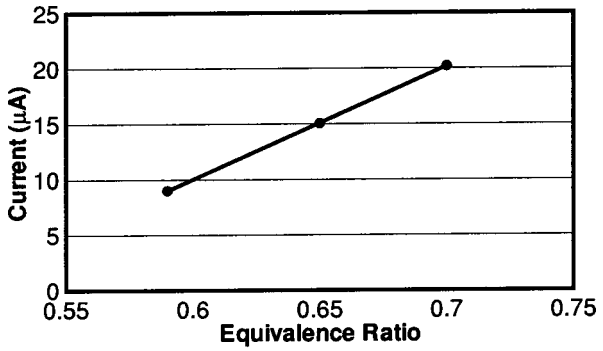

Fig. 10 Average *guard* current computed from the 60 ms time series data shown in Fig. 8

upstream of the *sense* electrode. Notice that in Fig. 8*(C)* the current measured from the *sense* electrode is greater than the current from the *guard* electrode when the pressure cycle is near a minimum. It is important to note that the potential gradient [i.e., all of the contour lines converge to the upstream corner of the *sense* electrode (see Fig. 6)] upstream of the *sense* electrode is much higher along the center body than the gradient surrounding the *guard* electrode. Therefore, the *sense* electrode should be more sensitive to charge carriers that are upstream of the electrodes than the *guard* electrode. Similarly, the *guard* electrode is more sensitive to charge carriers located downstream of the electrodes. Therefore, the amount of current from the *sense* to the upstream center-body surface is more than the current observed through the *guard* electrode.

The data in Fig. 10 shows the time-averaged *guard* current, calculated using the current signals shown in Fig. 8, and plotted as a function of the equivalence ratio. This data show a linear relationship between the average current and the inlet or bulk equivalence ratio of the combustion system. Due to the limited amount of available data more testing is needed to ascertain the relationship for this configuration. Furthermore, this test plan called for separating the effects of fuel flow (heat rate) from the equivalence ratio, instead of separating the bulk flow from the equivalence ratio effect. Both the bulk flow and the equivalence ratio will effect the ion density and therefore effect the measured current. These effects were observed in previous experiments conducted in NETL's atmospheric combustion rig [13]. Therefore, more work is required to understand and establish the relationship between the CCADS measurements and the equivalence ratio of the combustion system.

Next Steps

It is now clear that with the proper design of ion sensing electrodes much information about flame location and condition can be ascertained. Our experimental work will be combined with FEA and CFD to optimize the sensor design for a particular combustor configuration. Furthermore, achieving adequate sensor life will require close attention to material properties for the electrodes, dielectric insulators, and electrical connections. Our next generation design will evaluate new ideas to improve durability at an acceptable component cost.

The ion signal depends upon obtaining a low-impedance path from the electrode, through the flame ion field, and ultimately to electrical ground. Modern combustors have thermal barrier coatings covering much of the surface area of the hot section. These coatings have electrical properties that vary with temperature, and some TBC designs may interfere with ion signal strength. The electrical characteristics of these coatings will also be evaluated in NETL laboratories.

Combustion sensing must be integrated into the engine control system. Woodward already offers sophisticated controls for the fuel, air, and ignition systems. Our intent is to integrate ion sensing into electronic modules already available on modern DLN control systems. Our vision is that combustion feedback is integrated with the fuel system such that mitigating action can be taken once combustion dynamics, flashback, or other undesirable combustion conditions are detected. Some mitigating actions may simply require changing the power setting to avoid difficult operating regimes, but other solutions such as pilot trim valves, variable geometry nozzles, or high-frequency fuel injection valves may offer the better solution.

Conclusions

Researchers at the National Energy Technology Laboratory (NETL) and Woodward Industrial Controls are developing a durable, low-cost, in situ monitoring technique for control and diagnostics of natural gas combustion systems. This technique is based on the flow of electrical current through a hydrocarbon flame resulting from an applied electric field across the flame and the flame ionization reactions. This CCADS technique uses two electrically isolated electrodes on the premixing fuel injector center body, near the tip and the combustion flame anchor. Previous investigations at NETL have demonstrated the CCADS technique to detect flashback, the presence of the combustion flame, and to indicate the frequency of dynamic pressure of the combustion oscillations.

Woodward has designed a prototype fuel injector with the sensor electrodes on the center body. The initial evaluation of the prototype shows that the CCADS can potentially be used for multiple sensor functions. The data presented here show that the CCADS technique can be used to detect flashback, detect the presence of flame in the combustion zone, and detect the presence of dynamics pressure oscillations during operations. In addition, the CCADS technique can potentially provide a signal relative to the operating equivalence ratio of the combustion system. However, a more comprehensive evaluation of this measurement relationship, and an improved understanding of the physics are needed to fully develop this capability.

Acknowledgments

The authors wish to gratefully acknowledge the technical support of personnel from Woodward, Mr. Patrick Riley and Mr. Dan Burke, and from NETL, Dr. Ben Chorpening, Mr. Mark Tucker, and Mr. Mike Dera.

References

[1] Docquier, N., and Candel, S., 2002, "Combustion Control and Sensors: a Review," Prog. Energy Combust. Sci., **28**, pp. 107–150.
[2] Fric, T. F., Correa, S. M., and Bigelow, E. C., 1994, "Fuel Trim Control for Multi-Burner Combustors Based on Emissions Sampling," *Proceedings of ASME COGEN-TURBO 1994*, ASME, New York, NY IGTI-Vol. 9, pp. 503–511.
[3] St. John, D., and Samuelson, G. S., 1994, "Active Optimal Control of a Model Industrial Natural Gas Fired Burner," *Proceedings of the Twenty-Fifth International Symposium on Combustion*, editors, The Combustion Institute, Pittsburgh, PA, pp. 307–316.
[4] Jackson, M. D., and Agrawal, A. K., 1999, "Active Control of Combustion for Optimal Performance," ASME J. Eng. Gas Turbines Power, **121**, pp. 437–443.
[5] Corbett, N. C., and Lines, N. P., 1994, "Control Requirements for the RB 211 Low-Emission Combustion System," ASME J. Eng. Gas Turbines Power, **116**, pp. 527–533.
[6] Pandalai, R. P., and Mongia, H. C. 1998, "Combustion Instability Characteristics of Industrial Engine Dry Low Emission Combustion Systems," AIAA Paper No. 98-3379.
[7] Scott, D. A., King, G. B., and Laurendeau, N. M., 2002, "Chemiluminescence-Based Feedback Control of Equivalence Ratio for a Continuous Combustor," J. Propul. Power, **18**(2), pp. 376–382.
[8] Sandrowitz, A., Cooke, J. M., and Glumac, N. G., 1998, "Flame Emission Spectroscopy for Equivalence Ratio Monitoring," Appl. Spectrosc., **52**(5), pp. 285–289.

[9] Lee, J. G., Kim, K., and Santavicca, D. A., 2000, ''Measurement of Equivalence Ratio Fluctuation and Its Effect on Heat Release During Unstable Combustion,'' *Proceedings of the Twenty-Eighth International Symposium on Combustion*, The Combustion Institute, Pittsburgh, PA, pp. 415–421.
[10] Brown, D. M., Downey, E., Kretchmer, J., Michon, G., Shu, E., and Schneider, D., 1998, ''SiC Flame Sensor for Gas Turbine Control Systems,'' Solid State Electronics, **42**, pp. 755–760.
[11] Eriksson, L., and Nielsen, L., 1997, ''Ionization Current Interpretation for Ignition Control in Internal Combustion Engines,'' Control Engineering Practice, **5**, pp. 1107–1113.
[12] Waterfall, Roger C., He, Ruhua, and Beck, Christopher M., 1997, ''Visualizing Combustion Using Electrical Impedance Tomography,'' Chem. Eng. Sci., **52**, pp. 2129–2138.
[13] Thornton, J. D., Straub, D. L., Richards, G. A., Nutter, R. S., and Robey, E., 2001, ''An In-Situ Monitoring Technique for Control and Diagnostics of Natural Gas Combustion Systems,'' *Proceedings of the Second Joint Meeting of the U.S. Sections of the Combustion Institute*, The Combustion Institute, Pittsburgh, PA.
[14] Straub, D. L., Thornton, J. T., Chorpening, B. T., and Richards, G. A., 2002, ''In-Situ Flame Ionization Measurements In Lean Premixed Natural Gas Combustion Systems,'' *Proceedings of the Western States Section of the Combustion Institute Spring Technical Meeting*, The Combustion Institute, Pittsburgh, PA.
[15] Calcote, H. F., 1957, ''Mechanism for the Formation of Ions in Flames,'' Combust. Flame, **1**, pp. 385–403.
[16] Fialkov, A. B., 1997, ''Investigations on Ions in Flames,'' Prog. Energy Combust. Sci., **23**, pp. 399–528.
[17] Calcote, H. F., 1949, ''Ionization Flame Detectors,'' Rev. Sci. Instrum., **20**, pp. 349–352.
[18] Calcote, H. F., and Berman, C. H., 1989, ''Increased Methane-Air Stability Limits by a DC Electric Field,'' *Proceeding of the ASME Fossil Fuels Combustion Symposium*, ASME, New York, NY, Vol. 25, pp. 25–31.
[19] Cheng, W. K., Summers, T., and Collings, N., 1998, ''The Fast-Response Flame Ionization Detector,'' Prog. Energy Combust. Sci., **24**, pp. 89–124.
[20] Thornton, J. D., Richards, G. A., and Robey, E., 2000, ''Detecting Flashback in Premix Combustion Systems,'' presented at the American Flame Research Committee International Symposium, Newport Beach, California, September 17–21.
[21] Fluent Inc. 2001, *Fluent 6.0 User's Guide*, Lebanon, NH.
[22] Straub, D. L., and Richards, G. A. 1999, ''Effect of Axial Swirl-vane Location On Combustion Dynamics,'' ASME Paper 99-GT-109.
[23] Mansour, A., Benjamin, M., Straub, D. L., and Richards, G. A., 2000, ''Application of Macrolamination Technology to Lean Premix Combustion,'' ASME J. Eng. Gas Turbines Power, **123**, pp. 796–802.
[24] Straub, D. L., Richards, G. A., Baumann, W. T., and Saunders, W. R., 2001, ''Measurement of Dynamic Flame Response In A Lean Premixed Single-Can Combustor,'' ASME 2001-GT-0038.
[25] Mahan, J. R., and Karchmer, A. 1991, ''Combustion Core Noise,'' *Aeroacoustics of Flight Vehicles: Theory and Practice, Volume 1: Noise Sources, NASA Reference Publication 1258*, Harvey H. Hubbard, ed., NASA Langley Research Center, Chap. 9.
[26] Cannon, S. M., Adumitroaie, V., and Smith, C. E., 2001, ''3D LES Modeling of Combustion Dynamics in Lean Premixed Combustors,'' ASME Paper 2001-GT-0375.

Comparison of Linear and Nonlinear Gas Turbine Performance Diagnostics

Ph. Kamboukos
Research Assistant

K. Mathioudakis
Associate Professor

Laboratory of Thermal Turbomachines,
National Technical University of Athens,
P.O. Box 64069,
Athens 15710, Greece

The features of linear performance diagnostic methods are discussed, in comparison to methods based on full nonlinear calculation of performance deviations, for the purpose of condition monitoring and diagnostics. First, the theoretical background of linear methods is reviewed to establish a relationship to the principles used by nonlinear methods. Then computational procedures are discussed and compared. The effectiveness of determining component performance deviations by the two types of approaches is examined, on different types of diagnostic situations. A way of establishing criteria to define whether nonlinear methods have to be employed is presented. An overall assessment of merits or weaknesses of the two types of methods is attempted, based on the results presented in the paper. [DOI: 10.1115/1.1788688]

Introduction

Methods for diagnosing faults in the components of gas turbine engines have been in use for a long time now. The basic idea of all existing methods is that the deviation in values of characteristic component performance parameters are determined from measurement data. Measurements are compared to baseline values, namely, values from an engine considered to be in a new and clean condition. The problem of determining parameter deviations from measurement deviations and the assessment of engine condition based on these estimations is termed as the diagnostic problem.

A variety of techniques have been proposed by different authors, for solving the diagnostic problem. The first techniques that have been proposed (Urban [1]) were based on the formulation of a linear system of equations, interrelating measurement and parameter deviations. It results from the requirement that predicted values of performance variables should be as closely as possible to corresponding measurements. The system is linear, because it is set up by assuming small deviations of parameters, allowing the elimination of higher-order terms. This basic formulation has proven to be successful for practical purposes and forms the basis for most of the commercial systems available from the major jet engine manufacturers today (Doel [2], Urban and Volponi [3], Barwell [4]).

In the meantime, nonlinear methods have been proposed. The nonlinearity consists in the fact that measured variables are interrelated to parameters not through simplified linear relations, but through a fully nonlinear thermodynamic model. Formulation of the diagnostic problem is still based on the principle of minimizing difference of predictions from measurements. The minimization problem is formulated using various expressions, while various approaches are also used for its solution.

An objective function of the sum-of-squares type, minimized through conventional numerical algorithms, was employed by Stamatis, Mathioudakis, and Papailiou [5], in one of the first nonlinear methods to be proposed. Successive updates of the Jacobian matrix were employed by Escher and Singh [6], to formulate a nonlinear solver, consisting of successive applications of a linear one. Sum of absolute values, minimized through genetic algorithms, has been employed by Zedda and Singh [7]. Gronstedt [8] has investigated the exploitation of information from individual operating points to assess engine state using a genetic algorithm as an optimizer. Grodent and Navez [9] have used a statistical approach, with an objective function which is a combination of a quadratic and a modulus function. Composite objective functions, incorporating sum of squares and absolute values were proposed by Mathioudakis, Kamboukos, and Stamatis [10]. Finally, combinatorial approaches, solving a number of possible combinations of parameters and variables, and then selecting the most appropriate solutions, were proposed by Aretakis, Mathioudakis, and Stamatis [11].

Although such a wide variety of nonlinear techniques has become available, a systematic comparison of their effectiveness with respect to linear methods cannot be found in the literature. Results from particular cases have been presented by Escher and Singh [6] and Ogaji and Singh [12], for their particular formulations, to show the expected feature that their nonlinear method is superior to a linear one.

With the linear methods having the obvious advantage of simplicity, a question that can be posed is whether the superiority of nonlinear methods is substantial enough to justify the additional complexity. This is the main question that is addressed in the present paper. The degree of accuracy of the two types of methods is assessed, and the conditions under which the one or the other may present advantages are investigated. Although the investigation is based on a particular engine type, the method of study is general enough so that information can be provided to the engine diagnostician as to the kind of methods that would be expected to be most appropriate for a particular diagnostic problem in hand.

Linear and Nonlinear Methods

The purpose of a diagnostic method is to assess the engine condition when a set of measured quantities from the engine is available. Condition assessment is performed by estimation of the health parameters of engine components. The estimation is considered successful when quantities measured on the engine are reproduced in the best possible way, by an engine performance model incorporating the health parameters.

The engine can be represented though a functional relation between quantities that define the operating point, denoted as **u**, quantities expressing components health, denoted as **f**, and quantities measured for monitoring, denoted as **Y**:

$$\mathbf{Y} = \mathbf{F}(\mathbf{u}, \mathbf{f}). \tag{1}$$

Contributed by the International Gas Turbine Institute (IGTI) of THE AMERICAN SOCIETY OF MECHANICAL ENGINEERS for publication in the ASME JOURNAL OF ENGINEERING FOR GAS TURBINES AND POWER. Paper presented at the International Gas Turbine and Aeroengine Congress and Exhibition, Atlanta, GA, June 16–19, 2003, Paper No. 2003-GT-38518. Manuscript received by IGTI, October 2002, final revision, March 2003. Associate Editor: H. R. Simmons.

A computerized engine model materializes such a relationship. For a given operating point, Eq. (1) can be simplified to

$$\mathbf{Y}=\mathbf{F}(\mathbf{f}). \tag{2}$$

Health parameters for diagnostic purposes are derived by minimizing a cost function, usually represented by a relationship of the following form:

$$\mathrm{OF}=C_1\sum_{i=1}^{M}\left[\frac{Y_i^{\mathrm{given}}-Y_i^{\mathrm{calc}}(f)}{\sigma_{Y_i}Y_i^{\mathrm{ref}}}\right]^2+C_2\sum_{j=1}^{N}\left[\frac{f_j-f_j^0}{\sigma_{f_j}f_j^0}\right]^2 +C_3\sum_{j=1}^{N}\left|\frac{f_j-f_j^0}{\sigma_{f_j}f_j^0}\right|. \tag{3}$$

The first sum is used to satisfy the condition that model prediction will be as close as possible to measured quantities. The subsequent two terms express the empirical fact that health indices are not expected to deviate significantly from (known) reference values. The relative importance of the different terms is expressed through the weight factors *C*. Inclusion of these factors gives the possibility to adapt the objective function to the type of problem solved. For example, if the number of available measurements *M* is larger than the number *N* of unknown health parameters, then the values $C_1=1$ and $C_2=C_3=0$, can be used since the first group of terms is sufficient for obtaining a unique solution. More information about the significance of the different terms can be found in Ref. [10]. This generalized expression embeds different objective functions that have been employed by various diagnostic methods (for example, methods employing only sums of squares, only sums of absolute values, or both). In the following, linear and nonlinear methods comparison will be effected for cost functions using only sums of squares. This formulation is chosen as it is the basis for the main linear gas path analysis techniques that are in use today, e.g., Doel [13].

Taking $C_1=1$ and $C_3=0$ and using deltas, Eq. (3) becomes

$$\mathrm{OF}=\sum_{i=1}^{M}\left[\frac{\Delta Y_i^{\mathrm{given}}-\Delta Y_i^{\mathrm{calc}}(f)}{\sigma_{Y_i}}\right]^2+C_2\sum_{j=1}^{N}\left[\frac{(\Delta f_j-\Delta f_j^0)}{\sigma_{f_j}}\right]^2, \tag{4}$$

where

$$\Delta Y_i^{\mathrm{calc}}(\mathbf{f})=\frac{Y_i^{\mathrm{calc}}(\mathbf{f})-Y_i^{\mathrm{ref}}}{Y_i^{\mathrm{ref}}},\quad \Delta Y_i^{\mathrm{given}}=\frac{Y_i^{\mathrm{given}}-Y_i^{\mathrm{ref}}}{Y_i^{\mathrm{ref}}}, \tag{5}$$

$$\Delta f_j=\frac{f_j-f_j^{\mathrm{ref}}}{f_j^{\mathrm{ref}}},\quad \Delta f_j^0=\frac{f_j^0-f_j^{\mathrm{ref}}}{f_j^{\mathrm{ref}}} \tag{6}$$

(usually f^0 is taken to be equal to f^{ref}).

Calculated values in this expression come from an engine model. As shown in Appendix A, the general non-linear model can be reduced to a linear one, when parameter deviations are small, resulting into an expression of the form

$$\Delta Y_i^{\mathrm{calc}}=\sum_{j=1}^{N}\alpha_{ij}\Delta f_j \tag{7}$$

For a priori estimates of the health indices for those of a healthy engine ($f^0=f^{\mathrm{ref}}$), Eq. (4) becomes

$$\mathrm{OF}=\sum_{i=1}^{M}\left[\frac{\Delta Y_i^{\mathrm{given}}-\Sigma_{j=1}^{N}\alpha_{ij}\Delta f_j}{\sigma_{Y_i}}\right]^2+\sum_{j=1}^{N}\left[\frac{\sqrt{C_2}}{\sigma_{f_j}}\Delta f_j\right]^2. \tag{8}$$

Minimization of this expression is a least-squares problem and the vector $\Delta\mathbf{f}$ that minimizes this expression is given by the familiar matrix relation:

$$\Delta\mathbf{f}=[\mathbf{M}^{-1}+\mathbf{H}^T\cdot\mathbf{R}^{-1}\cdot\mathbf{H}]^{-1}\cdot\mathbf{H}^T\cdot\mathbf{R}^{-1}\cdot\mathbf{z}, \tag{9}$$

where $\mathbf{H}=[a_{ij}]$ is the system matrix, $\mathbf{z}=[\Delta Y^{\mathrm{given}}]$ is the vector of knowns, $\mathbf{R}=[\sigma_{Yi}^2]$ is the matrix containing the weight coefficients for measurement terms and $\mathbf{M}=[C_2/\sigma_{f_j}^2]$ is the matrix of a priori expected values for health-parameter estimation errors.

The particular aspects of linear and nonlinear diagnostic methods are now going to be examined using as test case an engine representative of a contemporary civil turbofan. The computer model that will be employed for simulating the performance of this engine has been presented by Stamatis et al. [14]. The engine layout, the measurements, and the health parameters considered are given in Appendix B.

Measurement Predictions From Nonlinear and Linear Models

The fundamental reason that the linear model, as expressed by Eq. (7), does not provide accurate solutions for $\Delta\mathbf{f}$ lies in the fact that it holds only approximately. Measurement Δ's evaluated by Eq. (7) differ from the actual ones by the magnitude of the higher-order terms, neglected in the linear approximation (*A*1) of Appendix A. It is thus useful to examine the amount of this difference for health-parameter deviation magnitudes encountered in usual fault situations.

An example of a measurement Δ evaluated by a linear and a nonlinear model is shown in Fig. 1. ΔT_6 variations for changes in the low-pressure turbine flow capacity between -5% and 5% are compared for linear and nonlinear models. It is apparent that for flow capacity changes larger than 2%, the deviation between the two Δ's is substantial.

The difference between linear and nonlinear predictions is not the same for all health parameters. In order to examine how close to linear a particular measurement Δ is, the difference between linear and nonlinear values is used. This quantity is defined as

$$\delta(\Delta Y_i^j)=\Delta Y_{ij}^{NL}-\Delta Y_{ij}^{L}, \tag{10}$$

where index *i* denotes the considered measurement and index *j* the deviated health parameter.

The sensitivity of this quantity to Δ's of different health parameters, for the exhaust gas temperature used as an example above, can be assessed from the results of Fig. 2. It is shown that for several health parameters (e.g., SE12, A8IMP, SW12, SW41) linear and nonlinear δ's are very close to each other, while a strong nonlinear dependence is shown for others, the most pronounced being SE26 and SE41.

Inspection of such results suggests that a first indicator can be established as to how strong the nonlinear impact of a particular parameter on measurement Δ's is. A nonlinearity Indicator NLI of a health parameter f_j is introduced as

$$\mathrm{NLI}_j=\frac{1}{M}\sum_{i=1}^{M}\delta(\Delta Y_i^j)^2. \tag{11}$$

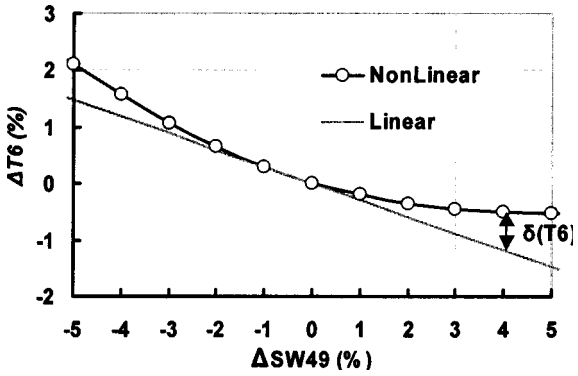

Fig. 1 Measurement deviation by linear and nonlinear model

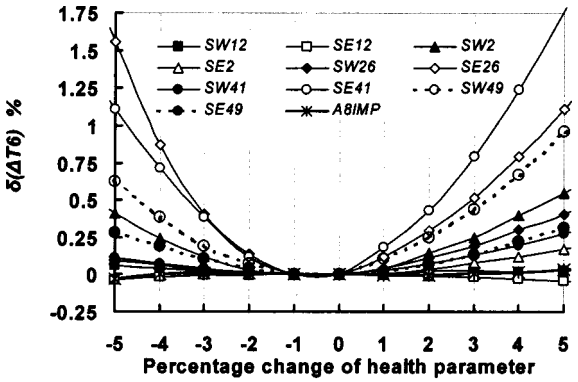

Fig. 2 Difference of the predictions of nonlinear and linear models

Health parameters with larger values of NLI, are prone to nonlinear behavior and for this reason special care must be applied when estimating them. The nonlinearity indicator for all health parameters of the engine considered here is given in Fig. 3. As expected, NLI is larger for larger health-parameter Δ's. On the other hand, this quantity indicates that some health indices are quite linear in behavior while others are not. SE26 and SE41 have the maximum nonlinearity. SW12 exhibits nonlinearity in a global sense, while its effect on T_6 was rather linear. For ease of interpretation, instances of this diagram may be presented separately, as for example shown in Fig. 4.

A last comment on the previous results is that NLI is zero for all health parameters for -1% change of each health parameter. The reason is that Jacobian matrix elements in the present case are evaluated by a -1% change of parameters and thus the predictions of both approaches for measurement changes coincide. In the Discussion section some particular aspects of the Jacobian matrix elements evaluation will be discussed.

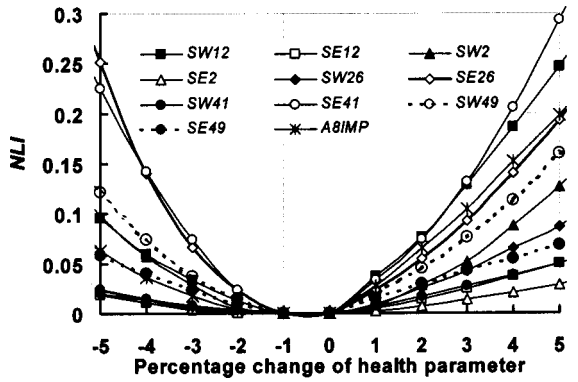

Fig. 3 Nonlinearity indicator for different health parameters

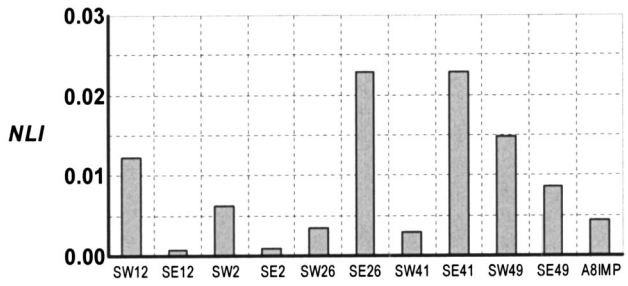

Fig. 4 NLI for -2% deviation of health parameters

Linear and Nonlinear Parameter Estimation

The effect of the difference between linear and nonlinear measurement Δ's on parameter estimation will now be examined. The method used for nonlinear parameter estimation is adaptive modeling, introduced by Stamatis et al. [5,17]. Measurement data have been generated by simulating changes of individual fault parameters. They were then provided as an input for the methods used to perform the estimations. The results shown below are for a 2% change in each parameter. A square diagnostic problem is considered at this stage (equal number of measurements and parameters), and C_2 is taken to be zero in Eq. (8). This initial choice is dictated by the fact that the result of the primary mechanism of parameter–measurement interrelation is to be explored, before examining other techniques that make use of additional information.

Three types of behavior have been observed, as shown from the representative results of Fig. 5. First, the nonlinear method produces an accurate estimation of the parameter deviations that have caused the measurement Δ's it was presented. For the linear method on the other hand, we have three types of behavior:

- Some parameters are estimated with sufficient accuracy. An example of such a parameter is fan efficiency parameter, SE12, as shown in Fig. 5(*a*).
- Other parameters are also estimated accurately, but additional spurious information is generated (would result in a false alarm). A high-pressure turbine (HPT) efficiency fault is correctly estimated, but at the same time a significant spurious deviation of the high-pressure compressor (HPC) flow capacity is also indicated, with smaller deviations spread over other health parameters too (Fig. 5(*b*)).
- Finally, some other parameters are estimated with a large deviation, while at the same time a false alarm on other parameters is generated. Fan flow capacity is an example of such a parameter, as shown in Fig. 5(*c*).

For every individual deviating parameter, the deviation of the linear value from the actual one increases with fault severity, as shown for example in Fig. 6 for SW12.

It is observed that these results are in agreement with the indications of the NLI chart, Fig. 3. The very small value for SE12

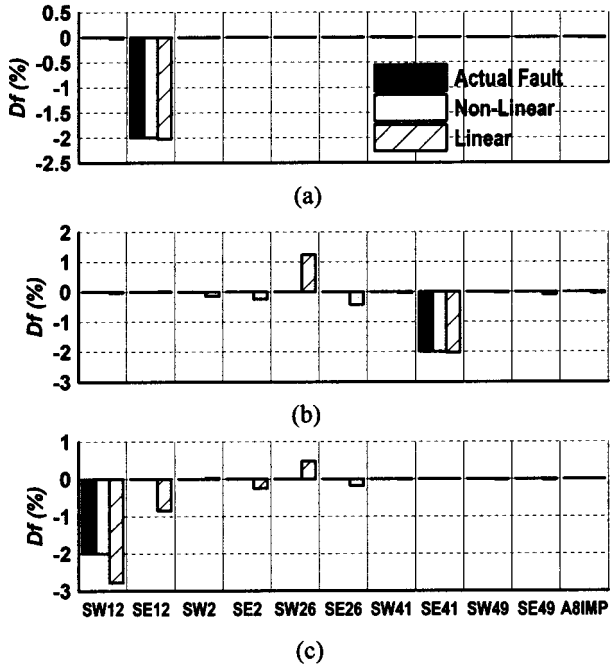

Fig. 5 Methods comparison for various fault situations

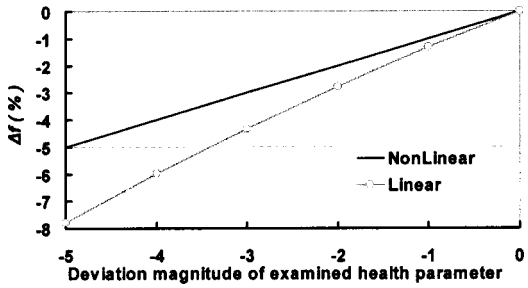

Fig. 6 Linear and nonlinear estimates of SW12 in function of fault level

actually indicates that this parameter assumes a linear behavior, as verified in Fig. 5(*a*). The large values for SW41 and SW12 also reflect the observations of Figs. 5(*b*) and 5(*c*). Of course the NLI does not distinguish between the latter two types of behavior.

A measure of the effectiveness of linear estimation for each health parameter can be given through the Eucleidian distance of solution vectors from the actual ones:

$$\mathrm{EUD}=\frac{1}{N}\sqrt{\sum_{j=1}^{N}[\Delta f_j^{NL}-\Delta f_j^{L}]^2}. \tag{12}$$

N is the number of estimated parameters (11 in the example considered here). Results for the 2% deviations are shown in Fig. 7. A small value indicates that the actual solution is very closely approximated, while a large value indicates that inaccuracies are produced, without knowing, however, if they express inaccuracy of the actual parameter or false values attributed to the remaining ones.

A way to reveal this behavior in a compact form is though the diagnostic response matrix, introduced by Mathioudakis, Kamboukos, and Stamatis [10]. This matrix is constituted from the results of a linear estimation, when measurement data are produced by disturbing each individual health parameter by 2%. The matrix for the present test case is shown in Table 1. It is reminded here that rows show the possibility of the method to identify isolated changes, while columns show how estimation of a particular parameter is influenced by deviations on other parameters. This matrix embeds the information illustrated in Fig. 5, covering the entire set of health indices employed.

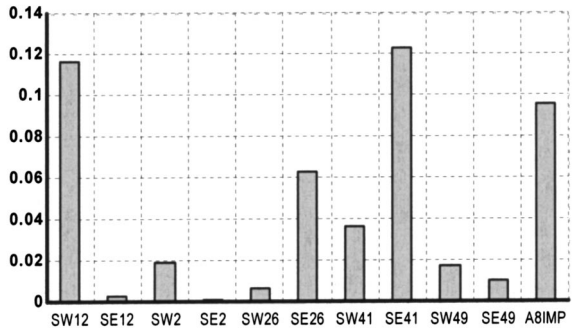

Fig. 7 Euclidian distance of linear estimations from nonlinear for faults with 2% deviations

Table 1 Diagnostic response matrix for linear parameter estimations

Disturbed Parameter	Estimated Values										
	SW12	SE12	SW2	SE2	SW26	SE26	SW41	SE41	SW49	SE49	A8IMP
SW12	-2.8	-0.8	0	-0.2	0.5	-0.2	0	0	0	0	0
SE12	0	-2.0	0	0	0	0	0	0	0	0	0
SW2	0	0	-2.1	-0.2	0	0	0	0	0	0	0
SE2	0	0	0	-2.0	0	0	0	0	0	0	0
SW26	0	0	0	0	-2.1	0	0	0	0	0	0
SE26	0	0	-0.1	-0.1	0.5	-2.4	0	0	0	0	0
SW41	0	0	0	0	0	0	-2.1	0	0	0	0
SE41	0	0	-0.1	-0.2	1.2	-0.4	0	-2.0	0	0	0
SW49	0	0	-0.1	-0.1	0.9	-0.3	0	0	-2.0	0	0
SE49	0	0	0	0	0	0	0	0	0	-2.1	0
A8IMP	-0.1	-0.1	0	0	0	0	0	0	0	0	-2.0

Fault Detection and Deterioration Tracking

Individual parameter estimation discussed in the preceding section covers the cases of faults that are manifested as individual parameter changes. Many cases of faults, however, include simultaneous changes on several parameters. Faults in a component usually imply change of both the component health indices. For such situations, the detection capabilities of a linear method will result from the combination of the effects on individual parameters discussed above. For illustration purposes a test case of faults reported to be realistic has been chosen, taken from Ganguli [15]. The results of estimation with linear and nonlinear method are shown in Table 2. Here too, small differences are observed for parameters with small NLI and larger ones for those with larger NLI. As a general remark, the faults are rather successfully identified, but the health index deviation estimation is not always that accurate.

Another type of situation with practical interest is the case of overall deterioration. The specific features of the diagnostic problem for this case and a nonlinear method for deterioration tracking was presented by Mathioudakis, Kamboukos, and Stamatis [10]. Their formulation estimated 11 parameters from 7 available measurements. When a linear model is used to support such methods, with all other specific features retained, the accuracy may deteriorate as a result of the approximate estimations of health parameters at the successive estimation steps.

An example of such an effect is demonstrated in Fig. 8. The result from the method of Ref. [10] implemented with a linear model is compared to the nonlinear one originally employed. The formulation of the original method is retained, apart from the fact that model estimations are produced through an equation of the form of Eq. (7) and not a fully nonlinear engine model. The much poorer performance of the method when supported by the linear model is observed. Overall effectiveness is assessed in Fig. 9, by presenting the results at the final point of the deterioration scenario considered. The overall picture is that most of the estimated parameters by the linear method exhibit a significant distance from the nonlinear estimations, which are very close to the actual values. A remarkable feature of this formulation is that differences in estimations occur not only for nonlinearly behaved parameters but also for parameters that do not exhibit interrelation with others according to the diagnostic response matrix for the 11×11 problem. This shows that for the present formulation the linearity-induced inaccuracies may influence all the parameters, a fact that can be attributed to the additional constraints implicitly imposed by the particular diagnostic algorithm.

It is interesting here to compare the previous results to estimations of a Kalman filter. An off-the-shelf routine was employed [16]. The observation equation used is the linear system equation (7), while the unity matrix was used as a state extrapolation matrix (formulation similar to the one presented in Ref. [3]). The estimation results for the final point of the scenario examined above are also shown in Fig. 9. This way of application gives much poorer results than the nonlinear method.

Table 2 Results of diagnostic methods for a typical set of faults [15]

Fault		SW12	SE12	SW2	SE2	SW26	SE26	SW41	SE41	SW49	SE49	A8IMP
FAN	Actual Fault	-2.50	-2.00									
	NonLinear	-2.50	-2.00									
	Linear	-2.45	-1.93	-0.03	-0.04	-0.04	0.00	0.00	0.00	-0.01	0.00	-0.01
LPC	Actual Fault			-2.20	-2.00							
	NonLinear			-2.20	-2.00							
	Linear	0.00	0.00	-2.22	-1.89	-0.06	-0.01	-0.01	0.00	-0.01	-0.01	-0.01
HPC	Actual Fault					-1.60	-2.00					
	NonLinear					-1.60	-2.00					
	Linear	-0.01	0.00	-0.05	-0.10	-1.97	-1.87	-0.01	0.00	-0.01	-0.02	-0.01
HPT	Actual Fault							1.50	-2.00			
	NonLinear							1.50	-2.00			
	Linear	-0.03	0.01	-0.19	-0.25	0.11	-0.07	1.38	-2.05	-0.03	-0.08	-0.04
LPT	Actual Fault									3.30	-2.00	
	NonLinear									3.30	-2.00	
	Linear	-0.02	-0.04	-0.26	-0.60	0.80	-0.45	0.00	0.01	3.18	-2.19	0.03

Discussion

The observations made and conclusions drawn from the results presented previously can be related to some particular aspects of the problem studied. The first such aspect is the way of deriving the influence coefficients for formulation of the linear model.

Numerical evaluation of the Jacobian matrix elements is through a numerical approximation of the partial derivatives (Eq. (16)). They can be evaluated using left, right, or central finite differences and different steps. The resulting linear model will be different for each case, as shown in Fig. 10. Although the overall comparison to the nonlinear model is similar for the different cases, the deviations will be of different magnitude in different ranges of values for the different models. For example, for negative deviations the linear model with left differences is closer to the nonlinear model, but it deviates more for positive values. The accuracy of estimation will thus depend on the particular fault and the discretization scheme for partial derivatives. An idea for the impact of such inaccuracies can be given from the difference that would be caused with critical operation parameters. As an example, the turbine inlet temperature for a given thrust demand at takeoff was calculated for different values of Δ(SE41). The situation at the left end of the x axis of Fig. 10 is considered. For $\Delta T6=2.4\%$, ΔSE41 ranges from -3% (linear estimation, right differences) to -2.3% (nonlinear). The corresponding difference in turbine inlet temperature is 9.3 K.

The discretization step for derivative evaluation also influences the accuracy of linear methods. In Fig. 11 the results from the estimation of a low-pressure turbine (LPT) flow capacity increase, using different discretization schemes, are shown. For a step of 1%, the forward (right) differences give a good estimate. If a reduction in flow capacity was considered, however, then the backward scheme would be the most accurate one. A much weaker sensitivity to the scheme is observed when a much smaller step for the discretization is employed, as shown in Fig. 12.

The formulations examined so far were the square problem of 11 parameters determined from 11 measurements and 7 parameters from 11 measurements. There are diagnostic methods that employ a series of reduced square problems for diagnosis (Aretakis, Mathioudakis, and Stamatis [11] and Gronsteadt [8]). It is thus interesting to examine how such situations are influenced when linear methods are used.

The diagnostic responses matrix for a 7×7 square problem for our engine test case is shown in Table 3. It is observed that the parameters exhibiting nonlinear behavior are here again those with differences in the estimated values. The differences observed are larger than those for the 11×11 problem in Table 1. Examination of different possible combinations of parameters for a given set of measurements has shown that differences are only encountered for the parameters that exhibit nonlinear behavior.

A further point in the comparison between linear and nonlinear methods is the assessment of two implementation aspects: calculation requirements and interaction with other engine systems.

Concerning calculation requirements, it is expected that the linear methods will possess an advantage, since they need much less computational resources and have a much quicker execution time.

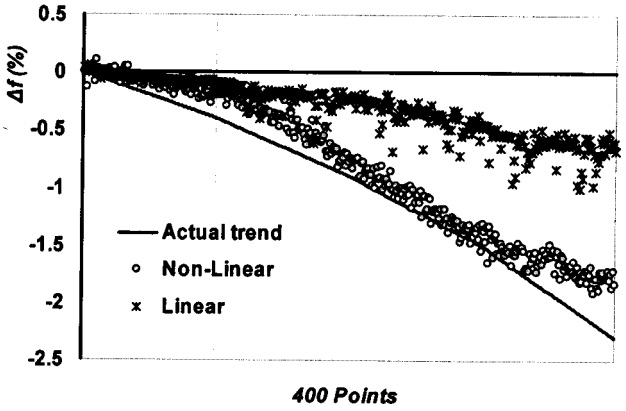

Fig. 8 Deterioration tracking for parameter SW26 using 400 operating points

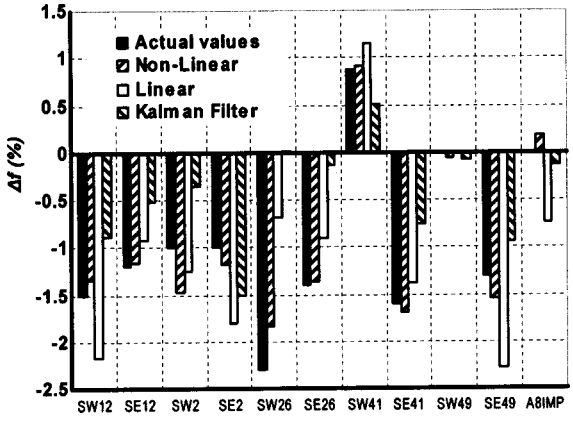

Fig. 9 Health parameters at the final point of deterioration scenario

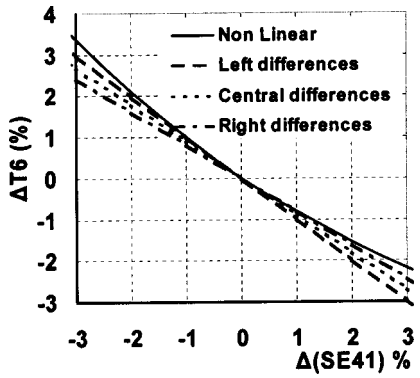

Fig. 10 Linear versus nonlinear model for different ways of derivative calculations

A comparative study of different methods computational characteristics is given in Refs. [17,18]. However, the present authors assess that slower execution times should not be considered as a significant disadvantage today, because current computing capabilities allow very fast execution times of nonlinear models, so they can be used even for real-time implementation.

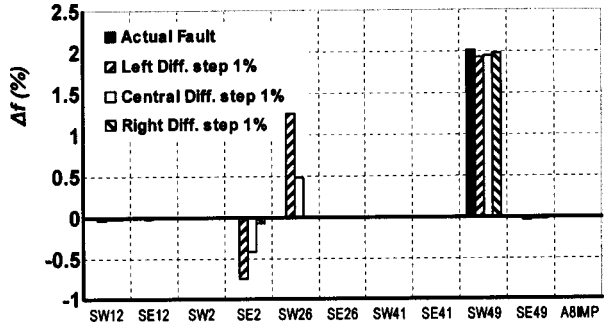

Fig. 11 Linear diagnoses with different ways of discretization for Jacobian matrix elements. Step: 1%.

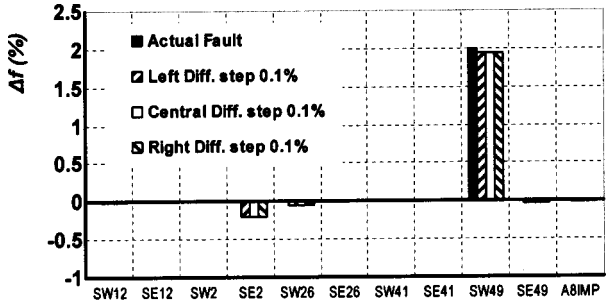

Fig. 12 Linear diagnoses with different ways of discretization for Jacobian matrix elements. Step: 0.1%.

Table 3 Diagnostic response matrix for linear parameter estimation. 7×7 diagnostic problem.

Disturbed Parameter	Estimated Values						
	SW12	SE12	SE2	SE26	SE41	SW49	A8IMP
SW12	-2.8	-0.8	0.4	-0.5	0	0.1	0
SE12	0	-2.0	0	0	0	0	0
SE2	0	0	-2.0	0	0	0	0
SE26	-0.1	0	0.5	-2.7	-0.1	0.1	-0.1
SE41	-0.1	0	1.2	-1.1	-2.2	0.2	-0.1
SW49	-0.1	0	0.9	-0.8	0	-2.0	0
A8IMP	-0.2	-0.1	-0.1	0	0	0	-2.0

A second matter related to implementation is the impact of inaccuracies in health parameters deviations on the values of performance related quantities. For example, the engine controller will exploit the information of a engine performance model for tuning the controlling procedure, as discussed by Turevskiy et al. [19] and Lietzau and Kreiner [20]. A critical parameter for such application is the turbine inlet temperature (TIT). TIT values produced by a model using health indices estimated by a linear model, for measurements from an engine with 2% drop on efficiency of HPT, are compared to the actual values and the values of the healthy engine. The results for given thrust demand are as follows:

- Healthy engine, 1488.7 K
- Faulty engine, 1508.3 K
- Estimation based on nonlinear method, 1508.3 K
- Estimation based on linear method, 1516.8 K

While the nonlinear method accurately predicts the resulting change on TIT, the deviation for the linear model is significantly different. A difference of about 8 deg is observed, which can be considered as significant, given that the difference of faulty from healthy operation is 20 deg.

As a final comment, it should be mentioned that the findings of the above analysis have been based on a particular type of engine that can be considered as one of the relatively more complex layouts in existence today. If another engine is to be analyzed, the steps and parameters defined above can be employed. For example, a single-spool, twin-shaft industrial gas turbine has been analyzed. It was found that nonlinearities are less pronounced in this case and inaccuracies become significant for larger fault sizes, in comparison to those of the test case examined above.

Conclusions

A comparison of linear and nonlinear diagnostic methods has been presented. The expected tendency for reduced accuracy of linear methods has been verified, but it was shown that the influence on accuracy is different for different health parameters. Some parameters were found to change with rates close to linear, and their estimation by linear methods was found to be very accurate. The difference is more substantial for those that change with a more pronounced nonlinearity.

Estimated parameters were found to be influenced to a larger or lesser degree and the influence is different for different types of diagnostic problem formulation. For square diagnostic problems, the diagnostic response matrix was found to be a good indicator of which parameters suffer inaccuracies, resulting from either inaccuracy of their own value estimation or from information spuriously attributed from other parameters. When fewer parameters than measurements are estimated, inaccuracies are spread over the entire set of parameters. It was shown that the difference in estimation can be significant, even though individual parameters exhibit only small differences.

Particular features of linear methods, such as the way of obtaining influence coefficients, were discussed. Finally, the impact on performance parameter estimation was also discussed and it was shown that use of linear methods may lead to substantial inaccuracies of significant parameters, such as the turbine inlet temperature.

Nomenclature

A8 = Exhaust area
A8IMP = Exhaust area deviation from datum value (Eq. (*B*3))
C = Weight factor (Eq. (3))
HPC = High-pressure compressor
HPT = High-pressure turbine
LPC = Low-pressure compressor
LPT = Low-pressure turbine
M = Number of measurements
N = Number of health parameters

NLI = Nonlinearity indicator of parameter f_j
f = Vector of engine component health parameters
OF = Objective function
P_i = Total pressure at station i of the engine
SE_i = Efficiency factor (Eq. (*B*2))
SW_i = Flow factor (Eq. (*B*1))
T_i = Total temperature at station i of the engine
TIT = Temperature inlet turbine
u = Vector of quantities defining operating point
W_i = Mass flow at the position i of the engine
$XNHP$ = High-pressure shaft rpm
$XNLP$ = Low-pressure shaft rpm
Y = Vector of measured quantities
ΔY = Percentage deviation of magnitude Y from nominal value $\Delta Y = 100(Y - Y^{\text{baseline}})/Y^{\text{baseline}}$
α_{ij} = Jacobian matrix elements (Eq. (*A*4))
η_i = Efficiency of component with entrance at station i
σ_{fj} = Normalized standard deviation of health parameter f_j
σ_{Yi} = Standard deviation normalized over mean value of measurement Yi

Subscripts and Superscripts

calc = Value of a quantity calculated by a model
f = Quantity referring to health parameters
given = Given value of a quantity, e.g., from measurement
i = Position along the engine
j = Index of health parameter f_j
L = Linear
NL = Nonlinear
0 = Baseline engine condition
ref = Quantity referring to the intact engine
Y = Quantity referring to measurements

Appendix A

The principles on which a linearized engine model is constituted are briefly presented here. Considering that the engine is represented through a functional model expressed through Eq. (2), and using Taylor's theorem we have:

$$Y_i = Y_i^{\text{ref}} + \sum_{j=1}^{N} \frac{\partial F_i}{\partial f_j}(f_j - f_j^{\text{ref}}) + \varepsilon. \tag{A1}$$

ε in this relation embodies all the higher-order terms of the series expansion. By assuming that the change of health parameters is small, higher-order terms are assumed to be negligible and we can thus write

$$\frac{Y_i - Y_i^{\text{ref}}}{Y_i^{\text{ref}}} = \sum_{j=1}^{N} \frac{f_j^{\text{ref}}}{Y_i^{\text{ref}}} \frac{\partial F_i}{\partial f_j} \frac{f_j - f_j^{\text{ref}}}{f_j^{\text{ref}}}. \tag{A2}$$

Using the notation for Δ's, this equation can be written as follows:

$$\Delta Y_i = \sum_{j=1}^{N} a_{ij} \Delta f_j \tag{A3}$$

with

$$a_{ij} = \frac{f_j^{ref}}{Y_i^{ref}} \frac{\partial F_i}{\partial f_j} \approx \frac{\dfrac{Y_i^j - Y_i^{\text{ref}}}{Y_i^{\text{ref}}}}{\dfrac{f_j - f_j^{\text{ref}}}{f_j^{\text{ref}}}}, \tag{A4}$$

where Y_i^j is the change of measurement Y_i due to change of parameter f_j.

Equation (*A*3) for all the measured variables can be written in a matrix form:

$$\mathbf{z} = \mathbf{H} \cdot \Delta \mathbf{f} \tag{A5}$$

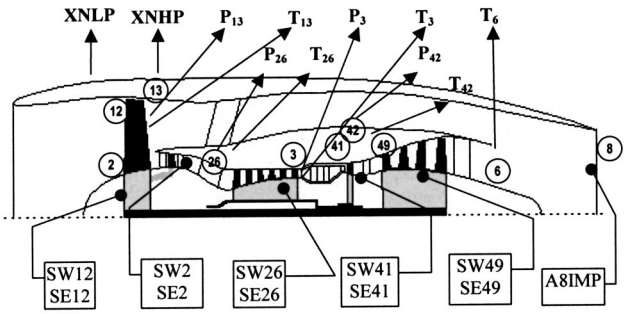

Fig. 13 Layout of a high bypass ratio partially mixed turbofan engine with station numbering

where **z** is the vector of known measured quantities $\Delta\mathbf{Y}$ and **H** is the influence matrix, also called Jacobian, containing the coefficients a_{ij}.

Equation (*A*3) provides the means for establishing a linearized engine performance model. If a performance variable Y_i is known at reference condition then its value at a condition that deviates from the reference by $\Delta\mathbf{f}$ can be calculated by using the linear relation:

$$Y_i^{\text{calc}} = Y_i^{\text{ref}} \left(1 + \sum_{j=1}^{N} a_{ij} \Delta f_j \right). \tag{A6}$$

Appendix B

The layout of the engine considered as a test case in the present study, together with station numbering, measurements, and health parameters are shown in Fig. 13. The nonlinear performance model for this engine has been developed by Stamatis et al. [14].

The parameters employed for characterize the health condition of each component of the engine are a flow factor SW and an efficiency factor SE. They determine how component flow capacity and efficiency are modified with respect to baseline condition. For a component with entrance at station i of the engine we define:

Flow factor:

$$SW_i = (W_i \sqrt{T_i}/p_i)/(W_i \sqrt{T_i}/p_i)_0. \tag{B1}$$

Efficiency factor:

$$SE_i = \eta_i / (\eta_i)_0. \tag{B2}$$

Exhaust area factor:

$$A8IMP = A_8 / (A_8)_0. \tag{B3}$$

References

[1] Urban, L. A., 1972, "Gas Path Analysis Applied to Turbine Engine Condition Monitoring," AIAA/SAE 8th Joint Propulsion Specialist Conference, AIAA paper 72-1082, December 1972.
[2] Doel, D., 1994, "TEMPER—a Gas Path Analysis Tool for Commercial Jet Engines," ASME J. Eng. Gas Turbines Power, **116**, pp. 82–89.
[3] Urban, L. A., and Volponi, A. J., 1992, "Mathematical Methods of Relative Engine Performance Diagnostics," S.A.E. technical paper 922048. J. Aerospace Trans., **101**, pp. 2025–2050.
[4] Barwell, M. J., 1987, "COMPASS—Ground Based Engine Monitoring Program for General Applications," S.A.E. Technical paper 871734.
[5] Stamatis, A., Mathioudakis, K., and Papailiou, K. D., 1990, "Adaptive Simulation of Gas Turbine Performance," ASME J. Eng. Gas Turbines Power, **112**, pp. 168–175.
[6] Escher, P. C., and Singh, R., 1995, "An Object-Oriented Diagnostics Computer Program Suitable for Industrial Gas Turbines," United 21st International Congress of Combustion Engines (CIMAC), Interlaken, Switzerland, 15–18, May 1995.
[7] Zedda, M., and Singh, R., 1999, "Gas Turbine and Sensor Diagnostics," ISABE paper 99-7238.
[8] Gronstedt, T. U. J., 2002, "Identifiability in Multipoint Gas Turbine Parameter Estimation Problems," ASME paper GT-2002-30020.

[9] Grodent, M., and Navez, A., 2001, ''Engine Physical Diagnosis Using a Robust Parameter Estimation Method,'' AIAA paper AIAA 2001-3768.
[10] Mathioudakis, K., Kamboukos, Ph., and Stamatis, A., 2002. ''Turbofan Performance Deterioration Tracking Using Non-Linear Models and Optimization Techniques,'' ASME J. Turbomach., **124**, pp. 580–587.
[11] Aretakis, N., Mathioudakis, K., and Stamatis, A., 2003, ''Non-Linear Engine Component Fault Diagnosis From a Limited Number of Measurements Using a Combinatorial Approach,'' ASME J. Eng. Gas Turbines Power, **125**, pp. 642–650.
[12] Ogaji, S. O. T., and Singh, R., 2002, ''Study of the Optimization of Measurements Sets for Gas Path Fault Diagnosis in Gas Turbines,'' ASME paper GT-2002-30050.
[13] Doel, L. D., 2002, ''Interpretation of Weighted Least Squares Gas Path Analysis Results,'' ASME paper GT-2002-30025.
[14] Stamatis, A., Mathioudakis, K., Ruiz, J., and Curnock, B., 2001, ''Real Time Model Implementation for Adaptive Control & Performance Monitoring of Large Civil Turbofans,'' ASME paper 2001-GT-0362.
[15] Ganguli, R., 2001, ''Data Rectification and Detection of Trend Shifts in Jet Engine Gas Path Measurement Using Median Filters and Fuzzy Logic,'' ASME paper 2001-GT-0014.
[16] Visual Numerics IMSL standard routines in Fortran. 1970–2002.
[17] Stamatis, A., Kamboukos, Ph., Aretakis, N., and Mathioudakis, K., ''On Board Adaptive Models: A General Framework and Implementation Aspects,'' Proceedings of ASME. Turbo Expo 2002 June 3–6, 2002, Amsterdam The Netherlands. ASME paper No. GT-2002-30622.
[18] Kamboukos, Ph., Mathioudakis, K., and Stamatis, A., 2003, ''A Comparative Study of Optimization Methods for Jet Engine Condition Diagnosis,'' Paper ISABE 2003-1231, 16th ISABE, Aug. 31–Sept. 5, Cleveland, OH.
[19] Turevskiy, A., Meisner, R., Luppold, R., Kern, R., and Fuller, J., 2002, ''A Model Based Controller for Commercial Aero Gas Turbines,'' ASME paper GT-2002-30041.
[20] Lietzau, K., and Kreiner, A., 2001, ''Model Based Control Concepts for Jet Engines,'' ASME paper 2001-GT-0016.

Prediction of the Transient Thermodynamic Response of a Closed-Cycle Regenerative Gas Turbine

T. Korakianitis
James Watt Professor of Mechanical Engineering,
University of Glasgow,
Glasgow G12 8QQ, UK
e-mail: t.Alexander@mech.gla.ac.uk

J. I. Hochstein
Professor of Mechanical Engineering,
Memphis State University,
Memphis, TN 38152

D. Zou
Department of Physical Therapy,
Washington University,
St. Louis, MO 63130

Instantaneous-response and transient-flow component models for the prediction of the transient response of gas turbine cycles are presented. The component models are based on applications of the principles of conservation of mass, energy, and momentum. The models are coupled to simulate the system transient thermodynamic behavior, and used to predict the transient response of a closed-cycle regenerative Brayton cycle. Various system transients are simulated using: the instantaneous-response turbomachinery models coupled with transient-flow heat-exchanger models; and transient-flow turbomachinery models coupled with transient-flow heat-exchanger models. The component sizes are comparable to those for a solar-powered Space Station (radial turbomachinery), but the models can easily be expanded to other applications with axial turbomachinery. An iterative scheme based on the principle of conservation of working-fluid mass in the system is used to compute the mass-flow rate at the solar-receiver inlet during the transients. In the process the mass-flow rate of every component at every time step is also computed. Representative results of different system models are compared and discussed.
[DOI: 10.1115/1.1806449]

Introduction

Models for the steady-flow performance of various configurations of gas-turbine engines have been presented in many previous studies and with various intentions such as cycle optimization (e.g., Korakianitis and Wilson [1]), or prediction of part-load performance (e.g., Korakianitis and Beier [2]). The transient behavior of turbomachinery components can be predicted with CPU-intensive unsteady Navier-Stokes computations (e.g., Korakianitis et al. [3]), but the effort required makes these computations unsuitable for preliminary analyses of the transient response of gas-turbine components and power plants through speed, load, and mass transients.

Transient-flow models for components where the flow may be assumed incompressible (such as some heat exchanger passages) are easier to develop because of the constant-density assumption. Similarly transient-flow models for ducts with compressible or incompressible flow are easy to model by predicting with characteristics the time of propagation of transients. Transient-flow models for axial and centrifugal compressor and turbine passages, where work is added to or extracted from the flow, are harder to develop. Non-CFD models suitable for predicting the transient performance of compressors and turbines fall into three main categories. The first category predicts the transient performance by obtaining equations resembling transfer functions in control theory using phenomenological analyses of component behavior (for example, Kuhlberg et al. [4]; Kalnitsky and Kwatny [5]). In the second category the unsteady conservation equations (mass, momentum, and energy) are written in a lumped-parameter approach (or alternatively finite volumes are considered along a mid-streamline) through one or more components. Many of the models in the second category use some assumption to minimize the effects of compressibility, or the effects of mass storage or mass depletion inside the component through the transient. For example, the system of equations is solved assuming either incompressible fluid, or no storage of mass in the component volumes through the transient, or another assumption that simplifies the transient for one or more of the flow properties (for example, Adams et al. [6]; Corbett and Elder [7]; Macdougal and Elder [8]). In the third category assumptions are made for the delay of the transport of perturbations from component inlet to exit (for example, Ray and Bowman [9]; Fink, Cumpsty, and Greitzer [10]). All three categories may incorporate routines for predicting relations between inlet and outlet properties from the component performance maps.

The purpose of this paper is to develop transient models of the second category (using the unsteady form of the conservation equations) suitable for predicting the performance of gas-turbine components, and to show how the models can be coupled to predict the transient performance of engines. The compressor and turbine models do not include assumptions (such as incompressible flow, constant density, no mass storage through the transient, or no pressure variation through the transient) that simplify the transient behavior for any of the flow properties. The transient models for flow through radial impellers use the unsteady forms of conservation of mass, angular momentum and energy. These can easily be modified for flow through axial stages by replacing the law of conservation of angular momentum with (the simpler equation of) the law of conservation of linear momentum through the mid streamline of each blade row. As an application the models are used to predict the transient thermodynamic performance of a regenerative gas-turbine engine that is approximately suitable for providing power to the Space Station. Various combinations of component models are evaluated by predicting the transient performance in constant-speed transients (suitable for alternator drives such as the one for the Space Station), and variable-speed transients (suitable for other drives for other applications).

System Description

The transient performance of gas turbines depend on the type and size of engine components, the working fluid, and the inputs

Contributed by the International Gas Turbine Institute (IGTI) of THE AMERICAN SOCIETY OF MECHANICAL ENGINEERS for publication in the ASME JOURNAL OF ENGINEERING FOR GAS TURBINES AND POWER. Paper presented at the International Gas Turbine and Aeroengine Congress and Exhibition, Cincinnati, OH, May 24–27, 1993; Paper 1993-GT-0136. Manuscript received by IGTI, December 1, 1992, final revision, March 1, 1993. Associate Editor: H. Lukas.

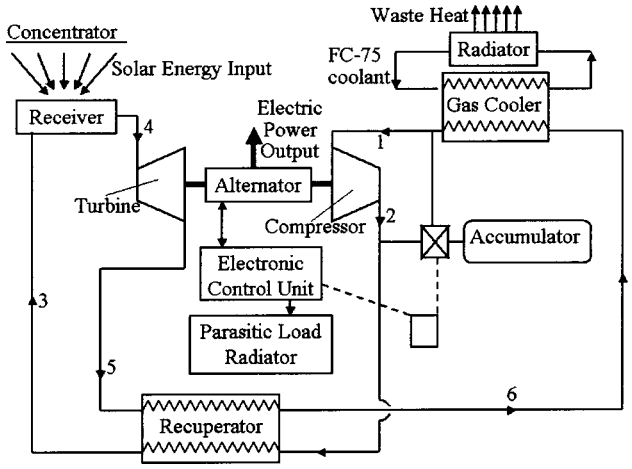

Fig. 1 Schematic of the solar-powered closed regenerative Brayton-cycle engine

driving the transient. These will vary from application to application. Simplified component and approximate temperature-entropy diagrams for the solar-powered closed regenerative Brayton-cycle engine under consideration to provide electrical power in space are shown in Figs. 1 and 2. Approximate dimensions and other information for the system are included in many NASA and NASA-contractor reports such as the two reports by Rocketdyne [11,12] and in the Appendix.

The working fluid is a mixture of helium and xenon (He-Xe). Solar energy is collected by the concentrator, focused onto the phase-change eutectic salt ($LiF\text{-}CaF_2$) in the receiver, and transferred to the working fluid. Energy is rejected from the cycle through the gas cooler. The gas cooler, in what is called the coolant loop, uses a liquid mixture of 75% $C_2H_3F_3O$ and 25% H_2O (called FC−75) to reject energy via the radiator to space. The centrifugal compressor, radial turbine, and alternator rotate as a single unit at (approximately) constant speed. The system rotates in space in and out of the shadow of the earth with a period of approximately 90 minutes, implying transients for the receiver and cooler. The receiver phase-change salt is used to provide energy at almost-constant temperature to the cycle. These and other system transients are handled by changing the mass-flow rate of the working fluid through the components (by adding and subtracting working fluid in the accumulator), and/or by shedding some of the electrical power output in the parasitic-load radiator.

Power for the system is partially provided by a photovoltaic module, and partially by two regenerative Brayton cycles similar to the one illustrated in Figs. 1 and 2, each providing approximately 30 kW. The compressor-turbine-alternator units rotate at 32,000 rpm (minimum 30,000 rpm, maximum 36,000 rpm). At the

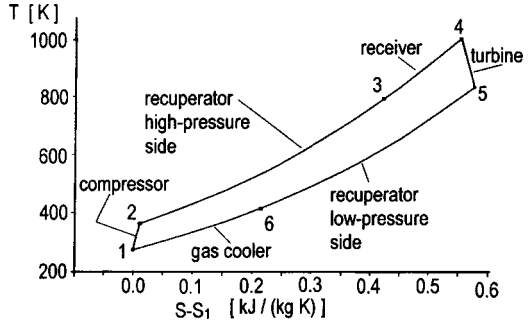

Fig. 2 Temperature-entropy diagram for the regenerative Brayton cycle. (The value of S_1 is arbitrary.)

design point the compressor and turbine pressure ratios are just below 2:1 (the turbine pressure ratio is a little lower than the compressor pressure ratio due to pressure losses), and the mass-flow rate is approximately 0.8 kg/s. The compressor and turbine are small radial impellers.

Although the following models are applied to the system illustrated in Fig. 1, the principles are general and they can be used in different gas-turbine engines with different components.

Component Models

The working fluid is modeled as a perfect gas with constant $c_p = 520.4$ J/(kg·K) and $c_v = 312.2$ J/(kg·K). It is assumed that the compressor and turbine are adiabatic.

Compressor and Turbine. The steady state compressor and turbine performance are modeled using the following equations:

$$\left(\frac{T_{T2}}{T_{T1}}\right) = \left(\frac{p_{T2}}{p_{T1}}\right)^{[R/(c_p\cdot\eta_c)]}$$

$$\left(\frac{T_{T5}}{T_{T4}}\right) = \left(\frac{p_{T5}}{p_{T4}}\right)^{[R\eta_t/c_p]} \tag{1}$$

$$\dot{W}_s = \dot{m}_t c_p (T_{T4} - T_{T5}) - \dot{m}_c c_p (T_{T2} - T_{T1}) - \dot{W}_{\rm fr}$$

where the efficiencies are read from compressor and turbine nondimensional performance maps typical for small radial impellers. The compressor and turbine performance maps used in this study have been obtained from similarly sized turbocharger-type compressor and turbine performance maps published by Heywood [13]. At design-point operation $\eta_c = 0.916$ and $\eta_t = 0.902$. $\dot{W}_{fr}$ represents bearing friction. The electrical power produced will be less than $\dot{W}_s$ because of the effects of alternator efficiency.

The transient radial compressor and turbine performance are modeled by considering the flow at three stations, at the inlet, middle, and outlet of the components. The whole component is considered as a control volume for which the conservation of mass, angular momentum, and energy are written as:

$$\frac{dm}{dt} = \dot{m}_{\rm in} - \dot{m}_{\rm ot} \tag{2}$$

$$\frac{d(m\Omega r_m^2)}{dt} = \pm \dot{m}\Omega r_{\rm tp}^2 + \frac{\dot{W}_c}{\Omega} - \frac{\dot{W}_t}{\Omega} \Rightarrow$$

$$\dot{W}_c - \dot{W}_t = \Omega^2 r_m^2 \frac{dm}{dt} + \Omega m r_m^2 \frac{d\Omega}{dt} \pm \dot{m}\Omega^2 r_{\rm tp}^2 \tag{3}$$

$$\frac{d(mc_vT)_m}{dt} = (\dot{m}c_pT)_{\rm in} - (\dot{m}c_pT)_{\rm ot} + \dot{W}_c - \dot{W}_t \Rightarrow$$

$$\frac{dT_m}{dt} = \frac{1}{mc_v}\left[(\dot{m}c_pT)_{\rm in} - (\dot{m}c_pT)_{\rm ot} + \dot{W}_c - \dot{W}_t - c_vT_m\frac{dm}{dt}\right] \tag{4}$$

where a component is either a compressor (with work $\dot{W}_c$ going into the control volume, and $\dot{W}_t = 0$), or a turbine (with work $\dot{W}_t$ going out of the control volume and $\dot{W}_c = 0$). The $r_{\rm tp}^2$ terms with "−" are for compressors, and the terms with "+" are for turbines. The flow is assumed going axially into the compressor impeller and going axially out of the turbine impeller (no tangential momenta at these stations).

For axial components the unsteady form for the conservation of angular momentum (Eq. (3)) is replaced with the unsteady form for the conservation of linear momentum in each stator and rotor blade row.

The equation of state for perfect gas is used for total (stagnation) and static properties, the isentropic relation connecting total and static properties, and the definition of total enthalpy ($h_T = h + U^2/2 \Rightarrow T_T = T + U^2/(2\cdot c_p)$) are used at each station in the com-

ponent. In order to obtain closure of the models, the following assumptions connecting properties at various locations and times are also used:

$$T_{T,m}(t)=\frac{1}{2}[T_{T,\mathrm{in}}(t)+T_{T,\mathrm{ot}}(t)]$$

$$\dot{m}_m(t)=\frac{1}{2}[\dot{m}_{\mathrm{in}}(t)+\dot{m}_{\mathrm{ot}}(t-\Delta t)]$$

$$m=\rho_m V_{cv}\,, \tag{5}$$

$$p_{T,m}(t)=p_{T,in}(t)\left[\frac{T_{T,m}(t)}{T_{T,\mathrm{in}}(t)}\right]^{[c_p/(R\cdot\eta_t)]}$$

$$p_{T,m}(t)=p_{T,\mathrm{in}}(t)\left[\frac{T_{T,m}(t)}{T_{T,\mathrm{in}}(t)}\right]^{[c_p\eta_c/R]}$$

It is assumed that the efficiencies from the inlet to the middle of the component are equal to the efficiencies from the inlet to the outlet of the component. This is an approximation. (The efficiencies from the inlet to the outlet of the component are read as functions of pressure ratio, $\dot{m}$ and Ω, from the nondimensional performance maps.) The mass-flow rate through the inlet of the component at time t is assumed equal to the average of the mass-flow rate through the inlet of the component at the same time t and the mass-flow rate through the outlet of the component at time $t-\Delta t$. This lagged assumption for the mass-flow rate provides the required stability to the numerical scheme.

One additional word of caution is due here. This transient scheme will predict an immediate response at the outlet of the compressor or turbine due to a variation of properties at the inlet. This is correct only if the time step is large enough for the disturbance to travel through the impeller passage and reach the outlet, thus imposing a minimum time-step limit to the numerical scheme. The resultant mixture of algebraic and differential equations is a "stiff" system of equations, so that its integration in time imposes a maximum time-step limit. The time step used in the numerical integration to predict engine transients must be between these two limits.

Equation (3) can be used to model a constant-speed variable-work component ($d\Omega/dt=0$ and $d\dot{W}_s/dt\neq 0$); a constant-work variable-speed component ($d\Omega/dt\neq 0$ and $d\dot{W}_s/dt=0$); and a component in which the interdependence of $(\dot{W},\Omega)$ can be used to identify the system transient.

Heat Exchangers. The steady-state performance of heat exchangers (receiver, regenerator, and gas cooler) is evaluated using the method of the number of heat transfer units (N_{tu}, Kays and London [14]). Heat-exchanger effectiveness (depending on heat-exchanger purpose) is defined by one of:

$$\epsilon\equiv\frac{C_{\mathrm{ht}}(T_{\mathrm{ht,in}}-T_{\mathrm{ht,ot}})}{C_{\min}(T_{\mathrm{ht,in}}-T_{\mathrm{cd,ot}})}$$

$$\epsilon\equiv\frac{C_{\mathrm{cd}}(T_{\mathrm{cd,ot}}-T_{\mathrm{cd,in}})}{C_{\min}(T_{\mathrm{ht,in}}-T_{\mathrm{cd,ot}})}$$

The number of heat transfer units N_{tu} are defined as:

$$N_{tu}\equiv f(A,h,C_{\min}).$$

In general it is possible to express

$$\epsilon=f\left(N_{tu},\frac{C_{\min}}{C_{\max}},\ \ flow\ \ arrangement\right)$$

and

$$\dot{Q}=Ah\Delta T_{me}=C_{\mathrm{ht}}(T_{\mathrm{ht,in}}-T_{\mathrm{ht,ot}})=C_{\mathrm{cd}}(T_{\mathrm{cd,ot}}-T_{\mathrm{cd,in}})$$

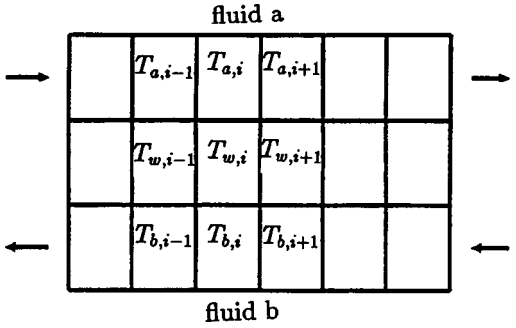

Fig. 3 Heat-exchanger finite-difference scheme

where T_{me} is a suitably defined mean temperature difference (such as the logarithmic mean temperature difference). The above are manipulated into:

$$T_{\mathrm{cd,ot}}=T_{\mathrm{ht,in}}-\left(1-\epsilon\frac{C_{\mathrm{ht}}}{C_{\mathrm{cd}}}\right)(T_{\mathrm{ht,in}}-T_{\mathrm{cd,in}})$$

$$T_{\mathrm{ht,ot}}=T_{\mathrm{cd,in}}-(1-\epsilon)(T_{\mathrm{ht,in}}-T_{\mathrm{cd,in}}) \tag{6}$$

$$\epsilon=\frac{1-\exp[-N_{tu}(1-C_{\mathrm{rat}})]}{1-C_{\mathrm{rat}}\exp[-N_{tu}(1-C_{\mathrm{rat}})]}$$

$$N_{tu}=\frac{Ah}{C_{\min}}\quad\text{and}\quad C_{\mathrm{rat}}=\frac{C_{\min}}{C_{\max}}$$

In the receiver the salt temperature ($T_{\mathrm{sl}}=T_{\mathrm{ht}}$) remains approximately constant during normal operation, so that C_{rat} is small. (In the following we are using variations in salt temperature to study system transients. Transients in sink temperature, or a combination of such transients could also be used). In the recuperator $C_{\mathrm{ht}}=C_{\mathrm{cd}}$, so that $C_{\mathrm{rat}}=1$. In the gas cooler C_{rat} has a value smaller than unity. The values of ϵ, N_{tu}, and C_{rat} for the design-point operation of the receiver, recuperator, and gas cooler are given in the Appendix. The pressure drops in the heat-exchanger passages are modeled as a function of working-fluid properties, flow arrangement, and heat transfer characteristics using models presented in Kays and London [14]. Similarly the pressure drops in other system ducts are modeled as a function of the local properties in the ducts.

For transient performance the counter-flow and cross-counter-flow heat exchangers are modeled by dividing the control volume into sections along the flow direction, with three elements in each section for fluids a and b and the wall w, as illustrated in Fig. 3. Fluid b may be flowing in the counter-flow or cross-counter-flow direction with respect to fluid a. It is assumed that the net energy transfer by convective transport dominates the conduction by diffusion between adjoining fluid elements. The transient continuity equation for fluids a and b along the control volumes i can be written as:

$$\frac{dm_a}{dt}=\dot{m}_{a,i-1}-\dot{m}_{a,i}$$

$$\frac{dm_b}{dt}=\dot{m}_{b,i+1}-\dot{m}_{b,i} \tag{7}$$

The transient energy balances can be written as:

$$\frac{\partial(mc_vT)_a}{\partial t}=(Ah)_a(T_w-T_a)+\frac{\partial(\dot{m}c_pT)_a}{\partial x}dx$$

$$(mc)_w\frac{\partial T_w}{\partial t}=(Ah)_a(T_a-T_w)+(Ah)_b(T_b-T_w) \tag{8}$$

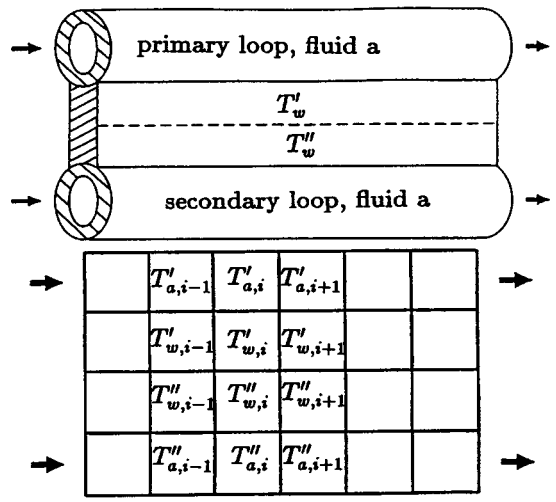

Fig. 4 Radiator finite-difference scheme

$$\frac{\partial(mc_vT)_b}{\partial t}=(Ah)_b(T_w-T_b)+\frac{\partial(\dot{m}c_pT)_b}{\partial x}dx$$

By writing the partial differences as finite differences and letting superscript n represent time steps, Eq. (8) are manipulated into:

$$\begin{aligned}(mc_v)_{a,i}\left[\frac{T^n_{a,i}-T^{n-1}_{a,i}}{\Delta t}\right]&=(Ah)_{a,i}[T^n_{w,i}-T^n_{a,i}]\\&\quad+(\dot{m}c_p)_{a,i}[T^n_{a,i-1}-T^n_{a,i}]\\(mc)_{w,i}\left[\frac{T^n_{w,i}-T^{n-1}_{w,i}}{\Delta t}\right]&=(Ah)_{a,i}[T^n_{a,i}-T^n_{w,i}]+(Ah)_{b,i}[T^n_{b,i}-T^n_{w,i}]\\(mc_v)_{b,i}\left[\frac{T^n_{b,i}-T^{n-1}_{b,i}}{\Delta t}\right]&=(Ah)_{b,i}[T^n_{w,i}-T^n_{b,i}]\\&\quad+(\dot{m}c_p)_{b,i}[T^n_{b,i+1}-T^n_{b,i}]\end{aligned}\tag{9}$$

(it can be shown analytically that the temperature variations in time dominate the temporal changes in mass-flow rates). These equations are rearranged to produce a matrix equation of the form $[A]\{T\}=\{B\}$, where $\{T\}$ is the vector of unknown temperatures, which is solved using a Gaussian elimination method with scaling and partial pivoting.

The pressure drops in the heat-exchanger passages during transient flow are modeled assuming an equilibrium state at every time step (similar to the corresponding pressure drops during steady flow). The pressure distribution is assumed linear along the flow passages. The equation of state for perfect gas is used to find the density in each elemental volume from the local pressure and temperature, and the mass of fluid in each elemental volume and at each time is found from $m_i=\rho_i V_{cv,i}$.

The recuperator, receiver and gas-cooler transient models are developed from Eqs. (9), with appropriate variations in constants to account for design details. Some information about these components is given in the Appendix. In the recuperator the values of c_p and c_v for the He-Xe mixture are used for both fluids *a* and *b*. In the gas-cooler fluid *a* is the He-Xe mixture, and fluid *b* is liquid $FC-75$, for which $c_{p,b}=c_{v,b}=c_b=1.0207$ kJ/(kg·K) and $\rho_b=1682.1$ kg/m^3 (assumed constant). In the receiver fluid *a* is the He-Xe mixture, and fluid *b* is the LiF-CaF_2 eutectic salt.

Radiator. The radiator consists of two coolant loops, a primary and a secondary one, as shown in Fig. 4. The steady-flow model for each radiator loop is developed by considering differential slices along its length. The heat rejected from each differential slice is evaluated by assuming that heat is radiated along the length of the radiator, but not from its two ends; heat radiates according to the Stefan-Boltzmann law; and the emissivity of the surface is constant. The liquid $FC-75$ temperature at the radiator outlet is evaluated by integrating the resulting equation along the radiator length:

$$\begin{aligned}d\dot{Q}=\sigma T^4D\,dL=-\dot{m}c_p\,dT\Rightarrow\\T_{ot}=\left[\frac{3\sigma DL}{\dot{m}c_p}+\frac{1}{T^3_{\text{in}}}\right]^{(-1/3)}\end{aligned}\tag{10}$$

where $\sigma=(\text{emissivity})\times(\text{Stefan-Boltzmann constant})=(0.9)\times(56.70\times10^{-9})=51.03\times10^{-9}$ W/(m$^2\cdot$K^4). For the transient model it is assumed that the sink temperature is a function of time, but constant along the length of the panel, in addition to the above assumptions for steady flow. The model is developed by dividing the radiator into segments as shown in Fig. 4. The energy balance for the fluid *a* and the wall *w* become:

$$\begin{aligned}\frac{\partial(mc_vT)_a}{\partial t}&=(Ah)_a(T_w-T_a)+\frac{\partial(\dot{m}c_pT)_a}{\partial x}dx\\(mc)_w\frac{\partial T_w}{\partial t}&=(Ah)_a(T_a-T_w)+\sigma A_r(T^4_{sk}-T^4_w)-kA_x\frac{\partial T_w}{\partial x}\\&\quad-kA_y\frac{\partial T_w}{\partial y}\end{aligned}\tag{11}$$

If $'$ and $''$ denote the primary and secondary loops, respectively, Eqs. (11) for an arbitrary element *i* in the primary loop can be written as (explicit formulation):

$$\left[\frac{\partial T'_a}{\partial t}\right]_i=\frac{1}{(mc_v)'_{a,i}}[(Ah)'_{a,i}(T'_{w,i}-T'_{a,i})+(\dot{m}c_p)'_{a,i}(T'_{a,i-1}-T'_{a,i})]\tag{12}$$

$$\begin{aligned}\left[\frac{\partial T'_w}{\partial t}\right]_i&=\frac{1}{(mc)'_{w,i}}[(Ah)'_{a,i}(T'_{a,i}-T'_{w,i})+(\sigma A_r)'_{w,i}(T^4_{sk}-T'^4_{w,i})]\\&\quad-\frac{1}{(mc)'_{w,i}}\cdot\left[\left(\frac{kA_x}{\Delta x}\right)'_{w,i}(2T'_{w,i}-T'_{w,i-1}-T'_{w,i+1})\right.\\&\quad\left.-\left(\frac{kA_y}{\Delta y}\right)'_{w,i}(T'_{w,i}-T''_{w,i})\right]\end{aligned}$$

Similarly, Eqs. (11) for an arbitrary element *i* in the secondary loop can be written as (explicit formulation):

$$\left[\frac{\partial T''_a}{\partial t}\right]_i=\frac{1}{(mc_v)''_{a,i}}[(Ah)''_{a,i}(T''_{w,i}-T''_{a,i})]\tag{13}$$

$$\begin{aligned}\left[\frac{\partial T''_w}{\partial t}\right]_i&=\frac{1}{(mc)''_{w,i}}[(Ah)''_{a,i}(T''_{a,i}-T''_{w,i})+(\sigma A_r)''_{w,i}(T^4_{sk}-T''^4_{w,i})]\\&\quad-\frac{1}{(mc)''_{w,i}}\cdot\left[\left(\frac{kA_x}{\Delta x}\right)''_{w,i}(2T''_{w,i}-T''_{w,i-1}-T''_{w,i+1})\right.\\&\quad\left.-\left(\frac{kA_y}{\Delta y}\right)''_{w,i}(T''_{w,i}-T'_{w,i})\right]\end{aligned}$$

Steady-flow and transient pressure drops in the receiver and other duct-type passages are modeled as described in the heat exchangers.

Rotor Inertia. For constant-speed transients the inertia of the rotating unit is not needed in the models. For variable speed operation the dynamic equation of the unit is used to evaluate the instantaneous acceleration:

$$\frac{d}{dt}\left(\frac{I\Omega^2}{2}\right)=\dot{W}_s-\dot{W}_{\rm al}=\dot{W}_t-\dot{W}_c-\dot{W}_{\rm fr}-\dot{W}_{\rm al}\Rightarrow$$
$$\dot{\Omega}=\frac{\dot{W}_t-\dot{W}_c-\dot{W}_{\rm fr}-\dot{W}_{\rm al}}{I\Omega} \tag{14}$$

where for the compressor-alternator-turbine rotating unit $I=23.39\times10^{-6}\,\mathrm{kg\cdot m^2}$. The instantaneous acceleration $\dot{\Omega}$ is integrated in time to give the rotational speed of the unit at the next time instant.

System Model

The above component models are coupled to form the system model. The rate of change of energy in the system is equal to the rate of collected solar energy, minus the output power, minus the rate of waste heat radiated to space. The transient formulations conserve energy, and therefore at every instant the temperature-entropy diagram for the cycle is a closed shape similar to the one shown in Fig. 2. The exact location of the diagram changes at different time instants, as driven by transients in eutectic-salt and sink temperatures, or other system transients. The new position of the diagram is found by iteratively evaluating the correct mass-flow rate through the components at each instant. The control equation for the overall system is the equation of conservation of mass through the transient. The total mass of working fluid and coolant in the system are assumed constant. The resultant transients can also be manipulated by specifying the mass of the working fluid in the system as a function of time through the period of the transient (modeling the working-fluid mass in the accumulator during the transient).

The state of the system at all times is represented by the combination of $\{T,p,\dot{m}\}$ at all junction points between the components. (During transients the mass flow rate is different at each flow station.) Transient iterations start from an initial steady state. Starting from an imposed transient for properties at one or more junctions between components, the He-Xe mass flow rate between the recuperator high-pressure-side outlet and receiver inlet ($\dot{m}_3$ at station 3 in Fig. 2) is iteratively increased and decreased using an under-relaxation technique until the conservation of total mass m in the system is satisfied, i.e., the sum of the mass in all components is (within a user-specified accuracy) equal to the specified total mass of the working fluid. The under-relaxation factor is increased and decreased throughout the iterations by monitoring the effect of changes of $\dot{m}_3$ on the total system mass.

Transient Performance

Transients considered include 90 minute (orbital) sinusoidal transients in salt and sink temperature ($T_{\rm sl}$ and $T_{\rm sk}$); loss of coolant pumps; loss of some of the radiator panels; and others have been simulated using the above models. The following system transients are illustrative of typical results for units of the size described above. For illustration purposes the results show transients driven by varying the eutectic salt temperature T_{sl}, while keeping the sink temperature T_{sk} constant. The recuperator, receiver, and gas cooler are divided into eight elements, while the radiator is divided into ten elements (for each fluid each wall section). Initially the models have been run to an initial state of full convergence by specifying no changes in the variable driving the transients. This operating point is identical (within numerical accuracy) to the corresponding point using the steady-state models. At that operating point key parameters of the cycle have the values shown in Table 1. The figures show the time-evolution of various parameters (nondimensionalized with their values at the beginning of the transients, shown in Table 1).

Figure 5 has been produced with a system model using the transient heat exchanger models coupled to the instantaneous-response turbomachinery models (Eqs. (1)). It shows the select output of the system response to a double-step transient of 20 K (about 2%) in salt temperature over 1080 s (18 min, about 20% of the 90 minute orbital transient). The time step in the calculations is 1 s. As seen from the figure, it takes over 18 min for the system to reach a new steady state. T_4 settles to its new value in about 800 s, but p_4, $\dot{m}_3$, and $\dot{W}_s$ require about 2000 s after the step to reach a new steady state. The final steady state after 4000 s is identical (within numerical accuracy) to the initial state at the beginning of the transient.

Table 1 Values at the beginning of transients

Variable	Value
T_{sk}	186.0 K
T_{sl}	1042.0 K
T_4	1012.2 K
p_4	354.8 kPa
$\dot{m}_3$	0.835 kg/s
Ω	3351 rad/s (32,000 rpm)
$\dot{W}_s$	41.1 kW

Figure 6 has also been produced with a system model using the transient heat-exchanger models coupled to the instantaneous-response turbomachinery models. It shows the select output of the system response to a sinusoidal transient in salt temperature of amplitude 5 K (0.47%) over 628 s (about 11.6% of the 90 min orbital transient). The time step in the calculations is 1 s. As seen from the figure, the relatively long thermal transient behavior of the heat exchangers causes the transients to reach the various components at different phases. The peaks in T_4 are about 60 s later than the corresponding peaks in $T_{\rm sl}$, and they are of a slightly lower amplitude. The sinusoidal variations in p_4, $\dot{m}_3$, and $\dot{W}_s$ (after an initial system transient during the first two or three cycles) follow a sinusoidal pattern similar to that for T_4.

Figure 7 shows the select output of the response of two different system models to a sinusoidal transient in salt temperature of

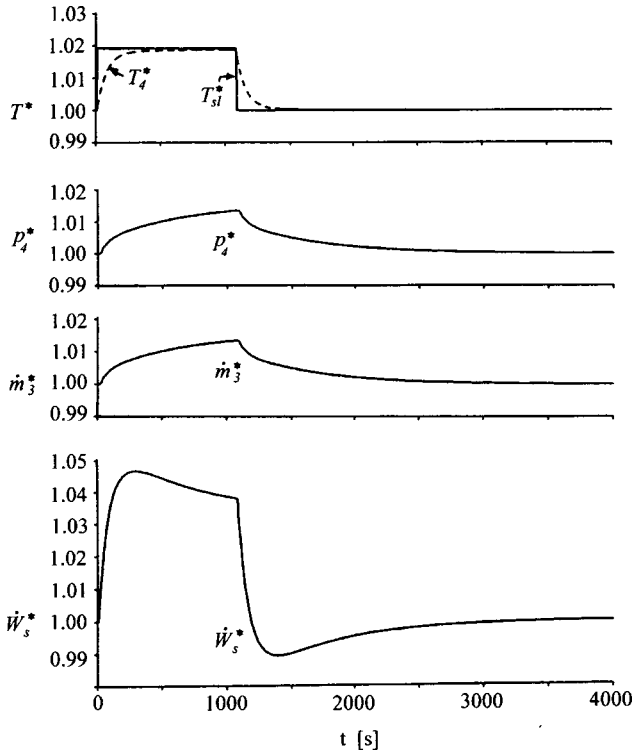

Fig. 5 Instantaneous-response turbomachinery/transient heat exchangers. System response to double step in T_{sl}.

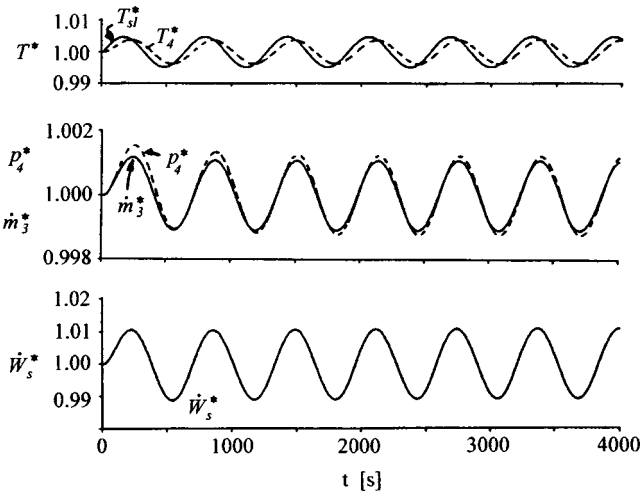

Fig. 6 Instantaneous-response turbomachinery/transient heat exchangers. System response to sinusoidal variation in T_{sl}.

amplitude 50 K (4.7%) over 0.628 s. The first system model (dashed lines) has been produced with transient heat-exchanger models coupled to the instantaneous-response turbomachinery models. The time step in these calculations is 0.0025 s. The second system model (solid lines) has been produced with transient heat exchanger models coupled to the transient turbomachinery models (Eqs. (2), (3), (4) and (5)). The time step in these calculations is 0.000025 s. Using working-fluid properties and component sizes, it was estimated that acoustic disturbances travel through the compressor passages in 0.000015 s, and through the turbine passages in 0.000020 s. The short period of the transient has been used in this case to show the differences in the system output from the transient and instantaneous-response turbomachinery. In transients with longer periods the slow thermal response of the heat exchangers dominates the transient turbomachinery behavior.

Figure 7 indicates that the system responds at a frequency similar to the driving frequency, and that the peaks in T_4 are about 0.168 s later than the peaks in T_{sl}. (The delay between the peaks is a function of the driving frequency.) The T_4 responses of the two system models are identical. The sinusoidal patterns in T_4, p_4, $\dot{m}_3$, and $\dot{W}_s$ are similar, and there is little difference in p_4 and $\dot{m}_3$ between the two models. Because the overall system takes about 2000 s to reach a new steady state (Fig. 5), once T_4, p_4, $\dot{m}_3$, and $\dot{W}_s$ have started increasing (the first cycle in Fig. 7), they drop very little below their initial values within the 2 s shown in Fig. 7. (They drop below their values at the beginning of the transient at later times.) The response of $\dot{W}_s$ (and other related temperatures and pressures at the inlet and exit of the compressor and turbine) have substantially different amplitudes between the instantaneous-response and transient-turbomachinery models. In gas-turbine cycles with heat exchangers the long thermal-response times of the heat exchangers dominates the turbomachinery response. It is concluded that the transient turbomachinery models are required for fast transients only. Such high-frequency transients may be introduced by the electronic control systems (such as some of those required to control the system by changing the distribution of mass between the system and the accumulator). The transient turbomachinery models are also required in simple cycles (those without heat exchangers).

Figure 8 has been produced with a system model using the transient heat exchanger models coupled to the instantaneous response turbomachinery models. It shows the select output of the system response to a sinusoidal transient in a salt temperature of amplitude 5 K (0.47%) over 628 s (about 11.6% of the 90 min orbital transient). The input to this transient is the same as that

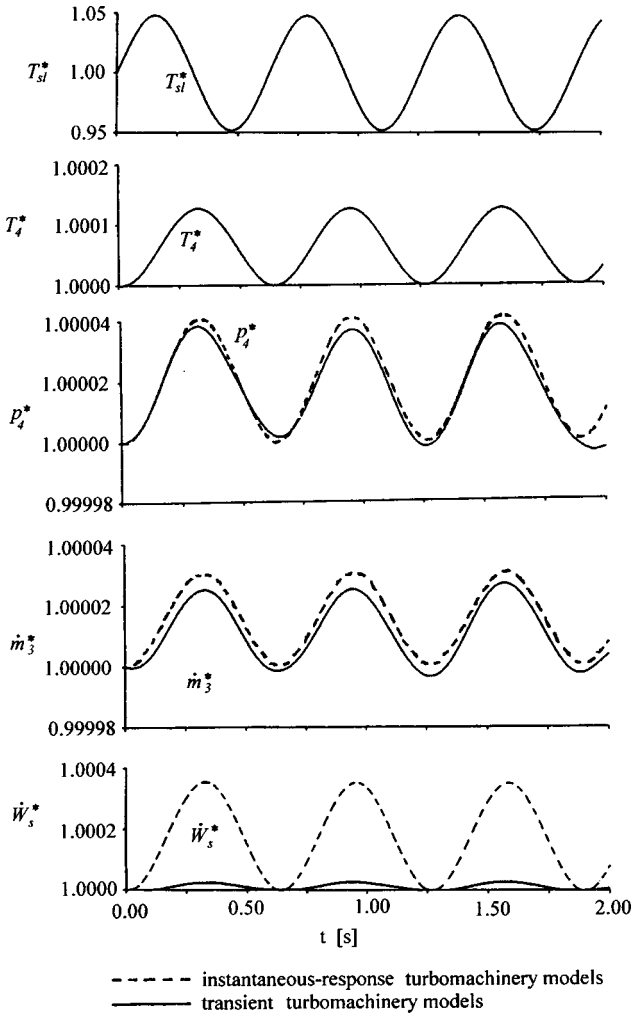

Fig. 7 System response to sinusoidal variation in T_{sl}. A comparison of system models with instantaneous-response turbomachinery (dashed lines) and with transient turbomachinery models (solid lines).

shown in Fig. 6. The time step in the calculations is 1 s. Two different transient system models are shown. The first system model (dashed lines) simulates constant-speed operation. The second system model (solid lines) simulates a system model with a power-speed law of the form $\dot{W}_{al}=k\Omega^3$. The T_4 responses of the two system models are identical. The sinusoidal variations in p_4, $\dot{m}_3$, and $\dot{W}_s$ (after an initial system transient during the first two or three cycles) follow a sinusoidal pattern similar to that for T_4. The Ω variations in the variable-speed model are 0.25%. The amplitude of $\dot{W}_s$ for the variable-speed model is less than that for the constant-speed model because of the shape of the turbine-efficiency contours (wider plateaus along constant-speed lines and narrower plateaus across the speed lines).

Conclusions

Steady-state and transient models suitable for predicting the behavior of gas-turbine components have been developed. The component models are based on the transient form of the conservation of mass, energy, and momentum within each component. The component models have been coupled to simulate a closed-cycle regenerative gas-turbine cycle with components suitable as powering units of small space systems. During transients the cycle parameters of the overall system are iteratively evaluated. A converged solution for each time step is obtained by an iterative

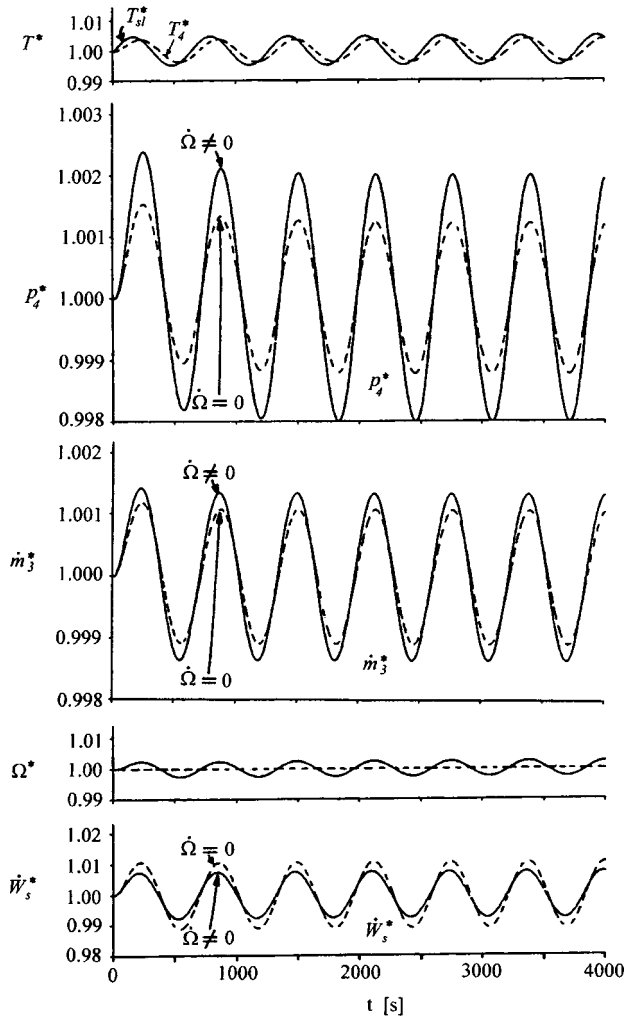

Fig. 8 System response to sinusoidal variation in T_{sl}. A comparison of constant and variable rotational speed models.

scheme based on the principle of conservation of working-fluid mass in the system. Various system transients have been studied. For an illustration, transients driven by step and sinusoidal variations in eutectic salt temperature (variations in energy input to the cycle), and under constant and varying shaft speed, have been included. In gas-turbine cycles with heat exchangers the long thermal-response times of the heat exchangers dominates the turbomachinery response. System models based on instantaneous-response turbomachinery/transient heat-exchanger component models can be used to predict low-frequency transients. The transient turbomachinery models are required for higher-frequency transients, such as those that may be introduced by the engine control system. The transient turbomachinery models are also required in simple cycles (those without heat exchangers).

Nomenclature

A = heat transfer area
c = specific heat capacity
C = heat capacity rate $C \equiv \dot{m} c_p$
D = diameter of a component
h = heat-transfer coefficient
I = rotating-unit inertia
k = heat conductivity of the wall
L = length of a component
m = mass
N_{tu} = number of heat transfer units
p = pressure
Q = energy transferred as heat
r = radius
R = (universal gas constant)/(molecular weight)
t = time
T = temperature
U = absolute flow velocity
V = volume
$W, \dot{W}$ = work, power
ϵ = heat-exchanger effectiveness
η = total-to-total polytropic efficiency
σ = (emissivity)×(Stefan-Boltzmann constant)
Ω = angular velocity

Subscripts

1, 2, . . . , 6 = thermodynamic-cycle points
a, b = fluids in heat exchangers
al = input to alternator shaft
c = compressor
cv = control volume
cd = cold fluid
fr = friction
ht = hot fluid
i = element counter in difference equations
in = into component
m = middle of component
max = maximum
min = minimum
ot = out of component
p = at constant pressure (c_p)
r = radiation
s = shaft power to alternator
sk = sink (temperature)
sl = eutectic salt (temperature)
T = total property
t = turbine
tp = impeller tip
v = at constant volume (c_v)
w = wall
x, y = Cartesian directions

Superscripts

n = counter in time-difference equations
$', ''$ = primary and secondary coolant loops
$*$ = nondimensional quantity (nondimensionalized with values shown in Table 1)

Appendix: Description of Components

(Note that the components of the Space Station were under development at the time of writing.) The following information was used to produce the results shown in this study. The receiver has 82 tubes of Haynes 188 steel of outlet diameter 22.2 mm and active tube length 2.5 m. At a design-point receiver operation $\epsilon = 0.8730$, $N_{tu} = 2.0635$, and $C_{rat} = 0.0000$. The recuperator is a pure counterflow plate-fin unit of length 0.37 m, width 0.32 m, and height 0.49 m. The high-pressure side has 62 sandwiches of fins, with 630 (0.15 mm thick) CRES 304L fins per m, with height 3.2 mm. The low-pressure side has 63 sandwiches of fins, with 630 (0.15 mm thick) CRES 304L fins per m, with height 3.9 mm. At design-point recuperator operation $\epsilon = 0.9404$, $N_{tu} = 15.7763$, and $C_{rat} = 1.0000$. The gas cooler is an eight-pass cross-counterflow plate-fin heat exchanger. The fin sandwiches are rectangular offset, 2.3 mm high. The gas side has 470 (0.15 mm thick) CRES 304L fins per m, with height 2.3 mm. The liquid side has 790 (0.15 mm thick) CRES 304L fins per m, with height 1.9 mm. At design-point gas-cooler operation $\epsilon = 0.9430$, $N_{tu} = 6.4501$, and $C_{rat} = 0.7428$. The radiator has 8 aluminum 2.3 m×8.0 m panels. Key turbomachinery parameters are shown below.

References

[1] Korakianitis, T., and Wilson, D. G., 1994, ''Models for Predicting the Performance of Brayton-Cycle Engines,'' ASME J. Eng. Gas Turbines Power, **116**, pp. 381–388.

[2] Korakianitis, T., and Beier, K. J., 1994, ''Investigation of the Part-Load Performance of Two 1.12 MW Regenerative Marine Gas Turbines,'' ASME J. Eng. Gas Turbines Power, **116**, pp. 418–423.

[3] Korakianitis, T., Papagiannidis, P., and Vlachopoulos, N., 2002, ''Unsteady-Flow/Quasi-Steady Heat Transfer Computations on a Turbine Rotor and Comparison With Experiments,'' ASME J. Turbomach., **124**, pp. 152–159.

[4] Kuhlberg, J. F., Sheppard, D. E., King, E. O., and Baker, J. R., 1969, ''The Dynamic Simulation of Turbine Engine Compressors,'' AIAA Paper No. 69-486.

[5] Kalnitsky, K. C., and Kwatny, H. G., 1981, ''A First Principles Model for Steam Turbine Control Analysis,'' ASME J. Dyn. Syst., Meas., Control, **103**, pp. 61–68.

[6] Adams, J., Clark, D. R., Louis, J. R., and Spanbauer, J. P., 1965, ''Mathematical Modeling of Once-Through Boiler Dynamics,'' Trans. IEEE, Power Apparatus Syst., **84**, pp. 146–156.

[7] Corbett, A. G., and Elder, R. L., 1974, ''Stability of an Axial Flow Compressor With Steady Inlet Conditions,'' J. Mech. Eng. Sci., **16**, pp. 377–385.

[8] Macdougal, I., and Elder, R. L., 1983, ''Simulation of Centrifugal Compressor Transient Performance for Process Plant Applications,'' ASME J. Eng. Gas Turbines Power, **105**, pp. 885–890.

[9] Ray, A., and Bowman, H. F., 1976, ''A Nonlinear Dynamic Model of a Once-Through Subcritical Steam Generator,'' ASME J. Dyn. Syst., Meas., Control, **98**, pp. 332–339.

[10] Fink, D. A., Cumpsty, N. A., and Greitzer, E. M., 1992, ''Surge Dynamics in a Free-Spool Centrifugal Compressor System,'' ASME J. Turbomach., **114**, pp. 321–332.

[11] Rocketdyne, 1986, ''Space Station Work Package WP-04 Power System Preliminary Analysis and Design Document,'' Rocketdyne RI/RD85-320-2, December.

[12] Rocketdyne, 1989, ''Allied-Signal Interim Design Review for the CBC/PGS for the NASA Space Station Freedom,'' Rocketdyne Report No. 41-9311, November.

[13] Heywood, J. B., 1988, *Internal Combustion Engine Fundamentals*, McGraw-Hill, New York.

[14] Kays, W. M., and London, A. L., 1984, *Compact Heat Exchangers*, McGraw-Hill, New York.

Parametric Performance of Combined-Cogeneration Power Plants With Various Power and Efficiency Enhancements

T. Korakianitis
James Watt Professor of Mechanical Engineering,
University of Glasgow,
Glasgow G12 8QQ, Scotland UK
e-mail: t.alexander@mech.gla.ac.uk

J. Grantstrom

P. Wassingbo

Department of Heat and Power Engineering,
Royal Institute of Technology,
Stockholm, Sweden

Aristide F. Massardo
University of Genova,
Genova, Italy

The design-point performance characteristics of a wide variety of combined-cogeneration power plants, with different amounts of supplementary firing (or no supplementary firing), different amounts of steam injection (or no steam injection), different amounts of exhaust gas condensation, etc., without limiting these parameters to present-day limits are investigated. A representative power plant with appropriate components for these plant enhancements is developed. A computer program is used to evaluate the performance of various power plants using standard inputs for component efficiencies, and the design-point performance of these plants is computed. The results are presented as thermal efficiency, specific power, effectiveness, and specific rate of energy in district heating. The performance of the simple-cycle gas turbine dominates the overall plant performance; the plant efficiency and power are mainly determined by turbine inlet temperature and compressor pressure ratio; increasing amounts of steam injection in the gas turbine increases the efficiency and power; increasing amounts of supplementary firing decreases the efficiency but increases the power; with sufficient amounts of supplementary firing and steam injection the exhaust-gas condensate is sufficient to make up for water lost in steam injection; and the steam-turbine power is a fraction (0.1 to 0.5) of the gas-turbine power output. Regions of "optimum" parameters for the power plant based on design-point power, hot-water demand, and efficiency are shown. A method for fuel-cost allocation between electricity and hot water is recommended. [DOI: 10.1115/1.1808427]

Introduction

The popular use of the phrase ''energy crisis'' implies that this ''energy'' is something that is degraded as we try to capture its usefulness. In engineering thermodynamics energy must be conserved (or with Einstein's theory of relativity, mass and energy are conserved through $\Delta E = \Delta m c^2$, and a small reduction in mass leads to the release of huge amounts of energy). Clearly there is an abundance of energy on earth. At the same time there is concern about our ability to efficiently convert this energy into the thermodynamic equivalent of work, a concept known as thermodynamic availability or exergy. We do not have an energy crisis; but, we should be concerned about our continued ability to derive exergy from fossil fuels indefinitely. Power plants with high efficiency and power density are essential.

In order to improve the ability of power plants to convert energy into exergy, utility companies have introduced combined power plants, using more than one prime mover. There are several ways to accomplish this, but the most common solution is a topping Brayton-cycle (gas turbine) plant and a bottoming Rankine-cycle (steam turbine) plant, with claimed combined thermal efficiencies up to 0.60 and higher. The performance of these plants may be improved further by various configurations of steam injection in the gas turbine, supplementary firing (in the Rankine cycle or other parts of the overall cycle), and other similar schemes. (For example: steam-injected gas turbine, Cheng, [1]; STIG, Fraize and Kinney, [2]; Tuzson, [3]; evaporative, Frutschi and Plancherel, [4], and El-Masri, [5]; water-injected stoichiometric combustion, WISC, Patton and Shouman, [6]; humid air turbine, HAT, and recuperated water-injected cycle, RWI, Chiesa et al., [7], and Macchi et al., [8]; cascaded humidified advanced turbine, CHAT, Nakhamkin et al., [9]; supplementary firing, Finckh and Pfost, [10]). Frequently, as a by-product of combined power plants one can also extract additional useful energy in the form of hot water, a concept known as ''cogeneration'' of electric power and hot water, usually for district heating (for instance, International Energy Agency, [11]; Horlock, [12]). The products of combustion (particularly of biomass) contain relatively large amounts of water, which may be condensed to provide district hot-water heating, or it may be condensed in the boiler (preheater) of the steam turbine plant, thus increasing thermal efficiency further (for instance, Nasholm et al., [13]; Nguyen and den Otter, [14]; Macchi and Poggio, 1994 [15]).

While steam injection increases power output, it has the major disadvantages of treated water consumption (which must be replaced in the water-treatment component of the plant) and the large thermal loss related to the latent heat of steam discharged to the atmosphere with the exhaust. Exhaust-gas condensation is a way to recuperate the latent heat in the combined cycle, and also to recycle the condensate into the plant. Some of the above studies directly or indirectly imply that supplementary firing into the Rankine-cycle boiler can improve the efficiency of the combined cycle. This appears contrary to basic thermodynamic principles, which demand that, for maximum efficiency, energy (heat) addition to the cycle must contribute to increasing maximum cycle temperature. Most published results on cogeneration plants concentrate on measures of efficiency, without mentioning the equally important parameter of power density. Various studies have been published on predicting the theoretical efficiency, or power, or size, of very restricted regions of combinations of these power plants [16–19,12,20,21]. We have not been able to find in the open literature a parametric study of combined-cogeneration plants that involves all three concepts of steam injection, supplementary firing, and exhaust gas condensation.

Contributed by the International Gas Turbine Institute and presented at the 42nd International Gas Turbine and Aeroengine Congress and Exposition, Orlando, FL, June 2–5 1997. Manuscript received November 1, 1996; final revision received February 1, 1997. Paper No. 1997-GT-0285. Associate Editor: H. A. Kidd.

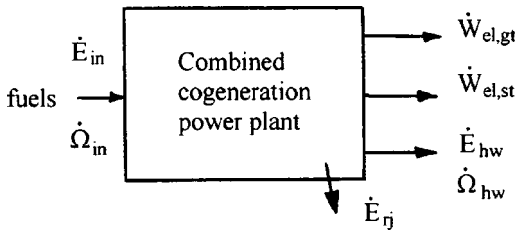

Fig. 1 Energy and exergy inputs and outputs in an arbitrary combined-cogeneration power plant

Several studies have addressed the issue of "optimizing" the performance of combined or cogeneration power plants, based on several different optimizing functions (for example, von Spakovsky and Evans, [22]; Frangopoulos, [23]; Yantovskii, [24]; Agazzani and Massardo, [25]). Other studies [26] have introduced the concept of combining the capital, maintenance, and operating costs of a power plant with the thermodynamic optimization. The optimization results are highly dependent on the necessary inputs of present capital costs and of future fuel and maintenance costs; they do not directly answer the question of trends as cycle parameters change. However, once the cycle parameters have been restricted in a narrower range, these studies are useful in optimizing a specific plant.

The trends of the effect of steam injection, supplementary firing, exhaust-gas condensation, etc. on the efficiency, power, and hot water for district heating derived from the above references are confusing and occasionally contradict each other. At present we do not have design-point performance figures ("carpet plots") of efficiency versus power versus energy in hot water as a function of combined-cogeneration cycle parameters. This is in contrast to the performance plots available for simple, regenerative, intercooled-regenerative, etc. gas turbines (such as those, for example among several others for gas turbines, derived by Korakianitis and Wilson (1994) [27]). This paper derives such design-point performance plots for combined-cogeneration cycles as a function of steam injection, supplementary firing, and exhaust-gas condensation. The purpose of these plots is to enable us to study the general effects (trends) of varying these cycle parameters, rather than to pinpoint the exact performance of a specific plant.

Plant-Performance Parameters

The concept of exergy grades the amount work that can be extracted out of any stream of energy interacting isentropically with the local environment [28]. Electric work can readily be converted into heat (resistance heaters), but only a fraction of heat can be converted to work (second law of thermodynamics, via a power plant). Furthermore, this fraction is reduced the lower the exergy of the available heat. For example, in a cogeneration plant the part of the energy available as heat in the district hot-water heating is relatively large, but it has small potential to do work. Clearly 1 kW h of electricity is worth a lot more than 1 kW h of hot water. This raises the issue of appropriate allocation of costs (capital costs, fuel costs, maintenance costs, etc.) between electricity and hot water in cogeneration plants.

The performance of any combined-cogeneration power plant of arbitrary complexity (including steam injection, supplementary firing, exhaust-gas condensation, and any other performance-enhancing measure) can be measured in terms of the energy E and exergy Ω inputs and outputs as shown in Fig. 1. With the aid of this figure, we define the following combined-cogeneration cycle performance parameters:

$$\eta_{th} \equiv \frac{\dot{W}_{el,gt} + \dot{W}_{el,st}}{\dot{E}_{in}} \quad \text{thermal efficiency} \tag{1}$$

$$\epsilon \equiv \frac{\dot{W}_{el,gt} + \dot{W}_{el,st} + \dot{\Omega}_{hw}}{\dot{E}_{in}} \quad \text{effectiveness} \tag{2}$$

$$\dot{W}' \equiv \frac{\dot{W}_{el,gt} + \dot{W}_{el,st}}{\dot{m}_{in,gt} C_p T_0} \quad \text{specific power} \tag{3}$$

$$\dot{E}'_{hw} \equiv \frac{\dot{E}_{hw}}{\dot{m}_{in,gt} C_p T_0} \quad \text{specific hot-water energy rate} \tag{4}$$

where the specific (nondimensional) values $\dot{W}'$ and $\dot{E}'_{hw}$ are nondimensionalized with the product of mass-flow rate of air at the gas turbine inlet, $\dot{m}_{in,gt}$, times the isobaric specific heat capacity of air at ambient conditions, C_p, times the ambient temperature, T_0. Therefore, $\dot{W}'$ and $\dot{E}'_{hw}$ are a function of the size of the gas turbine, and they are in direct correspondence with similar specific-power values for gas turbines available in the literature.

The denominator of thermal efficiency, η_{th}, and effectiveness, ϵ, is the energy flow rate into the power plant from all sources, $\dot{E}_{in}$, typically from the fuel input (or inputs, in the case of supplementary firing). This denominator could instead be the exergy rate of the fuel input(s), Ω_{in}, which would involve calculations of the partial pressures of the exhaust constituents and their corresponding chemical potentials with respect to standard atmosphere. The exergy content of most fuels is within 6.5% of the fuel energy-flow rate [29], and it is much harder to compute than the energy rate, particularly for multicomponent fuels such as natural gas and biomass. Since the constituents of these fuels vary with the fuel source, η_{th} and ϵ are usually defined with the energy flow rate of the fuel, which is easier to compute as the mass flow rate of fuel times the lower heating value of the fuel.

Combined-Cogeneration Plant

The representative combined-cogeneration power plant shown in Fig. 2 was developed for the design-point parametric studies, with component characteristics, where appropriate, derived from the GE LM5000 engine. The purpose of this representative plant is to investigate the design-point performance of widely different combined-cogeneration power plants as functions of turbine rotor-inlet temperature, compressor pressure ratio, supplementary firing, steam injection, and exhaust-gas condensation. We did not impose limits of a minimum power demand, or district-heating demand, or compressor surge, etc. For example, steam-injected gas turbines today are redesigned gas turbines, and therefore can accommodate a moderate amount of steam injection. In order to assess the impact of steam injection on the cycle, the steam injection capacity was not limited in the simulations by component considerations.

The gas turbine receives energy input from the primary fuel (F1) and from steam injection (station 5). The boiler of the Rankine plant receives energy inputs from gas-turbine exhaust and from the secondary fuel (F2, supplementary firing). The total energy into the plant is

$$\dot{E}_{in} = \dot{m}_{F1} LHV_{F1} + \dot{m}_{F2} LHV_{F2}. \tag{5}$$

Part of the exhaust gas is condensed and used to make up for steam injection in the gas turbine (station 17; the amount is computed as explained below); and this energy (latent heat) is used in part to preheat the Rankine-cycle feedwater (station 16), and in part to preheat the district hot water (stations 13–14). The plant includes one each (representative) open-and closed feed water heaters, and the pressure at the HP turbine inlet is the representative 120 bar. Although in practice steam injection can occur in several parts of the gas-turbine cycle, in this representative plant steam injection is at combustor outlet. The steam is extracted from the steam turbine (station 5) at the pressure of the gas turbine

Representative cycle symbols and inputs:
fuel F1 is into gas turbine combustor
fuel F2 is into Rankine-cycle boiler
energy ratio F2/F1 = 0.0, 0.1, 0.2, 0.3
$\dot{m}_{15}$ is $\dot{m}_{in,gt}$ (equations 3, 4)
$\dot{m}_3$ is Rankine HP-turbine mass-flow rate
$\dot{m}_5$ is steam injection mass-flow rate extracted at gas-turbine compressor-outlet pressure
$\dot{m}_5$ is steam-injection mass-flow rate
$\dot{m}_{10}$ is district hot water
stack temperature $T_{12} = 50\ ^\circ C$
district water inlet temperature $T_{10} = 40\ ^\circ C$
district water outlet temperature $T_{11} = 105\ ^\circ C$
$p_{10} = p_{11} = 5$ bar
condenser temperature $T_8 = 110\ ^\circ C$)
condenser pressure $p_8 = 1.433$ bar)
total-to-total compressor (turbine)
isentropic efficiency 85% (90%)
pressure losses, gas turbine cycle, 12%
TIT = 1500 K, 1600 K, 1700 K
r = 10, 20, 30, 40
Boiler inlet pressure $p_2 = 120$ bar
gas-turbine generator efficiency 0.958
steam-turbine generator efficiency 0.958

Lines in performance plots:

$\frac{\dot{E}_{F2}}{\dot{E}_{F1}}$:

$\frac{\dot{m}_5}{\dot{m}_{in,gt}}$:

$\frac{\dot{m}_5}{\dot{m}_3}$:

$\frac{\dot{W}_{el,st}}{\dot{W}_{el,gt}}$:

$\frac{\dot{m}_{10}(h_{13} - h_{14})}{\dot{E}_{F1} + \dot{E}_{F2}}$:

$\frac{\dot{m}_{17}}{\dot{m}_5}$:

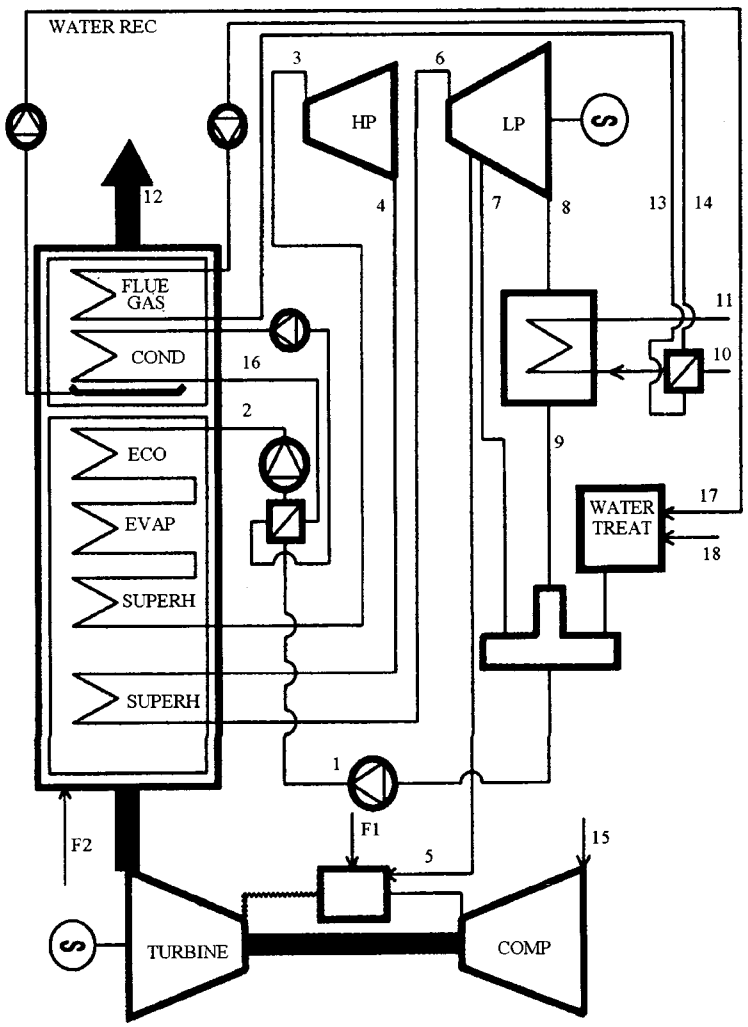

Fig. 2 Illustration of representative combined-cogeneration power plant

compressor, which in the parametric study was operating at one of the pressure ratios 10, 20, 30, or 40. The district hot water receives additional energy from the Rankine-cycle condenser. The performance figures below indicate that in some cases the water condensed from the exhaust is not sufficient to make up for steam injection in the gas turbine. When that happens the plant then needs additional water coming into the water treatment plant (station 18). This power-plant description is used to represent different sizes of components in different power plants in the calculations below. The size of the plant components would be different in different regions of the performance maps shown below.

Typically, exhaust-gas condensation occurs between 20°C and 80°C, depending on the partial pressure of the vapor and the moisture content of the fuels. The major disadvantage of exhaust-gas condensation is the corrosive effect of acids generated by several trace constituents in the fuels such as sulfur, vanadium, chlorium, and bromium. Natural gas and biomass have low contents of these corrosive constituents, making them suitable for plants with exhaust-gas condensation. Without loss of generality it was assumed that the primary fuel (F1) is natural gas, and the secondary fuel (F2) is ground biomass pellets with 10% moisture content, injected in the boiler, with the constituent concentrations by mass shown in Table 1. After combustion and before exhaust-gas condensation in the boiler, we have a mixture of

Table 1 Concentrations of dry air, Swedish natural gas, and typical dry biomass, all by mass

Constituent	Air	Natural gas	Biomass
O_2	23.14	—	42.5
N_2	75.54	0.9	0.9
Ar	1.28	—	—
CO_2	0.04	1.2	—
CH_4	—	81.1	—
C_2H_6	—	7.9	—
C_3H_8	—	4.2	—
n-C_4H_{10}	—	4.7	—
C	—	—	50.5
H_2	—	—	6.1

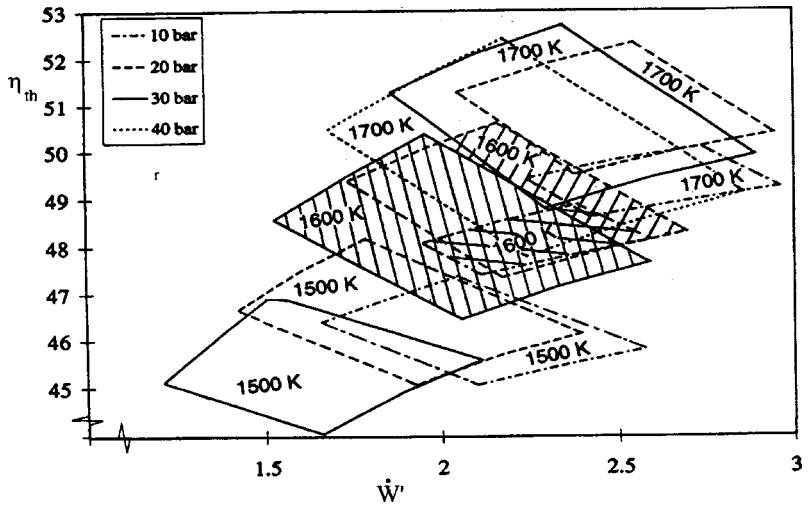

Fig. 3 Regions of plant η_{th} versus $\dot{W}'$ as functions of gas turbine TIT and r

O_2 (excess air from all combustion processes);

N_2 (from air, natural gas and biomass);

CO_2 (from complete combustion of F1 and F2, plus what comes in with the natural gas, plus what comes in with $\dot{m}_{in,gt}$, plus what comes in with combustion air);

Ar from all incoming air streams; and

H_2O from the combustion of H_2 in F1 and F2, plus from moisture in biomass, plus water from steam injection $\dot{m}_5$, plus from the humidity of all incoming air streams.

These exhaust products are treated as a saturated vapor mixture at 50°C and one atmosphere (temperature and pressure at station 12, with saturated vapor pressure $p_{sa,12}=0.1233$ bar) to evaluate the mass flow rate of water vapor in the saturated exhaust. The water mass fraction in the saturated exhaust, x, is computed by

$$x=\frac{MW_{H_2O}}{MW_d}\frac{p_{sa,12}}{p_{12}-p_{sa,12}} \tag{6}$$

It is assumed that the remaining water is condensed ($\dot{m}_{17}$), and recirculated in the water treatment plant. If the condensed water is less than the injected steam $\dot{m}_5$, then the plant needs make up water, $\dot{m}_{18}$.

The performance of the power plant was computed using the thermodynamic part of the model developed by Agazzani and Massardo [25], modified to include exhaust-gas condensation and steam injection. This program can be used for the overall optimization of power plants, but for this paper it was used to evaluate the performance of the power plants as specified by the inputs above. Since the representative power plant has only one open and one closed feedwater heaters, the computed performance is representative of the complexity of the plant (i.e., it is not as high as more-complex plants with additional performance-enhancing schemes). The calculations are used to discuss the trends in the performance figures below, and not the exact value of maximum plant efficiency.

Performance Figures

Figures 3 and 4 show regions of operation of different gas turbines on the η_{th} versus $\dot{W}'$ and ϵ versus $\dot{E}'$ maps. The performance of the power plants within these regions is explained below. For 1700 K engines the *regions* corresponding to increasing pressure ratios of 10, 20, 30, and 40 move counterclockwise similar to the typical performance *points* for simple-cycle gas turbines

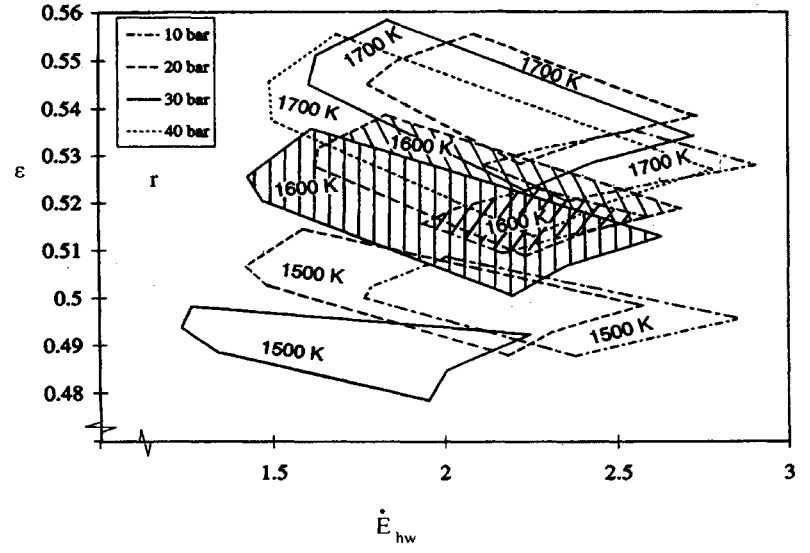

Fig. 4 Regions of plant ϵ versus E'_{hw} as functions of gas turbine TIT and r

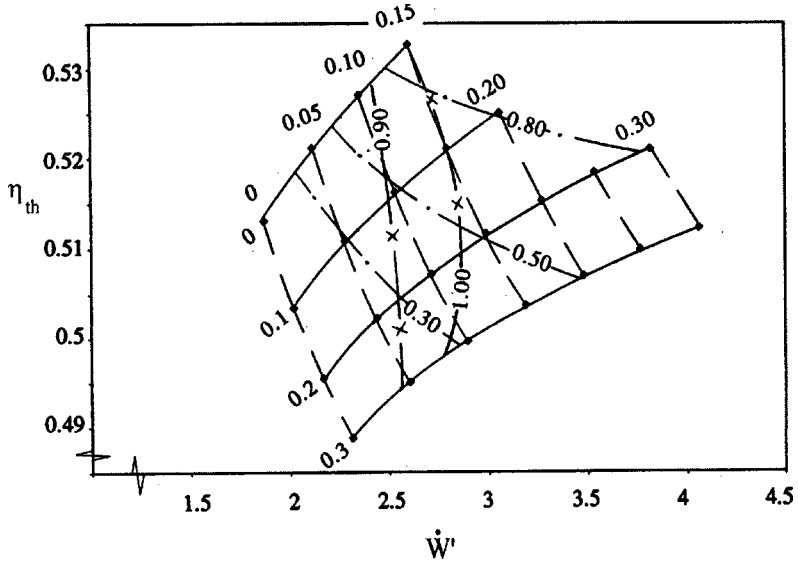

Fig. 5 η_{th} **versus** $\dot{W}'$ **for power plant with TIT=1700 K and** $r=30$

(as shown, for example, by Korakianitis and Wilson (1994) [27]). Just as in simple-cycle gas turbines, for each TIT as the gas turbine pressure ratio increases the performance figures indicate an optimum for specific power at compressor pressure ratios of around 10, and a different optimum for thermal efficiency at a higher pressure ratio of around 30. Increasing the pressure ratio further results in decreases in both power and efficiency. The region for 1700 K and $r=30$ appears ''optimum'' for thermal efficiency and for effectiveness, but we will explore the meaning of these ''optima'' further below.

Similarly, for 1600 K (shaded regions for $r=10$, 20, 30) the regions move counterclockwise with increasing r; and for 1500 K (for $r=10$, 20, 30) the regions move counterclockwise with increasing r.

Figures 5 and 6 show the design-point performance of power plants with TIT=1700 K and $r=30$. These figures are typical of the performance figures obtained for all other combinations of TIT and r. The legend for the lines of these figures is included in the table to the left of Fig. 2. The solid lines in Fig. 5 correspond to different values of $\dot{E}_{F2}/\dot{E}_{F1}$, which is the rate of energy input from fuel F2 (supplementary firing) divided by the rate of energy input from fuel F1 (primary firing), in the range of 0.0 to 0.3. The long dashed lines correspond to $\dot{m}_5/\dot{m}_{in,gt}$ (mass flow rate of steam injection into the gas turbine divided by mass flow rate of air at gas turbine inlet) in the range of 0.0 to 0.40. The dashed lines with one dot correspond to $\dot{m}_5/\dot{m}_3$ (mass flow rate of steam injection into the gas turbine divided by mass flow rate of steam into the HP steam turbine inlet) in the range of 0.3 to 0.80. The (almost vertical) dashed lines with an ''x'' correspond to $\dot{m}_{17}/\dot{m}_5$ (mass flow rate of condensed water from the exhaust divided by mass flow rate of steam injection into the gas turbine) in the range of 0.8 to 1.0. Clearly, when $\dot{m}_{17}/\dot{m}_5=1.0$ there is just enough water available in the condensed exhaust to make up for the steam injection, or the plant does not need the addition of new water in the water-treatment plant. When $\dot{m}_{17}/\dot{m}_5>1.0$ (to the right of the $\dot{m}_{17}/\dot{m}_5=1.0$ line) the plant ''makes water.'' When $\dot{m}_{17}/\dot{m}_5<1.0$ (to the left of the $\dot{m}_{17}/\dot{m}_5=1.0$ line) the plant needs additional water in the water treatment plant. (Tuzson (1992) [3] estimates the cost of treated water at 5% of the fuel cost.)

In Fig. 6 the solid lines (again) correspond to different values of

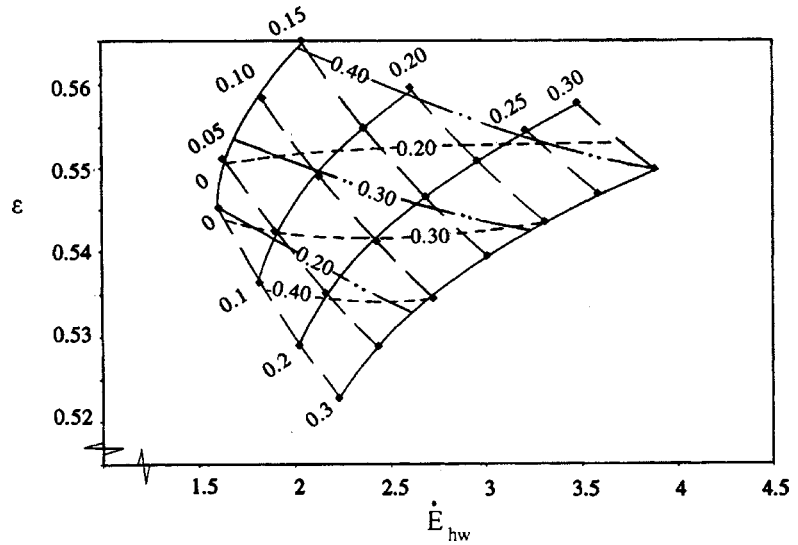

Fig. 6 ϵ **versus** E'_{hw} **for power plant with TIT=1700 K and** $r=30$

$\dot{E}_{F2}/\dot{E}_{F1}$ in the range of 0.0 to 0.3. The long dashed lines (again) correspond to $\dot{m}_5/\dot{m}_{in,gt}$ in the range of 0.0 to 0.40. The short dashed lines correspond to $\dot{W}_{el,sg}/\dot{W}_{el,gt}$ (power produced by the steam turbine divided by power produced by the gas turbine) in the range of 0.2 to 0.4. The dashed lines with double dots correspond to the rate of energy from the exhaust-gas condensation used for district hot-water heating $\dot{m}_{10}(h_{13}-h_{14})$ divided by the total rate of energy input from the two fuels $\dot{E}_{F1}+\dot{E}_{F2}$.

Combinations of figures such as Figs. 5 and 6 for several combined-cogeneration power plants are included in Korakianitis et al., 1997 [30]. With the information in these figures one can obtain an understanding of the relative sizes of these components, and compare them with components of other combined/cogeneration power plants with the same electricity and district heating output (with different $\dot{E}_{F2}/\dot{E}_{F1}$, $\dot{m}_5/\dot{m}_{in,gt}$, etc.) giving the same electric power and hot-water energy-rate outputs from the same region of performance (1700 K, $r=30$), or from another region of performance (e.g., 1600 K, $r=20$).

In these comparisons: (a) the lines of $\dot{E}_{F2}/\dot{E}_{F1}=0.0$ correspond to cases of combined power plants without supplementary firing but with different steam-injection rates; (b) the lines of $\dot{m}_5/\dot{m}_{in,gt}=0.0$ correspond to cases of no steam injection in the gas turbine but with different rates of supplementary firing; (c) the points of $\dot{E}_{F2}/\dot{E}_{F1}=0.0$ and $\dot{m}_5/\dot{m}_{in,gt}=0.0$ correspond to cases of no steam injection in the gas turbine and no supplementary firing, identical to the left-corner point of regions in Figs. 3 and 4; and (d) combinations of performance figures such as Figs. 5 and 6 correspond to general performance plots of several types of simplifications of the model power plant.

Discussion

In all cases steam injection will increase thermal efficiency. In all cases supplementary firing decreases thermal efficiency and effectiveness but increases specific power and specific rate of energy. As expected, in all cases the contribution of exhaust-gas condensation to preheating district hot-water heating increases with increasing steam injection and increasing supplementary firing. The $\dot{m}_5/\dot{m}_{in,gt}$ lines have a higher slope than the $\dot{m}_5/\dot{m}_3$ lines, particularly with increasing $\dot{E}_{F2}/\dot{E}_{F1}$ (meaning that the size of the steam plant increases with supplementary firing, as expected).

In all cases the electric power produced by the steam turbine plant is 10 to 50 percent of the electric power produced by the gas turbine. This means that the gas turbine dominates the overall power plant performance. It explains why the regions of performance shown in Figs. 3 and 4 resemble the points of simple-cycle performance. Steam injection in general increases specific power output and thermal efficiency. From these, one can conclude that in order to optimize the performance of combined/cogeneration power plants the order of importance of parameter choices is the following:

1. Maximize turbine-inlet temperature;
2. Chose compressor pressure ratio and region of operation (Figs. 3 and 4); and
3. Maximize steam injection.

In all cases either enough water is condensed from the exhaust gas to make up for steam injection in the gas turbine, or a relatively small percentage of additional water is needed (up to 20% of steam flow rate).

Figure 7 shows η_{th} versus $\dot{m}_3/\dot{m}_{in,gt}$ for TIT=1700 K and $r=30$ as a function of $\dot{E}_{F2}/\dot{E}_{F1}$ and $\dot{m}_5/\dot{m}_{in,gt}$ (corresponding to Fig. 6). It shows that increased supplementary firing and/or increased steam injection will increase the size of the steam power plant in relation to the gas turbine power plant. Similar trends are shown for all the other regions of (TIT,r).

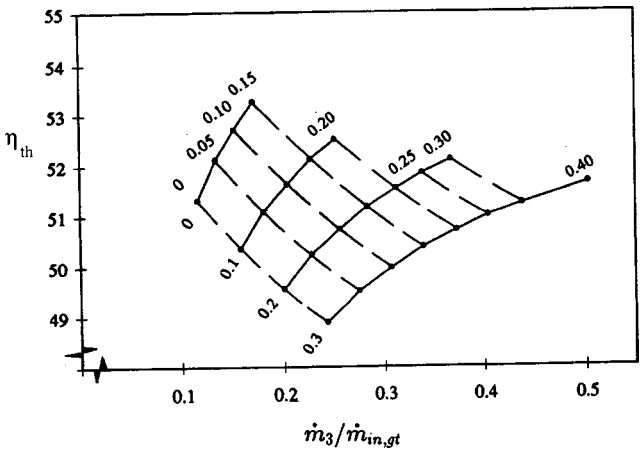

Fig. 7 η_{th} **versus** $\dot{m}_3/\dot{m}_{in,gt}$ **for power plant with TIT=1700 K and** $r=30$

Figure 8 shows η_{th} versus $\dot{W}'$ for TIT=1700 K and $r=10$, 20, 30, 40 as a function of $\dot{E}_{F2}/\dot{E}_{F1}$ (0.0 solid lines and 0.1 dashed lines) and $\dot{m}_5/\dot{m}_{in,gt}$ (0.0, 0.05, 0.10, corresponding to Figs. 5 and 6). The lines of increasing pressure ratio move counterclockwise. Similar trends are shown for all the other regions of (TIT,r). Clearly, the performance plots indicate that the performance of the gas turbine dominates the performance characteristics of the overall power plant. The lines with question marks in the figure approximate the extrapolated limit of $\dot{m}_5/\dot{m}_3=1.0$, which would correspond to a steam plant without a low-pressure turbine and without a condenser. (This is an approximation that neglects some auxiliary uses, such as the steam required for the deaerator, etc). The nearest points for these extrapolations are shown with "x" marks, using for the extrapolations values up to $\dot{m}_5/\dot{m}_3=0.87$ shown in Figs. 5 and 6). In these limiting power plants, all the steam released from the HP turbine is injected into the gas turbine, and exhaust-gas condensation takes the place of the condenser and district water preheating.

It is not surprising that the thermal efficiencies of the power plants shown are in the 50 percent range, and they do not quite approach the 60 percent range, if one considers that the steam turbine plants are not "optimized" (for instance, boiler pressure), and that a significant amount of power output is sacrificed to produce even more significant amounts of district hot-water heating (high condenser pressure).

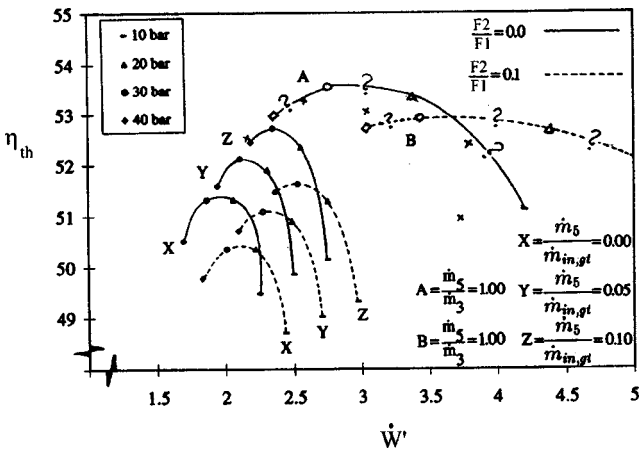

Fig. 8 η_{th} **versus** $\dot{W}'$ **for power plants with TIT=1700 K and** $r=10, 20, 30, 40$

Fuel-Cost Allocation

The performance figures indicate that in each case the energy rate in district hot water is comparable to the electric power produced. Several complex methods to allocate capital, maintenance, and fuel costs in combined-cogeneration power plants have been published (for instance, Frangopoulos, 1992 [23]; Yantovskii, 1994 [24]; Tsatsaronis and Chen, 1995 [26]). However, once the power plant is in operation, there will be seasonal variations between hot-water demand and electricity, and then one must address the question of distributing the fuel cost alone. All methods indicate that, if the fuel costs are allocated based on energy values, then the low-exergy district heating bears a disproportionately large portion of the fuel cost. Some of these methods allocate costs based on individual component losses (or entropy increases due to irreversibility). This is rather cumbersome in complex power plants, particularly in cases where some components are shared between plant functions. Such is the case, for instance, in the boiler of the representative power plant (to which side should one charge the entropy generated by irreversibility across the finite temperature difference in the heat exchanger?); or in steam injection in the gas turbine; and several other components.

We recommend that in answering the question of fuel-cost allocation between electricity and hot water, the plant is considered as shown in Fig. 1, and fuel costs are allocated based on exergy values. Thus, the fraction of the total fuel cost for F1 and F2 is allocated by

$$\dot{W}_{el}\ \text{fraction} = \frac{\dot{W}_{el,gt} + \dot{W}_{el,st}}{\dot{W}_{el,gt} + \dot{W}_{el,st} + \dot{\Omega}_{hw}} \tag{7}$$

$$\dot{E}_{hw}\ \text{fraction} = \frac{\dot{\Omega}_{hw}}{\dot{W}_{el,gt} + \dot{W}_{el,st} + \dot{\Omega}_{hw}} \tag{8}$$

where

$$\dot{\Omega}_{hw} = \dot{m}_{10}[(h_{11} - h_{10}) - T_0(s_{11} - s_{10})] \tag{9}$$

With this approach the fuel cost per kw h of hot water is appropriately lower than the fuel cost per kW h of electricity.

Conclusions

The design-point performance of a wide variety of combined-cogeneration power plants has been computed using a baseline representative power plant, without imposing limitations of using existing components. General trends of parametrically varying these performance-enhancing schemes are illustrated, clarifying some misconceptions of the effect of each of these enhancing schemes on thermal efficiency, power, plant effectiveness, energy rate in district heating, and relative size between gas turbine and steam turbine.

The performance of combined-cogeneration power plants is dominated by the gas-turbine performance. The performance of these plants is optimized by: (a) maximizing turbine rotor inlet temperature in the gas turbine; (b) optimizing the gas turbine pressure ratio for gas-turbine performance; (c) optimizing steam-turbine boiler pressure; and (d) maximizing steam injection in the gas turbine.

Supplementary firing should only be considered as a power-enhancing scheme, but it lowers plant thermal efficiency because it occurs at boiler temperatures, which are usually lower than the maximum cycle temperature (which occurs in the gas turbine). The exhaust-gas condensate is usually but not always sufficient to make up for water injected in the gas turbine. The gas turbine produces most of the plant power.

Limits in overall cycle parameters and performance are imposed by steam injection in the gas turbine, the temperature of district hot-water heating, the combination of condenser pressure and pinch point in the boiler, and the available amount of water vapor in the exhaust.

There is still a need to investigate the off-design performance of the plants; and to carry out the thermoeconomic optimization of the overall power plant including the costs and benefits of steam injection and exhaust-gas condensation.

Nomenclature

C_p = isobaric specific heat capacity
$E, \dot{E}, \dot{E}'$ = energy, energy rate, specific energy rate
F1, F2 = primary, secondary (supplementary) fuels
LHV = lower heating value of fuel
$m, \dot{m}$ = mass, mass-flow rate
MW = molecular weight
p = pressure
r = compressor pressure ratio
T = temperature
TIT = turbine rotor-inlet temperature
$W, \dot{W}, \dot{W}'$ = work, power, specific power
x = H_2O fraction in saturated exhaust
ϵ = power-plant effectiveness
η_{th} = thermal efficiency
$\Omega, \dot{\Omega}$ = exergy, exergy rate

Subscripts

d = dry (all constituents except H_2O)
el = electric output
gt = gas-turbine output
hw = hot water
in = into cycle
rj = rejected from cycle
st = steam-turbine output

References

[1] Cheng, D. Y., 1976, Parallel-Compound Dual-Fluid Heat Engine, U.S. Patent No. 3,978,661.
[2] Fraize, W. E., and Kinney, K. R., 1979, "The Thermodynamics of Steam Injection on the Performance of Gas Turbine Power Cycles," ASME J. Eng. Gas Turbines Power, **101**, pp. 217–227.
[3] Tuzson, J., 1992, "Status of Steam-Injected Gas Turbines," ASME J. Eng. Gas Turbines Power, **114**, pp. 682–686.
[4] Frutschi, H. U., and Plancherel, A. A., 1988, "Comparison of Combined Cycles With Steam Injection and Evaporation Cycles," Proceedings, ASME Cogen-Turbo II, pp. 137–145.
[5] El-Masri, M. A., 1988, "A Modified High Efficiency Recuperated Gas Turbine Cycle," ASME J. Eng. Gas Turbines Power, **110**, pp. 233–242.
[6] Patton, J. T., and Shouman, A. R., 1989, "Very High Efficiency Hybrid Steam/Gas Turbine Power Plant With Bottoming Vapor Rankine Cycle," US Patent No. 4,841,721.
[7] Chiessa, P., Lozza, G., Macchi, E., and Conconni, S., 1995, "An Assessment of the Thermodynamic Performance of Mixed Gas-Steam Cycles.—Part B: Water Injected and HAT Cycles," ASME J. Eng. Gas Turbines Power, **117**, pp. 489–499.
[8] Macchi, E., Conconni, S., Lozza, G., and Chiessa, P., 1995, "An Assessment of the Thermodynamic Performance of Mixed Gas-Steam Cycles. Part A—Intercooled and Steam-Injected Cycles," ASME J. Eng. Gas Turbines Power, **117**, pp. 499–508.
[9] Nakhamkin, M., Swensen, E. C., Wilson, J. M., Gaul, G., and Polsky, M., 1996, "The Cascaded Humidified Advanced Turbine [CHAT]," ASME J. Eng. Gas Turbines Power, **118**, pp. 565–571.
[10] Finckh, H. H., and Pfost, H., 1992, "Development Potential of Combined-Cycle (GUD) Power Plants With and Without Supplementary Firing," ASME J. Eng. Gas Turbines Power, **114**, pp. 653–659.
[11] International Energy Agency, 1983, *District Heating and Combined Heat and Power Systems. A Technology Review*, International Energy Agency, OECD, Paris, France.
[12] Horlock, J. H., 1996, *Cogeneration: Combined Heat and Power. Thermodynamics and Economics*, Krieger, Melbourne, FL.
[13] Nasholm, A. S. E., Svedberg, G., and Westermark, M. O. J., 1993, "Exergy Analysis of Biomass-Fired Cogeneration Plant in a Pulp and Paper Mill," ASME Paper 93-GT-354.
[14] Nguyen, H. B., and den Otter, A., 1994, "Development of Gas Turbine Steam Injection Water Recovery (SWIR) System," ASME J. Eng. Gas Turbines Power, **116**, pp. 68–74.
[15] Macchi, E., and Poggio, A., 1994, "A Cogeneration Plant Based on a Steam Injection Gas Turbine With Recovery of the Water Injected: Design Criteria and Initial Operating Experience," ASME Paper 94-GT-17.
[16] Boyle, R. J., 1976, "Effect of Steam Addition for Cycle Performance of Simple and Recuperated Gas Turbines," NASA Technical Paper TR 1440.
[17] El-Masri, M. A., 1987, "Exergy Analysis of Combined Cycles. Parts 1 and 2,"

ASME J. Eng. Gas Turbines Power, **109**, pp. 228–236, **109**, pp. 237–243.
[18] Horlock, J. H., 1992a, *Combined Power Plants*, Pergamon Press, Oxford.
[19] Horlock, J. H., 1992b, ''The Rational Efficiency of Power Plants and Their Components,'' ASME J. Eng. Gas Turbines Power, **114**, pp. 603–611.
[20] Kehlhofer, R., 1991, *Combined Cycle Gas and Steam Turbine Power Plants*, The Fairmont Press, Lilburn, GA.
[21] Boland, O., and Stadaas, J. F., 1995, ''Comparative Evaluation of Combined Cycles and Gas Turbine Systems With Water Injection, Steam Injection, and Recuperation,'' ASME J. Eng. Gas Turbines Power, **117**, pp. 139–145.
[22] von Spakovsky, M. R., and Evans, R. B., 1990, ''The Design and Performance Prediction of Thermal Systems,'' ASME J. Eng. Gas Turbines Power, **112**, pp. 86–93.
[23] Frangopoulos, C. A., 1992, ''Optimal Synthesis and Operation of Thermal Systems by the Thermoeconomic Functional Approach,'' ASME J. Eng. Gas Turbines Power, **114**, pp. 707–714.
[24] Yantovskii, E. I., 1994, *Energy and Exergy Currents*, Nova Science, New York.
[25] Agazzani, A., and Massardo, A. F., 1997, ''A Tool for Thermoeconomic Analysis and Optimization of Gas, Steam, and Combined Plants,'' ASME J. Eng. Gas Turbines Power, **119**, pp. 885–892.
[26] Tsatsaronis, G., and Chen, Y., 1995, ''Exergoeconomic Evaluation and Optimization of Cogeneration Systems,'' Int. J. Global Energy Issues, **7**, No. 3/4, pp. 148–161.
[27] Korakianitis, T., and Wilson, D. G., 1994, ''Models for Predicting the Performance of Brayton-Cycle Engines,'' ASME J. Eng. Gas Turbines Power, **116**, pp. 381–388.
[28] Gyftopoulos, E. P., and Beretta, G. P., 1991, *Thermodynamics: Foundations and Applications*, MacMillan, New York.
[29] Wark, K., 1996, *Advanced Engineering Thermodynamics*, McGraw-Hill, New York.
[30] Korakianitis, T., Grantstroem, J., Waessingbo, P., and Massardo, A. F., 1997, ''The Performance of Combined-Cogeneration Power Plants With Supplementary Firing, Steam Injection, and Exhaust Gas Condensation,'' Washington University Report WU-ICE 96-05.

Using Hydrogen as Gas Turbine Fuel

Paolo Chiesa

Giovanni Lozza

Dipartimento di Energetica,
Politecnico di Milano,
Milano, Italy

Luigi Mazzocchi
CESI,
Milano, Italy

This paper addresses the possibility to burn hydrogen in a large size, heavy-duty gas turbine designed to run on natural gas as a possible short-term measure to reduce greenhouse emissions of the power industry. The process used to produce hydrogen is not discussed here: we mainly focus on the behavior of the gas turbine by analyzing the main operational aspects related to switching from natural gas to hydrogen. We will consider the effects of variations of volume flow rate and of thermophysical properties on the matching between turbine and compressor and on the blade cooling of the hot rows of the gas turbine. In the analysis we will take into account that those effects are largely emphasized by the abundant dilution of the fuel by inert gases (steam or nitrogen), necessary to control the NO_x emissions. Three strategies will be considered to adapt the original machine, designed to run on natural gas, to operate properly with diluted hydrogen: variable guide vane (VGV) operations, increased pressure ratio, re-engineered machine. The performance analysis, carried out by a calculation method including a detailed model of the cooled gas turbine expansion, shows that moderate efficiency decays can be predicted with elevated dilution rates (nitrogen is preferable to steam under this point of view). The combined cycle power output substantially increases if not controlled by VGV operations. It represents an opportunity if some moderate re-design is accepted (turbine blade height modifications or high-pressure compressor stages addition).
[DOI: 10.1115/1.1787513]

1 Introduction

Hydrogen, as a carbon-free energy carrier, is likely to play a important role in a world with severe constraints on greenhouse gas emissions. In the power industry, its utilization as gas turbine fuel can be proposed under several possible scenarios, depending on the mode of H_2 production. For instance, hydrogen can be produced remotely from renewable energy sources (solar or wind) or from nuclear energy (via direct thermal conversion or by electrolysis), but in a more realistic and near-term vision it will be derived from conventional fossil fuels by conversion processes including CO_2 sequestration. Possible solutions include: (i) remote coal conversion to hydrogen (via gasification, shift, and separation from CO_2) and H_2 pipeline transport to the power station, (ii) integrated hydrogen and electricity production from coal or natural gas, exporting pure hydrogen to remote users, and using on-site low-grade hydrogen to produce power [1], (iii) electricity generation from combined cycles integrated to fossil fuel decarbonization (applicable to coal, oil, or gas) and to CO_2 capture [2]. Fuel cells and H_2-O_2 semiclosed cycles may represent future options for power generation, but combined cycles coupled to H_2 production/CO_2 sequestration processes can be proposed as a short/mid-term solution for massive greenhouse gas emission reduction.

This paper addresses the possibility to burn hydrogen in a large size, heavy-duty gas turbine designed to run on natural gas, for a prompt application of the above general concepts, regardless of the process used to produce hydrogen and its integrations with the combined cycle. We will focus on the behavior of the gas turbine, by considering the effects of the variation of volume flow rates and of thermophysical properties, related to switching from natural gas to hydrogen. These effects are emphasized by the fact that NO_x emission control relies on fuel dilution with large quantities of inert gases, like steam or nitrogen, as discussed in Sec. 2. The consequent variation of the operating conditions is therefore much larger than for the mere fuel substitution, calling for an analysis of the opportunity (or necessity) of design modifications to the gas turbine. The paper discusses these issues by considering some possible adaptation techniques, by discussing their operational limits and, mostly, by predicting the resulting combined cycle efficiency and power output.

2 NO_x Control

Generally speaking, three methods have been used to reduce NO_x emissions from gas turbine power plants: (i) premixed combustion, including catalytic combustion, (ii) fuel dilution, mostly by steam, water or nitrogen; (iii) removal from exhaust gases. For natural gas applications, the first technique is the preferred one: at present, the ''dry low-emission'' combustors are proposed by manufacturers for virtually any gas turbine model. Their basic principle is to achieve a moderate flame temperature by forcing more air than stoichiometric in the primary zone; this is obtained by mixing air to fuel before the combustion. Catalytic combustors, often referenced as the future technology for extremely low emissions, just enhance the same principle, allowing for a much larger rate of premixing, no longer limited by flame stability limits. When switching to hydrogen (or to hydrogenated fuels, such as the coal syngas used in IGCC plants) premixing becomes a very questionable practice, due to the much larger flammability limits and the lower ignition temperatures of hydrogen with respect to natural gas [3]. Therefore both dry low-emission and catalytic combustors cannot be safely proposed for large industrial applications, to the authors' knowledge, simply because hydrogen promptly reacts when mixed to air at typical gas turbine conditions, at virtually any rate. In fact, IGCC combustors, handling a CO-H_2 mixture with H_2 content from 25 to 40%, are diffusion burners and pre-mixed combustion was never attempted. Massive steam or nitrogen dilution is extensively used in these combustors [4] to control NO_x. In diffusion burners, the stoichiometric flame temperature (SFT) is representative of the actual flame temperature, strictly related to the NO formation rate.

Figure 1 shows a collection of literature data, mostly retrieved from a GE experimental investigation with hydrogenated fuels

Contributed by the International Gas Turbine Institute (IGTI) of THE AMERICAN SOCIETY OF MECHANICAL ENGINEERS for publication in the ASME JOURNAL OF ENGINEERING FOR GAS TURBINES AND POWER. Paper presented at the International Gas Turbine and Aeroengine Congress and Exhibition, Atlanta, GA, June 16–19, 2003, Paper No. 2003-GT-38205. Manuscript received by IGTI October 2002; final revision March 2003. Associate Editor: H. R. Simmons.

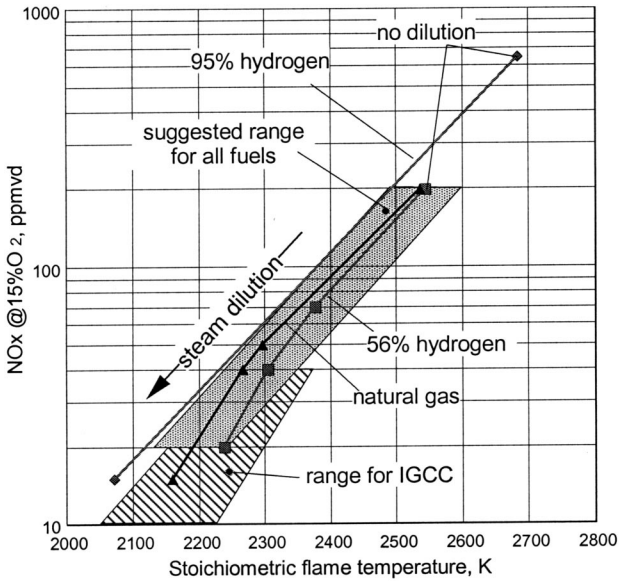

Fig. 1 Relation between NO_x emission and stoichiometric flame temperature, progressively reduced by steam dilution, for gas turbine diffusive combustion at 12–16 bar with different fuels. Nitrogen is the balance gas for 56% and 95% hydrogen.

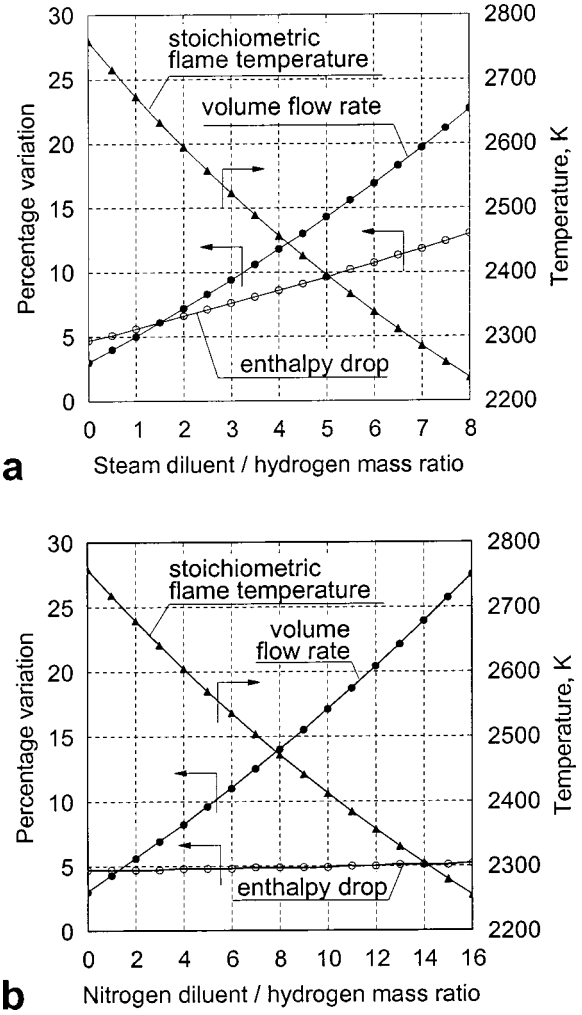

Fig. 2 Variation of the SFT and of the inlet volume flow rate and isentropic enthalpy drop of a hydrogen fueled gas turbine with respect to the reference natural gas case. Curves are drawn as a function of the added diluent flow rate: the upper diagram refers to steam, the lower diagram to nitrogen.

reported by Todd and Battista [5], showing a relation between SFT and NO_x emission for various fuels in typical gas turbine conditions. It is clear that the utilization of undiluted H_2 brings about unacceptable levels of emission and that the SFT must be greatly reduced to have emissions comparable to power industry standards (25–45 ppmvd). A reasonable value of 2300 K for SFT can be stipulated to meet this standards, even if more experience must be gained to set precise indications.

The third technique mentioned above (removal from exhausts) includes: (i) selective catalytic reduction (SCR) by means of ammonia injection (a very well-known method), (ii) the Sconox process, recently proposed for extremely elevated removal rates, using adsorption-desorption on potassium carbonate beds. These techniques can be used downstream of H_2-fueled gas turbines, as well as for conventional units. However, their cost and size are basically related to the amount of NO_x removed (about 2000 $/ton for SCR, 6000–8000 for Sconox (Major and Powers [6])). Their utilization can be proposed to reduce emissions starting from a moderate concentration (for instance from 100 to 10 ppm), but the incidence on the electricity cost would be excessive when starting from many hundreds of ppm, as for H_2 combustion (especially for Sconox). Therefore, excluding premixed combustors and limiting the SCR to ''finishing'' applications, dilution techniques seem mandatory for hydrogen utilization in gas turbine combustors.

The selection of steam and nitrogen as the possible diluents is quite straightforward. Steam is always available in a combined cycle and can be extracted from the steam turbine at any pressure and at any reasonable rate. Nitrogen is available ''for free'' in processes including air separation, i.e., in any coal or refinery residual gasification plant: if the hydrogen used by the gas turbine is produced on site from decarbonization of syngas from heavy fuels, nitrogen will be surely present in large quantities[1] (see, for instance, Lozza and Chiesa [2]). In such plants, it is also possible to use saturation of the hydrogen-rich gas by means of warm water coming from the syngas cooling: it makes available a steam-diluted fuel without extractions from the steam turbine. In some other hydrogen production processes, nitrogen is ''naturally'' available: this is the case of natural gas decarbonization by means of an air-blown autothermal reformer [7,8], producing a synthesis fuel consisting of a 50–50% (approximately, by volume) mixture of H_2 and N_2, perfectly suited for NO_x abatement.

[1]Throughout the discussion we will assume that nitrogen for dilution is available at no energy cost at atmospheric pressure. This assumption is actually verified if the plant incorporates a low-pressure air separation unit.

3 Effects of Hydrogen Combustion on Turbomachinery

Compared to natural gas, hydrogen combustion leads to a lower mass flow rate and to a different composition of the product gases, with an higher water content that in turn influences the molecular weight and the specific heat of the mixture. The most relevant effects on the operation of a gas turbine are: (i) a variation of the enthalpy drop in the expansion, (ii) a variation of the flow rate at the turbine inlet which, in turn, affects the turbine/compressor matching, (iii) a variation of the heat-transfer coefficient on the outer side of the turbine blades, affecting the cooling system performance.

3.1 Influence of Fluid Composition Variation on Turbine Enthalpy Drop and Inlet Volume Flow Rate. Figure 2(*a*) shows the influence of hydrogen combustion (in presence of a variable flow of diluting steam) on the isentropic enthalpy drop of a turbine at a given inlet condition ($T=1450°C$, $p=17$ bar) and

atmospheric outlet pressure, compared to the corresponding natural gas fired case. Compared to natural gas, the simple hydrogen combustion increases the enthalpy drop by about 5%, a variation that increases as long as the amount of added steam rises. Assuming the working fluid as an ideal gas, since the isentropic enthalpy drop can be evaluated through the expression

$$\Delta h_{is} = \int_{T_{FIN,IS}}^{T_{IN}} c_P(T)dT = \overline{c_P}(T_{IN} - T_{FIN,IS}),$$

it is possible to distinguish the effect due to the variation of average c_P and the one due to the variation of the temperature drop through the expansion (being the latter influenced by the exponent of the isentropic transformation γ, i.e., the specific-heat ratio). Increasing steam dilution entails an enhancement of the mixture specific heat but a simultaneous decrease of the exponent γ that reduces the temperature drop and consequently increases the turbine outlet temperature.

The second *y* axis reports the stoichiometric flame temperature resulting from the combustion. It shows that a diluent to H_2 mass ratio of about 7 is required to keep this temperature at 2300 K: correspondingly the enthalpy drop increases by about 12% with respect to the natural gas case.

Figure 2(*a*) also quantifies the variation of the volume flow rate at turbine inlet resulting from the hydrogen combustion (always in comparison with the natural gas fired case). The same amount of combustion air and the same combustion temperature (1450°C) are assumed for all the cases and therefore also the H_2 flow rate increases as long as the diluent flow rate increases. Notice that in the case of no dilution, although the mass flow rate of combustion products reduces (about 2%, considered that hydrogen LHV is 119.95 MJ/kg versus 44.77 of natural gas), the volume flow rate increases by about 3% due to the change in composition (molecular weight of this mixture reduces from 28.27 to 26.93 kg/kmol). This effect amplifies when dilution is considered. At steam to H_2 mass ratio of 7 the mass and volume flow rate increase by 11% and 20%, respectively.

Figure 2(*b*) reports the analysis as far as nitrogen is considered for dilution. The different scale on the abscissa reflects that a much larger diluent to fuel ratio is required to determine a given SFT abatement (about twice, since c_P of N_2 is approximately one-half of c_P of steam). Therefore dilution greatly affects the mass flow rate and, consequently, the volume flow rate (black dotted line). On the contrary the effect of nitrogen dilution on the turbine enthalpy drop is virtually negligible since a large amount of nitrogen (from combustion air) is already contained in the mixture so that even a large diluent addition does not substantially modify the fluid properties.

3.2 Compressor/Turbine Matching. Because of the variation of the volume flow rate caused by the different fuel (and additional diluent), using hydrogen affects the original matching between compressor and expander in a gas turbine originally designed to run on natural gas. A different running point will be set where mass flow rate and pressure ratio will restore the fluid-dynamic equilibrium between the two turbomachines. Typical operational curves are shown in Figs. 3 and 4, for a single shaft arrangement operating at fixed rotational speed (the only solution adopted for large industrial gas turbines). For high performance axial compressors with several transonic stages, used in advanced gas turbines, the characteristics show that the mass flow rate is virtually constant when the inlet is choked. To improve partial load operations, variable geometry guide vanes (VGV's) are used on several stator rows, affecting the characteristic lines as shown by Fig. 3.

The operating line of the expander at constant speed is reported in Fig. 4. When the machine is fueled with hydrogen, having a higher heating value than natural gas, the mass flow rate $G_{T,IN}$ reduces for a give compressor airflow. Nevertheless the nondimensional flow $G_{R,T,IN}$ slightly increases, because of the molecular mass reduction. This increase becomes more and more important when $G_{T,IN}$ grows up due to the diluent addition. Therefore switching from natural gas to hydrogen makes impossible to operate the gas turbine on the same running point (i.e., at the same VGV angle, pressure ratio, $G_{C,IN}$ and $T_{T,IN}$).

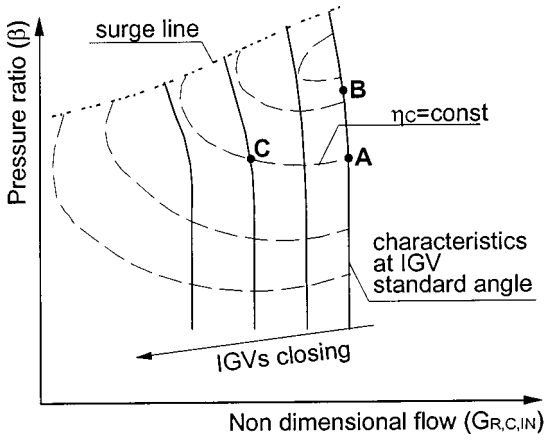

Fig. 3 Typical compressor characteristic curve at constant rotational speed. Different lines correspond to different settings of the variable guide vanes angle.

Assuming that A and A' are the design points on the compressor and turbine maps (Figs. 3 and 4) of the natural gas fueled machine, three different regulation strategies can be envisaged:

(i) Letting the compressor to work at the same point (*A*, at the same VGV angle) and reducing the $T_{T,IN}$, to restore the fluid-dynamic matching between compressor and turbine. The expander runs at the design point A':

(ii) Letting the VGV angle and $T_{T,IN}$ at their original value, $G_{R,T,IN}$ can be adjusted by increasing the pressure ratio, (i.e. moving from A to B on the compressor characteristics while the turbine running point moves from A' to B'). If the compressor is not choked, the higher β also reduces the mass flow rate and helps to reset the matching. If the required pressure ratio exceeds the available surge margin, one or more high-pressure stages must be added to the compressor.

(iii) Letting $T_{T,IN}$ and β at their value, equilibrium can be found by closing the VGV's and reducing $G_{C,IN}$. The corresponding running point moves from A to C in Fig. 3. If condition depicted by point C exceeds the available surge margin, additional stages are required. The turbine running point remains unaffected so that C' overlaps A'.

Remarking that the actual regulation can be carried out by adopting all the three strategies at the same time, it is evident that the first one seems the least interesting since the performance of a combined cycle substantially decays when $T_{T,IN}$ reduces. The effects of the latter strategies on the cycle performance will be dis-

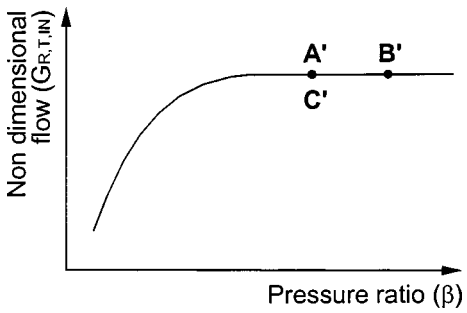

Fig. 4 Typical turbine characteristic curve at constant rotational speed

Table 1 Thermophysical properties at 1000°C and 10 bars

	ρ, kg/m^3	c_P, kJ/kg K	$\mu\times10^6$, Pa s	k$\times10^3$, W/m K	$\rho^{0.63}c_P^{1/3}k^{2/3}/\mu^{0.7}$
Air	2.736	1.183	50.109	83.164	73.84
Steam	1.702	2.482	48.241	135.465	98.15
CO_2	4.158	1.289	49.524	81.696	98.09

cussed later (Sec. 5), but it can be anticipated that off-design operations imply a substantial change of the gas turbine power output. Therefore considerations about mechanical stresses can heavily influence the regulation strategy: dealing with such limits is beyond the scope of the present analysis but they must be carefully considered.

The hydrogen combustion (and related dilution) also entails substantial changes in the shape of the velocity triangles, due to the increase of the enthalpy drop and volume flow rate that influence the flow velocity and its axial component, respectively. Given that the flow is accelerated along the gas path, the turbine blades can operate efficiently even for incidence angles sensibly different from the design value and these changes in the velocity triangles consequently have small effects on the turbine performance. A more relevant efficiency decay can be caused by the increase of the kinetic energy loss at the exhaust due to the increased flow rate for the same exhaust area.

3.3 Blade Cooling. Hydrogen combustion and additional dilution affect the cooling system under two different aspects:

- the varied composition of the hot stream enhances the convective heat-transfer coefficient on the outer side of the blade increasing the thermal flux with negative consequences on the performance of the cooling circuit;
- the higher pressure ratio increases the convective heat-transfer coefficients on both blade sides and the temperature of air used in the cooling circuit whose performance decays.

Effect of Flow Composition. The correlation proposed by Louis [9] allows us to evaluate the average heat-transfer coefficient on the outer side of the blade:

$$h_{\mathrm{OUT}}=0.285\frac{(\rho v)^{0.63}c_P^{1/3}k^{2/3}}{D^{0.37}\mu^{0.7}},$$

where v is the main stream speed referred to the cascade exit. Replacing steam to CO_2 (as it actually occurs when H_2 replaces natural gas as fuel) has no significant consequences on the heat flux imposed on the blade outer surface, as it can be argued from Table 1. On the contrary, steam dilution determines an increase of the thermal flux since the heat-transfer coefficient for steam is higher than for air. A secondary effect is an increase of h_{OUT} due to the higher average velocity of the gas stream along the flow path related to the higher available enthalpy drop.

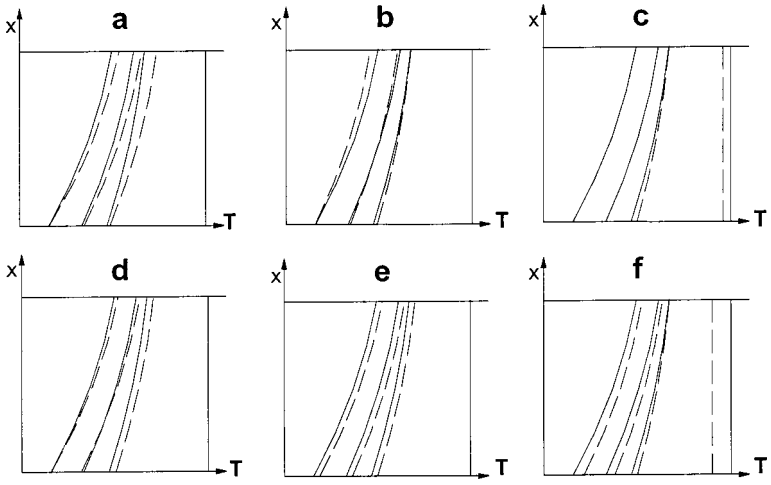

Fig. 6 Temperature–heat-transfer area diagrams showing different situations in the simplified cooling circuit of Fig. 5. Temperature profiles have the same meaning of Fig. 5: from left, they refer to coolant, inner blade wall, outer blade wall, main gas stream. The continuous lines refer to the original situation, the dashed ones to modified conditions.

Although the calculation model used for the final discussion (Sec. 5) considers the current gas turbine cooling circuits including film cooling and multipass channels, the behavior of a cooling circuit in consequence of a change in the main stream composition can be better discussed by considering a very simplified convective cooling circuit. It consists of a single internal duct run by the cooling fluid whose blade transverse section is schematically shown on the left side of Fig. 5. The temperature profiles along the blade height are shown in Fig. 5, right side. The blade can be considered a cross-flow heat exchanger, where the cooling flow ensures that the highest metal temperature remains within the stipulated limit.

Enhancing the thermal flux on the blade at constant cooling flow rate causes an increase of the temperatures along the profiles as shown in Fig. 6(*a*). The constraint on the maximum metal temperature can be restored either by increasing the cooling flow

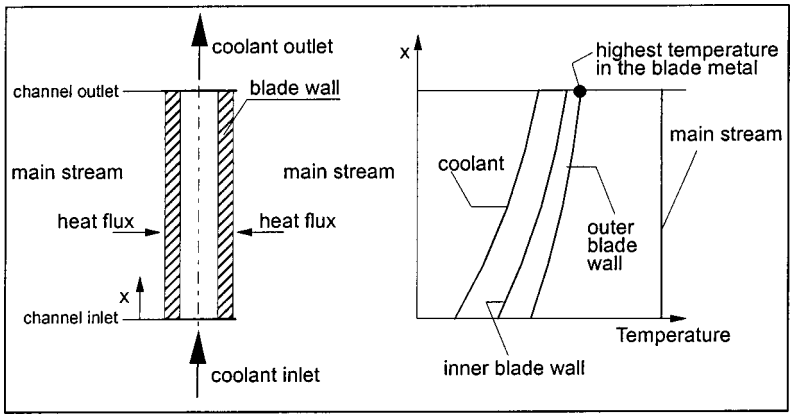

Fig. 5 Simplified blade cooling model. Blade is assumed as a cross-flow heat exchanger where heat capacity of the outer stream is infinitely larger than the one of the inner stream. Main temperature profiles are reported in the right diagram.

rate (Fig. 6(*b*)) or by reducing the temperature of the outer stream (Fig. 6(*c*)). In hydrogen operation of a gas turbine designed to run on natural gas, it seems straightforward that the cooling circuit does not change and therefore the solution of Fig. 6(*b*) cannot be adopted. Decreasing the turbine inlet temperature (Fig. 6(*c*)) appears the only feasible alternative.[2]

Effect of Pressure Ratio. An increase of the cycle pressure ratio influences the blade cooling mechanisms in three main aspects: (i) the heat-transfer coefficients enhance on both the inner and the outer blade side due to the fluid density increase; (ii) the temperature of the cooling air from compressor increases; (iii) the coolant mass flow rate increases because of coolant density increase for a given circuit geometry. About the first point, we already discussed the negative effects of an h_{OUT} enhancement. On the contrary, an enhancement of h_{COOL} has positive effects because it reduces the temperature difference between the fluid and the metal blade. Nevertheless, the simultaneous and proportional enhancement of the heat-transfer coefficient on both the blade sides due to the pressure ratio increase is not neutral because it increases the heat flux (and consequently the temperature drop) across the blade wall, bringing the maximum metal temperature beyond its admissible value (Fig. 6(*d*)). Finally, a coolant temperature increase causes the shift of all the temperature profiles as shown in Fig. 6(*e*). A temperature decrease of the flow at the turbine inlet is then required to restore the capability of the cooling circuit to meet the imposed limits (Fig. 6(*f*)) although this effect is somehow mitigated by the coolant flow increase allowed by the higher β.

4 Calculation Methodology

The performance prediction was carried out by a computer code developed by the authors' research group during several years of activities about gas turbine power plants. For a comprehensive description, see Chiesa and Macchi [10]. As a brief reminder, the main features of the code include the capability of reproducing very complex plant schemes by assembling basic modules (such as turbine, compressor, combustor, steam section, heat exchanger, etc.) and an effective prediction of the efficiency of turbomachines (gas and steam turbine stages, compressors) at their design point by means of built-in correlations. The calculation process also includes the one-dimensional design of the gas turbine stages, useful to establish all the aerodynamic, thermodynamic, and geometric characteristics of each blade row necessary for an accurate estimation of the cooling flows and the evolution of the cooled expansion. The cooling model accounts for film cooling, thermal coatings, and multipassage internal channels with enhanced heat-transfer surfaces. These effects are evaluated by means of some parameters, calibrated to reproduce the performance of advanced gas turbines. The complete procedure is reported in Ref. [10].

Even if the code is conceived for prediction of gas turbine performance at the design point only, introduction of convenient hypotheses on off-design behavior of turbomachines has made possible calculating the performance of hydrogen fueled combined cycles. We suppose that off-design operations are limited to the gas turbine because of the extreme rigidity of its design. Heat recovery steam generator and steam turbine can be easily adapted to run at the different conditions resulting from H_2 combustion, due to a more flexible manufacturing.

The ''reference'' natural gas combined cycle was calculated by using a set of assumptions reported by Table 2. The main data for the gas turbine are tuned to describe a Siemens V94.3A unit, representative of a state-of-the-art, heavy-duty, single-shaft machine [11]. The assumptions for the steam cycle calculation reproduce the present technological standards. The efficiency (38.17 and 57.57%) predicted for the gas turbine and the combined cycle, respectively, are in good agreement with declared data (38.20 and 57.30%). The same holds for power output (259.4 and 387.2 MW versus 260 and 390 MW). The assumptions of Table 2 were used for all the cases considered, apart from the gas turbine air flow, pressure ratio, and TIT, varied according to the following discussion. In fact, according to Sec. 3, different approaches can be adopted to use hydrogen as the fuel; three alternatives will be considered in the paper:

[2]The rationale underlying this strategy is that the same lifetime of a machine running on natural gas can be preserved in hydrogen operations by maintaining the same maximum metal temperature.

Table 2 Main assumptions for reference cycle calculations

Gas turbine	
	Ambient condition: 15°C, 1.0132 bar, 60% RH
	Inlet/outlet pressure losses=1/3 kPa
	Air/exhaust gas flow=633.8/644 kg/s
	Pressure ratio=17, TIT=1350°C
	Natural gas LHV=44.769 MJ/kg, preheated at 185°C
Steam cycle (three pressure levels, reheat)	
	Evaporation pressures: 166/36/4 bar
	Condensing pressure: 0.0406 bar
	Maximum steam temperature at SH/RH outlet=565°C
	ΔT at pinch point=8°C, at SH approach point=25°C
	Auxiliaries consumption=1% of heat rejected

VGV Operation. In this case no major modifications are required to the gas turbine provided that the stall margin is guaranteed. Additional high-pressure compressor stages can help to recover this margin. Calculation proceeds keeping the pressure ratio at the design value, with an inlet airflow reduced to recover the matching between compressor and turbine. Given the shape of efficiency curves on the compressor map (Fig. 3), it has been assumed to keep the compressor efficiency at the design value (the actual variation of efficiency depends on specific design criteria and cannot be generalized). The turbine maintains the original geometry (diameters, blade heights, angles) and cooling circuit characteristics but runs on a lower TIT in order to maintain the same blade metal temperature of the natural gas case. The different enthalpy drop is accommodated by varying the load on each stage at constant degree of reaction: according to Sec. 3, effects of loading on the stage efficiency have been neglected, but variations of the kinetic energy at the turbine outlet were kept into account.

Increased β. The second approach assumes that the VGV's remain full open and compressor/turbine matching is reset by increasing the operating pressure ratio. Calculation proceeds by assuming that the compressor characteristics is vertical (constant airflow). Given the stall margins available on the actual machines, it is really doubtful that this strategy can be adopted without any modification to the machine design, especially when SFT of 2300 K are demanded. Probably, one or more high-pressure compressor stages must be added [12,13] shifting upward the surge limit. In this case every compressor stage operates very close to the design point so that their efficiency can be correctly predicted by the code built-in correlations. Assumptions for turbine calculation are the same used in the previous case. TIT experiences a more significant decrease, justified by the warmer cooling flows and the higher heat-transfer coefficients related to the higher β.

Re-engineered Machine. In this case the standard machine is re-designed to comply with the larger flow rate at the turbine inlet. The compressor is virtually unchanged and the turbine blade height is increased to accommodate the larger gas flow. In this approach, turbine geometry and blade cooling flows are adapted to operate the gas turbine at the same β and TIT of the standard machine. Since the calculation is based on the very same assumptions used for the natural gas fired machine, this case represents the highest performance limit attainable with a hydrogen fueled gas turbine of the assigned technology level.

Table 3 Main results of the investigation (GT: gas turbine, SC: steam cycle)

Fuel	Nat. gas	Hydrogen, VGV operation			Hydrogen, increased β			Hydrogen, re-engineered		
Diluent	none	none	steam	nitrogen	none	steam	nitrogen	none	steam	nitrogen
Dil./fuel mass ratio	0.00	0.00	6.78	14.44	0.00	6.92	15.36	0.00	6.83	14.45
SFT, K	2545	2745	2300	2300	2746	2300	2300	2745	2300	2300
Pressure ratio	17.00	17.00	17.00	17.00	17.05	18.47	19.73	17.00	17.00	17.00
TIT, °C	1350	1339	1316	1340	1339	1305	1319	1350	1350	1350
TOT, °C	585.1	574.7	577.2	574.2	574.1	562.7	548.6	584.0	591.4	569.5
Air flow, kg/s	633.8	631.9	584.1	550.7	633.8	633.8	633.8	633.8	633.8	633.8
Gas flow, kg/s	644.0	632.7	623.5	631.1	634.6	676.5	728.2	634.7	678.1	725.9
Fuel flow, kg/s	15.02	5.58	5.67	5.52	5.59	6.02	6.11	5.66	6.31	6.31
Diluent flow, kg/s	0.00	0.00	38.44	79.67	0.00	41.71	93.78	0.00	43.10	91.21
Ma_{AX}	0.441	0.437	0.442	0.437	0.439	0.479	0.504	0.441	0.441	0.441
Cooling flows, kg/s	139.8	138.0	138.4	138.1	138.3	146.2	149.0	143.6	168.9	163.1
GT output, MW	256.8	264.5	292.0	297.6	265.1	314.4	340.5	266.3	323.8	342.7
SC net output, MW	130.4	125.6	91.5	125.3	125.7	92.1	132.4	130.1	104.9	142.1
N_2 compressor, MW	0.0	0.0	0.0	42.7	0.0	0.0	54.3	0.0	0.0	48.9
Total output, MW	387.2	390.1	383.5	380.2	390.9	406.4	418.6	396.4	428.7	436.0
LHV efficiency, %	57.57	58.32	56.38	57.46	58.32	56.25	57.15	58.35	56.60	57.57

5 Discussion of Results

The general results of the investigation are reported in Table 3, showing details of (i) the reference natural gas cycle, (ii) the three pure hydrogen fueled cases, calculated according to the strategies described in Sec. 4, (iii) the three hydrogen cases with steam dilution to achieve 2300-K SFT, (iv) the same cases repeated for nitrogen dilution. Figures 7(*a*)–(*f*) reports the most relevant parameters of the calculated cycles as a function of the SFT, i.e., by varying the hydrogen dilution rate.

5.1 Results With VGV Operations (Constant β). As discussed in Sec. 3, pure hydrogen combustion products show superior heat-transfer capabilities and a lower TIT must be selected (11 K—see Table 3). To keep the same pressure ratio, the airflow remains almost unchanged, as well as the heat input (LHV), for a number of reasons related to the variations of molecular mass, inlet temperature, nozzle cooling flow. The gas turbine power increases (3%), due to a larger turbine enthalpy drop, but the steam cycle loses some power (5 MW), due to a lower TOT (about 8 K) and gas flow. The total power slightly increases (0.7%) and a better efficiency is predicted. Note that this efficiency increase is not related to any improvement in the power cycle. It just depends on the thermodynamic properties and on the different lower heating value of the fuels (in fact, the higher heating value reduces efficiency).

When using steam dilution, we obtain (with respect to the undiluted H_2 case) (i) a lower TIT (Fig. 7(*c*), i.e., 23 K at dilution for SFT=2300 K), due to the higher heat-transfer capabilities of hot gases with larger water content, (ii) a reduced air flow (Fig. 7(*d*)), to accommodate for the added diluent flow, (iii) a relevant improvement of the gas turbine output (lower compressor power due to lower air flow, elevated turbine power due to a larger enthalpy drop), (iv) a reduced steam turbine output, due to the steam extraction. Therefore the total output does not change dramatically (Fig. 7(*a*)) but a different gas to steam turbine power ratio can be depicted (Fig. 7(*f*)). A loss of efficiency is predicted (Fig. 7(*b*): 2 percentage points at elevated dilution), because of the detrimental effects of steam/air mixing (typical of mixed gas/steam cycles, as discussed by Macchi et al. [14]).

The situation is different with nitrogen dilution, because: (i) the TIT and the TOT do not change significantly, the gas properties being very little affected by N_2 addition, (ii) the compressor air flow must be reduced because of nitrogen injection, to keep the $G_{R,T,\mathrm{IN}}$ unchanged, (iii) the gas turbine power increases due to the lower compression power, (iv) the steam turbine power remains unchanged (same TOT and gas flow), (v) the N_2 compressor power requirement is larger than the power augmentation of the gas turbine (42.7 MW versus 33 for the cases reported in Table 3), because it is less efficient than the gas turbine compressor (85.0% versus 92.4 on a polytropic basis) and brings the nitrogen (from atmospheric pressure) to a larger pressure than combustion air (1.2 times), sufficient for fuel mixing. Therefore the power output and the efficiency reduce with N_2 injection, mostly due to the above quoted effects regarding N_2 compression: the cycle thermodynamics is practically unmodified (differently from steam injection, strongly affecting the cycle with larger efficiency losses).

5.2 Results at Increased β (Constant Air Flow). When using pure hydrogen as the fuel, results are very similar to the previous case (a negligible variation of β here, of airflow there). On the contrary, significant differences arise with large dilution ratios: a larger pressure ratio is required to accommodate for the larger gas flow at the same airflow and turbine nozzle area. TIT must be reduced to keep into account for the higher coolant temperature (a consequence of the larger β), in addition to different heat-transfer properties of steam-rich mixtures. Figure 7(*e*) and Table 3 show that β must be increased to 18.5 for steam and to 19.7 for N_2 if the SFT should be kept at 2300 K, requiring the addition of at least one compressor stage. Compared to VGV operations, the TIT reduction is much larger (Fig. 7(*c*)) because of the higher coolant temperature (436°C at β=19.7 versus 406 at β=17), even if slightly larger cooling flow rates result from increased β, assuming that coolant passages are unmodified.

The lower TIT is the main reason for the lower efficiency obtained for the present cases (Fig. 7(*b*)); another reason is the increased kinetic energy loss at the turbine exhaust because of the higher flow rate through the same annulus area. The power output (Fig. 7(*a*)) is much higher than for the cases with VGV operations, because the air flow rate is no longer reduced and full advantage is taken from the added diluent flow. For the 2300-K dilution the gas turbine power rises to 314 MW (steam) and 340 MW (N_2) from an original value of 257 MW. Such a large modification will require a number of mechanical adaptations and a larger generator in addition to a modified compressor. Similar situations were encountered in the development of gas turbines for IGCC applications [12,13].

5.3 Results for the Re-engineered Machine. This is the situation showing the minimum impact on the cycle efficiency and the maximum improvement of the power output. With respect to the previous case, a larger power output is accomplished because a TIT reduction is no longer necessary, due to the same coolant temperature (unmodified pressure ratio) and to the adaptation of the cooling circuit to the different heat transfer capabilities (Table 3 shows that cooling flows vary according to the turbine flow, determining the blade surface). On another side, keeping the design pressure ratio allows for the optimum cycle configurations:

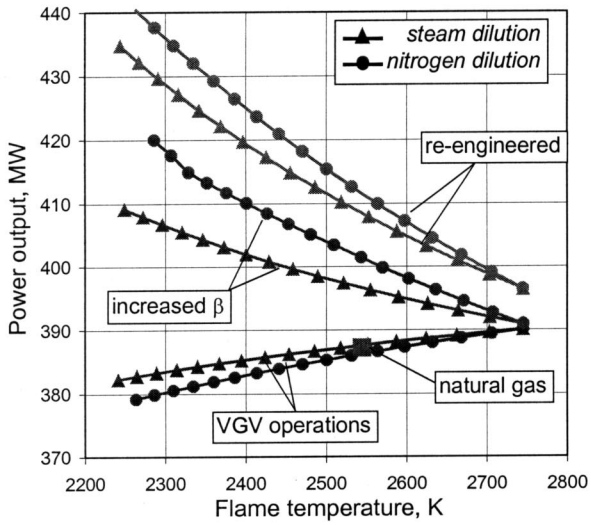

Fig.7a: Combined cycle net power output

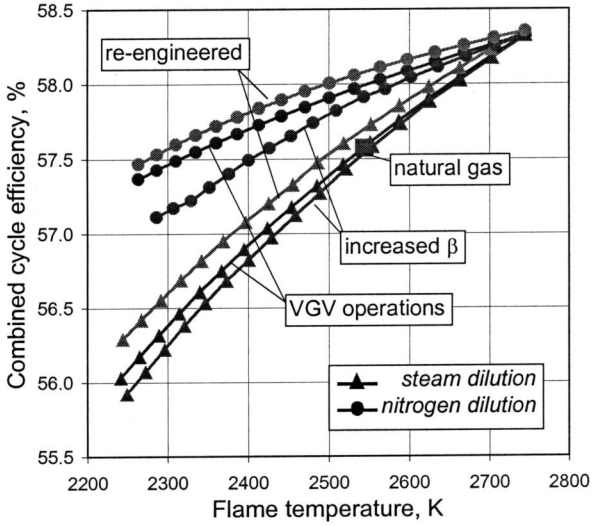

Fig.7b: Combined cycle net efficiency

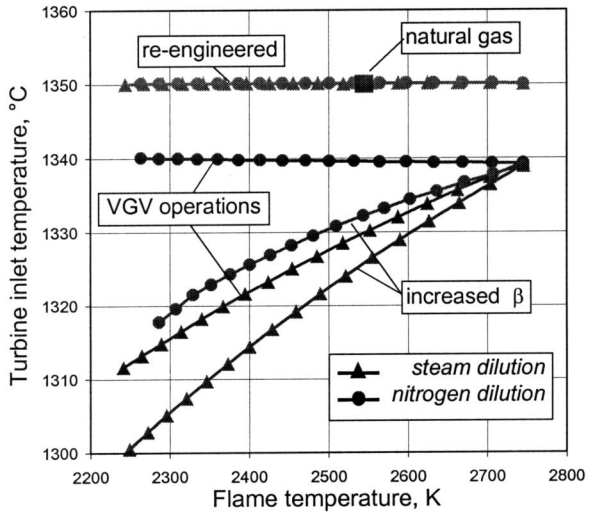

Fig.7c: Total temperature at first rotor inlet (TIT)

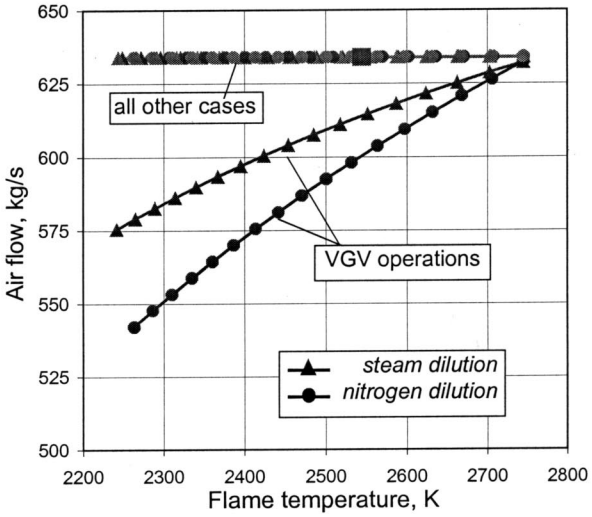

Fig.7d: Air flow at compressor inlet

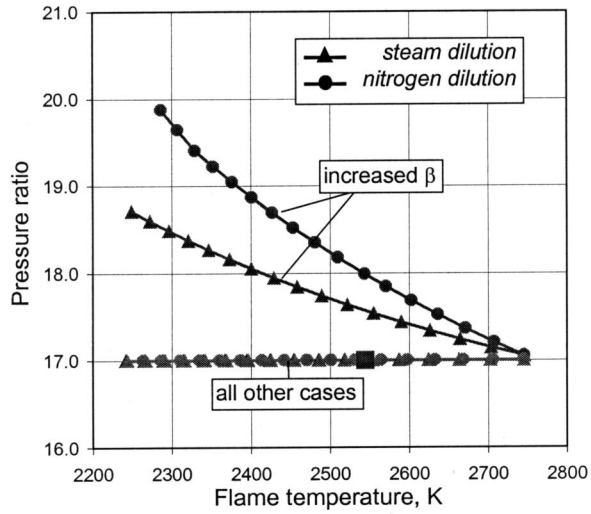

Fig.7e: Gas turbine pressure ratio

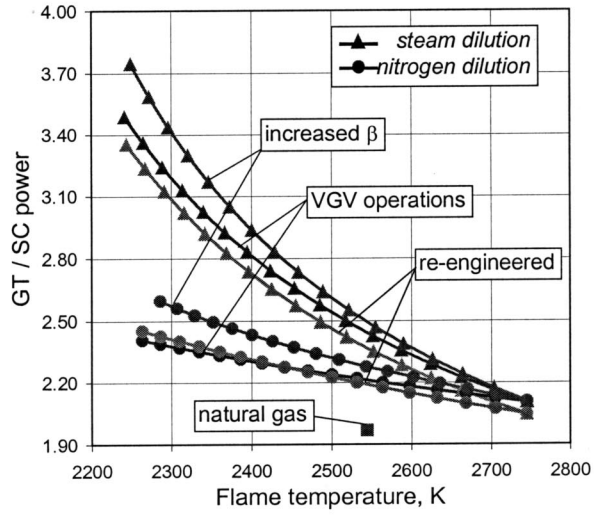

Fig.7f: Gas turbine / steam cycle power output

Fig. 7 (*a*) Combined cycle net power output, (*b*) combined cycle net efficiency, (*c*) total temperature at first rotor inlet (TIT), (*d*) air flow at compressor inlet, (*e*) gas turbine pressure ratio, (*f*) gas turbine/steam cycle power output

the efficiency decays for the same reasons described for VGV operations (steam mixing or higher pressure of compressed N_2, depending on the diluent).

6 Conclusions

The simulations carried out in this work allow a positive answer to the issues related to hydrogen combustion in modern gas turbines. However, a SFT abatement to about 2300 K seems necessary to comply with NO_x emission limits without incurring excessive operating costs of the end-of-pipe de-nitrification systems. This is possible without dramatic performance losses by means of a massive fuel dilution with steam or nitrogen (the latter providing minor losses of efficiency). Different strategies have been envisaged to operate the gas turbine in presence of dilution. Looking at the VGV operated solution (which appears the most likely for the first realizations) the efficiency loss is limited to 0.9 points for nitrogen dilution and 1.9 for steam dilution. Equally small is the influence on the combined cycle power output provided that the gas turbine power output can be increased (by about 10%) in consequence of the compressor airflow reduction. The other solutions here investigated (increased pressure ratio and re-engineered machine) are not particularly attractive in terms of efficiency but provide a much larger power output, an opportunity to reduce the specific costs provided that engineering costs are divided upon a sufficient number of units. It must also be noticed that VGV operations reduce the part-load capabilities of the machine, but make the gas turbine rather insensitive to elevated ambient temperatures (the ''natural'' power loss can be compensated by re-opening the VGV's). As a final consideration on system costs, it can be said that steam dilution allows for reduced capital cost compared to nitrogen, even if providing lower efficiency. In fact, a smaller steam turbine and condenser can be adopted, while the N_2 dilution requires a bulky and expensive additional compressor.

Acknowledgment

The work has been performed within the research on the Italian Electrical System ''Ricerca di Sistema'' Ministerial Decrees of January 26, 2000, and April 17, 2001.

Nomenclature and Acronyms

c_P = specific heat at constant pressure, J/kg K
D = reference blade dimension (chord), m
G = mass flow rate, kg/s
G_R = nondimensional mass flow rate ($G\sqrt{RT}/p$)
h = heat transfer coefficient, W/m^2 K
k = thermal conductivity, W/m K
LHV = lower heating value, MJ/kg
Ma_{AX} = axial Mach number at turbine outlet
p = pressure, Pa
SFT = stoichiometric flame temperature, K
T = temperature, °C or K
TIT = first rotor total inlet temperature, °C
TOT = turbine outlet temperature, °C
v = flow velocity, m/s
VGV = variable guide vanes
β = compressor pressure ratio
Δh = enthalpy drop, J/kg
γ = specific heat ratio
η = efficiency
μ = dynamic viscosity, Pa s
ρ = density of the gas stream, kg/m^3

Subscripts

C = relative to the compressor
COOL = coolant side of the blade wall
FIN = final condition
IN = inlet condition
IS = isentropic
OUT = outer side of the blade wall
T = relative to the turbine

References

[1] Kreutz, T. G. et al., 2002, ''Production of Hydrogen and Electricity From Coal With CO_2 Capture,'' *Proc. of the Sixth International Conference on "Greenhouse Gas Control Technologies"*, Kyoto, Japan.
[2] Lozza, G., and Chiesa, P., 2002, ''CO_2 Sequestration Techniques for IGCC and Natural Gas Power Plants: A Comparative Estimation of Their Thermodynamic and Economic Performance,'' *Proc. of the Int'l Conference on Clean Coal Technologies (CCT2002)*, Chia Laguna, Italy.
[3] Drell, I. L., and Belles, F. E., 1957, ''Survey of Hydrogen Combustion Properties,'' NACA Report 1383, Research Memorandum E57D24.
[4] Huth, H., Heilos, A., Gaio, G., and Karg, J., ''Operation Experiences of Siemens IGCC Gas Turbines Using Gasification Products From Coal and Refinery Residues,'' ASME paper 2000-GT-0026.
[5] Todd, D. M., and Battista, R. A., 2000, ''Demonstrated Applicability of Hydrogen Fuel for Gas Turbines,'' *Proc. of the IchemE Gasification 4 Conference*, Noordwijk, The Netherlands.
[6] Major, B., and Powers, B., 1999, ''Cost Analysis of NO_x Control Alternatives for Stationary Gas Turbines,'' Contract DE-Fc02-97CHIO877.
[7] Lozza, G., and Chiesa, P., 2002, ''Natural Gas Decarbonization to Reduce CO2 Emission From Combined Cycles. Part A: Partial Oxidation–Part B: Steam-Methane Reforming,'' ASME J. Eng. Gas Turbines Power, **124**(1), pp. 82–95.
[8] Andersen, T., Kvamsdal, H. M., and Bolland, O., 2000, ''Gas Turbine CC With CO_2 Capture Using Auto-Thermal Reforming of Natural Gas,'' ASME paper 2000-GT-0162.
[9] Louis, J. F., 1977, ''Systematic Studies of Heat Transfer and Film Cooling Effectiveness,'' in AGARD CP-229, Neuilly sur Seine, France.
[10] Chiesa, P., and Macchi, E., 2002, ''A Thermodynamic Analysis of Different Options to Break 60% Electric Efficiency in Combined Cycle Power Plants,'' ASME paper GT-2002-30663.
[11] Siemens Power Generation website: www.pg.siemens.com
[12] Heilos, A., Huth, M., Bonzani, F., and Pollarollo, G., 1998, ''Combustion of Refinery Residual Gas With a Siemens V94.2K Burner,'' Power Gen Europe, Milan, Italy.
[13] Huth, M., Vortmeyer, N., Schetter, B., and Karg, J., 1997, ''Gas Turbine Experience and Design for Syngas Operation,'' Gasification Technology in Practice, Institution of Chemical Engineers, Milan, Italy.
[14] Macchi, E., Consonni, S., Lozza, G., and Chiesa, P., 1995, ''An Assessment of the Thermodynamic Performance of Mixed Gas-Steam Cycles. Part A: Intercooled and Steam-Injected Cycles–Part B: Water-Injected and HAT Cycles,'' ASME J. Eng. Gas Turbines Power, **117**(3), pp. 489–498.

Advanced Zero Emissions Gas Turbine Power Plant

Timothy Griffin
ALSTOM Power Technology Center,
CH-5405 Dättwil/Baden, Switzerland

Sven Gunnar Sundkvist
Demag Delaval Industrial Turbomachinery AB,
SE-612 83 Finspong, Sweden

Knut Åsen

Tor Bruun
Norsk Hydro Oil & Energy Research Center,
N-3960 Porsgrunn, Norway

The AZEP "advanced zero emissions power plant" project addresses the development of a novel "zero emissions," gas turbine-based, power generation process to reduce local and global CO_2 emissions in the most cost-effective way. Process calculations indicate that the AZEP concept will result only in a loss of about 4% points in efficiency including the pressurization of CO_2 to 100 bar, as compared to approximately 10% loss using conventional tail-end CO_2 capture methods. Additionally, the concept allows the use of air-based gas turbine equipment and, thus, eliminates the need for expensive development of new turbomachinery. The key to achieving these targets is the development of an integrated MCM-reactor in which (a) O_2 is separated from air by use of a mixed-conductive membrane (MCM), (b) combustion of natural gas occurs in an N_2-free environment, and (c) the heat of combustion is transferred to the oxygen-depleted air by a high temperature heat exchanger. This MCM-reactor replaces the combustion chamber in a standard gas turbine power plant. The cost of removing CO_2 from the combustion exhaust gas is significantly reduced, since this contains only CO_2 and water vapor. The initial project phase is focused on the research and development of the major components of the MCM-reactor (air separation membrane, combustor, and high temperature heat exchanger), the combination of these components into an integrated reactor, and subsequent scale-up for future integration in a gas turbine. Within the AZEP process combustion is carried out in a nearly stoichiometric natural gas/O_2 mixture heavily diluted in CO_2 and water vapor. The influence of this high exhaust gas dilution on the stability of natural gas combustion has been investigated, using lean-premix combustion technologies. Experiments have been performed both at atmospheric and high pressures (up to 15 bar), simulating the conditions found in the AZEP process. Preliminary tests have been performed on MCM modules under simulated gas turbine conditions. Additionally, preliminary reactor designs, incorporating MCM, heat exchanger, and combustor, have been made, based on the results of initial component testing. Techno-economic process calculations have been performed indicating the advantages of the AZEP process as compared to other proposed CO_2-free gas turbine processes. [DOI: 10.1115/1.1806837]

The AZEP Concept

The AZEP concept (see Ref. [1]) is shown in Fig. 1. The combustor in an ordinary gas turbine is here replaced by the MCM-reactor, which includes a combustor, an air preheater, a membrane section (mixed conducting membrane, MCM), and a high temperature heat exchanger section (see [2]). As shown in the figure, air is compressed in a conventional gas turbine compressor. Typically air can be extracted from the compressor at 20 bar and 450 °C. A major part, about 90%, of the extracted compressed air is preheated to about 900–1100 °C in the lower section of the MCM-reactor. The reason for this high preheating temperature is to reduce the membrane area.

The transport of oxygen through the membrane is increasing with increasing temperature. However, in order to avoid significant degradation of the membrane there is also an upper temperature limit, which is material dependent. In the membrane section 40%–50% of the oxygen in the air stream is transported through the dense MCM.

The membrane is made from materials with both ionic and electronic conductivity (see Fig. 2). An oxygen partial pressure difference causes oxygen ions to be transported through the membrane by means of a diffusive process. Simultaneously the electrons flow from the permeate side back to the retentate side of the membrane.

Oxygen is picked up by means of a circulating sweep gas containing mainly CO_2 and H_2O (see [3]). The concentration of oxygen in the combustor inlet is about 10%. The natural gas is typically provided at pressures of 25 to 35 bar and the temperature in the combustor may be over 1200 °C. About 90% of the hot combusted gas then enters the high temperature heat exchanger section in the MCM-reactor in countercurrent flow to the air stream. The air stream then can be heated to above 1200 °C. About 10% of the combusted gas is bled off and heat is recovered by heating a minor part (10%) of the compressed air.

Hot compressed air then enters the turbine to generate electrical power. Waste heat in both the oxygen-depleted air stream and the CO_2 containing bleed gas stream is recovered by generating steam at different pressure levels. The steam is utilized in steam turbines for power generation. The CO_2 containing bleed gas is further cooled to condense water. CO_2 is recovered at about 20 bar and is then compressed to final pressure. Main features of the AZEP process are

- efficiency reduction of about 4% points after CO_2 removal,
- 100% capture of CO_2,
- no NOx emissions, and
- predicted 30%–50% CO_2 removal cost reduction compared with conventional tail-end CO_2 capture methods (see [4]).

The AZEP Project

A joint feasibility study on the AZEP concept was first performed by Norsk Hydro, Norway, the original inventor of the concept, and the gas turbine manufacturer ABB ALSTOM Power Sweden AB (today Demag Delaval Industrial Turbomachinery AB). As this study showed a high potential of the technology, not

Contributed by the International Gas Turbine Institute (IGTI) of THE AMERICAN SOCIETY OF MECHANICAL ENGINEERS for publication in the ASME JOURNAL OF ENGINEERING FOR GAS TURBINES AND POWER. Paper presented at the International Gas Turbine and Aeroengine Congress and Exhibition, Atlanta, GA, June 16–19, 2003, Paper No. 2003-GT-38426. Manuscript received by IGTI, October 2002, final revision, March 2003. Associate Editor: H. R. Simmons.

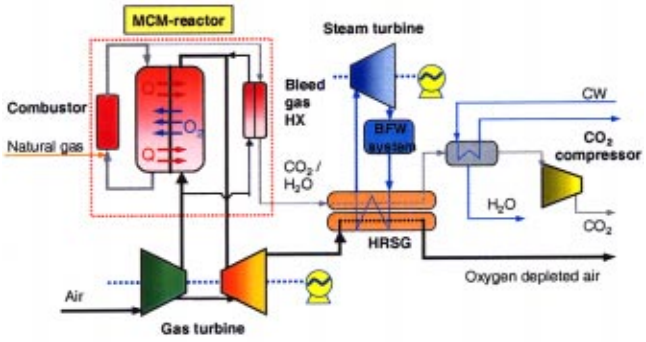

Fig. 1 AZEP process flow sheet

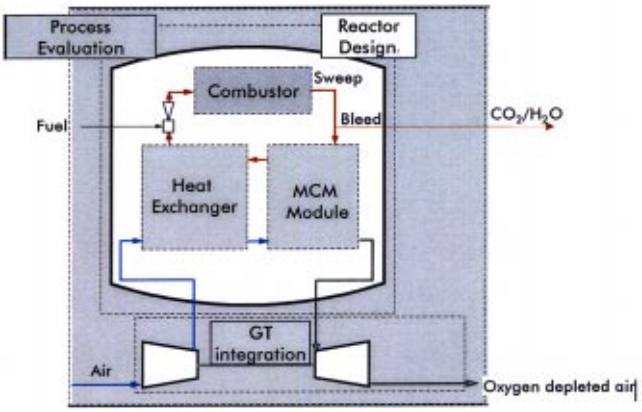

Fig. 3 AZEP project work packages

only on performance like gas turbine efficiency and CO_2 capture, but also indicated a much lower CO_2 avoidance cost compared to alternative technologies (see [5]), it was decided to develop this technology in a consortium by inviting other partners with complementing skills.

The project is characterized by a vertically integrated industrial involvement supplemented by well-established academic partners essential for this novel and important development. Ten partners from six European countries (see website www.azep.org) represent a combination of expertise covering all necessary skills (development of materials, ceramic manufacturing methods, high temperature heat exchanger, combustion technology for AZEP gas mixtures, gas turbine and power plant technology, and techno-economic and environmental analysis).

A modular approach has been adopted for the work such that know-how is developed within individual work packages, which deliver components, designs, and process data to the project (see Fig. 3). The on-going first three-year phase (started December 2001) primarily focuses on research and development of the MCM-reactor upon its constituent units, the combination of these components into an integrated reactor, and its subsequent scale-up for future integration in a gas turbine. After the components have been identified and manufactured, they will be integrated into a complete MCM-reactor design, and subsequently tested at simulated gas turbine conditions to verify overall functionality.

In order to develop the optimum AZEP with an integrated MCM-reactor, process simulation and economic evaluation is being continuously performed. The resulting data will be used to define benchmarks (e.g., cost of electricity, net present value). Market potential for AZEP plants will be identified considering the growing CO_2 market for oil and gas recovery as well as emerging financial measures to curb CO_2 emissions, including CO_2 trading.

Project cost for phase 1 is M€ 9.3 with funding by EC (M€ 3.4) and the Swiss government (M€ 1.5).

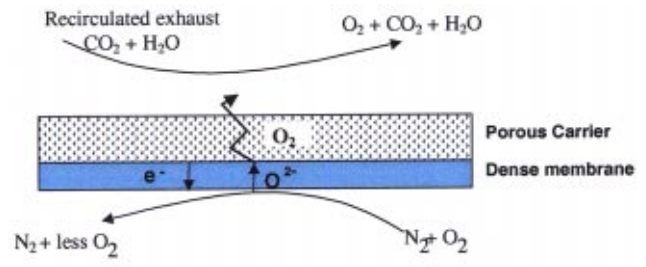

Fig. 2 Schematic drawing of MCM membrane, with oxygen swept from the permeate side of the membrane by recirculated exhaust gas

Technical Challenges

The technical challenges within the project are associated with the following areas:

- combustion of natural gas in highly diluted exhaust gas streams at low temperature (<1300 °C) and with little excess oxygen present,
- the air separation membrane and its stable operation within the gas turbine system (target >30,000 h),
- a heat exchanger stable at high temperatures (>1200 °C) and in the presence of steam and carbon dioxide,
- high temperature (>1100 °C) sealing between ceramic elements,
- achieving highest surface to volume ratios within ceramic components for the required oxygen and heat transport rates,
- integration of the MCM-reactor in the gas turbine system, and
- start-up philosophy and gas turbine trips.

The project is focusing its main efforts on addressing these challenges, and the present paper will discuss progress in some of these areas.

The MCM Reactor

The MCM-reactor is comprised of three main integrated process units: oxygen transporting membrane (MCM), low and high temperature heat exchangers, and a combustion section (see Figs. 3 and 4). Compressed low temperature air (at 20 bar, 450°C) from the gas turbine compressor enters the reactor through a transition duct leading to the inlet openings of the low temperature heat exchanger. This heat exchanger increases the temperature level above 800 °C, so that air may enter into the MCM section and ''give off'' oxygen to the recirculated exhaust gas stream. From the MCM section the air enters the high temperature heat exchanger where its temperature is raised to a value close to the hot

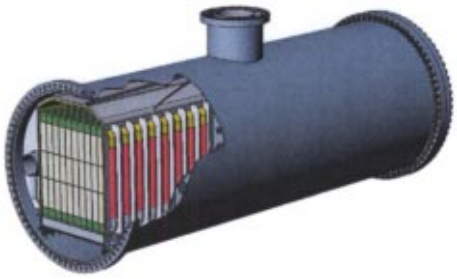

Fig. 4 MCM reactor showing the ceramic monolithic structure

exhaust gas temperature from the combustor (>1200 °C). From the high temperature section the now hot and oxygen-depleted air is led out of the reactor to the power-generating turbine.

Both the MCM and the heat exchangers are based on ceramic monolith structures (honeycombs) with high surface-to-volume ratio and low pressure drop. Exhaust gas from the combustion chamber flows counter-currently to the airflow, heating up air and picking up and transporting oxygen to the combustion section. The oxygen is transported through the ceramic walls of the MCM monolith structure. Materials are identified for the MCM and heat exchanger and have been demonstrated at laboratory scale and AZEP conditions.

Modeling has been performed to determine the optimal configuration of these process units, and to determine their boundary conditions. The pressures and mass flows of air and oxygen to the combustion cycle are set by the overall turbine process. By utilizing ceramic monolith structures for both heat transport and oxygen transport these operations can be performed in an integrated monolith stack.

A monolith structure with given channel width and wall thickness has a fixed specific surface to volume ratio (m^2/m^3) available for heat and mass (oxygen) transfer. The required total volume of the monolith structures can then be calculated. In principle the ratio between length and width can be chosen freely. However, in order to maintain laminar flow and avoid excessive pressure losses, the free flow area must be above a certain value.

In current design the total height of the monolithic stack is ca. 2 m, and the design is based on standard sized monoliths (with side length of ca. 15×15 cm). Internal channels sizes are in the range of 1–2 mm, giving surface to volume ratios in the range 500–1000 m^2/m^3. This unit or standard sized system has a thermal load between 50 and 100 kW (corresponding to an energy density of 1–2 MW/m^3). Based on such a modular system any size of capacity can be performed by simply increasing the number of standard ceramic monolith stacks. Thus the heat and oxygen transfer capacity is adjusted to fit the gas turbine system capacity by simply adjusting the number of standard sized monolithic stacks. This acts to increase the length of reactor (see [6]).

For comparison also plate and pipe solutions that have a similarity with SOFC design solutions have been evaluated together with honeycomb structures. Our membrane/heat exchanger structures differ from SOFC solutions in that electric circuit connectors are not necessary. The reason is that the membrane material transfers both oxygen ions and electrons internally and therefore is electrically neutral. This makes it possible to use ceramic monolithic structures. As honeycomb structures have both low pressure drop and high surface-to-volume ratios, the chosen design is based on monolithic structures both for the MCM membrane and the heat exchangers.

Combustion Methodology

The working fluid in the AZEP process consists of extremely diluted fuel/oxidant mixtures (e.g., 5% CH_4, 10% O_2, 28% CO_2, 57% H_2O, by volume). Since the exhaust gas is formed by stoichiometric methane combustion the molar ratio of H_2O and CO_2 is always 2:1. The reactivity of such mixtures in existing lean, premix burners and catalytic combustors is lower than those of standard CH_4/air mixtures at similar temperatures in the following ways:

- Ignition delay times are nearly an order of magnitude higher (based on CHEMKIN calculations).
- Residence times for complete burn out of CO and UHCs are higher.
- Flame speeds are lower.

On the positive side, there is very limited nitrogen within the gas (associated with the natural gas), and thus NO*x* formation is not an issue.

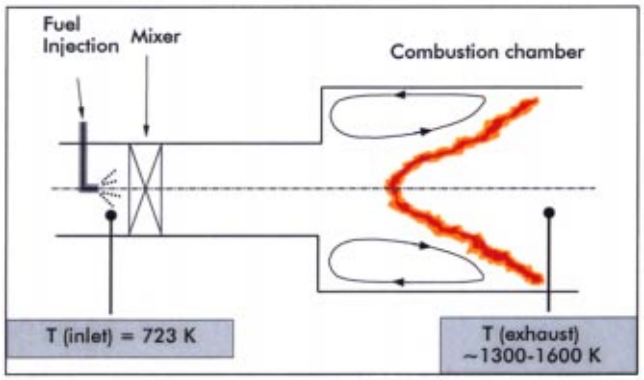

Fig. 5 Backward-facing step combustion stabilization

The situation is exacerbated by the fact that the overall temperature of the combustion products must be relatively low (e.g., 1200 °C). The low temperatures are dictated by the fact that the membrane materials are limited in their thermal stability. This signifies that current combustion methods may have to be considerably modified/developed.

Currently available burning methods are swirl-stabilized, diffusion burners, lean premixed burners, and catalytic burners. However, these on their own are not optimized for the AZEP processes. Traditional, vortex stabilized combustion methods, utilizing turbulent recirculation zones for flame stability may not be relevant to this process due to the low pressure drops and low velocities present.

In the present paper initial results on the combustion of AZEP mixtures at high-pressure conditions in a lab-scale combustion chamber will be discussed. (Previous results on AZEP combustion at atmospheric pressure may be found in [7]). In this experiment the combustion was stabilized by vortex regions formed after a sudden expansion of the inlet gases as shown in Fig. 5. The backward-facing step expansion, in a cylindrical configuration, was from 25 to 75 mm diameter.

Experiments were performed at a given inlet temperature and velocity. The gas was ignited and the fuel concentration was gradually reduced until the flame became unstable and the CO emissions rapidly increased. When the flame started to pulsate and unburned hydrocarbons started to be emitted the ''lean blow out'' (LBO) limit was recorded. The results of the testing are given in Fig. 6 in terms of the lean blow out limit as a function of the combustion pressure. Experiments were performed for both air and an AZEP mixture (O_2+exhaust gas).

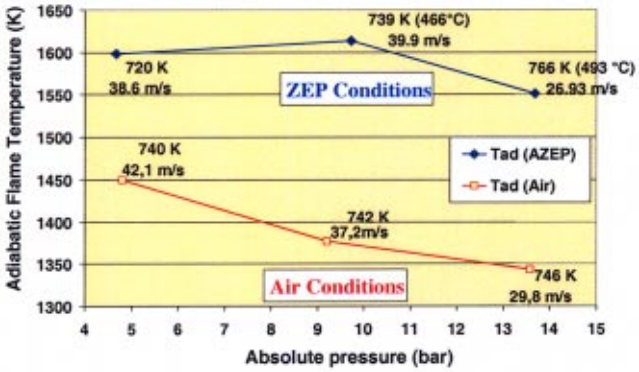

Fig. 6 Lean blowout limit of combustion for methane in both an air and AZEP (O_2+exhaust gas environment. (The inlet temperature and velocity of each data point are indicated.)

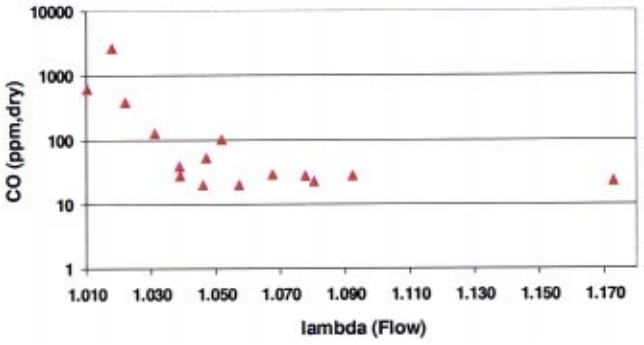

Fig. 7 CO emissions as a function of the excess oxidant ratio of combustion. The data were taken at flame temperatures between 1700 and 1800 K.

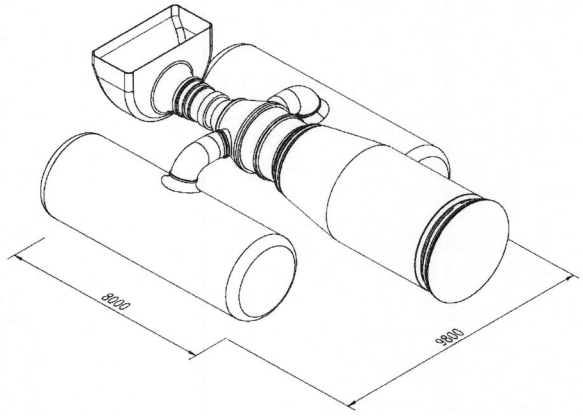

Fig. 8 Gas turbine GTX100 in the middle modified for AZEP with one MCM reactor on each side

As expected, the high levels of CO_2 and H_2O inhibit combustion, leading to an increase in the LBO of more than 150 K, as compared to the results obtained with air. Although the LBO decreases with increasing pressure, it is still at 1550 K (1277 °C) at a pressure of 14 bar, above the goal temperature of 1200 °C.

A further challenge associated with AZEP combustion is related to the complete burnout of the combustion intermediate CO. Figure 7 shows the CO emissions as a function of the lambda value (excess oxidant ratio of combustion). As seen, even at high flame temperatures, where flame stability is not an issue, an excess amount of oxygen is necessary to ensure that the CO will be fully converted to carbon dioxide. This is undesired since it would add to the cost and size of the required membranes.

Another option for flame stabilization is catalytic combustion, proposed to have advantages to homogeneous gas phase combustion for standard gas turbine systems with air as the oxidant. With catalytic combustion it is possible to obtain complete and stable combustion at much lower temperatures, allowing extremely lean fuel combustion outside the flammability limits of homogeneous reactions. More detailed description of the basics of catalytic combustion can be found in [8–12]. In the next phase of the project various catalytic combustion concepts will be evaluated regarding their application in the current AZEP process.

Integration in the Gas Turbine System

The AZEP gas turbine set and its auxiliary systems consist mainly of standard equipment with one exception: as mentioned the conventional combustion chamber in a standard gas turbine will be replaced by the MCM-reactor. Necessary turbine modifications are therefore essentially concentrated to the integration of the MCM-reactor to the gas turbine system, which substantially reduces technical and commercial risks.

Gas Turbine Selection. Several criteria have been put up for the selection of the gas turbine in AZEP:

- It must be a high performance, modern gas turbine with high turbine inlet temperature and potential for higher pressure ratio that can also form the basis for larger machine developments in the future.
- Its design should have a potential for retrofitting existing gas turbine systems with AZEP gas turbine systems in the future.
- Space must be available for a transition duct to the MCM-reactor.
- The start-up procedure for an AZEP gas turbine system must not be too complicated.

After evaluation of three alternative gas turbines the 43 MW (simple cycle) one-shaft gas turbine GTX100 has been selected as the best alternative for a future AZEP gas turbine system. It meets the above-mentioned criteria and it also has the following properties:

- The GTX100 is less complicated and safer to redesign than the other evaluated alternatives.
- A single shaft turbine facilitates the start-up of the AZEP gas turbine system.
- The gas turbine combustor has a double wall for convection cooling, which is the method that will be used in the AZEP-turbine, and this makes it easier to integrate the MCM-reactor to the gas turbine.

Transition Ducts Between Gas Turbine and MCM-Reactor. Due to the size of the MCM membrane and the heat transfer areas preliminary design has been made for two transition ducts between the gas turbine and two parallel MCM-reactors (see Fig. 8). The chosen principle for the transition duct is to use coaxial ducts with hot gas (depleted air) from the reactor in the inner duct cooled by the air from the compressor in the annulus between the ducts.

A non-insulated inner duct for the hot air (ca 1250 °C) air is proposed, which will allow a fairly simple design of the transition duct. In combination with thermal coating on the inside of the hot duct the maximum temperature of the wall material will be around 800 °C. With chosen design and a short length of the transition duct the temperature loss on the hot side can be kept around 16 °C and the heat expansion can be kept low.

Start-Up Philosophy. At start-up the ceramic core structure is heated up from ambient condition with an external heat source in such a way that temperature gradients are within acceptable limits. The gas turbine is speeded up from stand still with a starting motor. This must be done so that the outlet temperature of the gas turbine compressor matches the cool side of the sweep gas. The pressure difference between compressor outlet and sweep gas side must be controlled but is not critical since the membrane walls can withstand considerable pressure differences. When the temperature in the membrane core is sufficient to start the oxygen transport, fuel is fed to the combustion zone. Heat from the combustion is then transferred to the oxygen depleted air and the turbine inlet temperature increases. The starting motor power can then be reduced. Temperature and oxygen transport to the reactor core is thereafter increased until normal running conditions are achieved.

To facilitate start-up a by-pass duct will connect the cold air side with the turbine inlet. With a valve on the by-pass duct and a valve on the cold air transition duct to the reactor it is possible to gradually control the gas turbine almost as fast as burners at the ordinary gas turbine are controlled (see [13]). With this strategy

the outlet of the MCM-reactor will be kept at constant high temperature after the initial heating of the core irrespective of the load. The inlet temperature of the core will follow the outlet temperature of the compressor.

Transient calculations have been made to simulate the reactor temperature propagation at start-up. These calculations indicate a start-up time comparable with an ordinary GTCC start-up time. The challenge is here to avoid overheating and inhomogeneous temperature distributions in the ceramic structures in the MCM-reactor.

Gas Turbine Trips. The proposed valve arrangement will also make it possible to bypass the reactor at gas turbine trips. However, the pressure cannot be allowed to change too rapidly for reasons related to the mechanical integrity of the MCM-reactor. During shorter stops the temperature profile of the core can be maintained with the help of a small airflow through the core and a corresponding small amount of external firing. Controlling the mixing of heated and unheated air will then control the temperature at the turbine inlet.

Summary

The paper describes AZEP, a membrane based concept, to sequestrate CO_2 from gas turbine-based power generation processes. Results of the on-going EU funded development project are presented. The MCM-reactor, which replaces the combustion chamber in an ordinary gas turbine, is described together with its integrated components: the oxygen selective MCM membrane and the heat exchangers (all built on a monolithic ceramic structure) and the combustor. Alternative combustion methods for the extremely diluted fuel/oxidant mixtures in AZEP (e.g., 5% CH_4, 10% O_2, 28% CO_2, 57% H_2O) are investigated and results of lean blow out (LBO) limit and CO emissions are shown. Integration of the MCM-reactor (via transition ducts) to the selected gas turbine GTX100 for AZEP is described and start-up philosophy is given for the AZEP gas turbine system.

Acknowledgments

The AZEP project is partly funded by the European Commission in FP5, Contract No. ENK5-CT-2001-00514, and the Swiss Government.

References

[1] Linder, U., Eriksen, E. H., and Åsen, K. I., 2000, ''A Method for Operating a Combustion Plant and a Combustion Plant,'' SE Patent Application 0002037.

[2] Bruun, T., Werswick, B., Grönstad, L., Kristiansen, K., and Linder, U., 2000, ''A Device and a Method for Operating Said Device,'' NO Patent Application 20006690.

[3] Åsen, K. I., and Julsrud, S., 1997, ''Method for Performing Catalytic or Non-Catalytic Processes, Wherein Oxygen is One of the Reactants,'' NO Patent Application 19972630.

[4] Bill, A., Span, R., Griffin, T., Kelsall, G., and Sundkvist, S. G., 2001, ''Technology Options for Zero Emissions' Gas Turbine Power Generation,'' *International Conference Power Generation and Sustainable Development*, Liège, Belgium, 8–9 October.

[5] Hellberg, A. et al., 1999, ''Zero Emission Power Plant—Process Selection,'' Internal Report ABB ALSTOM Power, RT T10 57/99, July.

[6] Bruun, T., Werswick, B., Grönstad, L., and Kristiansen, K., 2001, ''Method and Apparatus for Feeding and Output of Two Gases to a Monolithic Structure,'' NO Patent Application 20015134.

[7] Reinke, M., Carroni, R., Winkler, D., and Griffin, T., 2002, ''Experimental Investigation of Natural Gas Combustion in Oxygen/Exhaust Gas Mixtures for Zero Emissions Power Generation,'' *Proceedings of 6th International Conference on Technologies and Combustion for a Clean Environment*, Porto, July 2001. (to appear in *International Journal on Environmental Combustion Technologies*, 2002).

[8] Kesselring, J. P., 1986, ''Catalytic Combustion,'' in *Advanced Combustion Methods*, edited by F. J. Weinberg, Academic, London, pp. 237–275.

[9] Trimm, D. L., 1985, ''Catalytic Combustion (Review),'' Appl. Catal., **7**, pp. 249–282.

[10] Pfefferle, L. D., and Pfefferle, W. C., 1987, ''Catalysis in Combustion,'' Catal. Rev. - Sci. Eng., **29**(2&3), pp. 219–267.

[11] Griffin, T., and Scherer, V., 1995, ''Katalytisch unterstützte Verbrennung in Gasturbinen: Potentiale und Grenzen,'' VGB Kraftwerkstechnik, **75**, Heft 5, pp. 421–426.

[12] Appel, C., Mantzaras, I., Scharen, R., Bombach, R., and Inauen, A., 2001, ''Catalytic Combustion of H_2/Air Mixtures Over Platinum,'' *accepted Sixth International Conference on Technologies and Combustion for a Clean Environment*, 9–12 July, Porto, Portugal.

[13] Hamrin, S., 2003, ''Styrning av Gasturbin Med MCM-Reaktor,'' SE Patent Application 0300131-0.

Performance Comparison of Internal Reforming Against External Reforming in a Solid Oxide Fuel Cell, Gas Turbine Hybrid System

Eric A. Liese
e-mail: eric.liese@netl.doe.gov

Randall S. Gemmen

National Energy Technology Laboratory,
3610 Collins Ferry Road,
Morgantown, WV 26507

Solid Oxide Fuel Cell (SOFC) developers are presently considering both internal and external reforming fuel cell designs. Generally, the endothermic reforming reaction and excess air through the cathode provide the cooling needed to remove waste heat from the fuel cell. Current information suggests that external reforming fuel cells will require a flow rate twice the amount necessary for internal reforming fuel cells. The increased airflow could negatively impact system performance. This paper compares the performance among various external reforming hybrid configurations and an internal reforming hybrid configuration. A system configuration that uses the reformer to cool a cathode recycle stream is introduced, and a system that uses interstage external reforming is proposed. Results show that the thermodynamic performance of these proposed concepts are an improvement over a base-concept external approach, and can be better than an internal reforming hybrid system, depending on the fuel cell cooling requirements.
[DOI: 10.1115/1.1788689]

Introduction

The National Energy Technology Laboratory (NETL) Strategic Center for Natural Gas (SCNG) is supporting the development of several solid oxide fuel cell based technologies. The Solid State Energy Conversion Alliance (SECA) was initiated in the fall of 1999 to encourage the development of environmentally friendly solid-oxide fuel cell modules for use with commonly available fossil fuels at low cost. The Alliance is coordinated by the U.S. Department of Energy's National Energy Technology Laboratory and Pacific Northwest National Laboratory. The basic building block of the proposed future fuel cell will be a compact and lightweight, 5-kW solid state module that can be efficiently mass-produced. The modularity of the system will remove a major contributor to current high fuel cell costs, namely the present need to separately design and custom-build fuel cell stacks for each particular application. In addition, the proposed solid state design will leverage numerous recent advances, such as production of thin-film solid electrolyte materials and precise, automated manufacturing technologies developed largely in the semiconductor industry. Reduced manufacturing costs, when combined with the traditional high efficiency and outstanding environmental performance of the fuel cell, will make the SECA module a prime option for a wide range of electric power needs—including those satisfied by hybrid fuel cell and gas turbine systems.

NETL/SCNG is also supporting the development of Fuel Cell/Gas Turbine (FC/GT) ''hybrids.'' These systems will increase electrical efficiencies by 10 to 15% compared to standalone fuel cells (10% for smaller systems). A 300-kW hybrid system with SECA fuel cells might have 40, 5 kW fuel cells with a 100 kW gas turbine. Plans for most SECA stack designs have reforming external to the fuel cell, at least initially. This design approach favors serviceability and does not link the fuel cell stack lifetime to the reformer. Also, a fuel cell has more general use if internal reforming is not used, since employing internal reforming will force an additional constraint—namely the operation on the specific fuel for which the internal reformer was designed. Much work must still be accomplished to understand exactly what opportunities exist for developing commercially viable systems based on the integration of these systems.

Hybrid Arrangements. To date, most of the literature discussion on SOFC hybrid design and performance has assumed an indirect-internal reforming fuel cell (IIR-SOFC). Two recent papers that discuss IIR-SOFC hybrid systems are Nishida et al. [1] and Kimijima and Kasagi [2]. Costamagna, Magistri, and Massardo [3] and Campanari [4] are papers based on the IIR-SOFC design of Siemens-Westinghouse Power Company (SWPC).

The lack of studies for SOFC hybrids using external reforming (ER-SOFC) could be for several reasons. Recently SWPC completed demonstration of a 250–300-kW IIR-SOFC hybrid system. As a result, this technology has had more exposure and has been given more attention than other technologies. Another reason could be that the ER-SOFC hybrid (a simple concept is shown in Fig. 2) appears less efficient, and thus is less likely to be promoted. As yet, no ER-SOFC hybrid designs have been proposed in the literature. As a result, the base-concept design in Fig. 2 was generated for this work. This paper will then show two more ER-SOFC hybrid system concepts, one employing cathode recycle with a reformer in the recycle loop and the other a staged fuel cell connected by a reformer. These will be compared with the base-concept ER-SOFC hybrid and the typical IIR-SOFC hybrid shown in the literature.

IIR-SOFC Versus ER-SOFC

In an IIR-SOFC, most of the fuel reforming occurs in a passage prior to entering the anode. In a planar stack of cells, reforming passages would be located in between cells (although not necessarily between each one). Since there is still a considerable amount of heat generated by the fuel cell beyond that which is

Contributed by the International Gas Turbine Institute (IGTI) of THE AMERICAN SOCIETY OF MECHANICAL ENGINEERS for publication in the ASME JOURNAL OF ENGINEERING FOR GAS TURBINES AND POWER. Paper presented at the International Gas Turbine and Aeroengine Congress and Exhibition, Atlanta, GA, June 16–19, 2003, Paper No. 2003-GT-38566. Manuscript received by IGTI, Oct. 2002; final revision, Mar. 2003. Associate Editor: H. R. Simmons.

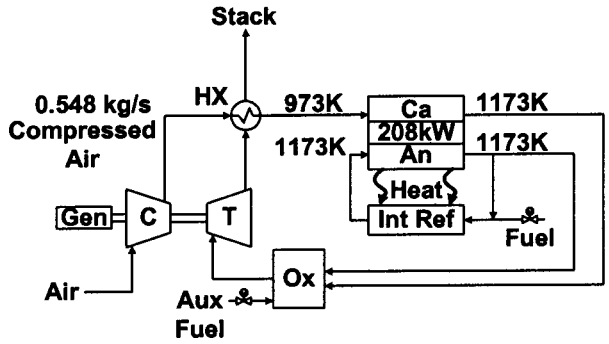

Fig. 1 Arrangement 1—typical hybrid with indirect internal reforming SOFC

necessary for the reforming, excess air in the cathode is still necessary for cooling. The tubular IIR-SOFC developed by SWPC uses 3.5 to 4 times more excess air than that required for stoichiometric reaction.

For a fuel cell that does not incorporate internal reforming, even more excess air is required for cooling since the endothermic reaction of the reforming would no longer be cooling the fuel cell in between cells of a stack. A study done by TIAX LLC and presented by Thijssen [5] estimates an excess air ratio of 7.7:1 for an ER-SOFC. While other design aspects will affect the excess air necessary, it is a reasonable estimate that an external reforming fuel cell would require twice the amount of air as an internal reforming design. It will be shown that in a hybrid configuration where the SOFC is pressurized by a gas turbine, an increase in excess air lowers the cycle thermal efficiency (assuming constant fuel cell efficiency). Therefore, it first appears that the ER-SOFC could have a disadvantage in performance within a pressurized hybrid configuration.

System Arrangements

In this paper, we compare the performance of four hybrid designs. First a typical configuration for an IIR-SOFC is described. It is then compared with a base-concept ER-SOFC hybrid. Then two arrangements are presented as concepts that improve the ER-SOFC hybrid performance.

Arrangement 1—Typical IIR-SOFC Hybrid. Thermodynamic calculations were performed for the hybrid arrangement shown in Fig. 1, which is similar to that given by Kimijima and Kasagi [2] for a 300-kW system. Air is compressed and then heated to a minimum of 973 K through the heat exchanger. For comparison, the maximum allowable air temperature increase across the cathode will be 200 K, as in Ref. [2]. This maximum has been given various values in the literature from 100 to 200 K and will of course depend on the particular fuel cell (design, size, etc.). The spent fuel from the anode is recycled through the reformer and the nonrecycle is burned with the air from the cathode exhaust in the oxidizer. If there is not enough heat for the recuperator to raise the compressed air temperature to 973 K, then supplemental fuel is added to the oxidizer.

Table 1 shows other parameters relevant to this case and the other cases that will be shown. The fuel cell electric efficiency was fixed at 51.4% for all cases, matching Campanari's value. [Some detailed modeling done at NETL has shown that there could be a slight (1–2%) variation in the fuel cell efficiency with oxygen concentration as might occur due to changes in air utilization or recycle.] Finally, the global fuel utilization is a result of the fuel recycle. A pressurized, desulfurized fuel source was assumed. The same flow of fresh fuel to the inlet of the internal reformer was used for all cases.

In order to illustrate a general point, let us assume the airflow is increased, and the cathode inlet temperature requirement kept the same (973 K). The resulting outlet cathode temperature would be lower, and assuming the same amount of spent fuel going to the oxidizer, the combustion temperature would decrease for the higher airflow as well. This means more supplemental fuel must be added to the oxidizer in order to keep the cathode inlet temperature at 973 K. Thus the system efficiency would be less (assuming the fuel cell efficiency is the same), although there will be more power from the turbine. Therefore, the idea is that since the ER-SOFC hybrid will require a higher airflow, its performance will suffer compared to the IIR-SOFC hybrid.

Table 1 Operating conditions

SOFC power	207.8 kW
SOFC electric efficiency	51.4%
Inverter efficiency	96%
SOFC/reformer heat loss	4%
Single-pass fuel utilization	0.80
Global fuel utilization (anode recycle)	0.91
CH_4 flow at SOFC inlet	0.0081 kg/s
Reformer steam to carbon ratio	1.8:1
Energy necessary for 96% methane conversion (4% reformed in FC)	90.7 kW
Energy needed to raise methane from 500 to 1173 K (assume methane is heated to 500 K in a stack exhaust HX)	21.7 kW
Energy content of methane–steam mixture with a 50-K temperature change. Used in calculations for Arrangements 2, 3, and 4.	6.7 kW
Air temperature increase across cathode	200 K
Compressor pressure ratio	4
Expander expansion ratio	0.98/3.6
Compressor isentropic efficiency	76%
Expander isentropic efficiency	85%
GT mechanical efficiency	95%
Alternator efficiency	98%
Recuperator effectiveness	85%
Blower isentropic efficiency	70%
Blower mechanical efficiency	90%
Blower pressure ratio	1.06

Arrangement 2—Base-Concept ER-SOFC Hybrid. The second arrangement, as shown in Fig. 2, is for an ER-SOFC hybrid with one reformer and one fuel cell. The placement of the reformer after the cathode is the most likely location due to the availability of heat. That is, the temperature of the cathode exhaust stream (1173 K) is a good match for the reformer inlet. Also, having the reformer pressurized on both the fuel and hot air/gas side is beneficial since the differential pressure is reduced and the air/gas side volume is reduced compared to atmospheric operation.

Table 2 compares results for Arrangements 1 and 2, showing the lower performance calculated for the external reforming case. Since the temperature requirements for both fuel cells are the same, they will have the same outlet temperature. But for Arrangement 2, the air must then pass through the reformer. The air

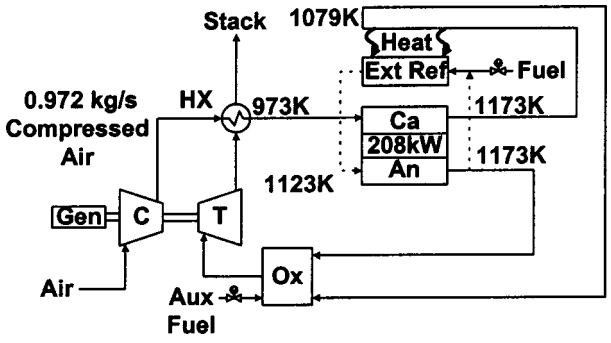

Fig. 2 Arrangement 2—base-concept hybrid with SOFC and external reformer

Table 2 Comparison of results

Arrangement	Efficiency (%)	Total power (kW)	Blower work (kW)	Fuel added to oxidizer (kg/s)	Compressor flow (kg/s)	Cathode flow (kg/s)	TIT[1] (K)	EGT[2] (K)
1 Internal	63.1	318		0.0020	0.548	0.548	1392	1053
2 External	55.5	403		0.0064	0.972	0.972	1397	1057
3 Cathode recycle	61.6	249	21.2	0	0.380	0.972	1269	960
4 Interstage reform	63.9	305		0.0014	0.486	0.486	1382	1052

[1]TIT denotes turbine inlet temperature.
[2]EGT denotes turbine exhaust gas temperature.

temperature exiting the reformer is 1079 K, 94 K lower than the cathode outlet temperature for Arrangement 1. Also, since the airflow rate is higher, and the spent fuel to the oxidizer is the same, an even lower temperature would exist at the turbine inlet. (Extra fuel is added in both cases since the temperature must be high enough to supply the heat necessary for the cathode inlet, but without the supplemental fuel the turbine inlet temperature would be 1239 K for Arrangement 1 and only 1120 K for Arrangement 2, a difference of 119 K.) Hence, Arrangement 2 is further burdened since it must raise the lower temperature while at a higher airflow rate. This explains the lower efficiency for Arrangement 2. One mitigating effect also related to the increase in flow is a potential improvement in the fuel cell performance. Since the airflow rate through the cathode is higher, the average oxygen concentration in the fuel cell will be higher than Arrangement 1, thereby slightly enhancing the fuel cell performance (1–2% according to a detailed analysis of a fuel cell).

In the comparison analysis, the pressure drop is assumed to be the same for both cases from compressor outlet to turbine inlet. This assumption offers a conservative approach to this study by slightly overestimating the ER performance. Although the flow rate is higher for Arrangement 2 the design could account for this by making the flow areas larger for Arrangement 2 by 60%. Obviously, increasing the flow area will also impact the size of Arrangement 2, but the present work does not consider such effects.

In this case, the reformer requires a total of 106 kW of heat: 90.7 kW for the endothermic reaction, 21.7 kW for the methane heating, and −6.7 kW supplied by the methane and steam gas itself. This assumes a reformer fuel outlet temperature of 1123 K. If the reformer fuel gas were allowed to cool even more, this would send a lower temperature fuel to the fuel cell and thus could be used to help fuel cell cooling. However, even for a low fuel temperature of 973 K to the anode inlet, the system efficiency would only be 1% higher. Also for a 973 K outlet reformer temperature, the kinetics would be too slow to have good methane conversion at the outlet.

Arrangement 3—Cathode Recycle Hybrid (Using the Heat Sink More Effectively). In order to improve the system thermal efficiency of the previous design, it is necessary to reduce the airflow work while maintaining adequate cooling for the fuel cell and supplying 106 kW of high-quality heat to the reformer. The first concept involves recycling the cathode exhaust through the reformer and back into the cathode inlet (see Fig. 3). The hot cathode exhaust that is recycled is cooled as it passes through the reformer prior to reentering the fuel cell inlet.

One concern with this arrangement is the amount of work the blower, or recycle device, must perform. For the results in Table 2, an improvement in thermal efficiency compared to Arrangement 2 is shown. This assumes a blower pressure ratio of 1.06:1 (5% total pressure loss). If a blower was used to do the recycle, it would need to withstand high temperatures, 1173 K if placed at the reformer inlet, or 1023 K if placed at the reformer outlet. Another concern is the reduced oxygen concentration compared to the other system arrangements. Again, detailed modeling done at NETL indicates the fuel cell efficiency could be slightly lower than Arrangement 1 due to the reduction in oxygen concentration resulting from recycle. The advantage to this arrangement is the lower turbine inlet temperature and hot-side heat exchanger inlet temperature (the turbine exhaust gas temperatue, EGT) compared to the other arrangements as shown in Table 2.

Arrangement 4—Interstage Reforming Hybrid. The final novel arrangement stages the reforming between two fuel cell modules, each providing 104 kW of power (see Fig. 4). Put in terms of SECA type fuel cells, each 104-kW module would be made up of 21 5-kW fuel cells in parallel. Note that the total fuel cell power in Arrangement 4 is the same as that for the single stack in the other arrangements (208 kW).

As shown in Fig. 4, the hot cathode exhaust from the first module is cooled by the reformer prior to entering the cathode

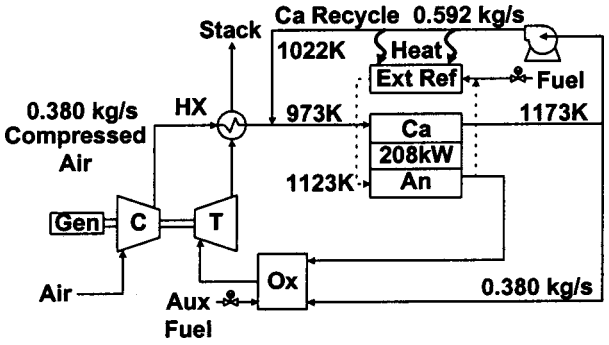

Fig. 3 Arrangement 3—cathode recycle through the external reformer

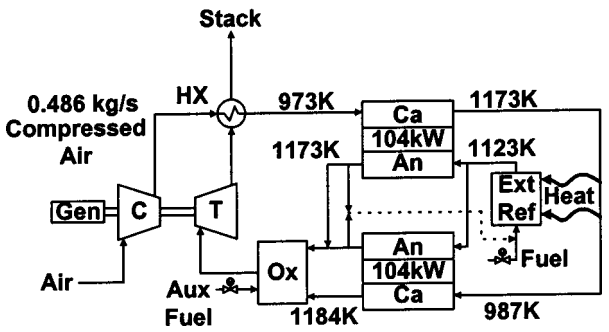

Fig. 4 Arrangement 4—interstage reforming

inlet of second. Thus, the first fuel cell module is used as a means to heat the air to a temperature necessary for the reformer, and the reformer is in turn used as a means to cool the air to an acceptable level for the second fuel cell module. The same amount of heat, 106 kW, is necessary in the reformer section as for Arrangement 3. However, this arrangement does not have the efficiency penalty related to the recycle blower. The improved performance result is shown and compared with the other cases in Table 2. Compared to Arrangement 1, the airflow for Arrangement 4 is slightly lower (11%) and thus explains the higher efficiency.

The issue of pressure drop is similar to the discussion given in Arrangement 2, with the exception that the air must now pass through two fuel cell modules in series. Therefore, unless the flow area were increased compared to the flow area of Arrangement 2, the pressure drop would double since the air is effectively going over twice the length. All arrangements assume a 10% (of 4 atm) pressure loss for the components between the compressor and expander. If that were doubled to 20% for Arrangement 4, the efficiency would decrease 1.1% (to 62.8%) and the total system power would decrease by 17 kW (to 288 kW).

Regarding the power electronics treatment of the dual stack versus single stack arrangements, it is proposed that the dual stack be operated in electric-series. With this approach, approximately the same total fuel cell voltage to the power electronics subsystem is achieved, thereby keeping the efficiency of the electricity processing system constant for the two cases studied. It also helps to keep the reactions in both stacks ''locked together'' so that heat generation in both stacks is very closely the same in keeping with the assumption for this study.

Figure 4 shows that there is a 14 K higher inlet and outlet temperature for the second fuel cell (987 and 1184 K, respectively). The requirement has been a minimum cathode inlet temperature of 973 K and maximum cathode air temperature increase of 200 K. If the cathode outlet temperature were also limited to 1173 K, then a few options are available. One solution would be to increase the airflow. The results then compare very close to Arrangement 1 with calculations showing an airflow rate of 0.518 kg/s and efficiency of 63.1%. This also lowers the cathode air temperature increase to 188 K. A second option would be to add a heat exchanger between the cathode outlet of the first fuel cell and the reformer, and exchange heat with the air entering the cathode inlet of the first fuel cell. This would require a very high temperature heat exchanger, but would also reduce the temperature requirement of the turbine exhaust heat exchanger. A third option would be to increase the fuel flow to the reformer, producing more hydrogen than is necessary for the fuel cell; hydrogen that could be used for other purposes. However, the amount of excess hydrogen produced in this case would seem too small to make it economical.

Finally, if the fuel cell electric efficiency was 54.2%, then the heat balance would be such that an exact match of inlet (973 K) and outlet (1173 K) temperature of both fuel cells would be obtained (the system electric efficiency would be higher as well of course, 65%).

The arrangement shown in Fig. 4 is for reforming between two fuel cell modules; however, a 3-fuel-cell arrangement (FC-Reformer-FC-Reformer-FC) could also be used. The result, given a 51.4% cell electric efficiency, would be a more pronounced increase in successive cathode inlet temperatures and the options mentioned above would again need to be employed to reduce the temperature. Note that this could begin to make excess hydrogen production an interesting option, but a more detailed analysis is needed in order to determine the advantages and disadvantages compared to stand-alone methods of hydrogen production.

Comparing Previous Work

Known Benefits of Staging. The staging of fuel cells has been analyzed by a number of investigators. Leaving aside the hybrid configurations, fuel cell staging has been considered by inventors George and Smith in Patent No. 6,033,794. However, the concept considers only internal reforming solid oxide fuel cells and furthermore does not consider pressurized systems. The purpose of staging for George and Smith is to attempt to maximize performance of the fuel cell by temperature, oxygen utilization, and fuel utilization considerations. If we look at the fuel flow path of a two-stage IIR-SOFC, there is in one sense a reformer in between the two fuel cells. However, the fuel flow path would be reformer-anode-reformer-anode, rather than anode-reformer-anode. As has been shown, the first does not make as effective a use of the reformer as a gas cooler.

The benefit of staging fuel cells in a hybrid configuration is discussed by Selimovic and Palsson [6]; however, they do not consider cooling with interstage reforming. The same applies to arrangements by Winkler and Lorenz [7] who consider staging fuel cells between expanders. Winkler and Lorenz also suggest other ideas to reduce the airflow, but again only for internal reforming fuel cells.

Nishida et al. [1] analyzed fuel cell staging for internal reforming fuel cells. In their analysis, the added benefit in electrical efficiency when staging internal reforming fuel cells is minimal since the flow rate of compressed air is not much less than that required for a single stage fuel cell. (In Ref. [1], the reader should compare the system efficiencies in Tables 6, 7, and 8 with Table 5).

Cathode Recycle Use and Potential Benefits. The original form of this paper was presented at the 2003 ASME Turbo Expo in Atlanta, GA [8]. Another paper presented at that same meeting also discussed the use and benefit of using cathode recycle [9]. The primary benefit discussed was the removal of a high-temperature heat exchanger, or with enough recycle, even the elimination of a heat exchanger altogether. This idea was also shown previously by Selimovic, Palsson, and Sjunnesson [10]. However, none of these concepts include the placement of an external reformer in the recycle loop, which improves the system efficiency. Furthermore, if more air is required for fuel cell cooling than what is presented in this paper, then there will be an efficiency penalty for all system arrangements; however, the penalty would seem much less for the cathode recycle case, Arrangement 3. For Arrangements 1, 2, and 4 the added compressor work requirement reduces efficiency, but in the case of the recycle cooling, the added work is done by the recycle blower, which is working against a much smaller pressure ratio. The increased recycle, however, will decrease the overall cathode oxygen concentration and thereby reduce the fuel cell efficiency by a small amount as discussed previously.

Conclusions

The main objective of this paper was to show that internal reforming may not be necessary in order to achieve high efficiency. Two novel concepts presented here shows that external reforming can be implemented efficiently in a hybrid fuel cell–gas turbine system. There are of course a number of issues other than cycle performance that must be considered when comparing internal and external reforming, i.e., fuel cell construction. Other interesting issues to consider would be off-design performance and controllability of heat and thermal loads. Even so, the present results suggest that these new concepts be investigated for achieving improved performance as well as ease of service.

References

[1] Nishida, K., Takagi, T., Kinoshita, S., and Tsuji, T., 2002, ''Performance Evaluation of Multi-Stage SOFC and Gas Turbine Combined Systems,'' ASME Paper No. GT-2002-30109.

[2] Kimijima, S., and Kasagi, N., 2002, ''Performance Evaluation of Gas Turbine-Fuel Cell Hybrid Micro Generation System,'' ASME Paper No. GT-2002-30111.

[3] Costamagna, P., Magistri, L., and Massardo, A. F., 2001, ''Design and Part-Load Performance of a Hybrid System Based on Solid Oxide Fuel Cell Reactor and a Micro Gas Turbine,'' J. Power Sources, **92**, pp. 352–368.
[4] Campanari, S., 1999, ''Full Load and Part Load Performance Prediction for Integrated SOFC and Microturbine Systems,'' ASME Paper No. 99-GT-65.
[5] Thijssen, J., 2002, ''SECA Fuel Cells for Larger Applications,'' *NETL Conference Proceedings of the 3rd Annual SECA Workshop*, Mar. 21–22, Washington, D.C.
[6] Selimovic, A., and Palsson, J., 2002, ''Networked Solid Oxide Fuel Cell Stacks Combined With a Gas Turbine Cycle,'' J. Power Sources, **106**, pp. 76–82.
[7] Winkler, W., and Lorenz, H., 2002, ''The Design of Stationary and Mobile Solid Oxide Fuel Cell-Gas Turbine Systems,'' J. Power Sources, **105**, pp. 222–227.
[8] Liese, E. A., and Gemmen, R. S., 2003, ''Performance Comparison of Internal Reforming Against External Reforming in a SOFC, Gas Turbine Hybrid System,'' ASME Paper No. GT-2003-38566.
[9] Agnew, G. D., Moritz, R. R., Berns, C., Spangler, A., Tarnowski, A., and Bozzolo, M., 2003, ''A Unique Solution to a Low Cost SOFC Hybrid Power Plant,'' ASME Paper No. GT-2003-38944.
[10] Selimovic, A., Palsson, J., and Sjunnesson, L., 1998, ''Integration of a Solid Oxide Fuel Cell Into a Gas Turbine Process,'' Fuel Cell Seminar, Palm Springs, CA.

A Study of Humidified Gas Turbines for Short-Term Realization in Midsized Power Generation—Part I: Nonintercooled Cycle Analysis

Michael A. Bartlett

Mats O. Westermark

Department of Chemical Engineering and Technology/Energy Processes, The Royal Institute of Technology, SE-100 44 Stockholm, Sweden

Humidified Gas Turbine (HGT) cycles are a group of advanced gas turbine cycles that use water-air mixtures as the working media. In this article, three known HGT configurations are examined in the context of short-term realization for small to midsized power generation: the Steam Injected Gas Turbine, the Full-flow Evaporative Gas Turbine, and the Part-flow Evaporative Gas Turbine. The heat recovery characteristics and performance potential of these three cycles are assessed, with and without intercooling, and a preliminary economic analysis is carried out for the most promising cycles.
[DOI: 10.1115/1.1788683]

Introduction

Humidified Gas Turbine (HGT) cycles are a group of advanced gas turbine cycles that have been studied as an alternative to the combined cycle and reciprocating engines for power generation. HGT cycles can be classified as gas turbine cycles that utilize water-air mixtures as the working fluid through the expander. Water vapor is obtained from evaporative processes in the cycle, for example, a heat recovery boiler, a humidification tower, or through water injection into the working fluid. As the expander flow increases without increasing the compressor flow, higher specific power outputs and efficiencies are achieved than those for the simple gas turbine cycle.

Many variations of the HGT have arisen, for example, the humid air turbine (HAT) cycle, the Steam Injected Gas Turbine (STIG) cycle, the Cheng cycle, the recuperated water injection (RWI) cycle, and the Evaporative Gas Turbine (EvGT) cycle. The main advantages identified with HGT cycles are electrical efficiencies similar to the combined cycle (CC) with higher specific power outputs [1–3] and significantly higher total efficiencies in combined heat and power (CHP) applications [4,5]. Furthermore, because the HGT cycles do not require a steam turbine for the bottoming cycle, specific investment costs ($/kW$_e$) are significantly lower than those for the CC [6]. Rydstrand, Westermark, and Bartlett [4] showed this to be especially true in combined heat and power applications due to the HGT's superior total efficiencies. Short start-up times and good load following characteristics have been reported [3,7] in addition to very low NO_x emissions with the use of only a diffusion burner [3]. Given this combination of characteristics, the focus of HGT commercialization falls naturally on distributed generation, peak-load plants, and industrial-sized applications (1–80 MW$_e$). Above this size, the flexibility and low investment costs of the HGT cycles become less important in the face of the mature performance and market position associated with large combined cycle.

The steam-injected gas turbine cycle uses exhaust gas heat to raise steam in a boiler that is then injected into the working fluid. This configuration has been investigated thoroughly in the literature, with Larsson and Williams [8] and Tuzson [9] presenting good overviews. In 1978, Cheng patented the Cheng cycle [10], a variation on the steam-injected cycle, which has since been commercialized based on the Allison 501 KM gas turbine. Kellerer and Spangenberg [7] report on operating experience from such a plant in Munich. Other gas turbine cycles with varying degrees of steam injection have been commercialized by General Electric, Aquarius, and Kawasaki. Macchi and Poggio [11] and dePaepe and Dick [12] have addressed water recovery systems for steam-injected cycles.

Evaporative gas turbine cycles can be defined as cycles which evaporate water directly into the working fluid. Water injection, i.e., spraying fine, warm droplets into the working fluid, was proposed by Gasparovic and Stapersma [13] and was further studied and developed by Mori et al. [14], and Frutschi and Plancherel [15]. Nakamura et al. [16] first patented an evaporative cycle which utilizes a humidification tower instead of direct water injection to evaporate the water. Fluor Daniel, Inc. investigated the humid air turbine (HAT) cycle [1,17], which also features a humidification tower instead of water injection, and patented some variations [18]. Amongst others, Chiesa et al. [19], Eidensten et al. [20] Stecco et al. [21], Rosén [22], and Yan, Eidensten, and Svedberg [23] have evaluated different configurations of evaporative gas turbine cycles.

In Sweden, evaporative gas turbine (EvGT) system studies were initiated at the Royal Institute of Technology (KTH) and Lund Institute of Technology (LTH), leading to the formation of the EvGT Consortium with industry and the Swedish Energy Agency in 1993. This consortium has concentrated on cycles with humidification towers for evaporation and has demonstrated the EvGT-technology for the first time in Lund, Sweden. A small-scale (600-kW$_e$) pilot plant was constructed with a humidification tower and recuperator, and later complemented with an aftercooler. Ågren et al. [24], Lindquist [3], Bartlett and Westermark [25], Dalili and Westermark [26], and Thern, Lindquist, and Torrison [27] have addressed different aspects of the EvGT pilot plant, including performance, operation characteristics, air and water quality, water recovery, humidification, and modeling.

Economic and technical simulation studies of midsize plants (70–80 MW) are also included in the EvGT project [6,28] along with application studies. Rydstrand, Westermark, and Bartlett [4] investigated natural gas-fired humidified gas turbines in district

Contributed by the International Gas Turbine Institute (IGTI) of THE AMERICAN SOCIETY OF MECHANICAL ENGINEERS for publication in the ASME JOURNAL OF ENGINEERING FOR GAS TURBINES AND POWER. Paper presented at the International Gas Turbine and Aeroengine Congress and Exhibition, Atlanta, GA, June 16–19, 2003, Paper No. 2003-GT-38402. Manuscript received by IGTI, October 2002; final revision, March 2003. Associate Editor: H. R. Simmons.

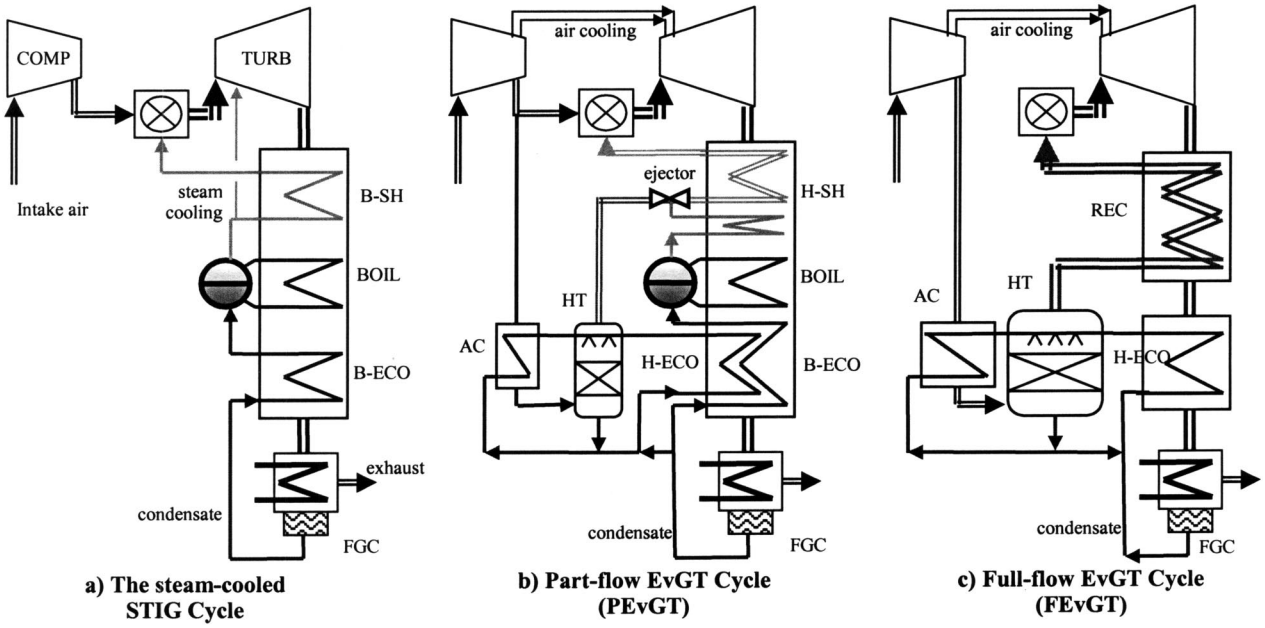

Fig. 1 Cycle layout of the nonintercooled HGT concepts to be studied

heating applications, while Bartlett et al. [29] examined cofired humidified cycles, also in district heating applications. Simonsson et al. [30] presented an analysis of EvGT cycles for industrial cogeneration using waste heat sources.

One important concept to arise from the EvGT project is the part-flow EvGT cycle (PEvGT), whereby only a fraction of the compressor air is used in the humidification tower. Westermark patented the concept [31] and Ågren [2] first introduced it to the literature. The authors studied this configuration with varying part-flow ratios for an industrial and an aeroderivative core engine and found that the optimal part-flow lies within the range 10–30% [2]. These studies, however, should be extended to a general thermodynamic and economic comparison with competing HGT concepts in power generation.

Scope

This two-paper series aims to identify the short-term thermodynamic and economic potential of HGT cycles with newly designed gas turbine machinery under 80 MW_e. An analysis is presented of three HGT concepts—the steam-injected cycle, the full-flow EvGT (FEvGT) cycle, and the PEvGT cycle—with and without intercooling. Favorable conditions for the different HGT concepts and configurations are identified and promising cycles are extracted for economic analysis. This paper, Part I, presents the background to the modeling and a thermodynamic analysis of the nonintercooled cycles, while the following paper, Part II, presents a thermodynamic analysis of intercooled HGT cycles (HGT-IC) and an economic comparison of the alternatives [36].

Table 1 Core engine characteristics

Inlet conditions	ISO
Inlet flow	50 kg/s
Compressor inlet ΔP	1%
Compressor isentropic efficiency	0.9
Intercooler ΔP (Part II cycles only)	2%
Compressor outlet ΔP	1%
Combustion chamber ΔP	3%
Turbine polytropic efficiency	0.87
Turbine exit ΔP	1.8%

Outline of the HGT Cycles for Analysis

The STIG Cycle. In the STIG cycle, shown in Fig. 1(*a*), steam is raised in a heat recovery steam generator (HRSG) and then injected into the working fluid after the compressor. Feed water preheating occurs in an economizer (B-ECO), evaporation in a boiler (BOIL), and high temperature heat recovery in a superheater (B-SH). Water vapor in the flue gas can be recovered in a flue gas condenser (FGC), then treated and recycled to the HRSG, making the cycle water self-sufficient. As the boiler is

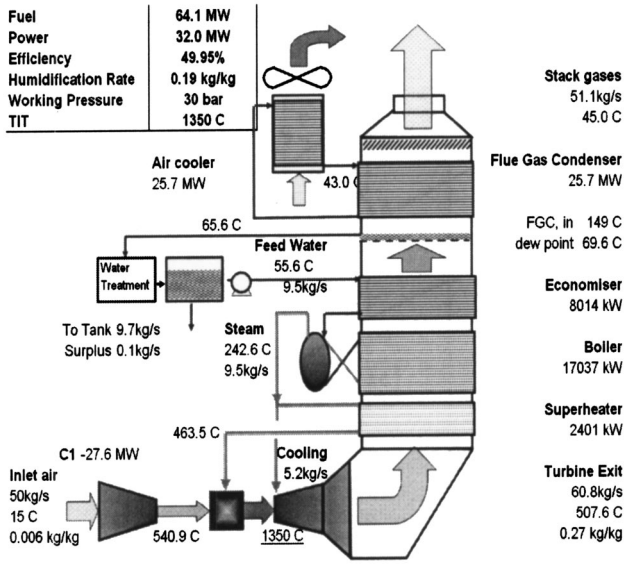

Fig. 2 STIG cycle used for the cost of electricity (CoE) analysis in Part II

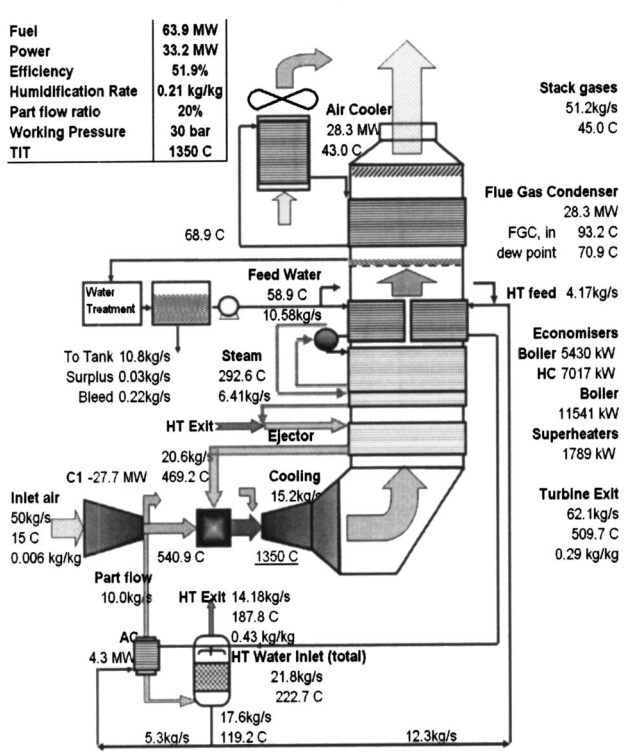

Fig. 3 PEvGT cycle used for the CoE analysis in Part II

limited to one pressure, superheated-STIG cycles typically have difficulty accessing low-quality heat and the flue gas can leave the HRSG at quite high temperatures. One way to increase heat recovery is to introduce steam cooling where slightly superheated steam is used to cool the gas turbine components instead of compressed air. This decreases the amount of steam for superheating, allowing more boiling and feed water preheating, thus increasing the amount of heat recovered.

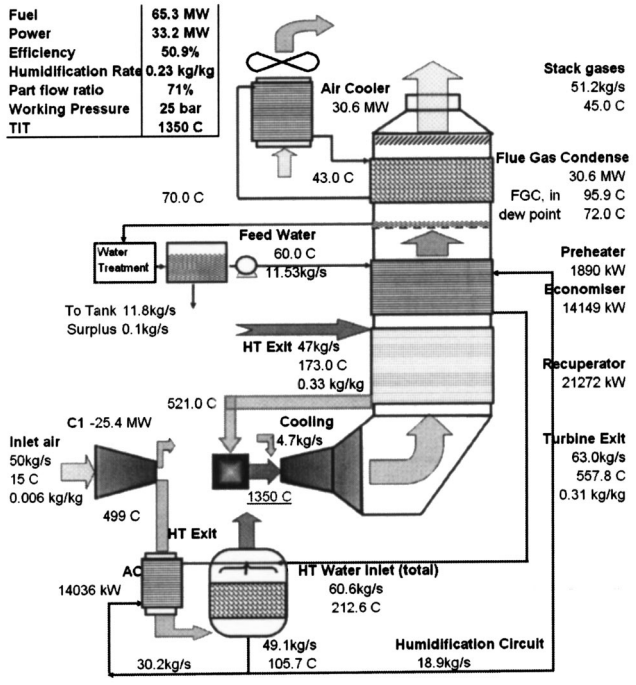

Fig. 4 FEvGT cycle used for the CoE analysis in Part II

Table 2 Pressure losses in the different HGT cycles

Area	STIG	PEvGT	FEvGT
Flue gas	3%	4%	7%[a]
HC	—	0[b]	5%
BC	[c]	[c]	—

[a]recuperator $\Delta P = 6\%$ [32].
[b]a steam ejector is used to overcome the pressure loss in the humidification circuit.
[c]5 bar overpressure is used to compensate for steam circuit pressure losses and the ejector.

Table 3 The modeling characteristics of cycle areas

Area	Item	Applicable cycle	Modeling characteristic	Value
Boiler circuit	B-ECO	STIG, PEvGT	Outlet sub cooling	10K
	BOIL	STIG, PEvGT	Pinch at drum	15K
	B-SH	STIG, PEvGT	Effectiveness[a]	85%
	H-SH			
Humidification circuit	H-ECO	PEvGT, FEvGT	Cold approach temperature	15K
	AC	PEvGT, FEvGT		
	IC	PEvGT, FEvGT		
	H-FWPH	PEvGT, FEvGT	Hot approach temperature	15K
	HT	PEvGT, FEvGT	Minimum driving force $(t - t_{ad})$	4K
Recuperator	REC	FEvGT	Effectiveness[a]	90%
Water recovery	WRU	All	Self-supporting temperature	—

[a]The effectiveness quoted is the enthalpy effectiveness. This expresses the heat transferred as a percentage of complete, ideal heat exchange.

The FEvGT Cycle. Instead of boiling the water separately, the EvGT cycle raises water vapor through evaporating water directly into the working medium in a humidification tower. In what is called the FEvGT concept in this article [see Fig. 1(*c*)], the entire compressor outlet passes through the humidification circuit, where it is cooled and humidified before being reheated and introduced to the combustion chamber. A primary surface recuperator (REC) is usually suggested for high-temperature heat recovery. The evaporation duty is extracted using an economizer (H-ECO) and an aftercooler (AC). In the humidification tower (HT), simultaneous mass and heat transfer takes place. Water heated to slightly below the boiling point is distributed across a packed bed where it is brought into countercurrent contact with compressed air. As the vapor pressure of the water exceeds the partial pressure

Table 4 The core engine parameters

Parameter		Values
CDP	Compressor discharge pressure (bar)	20, 25, 30, 35
TIT	Firing temperature (°C)	1200, 1350, 1500

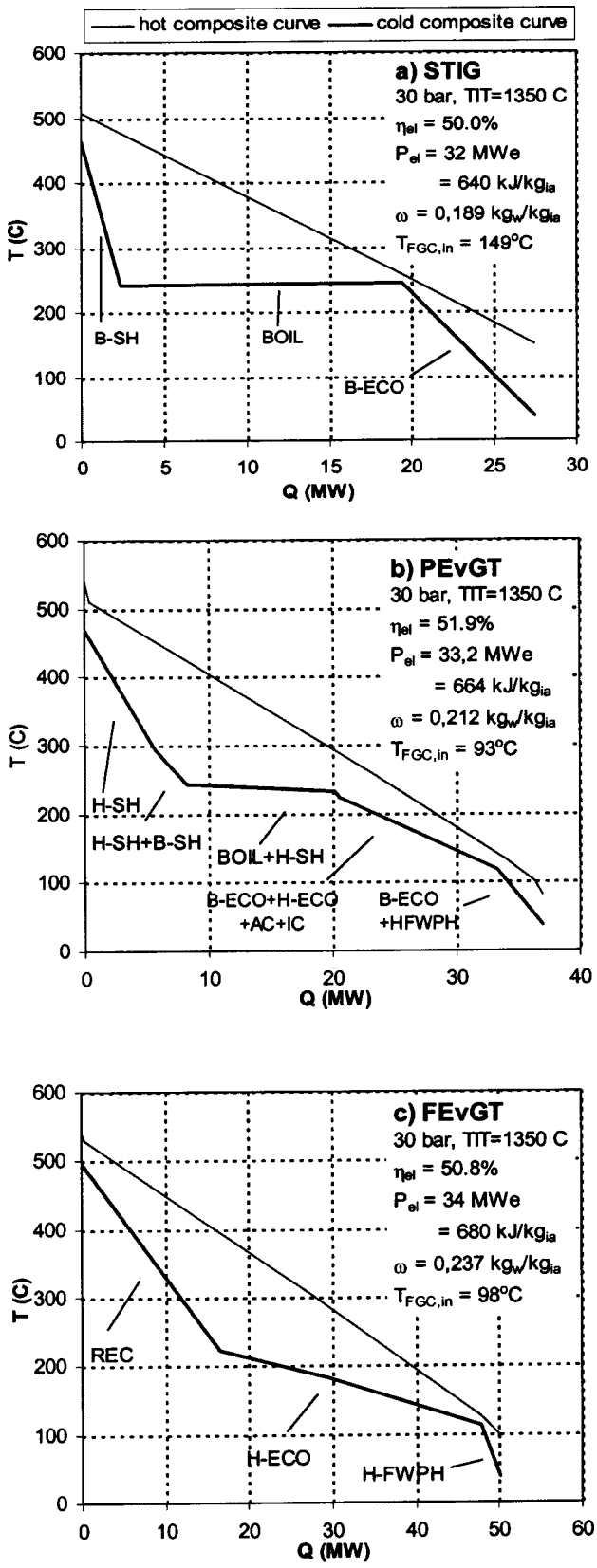

Fig. 5 Composite curves of the nonintercooled HGT cycles

of water in the air, evaporation takes place. This diabatic process takes most of the heat for evaporation from the water film, cooling the water as it flows down the tower. Hence a cold exit water stream from the HT is obtained, which can act effectively as an internal heat sink.

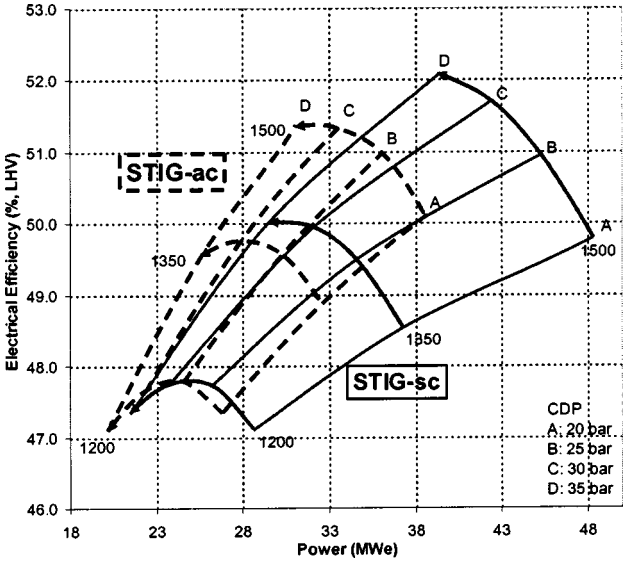

Fig. 6 Comparison of the performance maps of the air-cooled (ac) and steam cooled (sc) STIG cycle

The PEvGT Cycle. Ågren [2] presented and investigated the PEvGT concept introduced by Westermark [31]. The guiding principle of this concept is to reduce the heat exchange area and pressure drop penalties compared to a full-flow configuration while achieving the same heat recovery. To achieve this, only a part of the compressor outlet is extracted, cooled, humidified, reheated, and reinjected. The PEvGT cycle is illustrated in Fig. 1(*b*) and can be seen to combine features of the STIG and FEvGT cycle in one cycle. Like the STIG cycle, a HRSG is used to raise superheated steam, utilizing flue gas heat above the system boiling point. To fully exploit the heat remaining below the boiling point, a humidification tower with a part-flow from the compressor is used. Hence, the humidifier's purpose in this cycle is akin to the low-pressure boiler in a CC. The humidified part-flow is then heated with, or parallel to, the steam in a humid air superheater (H-SH). As the water vapor content is very high in the H-SH, excessive surface areas will not be required, nor the transition to a recuperator. Other PEvGT cycle configurations have been studied:

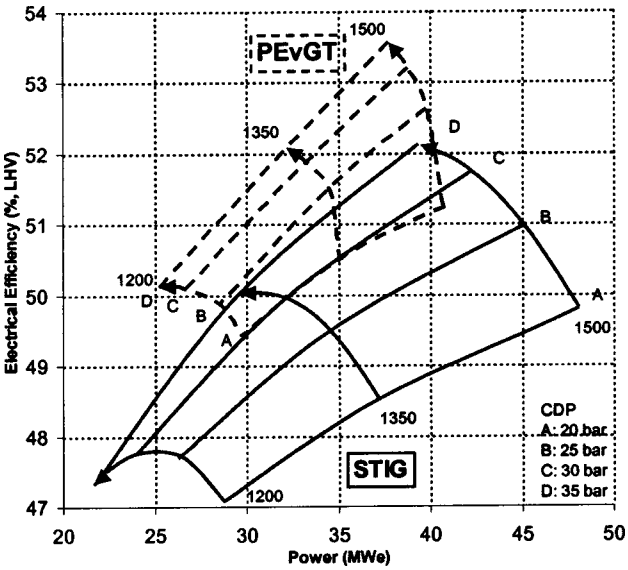

Fig. 7 The performance maps of the nonintercooled STIG and PEvGT cycles

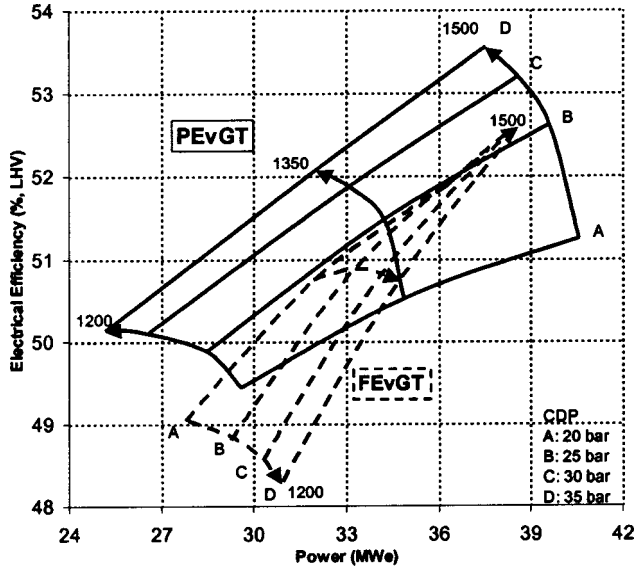

Fig. 8 The performance maps of the nonintercooled FEvGT and PEvGT cycles

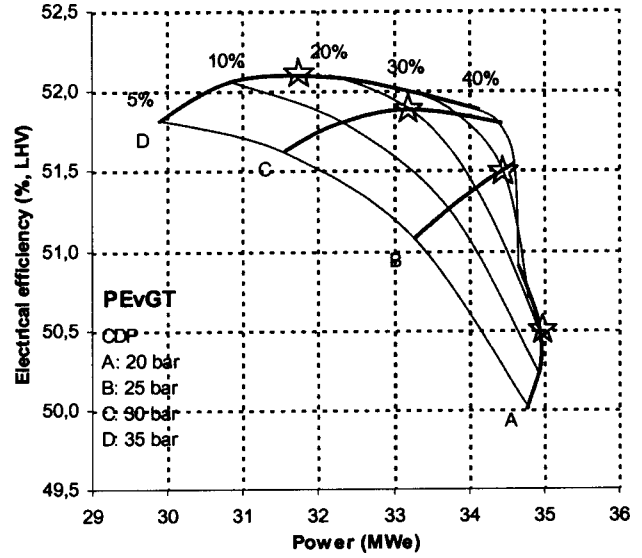

Fig. 9 The performance map of the nonintercooled PEvGT cycles for varying working pressures and part flows at a constant firing temperature of 1350°C

Table 5 Approach temperature and pressure drop sensitivity of the HGT cycles

Cycle	Configuration	Base η_{el}	$\Delta\eta_{el}$ (%, abs.) Low Δt	Low HC Δp	Low flue gas Δp
STIG-sc	30 bar 1350°C	50	+0.4	···	+0.2
PEvGT	35 bar 1350°C	52.1	+0.4	···	+0.2
FEvGT	25 bar, 1350°C	50.9	+0.75	+0.3	+0.3

first with a recuperator and two-stage humidifier but no boiler, and second with a recuperator, humidifier and boiler [2]. However, we have chosen to study the concept in Fig. 1(*b*) due to its simplicity. As an improvement over past configurations, we suggest using a steam ejector instead of a booster fan to overcome the pressure drop caused by the humidification process and heat exchangers.

Modeling the Cycles

The parameters for the cycle simulation have been chosen to represent current gas turbine technology in the midsize range. Furthermore, the heat exchangers and the humidification tower are modeled with somewhat conservative parameters so that their dimensions and costs are reasonable. GATECYCLE is used to model the gas turbine, heat exchangers, and cycle performance. The humidification tower and flue gas condensers are modeled using in-house programs linked with GATECYCLE through MS Excel.

The cycle can be divided into four areas: the core engine, the boiler circuit, the humidification circuit, and water recovery. Each section is discussed below and refers to both Parts I and II.

The Core Engine. The core engines for the different HGT cases are assumed to be purpose-built for humidified operation, i.e., they operate at their design point with a flow imbalance. The design constant is a compressor capacity of 50 kg/s air at ISO conditions. Consequently, the size of the turbine expander varies between cases following the degree of humidification, giving a cycle power output of 30–50 MW_e. As the heat exchange network is modeled conservatively, giving good driving forces and low costs, the thermodynamic data presented in the results may be scaled directly to smaller gas turbine cycles (5–15 MW_e) without adjusting the heat exchange network. However, the lower firing temperatures and pressures presented in this article are perhaps more applicable to smaller core engines. Table 1 outlines the constants used to model the core engine.

HGT cycles have cooling media other than the compressor air available, for example, saturated steam or cool humid air from the humidification tower. For reasons outlined in the section entitled ''Results and Discussion,'' the STIG cycle presented is steam cooled, while the evaporative cycles are cooled with compressor air. The cooling flow to the nozzle (stator) of the turbine is determined by GATECYCLE using the metal temperature of the turbine blades as expressed in Eq. (1). The reference parameters are taken from previous simulations [2]. The cooling flow to the rotor is set as equal to the cooling flow to the nozzle, a conservative assumption as rotor cooling flows are usually less than nozzle flows.

$$M_{cool} = M_{cool,ref}\left(\frac{C_{p,ref}}{C_p}\right)_{cool}\left(\frac{C_p}{C_{p,ref}}\right)_{gas}\left(\frac{\left(\frac{T_g - T_{metal}}{T_g - T_{cool}}\right)}{\left(\frac{T_g - T_{metal}}{T_g - T_{cool}}\right)_{ref}}\right)^{1.1}, \quad (1)$$

where M is the cooling flow rate, C_p is the specific heat, T is the temperature, and subscripts gas denote inlet gas value, cool denotes cooling gas value, and ref denotes the value at the reference condition.

While Eq. (1) is limited as heat transfer properties are not accounted for, it was judged to be more realistic than other GATECYCLE options. Typical cooling flows are given in the flow sheets contained in Figs. 2–4 and Figs. 6–9 in Part II [36].

The Heat Recovery Circuits. The boiler circuit (BC) is classified as the section of the HGT cycle which raises steam for delivery to the combustion chamber, in other words, the HRSG. This includes the B-ECO, the BOIL, and the superheaters (B-SH and H-SH).

The humidification circuit (HC) is the heat recovery section that delivers energy to the humidification process. This consists of the

HT, aftercooler (AC), humidification circuit economizer (H-ECO), and feed water preheater (H-FWPH). An intercooler is also included in paper II.

Table 2 shows the pressure drops resulting from the heat recovery systems, while Table 3 shows the performance characteristics of these items. The water flows through the AC, intercooler (IC), and H-ECO were adjusted such that the water outlet temperature was 10 K subcooled compared to the humidification tower pressure.

Humidification Model. While GATECYCLE contains a humidification tower model, which satisfactorily performs overall energy and mass balances, it does not check the internal conditions of the tower packing. Therefore, the model may converge on inoperable conditions where a point in the packing actually contravenes equilibrium. As such an in-house humidification tower model is integrated into the cycle calculations through a link with MS Excel for performance and dimensioning. The model is based on working-line theory common in unit operations [33,34] and uses a humid air properties model that account for nonideal mixing effects [35]. Importantly, the model has been experimentally verified for use with packed-bed and tubular humidifiers [26]. A description of this model can be found in Ågren [2] and Dalili and Westermark [26].

Parameter Study

Currently, there is a push for higher working pressures and firing temperatures for industrial midsized gas turbines. The parameters for this study are chosen to reflect these trends and are presented in Table 4. It was deemed infeasible to increase the working pressure beyond 35 bar without intercooling.

The optimal part-flow ratio in the PEvGT cycle will also vary with each core engine parameter. Ågren [2] showed that the probable optimum lies at lower part-flow ratios. Therefore, the part-flow ratio (ψ) in the PEvGT cycle is varied from 5–40%. Note that ψ is defined as the mass fraction of compressor intake air that is lead to humidification circuit.

Results and Discussion

This section examines and compares the performance of the nonintercooled HGT cycles. The results for the intercooled HGT cycles and a final economic analysis may be found in paper II.

Heat Recovery Comparison. Before analyzing the response of the HGT cycles to changes in pressure and the firing temperature, it is important to appreciate the nature of each cycle's heat recovery system. Figure 5 presents composite curves produced from the simulations at 30 bar and a combustor outlet of 1350°C. These curves show the amount and nature of the heat transferred in the cycle, including the aftercooler and flue gas. Composite curves are obtained through adding the $\dot{m} \cdot c_p$ values of all the heat sources or heat sinks for a temperature region, respectively, and multiplying the sum by the temperature change in that region.

Examining the three diagrams, it is clear that the FEvGT transfers the most heat between the streams (50 MW), nearly twice the amount of the STIG cycle (27 MW) and 35% more than the PEvGT (37 MW). This reflects the extra heat transfer required in the FEvGT's humidification circuit to cool and heat the entire airflow from the compressor in the aftercooler and recuperator. As the PEvGT passes only a fraction of the compressed air through the HC, it requires less heat transfer for this purpose. The STIG cycle has no humidification circuit. Importantly, the FEvGT cycle (16.6 MW) has seven times as much gas-gas heat transfer as the STIG (2.4 MW) and double that of the PEvGT (8.3 MW). Therefore, due to the amount of heat exchange in the FEvGT and the domination of gas-gas heat transfer therein, the FEvGT will require considerably more heat exchange area than either the STIG or the PEvGT.

It is important to note the different strategies to utilize low temperature heat in the different HGT cycles. It is these strategies which in turn have a critical consequence on the choice of turbine cooling media. In the STIG cycle, steam cooling is used to recover more low temperature heat. By decreasing the amount of steam for superheating, the amount of water that may be boiled and preheated is increased. For example, switching to steam cooling for the STIG cycle in Fig. 5(*a*) decreased the flue gas exit temperature from 167 to 150°C. The effect of this on the STIG performance is significant, as shown in Fig. 6. In the evaporative cycles, the humidification tower already allows the recovery of practically all the useful heat contained in the exhaust. Consequently, switching to direct steam- or humid air-cooling will not lower the flue gas temperature further, nor benefit the cycle efficiency greatly. Hence direct air-cooling was chosen for the evaporative cycles and direct steam-cooling was chosen for the STIG cycle.

The recovery of low temperature heat in the humidifier affords the PEvGT cycle 1.9% points more efficiency than the STIG cycle at an increased power density. The FEvGT cycle, however, only gains 0.8% points due to the pressure and temperature loss (the humid air enters the combustor colder than the compressor air) associated with the humidification process.

The Performance Maps. Figures 7–9 present the performance maps of the nonintercooled HGT cycles. As with all performance maps presented in this article, they show the power output versus the electrical efficiency of the cycle. The specific power output (kJ/kg_{ia}) is gained by multiplying the power output value (MW_e) by 20 (constant intake air flow for all cycles). The isobars [constant compressor discharge pressure (CDP)] and isotherms (constant firing temperature) outline an area in the map for each type of cycle. Only the optimal PEvGT cycles are considered, see the next section for details on this choice. It is useful to keep in mind the example composite curves in Fig. 5 when interpreting these maps.

In Fig. 7, the STIG cycle exhibits substantial increases in both specific power and efficiency with an increasing firing temperature. Increases in the turbine inlet temperature (TIT) imply a higher turbine outlet temperature (TOT), which allows more flue gas heat to be recovered by the single-pressure HRSG. Hence, more steam expands in the turbine and therefore the efficiency and specific power output increase. Increases in the compressor discharge pressure also lead to higher efficiencies, but with falling specific power outputs. The higher efficiencies are attributable to more work being extracted from the steam when at higher working pressures. However, because the TOT sinks with increases in the pressure, steam generation falls, and an efficiency maximum is therefore found on the isotherms (constant TIT and increasing CDP).

The PEvGT area can be considered a projection of the STIG area into a smaller region at higher electrical efficiencies (see Fig. 7). This projection is especially marked when there are significant amounts of heat left by the HRSG that the humidification tower in the PEvGT can utilize, i.e., at low turbine outlet temperatures. As the PEvGT can utilize low temperature heat, the efficiency maxima on the isotherms lie at much higher pressures than the STIG cycle because water vapor generation does not decrease as markedly with increases in the CDP. Compared to the STIG cycle, the specific power increases with an increased TIT are more moderate. The higher temperature of the turbine outlet, which follows a higher TIT, is mainly utilized for increased superheating and efficiency gains in the PEvGT rather than water vapor generation and power gains, as in the STIG cycle. Furthermore, steam cooling gives the STIG cycle an advantage in specific power (see Fig. 6).

The FEvGT area, Fig. 8, resides mostly within the PEvGT area and is a twisting, narrow, and steep surface. The isotherms show that the FEvGT efficiency only improves with pressure increases when the TIT is high. This is because a positive difference is required between the turbine outlet and compressor outlet temperatures for the recuperator to contribute positively to the effi-

ciency. This factor is also reflected in the marked efficiency increase along the isobars with an increasing TIT, which increases the TOT and hence the recuperator's impact. Unlike both the STIG and PEvGT cycles, the specific power of the FEvGT increases with the CDP, albeit marginally. This is attributable to the balance between the humidifier and recuperator. As the working pressure increases, the TOT decreases while the temperature out of the humidifier increases. Hence the recuperator recovers proportionately less flue gas heat at higher CDPs, allowing more humidification and therefore an increased power output. From Fig. 8, we can conclude the FEvGT has a lower efficiency than the PEvGT at CDPs over 25 bar and only a marginally better efficiency at a lower power output at lower CDPs.

Optimizing the PEvGT Cycle. Figure 9 shows the performance map of the PEvGT cycles (nonintercooled) at a constant firing temperature of 1350°C with varying pressures and part flow ratios. The trends are similar for the different firing temperatures studied. The stars represent the optimal part flow ratios chosen for use in the performance maps presented in Figs. 7 and 8.

It can be seen in Fig. 9 that at higher pressures (30–35 bar) an efficiency maximum exists, whereas a power maximum is found at lower pressures (20 bar). The characteristic of the part-flow curve is found to be dependent on two factors: the TOT and the temperature difference between the turbine and compressor outlets.

At a higher working pressure, the TOT encountered is low and colder than the compressor outlet temperature. The low TOT means large amounts of heat cannot be recovered by the high-pressure HRSG boiler and should be adsorbed by the H-ECO. As more air is passed through the humidification tower, the water outlet temperature is lowered and more heat is recovered from the flue gas, hence improving the efficiency and power output. However, as the turbine outlet is colder than the compressor outlet, the air sent to the humidifier will never recover its original temperature level, costing the cycle fuel and efficiency. The balance between these two factors will create an efficiency maximum, as seen for the 30- and 35-bar PEvGT cases in Fig. 9. While extra power may be gained at ψ values higher than the maximum, the gains become smaller while the heat exchanger area and thus costs increase linearly with ψ. A detailed economic study is required to find the optimal part-flow rate; however, in this article the maximum efficiency is chosen for further evaluation. Jonsson and Yan [28] carried out a detailed economic analysis of part-flows for three different core engines.

At low pressures, high TOTs and low COTs are found. In this case, the HRSG is well suited to the flue gas and little heat is left for the humidification tower. Therefore only a small part-flow percentage is needed to complete the heat recovery. Leading more air than this amount through the HC serves only to shift heat away from the HRSG to the H-SH, thus increasing sensible heat recovery and decreasing the humidity. As the power output is heavily dependent on the humidity, there is accordingly a power maximum at low to moderate part-flow ratios, illustrated by the 20-bar PEvGT case. Higher ψ values may deliver higher efficiencies, but again the heat exchange area and hence costs also increase. Hence the power maximum is chosen for evaluation in this study.

At moderate pressures (25 bar) both of the above effects are present. The turbine outlet temperature is low, but still slightly warmer than the compressor outlet. Hence sending more air through the humidification circuit in general, and the H-SH in particular, increases the efficiency weakly. Moreover, the HRSG also leaves significant amounts of heat available for the humidifier that is more effectively accessed with high ψ, due to a lower water temperature from the HT. Thus both the power output and the efficiency increase quickly with the part-flow ratio to an efficiency maximum at 30%, after which the gains are marginal.

Sensitivity Analysis. The parameters used in this study were chosen to conservatively model a feasible mid-sized gas turbine cycle. Hence the pressure drops and pinch points were chosen such that the HGT cycles' performances are not overstated nor the heat exchange size and costs ignored. Table 5 presents a study of the potential of the HGT cycles when these two parameters are lowered. For the case of low approach temperature differences, "low Δt", water–gas heat exchangers have an approach Δt of 5 K, the boiler drum pinch point is reduced to 5 K, the recuperator effectiveness is raised to 95%, and the effectiveness of the superheaters are raised to 90%. In the case "low HC Δp," the pressure drop associated with the humidification circuit is halved. Similarly, the flue gas pressure drop in the heat exchangers is halved in the case "low flue gas Δp."

Table 5 shows that the FEvGT benefits the most from all measures. This demonstrates that the FEvGT is the most sensitive HGT cycle to changes in approach temperatures and pressure drops. Therefore the FEvGT is more exposed to technology levels than the other cycles. A significant portion of the 0.75-point increase that occurs when improving the FEvGT's approach temperatures comes from the improved recuperator performance. Similarly, the recuperator contributes to most of the pressure drop penalties in the flue gas and humidification circuit. Therefore, the recuperator is essentially the determining factor of the competitiveness of the FEvGT.

It is important to stress that the potential of the HGT cycles cannot be found by adding the three end columns in Table 5. If the approach temperatures are reduced, then heat exchange area will increase and the pressure drop will also rise. Thus, in reality, any approach temperature changes will be partly counteracted by increased heat exchange pressure drop penalties.

Conclusions

In part I of this two-paper series, nonintercooled HGT cycles were examined for use in midsized power applications. The heat recovery characteristics of the STIG, FEvGT, and PEvGT cycles were analyzed using composite curves. Furthermore, the cycles' performances were mapped across a range of pressures and firing temperatures, with the PEvGT also examined with differing part flow ratios. The following points may be concluded.

- The full-flow EvGT (FEvGT) cycle is unsuitable for nonintercooled cycles. Much larger quantities of heat are transferred in the FEvGT cycle than the other HGT cycles, especially in gas–gas heat exchangers. This fact points to higher costs. Furthermore, the performance of the FEvGT cycle was found to be only moderate, with the part-flow EvGT cycle superior to the FEvGT for most relevant working pressure and firing temperature combinations.
- The STIG cycle shows good potential, with the lowest amount of heat transfer of the HGT cycles and very low amounts of gas–gas exchange; thus promising low heat exchange costs. The efficiency of the STIG cycle was not significantly lower than the other cycles, especially at high firing temperatures and working pressures.
- Steam cooling the turbine, rather than using air cooling, significantly benefits the STIG cycle by allowing more boiling and low-temperature heat recovery from the flue gas. The efficiency of the other cycles showed a lower dependency on the cooling media as the humidification tower already allows them to recover low-temperature heat.
- The part-flow EvGT (PEvGT) cycle is the most promising HGT cycle for nonintercooled core engines. Higher efficiencies than the other cycles are obtained, especially at moderate to high pressures, and good power densities. The total amount of heat transfer is kept 35% lower than the FEvGT, with gas–gas transfer 50% lower. The optimal part-flow ratio is dependent on the relationship between the compressor and turbine outlet temperatures, but was found to always be under 30%.
- HGT cycles are quite sensitive to how the heat exchange network is modeled, i.e., choices of approach temperatures and pressure drops. The FEvGT is especially sensitive and thus most dependent on component technology levels.

This article showed that the performances of the HGT cycles are quite similar, with at most a 2-percentage-point difference in the efficiency between the different optimized FEvGT, PEvGT, and STIG cycles. Furthermore, the power output at the optimal efficiencies also varied modestly. These facts point to the importance of an economic analysis to find the most attractive cycle.

In Part II of this series, intercooled HGT cycles examined and both intercooled and nonintercooled cycles are selected for economic analysis and comparison.

Acknowledgments

The authors would like to thank the financial and technical support of the EvGT Consortium members during this work: the Swedish Energy Agency, Vattenfall AB, Sydkraft AB, Energy E2, ALSTOM Power AB, and Elforsk.

Nomenclature

Cycle Abbreviations.

CC = Combined cycle
EvGT = Evaporative gas turbine
FEvGT = Full-flow evaporative gas turbine
HAT = Humid air turbine
HGT = Humidified gas turbine
PEvGT = Part-flow evaporative gas turbine
RWI = Recuperated-water-injected gas turbine
STIG = Steam-injected gas turbine

Heat Exchanger Abbreviations.

AC = Aftercooler
BC = Boiler circuit
B-ECO = Boiler circuit economizer
B-SH = Boiler circuit superheater
FGC = Flue gas condenser
HC = Humidification circuit
H-ECO = Humidification circuit economizer
H-FWPH = Humidification circuit feed water preheater
H-SH = Humid air superheater
HT = Humidification tower
IC = Intercooler
REC = Recuperator

Parameters.

CDP = Compressor discharge pressure, bar
COT = Compressor outlet temperature, °C
LHV = Lower heating value
P_{el} = Power output, MW_e (net)
t = Temperature
TIT = Turbine inlet temperature (combustor outlet temperature), °C
TOT = Turbine outlet temperature, °C
η_{el} = Cycle electrical efficiency, % LHV
ω = Cycle humidification rate, $kg_{H_2O}/kg_{intake\ air}$
ψ = Part-flow ratio, per kg compressor intake air

Subscripts.

ad = adiabatic
i.a. = intake air

References

[1] Rao, A. D., and Joiner, J. R., 1990, ''A Technical and Economic Evaluation of the Humid Air Turbine Cycle,'' Proc. 7th Annual International Pittsburgh Coal Conference, September 10–14.
[2] Ågren, N. D., 2000, ''Advanced Gas Turbine Cycles With Water-Air Mixtures as Working Fluid,'' Ph.D. thesis, Royal Institute of Technology, Dept of Chemical Engineering/Energy Processes, Stockholm, Sweden, ISSN 1104-3266 ISRN KTH/KET/R—120—SE.
[3] Lindquist, T., 2002, ''Evaluation, Experience and Potential of Gas Turbine Based Cycles With Humidification,'' Ph.D. Thesis, Lund University, Dept. of Heat and Power Engineering, Lund, Sweden, ISBN 91-628-5330-9.
[4] Rydstrand, M., Westermark, M., and Bartlett, M., 2002, ''An Analysis of the Efficiency and Economy of Humidified Gas Turbines in District Heating Applications,'' Proc. ECOS 2002, Vol. II, pp. 695–703.
[5] Poggio, A., and Strasser, A., 1996, ''CHENG Cycle Cogeneration System Application and Experience of Exhaust Gas Condensing,'' Proc. POWERGEN '96, June 26–28, Budapest.
[6] Nilsson, P. A., ed., 1996, ''EvGT—evaporative Gas Turbine—Block 3,'' Technical report, Lund Institute of Technology, Dept. of Heat and Power Technology, Lund, Sweden.
[7] Kellerer A., and Spangenberg C., 1998, ''Operating Experience With a Cheng-Cycle Unit,'' VGB PowerTech, November 1998, pp. 16–22.
[8] Larson, E. D., and Williams, R. H., 1987, ''Steam-Injected Gas Turbines,'' ASME J. Eng. Gas Turbines Power, **109**, pp. 55–63.
[9] Tuzson, J., 1992, ''Status of Steam-Injected Gas Turbines,'' ASME J. Eng. Gas Turbines Power, **114**, pp. 682–686.
[10] Cheng, D. Y., 1978, ''Regenerative Compound Dual-Fluid Heat Engine,'' US Patent No. 4,128,994.
[11] Macchi, E., and Poggio A., 1994, ''Cogeneration Plant Based on Steam Injection Gas Turbine With Recovery of Water Injected: Design Criteria and Initial Operating Experience,'' ASME Paper No. 94-GT-17.
[12] dePaepe, M., and Dick, E., 1999, ''Water Recovery in Steam-Injected Gas Turbines: A Technological and Economical Analysis,'' European J. Mech. Environ. Eng., **44**, pp. 195–204.
[13] Gasparovic, N., and Stapersma, D., 1973, ''Gas Turbine With Heat Exchanger and Water Injection in the Compressed Air,'' Combustion, **45**, pp. 6–16.
[14] Mori, T. R., Nakamura, H., Takahashi, T., and Yamamoto, K., 1983, ''A Highly Efficient Regenerative Gas Turbine System by New Method of Heat Recovery With Water Injection,'' Proc. 1983 Tokyo International Gas Turbine Congress, Vol. 1, pp. 297–303.
[15] Frutschi, H. U., and Plancherel, A., 1988, ''Comparison of Combined Cycle With Steam Injection and Evaporation Cycles,'' Proc. 2nd Sym. on Turbomachinery, Combined-Cycle Technologies and Cogeneration, IGTI, Vol. 3, pp. 137–145.
[16] Nakamura, H., Takahashi, T., Narazaki, N., Yamamoto, F., and Sayama, N., 1981, ''Regenerative Gas Turbine Cycle With Water Addition and Method of Operation Therefore,'' U.S. Patent No. 0,053,045 B1.
[17] Day, W. H., and Rao, A. D., 1992, ''FT4000 HAT With Natural Gas Fuel,'' ASME COGEN-TURBO, American Society of Mechanical Engineers, International Gas Turbine Institute, Vol. 7, pp. 239–245.
[18] Rao, A. D., 1989, ''Process for Producing Power,'' U.S. Patent No. 4,829,763.
[19] Chiesa, P., Lozza, G., Macchi, E., and Consonni, S., 1995, ''An Assessment of the Thermodynamic Performance of Mixed Gas-Steam Cycles: Part B—Water-Injected and HAT Cycles,'' ASME J. Eng. Gas Turbines Power, **117**, pp. 499–508.
[20] Eidensten, L., Svedberg, G., Yan, J., and Ågren, N., 1994, ''New Heat and Power Production Processes (Nya el- och värme-produktionsprocesser),'' Technical Report (in Swedish), Royal Institute of Technology, ISSN-1104-3466/TRITA-KET R19.
[21] Stecco, S. S., Desideri, U., Frachini, B., and Bettagli, N., 1993, ''The Humid Air Cycle: Some Thermodynamical Considerations,'' ASME Paper No. 93-GT-77.
[22] Rosén, P., 1993, ''Evaporative Gas Turbine Cycles—A Thermodynamic Evaluation of Their Potential,'' Licentiate Thesis, Department of Heat and Power Technology, Lund Institute of Technology, Lund, Sweden, ISRN LUTMDN/TMVK-7010-SE.
[23] Yan, J., Eidensten, L., and Svedberg, G., 1995, ''Investigation of the Heat Recovery System in Externally Fired Evaporative Gas Turbines,'' ASME Paper No. 95-GT-72.
[24] Ågren, N. D., Westermark, M. O., Bartlett, M. A., and Lindquist, T., 2000, ''First Experiments on an Evaporative Gas Turbine Pilot Plant—Water Circuit Chemistry and Humidification Evaluation,'' ASME Paper No. 2000-GT-168.
[25] Bartlett, M., and Westermark, M., 2001, ''Experimental Evaluation of Air Filters and Metal Ion Migration in Evaporative Gas Turbines,'' ASME Paper No. JPGC2001/PWR-19119.
[26] Dalili, F., and Westermark, M., 2002, ''Experimental Study on a Packed Bed Humidifier in an Evaporative Gas Turbine,'' ASME Paper No. IJPGC2002-26106.
[27] Thern, M., Lindquist, T., and Torrison, T., 2003, ''Theoretical and Experimental Evaluation of s Plate Heat Exchanger Aftercooler in an Evaporative Gas Turbine Cycle,'' ASME Paper No. GT2003-38099.
[28] Jonsson, M., and Yan, J., 2003, ''Economic Assessment of Evaporative Gas Turbine Cycles With Optimized Part Flow Humidification,'' ASME Paper No. GT2003-38009.
[29] Bartlett, M. A., Wikman, K., Holmgren, K., and Westermark, M., 2002, ''Effective Waste Utilisation in Hybrid Cycles for CHP Applications—A Cycle and System Study,'' Proc. ECOS 2002, Vol. II, pp. 804–813.
[30] Simmonsson, N., Anheden, M., Eidensten L., and Tollin, J., 2002, ''Evaporative Gas Turbines—Humidified Air Gives Flexible Power for the Future,'' Proc. POWERGEN 2002, Milan, Italy.
[31] Westermark, M., 1996, ''Method and Device for Generation of Mechanical Work and, if Desired, Heat in an Evaporative Gas Turbine Process,'' International Patent Application No. PCT/SE96/00936.
[32] Utriainen, E., 2001, ''Investigation of Some Heat Transfer Surfaces for Gas Turbine Recuperators,'' Ph.D. thesis, Lund University, Dept. of Heat and Power Engineering, Lund, Sweden. ISBN 91-7874-118-1.

[33] Mickley, H. S., 1949, ''Design of Forced Draught Air Conditioning Equipment,'' Chem. Eng. Prog., **45**, p. 739ff.
[34] Coulson, J. M., and Richardson, J. F., 1996, *An Introduction to Chemical Engineering Design*, Vol. 6 of *Chemical Engineering*, Butterworth-Heinemann.
[35] Dalili, F., Andren, M., Yan, J., and Westermark, W., 2001, ''The Impact of Thermodynamic Properties of Air-Water Vapor Mixtures on Design of Evaporative Gas Turbine Cycles,'' ASME Paper No. 2001-GT-098.
[36] Bartlett, M. A., and Westermark, M. O., 2004, ''A Study of Humidified Gas Turbines for Short-Term Realization in Midsized Power Generation—Part II: Intercooled Cycle Analysis and Final Economic Evaluation,'' J. Eng. Gas Turbines Power, **127**, pp. 100–108.

A Study of Humidified Gas Turbines for Short-Term Realization in Midsized Power Generation—Part II: Intercooled Cycle Analysis and Final Economic Evaluation

Michael A. Bartlett

Mats O. Westermark

Department of Chemical and Technology/Energy Processes,
The Royal Institute of Technology,
SE-100 44 Stockholm, Sweden

Humidified gas turbine (HGT) cycles are a group of advanced gas turbine cycles that use water–air mixtures as the working media. In this article, three known HGT configurations are examined in the context of short-term realization for small to mid-sized power generation: the steam injected gas turbine, the full-flow evaporative gas turbine, and the part-flow evaporative gas turbine. The heat recovery characteristics and performance potential of these three cycles are assessed, with and without intercooling, and a preliminary economic analysis is carried out for the most promising cycles.
[DOI: 10.1115/1.1788684]

Introduction

This paper is Part II of a two-part paper. It is strongly recommended that the two be read together to gain more insight into the processes described and for information on background, relevant literature, theory, and modeling. Part I [18] treats the research background for HGT cycles, while only a brief introduction is given here.

Humidified gas turbine (HGT) cycles are a group of advanced gas turbine cycles that have been studied as an alternative to the combined cycle and reciprocating engines for power generation. HGT cycles can be classified as gas turbine cycles that utilize water–air mixtures as the working fluid through the expander. Water vapor is obtained from evaporative processes in the cycle, for example, a heat recovery boiler, a humidification tower, or through water injection into the working fluid. As the expander flow increases without increasing the compressor flow, higher specific power outputs and efficiencies are achieved than for the simple gas turbine cycle.

The main advantages identified with HGT cycles are electrical efficiencies similar to the combined cycle (CC) with higher specific power outputs [1–3] and significantly higher total efficiencies in CHP applications [4,5]. Furthermore, because the HGT cycles do not require a steam turbine for the bottoming cycle, specific investment costs ($\$/kW_e$) are significantly lower than those for the CC [6]. Rydstrand, Westermark, and Bartlett [4] showed this to be especially true in combined heat and power applications due to the HGTs superior total efficiencies. Short start-up times and good load following characteristics have been reported [3,7] in addition to very low NO_x emissions with the use of only a diffusion burner [3]. Given this combination of characteristics, the focus of HGT commercialization falls naturally on distributed generation, peak-load plants and industrial-sized applications ($1-80\ MW_e$). Above this size, the flexibility and low investment costs of the HGT cycles become less important in the face of the mature performance and market position associated with large combined cycles.

While many HGT variations have been proposed (see Part I for details), the literature lacks a thorough thermodynamic and economic comparison of the leading configurations when applied to mid-sized power generation.

Scope

This two-part paper aims to identify the short-term thermodynamic and economic potential of HGT cycles with newly designed gas turbine machinery under $80\ MW_e$. An analysis is presented of three known HGT concepts—the steam injected cycle, the full flow evaporative gas turbine (FEvGT) cycle, and the part-flow evaporative gas turbine (PEvGT) cycle—with and without intercooling. Favorable conditions for the different HGT concepts and configurations are identified and promising cycles are extracted for economic analysis. Part I presented the background to the modeling and a thermodynamic analysis of the non-intercooled cycles [18], while this article presents a thermodynamic analysis of intercooled HGT cycles (HGT-IC) and an economic comparison of the alternatives.

Outline of the Intercooled HGT Cycles

The STIG-SIC Cycle. In the steam injected gas turbine with a spray intercooling (STIG-SIC) cycle, shown in Fig. 1(*a*), steam is raised in a heat recovery steam generator (HRSG) and then injected into the working fluid. Feed water preheating occurs in an economizer (B-ECO), evaporation in a boiler (BOIL), and sensible heat recovery in a superheater (B-SH). Water vapor in the flue gas can be recovered in a flue gas condenser (FGC), then treated and recycled to the HRSG, making the cycle water self-sufficient. Steam is used to cool the turbine blades. It was shown in Part I that this decreases the amount of steam for superheating, allowing more boiling and feed water preheating and improving heat recovery and cycle performance.

If the STIG cycle is to be intercooled, the heat rejected is at temperatures too low to be utilized in an HRSG. Furthermore, the compressor flow is not recuperated and conventional intercooling

Contributed by the International Gas Turbine Institute (IGTI) of THE AMERICAN SOCIETY OF MECHANICAL ENGINEERS for publication in the ASME JOURNAL OF ENGINEERING FOR GAS TURBINES AND POWER. Paper presented at the International Gas Turbine and Aeroengine Congress and Exhibition, Atlanta, GA, June 16–19, 2003, Paper No. 2003-GT-38403. Manuscript received by IGTI, October 2002, final revision, March 2003. Associate Editor: H. R. Simmons.

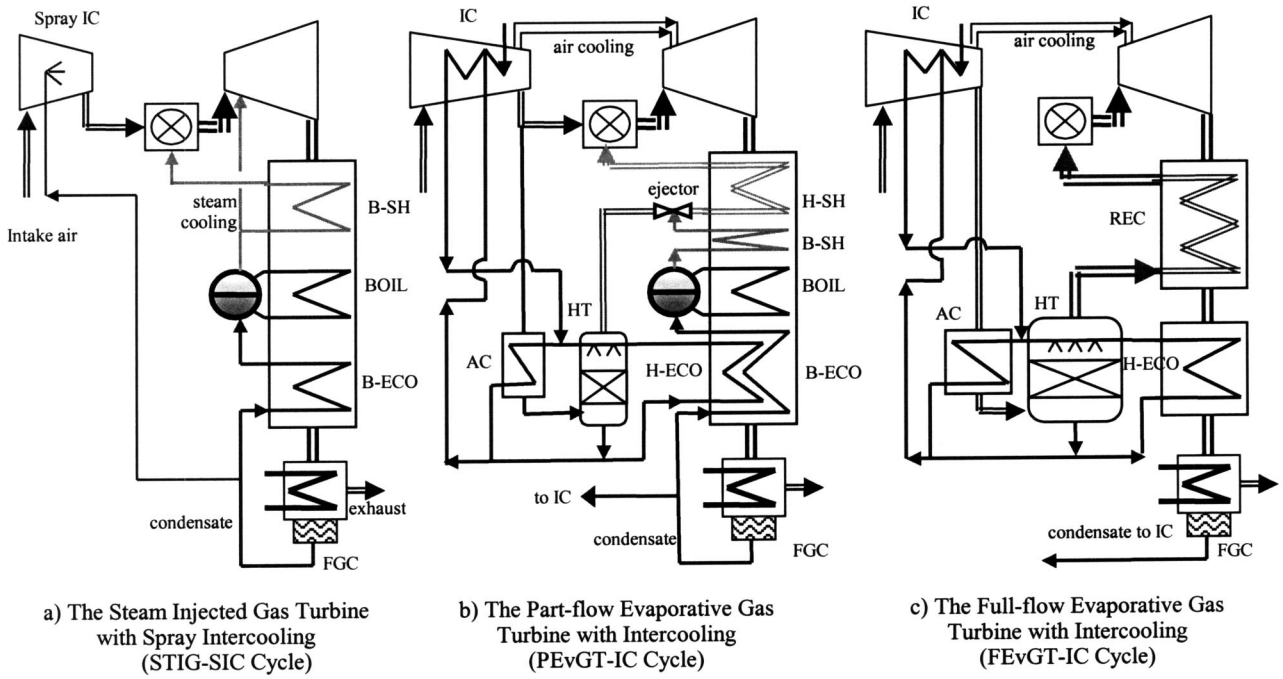

Fig. 1 Cycle layout of the intercooled HGT cycles to be studied

will thereby increase fuel consumption. Therefore, we have chosen to spray intercool the compressed air with fine water droplets in a single adiabatic step at low pressures. The optimal spray intercooling pressure for the cycle efficiency was found to be at approximately one-tenth of the working pressure. At these pressures, the trade off between the amount of compressor work saved and the amount of fuel consumed is balanced. The amount of water evaporated is quite low but sufficient to restrain the compressor outlet temperature. Spray intercooling is therefore viewed in this article mainly as a technique to allow high compressor discharge pressures while remaining within material temperature constraints.

The FEvGT-IC Cycle. Instead of boiling water separately, the evaporative gas turbine (EvGT) cycle raises water vapor through evaporating water directly into the working medium in a humidification tower. In what is termed the full-flow EvGT (FEvGT) concept in this article (see Fig. 1(*c*)), the entire compressor outlet (except cooling flows) is lead through the humidification circuit, where it is cooled and humidified before being reheated and introduced to the combustion chamber. A recuperator (REC) is used for sensible heat recovery. The evaporation duty is extracted using an economizer (H-ECO), an aftercooler (AC), and an intercooler (IC).

Similar to the intercooled-recuperator (ICR) cycle, the intercooler in the FEvGT-IC saves compressor work. Moreover, the heat rejected from the intercooler is used by the cycle in the humidification tower to generate extra water vapor. The choice of pressure for intercooling is chosen to suit the humidification circuit with the discharge temperature of the first compressor set to 15K above the water inlet temperature to the humidification tower (see Fig. 2). This results in somewhat higher pressure ratios for the low-pressure compressor compared to the high-pressure compressor. In order to maximize the duty of the intercooler, the feed water for the humidification circuit is preheated in the intercooler along with water from the tower exit. To prevent droplet formation before compressor 2, the intercooler gas outlet temperature is limited to 40 K above the dew point.

The PEvGT-IC Cycle. Ågren [2] presented and investigated the part-flow EvGT concept (PEvGT) patented by Westermark [8]. The guiding principle of this concept is to reduce the heat exchange area and pressure drop penalties, compared to the full flow EvGT cycle, while achieving the same heat recovery. To achieve this, only a minor part of the compressor outlet is extracted, cooled, humidified, re-heated, and re-injected. The PEvGT-IC cycle is illustrated in Fig. 1(*b*) and can be seen to combine features of the STIG-SIC and FEvGT-IC cycles. Like the STIG cycle, an HRSG is used to raise superheated steam, utilizing flue gas heat above the system boiling point. To fully exploit the heat remaining below the boiling point, a humidification tower with a part-flow from the compressor is used. This humidification circuit is analogous to the low-pressure boiler in a combined cycle. The tower can also collect heat from other cycle streams, e.g., intercooling, that the HRSG cannot utilize. The humidified part-flow is then heated together, or in parallel, with the steam in a humid air superheater (H-SH). This eliminates the need for a large recuperator. As an improvement over past configurations, we suggest using a steam ejector instead of a booster fan to overcome the pressure drop caused by the humidification process and heat exchangers. The intercooler is laid out as presented in the FEvGT-IC section.

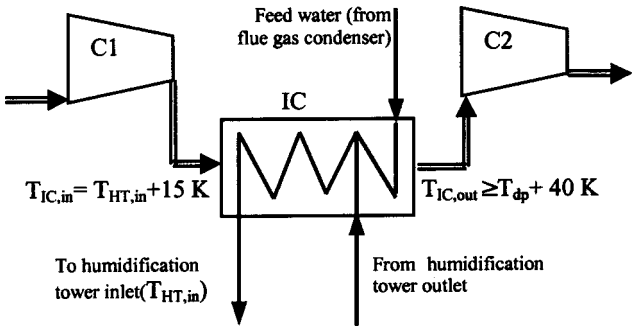

Fig. 2 FEvGT-IC and PEvGT-IC intercooling layout

Table 1 Core engine parameters

Parameter		*Values*
CDP	Compressor discharge pressure (bar)	20, 30, 40
TIT	Firing temperature (°C)	1200, 1350, 1500

Modeling the Cycles

As in Part I, the parameters for the cycle simulations have been chosen to represent current gas turbine technology in the mid-size range (below 80 MW_e). Furthermore, the gas turbines are assumed to be purposely built for humidified operation, i.e., they operate at their design point with a flow imbalance. The heat exchangers and humidification towers are modeled with somewhat conservative parameters so that their dimensions and costs are reasonable. GATECYCLE is used to model the gas turbine, heat exchangers, and cycle performance. The humidification tower and flue gas condensers are modeled using in-house programs [2,9] linked with GATECYCLE through MS Excel.

The cycle can be divided into four areas, as outlined in Part I: the core engine, the boiler circuit (BC), the humidification circuit (HC), and water recovery. Part I presented the modeling assumptions and variables used in each of these areas and Table 2 summarizes the factors used for the heat exchangers for performance modeling, dimensioning, and costing in each area.

Parameter Study. Reflecting the current push for higher working pressures and turbine inlet temperature (TIT) levels, the core engine parameters are shown in Table 1. The optimal part-flow ratio in the PEvGT-IC cycle will also vary with each core engine parameter. Ågren [2] showed that the probable optimum lies at lower part-flow ratios; thus the part-flow ratio (ψ) is varied from 5% to 40%. Note that ψ is defined as the mass fraction of compressor intake air that passes through the humidifier.

Dimensioning and Costing

It is not sufficient for a HGT to just be thermodynamically attractive; it must also be economically and technically attractive. Thus promising cases from the parameter studies in both Part I and this article are chosen for a preliminary economic analysis involving dimensioning, costing, and a cost of electricity (CoE) analysis.

Table 2 summarizes the characteristics and information used to provide the dimensions and costs of the heat exchange equipment in each cycle. Cost data for the genset (core engine plus generator) is supplied by Ref. [14] assuming a mature product. All figures shown in Table 2 refer to base equipment costs, except the flue gas condenser. The installed cost is obtained from the equipment purchase cost by using the factor methodology from Coulson and Richardson [10]. The fixed capital for investment is then obtained by adding 23% to the installed cost for (a) land purchase, surveys, site, preparations, etc. (5%), (b) specific services (1%), (c) fees in addition to the contractor fee (2%), (d) contingency (10%), (e) confidence limit (2%), and (f) contractor fee (3%).

CoE Analysis. The cost of electricity (CoE) is used as the main tool for economic appraisal. This factor is calculated using the assumptions and costs found in Table 3. No taxes were included in the study.

Table 2 The modeling, dimensioning, and costing characteristics of the boiler circuit, humidification circuit, and water recovery equipment

Area	*Item*	*Applicable Cycle*	*Modelling Characteristic*	*Value*	*Dimensioning characteristic*	*Value*	*Costing Characteristic*	*Value*
Boiler Circuit	B-ECO	STIG, PEvGT	Outlet sub cooling	10 K	Overall heat transfer coefficient	700 $W/m^2.K$	Finned-tube area[1]	290 $/m^2
	BOIL	STIG, PEvGT	Pinch at drum	15 K	Overall heat transfer coefficient	105 $W/m^2.K$	Smooth tube area[2]	80 $/m^2
	B-SH	STIG, PEvGT	Effectiveness	85 %	Overall heat transfer coefficient	90 $W/m^2.K$	Smooth tube area[3]	107 $/m^2
	H-SH	PEvGT						
Humidification Circuit	H-ECO	PEvGT, FEvGT	Cold approach temperature	15 K	Overall heat transfer coefficient	700 $W/m^2.K$	Finned-tube area[4]	345 $/m^2
	AC	PEvGT, FEvGT						
	IC	PEvGT, FEvGT						
	H-FWPH	PEvGT, FEvGT	Hot approach temperature	15 K				
	HT[6]	PEvGT, FEvGT	$(t\text{-}t_{ad})_{min}$ $(t_{w,in} - t_{w,bp})$[7]	4 K 10 K	Height of a transfer unit (HTU)	0.24	Vessel volume Packing volume[8]	2 k$/$m^3$ 2.4 k$/$m^3$
Recuperator	REC	FEvGT	Effectiveness	90 %	-	-	Duty[5]	43 $/kW
Water Recovery	WRU[9]	All	Self-supporting temperature	-	-	-	Condensate flow rate	167 k$/kg/s

1. B-ECO is carbon steel tubes with carbon steel fins [11]. Overall heat transfer coefficient (U) obtained from Hewitt et al. [12].
2. BOIL consists of smooth carbon steel tubes. Cost [11] includes factor for water/steam system cost. U is obtained from [12].
3. Superheaters are smooth stainless steel tubes. Costs from Wahlberg [11] and U from Hewitt et al. [12].
4. HC heat exchangers and the superheaters are stainless steel tubes with carbon steel fins. Costs from Wahlberg [11] and U from Hewitt et al [12].
5. The recuperator is a primary surface, laminar flow heat exchanger with the cost from Nilsson [6].
6. The size and pressure drop of the humidification tower are determined by the in-house model, which was verified by Dalili [9]. Cost data from Wahlberg [11].
7. Water entering the tower is 10 K under the boiling point. The minimum temperature driving force in the tower is 4 K.
8. Including water distributor and droplet separator.
9. WRU specific cost from Cataldi [13] for a dry air-cooling system, including a lamella flue gas condenser, air-cooled heat rejecters, water storage, plume prevention (diluting flue gas outlet with warm air from blast air coolers) and the water treatment process. Installed cost.

Table 3 Assumptions for the CoE analysis

Interest	6%
Amortisation Period	20 years
Fixed costs	2% of fixed capital/y
Variable costs	0.8 USD/MWh-fuel
Fuel costs	10 USD/MWh-fuel
Operating hours	6000 h/y

Results and Discussion

Heat Recovery Characteristics of the HGT-IC Cycles. Before analyzing the response of the HGT cycles to changes in pressure and the firing temperature, it is important to appreciate the nature of each cycle's heat recovery system. Figure 2 presents composite curves produced from the simulations at 30 bar and a firing temperature of 1350°C. These curves show the amount and nature of the heat transferred in the cycle, including the aftercooler and flue gas. Composite curves are obtained through adding the $m \cdot c_p$ values of all the heat sources or heat sinks for a temperature region and multiplying the sum by the temperature change in that region.

A striking aspect of Fig. 3(*c*) is the close match between the cold and hot composite curves for the FEvGT-IC. This indicates a thermodynamically sound heat recovery system with low levels of irreversibilities. The intercooler allows a low compressor outlet temperature (COT), which lowers the amount of high-temperature heat transfer in the aftercooler compared to the non-intercooled FEvGT cycle (Fig. 5 in Part I). Instead, most of this heat is taken out at a lower temperature in the intercooler. In total, compared to the FEvGT, the amount of heat transferred in the FEvGT-IC drops 3 MW. Approximately a third of the total heat transfer occurs in the gas–gas recuperator. Furthermore, this heat transfer has a small average temperature driving force; thus large heat exchange areas will still be needed for this cycle.

Unlike the nonintercooled case, where the PEvGT cycle has 35% less heat transfer than the FEvGT cycle, the PEvGT-IC cycle has a similar amount of heat transfer (only 6% less) to the FEvGT-IC cycle [Fig. 3(*b*)]. However, due to the presence of the boiler, the PEvGT-IC has 33% less gas–gas heat transfer than in the FEvGT-IC that, moreover, is carried out with a much higher mean temperature driving force. This fact points to a lower dependency on refined gas–gas heat exchange technology and an intrinsically lower total heat exchange area and cost. The high temperature heat not used for gas–gas heating is instead used for boiling, explaining the high humidity of the PEvGT-IC. Resulting from the high humidity is a larger release of energy from the cycle than the FEvGT-IC, despite the lower $T_{FGC,in}$. The PEvGT-IC composite curves are well matched for water heating where heat exchange properties are favorable.

In Fig. 3(*a*), the spray-intercooled STIG cycle is shown. The intercooling process cannot be shown as no heat is rejected from the compressor; it is just used to evaporate a small amount of water. The trends shown in Fig. 3(*a*) were explained in Part I. The flue gas leaves at high temperatures (149°C) and the intercooling process is not significantly beneficial to the cycle. As both the PEvGT-IC and FEvGT-IC can utilize nearly all the useful flue gas and intercooler energy, they have higher performance levels.

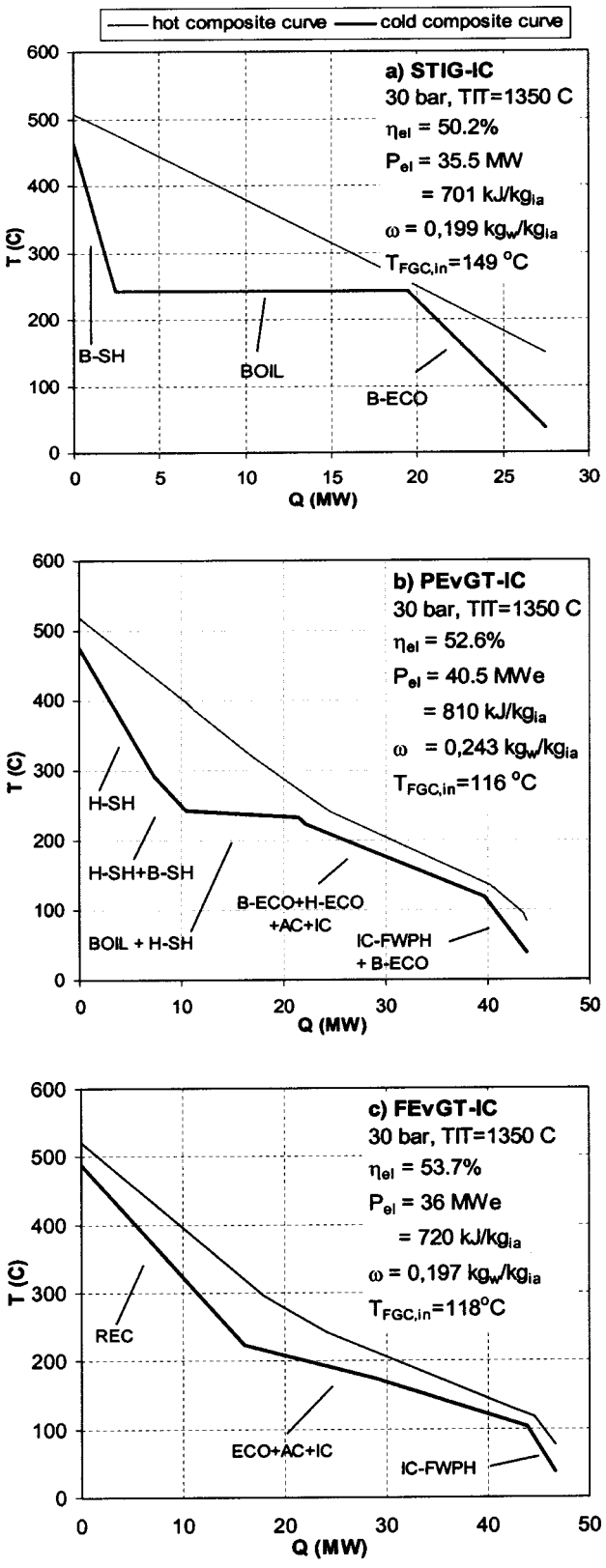

Fig. 3 Composite curves of the intercooled HGT cycles

Performance Maps of the HGT-IC Cycles. Figure 4 presents the performance map of the intercooled HGT cycles, with the isobars [constant compressor discharge pressure (CDP)] and isotherms (constant firing temperature) outlining an area in the map for each type of cycle. The intercooled HGT cycles were examined at three working pressures (20, 30, and 40 bar), and three firing temperatures (1200, 1350, and 1500°C). Only the power maximized PevGT-IC cycles are considered (see the next section for details on this choice). It is useful to keep in mind the example composite curves in Fig. 3 when interpreting the performance map.

Compared to the non-intercooled cycles (Fig. 7, Part I), the intercooled HGT cycle surfaces are more distinct in relation to

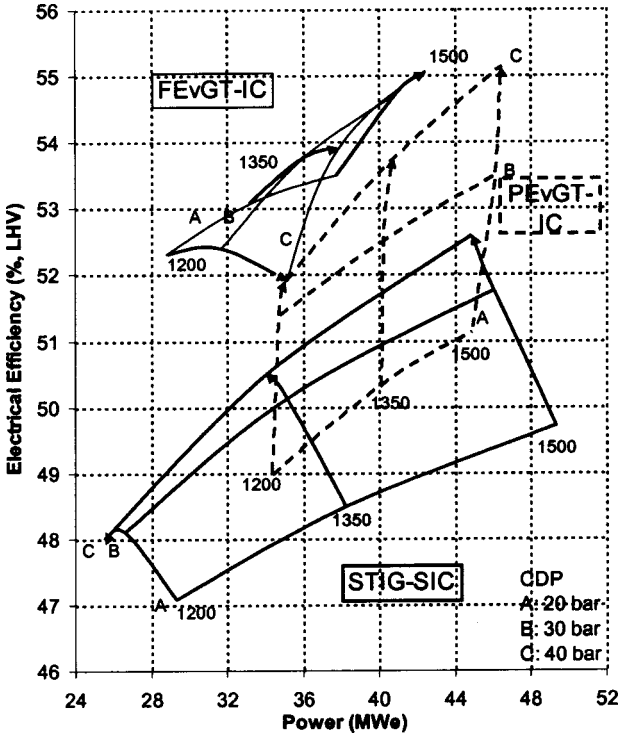

Fig. 4 Performance map of the intercooled HGT cycles

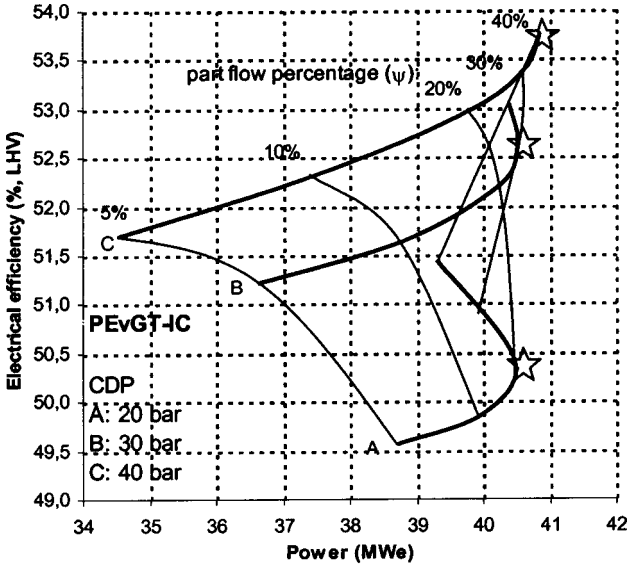

Fig. 5 Performance map of the intercooled PEvGT cycle with varying working pressures and part-flow ratios (constant firing temperature of 1350°C)

one another. Intercooling lifts the FEvGT cycle's efficiency significantly (cf. Fig. 8, Part I) and now has higher efficiencies than the other HGT cycles for most configurations. The PEvGT-IC also benefits in efficiency but more in power output. Similar to Part I, the STIG-SIC cycle has the lowest efficiencies but reaches among the highest power outputs. For all three HGT cycles, the interplay of cycle factors described in Part I are still valid in Fig. 4 with the difference being that the compressor outlet is always cooler then the turbine outlet due to intercooling.

The intercooled FEvGT cycle surface is characterized by bunched isotherms and isobars, occupying a region of high electrical efficiencies. Like the non-intercooled FEvGT, increases in pressure give mostly increases in the power outputs with an efficiency maximum. The location of the maximum depends heavily on the turbine outlet temperature and thereby lies at higher TITs at higher working pressures. Increases in the TIT along the isobars can result in significant efficiency gains if the CDP is over 20 bar.

The PEvGT-IC surface in Fig. 4 occupies a position of high power outputs at good to high efficiencies. Unlike the FEvGT-IC surface, the PEvGT-IC isobars are well spaced, indicating very good efficiency increases with pressure increases. As the isotherms extend nearly vertically, this efficiency increase occurs with little change in the power output. When the TIT increases at constant pressure, advances in both efficiency and power output are made. Consequently, the PEvGT-IC is well suited to simultaneous or separate increases in pressure and TIT. At a high CDP and TIT, the PEvGT-IC reaches the same efficiencies of the FEvGT-IC with a higher power output.

The STIG-SIC cycle surface covers a larger region of power outputs than the evaporative cycles and sits at lower efficiencies than the evaporative cycles by 2.5%–4% points. The lowest power outputs are lower than either the FEvGT-IC or PEvGT-IC while the highest outputs are equivalent to the PEvGT-IC. This reflects the dependency of water vapor generation in the HRSG on the turbine outlet temperature. Large gains in efficiency are made going from low to moderate pressures, but the marginal effect of increasing the pressure decreases once the compressor outlet temperature reaches its maximum of around 480°C. The isotherms show that increasing the working pressure will reduce the power output, unlike the PEvGT-IC or FEvGT-IC, a trend explained in Part I. Similar efficiency gains in efficiency are made as the PEvGT-IC when increasing the TIT.

Judging from Fig. 4, the PEvGT-IC shows the best potential for future intercooled cycles at very high pressures and firing temperatures. Further increases in pressure beyond 40 bars will be examined in future work.

Optimizing the Intercooled PEvGT Cycle. Figure 5 shows the performance map of the PEvGT cycles (intercooled) at a constant firing temperature of 1350°C with varying pressures and part-flow ratios. Interestingly, the optimal part flow ratio (ψ) marked with a star in Fig. 5 and used in Fig. 4, is only a function of pressure. Hence the optimal ψ values in Fig. 5 for each working pressure may be applied to firing temperatures besides 1350°C (this is not the case in Part I).

Examining Fig. 5, it is clear that a power maximum is found for each isobar. This is in contrast to the non-intercooled PEvGT where an isobar could have an efficiency or power maximum. Furthermore, the efficiency constantly increases with increasing part-flow ratios regardless of the pressure. As intercooling always gives a compressor outlet cooler than the turbine outlet, for the studied pressures, increasing the part flow will result in a higher combustion inlet temperature and hence efficiency. Increasing the part flow also serves to lower the outlet water temperature from the humidifier. This allows more low-temperature heat recovery from the cycle, which manifests in a higher humidity and the increasing power output in Fig. 5. Countering this effect is a decrease in the amount of steam generated in the HRSG due to the increase in superheating. This creates a humidity and power maximum.

The optimal part-flow ratio for the power-maximum can be seen to increase when the CDP is raised. This is attributable to coinciding decreases in the TOT and increases in the steam pressure leading to lower steam-generation levels. Therefore more heat is-available for the humidifier at higher pressures and a larger amount of air is required to keep the humidifier water outlet temperature low and effectively utilize the heat available in the cycle.

It was found that the two processes of part-flow humidification and intercooling need to be harmonised to gain the greatest effect. As the amount of humidifier feed water and the temperature out of the tower affect the duty of the intercooler (see Fig. 2), changes in

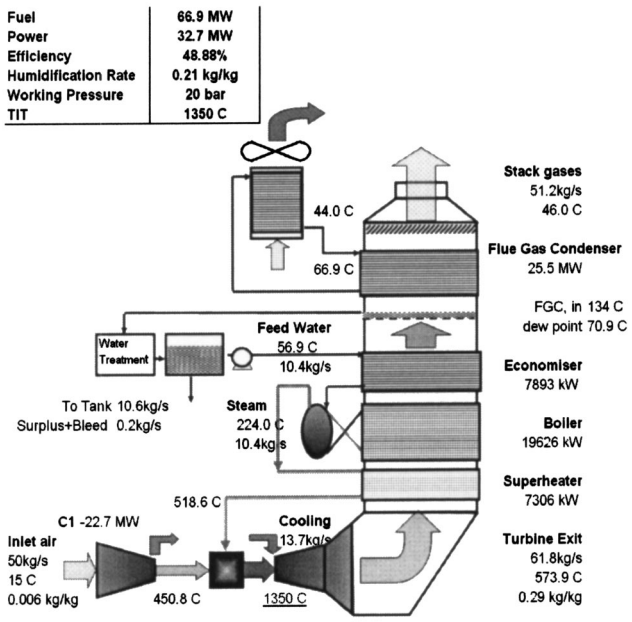

Fig. 6 Conventional STIG cycle flow sheet as used for dimensioning and costing

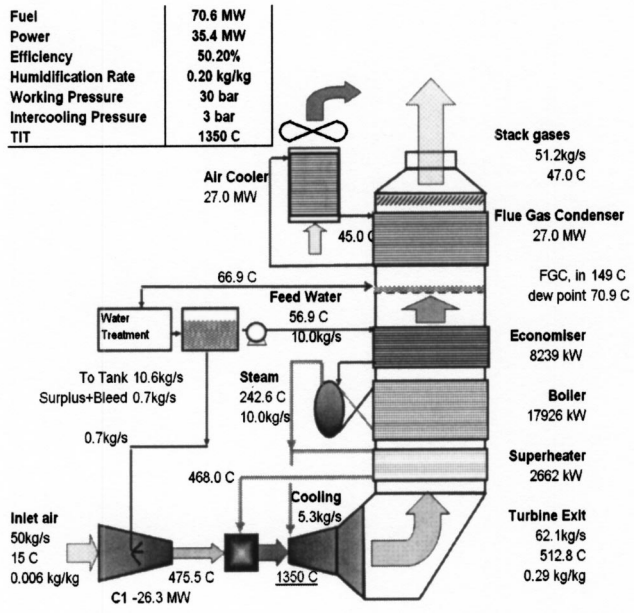

Fig. 7 Spray-intercooled, steam-cooled STIG cycle flow sheet as used for dimensioning and costing

the part flow have repercussions on the compressor work, the compressor outlet temperature, and hence cycle areas beyond flue gas heat recovery.

Economic Study of the HGT Cycles

A HGT concept for commercialization should be one that delivers a good economic performance, is technically feasible, and preferably has low development time, costs, and risks. Furthermore, the concept should show the potential to improve with time. We have chosen to limit the cycles to pressures under 30 bar and firing temperatures under 1350°C to reflect short-term technologies. One configuration of each type of HGT cycle is chosen for the intercooled and non-intercooled cycles. Furthermore, a combined cycle in the midsize range [14] as well as an air-cooled STIG cycle (data generated by the authors) is chosen as reference points. Flow sheets of the chosen cycles are shown in Figs. 2–4 in Part I and Figs. 6–9 here for the nonintercooled and intercooled HGT cycles, respectively.

Table 4 shows the HGT cycles chosen for economic analysis broken into the following sections: reference, nonintercooled, intercooled, and FEvGT-IC feasibility. The FEvGT-IC feasibility study shows what conditions must be placed on the FEvGT-IC cycle to become competitive with the other HGT cycles. Table 4 gives the configuration and performance, along with a percentage breakdown of the specific cost of the cycle components (genset, boiler circuit, humidification circuit, and water recovery unit), the investment cost index compared to the CC, and the final cost of electricity index, compared to the CC.

The first trend of note in Table 4 is that all HGT cycles have a lower CoE than the combined cycle due to their lower specific investment costs and good efficiencies. Another initial comment is that considering the very low investment costs (savings of 15%–35%), the differences in the short term CoE (3%–12%) are not particularly large. This reflects the dominating role of the variable part of the CoE, i.e., the fuel cost. The biggest investment saving is through the lack of a steam turbine. The actual specific cost ($/kW$_e$) of the humidified genset is quite stable, and therefore variations in the specific investment cost of the cycles are mostly due to fluctuations in the specific cost of the heat exchangers. The chosen length of operation (6000 h) is typical for the Nordic region and can be regarded as low from an international perspective.

The second point of interest is that the short-term HGT cycles can be broken into four groups related to their CoE performance.

1. The first group consists of the PEvGT, PEvGT-IC, STIG, and STIG-SIC cycles. These cycles return the lowest CoEs, about 88–89 on the index.

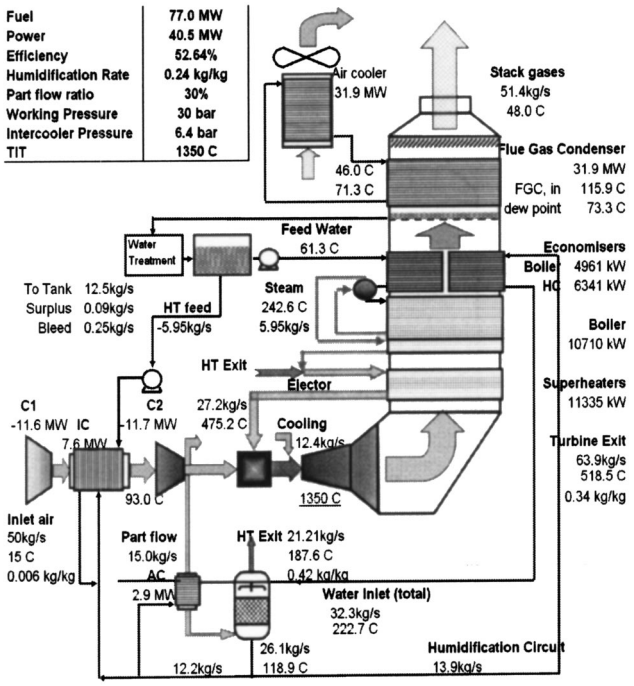

Fig. 8 PEvGT-IC cycle flow sheet as used for dimensioning and costing

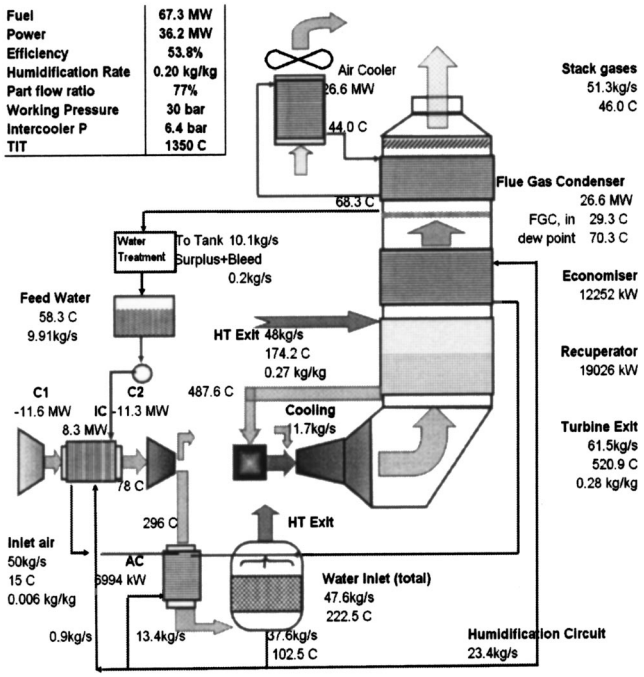

Fig. 9 FEvGT-IC cycle flow sheet as used for dimensioning and costing

2. A second group is formed by the conventional (air-cooled) STIG and the intercooled FEvGT cycle, which have a CoE index of 91.
3. The non-intercooled FEvGT is the lone HGT cycle with a CoE over 95 on the index.

Implicit in the first grouping is that intercooling marginally improves the economic performance of the STIG and PEvGT cycles but does not seem strictly necessary in any near-term PEvGT or STIG cycle. Furthermore, it is evident that the ''refined STIG cycles,'' i.e., STIG cycles complemented with steam cooling or a humidification tower, pay for their increased complexity over the conventional STIG cycle. Given the uncertainties in the costing and dimensioning data, and the small differences between the CoE of the PEvGT and STIG cycles, it is difficult to recommend one cycle over the other on economic grounds. However, the PEvGT-IC and PEvGT cycles do show a slight economic edge, which combined with the superior performance potential of the PEvGT cycle, is an important factor to consider in any decision between these cycles.

Unlike the STIG and PEvGT cycle, the FEvGT cycle requires an intercooler to approach the economic performance of the other cycles. Moreover, it is clear that recuperator prices or cycle performance must be improved for the FEvGT-IC to become competitive; the last grouping in Table 4 ''FEvGT-IC feasibility'' presents an analysis of this. The case ''Feasible FEvGT-IC'' shows that the recuperator price must be vastly reduced in order to attain a CoE equivalent to the other intercooled cycles. The recuperator cost in Table 4 is equivalent to 16 $\$/kW_{duty}$ compared to the 43 $\$/kW_{duty}$ used in the normal economic study (Table 2). In other terms, the recuperator can only cost the same as a finned-tube heat exchanger.

Another way to make the FEvGT-IC competitive is to raise its performance by decreasing the pressure drops and approach temperatures, increasing the humidification tower (HT) performance and cooling the turbine with humid air from the HT. This case is presented in the last column ''High performance FEvGT-IC'' and likens the cycle proposed by Lindquist [3]. The efficiency is raised 2% points over the base FEvGT-IC case and the power output increases 130 kJ_e/kg_{ia}. However, the heat exchangers become much larger and hence 50% more costly. Therefore the recuperator must still be 40% the cost of the original estimate, i.e., 28 $\$/kW_{duty}$ (purchase cost, see Table 2), for the cycle to be competitive. It is worth stressing that the high performance recuperator in this advanced case must fulfill demands for a higher effectiveness (96%) and a lower pressure drop (4.5%) at the same time. This is without mentioning the difficulties of recuperator operation at the higher working pressures studied in this paper. In conclusion, while the FEvGT-IC has the potential to deliver very high efficiencies, it is heavily reliant on the existence of a recuperator with a low cost, a high effectiveness, and low pressure drops. Consequently, near-term HGT cycles are more likely to be of the PEvGT or STIG configuration.

Table 4 Summary of the economic performance of the HGT cycles

	Reference Cycles		Non-intercooled HGT Cycles			Intercooled HGT Cycles			FEvGT-IC Feasiblity Study		
	CC	Conv. STIG	Steam cooled STIG	PEvGT	FEvGT	Steam cooled STIG-SIC	PEvGT-IC	FEvGT-IC	Feasible FEvGT-IC[a]	High Perfrom. FEvGT-IC[b]	Feasible High Perform FEvGT-IC[a, b]
Electrical Efficiency (%)	53	48.9	50.0	51.9	50.9	50.2	52.6	53.8	53.8	55.8	55.8
Specific Power (kJ_e/kg_{ia})	529	654	640	663	664	708	810	724	724	854	854
CDP (bar)	20	20	30	30	25	30	30	30	30	29	29
TIT (°C)	-	1350	1350	1350	1350	1350	1350	1350	1350	1400	1400
IC	N	N	N	N	N	spray	Y	Y	Y	Y	Y
ψ (part flow %)	-	-	-	20%	-	-	30%	-	-	-	-
Genset (% installed cost)	n/a	79	81	76	65	81	74	66	73	60	65
Σ BC (% installed cost)	-	8	7	7	0	7	7	0	0	0	0
Σ HC (% installed cost)	-	0	0	5	7	0	8	10	11	15	16
REC (% installed cost)	-	0	0	0	17	0	0	15	6	16	9
WRU (% installed cost)	-	13	12	12	11	12	12	9	10	9	9
Specific Investment Cost Index	100.0	65.5	63.7	69.0	85.3	62.7	69.2	80.0	72.5	83.2	77.0
CoE Index	**100.0**	**91.0**	**89.0**	**88.7**	**96.5**	**88.2**	**87.9**	**91.0**	**88.0**	**90.2**	**88.0**

a. Recuperator cost varied to attain a CoE competitive with other IC cycles, i.e. CoE index=88.
b. Dimensioning, and costing parameters constant. Performance characteristics improved as follows: water-gas approach temperature = 5 °C, $(t_{w,in}-t_{w,bp})_{HT}$=5°C, $(t_w-t_{ad})_{min,\ HT}$ = 3 °C recuperator effectiveness = 96% ΔP flue gas = 3.7%, ΔP working fluid = 3.3%, humid air cooling. Recuperator cost increase ($/$kW_{duty}$) assumed to be 20% to account for larger area

Discussion: Commercializing HGT Cycles

Despite extensive research on humidified gas turbine concepts (see Part I, Introduction), they have remained unpopular with gas turbine manufacturers. Three main areas are often cited as obstacles for commercializing HGT cycles.

First, the costs associated with water consumption or water recovery have been cited as too expensive, offsetting any benefits from a decreased plant investment cost. Furthermore, water impurities may carry over to the gas turbine and endanger the turbine lifetime. Recent reports, however, have shown water self-sufficient humidified plants to be technically and economically feasible [13,15,16] while at the same time ensuring good air quality for the turbine [17]. The HGT plant costs in this article include a very capital-intensive water recovery system [13] (closed-circuit cooling with blast-air coolers), yet the cycles still have a reasonable economic edge over the combined cycle.

Second, the recuperator is seen as a large risk for evaporative cycles on top of the risk of designing a new gas turbine. An important result of this study, however, has been to identify the PEvGT configuration as the most cost-effective way to obtain the heat recovery advantages of the humidification tower without the risk of developing a high-performance recuperator.

The third and most crucial area is the investment and risk involved for manufacturers to develop a new gas turbine especially designed for humidified operation. Results produced by the EvGT consortium, including this article, point to the advantages of HGT cycles when a new gas turbine designed for humidified operation is used. However, most design efforts in industry concentrate on adapting existing gas turbines to humid operation in order to minimize costs and risk. The result of this approach is basically to compromise the core advantage of humidified operation (a large expander flow with a small compressor flow) and the adapted gas turbine is rarely competitive. To justify the risks involved in developing a humidified gas turbine, manufacturers must be convinced a strong market exists for the product, something beyond the scope of this article.

Conclusions

By examining the thermodynamic performance of the intercooled HGT cycles, the following could be concluded:

- Both the PEvGT-IC and FEvGT-IC are well suited to conventional intercooling. Both cycles' efficiencies and power outputs benefit, but intercooling favors the FEvGT cycle more in terms of efficiency and the PEvGT more in terms of power output.
- The STIG cycle utilizes spray-intercooling, which allows higher pressures but only a marginal performance improvement over a non-intercooled STIG cycle.
- With the introduction of the intercooler, the FEvGT-IC concept appears to have a performance edge on the PEvGT-IC concept for most conventional core engine designs. The PEvGT-IC, however, responds best to increases in pressure and has the highest potential performance of the HGT cycles. The STIG-SIC is usually 2.5%–4% points below the evaporative cycles.
- Due to lower amounts of gas-gas heat exchange at higher driving forces, the PEvGT-IC will intrinsically have less heat exchange area than the FEvGT-IC. The STIG-SIC has only half the amount of heat transfer of these two cycles.
- Higher part-flow ratios are required for the PEvGT-IC than the PEvGT to accommodate the extra energy transfer from the intercooler. The optimal part flow ratio for the PEvGT-IC is constant with constant CDP.

From an economic analysis that compared both intercooled and non-intercooled HGT cycles to the combined cycle, the following may be concluded:

- All near-term HGT cycles were found to have lower specific investment costs (15%–35%) and CoE (3%–12%) than the CC.
- Given their low investment costs, good performances, and relatively conventional components, the PEvGT and the steam-cooled STIG cycle seems the most promising advanced HGT cycles for near-term commercialization. The PEvGT cycle has a greater performance potential for future development than the STIG cycle, both in intercooled and non-intercooled configurations.
- An intercooler does not significantly improve the economic performance of the PEvGT or STIG cycle at working pressures under 30 bars. Hence intercooling is unnecessary for a near-term cycle.
- To be competitive with the boiler-based HGT cycles, the full-flow EvGT cycle must be intercooled and requires the development of a recuperator that is 40%–60% of the current estimated price. The non-intercooled full-flow EvGT is the least cost-effective HGT cycle studied.

Acknowledgments

The authors would like to thank the financial and technical support of the EvGT Consortium members during this work: the Swedish Energy Agency, Vattenfall AB, Sydkraft AB, Energy E2, ALSTOM Power AB, and Elforsk.

Nomenclature

Cycle Abbreviations

CC = Combined cycle
EvGT = Evaporative gas turbine
FEvGT = Full-flow evaporative gas turbine
HGT = Humidified gas turbine
ICR = Intercooled recuperated gas turbine
PEvGT = Part-flow evaporative gas turbine
STIG = Steam-injected gas turbine

Heat Exchanger Abbreviations

AC = Aftercooler
BC = Boiler circuit
B-ECO = Boiler circuit economiser
B-SH = Boiler circuit superheater
FGC = Flue gas condenser
HC = Humidification circuit
H-ECO = Humidification circuit economiser
H-FWPH = Humidification circuit feed water preheater
H-SH = Humid air superheater
HT = Humidification tower
IC = Intercooler
REC = Recuperator
WRU = Water recovery unit

Parameters

CDP = Compressor discharge pressure, bar
CoE = Cost of electricity, $\$/MWh_e$
COT = Compressor outlet temperature, °C
LHV = Lower heating value
P_{el} = Power output, MW_e (net)
t = Temperature
TIT = Turbine inlet temperature (combustor outlet temperature), °C
TOT = Turbine outlet temperature, °C
η_{el} = Cycle electrical efficiency, % LHV
ω = Cycle humidification rate, $kg_{H2O}/kg_{intake\ air}$
ψ = Part-flow ratio, per kg compressor intake air

Subscripts

ad = adiabatic
bp = boiling point
i.a. = intake air
w = water

References

[1] Rao, A. D., and Joiner, J. R., 1990, ''A Technical and Economic Evaluation of the Humid Air Turbine Cycle,'' Proc. 7th Annual International Pittsburgh Coal Conference, September 10–14.

[2] Åagren, N. D., 2000, ''Advanced Gas Turbine Cycles With Water-Air Mixtures as Working Fluid,'' Ph.D. Thesis, Royal Institute of Technology, Dept of Chemical Engineering/Energy Processes, Stockholm, Sweden. ISSN 1104-3266 ISRN KTH/KET/R-120-SE.

[3] Lindquist, T., 2002, ''Evaluation, Experience and Potential of Gas Turbine Based Cycles With Humidification,'' Ph.D. Thesis, Lund University, Dept. of Heat and Power Engineering, Lund, Sweden. ISBN 91-628-5330-9.

[4] Rydstrand, M., Westermark, M., and Bartlett, M., 2002, ''An Analysis of the Efficiency and Economy of Humidified Gas Turbines in District Heating Applications'', Proc. ECOS 2002, Vol. II, pp. 695–703.

[5] Poggio, A., and Strasser, A., 1996, ''CHENG Cycle Cogeneration System Application and Experience of Exhaust Gas Condensing,'' Proc. POWERGEN '96, June 26–28, Budapest.

[6] Nilsson, P. A., ed., 1996, ''EvGT—Evaporative Gas Turbine—Block 3'', Technical report, Lund Institute of Technology, Dept. of Heat and Power Technology, Lund, Sweden.

[7] Kellerer, A., and Spangenberg, C., 1998, ''Operating Experience With a Cheng-Cycle Unit,'' VGB PowerTech, November 1998, pp. 16–22.

[8] Westermark, M., 1996, ''Method and Device for Generation of Mechanical Work and, if Desired, Heat in an Evaporative Gas Turbine Process,'' International Patent Application No. PCT/SE96/00936.

[9] Dalili, F., and Westermark, M., 2002, ''Experimental Study on a Packed Bed Humidifier in an Evaporative Gas Turbine,'' ASME Paper No. IJPGC2002-26106.

[10] Coulson, J. M., and Richardson, J. F., 1996, *An Introduction to Chemical Engineering Design*, Vol. 6 of *Chemical Engineering*, Butterworth-Heinemann, Stoneham, MA.

[11] Wahlberg, P.-E., 2001, ''Design and Comparison Between a Finned Tubed Humidifier and a Packed-Bed Humidifier Concerning Performance and Costs,'' Masters Thesis, Royal Institute of Technology, Dept. of Chemical Engineering and Technology/Energy Processes, Stockholm, SE-10044, Sweden.

[12] Hewitt, G. F., Shires, G. L., and Bott, T. R., 1994, *Process Heat Transfer*, CRC Press, Boca Raton, FL, pp. 220–229.

[13] Cataldi, G., 2001, ''Dry Air-Cooling for Water Recovery in Humidified Gas Turbine Cycles,'' Masters thesis, Royal Institute of Technology, Department of Chemical Engineering and Technology/Energy Processes, Stockholm, SE-10044, Sweden.

[14] Nilsson, K.-J., ALSTOM Power AB, Sweden.

[15] Åagren, N. D., Westermark, M. O., Bartlett, M. A., and Lindquist, T., 2000, ''First Experiments on an Evaporative Gas Turbine Pilot Plant—Water Circuit Chemistry and Humidification Evaluation,'' ASME Paper No. 2000-GT-168.

[16] dePaepe, M., and Dick, E., 1999, ''Water Recovery in Steam-Injected Gas Turbines: A Technological and Economical Analysis,'' European J. Mech. Environ. Eng., **44**, pp. 195–204.

[17] Bartlett, M., and Westermark, M., 2001, ''Experimental Evaluation of Air Filters and Metal Ion Migration in Evaporative Gas Turbines,'' ASME Paper No. JPGC2001/PWR-19119.

[18] Bartlett, M. A., and Westermark, M. O., 2004, ''A Study of Humidified Gas Turbines for Short-Term Realization in Midsized Power Generation—Part I: Nonintercooled Cycle Analysis,'' J. Eng. Gas Turbines Power, **127**, pp. 91–99.

The Effect of Turbine Blade Cooling on the Cycle Efficiency of Gas Turbine Power Cycles

R. C. Wilcock

J. B. Young
e-mail: jby@eng.cam.ac.uk

J. H. Horlock

Hopkinson Laboratory,
Engineering Department,
Cambridge University,
Trumpington Street,
Cambridge CB2 1PZ, UK

A thermodynamic cycle analysis computer code for the performance prediction of cooled gas turbines has been used to calculate the efficiency of plants with varying combustor outlet temperature, compressor pressure ratio, and turbomachinery polytropic efficiency. It is shown that the polytropic efficiency exerts a major influence on the optimum operating point of cooled gas turbines: for moderate turbomachinery efficiency the search for enhanced combustor outlet temperature is shown to be logical, but for high turbomachinery efficiency this is not necessarily so. The sensitivity of the cycle efficiency to variation in the parameters determining the cooling flow rates is also examined. While increases in allowable blade metal temperature and film cooling effectiveness are more beneficial than improvements in other parameters, neither is as important as increase in turbomachinery aerodynamic efficiency. [DOI: 10.1115/1.1805549]

1 Introduction

The single most important factor responsible for the steady increase in gas turbine efficiency over the last half century has been the increase in combustor outlet temperature T_{cot}. Advances have been made possible by remarkable developments in both blade materials and cooling technology. So successful has this development program proved that few engineers would challenge the principle that the surest way to raise the efficiency of the next generation of machines is to increase the top temperature.

Nevertheless, MacArthur [1] and Horlock et al. [2] have recently argued that the efficiency benefits of higher temperatures may be more than offset by the increased losses associated with the cooling flow rates required. Using a computer code in which real gas effects were included, Horlock et al. [2] presented calculations of the variation of cycle efficiency with T_{cot} at various fixed pressure ratios. These displayed efficiency maxima at temperatures not significantly higher than those of machines currently in operation.

Surprisingly, the calculations gave similar maxima even without turbine cooling. A detailed study was therefore made of gas properties, as a limit on performance in the absence of cooling, by Wilcock et al. [3]. This work focused on the effects of increased water content in the combustion products at higher fuel/air ratios leading to higher specific heat capacities c_p and c_v, but a lower ratio γ. It was shown that these real gas effects are responsible for the peaks in cycle efficiency with T_{cot} well below the stoichiometric limit.

This paper presents more comprehensive calculations of gas turbine performance using an improved code. Cycle efficiencies with and without turbine cooling are compared for a range of turbomachinery efficiencies. The calculations provide an overview, which is lacking in less general studies, and lead to conclusions which are of considerable importance for the gas turbine designer.

2 Cycle Analysis Computer Code

The cycle analysis computer code is based on the theory of Young and Wilcock [4,5] and models a simple-cycle industrial gas turbine with cooling as shown in Fig. 1. The main parameters defining the cycle are the pressure ratio r_p, the combustor outlet temperature T_{cot}, and the compressor and turbine polytropic efficiencies $\eta_{\text{poly},C}$ and $\eta_{\text{poly},T}$. The latter refers to an uncooled turbine, the cooling losses being estimated separately as described below.

The working fluid is assumed to be a mixture of the four semi-perfect gases N_2, O_2, CO_2, and H_2O. Semi-perfect implies that the specific heat capacities depend on temperature but not pressure. They were represented by polynomial curve fits to the data in the JANAF tables (Chase et al. [6]). Combustion for a given fuel was modeled in the usual way using enthalpies and entropies of formation also taken from the JANAF tables.

As shown in Fig. 2, the cooled turbine is divided into stages, each stator and rotor being treated separately. In order to avoid specifying the blade geometry, the relative total temperature at rotor inlet is estimated from a given stage loading coefficient, as described in Ref. [5]. Coolant from the compressor enters the internal passages of the blade where it receives heat from the mainstream flow after conduction through the thermal barrier coating (if present) and the blade metal. A special treatment for rotating blades is described in Ref. [5]. For film-cooled blades, the coolant flows over the blade surface before mixing out with the mainstream flow. Mixing is assumed to be complete at entry to the next blade row.

Full details of the theory are given in Ref. [5] but it will be evident that, in order to fix the thermodynamic state downstream of a blade row, it is necessary to know, not only the cooling flow rate, but also the rate of entropy creation (over and above the basic uncooled loss represented by $\eta_{\text{poly},T}$). These crucial aspects of the procedure are now discussed.

2.1 Prediction of the Cooling Flow Rates. The cooling flow rates were estimated using the method of Holland and Thake [7], modified to allow for the temperature variations across the metal and thermal barrier coating (TBC). The Appendix provides a description of the method, and full details can be found in Ref. [5]. The procedure models both convection and film cooling, and is particularly attractive because the cooling flow fraction ψ (the ratio of the coolant mass flowrate m_c to the mainstream mass flow rate m_g) is expressed in terms of just six parameters [see Eqs. (A2)]. These are, ε_0 (blade cooling effectiveness), K_{cool} (cooling flow factor), η_{int} (internal cooling efficiency), ε_f (film cooling effectiveness), Bi_{met} (metal Biot number), and Bi_{tbc} (TBC Biot number). Of these, ε_0 is fully specified by the gas and coolant inlet temperatures, and the allowable blade metal temperature. The remaining five parameters are specified as input data. Table 1

Contributed by the Power Division of THE AMERICAN SOCIETY OF MECHANICAL ENGINEERS for publication in the ASME JOURNAL OF ENGINEERING FOR GAS TURBINES AND POWER. Manuscript received by the Power Division July 10, 2003; final revision received September 23, 2003. Editor: L. S. Langston.

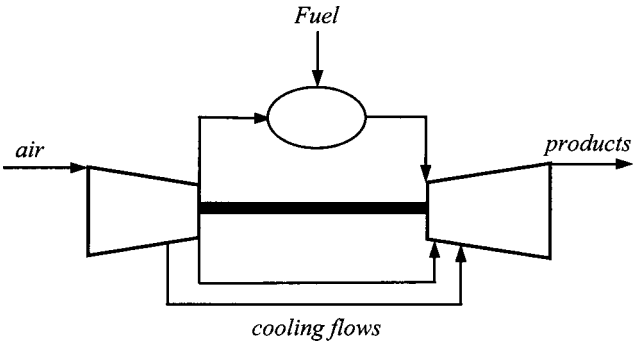

Fig. 1 Schematic diagram of simple-cycle cooled industrial gas turbine

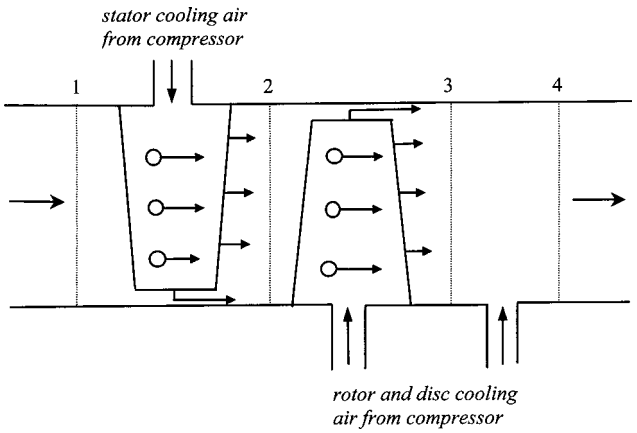

Fig. 2 Schematic diagram of a cooled turbine stage. Complete mixing is assumed at planes 1, 2, 3, and 4.

Table 1 Parameter values for different levels of aeroderivative cooling technology

Cooling Technology	K_{cool}	η_{int}	ε_f	Bi_{met}	Bi_{tbc}
Current	0.045	0.70	0.40	0.15	0.30
Advanced	0.045	0.75	0.45	0.15	0.40
Super-advanced	0.045	0.80	0.50	0.15	0.50

lists some typical values for current aeroderivative cooling technology and for two advanced technologies which might be achievable within the next few years.

With the cooling flow fraction known, application of the steady-flow energy equation gives the values of the various temperatures introduced in the Appendix and also the specific total enthalpy of the mixed-out flow downstream of the blade row.

2.2 Estimation of the Cooling Irreversibilities. The irreversible entropy creation is calculated as described by Young and Wilcock [5]. In this approach, the total irreversibility is divided into an ''uncooled loss'' and various ''cooling losses.'' The uncooled loss refers to the profile, secondary, and tip-leakage losses in an uncooled expansion and is obtained from a given stage ''uncooled'' polytropic efficiency $\eta_{poly,T}$. A major assumption is that the uncooled loss is unchanged in the presence of cooling flows. Additional entropy creation results from the following processes, depicted in Fig. 3:

i. Heat transfer from the mainstream flow to the blade outer surface
ii. Heat transfer through the thermal barrier coating if present
iii. Heat transfer through the blade metal
iv. Heat transfer from the blade inner surface to the coolant
v. Frictional pressure loss between compressor offtake and coolant injection
vi. Thermal mixing (i.e., the turbulent mixing process wherein the injected coolant and mainstream static temperatures equilibrate)
vii. Kinetic energy dissipation (i.e., the turbulent mixing process wherein the injected coolant and mainstream flow velocities equilibrate)

Reference [5] gives model expressions for the entropy production rate in each of these processes and the Appendix provides a brief description and statement of the parameters which need to be specified. Once the entropy creation terms are known, the mixed-out entropy downstream of the blade row can be found. Knowing the total enthalpy and entropy at exit to each stage, the cycle efficiency and all other quantities can be determined.

It is not essential to express the losses in terms of the entropy created. Horlock et al. [2], for example, use a similar mixing calculation to estimate the mainstream total pressure downstream of the coolant injection, and this provides equivalent information for fixing the thermodynamic state. The advantage of working in terms of entropy, however, is that the source and magnitude of each irreversibility is well defined. The effect of changes in the cooling parameters can then be assessed at a local as well as an overall level.

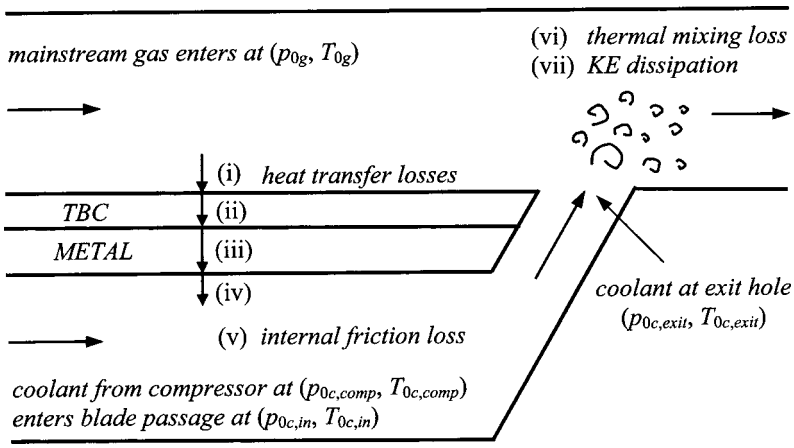

Fig. 3 Schematic diagram illustrating the cooling irreversibilities

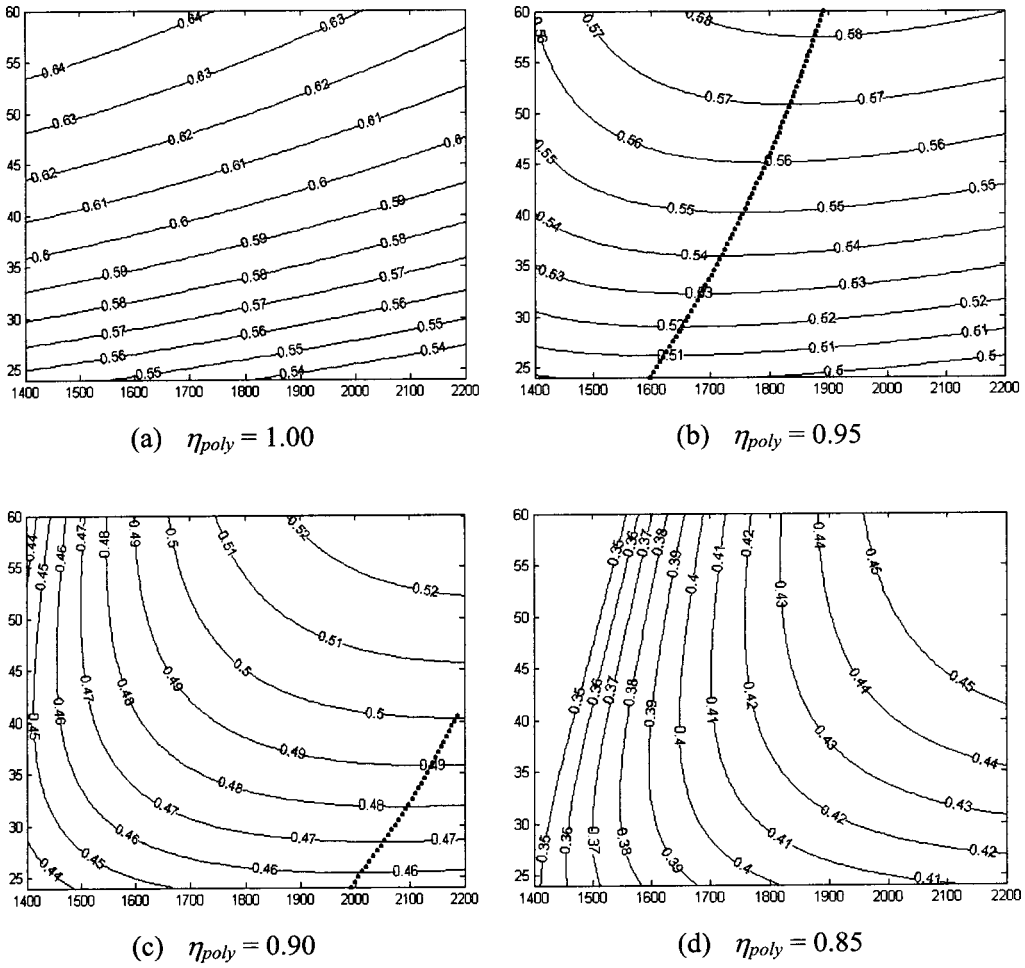

Fig. 4 Uncooled GT with $\eta_{poly,C} = \eta_{poly,T} = \eta_{poly}$. Contours of constant cycle efficiency η_{cyc} with contour interval 0.01. Combustor outlet temperature T_{cot}=1400–2200 K on abscissa, compressor pressure ratio r_p=24–60 on ordinate. Dotted lines are loci of $T_{cot,opt}$ (T_{cot} for maximum η_{cyc} at constant r_p).

3 Cycle Calculations Without Cooling

A set of ''real gas'' computer calculations for an uncooled turbine was described in Ref. [3]. The calculations showed how varying composition and specific heat capacity result in the occurrence (at constant pressure ratio) of a maximum cycle efficiency at temperatures well below stoichiometric. A mathematical analysis of this behavior was given in Ref. [3] and is not repeated here. A brief description of the results is appropriate, however, because this high-temperature real gas behavior represents the limiting case of zero-cooling flow rate.

For the calculations, the air entering the compressor was assumed to be at a temperature of 25 °C and a pressure of 1 atm. For convenience, the compressor and turbine polytropic efficiencies were taken to be equal, $\eta_{poly,C} = \eta_{poly,T} = \eta_{poly}$. The fuel was assumed to be supplied at 25 °C and combustor pressure, and had the composition of methane with LHV 50 MJ/kg. A 4% combustor pressure loss was assumed for all calculations, but pressure losses in the inlet and outlet ducts were neglected. Because of these and other minor approximations, the calculated efficiencies are a little higher than might be expected, and attention should be directed at changes in efficiency rather than absolute values.

Contour plots of cycle efficiency η_{cyc} on axes of combustor outlet temperature T_{cot} and pressure ratio r_p are presented in Fig. 4. Figure 4(*a*) refers to the case when $\eta_{poly} = 1.0$ (reversible turbomachinery). An ideal Joule-cycle analysis with constant specific heat capacities would give straight horizontal contour lines because η_{cyc} would be a function of r_p only, independent of T_{cot}. The inclusion of real gas effects in Fig. 4(*a*) results in an anticlockwise rotation of the contours, showing that η_{cyc} would actually decrease with increasing T_{cot} at fixed r_p. Thus, although the turbine work output increases with T_{cot}, this is more than offset by an increase in fuel/air ratio.

Figure 4(*b*) shows contours of constant η_{cyc} for turbomachinery with $\eta_{poly} = 0.95$. With respect to Fig. 4(*a*), the contours have rotated clockwise and have moved toward the bottom left of the diagram. This results in η_{cyc} passing through a maximum with increasing T_{cot} at fixed r_p. The locus of these maxima is marked by the dotted line, and it can be seen that the ''optimum value'' $T_{cot,opt}$ increases with pressure ratio. For $\eta_{poly} = 0.9$, Fig. 4(*c*) shows that the clockwise rotation and movement of the contours is enhanced and the locus of $T_{cot,opt}$ has migrated to higher temperatures. Finally, for $\eta_{poly} = 0.85$, Fig. 4(*d*) shows that, for *any* fixed pressure ratio, η_{cyc} increases monotonically with T_{cot} and does not display a maximum.

These calculations show that, for a gas turbine requiring no cooling, it would only be at low polytropic efficiency that a case could be made for continually increasing T_{cot} (at constant r_p) as a means of increasing the cycle efficiency. Indeed, for an uncooled plant operating at specified r_p, T_{cot}, and η_{poly}, the optimum design path for increasing η_{cyc} is in a direction normal to the contour at that point. At high η_{poly} this may, surprisingly, involve decreasing T_{cot} while increasing r_p. These findings are very important.

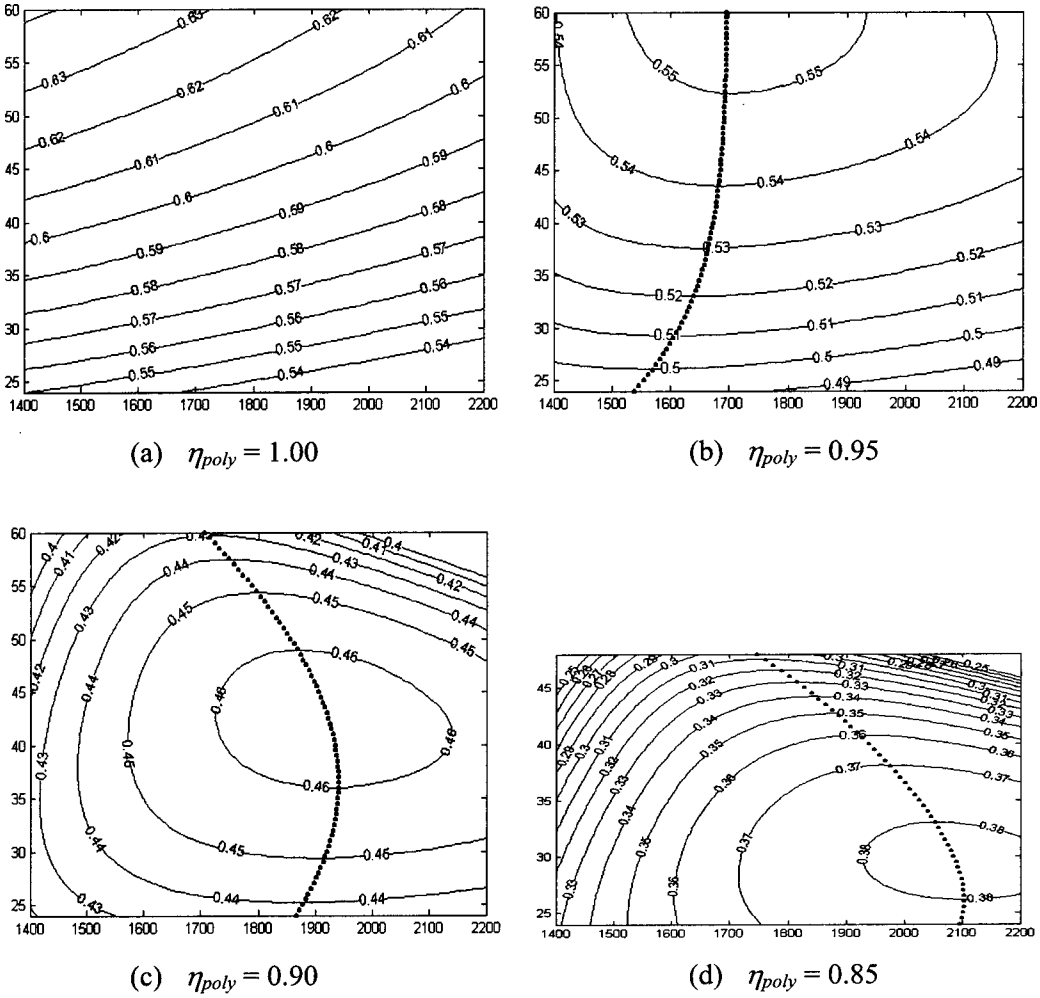

Fig. 5 Cooled GT with "current cooling technology" from Table 1 and $\eta_{poly,C} = \eta_{poly,T} = \eta_{poly}$ ($\eta_{poly,T}$ refers to an *uncooled* mainstream expansion). Contours of constant cycle efficiency η_{cyc} with contour interval 0.01. Combustor outlet temperature T_{cot}=1400–2200 K on abscissa, compressor pressure ratio r_p=24–60 on ordinate. Dotted lines are loci of $T_{cot,opt}$ (T_{cot} for maximum η_{cyc} at constant r_p).

4 Cycle Calculations With Current Cooling Technology

The computer code for cooled gas turbines described in Section 2 was used to calculate a set of contour plots for the four turbomachinery polytropic efficiencies exactly as in Section 3. The cooling parameters were set at a level representative of "current cooling technology" as listed in Table 1 and were maintained constant for all the calculations.

Figure 5(*a*) shows contours of η_{cyc} for a gas turbine with $\eta_{poly,C} = \eta_{poly,T} = \eta_{poly} = 1.0$. As discussed in Section 2.2, $\eta_{poly,T}$ refers to the efficiency of an uncooled turbine expansion. The actual expansion with coolant injection is not isentropic because of the entropy creation associated with the cooling losses. As with the "uncooled" plots of Fig. 4(*a*), the cycle efficiency at constant r_p decreases with increasing T_{cot}. In fact, the shape of the contours in Figs. 4(*a*) and 5(*a*) is very similar, the only real difference being in the magnitude of the efficiencies, which are lower by 0.5–1.5 percentage points in Fig. 5(*a*). Considering the magnitude of the cooling flow fractions, especially at high T_{cot} and r_p, this is a remarkably small penalty to pay for cooling the blades. The explanation will emerge below.

Figure 5(*b*) shows contours of η_{cyc} for $\eta_{poly} = 0.95$. A comparison with Fig. 4(*b*) shows a more substantial shift of the contours and a larger efficiency penalty due to cooling. It will also be noted that the locus of $T_{cot,opt}$ has shifted to lower temperatures (by 60–100 K) and there is evidence of a global maximum cycle efficiency. Although this cannot quite be observed in Fig. 4(*b*), examination into the region of higher-pressure ratios reveals a maximum of $\eta_{cyc,max} = 0.555$ at $T_{cot,max} = 1690$ K and $r_{p,max} = 63$. This combustor outlet temperature is lower than present-day aeroderivative operating temperatures.

Figure 5(*c*) shows the results with $\eta_{poly} = 0.9$. A comparison with Fig. 4(*c*) reveals substantial changes in contour pattern and efficiency level. Also, the global maximum has moved to the much higher temperature and lower pressure ratio of $T_{cot,max} = 1930$ K and $r_{p,max} = 41$ with the reduced value $\eta_{cyc,max} = 0.463$. This trend continues in Fig. 5(*d*) for $\eta_{poly} = 0.85$. The maximum cycle efficiency is now $\eta_{cyc,max} = 0.382$, and it occurs at the even higher temperature and lower pressure ratio of $T_{cot,max} = 2090$ K and $r_{p,max} = 30$.

To summarize, the cycle efficiency penalty at very high turbomachinery efficiency is surprisingly small, even at combustor outlet temperatures and pressure ratios where the cooling flow fractions are very high. As η_{poly} drops, much larger differences between cooled and uncooled operation appear, characterized by substantial changes in the cycle efficiency contour patterns and the magnitude of the cooling efficiency penalty. The changing contour pattern reveals the existence of a global maximum of η_{cyc} which migrates from low T_{cot} and high r_p at $\eta_{poly} = 0.95$ to much higher T_{cot} and lower r_p at $\eta_{poly} = 0.85$.

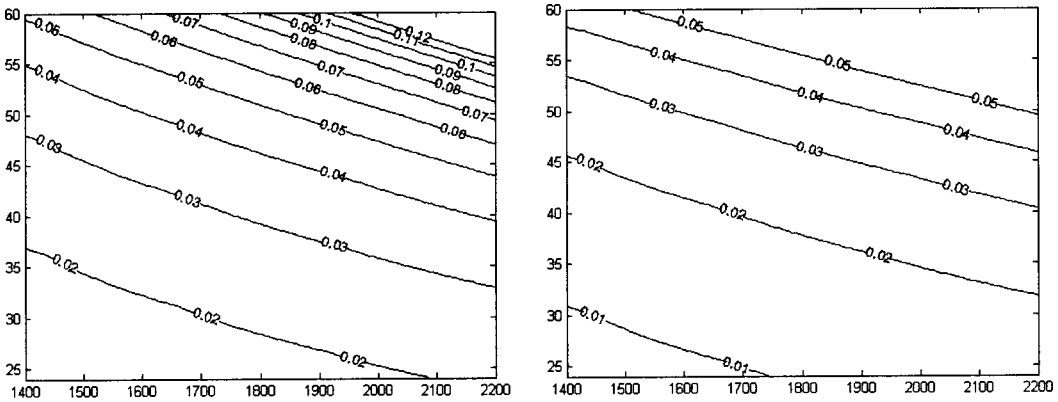

(a) Full computer calculation (b) Approximate result from Eq. (1)

Fig. 6 Cycle efficiency cooling penalty $\Delta\eta_{cyc}$ for current cooling technology and $\eta_{poly}=0.90$. Combustor outlet temperature $T_{cot}=1400-2200$ K on abscissa, compressor pressure ratio $r_p=24-60$ on ordinate. At each condition (T_{cot},r_p), the contours represent the difference in cycle efficiency between Figs. 4(*c*) and 5(*c*).

To set the calculations in context, modern aeroderivative gas turbine power plants have polytropic efficiencies around 0.9 (a little lower for the turbine) and operate on design at around $T_{cot} \approx 1750-1850$ K and $r_p \approx 30-36$. These conditions are quite close to the global maximum in Fig. 5(*c*). The implications are, (i) at current levels of turbomachinery efficiency and cooling technology, increasing T_{cot} (at any pressure ratio) would result in only a small increase (and possibly even a decrease) in cycle efficiency and, (ii) at the current level of cooling technology, an increase in η_{poly} should warrant a decrease in T_{cot}.

5 The Cycle Efficiency Penalty Due to Cooling

The cycle efficiencies for the uncooled and cooled gas turbines of Figs. 4 and 5 may be subtracted to give the cycle efficiency penalty due to cooling $\Delta\eta_{cyc}$. Figure 6(*a*) shows contours of $\Delta\eta_{cyc}$ for $\eta_{poly}=0.90$. The penalty increases both with r_p at a given T_{cot} and with T_{cot} at a given r_p. At the point of maximum η_{cyc} ($T_{cot,max}=1930$ K, $r_{p,max}=41$), the efficiency penalty is 3.7 percentage points. At higher temperatures and pressure ratios, the penalty is much greater, for example at $T_{cot}=2100$ K, $r_p=50$, the penalty is 6.5 percentage points. As the conditions become more extreme, however, the calculations become less reliable because the cooling flows are impracticably high. This can be seen in Fig. 7(*a*), which shows the calculated cooling flow fraction for the first stator row and in Fig. 7(*b*), which shows the cooling flow fraction for the whole machine (including an allowance for disc cooling).

A simple method for estimating $\Delta\eta_{cyc}$ is given by Horlock [8]. Assuming perfect gas behavior, he derived approximate expressions for $\Delta\eta_{cyc}$ in one-step, two-step, and multistep cooling processes. For two-step cooling with HP and LP cooling flow fractions ψ_{HP} and ψ_{LP}, Horlock's expression (rewritten for polytropic rather than isentropic efficiency) is

$$\Delta\eta_c=\frac{1}{(\theta-\xi_{HP})}\left[\psi_{HP}\left(\frac{\xi_{HP}}{\zeta_{HP}}-1\right)+\psi_{LP}\left(\frac{\xi_{LP}}{\zeta_{LP}}-1\right)\right], \qquad (1)$$

where $\theta=T_{cot}/T_{ambient}$. The compression temperature ratio is ξ

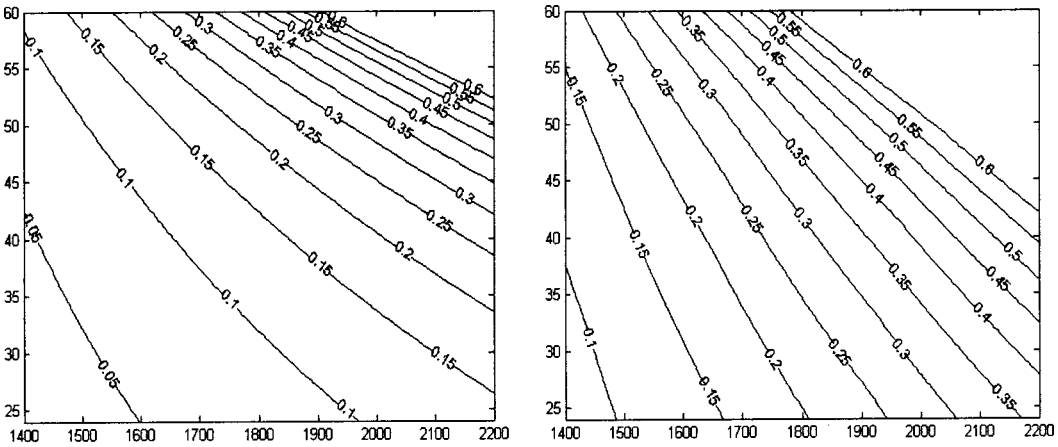

(a) First stator only (b) Complete machine with disc flows

Fig. 7 Fractional cooling flowrates ψ for current cooling technology and $\eta_{poly}=0.90$. Combustor outlet temperature $T_{cot}=1400-2200$ K on abscissa, compressor pressure ratio $r_p=24-60$ on ordinate. In (*a*) ψ is based on the exit flow from the first stator and in (*b*) on the exit flow from the final stage.

Table 2 Sensitivity of cooling flow fraction ψ (whole turbine) and cycle efficiency η_{cyc} to changes in cooling parameters at constant $T_{cot}=1800$ K, $r_p=36$, and $\eta_{poly}=0.90$

Cooling parameter	Cooling flow fraction	Cycle efficiency
Max metal temp (rotors and stators) 1175 K−(1125 K)−1075 K	0.198−(0.258)−0.355	0.465−(0.459)−0.448
Film cooling effectiveness ε_f 0.5−(0.4)−0.3	0.203−(0.258)−0.318	0.465−(0.459)−0.452
Internal cooling efficiency η_{int} 0.8−(0.7)−0.6	0.242−(0.258)−0.279	0.461−(0.459)−0.452
TBC Biot number Bi_{tbc} 0.4−(0.3)−0.2	0.244−(0.258)−0.279	0.460−(0.459)−0.457
Metal Biot number Bi_{met} 0.1−(0.15)−0.2	0.249−(0.258)−0.269	0.460−(0.459)−0.458
Combustion Pattern Factor K_{comb} 0.10−(0.15)−0.20	0.239−(0.258)−0.278	0.461−(0.459)−0.457

$=r^m$, where $m=(\gamma-1)/(\gamma\eta_{poly})$ and r is the pressure ratio over which the coolant stream is compressed (from ambient to supply). The expansion temperature ratio is $\zeta=r^n$, where $n=\eta_{poly}(\gamma-1)/\gamma$ and r is the pressure ratio over which the coolant is expanded (to ambient) after mixing in the turbine.

Horlock obtained Eq. (1) by considering the difference between the work required to compress the coolant and the work produced by its expansion after mixing with the mainstream flow. If these processes were isentropic (and the coolant behaved as a perfect gas with constant c_p and γ), then m and n would be equal and $\Delta\eta_{cyc}$ would be zero. For nonisentropic compression and expansion, m and n differ and $\Delta\eta_{cyc}$ takes positive values. It is important to appreciate, therefore, that Horlock's analysis ignores the combustor pressure loss, the entropy production due to friction in the internal blade passages, and the kinetic energy dissipation during mixing (losses (v) and (vii) in Section 2.2).

By way of illustration, the cooling flow fractions for $\eta_{poly}=0.90$, determined in Section 4, were substituted for ψ_{HP} and ψ_{LP} in Eq. (1) to produce estimates of $\Delta\eta_{cyc}$. These are plotted in Fig. 6(*b*) for comparison with the full computer calculations of Fig. 6(*a*). Because of the neglect of some sources of loss $\Delta\eta_{cyc}$ in Fig. 6(*b*) is everywhere smaller than in Fig. 6(*a*). Nevertheless, the slopes of the curves are remarkably similar showing that Horlock's result is successful in explaining part, but not all, of the efficiency penalty due to cooling.

The preceding analysis and discussion also provides an explanation for the extremely modest uncooled-to-cooled contour shifts at high turbomachinery efficiency described in Section 4. As noted above, the approximation to $\Delta\eta_{cyc}$ from Eq. (1) tends to zero as $\eta_{poly}\to 1$ because the parameters m and n become equal. Hence, with Horlock's assumptions (perfect gas behavior throughout the cycle and neglect of the coolant internal friction and kinetic energy mixing losses), η_{cyc} would be truly independent of cooling flow fraction at $\eta_{poly}=1$. Now, although the inclusion of a real gas model has a substantial effect on the *absolute* level of cycle efficiency, the *change* (uncooled-to-cooled) is not strongly dependent on the cooling flow fraction. These comparatively minor real gas effects and the further inclusion of the neglected losses are together responsible for the rather small differences in cycle efficiency observed between Figs. 4(*a*) and 5(*a*). As η_{poly} decreases, however, so m and n become significantly different and $\Delta\eta_{cyc}$ [as can be seen from Eq. (1)] not only increases, but also becomes proportional to the cooling flow fractions. This results in the much larger changes in cycle efficiency contour patterns, which are evident at low values of η_{poly}.

6 Sensitivity to Variation in the Cooling Parameters

In the preceding sections it has been shown that, as the turbomachinery efficiency decreases, the cycle efficiency of a cooled gas turbine becomes very dependent on the cooling flow fraction ψ delivered to each blade row and, therefore, on the choice of parameters involved in the estimation of ψ. The sensitivity of ψ to changes in these parameters can be investigated by differentiating the expression for ψ (Eq. (*A*2*a*) in the Appendix) to give

$$\frac{\delta\psi}{\psi}=\frac{\delta K_{cool}}{K_{cool}}-\left(\frac{\varepsilon_0-\varepsilon_f}{\varepsilon_0-C\varepsilon_f}\right)\frac{\delta\eta_{int}}{\eta_{int}}-\left[\frac{C}{\varepsilon_0-C\varepsilon_f}+\frac{Bi_{met}}{(1-\varepsilon_0)(1+B)}\right]\delta\varepsilon_f-\frac{\delta Bi_{tbc}}{(1+B)}+\left(\frac{\varepsilon_0-\varepsilon_f}{1-\varepsilon_0}\right)\frac{\delta Bi_{met}}{(1+B)}+\left[\frac{(1+\varepsilon_f)}{(\varepsilon_0-C\varepsilon_f)(1-\varepsilon_0)}+\frac{Bi_{met}}{(1-\varepsilon_0)^2(1+B)}\right]\delta\varepsilon_0 \quad (2)$$

where $B=Bi_{tbc}-Bi_{met}(\varepsilon_0-\varepsilon_f)/(1-\varepsilon_0)$ and $C=1-\eta_{int}(1-\varepsilon_0)$.

As an example, consider an HP aeroderivative stator blade operating with a combustor outlet temperature of 1800 K, a combustor pattern factor 0.15, a coolant supply temperature of 875 K, and a maximum outer surface metal temperature of 1125 K. Equations (*A*1)–(*A*7) with the "current technology" values of Table 1 ($\eta_{int}=0.7$, $\varepsilon_f=0.4$, $Bi_{met}=0.15$, $Bi_{tbc}=0.30$) then give $\varepsilon_0=0.765$ and the required cooling flow fraction for the first stator row as $\psi=0.110$. Inserting these values into Eq. (2) gives

$$\frac{\delta\psi}{\psi}=\frac{\delta K_{cool}}{K_{cool}}-1.21\delta\eta_{int}-[1.94+0.60]\delta\varepsilon_f-0.94\delta Bi_{tbc}+1.46\delta Bi_{met}+[13.83+2.55]\delta\varepsilon_0 \quad (3)$$

which shows clearly the relative effect of changing each parameter. Of particular interest is the significant contribution to the coefficient of $\delta\varepsilon_f$ from the term involving Bi_{met} (the second term in the square brackets). This indicates the importance of allowing for the metal temperature drop, an effect neglected in the original Holland and Thake theory [7].

To continue, suppose improvements in cooling technology resulted in an increase of 0.05 in each of η_{int}, ε_f, and Bi_{tbc} while maintaining K_{cool} and Bi_{met} constant. Equations (A2*a*) and (A2*b*) then show that ψ could be reduced from 0.110 to 0.088 for the same value of ε_0. Alternatively, ε_0 could be increased from 0.765 to 0.795 with ψ unchanged. For the same allowable metal temperature of 1125 K, this would correspond to an increase in T_{cot} of about 130 K.

Calculations such as these provide useful information on the sensitivity of the cooling flow rates to changes in the cooling parameters, but they give no indication of the resulting variations in cycle efficiency. It is therefore informative to present the results of a few sample calculations to illustrate the sensitivity of η_{cyc} to variations in the cooling parameters. These calculations, it should be noted, have been carried out on the assumption that the compressor and uncooled turbine polytropic efficiencies remain unchanged.

A reference point was taken at $T_{cot}=1800$ K, $r_p=36$, and $\eta_{poly}=0.90$, and this was maintained constant. All the cooling parameters except one were then also fixed and the remaining

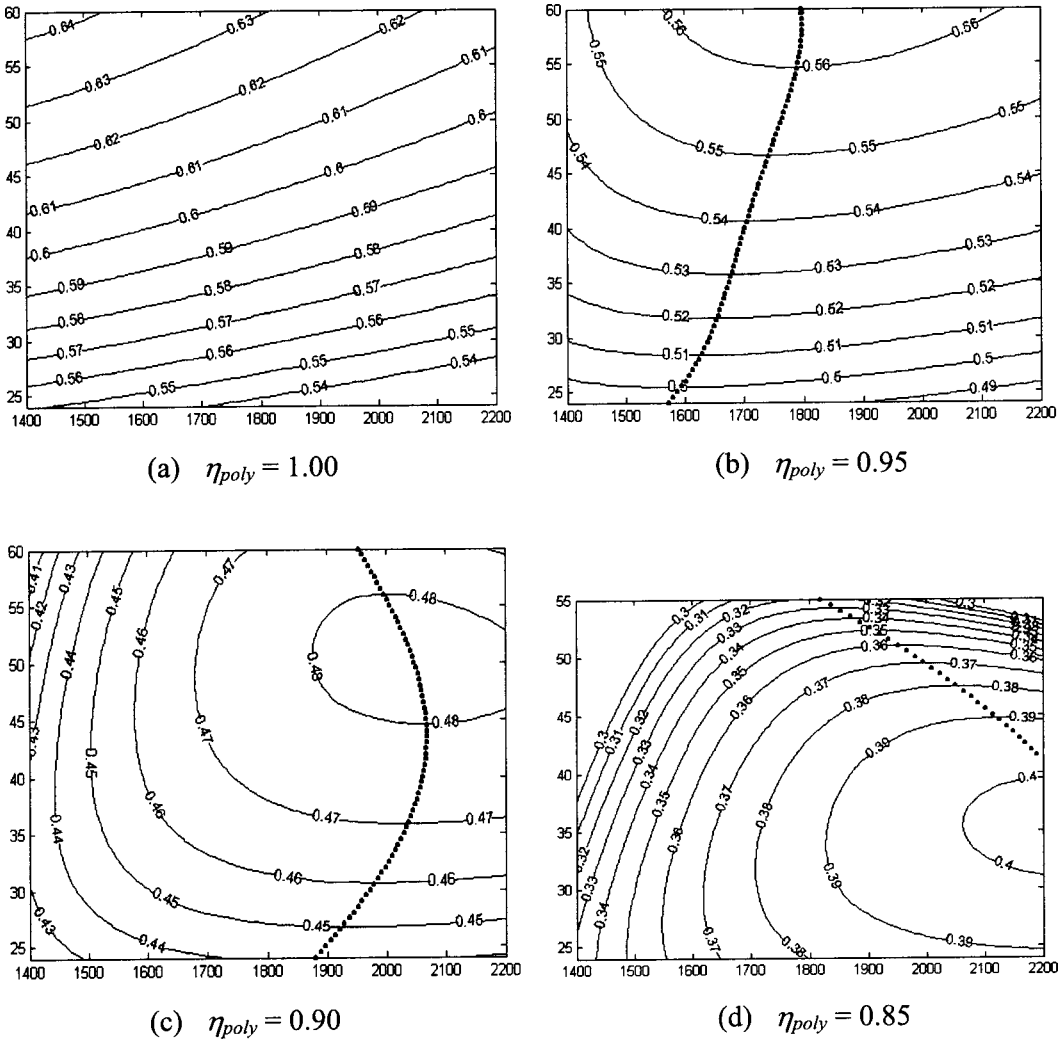

Fig. 8 Cooled GT with "advanced cooling technology" from Table 1. Contours of constant cycle efficiency η_{cyc} with contour interval 0.01. Combustor outlet temperature T_{cot}=1400–2200 K on abscissa, compressor pressure ratio r_p=24–60 on ordinate. Dotted lines are loci of $T_{cot,opt}$ (T_{cot} for maximum η_{cyc} at constant r_p).

parameter varied as shown in the left-hand column of Table 2 (with the reference value given in brackets). The corresponding range of cooling flow fractions and cycle efficiencies resulting from the variations are tabulated in the other columns.

An improvement in η_{cyc} of about 0.6 percentage point would result from an increase of 50 K in the allowable metal temperature or from an increase in film cooling effectiveness from 0.4 to 0.5. Smaller improvements in η_{cyc} would be obtained from increasing the internal cooling efficiency or TBC Biot number or decreasing the metal Biot number; the combustion pattern factor is not a very significant parameter. Although these changes in efficiency are relatively small, the changes in the cooling flow fraction are more substantial.

However, it is important to note that none of the changes in Table 2 would match the improvement resulting from an increase of one percentage point in the compressor *and* uncooled turbine polytropic efficiencies. This would increase η_{cyc} by 1.5 percentage points from 0.459 to 0.474 (the cooling flow fraction dropping from 0.258 to 0.250).

7 Cycle Calculations With Improved Technologies

7.1 Improved Cooling Technologies. In Sections 3 and 4, the contour plots of cycle efficiency for an uncooled gas turbine (Fig. 4) and for a cooled gas turbine with "current cooling technology" (Fig. 5) were examined in detail. It is now of interest to see how improvements in cooling technology result in a gradual transition from the plots of Fig. 5 to those of Fig. 4. To this end, two improved technologies, defined in Table 1, were investigated. The "advanced cooling technology" features modest improvements which might be representative of the next generation of aeroderivative machines. Typically, such improvements produce about a 25% reduction in cooling flow fraction at a given T_{cot} and r_p compared with "current technology" values. A "super-advanced cooling technology" is also defined in Table 1. These parameters provide about a 50% reduction in cooling flow fraction compared with current technology and, therefore, represent a major advance in cooling development. Figures 8 and 9 show the contour plots for the two improved technologies.

Consider first the calculations for η_{poly}=1.0. The most instructive way of examining the plots is to observe the shift of the contours through the sequence Figs. 5(*a*)→8(*a*)→9(*a*)→4(*a*) as the technology improves from its current level to the ultimate uncooled case. Clearly, only very small changes in cycle efficiency result from these improvements. This reinforces the conclusion that, at very high η_{poly}, η_{cyc} is almost independent of cooling flow fraction.

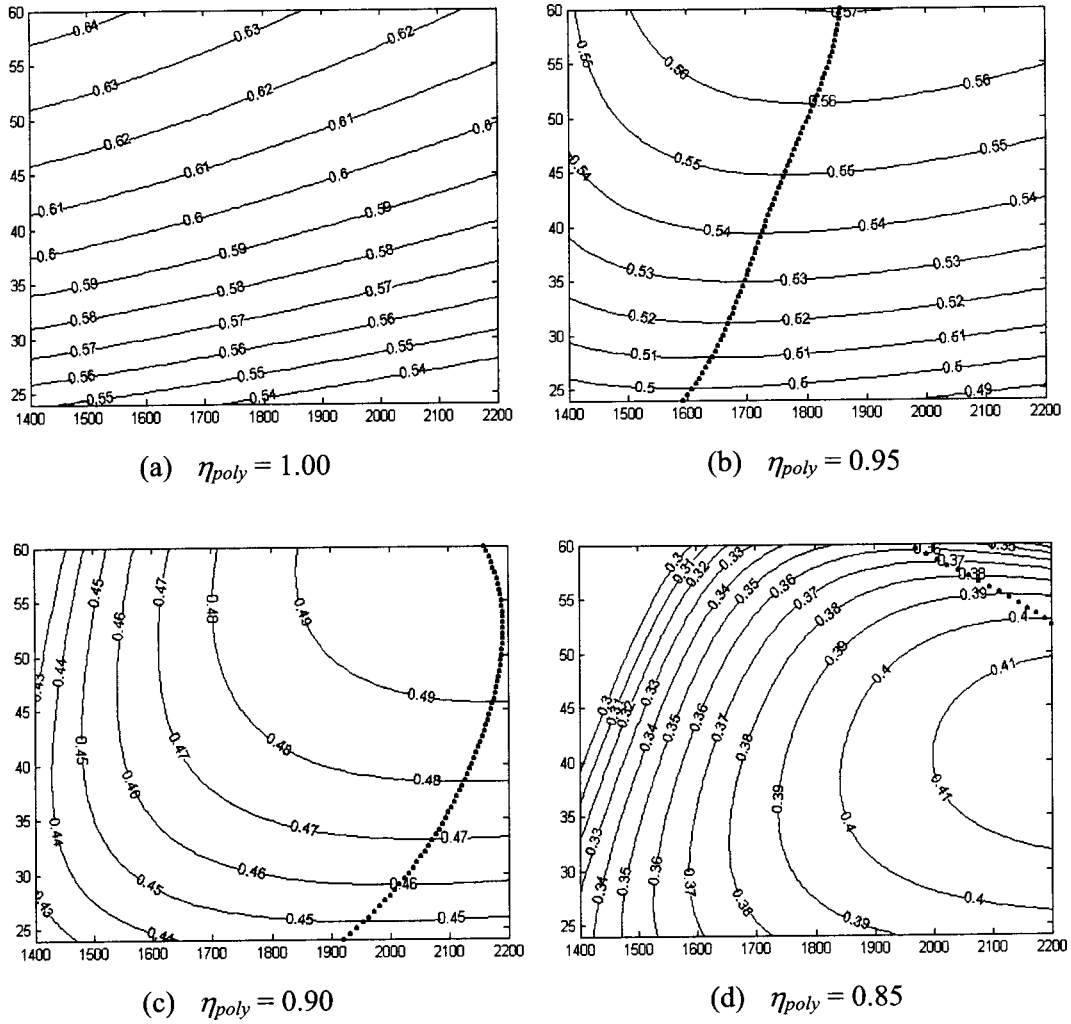

Fig. 9 Cooled GT with "super-advanced cooling technology" from Table 1. Contours of constant cycle efficiency η_{cyc} with contour interval 0.01. Combustor outlet temperature T_{cot}=1400–2200 K on abscissa, compressor pressure ratio r_p=24–60 on ordinate. Dotted lines are loci of $T_{cot,opt}$ (T_{cot} for maximum η_{cyc} at constant r_p).

For $\eta_{poly}=0.95$, the plots are best examined in the reverse sequence Figs. 4(*b*)→9(*b*)→8(*b*)→5(*b*). Although the changes are not dramatic, the curvature of the contours clearly increases, culminating in the formation of the global maximum of η_{cyc} already noted in Fig. 5(*b*) at $T_{cot,max}=1690$ K, $r_{p,max}=63$. More importantly, there is little variation in the locus of $T_{cot,opt}$, particularly at low r_p. In the unlikely event that turbomachinery polytropic efficiencies reach values of 0.95, the optimum T_{cot} at given r_p would be largely independent of the cooling technology and would not exceed 1900 K, even at pressure ratios of 60.

For $\eta_{poly}=0.90$, the forward sequence Figs. 5(*c*)→8(*c*)→9(*c*)→4(*c*) shows the locus of $T_{cot,opt}$ moving to regions of higher temperature, the global maximum of η_{cyc} increasing in both temperature and pressure ratio. Similar comments apply for $\eta_{poly}=0.85$, and the sequence Figs. 5(*d*)→8(*d*)→9(*d*)→4(*d*).

These observations indicate that, for improved cooling technology but essentially constant η_{poly} of around $\eta_{poly}=0.9$ (Figs. 5(*c*)→8(*c*)→9(*c*)), an increase in both T_{cot} and r_p might be justified by the resulting increase in η_{cyc}. However, with improvements in *both* cooling technology and η_{poly}, an increase in r_p is more important than an increase in T_{cot}. Indeed, depending on the level of improvement in η_{poly}, the optimum combustor outlet temperature may actually decrease as the cooling technology gets better (Figs. 5(*c*)→8(*b*)→9(*b*)).

7.2 Ultimate Turbomachinery Efficiency. The theoretical behavior for $\eta_{poly}=1.0$, although providing understanding and interpretation, can obviously never be realized in practice. Indeed, even values of 0.95 probably exceed the maximum achievable turbomachinery efficiency, which, according to most authorities, is likely to be around $\eta_{poly}=0.92-0.93$ for both compressors and turbines. Hence, in an attempt to represent the ultimate realizable technology for turbomachinery aerodynamic design, Fig. 10 presents contour plots for the four levels of cooling technology discussed previously, all calculated with $\eta_{poly}=0.925$. It shows clearly the gradual transition, at constant $\eta_{poly}=0.925$, from current cooling technology (*a*), through advanced (*b*) and super-advanced (*c*) technologies, to a hypothetical uncooled machine (*d*).

Figure 10(*a*) shows a global maximum cycle efficiency of 0.507 at $r_p=50$, $T_{cot}=1810$ K, compared with 0.463 at $r_p=41$ and $T_{cot}=1930$ K for $\eta_{poly}=0.90$ (Fig. 5(*c*)). This emphasises the im-

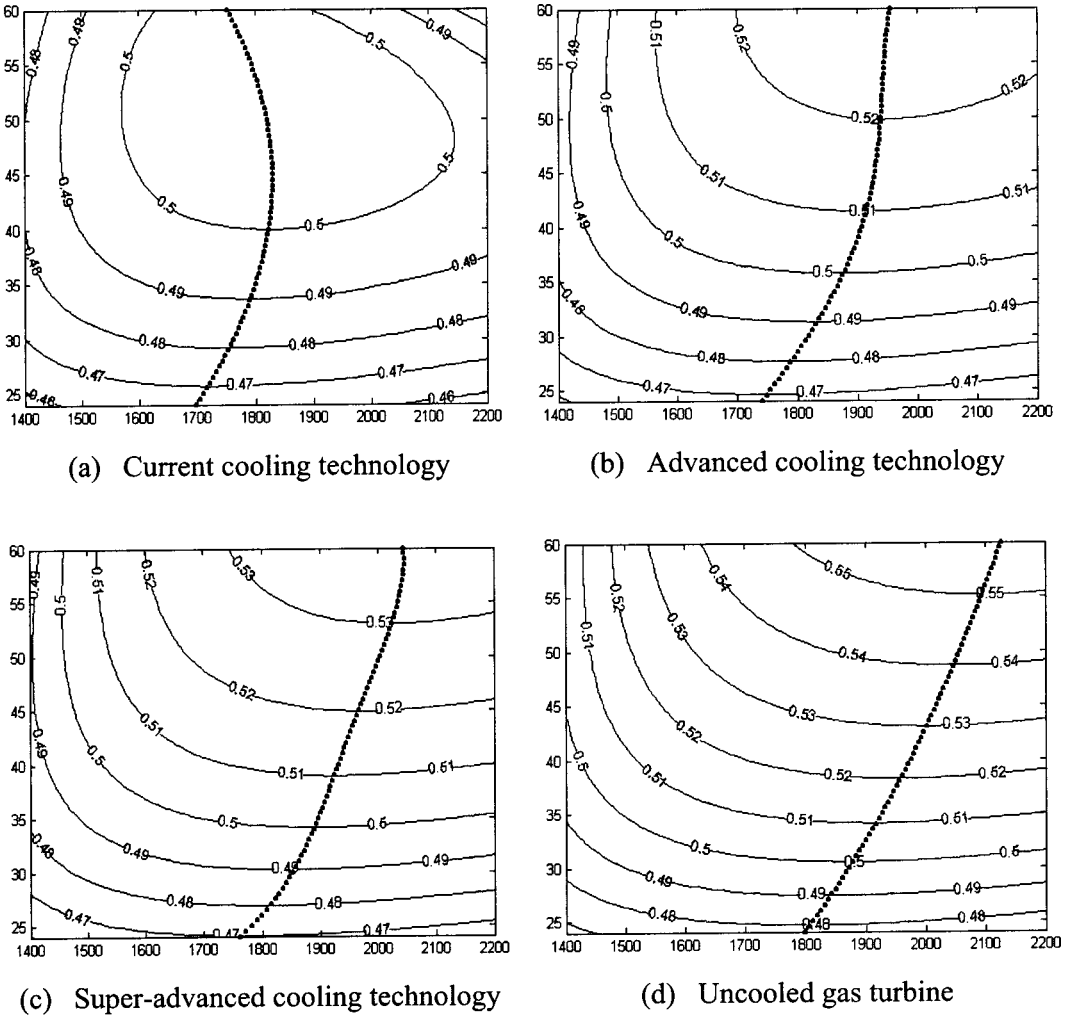

Fig. 10 GT with the "ultimate turbomachinery efficiency" of $\eta_{poly}=0.925$. Contours of constant cycle efficiency η_{cyc} with contour interval 0.01. Combustor outlet temperature $T_{cot}=1400-2200$ K on abscissa, compressor pressure ratio $r_p=24-60$ on ordinate. Dotted lines are loci of $T_{cot,opt}$ (T_{cot} for maximum η_{cyc} at constant r_p).

portant point made in Section 4 that the optimum T_{cot} for current cooling technology falls as the turbomachinery becomes more efficient.

Figures 10(*b*)–10(*d*) are remarkable for the similarity of the contour patterns and the fact that the locus of $T_{cot,opt}$ is almost independent of the level of cooling technology. Furthermore, it will be noted that the contour lines for high T_{cot} run almost parallel to lines of constant r_p indicating a very weak dependence of η_{cyc} on T_{cot} for constant r_p. Thus, if the gas turbine designer, having achieved ultimate turbomachinery polytropic efficiency of 0.925 and chosen a pressure ratio of 50 with a combustion temperature of 1810 K (the optimum conditions of Fig. 10(*a*)), were prepared to compromise by, say, 0.5% on cycle efficiency, the required combustor outlet temperature would fall by some 200 K.

8 Summary and Conclusions

The calculations presented in this paper show that, just as for uncooled machines, the cycle efficiency of a cooled gas turbine is primarily dependent on the combustor outlet temperature T_{cot}, the pressure ratio r_p, and the turbomachinery polytropic efficiency η_{poly}. The operating condition for maximizing cycle efficiency depends, however, on a subtle combination of these parameters. Using a computer code incorporating accurate modeling of gas properties and the cooling methodology of Young and Wilcock [5], the paper has explored the variation in cycle efficiency for a range of turbomachinery aerodynamic efficiencies and cooling technologies. In an attempt to summarize the results in as digestible a form as possible, Fig. 11 presents a montage of the 20 contour plots comprising Figs. 4, 5, 8, 9, and 10. A study of the trends exhibited in this figure clearly shows that, contrary to widespread opinion, improved cycle efficiencies will not necessarily result from increased combustor outlet temperatures.

These findings should lead the designer to search for a suitable compromise between increased combustor outlet temperature and improved turbomachinery efficiency. If high η_{poly} is not possible, then it is logical to seek a higher T_{cot}. However, if high η_{poly} can be attained, then the search for high T_{cot} may not be appropriate. At very high (unattainable) η_{poly}, the cycle efficiency is almost independent of the level of cooling technology. Even at $\eta_{poly}=0.925$ (the generally accepted ultimate aerodynamic efficiency), the value of T_{cot} giving maximum η_{cyc} for a given r_p is, not only remarkably insensitive to the cooling flow fraction, but also comparable to, or even lower than, present-day operating temperatures.

Finally, it must be emphasised that this study has concentrated on gas turbine performance in terms of cycle efficiency only. In some circumstances there may be other valid reasons for increasing the combustor outlet temperature (such as the desire to in-

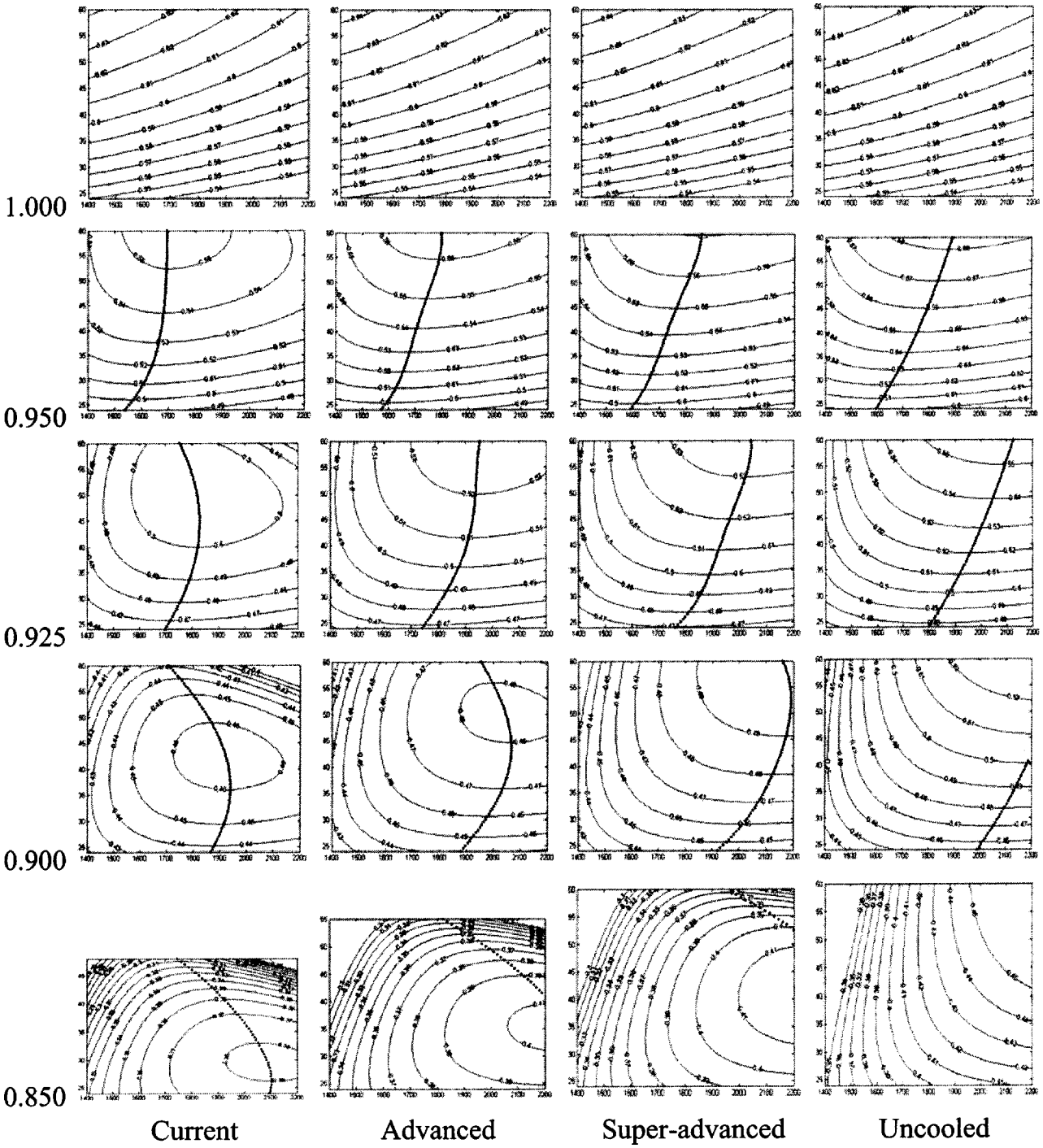

Fig. 11 Contours of constant η_{cyc} (contour interval=0.01) with $\eta_{poly,C}=\eta_{poly,T}=\eta_{poly}$. Each plot has T_{cot} =1400–2200 K on abscissa, r_p=24–60 on ordinate. Dotted lines are loci of T_{cot} for maximum η_{cyc} at constant r_p. Left to right, increasing cooling technology. Bottom to top, increasing turbomachinary η_{poly}.

crease the specific work output) which outweigh efficiency considerations. It is also appreciated that other limits, such as those on emissions, may have to be imposed which will restrict increases in combustion temperature beyond those in use at present.

Acknowledgments

R.C.W. gratefully acknowledges the receipt of an EPSRC studentship, a Rolls-Royce CASE award, and a maintenance contribution from the Ford of Britain Trust of the Cambridge University Engineering Department. The authors are grateful to A. Aramayo-Prudencio for his help in preparing the contour plots.

Nomenclature

Bi = Biot number
K_{comb} = combustion pattern factor
K_{cool} = cooling flow factor
p_0 = total pressure
r_p = compressor pressure ratio
T_{cot} = combustor outlet temperature

T_0 = total temperature
ε_0 = blade cooling effectiveness
ε_f = film cooling effectiveness
η_{cyc} = cycle efficiency
η_{int} = internal cooling efficiency
η_{poly} = turbomachinery polytropic efficiency
ψ = cooling flow fraction (m_c/m_g)

η_{cyc} is based on the net work output, uncorrected for mechanical and generator efficiencies, and on the LCV of methane. η_{poly} is a total-to-total polytropic efficiency. All states in the cycles are stagnation states. The maximum cycle temperature is the combustor outlet temperature not the rotor inlet temperature.

Subscripts.

C = compressor
c = coolant
g = mainstream gas
T = turbine

Appendix

Determination of the Cooling Flow Rates. Various approaches for estimating the required cooling flow fraction ψ (the ratio of the coolant mass flowrate m_c to the mainstream flowrate m_g) are described by Holland and Thake [7], El Masri [9], Consonni [10], and Chiesa and Macchi [11]. The Holland and Thake approach is attractive because it expresses ψ in terms of a small number of parameters representive of a ''technology level.'' The method was extended by Young and Wilcock [5] to allow for the temperature drop through the thermal barrier coating (TBC) and blade metal.

The analysis starts by defining the *blade cooling effectiveness* ε_0 by

$$\varepsilon_0 = \frac{T_{0g} - T_{\text{met,ext}}}{T_{0g} - T_{0c,\text{in}}} \tag{A1}$$

where T_{0g} is the relative total temperature of the mainstream gas, $T_{0c,\text{in}}$ is the relative total temperature of the coolant entering the blade passages, and $T_{\text{met,ext}}$ is the allowable external surface metal temperature (assumed constant over the blade). The problem is to find the value of ψ (for each blade row) which will ensure that the required value of ε_0 is achieved.

An expression for ψ is derived in Appendix 2 of [5]. The result can be expressed as

$$\psi = \frac{m_c}{m_g} = \frac{K_{\text{cool}}}{(1+B)} \left\{ \frac{\varepsilon_0 - \varepsilon_f[1 - \eta_{\text{int}}(1-\varepsilon_0)]}{\eta_{\text{int}}(1-\varepsilon_0)} \right\} \tag{A2a}$$

$$B = \text{Bi}_{\text{tbc}} - \left(\frac{\varepsilon_0 - \varepsilon_f}{1-\varepsilon_0} \right) \text{Bi}_{\text{met}} \tag{A2b}$$

In Eqs. (*A2a*) and (*A2b*), K_{cool} is the *cooling flow factor*, η_{int} is the *internal cooling efficiency*, ε_f is the *film cooling effectiveness*, Bi_{met} is the *metal Biot number*, and Bi_{tbc} is the *TBC Biot number*.

The cooling flow factor K_{cool} is defined by

$$K_{\text{cool}} = (1+\alpha) \frac{A_{\text{surf}}}{A_g} \frac{c_{pg}}{c_{pc}} St_g \tag{A3}$$

A_{surf} is the blade surface area, and A_g is the exit flow area normal to the axial direction. c_{pg}/c_{pc} is the gas to coolant specific heat ratio, and St_g is a Stanton number defined by $St_g = h_g A_g / m_g c_{pg}$ (h_g being the gas to blade surface *mean* heat transfer coefficient). The factor α allows for other primary cooling flows (mainly end-wall cooling) and is roughly equal to the ratio of the end-wall area to A_{surf}. It does not encompass secondary cooling flows for sealing, etc. For convenience, all the parameters were combined into the single parameter K_{cool} of Eq. (A3) which was ''tuned'' to engine data and then fixed for all the calculations.

Returning to Eq. (*A2a*), the internal cooling efficiency η_{int} is defined by

$$\eta_{\text{int}} = \frac{T_{0c,\text{exit}} - T_{0c,\text{in}}}{T_{\text{met,int}} - T_{0c,\text{in}}} \tag{A4}$$

where $T_{0c,\text{exit}}$ is the relative total temperature of the coolant at exit from the internal blade passage and $T_{\text{met,int}}$ is the internal surface metal temperature. η_{int} represents the quality of the ''internal cooling technology.'' It can, as discussed by Chiesa and Macchi [11], be related to the internal heat transfer coefficient and the surface area of the internal flow passages, but this is deliberately not done in the present paper. Instead, in order to bypass a difficult internal heat transfer calculation, a value of η_{int} is specified directly as input data.

The film-cooling effectiveness ε_f is defined by

$$\varepsilon_f = \frac{T_{\text{recov}} - T_{\text{adwall}}}{T_{\text{recov}} - T_{0c,\text{exit}}} \cong \frac{T_{0g} - T_{\text{adwall}}}{T_{0g} - T_{0c,\text{exit}}} \tag{A5}$$

where T_{recov} is the mainstream recovery temperature (approximately equal to T_{0g}) and T_{adwall} is the adiabatic outer wall temperature. Equation (*A2a*) requires a surface-area-averaged value of ε_f, and this is difficult to estimate because it depends on the geometry and layout of the injection holes, the blowing ratio, and other parameters. In order to avoid this problem, a value of ε_f representative of current ''film cooling technology'' was specified directly. When film cooling was employed, it was assumed that all the air emerges from the cooling holes.

The final parameters in Eqs. (*A2a*) and (*A2b*) are the metal and TBC Biot numbers defined by

$$\text{Bi}_{\text{met}} = \frac{h_g t_{\text{met}}}{\lambda_{\text{met}}}, \quad \text{Bi}_{\text{tbc}} = \frac{h_g t_{\text{tbc}}}{\lambda_{\text{tbc}}} \tag{A6}$$

where t is the thickness and λ is the thermal conductivity of the metal or TBC.

If T_{0g} in Eq. (*A1*) corresponds to the mass-averaged total temperature, the predicted coolant flow rate is invariably lower than that used in a real engine. This is because allowance must be made for temperature nonuniformity in the combustor outlet flow. A common way of doing this is to replace T_{0g} by a temperature $T_{0g,\text{max}}$ given by

$$T_{0g,\text{max}} = T_{0g} + K_{\text{comb}} \Delta T_{\text{comb}} \tag{A7}$$

where ΔT_{comb} is the combustion temperature rise and K_{comb} is a ''pattern factor,'' depending on the type of combustor and the position of the blade row (Kawaike et al. [12]). Typically, K_{comb} is about 0.15 for the first stator, reducing progressively for subsequent cooled rows. Having obtained ψ by this method, the calculations revert to using the mass-averaged T_{0g}.

Determination of the Cooling Irreversibilities. Figure 3 is a schematic diagram showing the coolant and mainstream flow paths. The Holland and Thake analysis and energy equation provide values of the coolant flow fraction, heat transfer rate and temperatures defined earlier in this appendix. Process (i) in Section 2.2 refers to entropy creation due to heat transfer to the outer blade surface. As shown in Ref. [5], this can be written in terms of the mainstream static and blade surface temperatures. The former requires knowledge of the average mainstream Mach number, but the value is not critical. Processes (ii) and (iii) refer to entropy creation due to conduction through the TBC and blade metal and can be computed from the known heat transfer rate and temperature drops.

Processes (iv) and (v) refer to entropy creation in the coolant stream between compressor offtake and injection into the mainstream. At compressor offtake, $T_{0c,\text{comp}}$ and $p_{0c,\text{comp}}$ are prescribed and $T_{0c,\text{exit}}$ is known from the heat transfer analysis. If $p_{0c,\text{exit}}$ can be found, this defines the specific entropy at the exit holes and hence fixes this ''internal loss.''

One way of finding $p_{0c,\mathrm{exit}}$ is to estimate the pressure loss in the internal passages using the method of Consonni [10]. This, however, requires detailed knowledge of the internal flow. An alternative approach is to assume that the design of the passages has been such as to achieve a certain ''momentum flux blowing ratio'' I at the holes. I is defined by

$$I = \frac{\rho_{c,\mathrm{exit}} V_{c,\mathrm{exit}}^2}{\rho_{g,\mathrm{exit}} V_{g,\mathrm{exit}}^2} = \frac{\gamma_c M_{c,\mathrm{exit}}^2}{\gamma_g M_{g,\mathrm{exit}}^2} \tag{A8}$$

where $M_{c,\mathrm{exit}}$ is the exit coolant Mach number and $M_{g,\mathrm{exit}}$ is the local mainstream Mach number. As shown in Ref. [5], specifying $M_{g,\mathrm{exit}}$ and I is sufficient to define $p_{0c,\mathrm{exit}}$ if it is assumed that the coolant and gas *static* pressures at the holes are equal.

This method of estimating the internal loss parallels the calculation of the internal heat transfer described earlier in this appendix. There, the difficult problem of estimating the internal heat transfer coefficient was avoided by the direct specification of the parameter η_{int}. Here, the problem of estimating the mean friction factor is avoided by specifying the parameter I.

Finally, it is necessary to calculate the entropy creation due to the mixing processes (vi) and (vii). As explained in Ref. [5]. This is achieved using the method of Hartsel [13] under the assumption that the *static* pressure remains constant during mixing. The only extra parameter required to perform this calculation is the injection angle of the coolant ϕ.

The advantage of this approach is that the heat transfer analysis together with the specification of just three parameters $M_{g,\mathrm{exit}}$, I and ϕ allows the estimation of *all* the cooling irreversibilities. The disadvantage is in the difficulty of choosing suitable average values for the parameters in order to provide accurate representations of cooling systems which are invariably very complex.

References

[1] MacArthur, C. D., 1999, ''Advanced Aero-Engine Turbine Technologies and Their Application to Industrial Gas Turbines,'' *ISABE 14th Int. Symp. on Air-Breathing Engines*, Florence, Paper 99-7151.

[2] Horlock, J. H., Watson, D. T., and Jones, T. V., 2001, ''Limitations on Gas Turbine Performance Imposed by Large Turbine Cooling Flows,'' ASME J. Eng. Gas Turbines Power, **123**, pp. 487–494.

[3] Wilcock, R. C., Young, J. B., and Horlock, J. H., 2002, ''Gas Properties as a Limit To Gas Turbine Performance,'' *ASME Turbo-Expo 2002*, Amsterdam, Paper GT-2002-30517.

[4] Young, J. B., and Wilcock, R. C., 2002, ''Modelling the Air-Cooled Gas Turbine: Part 1-General Thermodynamics,'' ASME J. Turbomach., **124**, pp. 207–213.

[5] Young, J. B., and Wilcock, R. C., 2002, ''Modelling the Air-Cooled Gas Turbine: Part 2-Coolant Flows and Losses,'' ASME J. Turbomach., **124**, pp. 214–221.

[6] Chase, Jr., M. W., Davies, C. A., Downey, Jr., J. R., Frurip, D. J., McDonald, R. A., and Syverud, A. N., 1986, ''JANAF Thermochemical Tables,'' Third Edition, American Institute of Physics, New York.

[7] Holland, M. J., and Thake, T. F., 1980, ''Rotor Blade Cooling in High Pressure Turbines,'' J. Aircr., **17**, pp. 412–418.

[8] Horlock, J. H., 2001, ''Basic Thermodynamics of Turbine Cooling,'' ASME J. Turbomach., **123**, pp. 583–592.

[9] El-Masri, M. A., 1987, ''Exergy Analysis of Combined Cycles: Part 1, Air-Cooled Brayton-Cycle Gas Turbines,'' ASME J. Eng. Gas Turbines Power, **109**, pp. 228–235.

[10] Consonni, S, 1992, ''Performance Prediction of Gas/Steam Cycles for Power Generation,'' Ph.D. thesis no. 1983-T, MAE Dept. Princeton Univ.

[11] Chiesa, P., and Macchi, E., 2002, ''A Thermodynamic Analysis of Different Options to Break 60% Electric Efficiency in Combined Cycle Power Plant,'' *ASME Turbo-Expo 2002*, Amsterdam, Paper 2002-GT-30663.

[12] Kawaike, K., Kobayishi, N., and Ikeguchi, T., 1984, ''Effect of Blade Cooling System With Minimized Gas Temperature Dilution on Gas Turbine Performance,'' ASME J. Eng. Gas Turbines Power, **106**, pp. 756–764.

[13] Hartsel, J. E., 1972, ''Prediction of Effects of Mass-Transfer Cooling on the Blade-Row Efficiency of Turbine Airfoils,'' *AIAA, 10th Aerospace Sciences Meeting*, San Diego, Paper AIAA-72-11.

Effects of Pore Size Variations on Regenerative Wheel Performance

Wei Shang

Robert W. Besant

Department of Mechanical Engineering,
University of Saskatchewan,
57 Campus Drive,
Saskatoon SK S7N 5A9, Canada

Manufacturing tolerances usually cause the air flow channel pore sizes to have a random variation in the matrices of regenerative wheels. The effects of random pore size distribution on pressure drop across a regenerative energy wheel transferring heat and moisture and effectiveness are investigated using analytical methods. Compared to an identical wheel with no pore size variation, simple algebraic expressions for pressure drop ratio, $\Delta p/\Delta p_0$, and effectiveness ratio, ϵ/ϵ_0, are developed for a Gaussian distribution of flow channel hydraulic diameters. Graphical results are presented showing that large random variations in flow channel pore size decrease the pressure drop across a wheel and the effectiveness (sensible, latent, and total) significantly for a regenerative wheel. Optical and micrometer measurements of four typical regenerative wheels showed a random variation in flow channel hydraulic diameters. These data imply significant decreases in $\Delta p/\Delta p_0$ and ϵ/ϵ_0 for each wheel. [DOI: 10.1115/1.1804539]

1 Introduction

Most heat exchangers are designed with large fluid flow or pore channel diameters so that the problem of geometric variations among the flow channels is not a concern. This may not be the case for desiccant coated wheel dehumidifiers, heat wheels, and desiccant coated energy wheels with small flow channel pore diameters for fluid flow.

In two recent papers by Shang and Besant [1] a typical energy wheel with a large heat and mass transfer surface area per unit volume (e.g., a specific surface area of about 4000 m^2/m^3) and a large number of flow passages per unit surface area (e.g., about 40 000 pores per m^2) indicated variations in the downstream outlet velocities across the face of the wheel and significant variations in outlet temperatures and humidities. It is speculated that these velocity and property variations are mostly caused by variations in the pore size of the wheel matrix.

The problem of variations in fluid flow passage sizes has been mentioned in several conference proceedings and handbooks on heat exchanger design [2–4] as an important design consideration. In 1970 London [5] considered laminar flow through gas turbine regenerators and the influence of manufacturing tolerances for two sizes of channel passages and showed that the pressure drop would decrease and the effective number of heat transfer units of the heat exchanger would decrease as the deviation in flow channel sizes increased. Mondt [6] used scanned photographs of heat exchanger inlet faces to present measured deviations of spacings in deepfold compact heat exchangers and showed that standard deviations in the characteristic lengths of the flow channels varied between 0.85% and 4.09% for three types of flow channel geometries. London [7] reviewed the paper by Mondt and recommended more precise experimentation and more sophisticated statistical techniques and concluded that this is a nagging problem for industry and it is one that will not go away. Rohsenow [8] discussed the problem for laminar flow through parallel flow channels considering two different hydraulic diameters and showed that the change in effective heat transfer coefficient always decreases with increasing size differences compared to the case of equal hydraulic diameters. In a comprehensive heat transfer analysis, Shah and London [9] extended the work of London [5] by investigating a number of heat transfer problems with variations in the hydraulic diameters of compact heat exchanger flow channels. They presented the equations for pressure drop ratio gain and fractional reduction in heat exchanger performance for various steady state heat transfer boundary conditions. Effective friction factor Reynolds number product and Nusselt number results are presented as a function of the channel deviation parameter for rectangular and triangular channels for a Gaussian distribution when the number of discrete flow passage sizes range from 2 to 11. When this channel deviation or standard deviation parameter is allowed to increase from 0 to 0.25 the effective Nusselt number decreases by up to 45% for a rectangular channel with an aspect ratio of 0.125 and by 26% for an aspect ratio of 1.0.

An important question not previously considered by other researchers investigating regenerative air-to-air heat and water vapor exchange between two air flow streams [10–13] is—what effect does a variation in pore size have on the performance factors of a regenerative wheel which transfers both heat and water vapor between air streams? That is, how will the effectiveness (sensible, latent, and total) and the pressure drop change between two wheels differ if one wheel has only one uniform size of pore for air flow and the other is identical except that there is a random variation in pore size about the same mean value? This is the problem to be considered in this paper.

The literature states that variations in flow channel size in heat exchangers are important and, for steady state operating conditions, indicates just how the pressure drop and Nusselt number will vary with several sizes and aspect ratios of flow channels. Now there is a need to investigate the impact that these variations will have on the performance factors of regenerative wheels which transfer both heat and water vapor between air streams. The heat transfer results of Shah and London [9] need to be extended to the transient boundary conditions of these regenerative wheels and for a wide range of operating conditions [14] with channel size and aspect ratio distributions that are completely random as they are in typical wheels.

2 Problem Formulation and Theoretical Considerations

According to ASHRAE Std. 84-91R [15], the performance of an air-to-air heat/energy recovery can be characterized by the effectiveness for sensible, latent, and total energy as well as pressure drop, crossover, and mass flows. Figure 1 shows a schematic diagram for an energy wheel with a typical air counter-flow arrangement and flow property measurement stations for supply flow inlet (1) and outlet (2) and exhaust flow inlet (3) and outlet (4).

In this problem, two nearly identical energy wheels are considered—one with a uniform pore size and the other with a

Contributed by IGTI of THE AMERICAN SOCIETY OF MECHANICAL ENGINEERS for publication in the ASME JOURNAL OF ENGINEERING FOR GAS TURBINES AND POWER. Manuscript received by IGTI Division April 2, 2003; final revision received September 1, 2003. IGTI Heat Transfer Chair: R. Bunker.

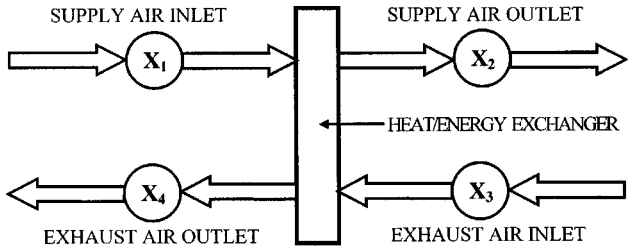

Fig. 1 Schematic of airflow for air-to-air heat/energy exchangers

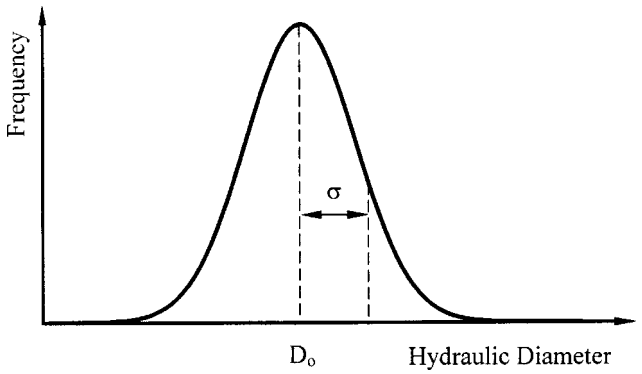

Fig. 3 Number of wheel matrix pores versus pore hydraulic diameter for a Guassian distribution of diameters

random variation in pore size but with the same total flow area and exchanger surface area for all the flow channels. These wheels are considered to be identical in thickness, outer diameter, hub diameter, and desiccant coating type and thickness but there is a variation in pore size in one but not the other. The wheel speed and mass flow rates of air are the same for each.

It is assumed that the shape of the flow channel in each of the pores is similar for both wheels (i.e., if the pores in the matrix are parallel surface, hexagon honeycomb, or corrugated in one wheel then they will have a similar parallel plate, honeycomb, or corrugation geometry in the other, etc.). Generally, the airflow within the pores of energy wheels is low in Reynolds number (e.g., $300 < \mathrm{Re} < 1500$), so the flow is laminar. Simonson and Besant [10] showed that the entrance effects in the flow channels are usually small, therefore the flow is essentially a fully developed channel flow. In this study the entrance effects are considered to be negligible so that each channel has only fully developed laminar flow. Shah and London [16] have compiled an extensive data base for fully developed laminar flow in channels including parallel plates, corrugated channels, and polygon channels including equilateral triangle, square, hexagonal, and circular flow channels. These channel shapes along with some others have been used in regenerative wheels, but most have a corrugated channel shape for desiccant coated energy wheels as shown in Fig. 2.

For fully developed flow in a channel with parallel walls it can be shown that [16]

$$f' \,\mathrm{Re} = \frac{D^2}{2\mu V}\frac{dp}{dx} \tag{1}$$

is a constant dependent only on the channel geometry. That is, for flow channels with a geometry variation $f'\,\mathrm{Re}$ may take on different values; however, for similar geometry the same constant applies to each. For example, all circular tubes have $f'\,\mathrm{Re}=16$, all regular hexagonal honeycombs have $f'\,\mathrm{Re}=15.05$, and parallel surfaces have $f'\,\mathrm{Re}=24$. For corrugated channels (sine wave ducts) with a complete range of aspect ratios $0<2b/2a<\infty$, where $2a$ is the wave length and $2b$ is the wave height, the range of $f'\,\mathrm{Re}$ is $9.6<f'\,\mathrm{Re}<15.3$ [19]. For typical regenerative wheel pores with an aspect ratio range $0.25<2b/2a<1.5$, the range of $f'\,\mathrm{Re}$ is $10.1<f'\,\mathrm{Re}<13.0$ or a variation of 12.5% about the mean value of 11.6.

In this study, it will be first assumed that the variation in $f'\,\mathrm{Re}$ from channel to channel in the same wheel can be neglected which is usually the case for parallel surface, triangular, square, hexagonal, and circular cylinder pores in regenerative wheels even though there may be a significant variation in the channel hydraulic diameter, D. Later, variations in $f'\,\mathrm{Re}$ will be included for typical corrugated flow channels.

Equation (1) is often expressed in the integrated form when ρ is constant for a finite channel length, L, giving the total pressure drop

$$\Delta p = 2f'\frac{L}{D}\rho V^2 \tag{2}$$

where the Reynolds number has been replaced by its definition, $\mathrm{Re}=\rho VD/\mu$.

2.1 Parallel Plates. For a parallel surface regenerative wheel of thickness, L, with a very large number of flow channels the pressure drop for each channel is the same while the mean flow speed, V, changes with the channel hydraulic diameter, D.

If the distribution of flow channel hydraulic diameter is Gaussian as shown in Fig. 3 where the mean hydraulic diameter is D_0

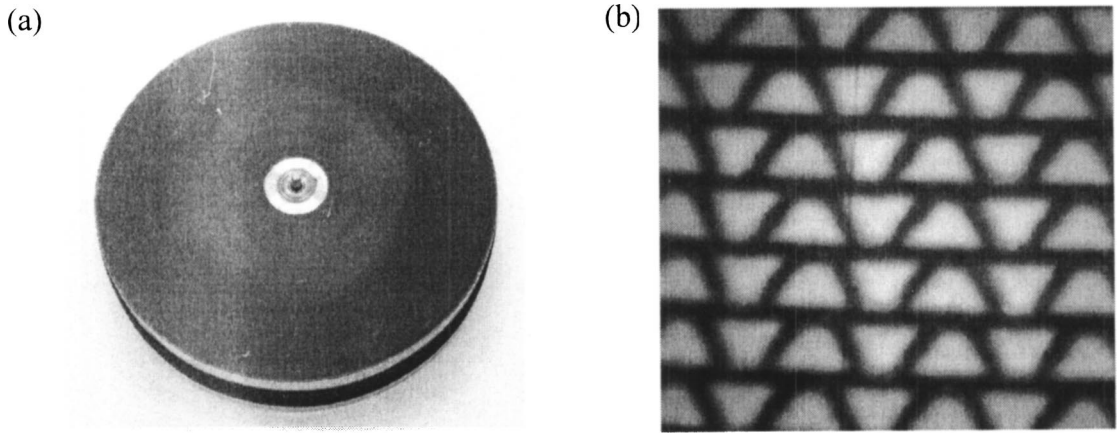

Fig. 2 (*a*) A typical energy wheel with desiccant coating, (*b*) corrugated channels for the same energy wheel with flow through each pore

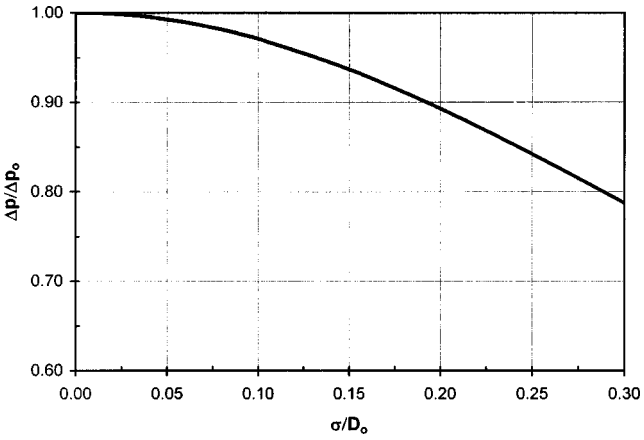

Fig. 4 Pressure drop ratio for parallel surface wheel with random variations in pore sizes to one without versus the standard deviation in pore hydraulic diameters with respect to the mean value

and its standard deviation is σ we can compare the pressure drop in a wheel with variable pore diameters, Δp, (i.e., σ is finite) to a wheel with no variation in pore diameters, Δp_0. Assuming the same mass flow rate for both wheels and $f'\,\mathrm{Re}=$constant, the ratio of pressure drop for a wheel with pore diameter variations to one without is given by

$$\frac{\Delta p}{\Delta p_0}=\left[\frac{1}{N}\sum_{i=1}^{N}\left(\frac{D_i}{D_0}\right)^3\right]^{-1} \tag{3}$$

The reader is referred to Appendix A for a more detailed derivation of this equation.

Taking the limit as $N\rightarrow\infty$ and integrating Eq. (3) for an assumed Gaussian distribution of hydraulic diameters gives the integral

$$\frac{\Delta p}{\Delta p_0}=\left\{\frac{1}{\sqrt{2\pi}}\int_{-\infty}^{\infty}\left[1+3\tau\left(\frac{\sigma}{D_0}\right)+3\tau^2\left(\frac{\sigma}{D_0}\right)^2+\tau^3\left(\frac{\sigma}{D_0}\right)^3\right]e^{-\tau^2/2}d\tau\right\}^{-1} \tag{4}$$

where the nondimensional deviation from the mean hydraulic diameter is

$$\tau=\frac{D-D_0}{\sigma} \tag{5}$$

Integrating each term in Eq. (4) by parts and noting that $1/\sqrt{2\pi}\int_{-\infty}^{\infty}e^{-\tau^2/2}d\tau=1$ results in an explicit equation for the pressure drop ratio as a function of (σ/D_0). This is

$$\frac{\Delta p}{\Delta p_0}=\left[1+3\left(\frac{\sigma}{D_0}\right)^2\right]^{-1} \tag{6}$$

Equation (6) is plotted in Fig. 4 to clearly illustrate that as (σ/D_0) increases this pressure drop ratio decreases such that this ratio decreases by more than 10% when $\sigma/D_0=0.2$. In general, for the same flow rate, a wheel with a uniform pore size will result in the maximum pressure drop and all others with a variation in pore size $(\sigma/D_0>0)$ will have lower pressure drops. The reader is referred to Appendix A for a more detailed derivation of Eq. (6) and a discussion of transient effects.

A lower pressure drop might be considered to be a desirable design feature for a regenerative wheel if all the other performance characteristics remained constant. The most important performance factor for energy wheels is the effectiveness (sensible, latent, and total) defined in ASHRAE Std 84-1991R [15] as

$$\epsilon=\frac{\dot{m}_s(X_1-X_2)}{\dot{m}_{\min}(X_1-X_3)} \tag{7}$$

Generally, each effectiveness decreases with mass flow rate [14]. Some typical values for effectiveness for an energy wheel versus mass flow rate are shown in Fig. 5 for the ARI Std 1060 [18] test conditions for rating air-to-air energy exchangers shown in Table 1. These effectiveness curves illustrate that for these op-

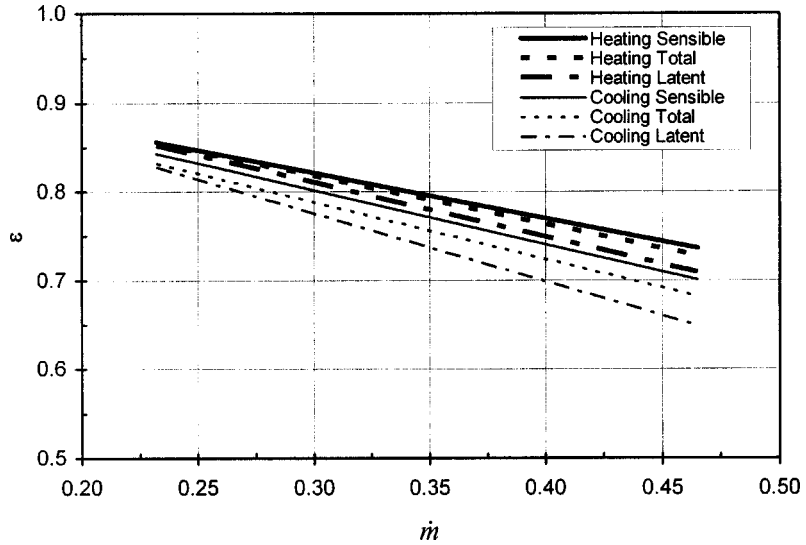

Fig. 5 Effectiveness versus mass flow rate under the ARI Std 1060 test conditions based on the correlations of Simonson and Besant (see Ref. [17]) for a desiccant coated energy wheel for ventilation air heat and moisture exchange (wheel width 229.5 mm, wheel diameter 638.5 mm, wheel rotational speed 27.6 rpm, and silica gel desiccant coating)

Table 1 Operating conditions for energy wheel tests, ARI Std 1060-2001

Item	Conditions	
	Heating	Cooling
(1) Entering supply air		
(*a*) Dry bulb temperature	1.7±1°C (35±1.8°F)	35±1°C (95±1.8°F)
(*b*) Relative humidity	82.5%±2%	47.4%±2%
(2) Entering exhaust air		
(*a*) Dry bulb temperature	21.1±1°C (70±1.8°F)	23.9±1°C (75±1.8°F)
(*b*) Relative humidity	49.2%±2%	51.2%±2%

erating conditions and over a significant variation in mass flow rate, these effectiveness curves have a constant slope, $\partial\epsilon/\partial\dot{m}$. As an energy wheel is subjected to a wide range of different operating conditions, Simonson et al. [14] show that this slope may change because, for some operating conditions with especially low face mass velocities, the effectiveness may increase for some (e.g., sensible effectiveness) and decrease for others (e.g., latent and total effectiveness).

For any given operating condition with a specified wheel speed and inlet air temperatures, humidities, and total mass flow rates (see Table 1 for typical temperatures and humidities), the effectiveness (sensible, latent, or total) of the whole wheel is the sum of the parts

$$\epsilon = \frac{1}{N\dot{m}_0}\sum_{i=1}^{N} \epsilon_i \dot{m}_i \tag{8}$$

where

$$\dot{m}_0 = \frac{1}{N}\sum \dot{m}_i\,, \tag{9}$$

$$\dot{m}_i = \rho_i V_i w z_i \tag{10}$$

and it is assumed that for any particular operating condition

$$\epsilon_i \dot{m}_i = \epsilon_0 \dot{m}_0 + \left.\frac{\partial\epsilon}{\partial\dot{m}}\right|_{\dot{m}=\dot{m}_0} (\dot{m}_i - \dot{m}_0)\dot{m}_i \tag{11}$$

Again it is convenient to consider the ratio of the effectiveness of a wheel with variations in pore diameter to one without (ϵ_0) and assume that the air density is a constant independent of these slight changes in operating conditions for each flow channel. The result when Eqs. (8), (9), (10), and (11) are combined, as in Appendix A, is

$$\frac{\epsilon}{\epsilon_0} = \frac{1}{N}\sum_{i=1}^{N}\left\{1+\left(\frac{\dot{m}}{\epsilon_0}\frac{\partial\epsilon}{\partial\dot{m}}\right)\right|_{\dot{m}=\dot{m}_0}\left[\left(\frac{\Delta p}{\Delta p_0}\right)^2\left(\frac{D_i}{D_0}\right)^6 - \left(\frac{\Delta p}{\Delta p_0}\right)\left(\frac{D_i}{D_0}\right)^3\right]\Bigg\} \tag{12}$$

The discussion in Appendix A points out that the heat and mass transfer processes are, unlike the mass flow rate, always transient in regenerative wheels—so there is a more complex relationship between ϵ and Nusselt number than is the case for steady state boundary conditions on each flow channel. As a consequence $(\dot{m}_0/\epsilon_0)(\partial\epsilon/\partial\dot{m})|_{\dot{m}=\dot{m}_0}$ must be determined by accurate experimental data or validated numerical simulation [17].

Again assuming that as $N\to\infty$ for a Gaussian distribution this results in the integral

$$\frac{\epsilon}{\epsilon_0} = \frac{1}{\sqrt{2\pi}}\int_{-\infty}^{\infty}\Bigg\{1+\partial\epsilon_m\Bigg[\left(\frac{\Delta p}{\Delta p_0}\right)^2\Bigg[1+6\tau\left(\frac{\sigma}{D_0}\right)+15\tau^2\left(\frac{\sigma}{D_0}\right)^2 + 20\tau^3\left(\frac{\sigma}{D_0}\right)^3+15\tau^4\left(\frac{\sigma}{D_0}\right)^4+6\tau^5\left(\frac{\sigma}{D_0}\right)^5+\tau^6\left(\frac{\sigma}{D_0}\right)^6\Bigg] - \left(\frac{\Delta p}{\Delta p_0}\right)\left[1+3\tau\left(\frac{\sigma}{D_0}\right)+3\tau^2\left(\frac{\sigma}{D_0}\right)^2+\tau^3\left(\frac{\sigma}{D_0}\right)^3\right]\Bigg]\Bigg\}e^{-\tau^2/2}d\tau \tag{13}$$

where $(\Delta p/\Delta p_0)$ is given as a function of only (σ/D_0) in Eq. (6) and the nondimensional effectiveness sensitivity coefficient is

$$\partial\epsilon_m = \frac{\dot{m}_0}{\epsilon_0}\left.\frac{\partial\epsilon}{\partial\dot{m}}\right|_{\dot{m}=\dot{m}_0} \tag{14}$$

is assumed to be a constant for any typical operating condition. Figure 5 shows that this parameter is about -0.3 for all three effectivenesses for this particular silica gel coated wheel with $0.6<\epsilon<0.8$ using the ARI [18] rating conditions. Other wheels, coated with molecular sieve coatings for example, will have much lower values for $\partial\epsilon_m$. Higher values of $\partial\epsilon_m$ will occur for special operating conditions and, in somewhat unusual operating conditions, it can even be positive [14] for the sensible effectiveness. For counterflow heat exchangers with equal supply and exhaust mass flow rates, it can be shown that $\partial\epsilon_m=(\epsilon-1)\epsilon/\epsilon_0$ where $(\epsilon-1)$ should be determined by direct experimental testing or analysis using design specifications [14] and ϵ/ϵ_0 is found from this analysis to be a constant. For the energy wheels tested, a value is found such that $0.87\leqslant\epsilon/\epsilon_0\leqslant0.99$. It is interesting to note that this relationship will only be altered by a small amount for typical regenerative heat wheels unless the wheels are rotated slowly with respect to the air capacity rate [17].

Integrating each term in Eq. (13) by parts results in an explicit relationship for (ϵ/ϵ_0) as a function of (σ/D_0) and the parameter $\partial\epsilon_m$:

$$\frac{\epsilon}{\epsilon_0} = 1+\partial\epsilon_m\Bigg\{\left(\frac{\Delta p}{\Delta p_0}\right)^2\left[1+15\left(\frac{\sigma}{D_0}\right)^2+45\left(\frac{\sigma}{D_0}\right)^4+15\left(\frac{\sigma}{D_0}\right)^6\right] - \left(\frac{\Delta p}{\Delta p_0}\right)\left[1+3\left(\frac{\sigma}{D_0}\right)^2\right]\Bigg\} \tag{15}$$

The effectiveness ratio given by Eq. (15) is plotted in Fig. 6 as a function of (σ/D_0) with $\partial\epsilon_m$ as a parameter. This figure shows that for most parallel surface energy wheel operating conditions with $-0.5<\partial\epsilon_m<-0.1$ the effectiveness will decrease as (σ/D_0) increases.

2.2 Symmetrical Cylinders. In this section, we consider flow through cylinders or channels in matrices that are symmetric about a single axis of symmetry along the air flow direction and have only one characteristic dimension. Examples of such matrices are flow channels with pores that have only equilateral triangle, square, pentagonal, hexagonal, and so on with increasing number of sides up to perfect circle geometric shapes. For conve-

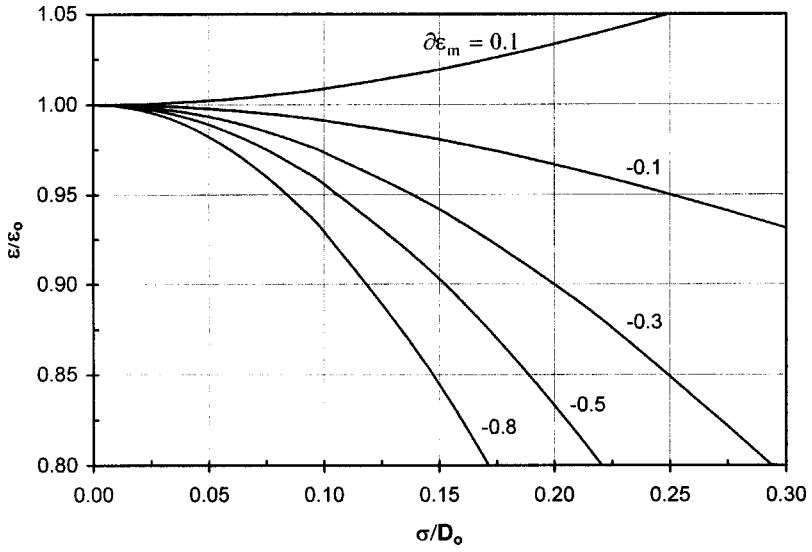

Fig. 6 Ratio of effectiveness for a parallel surface wheel with a random variation in pore sizes to one without versus standard deviation in pore hydraulic diameters with respect to the mean value

nience, we refer to this class of pore shapes as symmetrical cylinders. Perhaps the lowest cost shape for a manufacturer to make in a regenerative wheel matrix using symmetrical cylinders is the hexagonal (honeycomb) shape because, for a given wall thickness and pore flow area, it contains the least mass of material in a wheel.

Similar to the parallel surfaces in regenerative energy wheels, the manufactured distribution of flow channel hydraulic diameters of these flow channels is assumed to be Gaussian. Using the mean hydraulic diameter, D_0, and its standard deviation, σ, we can compare the pressure drop through a wheel with variable pore diameters, Δp, (i.e., σ is finite) to a wheel with no variation in pore diameters, Δp_0. Again, assuming that $f'\,\mathrm{Re}$=constant and the mass flow rates for both wheels to be equal, the ratio of pressure drop for a wheel with pore diameter variations to one without results in an equation similar to Eq. (3) (see Appendix A)

$$\frac{\Delta p}{\Delta p_0}=\left[\frac{1}{N}\sum_{i=1}^{N}\left(\frac{D_i}{D_0}\right)^4\right]^{-1} \tag{16}$$

The mass flow rate can be calculated using

$$\dot{m}_i=\rho_i V_i A_i \tag{17}$$

For pores that are equilateral triangle, square, hexagonal, and circular shapes, the flow channel flow areas as a function of the hydraulic diameters are, respectively,

$$A_i=\frac{3\sqrt{3}}{4}D_i^2 \tag{18a}$$

$$A_i=D_i^2 \tag{18b}$$

$$A_i=\frac{\sqrt{3}}{2}D_i^2 \tag{18c}$$

$$A_i=\frac{\pi}{4}D_i^2 \tag{18d}$$

For each of these flow channel shapes the corresponding $f'\,\mathrm{Re}$ values in Eq. (1) are, respectively, $f'\,\mathrm{Re}$=13.3, 14.2, 15.05, and 16 [19].

Taking the limit as $N\to\infty$, defining τ as in Eq. (5), and integrating Eq. (16) for an assumed Gaussian distribution of hydraulic diameters gives an explicit equation for the pressure drop ratio as a function of (σ/D_0), which is similar to Eq. (6):

$$\frac{\Delta p}{\Delta p_0}=\left[1+6\left(\frac{\sigma}{D_0}\right)^2+3\left(\frac{\sigma}{D_0}\right)^4\right]^{-1} \tag{19}$$

This equation, plotted in Fig. 7, shows a greater decrease in $\Delta p/\Delta p_0$ with increasing σ/D_0 than that for the parallel surfaces in Fig. 4.

The ratio of the effectiveness with variations in pore diameter (ϵ) to one without (ϵ_0) for wheels that have flow pores that are symmetrical cylinders is determined using Eqs. (8), (9), (11), (17), and (18), as in Appendix A. This equation is similar to Eq. (12):

$$\frac{\epsilon}{\epsilon_0}=\frac{1}{N}\sum_{i=1}^{N}\left\{1+\left(\frac{\dot{m}}{\epsilon_0}\frac{\partial\epsilon}{\partial\dot{m}}\right)\Big|_{\dot{m}=\dot{m}_0}\left[\left(\frac{\Delta p}{\Delta p_0}\right)^2\left(\frac{D_i}{D_0}\right)^8-\left(\frac{\Delta p}{\Delta p_0}\right)\left(\frac{D_i}{D_0}\right)^4\right]\right\} \tag{20}$$

Integrating Eq. (20) for a Gaussian distribution of diameters gives the effectiveness ratio equation similar to Eq. (15):

$$\frac{\epsilon}{\epsilon_0}=1+\partial\epsilon_m\left\{\left(\frac{\Delta p}{\Delta p_0}\right)^2\left[1+28\left(\frac{\sigma}{D_0}\right)^2+210\left(\frac{\sigma}{D_0}\right)^4+420\left(\frac{\sigma}{D_0}\right)^6\right]-\left(\frac{\Delta p}{\Delta p_0}\right)\left[1+6\left(\frac{\sigma}{D_0}\right)^2+3\left(\frac{\sigma}{D_0}\right)^4\right]\right\} \tag{21}$$

The effectiveness ratio given by Eq. (21) is plotted in Fig. 8 as a function of (σ/D_0) with $\partial\epsilon_m$ as a parameter. For typical pore variations in wheels, the $(\sigma/D_0)^8$ and higher order terms are negligible. This figure shows that for most regenerative energy wheels with $-0.5<\partial\epsilon_m<-0.1$, the effectiveness will decrease significantly as (σ/D_0) increases. Comparing Figs. 8 and 6 indicates that the changes in ϵ/ϵ_0 with increasing σ/D_0 are greater for this case than they are for the parallel surfaces.

2.3 Corrugated Pore Matrices. This section for corrugated pores is similar to the previous sections where pressure drop and effectiveness ratios were developed for pores with parallel surfaces and symmetrical cylinders. This commonly used matrix pore geometry is shown in Fig. 9. Unlike symmetrical cylinder pore matrices, corrugated matrices have two characteristic dimensions,

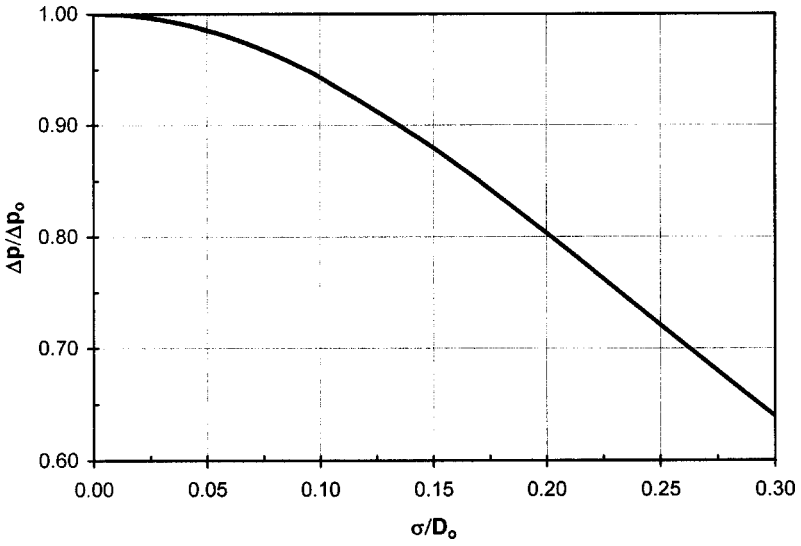

Fig. 7 Pressure drop ratio for a regenerative wheel with a matrix containing symmetrical cylinder pores with random variations in pore sizes to one without versus the standard deviation in pore hydraulic diameters with respect to the mean value

the wave amplitude, b, and the wave half width, a. Other cylindrical type pore geometries, which have two characteristic dimensions are isosceles triangles, rectangles, and ellipse, are more difficult to manufacture—so they are not considered in detail. For the corrugated flow channels, the resulting dimensionless pressure drop ratio and effectiveness ratio will, therefore, depend on both the standard deviation of hydraulic diameters divided by the mean hydraulic diameter (σ/D_0) and the mean ratio of characteristic pore dimensions, b/a, called the aspect ratio, η_0. The flow constant, f' Re, given by Eq. (1) will differ with variations in the aspect ratio, η, as well as the hydraulic diameter, D, for corrugated matrices. These relationships are expressed explicitly in this section.

For a corrugated wheel matrix the relationship between average velocity, V_i, through a pore of hydraulic diameter, D_i, we find that f' Re is nearly a constant, K_{fi}, which depends on the aspect ratio of the pore, η. Thus the average velocity can be written for fully developed laminar flow as

$$V_i = \frac{\Delta p D_i^2}{2\mu K_{fi} L} \tag{22}$$

where $K_{fi}(\eta_i)$ is a friction coefficient which is a different constant for different corrugation aspect ratios as shown in Fig. 10 [16]. The flow area of pore i is

$$A_i = \frac{1}{4} D_i P_i \tag{23}$$

where the wetted perimeter P_i can be written as

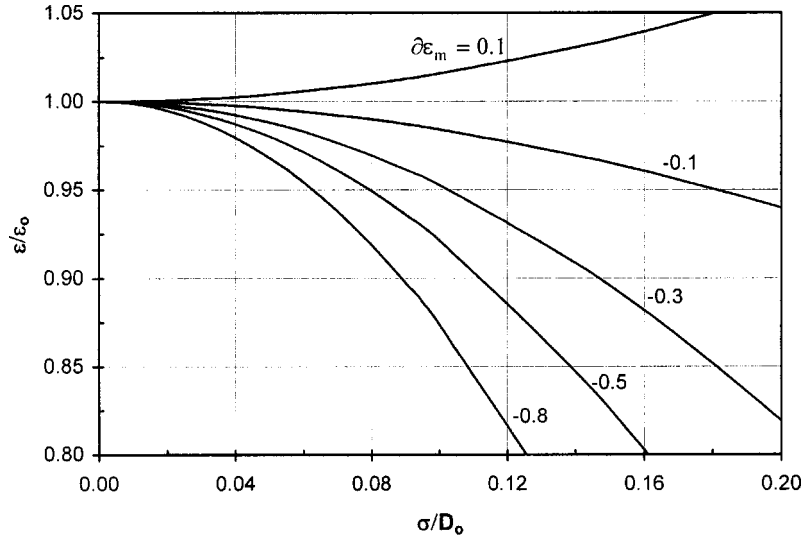

Fig. 8 Ratio of effectiveness for a regenerative wheel with a matrix containing symmetrical cylinder pores with a random variation in pore sizes to one without versus standard deviation in pore hydraulic diameters with respect to the mean value

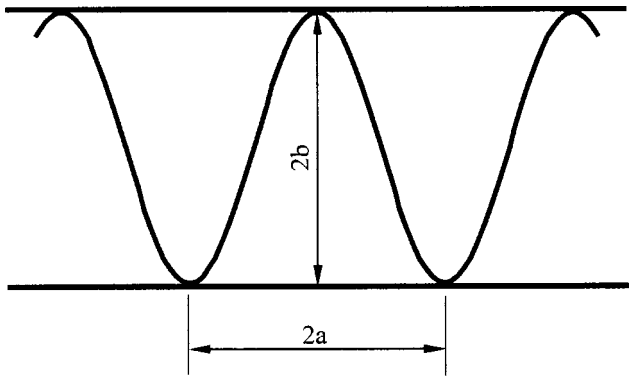

Fig. 9 Schematic of a corrugated shaped matrix channel for a regenerative wheel

$$P_i = K_{pi} D_i \tag{24}$$

where K_{pi} is a wetted perimeter coefficient that depends on the aspect ratio η_i as shown in Fig. 11.

Again assuming that the pressure drop is the same for each pore and the mass flow rate is the same for the wheel with variable pore sizes and the wheel with no variation in pore size, then the ratio of pressure drop for the wheel with variable pore sizes to the one without is

$$\frac{\Delta p}{\Delta p_0} = \left[\frac{1}{N} \sum_{i=1}^{N} K_i \left(\frac{D_i}{D_0} \right)^4 \right]^{-1} \tag{25}$$

where

$$K_i = \frac{K_{pi} K_{fo}}{K_{fi} K_{po}} \tag{26}$$

and $K_{fo} = K_{fi}$ for $D_i = D_0$, $K_{po} = K_{pi}$ for $D_i = D_0$.

Defining $\Delta \eta_i = \eta_i - \eta_0$, Fig. 12 shows how K_i varies with $\Delta \eta_i$ with η_0 as a parameter. It is clear from Fig. 12 that $K_i = 1.0$ at $\Delta \eta_i = 0$ and increases dramatically as $\Delta \eta_i$ goes to large negative values. The dimensionless ratio, K_i, is a function of only the aspect ratio $\Delta \eta / \eta_0$ with η_0 as a constant parameter for any par-

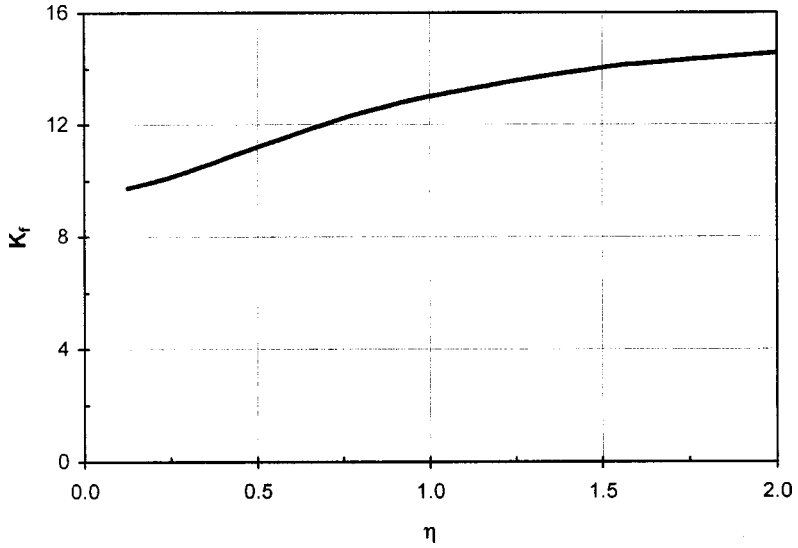

Fig. 10 K_f versus aspect ratio η for a corrugated channel

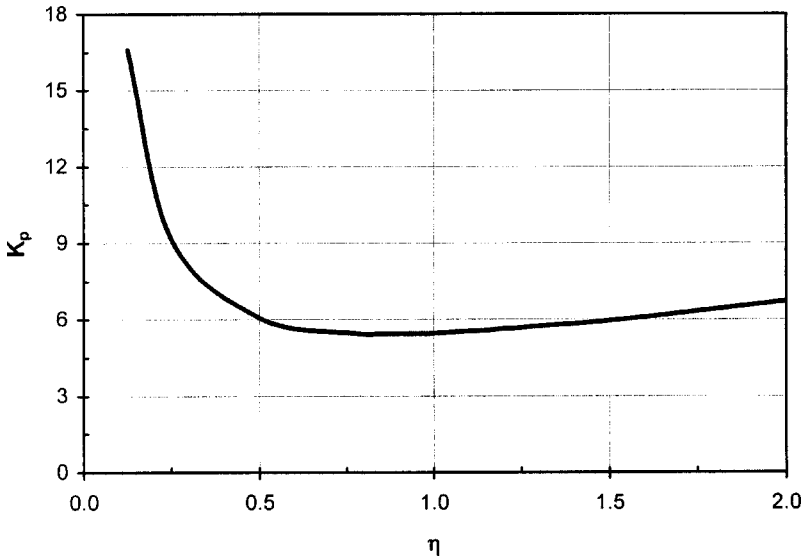

Fig. 11 K_p versus aspect ratio η for a corrugated channel

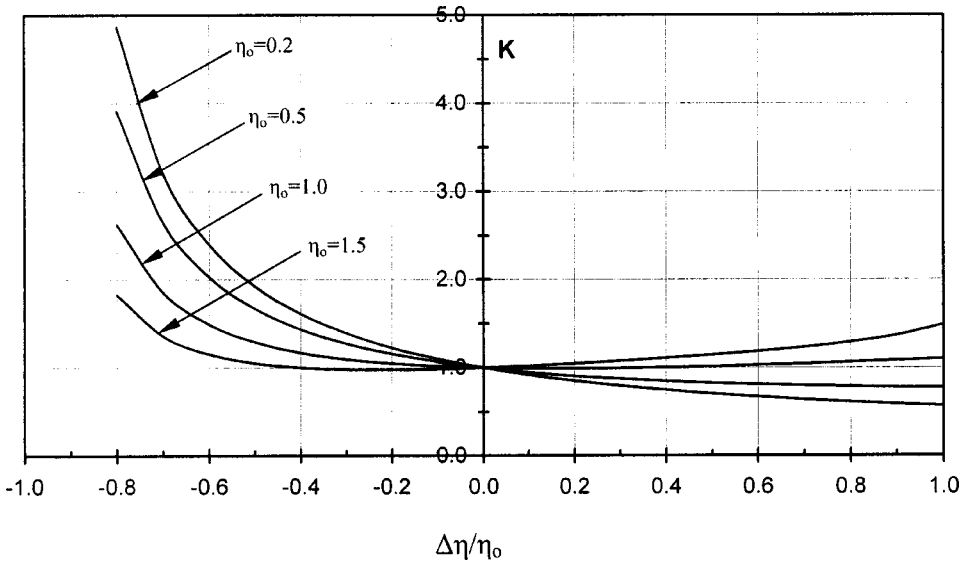

Fig. 12 ***K*** **versus** $\Delta\eta/\eta_0$ **for a corrugated pore geometry with** η_0 **as a parameter**

ticular wheel because $K_{pi}=P_i/D_i$ and both $P_i/2a_i$ and $2a_i/D_i$ are only functions of η_i. Figure 13 shows the variation of $D_i/2a_i$ with η_i [16]. A polynomial can be used to relate K_i to $\Delta\eta_i/\eta_0$ with η_0 as a parameter in an equation of the functional form

$$K_i = K_i\left(\frac{\Delta\eta_i}{\eta_0}, \eta_0\right) \tag{27}$$

where for any particular wheel η_0 is a constant.

When the range of η_i is not too large and $2a$ is nearly constant as it is with typical wheels, we can assume a linear relationship between the aspect ratio and the dimensionless hydraulic diameter ratio (D_i/D_0), as implied in Fig. 13. For $2a=$constant, this gives

$$\frac{\eta_i}{\eta_0} - 1 = \alpha_0 \frac{\sigma}{D_0}\tau_i \tag{28}$$

where α_0 is sensitivity coefficient for aspect ratio as a function of hydraulic diameter and it is a constant for any wheel. It is evaluated from the equation

$$\alpha_0 = \frac{1}{\eta_0}\left[\frac{\partial\eta}{\partial(D/2a)}\right]_{\eta_i=\eta_0}\left(\frac{D_0}{2a}\right) \tag{29}$$

Finally, when Eq. (28) is substituted into the functional Eq. (27), we get

$$K_i = 1 + \sum_{j=1}^{4} \beta_j \left(\frac{\sigma}{D_0}\tau_i\right)^j \tag{30}$$

where β_j are assumed to be constants that depend only on the mean value of the aspect ratio η_0 as presented in Table 2. The values of β_j, which are developed by curve fitting, are selected from this table for a known average aspect ratio η_0.

When Eq. (30) is substituted into Eq. (25) for the ratio of pressure drop and integrated for a Gaussian distribution of diameters in the same manner as Eq. (4), we get an equation with the first three terms the same as Eq. (19) for matrices containing sym-

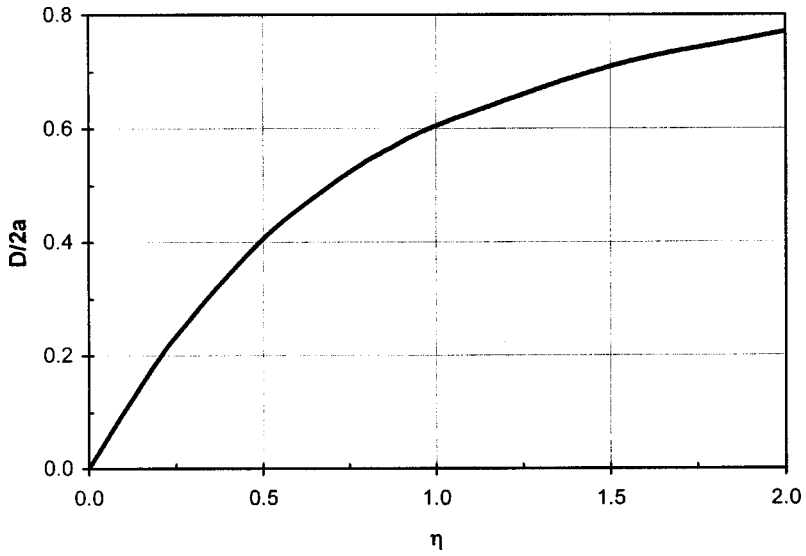

Fig. 13 ***D*****/2*a*** **versus aspect ratio** η **for a corrugated channel**

Table 2 For corrugated flow channels with selected values of η_0 corresponding values of β_j ($j=1, 2, 3,$ and 4) and α_0

η_0	α_0	β_1	β_2	β_3	β_4
0.2	1.130	−0.8192	0.7431	−3.1253	4.200
0.5	1.421	−0.6532	0.9470	−4.8442	8.114
1.0	2.184	−0.0734	1.3341	−11.127	28.787
1.5	3.145	0.7540	1.6455	−20.016	84.966

metrical cylinders and three more terms which modify the symmetrical cylinder result for the corrugated pore geometry

$$\frac{\Delta p}{\Delta p_0}=\left[1+6\left(\frac{\sigma}{D_0}\right)^2+3\left(\frac{\sigma}{D_0}\right)^4+(4\beta_1+\beta_2)\left(\frac{\sigma}{D_0}\right)^2+(12\beta_1+18\beta_2+12\beta_3+3\beta_4)\left(\frac{\sigma}{D_0}\right)^4+(15\beta_2+60\beta_3+90\beta_4)\left(\frac{\sigma}{D_0}\right)^6\right]^{-1} \quad (31)$$

where the terms $(\sigma/D_0)^8$ and higher have been deleted because they are not significant for typical aspect ratio variations in wheels. For the case of $K_i=1.0$, Eq. (31) is the same as Eq. (19) (i.e., the same curve as Fig. 7). Figure 14 graphically presents the results of Eq. (31) for $\eta_0=0.2$, 0.5, 1.0, and 1.5. This result implies a negligible correction of $(\Delta p/\Delta p_0)$ for $\sigma/D_0<0.05$; however, as η_0 takes different values, the pressure ratio increases relative to the case of $K=1.0$ for small values of η_0 (i.e., $\eta_0<1$) and decreases for $\eta_0\geqslant 1$. This finding needs some explanation because it may suggest that the aspect ratio η_0 should be selected to be as small as possible. Small aspect ratio matrices appear more convenient to manufacture because they have small wave amplitudes for a given wave length. Nonetheless, controlling the variation in relative wave amplitude in a manufacturing process appears to be more problematic than controlling the wave length. Thus small amplitude corrugation pores may tend to give rise to a greater range of variations in relative amplitudes in a manufacturing process. This can then result in a large standard deviation in the hydraulic diameters. In any case, the value of η_0 should not be selected based on pressure ratio alone for regenerative wheels because the effectiveness is usually much more important.

Corresponding to the effectiveness ratio for symmetrical cylinders derived from Eq. (20) to get Eq. (21), the effectiveness ratio of a corrugated wheel matrix is

$$\frac{\epsilon}{\epsilon_0}=1+\partial\epsilon_m\left\{\left(\frac{\Delta p}{\Delta p_0}\right)^2\left[1+B_{2,2}\left(\frac{\sigma}{D_0}\right)^2+B_{2,4}\left(\frac{\sigma}{D_0}\right)^4+B_{2,6}\left(\frac{\sigma}{D_0}\right)^6\right]-\left(\frac{\Delta p}{\Delta p_0}\right)\left[1+B_{1,2}\left(\frac{\sigma}{D_0}\right)^2+B_{1,4}\left(\frac{\sigma}{D_0}\right)^4+B_{1,6}\left(\frac{\sigma}{D_0}\right)^6\right]\right\} \quad (32)$$

where the term of order $(\sigma/D_0)^8$ and higher are dropped because they are negligible (see Appendix A for more discussion and details). The coefficients B_{ij} are explicitly given in Appendix B. It is recommended that this series expansion of (ϵ/ϵ_0) as a function of (σ/D_0) for a corrugated flow channel should not be used for high values of (σ/D_0), i.e., the recommended range is $\sigma/D_0\leqslant 0.15$ but the errors will be negligible or small even at $\sigma/D_0=0.2$.

The curves in Fig. 15 are presented using Eq. (32) for $\eta_0=1.0$. For greater clarity of these lines and for other values of η_0, Fig. 16 shows this result for only $\partial\epsilon_m=-0.3$. Other values of $\partial\epsilon_m$ have the same sequence of curves for each value of the mean aspect ratio, η_0.

Figure 16 shows that the effectiveness is significantly improved compared to $K_i=1.0$ for $0.2\leqslant\eta_0\leqslant 1.5$ for the same standard deviation ratio except for the case of $\eta_0\cong 1.0$ where the difference between curve for $K_i=1.0$ and $\eta_0=1.0$ is very small for $\sigma/D_0<0.075$. This result, plotted in Figs. 15 and 16, suggests that a wheel designer should select η_0 to be small, but it is likely to be just the reverse. Controlling the relative size of the standard deviation in hydraulic diameters is much more important than the decision about the aspect ratio. Using Eq. (28) it can be shown that if the aspect ratio is known to have a typical standard deviation then the standard deviation of the hydraulic diameters will be inversely proportional to the sensitivity coefficient for aspect ratio, α_0. Table 2 shows that α_0 increases significantly with increasing η_0.

3 Measurement of Flow Channel Pore Size Variations

An optical magnifying system can be used to directly measure the apparent variations in pore geometry for a regenerative wheel exchanger as shown in Fig. 17. This system requires a parallel light source, an optical magnifying system, and a screen and micrometer from which size variations can be accurately measured. The only hypothesis implied when this method is used is that the

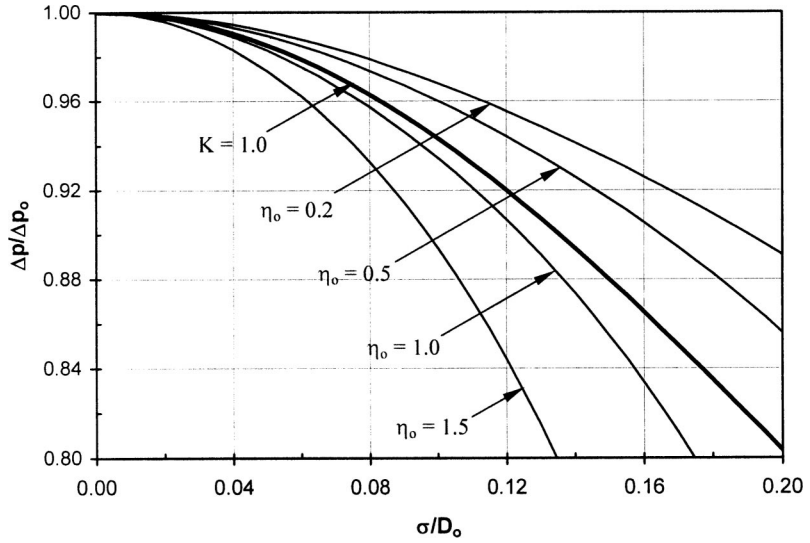

Fig. 14 Modified pressure drop ratio for a corrugated matrix energy wheel versus standard deviation divided by mean value of hydraulic diameter

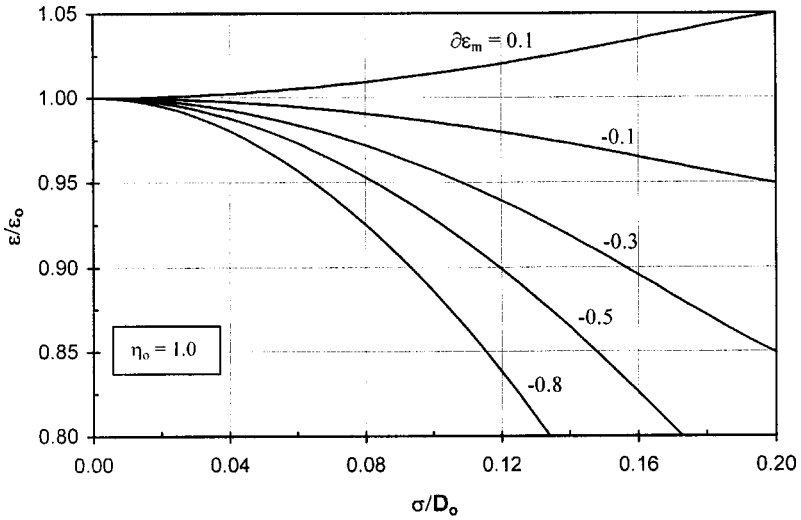

Fig. 15 Modified effectiveness ratio for a corrugated matrix energy wheel versus standard deviation divided by mean value of hydraulic diameter

walls of flow channels or pores are parallel to the light source. This optical method permits the direct evaluation of this hypothesis once the wall thicknesses of the flow channels are accurately known by independent micrometer measurements of the wall thickness and when the distance between many flow channels can be accurately measured (e.g., 20–50 flow channels). The method also permits the measurement of the apparent wall thickness of each flow channel.

These channel wall thicknesses should be consistent with any direct micrometer measurement of thicknesses. Apparent thickness deviations in the wall thickness which are larger than the expected values may be due to obstructions in the flow channels caused by extra thick pore walls or slight deviations in the pore wall angles with respect to the light beam. Of course, if angle deviations occur for one pore wall, they should be similar for adjacent pore walls. When the apparent wall thicknesses differed from the micrometer data, corrections were made to the data for wall thickness. Because the bias errors were small and the measured distances were all differences between two points only the precision uncertainty is significant for the combined optical-micrometer data.

Four different energy wheel matrices were investigated to illustrate the method of testing and analysis—one with parallel channel surfaces, one with honeycomb pores, and two with corrugated pores. These wheels were selected for their different flow channel or pore shapes and materials of construction and are not expected to be representative of a particular manufacturing method. Typical optical images are shown in Fig. 18 for each matrix. The overall geometric properties of these wheels are presented in Table 3. The optical magnification was 20× and the uncertainties for the micrometer and optical-micrometer system are presented in Table 4.

Sixty measurement positions $P(r_i, \theta_j)$ on each wheel were selected from a random set of coordinate numbers r_i, and θ_j as shown in Fig. 19.

A chi squared analysis of each of these characteristic dimension distributions for each wheel show that they are all random or

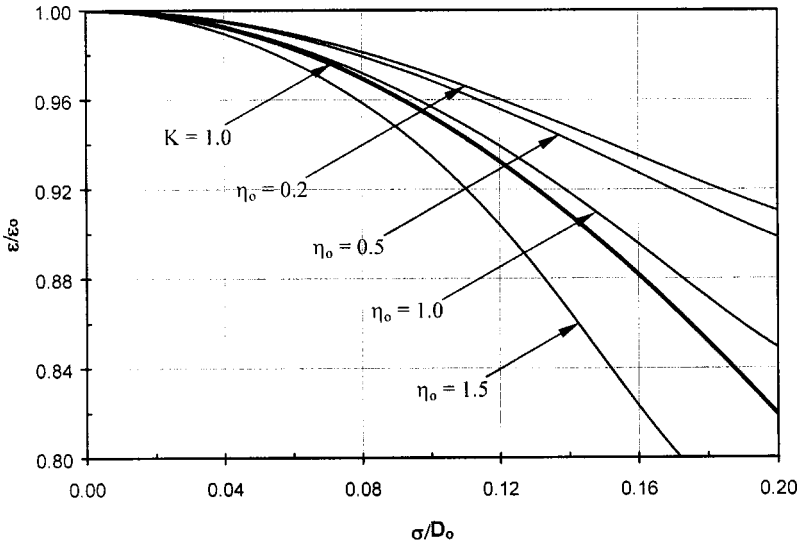

Fig. 16 Modified effectiveness ratio for a corrugated matrix energy wheel versus standard deviation divided by mean value of hydraulic diameter $\partial\epsilon_m = -0.3$

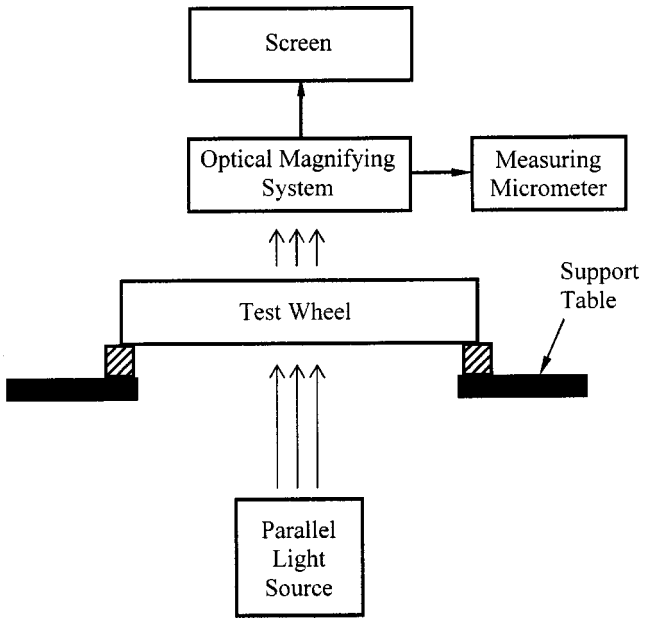

Fig. 17 A schematic of the optical system used to measure pore geometries

Gaussian for the 60 random positions selected for each wheel [20]. That is, $\chi^2 \leqslant 6$ for each wheel. Figure 20 shows the chi squared analysis of the characteristic dimension distributions of the four wheels where the bars give the data and the lines give the Gaussian distribution. For the corrugated wheels, the variation in the wave length, $2a$, was always small, so the prime reason for variation in the hydraulic diameter, D, is due to variations in the wave amplitude, b, as shown in Fig. 20.

A summary of the optical-micrometer results for the ratio of standard deviation in pore hydraulic diameter to mean hydraulic diameter and the estimated uncertainty is presented in Table 5. The results, summarized in Table 5, illustrate that variations in optical-micrometer determined pore size standard deviation are significant for each wheel but are especially large for the wheel with parallel surface flow channels.

Using the methods and results of this paper, σ/D_0 can be used to calculate the effectiveness ratio, ϵ/ϵ_0. Such results could be used by manufacturers to trade-off the flow channel quality control geometry specifications and costs relative to the expected acceptable performance degradation in effectiveness.

4 Conclusions

It has been shown that variations in pore sizes appear to be inevitable in the manufacture of regenerative wheels. This work will permit the manufacturer and the user of regenerative wheels to quantitatively determine how these variations impact the performance.

It is concluded from this theoretical development and the resulting simple algebraic expressions for pressure drop ratio and effectiveness ratios and corresponding graphs of performance for regenerative wheels that:

1. Large random variations in flow channel pore diameters in the matrix of regenerative wheels will significantly alter the pressure drop and effectiveness performance factors for a wheel compared to an identical wheel with no pore size variation.
2. For regenerative wheels with only one characteristic pore size dimension (e.g., parallel surfaces and symmetrical cylinders), the performance factors, such as pressure drop ratio $(\Delta p/\Delta p_0)$ or effectiveness ratio (ϵ/ϵ_0), usually decrease with increasing ratio of flow channel pore standard deviation to mean pore hydraulic diameter and simple algebraic expressions or graphs can be used to predict these ratios.
3. For regenerative wheels with two characteristic flow channel pore size dimensions (e.g., corrugated cylindrical pores) the

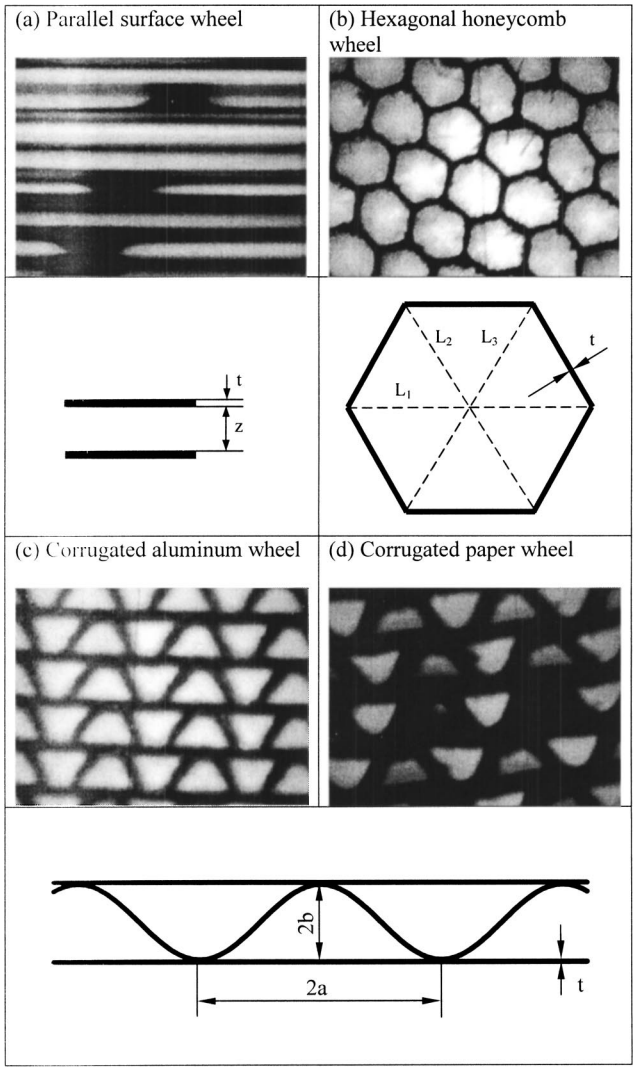

Fig. 18 Photos of the matrices for four different energy wheels

Table 3 Geometric properties for different regenerative wheels

Energy wheel	Pore material	Pore shape	Hub diameter (mm)	Wheel thickness (mm)	Wheel diameter (mm)
1	Plastic	Parallel	130±0.5	38±0.1	750±0.5
2	Paper	Honeycomb	55±0.5	101±0.5	508±0.5
3	Aluminum	Corrugated	80±0.5	99±0.5	508±0.5
4	Paper	Corrugated	104±0.5	101±0.5	508±0.5

Table 4 Bias and precision uncertainties for the micrometer and optical measurement system

	Bias uncertainty (mm)	Precision uncertainty (mm)
Micrometer	±0.001	±0.001
Optical system	±0.002	±0.002

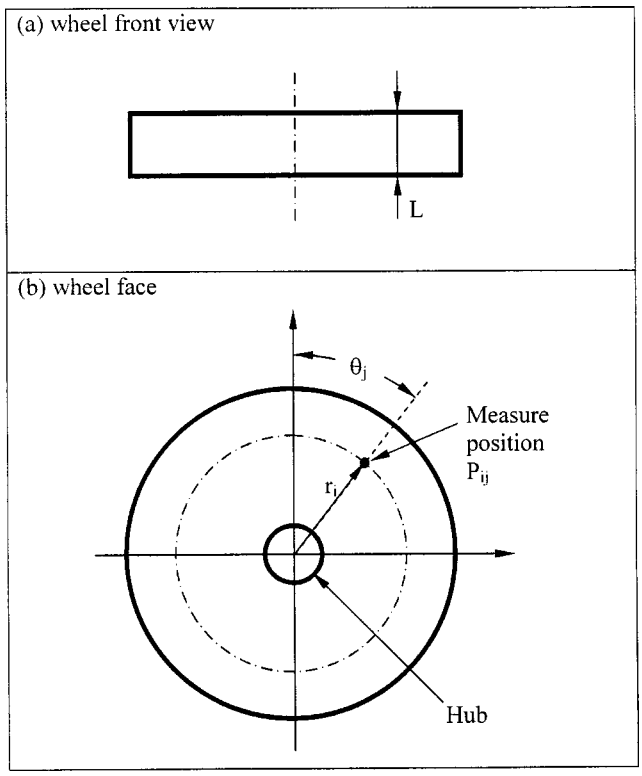

Fig. 19 A schematic diagram showing the optical measure position P_{ij} on an energy wheel face

Table 5 Comparison of the optical-micrometer results for four energy wheels

Wheel matrix	(σ/D_0) optical
Parallel surface	23.4%±3.0%
Honeycomb	7.6%±1.0%
Aluminum corrugated	6.4%±3.0%
Paper corrugated	11.8%±4.2%

performance ratios $(\Delta p/\Delta p_0)$ and (ϵ/ϵ_0) depend on a mean pore geometry aspect ratio as well as the standard deviation ratio for hydraulic diameter and simple algebraic equations or graphs can be used to predict these ratios.

In the experimental study of four regenerative wheels the random variation in flow channel pore sizes and the ratio of the standard deviation of hydraulic diameter to mean hydraulic diameter for each wheel matrix allowed the calculation of the pressure drop $(\Delta p/\Delta p_0)$ and effectiveness (ϵ/ϵ_0) ratios for these wheels. These are shown in Table 6.

The value of $(1-\epsilon/\epsilon_0)$ represents the lost fraction of recovered energy rate for any device operating at full capacity. This lost energy rate when integrated over a year will give an annual energy cost which can then be traded off with the cost of better quality control in the manufacture of regenerative wheels for recovering heat and moisture.

These experimental results, presented to illustrate the method to determine σ/D_0, show small but significant effects for $\Delta p/\Delta p_0$ and ϵ/ϵ_0 for each wheel and point to opportunities to increase energy recovery cost effectively.

All results presented in graphical form are restricted to a range of standard deviation to mean hydraulic diameter. Extrapolation of these curves is not advised.

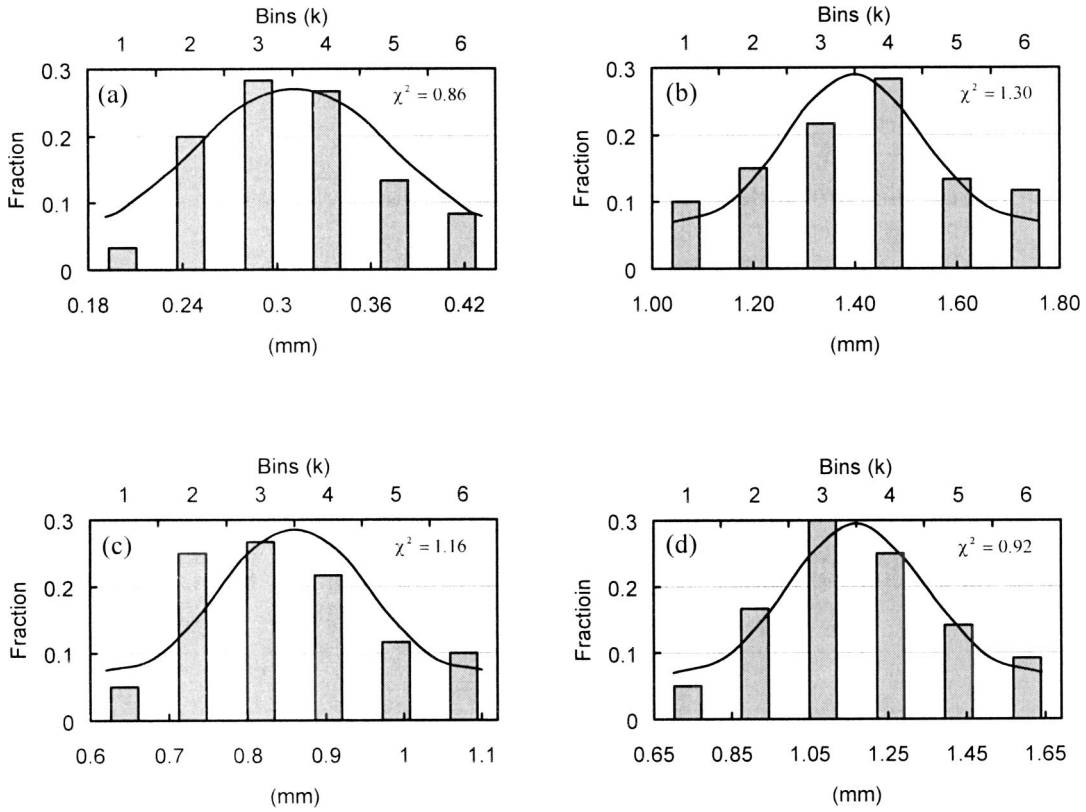

Fig. 20 A chi squared analysis of the characteristic dimension distributions of the four wheels; (*a*) parallel surface wheel (*D*/2), (*b*) hexagonal honeycomb wheel (*D*), (*c*) corrugated aluminum wheel (2*b*), and (*d*) corrugated paper wheel (2*b*) each compared with a Gaussian distribution line

Table 6 Optical-micrometer system determined pressure drop ($\Delta p/\Delta p_0$) and effectiveness (ϵ/ϵ_0) ratios for $\partial\epsilon_m = -0.3$

Wheel matrix	$\Delta p/\Delta p_0$ (%)	ϵ/ϵ_0 (%)
Parallel surface	85.8	86.5
Honeycomb	96.7	97.3
Aluminum corrugated	98.2	98.6
Paper corrugated	94.5	95.6

Acknowledgments

This research was supported by NSERC Canada. The energy wheels used for testing were provided by Venmar, CES, Saskatoon, SK, Canada.

Nomenclature

A = cross-sectional flow area of a pore channel, m^2
a = one half corrugated pore wave length, m
b = corrugated pore wave amplitude, m
D = hydraulic diameter of a pore channel in a wheel, m
D_0 = mean hydraulic diameter of all the pore channels in a wheel, m
f' = channel averaged skin friction factor (Fanning friction factor), dimensionless
h = enthalpy of a unit mass of dry air, J/kg
K = dimensionless constant, defined by Eq. (27) and illustrated in Fig. 12
K_f = dimensionless constant, defined by Eq. (22) and illustrated in Fig. 10
K_p = dimensionless constant, defined by Eq. (24) and illustrated in Fig. 11
L = thickness of a regenerative wheel, m
$\dot{m}$ = mass flow rate of dry air in an air stream, kg/s
N = number of flow channels in a regenerative wheel
P = wetted perimeter of a pore channel, m
Δp = pressure drop across a regenerative wheel with non-uniform pores, Pa
Δp_0 = pressure drop across a regenerative wheel with uniform pores, Pa
dp/dx = pressure gradient, Pa/m
Re = Reynolds number, $\rho VD/\mu$, dimensionless
T = dry bulb temperature, K or °C
V = mean flow velocity, m/s
W = humidity ratio (mass of water vapor per mass of dry air), kg_w/kg_a
w = width of flow channel for parallel plates for $z/w \to 0$, m
x = dimension along flow direction, m
z = height of flow channel for parallel plates, m
α_0 = dimensionless constant, defined by Eq. (29) and presented in Table 2
β_j = dimensionless constants, defined by Eq. (30) and presented in Table 2
ϵ = effectiveness of regenerative wheel with non-uniform pores, dimensionless
ϵ_0 = effectiveness of regenerative wheel with uniform pores, dimensionless
$\partial\epsilon_m$ = dimensionless ratio of effectiveness change as a function of mass flow rate, defined in Eq. (14)
η = aspect ratio, $2b/2a$, dimensionless
μ = viscosity, Pa s
ρ = density of air, kg/m^3
σ = standard deviation of hydraulic diameters, m

Subscripts

e = exhaust air stream
i = pore channel
m = related to mass flow rate
min = minimum value of supply or exhaust flow
s = supply air stream
0 = mean value for all pore channels
1 = supply air inlet
2 = supply air outlet
3 = exhaust air inlet
4 = exhaust air outlet

Appendix A: Development of Eqs. (3), (16), (12), (20), and (32)

1 Development of Eqs. (3) and (16). Due to the rotation of the wheel, the flow in the channels of a regenerative wheel typically reverses direction every few seconds (e.g., 1–5 s). This results in a quasisteady viscous flow field for all but the flow direction switch from the supply to the exhaust and vice versa.

Substituting the continuity Eq. (10)

$$\dot{m}_i = \rho_i V_i A_i \tag{A1}$$

into Eq. (2) written in the form

$$\Delta p_i = 2f' \frac{L}{D_i} \rho_i V_i^2 \tag{A2}$$

gives

$$\Delta p_i = C_i \frac{\dot{m}_i}{wD_i^3} \tag{A3a}$$

$$\Delta p_i = C_i \frac{\dot{m}_i}{D_i^4} \tag{A3b}$$

for parallel plates and symmetrical cylinders, respectively,

$$\text{where} \quad C_i = f' \,\mathrm{Re} \frac{8\mu L}{\pi \rho_i} \tag{A4}$$

is a constant, C, when the changes in ρ_i are negligible with respect to ρ_0. For ventilation air-to-air applications this assumption will cause a negligible error but for gas turbine applications with a large temperature difference between inlet air temperatures this assumption may cause some error. The f' Re correlation for laminar flow in the flow channels applies because the viscous flow field sets up and becomes fully developed in about 1% or less of the flow time duration for each half cycle.

The corresponding pressure drops to Eqs. (*A*3) and (*A*4) for wheels with equal total mass flow rate $N\dot{m}_0$ for parallel surfaces and symmetrical cylinders are, respectively,

$$\Delta p_0 = C \frac{\dot{m}_0}{wD_0^3} \tag{A5a}$$

$$\Delta p_0 = C \frac{\dot{m}_0}{D_0^4} \tag{A5b}$$

Combining Eqs. (*A*3*a*) and (*A*5*a*) and (*A*3*b*) and (*A*5*b*) for parallel surfaces and symmetrical cylinders gives

$$\frac{\Delta p_i}{\Delta p_0} = \frac{\dot{m}_i}{\dot{m}_0} \left(\frac{D_i}{D_0} \right)^{-3} \tag{A6a}$$

$$\frac{\Delta p_i}{\Delta p_0} = \frac{\dot{m}_i}{\dot{m}_0} \left(\frac{D_i}{D_0} \right)^{-4} \tag{A6b}$$

and noting that

$$N\dot{m}_0 = \sum_{i=1}^{N} \dot{m}_i \tag{A7}$$

which is the total mass flow rate. When we use the fact that pressure drop through each flow channel is the same as the others in the same wheel we get for the two types of pores

Table A1 Values of C/C_0 as a function of η_0 and σ/D_0 for a corrugated wheel

η_o \ σ/D_o	0.1	0.12	0.15
0.2	1.0001	1.0002	1.0003
0.315	1.0003	**1.0005***	1.0008
1.5	0.992	0.989	0.983

*This value corresponds to the case of the corrugated paper wheel with $\eta_0=0.315$, $\alpha_0=1.225$, and $\sigma/D_0=0.120$.

$$\frac{\Delta p}{\Delta p_0}\left(\frac{\dot m_0}{\dot m_i}\right)=\left(\frac{D_i}{D_0}\right)^{-3} \tag{A8a}$$

$$\frac{\Delta p}{\Delta p_0}\left(\frac{\dot m_0}{\dot m_i}\right)=\left(\frac{D_i}{D_0}\right)^{-4} \tag{A8b}$$

Now summing both sides over all N flow channels in the wheel gives

$$\frac{\Delta p}{\Delta p_0}=\left[\frac{1}{N}\sum_{i=1}^{N}\left(\frac{D_i}{D_0}\right)^3\right]^{-1} \tag{A9a}$$

$$\frac{\Delta p}{\Delta p_0}=\left[\frac{1}{N}\sum_{i=1}^{N}\left(\frac{D_i}{D_0}\right)^4\right]^{-1} \tag{A9b}$$

for the parallel surface and symmetrical cylinder pores respectively. These are Eqs. (3) and (16).

2 Development of Eqs. (12) and (20). The heat and mass transfer fields inside each channel are transient during the entire half cycle when another flow direction reversal occurs for another transient heat and mass transfer process. This transient heat and mass transfer in each flow channel air over each entire half cycle is coupled to the solid matrix of the wheel undergoing a transient process of heat and mass transfer. The Nu correlations for steady state heat (or mass) transfer or for even transient fixed constant isothermal or heat flux wall boundary conditions and uniform initial condition (i.e., f' Re=constant) do not apply. In general, these complex transient heat and mass transfer processes are coupled in a relationship that has only been solved numerically [10]. Using such a fully validated simulation, one can then predict effectiveness as a complex function of seven independent non-dimensional parameters plus inlet conditions [17].

The following equation is the Eq. (8) in the paper

$$\epsilon=\frac{1}{N\dot m_0}\sum_{i=1}^{N}\epsilon_i\dot m_i \tag{A10}$$

Using Eqs. (*A*1) and (*A*7) and assuming that for any particular operating Eq. (11) in the paper is

$$\epsilon_i\dot m_i=\epsilon_0\dot m_0+\left.\frac{\partial\epsilon}{\partial\dot m}\right|_{\dot m=\dot m_0}(\dot m_i-\dot m_0)\dot m_i \tag{A11}$$

Substituting Eq. (*A*11) into Eq. (*A*10), we get

$$\epsilon=\epsilon_0+\frac{\dot m_0}{N}\left.\frac{\partial\epsilon}{\partial\dot m}\right|_{\dot m=\dot m_0}\sum_{i=1}^{N}\left[\left(\frac{\dot m_i}{\dot m_0}\right)^2-\left(\frac{\dot m_i}{\dot m_0}\right)\right] \tag{A12}$$

or

$$\frac{\epsilon}{\epsilon_0}=1+\frac{\dot m_0}{\epsilon_0}\left.\frac{\partial\epsilon}{\partial\dot m}\right|_{\dot m=\dot m_0}\frac{1}{N}\sum_{i=1}^{N}\left[\left(\frac{\dot m_i}{\dot m_0}\right)^2-\left(\frac{\dot m_i}{\dot m_0}\right)\right] \tag{A13}$$

For each flow channel, i, the pressure drop can be calculated for the parallel surface and symmetrical cylinder matrix pores using Eqs. (*A*3*a*) and (*A*3*b*). Substituting Eqs. (*A*6*a*) and (*A*6*b*) into Eq. (A13) gives for $\Delta p_i/\Delta p_0=\Delta p/\Delta p_0$:

$$\frac{\epsilon}{\epsilon_0}=\frac{1}{N}\sum_{i=1}^{N}\left\{1+\left(\frac{\dot m}{\epsilon_0}\frac{\partial\epsilon}{\partial\dot m}\right)\Big|_{\dot m=\dot m_0}\left[\left(\frac{\Delta p}{\Delta p_0}\right)^2\left(\frac{D_i}{D_0}\right)^6-\left(\frac{\Delta p}{\Delta p_0}\right)\left(\frac{D_i}{D_0}\right)^3\right]\right\} \tag{A14a}$$

$$\frac{\epsilon}{\epsilon_0}=\frac{1}{N}\sum_{i=1}^{N}\left\{1+\left(\frac{\dot m}{\epsilon_0}\frac{\partial\epsilon}{\partial\dot m}\right)\Big|_{\dot m=\dot m_0}\left[\left(\frac{\Delta p}{\Delta p_0}\right)^2\left(\frac{D_i}{D_0}\right)^8-\left(\frac{\Delta p}{\Delta p_0}\right)\left(\frac{D_i}{D_0}\right)^4\right]\right\} \tag{A14b}$$

These are the Eqs. (12) and (20) for the parallel surface and symmetrical cylinder pore wheels.

3 Development of Eq. (32). For the case of corrugated flow channels, the value of C_i in Eqs. (*A*3*a*) and (*A*3*b*) is no longer a constant if variations in the hydraulic diameter occur.

In this case

$$\left(\frac{\Delta p}{\Delta p_0}\right)=\left(\frac{\dot m_i}{\dot m_0}\right)\left(\frac{D_0}{D_i}\right)^4\left(\frac{C_i}{C_0}\right) \tag{A15}$$

Now it will be shown that the term, (C_i/C_0), when averaged for a Gaussian distribution of pore diameters, will be very close to 1.0. To do this we expand (C_i/C_0) in the form:

$$\frac{C_i}{C_0}=\frac{K_{fi}}{K_{fo}}\cong 1+\frac{K'_{fo}}{K_{fo}}\eta_0\alpha_0\frac{\sigma}{D_0}\tau+\frac{K''_{fo}}{2!K_{fo}}\eta_0^2\alpha_0^2\left(\frac{\sigma}{D_0}\right)^2\tau^2 \tag{A16}$$

where $K_f(\eta)$ is shown in Fig. 10 and where $K'_{fo}=dK_f/d\eta\big|_{\eta=\eta_0}$ and $K''_{fo}=d^2K_f/d\eta^2\big|_{\eta=\eta_0}$. Values of K''_{fo} are determined by curve fitting K_f as a polynomial in η over each range of η to get a fit with $0.999<r^2<1.001$.

An order of magnitude analysis of these terms in Eq. (*A*16) can be done using the same method of analysis that used to obtain explicit equations for $(\Delta p/\Delta p_0)$ and (ϵ/ϵ_0) in Eqs. (6), (19), (15), and (21). That is, the average value of (C_i/C_0), for a Gaussian distribution of pore sizes is

$$\frac{C}{C_0}=\frac{1}{\sqrt{2\pi}}\int_{-\infty}^{\infty}\left[1+\frac{K'_{fo}}{K_{fo}}\eta_0\alpha_0\frac{\sigma}{D_0}\tau+\frac{K''_{fo}}{2!K_{fo}}\eta_0^2\alpha_0^2\left(\frac{\sigma}{D_0}\right)^2\tau^2\right]e^{-\tau^2/2}d\tau \tag{A17}$$

Integration gives

$$\frac{C}{C_0}=1+\frac{1}{2}\frac{K''_{fo}}{K_{fo}}\eta_0^2\alpha_0^2\left(\frac{\sigma}{D_0}\right)^2 \tag{A18}$$

Values of C/C_0 are presented in Table A1 later.

It is evident from these results for $0.2\leqslant\eta_0\leqslant1.5$ and $0.1\leqslant\sigma/D_0\leqslant1.5$ that C/C_0 in Eq. (*A*15) would differ from 1.0 by no more than 1.7% for $\eta_0=1.5$ and $\sigma/D_0=0.15$. However, for the wheels optically investigated this difference is equal to or less

than 0.05%. Such small corrections could not be seen on the graphical results and they are much smaller than the uncertainty in determining the experimental value of σ/D_0.

It was concluded from this analysis that Eq. (20) can be used with no significant error for both the corrugated and symmetrical cylinder matrices. Using Eq. (20) for corrugated pores finally gives Eq. (32) as explained in Sec. 2.3.

Appendix B: Determination of the Coefficients for the Calculation of the Effectiveness Ratio for Corrugated Energy Wheels

The effectiveness ratio for corrugated energy wheels can be calculated using Eq. (32):

$$\frac{\epsilon}{\epsilon_0}=1+\partial\epsilon_m\left\{\left(\frac{\Delta p}{\Delta p_0}\right)^2\left[1+B_{2,2}\left(\frac{\sigma}{D_0}\right)^2+B_{2,4}\left(\frac{\sigma}{D_0}\right)^4+B_{2,6}\left(\frac{\sigma}{D_0}\right)^6\right]-\left(\frac{\Delta p}{\Delta p_0}\right)\left[1+B_{1,2}\left(\frac{\sigma}{D_0}\right)^2+B_{1,4}\left(\frac{\sigma}{D_0}\right)^4+B_{1,6}\left(\frac{\sigma}{D_0}\right)^6\right]\right\} \quad (B1)$$

where

$$B_{1,2}=6+4\beta_1+\beta_2 \quad (B2)$$

$$B_{1,4}=3+12\beta_1+18\beta_2+12\beta_3+3\beta_4 \quad (B3)$$

$$B_{1,6}=15\beta_2+60\beta_3+90\beta_4 \quad (B4)$$

$$B_{2,2}=28+16\beta_1+2\beta_2+\beta_1^2 \quad (B5)$$

$$B_{2,4}=210+336\beta_1+168\beta_2+48\beta_3+6\beta_4+48\beta_1\beta_2+6\beta_1\beta_3+84\beta_1^2+3\beta_2^2 \quad (B6)$$

and

$$B_{2,6}=420+1680\beta_1+2100\beta_2+1680\beta_3+840\beta_4+1680\beta_1\beta_2+840\beta_1\beta_3+240\beta_1\beta_4+240\beta_2\beta_3+30\beta_2\beta_4+1050\beta_1^2+420\beta_2^2+15\beta_3^2 \quad (B7)$$

References

[1] Shang, W., and Besant, R. W., 2001, ''Energy Wheel Effectiveness Evaluation, Part I: Outlet Airflow Property Distributions Adjacent to an Energy Wheel; Part II: Testing and Monitoring Energy Wheels in HVAC Applications,'' ASHRAE Trans., **107**, pp. 266–280.

[2] Mahbub-Uddin, A. K. M., and Bell, K. J., 1988, ''Effect of Uncertainties on the Design and Operation of Systems of Heat Exchangers,'' *Heat Transfer Equipment Design*, R. K. Shah, E. C. Subbarao, and R. A. Meshelkar, eds., Hemisphere, New York, pp. 39–47.

[3] Fraas, A. P., 1989, *Heat Exchanger Design*, Wiley, New York.

[4] Kuppan, T., 2000, *Heat Exchanger Design Handbook*, Marcel Dekker, New York.

[5] London, A. L., 1970, ''Laminar Flow Gas Turbine Regenerators—The Influence of Manufacturing Tolerances,'' ASME J. Eng. Power, **92**, pp. 46–56.

[6] Mondt, J. R., 1977, ''Effects of Nonuniform Passages on Deepfold Heat Exchanger Performance,'' ASME J. Eng. Power, **99**, pp. 657–663.

[7] London, A. L., 1980, ''Discussion on the Paper by Mondt [6]—Effects of Nonuniform Passages on Deepfold Heat Exchanger Performance,'' ASME J. Eng. Power, **102**, pp. 510–511.

[8] Rohsenow, W. M., 1981, ''Why Laminar Flow Heat Exchangers Can Perform Poorly,'' *Heat Exchangers: Thermal-Hydraulic Fundamentals and Design*, S. Kakac, A. E. Bergles, and F. Mayinger, eds., McGraw-Hill, New York, pp. 1057–1071.

[9] Shah, R. K., and London, A. L., 1980, ''Effects of Nonuniform Passages on Compact Heat Exchanger Performance,'' ASME J. Eng. Power, **102**, pp. 653–659.

[10] Simonson, C. J., and Besant, R. W., 1997, ''Heat and Moisture Transfer in Desiccant Coated Rotary Energy Exchangers, Part I: Numerical Model; Part II: Validation and Sensitivity Studies,'' Int. J. HVAC&R Research, **3**, pp. 325–368.

[11] Stiesch, G., Klein, S. A., and Mitchell, J. W., 1995, ''Performance of Rotary Heat and Mass Exchangers,'' Int. J. HVAC&R Research, **1**, pp. 308–323.

[12] Nimmo, B. G., Collier, Jr., R. K., and Rengarajan, R., 1993, ''DEAC: Desiccant Enhancement of Cooling-Based Dehumidification,'' ASHRAE Trans., **99**, pp. 842–848.

[13] Zheng, W., Worek, W. M., and Novosel, D., 1993, ''Control and Optimization of Rotational Speeds for Rotary Dehumidifiers,'' ASHRAE Trans., **99**, pp. 825–833.

[14] Simonson, C. J., Ciepliski, D. L., and Besant, R. W., 1999, ''Determining the Performance of Energy Wheels, Part I: Experimental and Numerical Methods; Part II: Experimental Data and Numerical Validation,'' ASHRAE Trans., **105**, pp. 174–205.

[15] ASHRAE, 1991, *ANSI/ASHRAE Standard 84-1991R: Method of Testing Air-to-Air Heat Exchangers*, American Society of Heating, Refrigerating and Air-Conditioning Engineers, Inc., Atlanta.

[16] Shah, R. K., and London, A. L., 1978, *Laminar Flow Forced Convection in Ducts*, Supplement 1 to Advances in Heat Transfer, Academic, New York.

[17] Simonson, C. J., and Besant, R. W., 1999, ''Energy Wheel Effectiveness, Part I: Development of Dimensionless Groups; Part II: Correlations,'' Int. J. Heat Mass Transfer, **42**, pp. 2161–2185.

[18] ARI, 2001, *ARI Standard 1060: Rating Air-to-Air Energy Recovery Ventilation Equipment*, Air-Conditioning & Refrigeration Institute, Arlington, Virginia.

[19] Bejan, A., 1984, *Convection Heat Transfer*, Wiley, New York.

[20] Taylor, J. R., 1982, *An Introduction to Error Analysis*, University Science Books, Mill Valley, CA.

Investigation of Brush Seal Flow Characteristics Using Bulk Porous Medium Approach

Yahya Dogu
Department of Mechanical Engineering,
Kirikkale University,
71450 Yahsihan, Kirikkale, Turkey

The flow behavior through a brush seal has been investigated by developing a flow analysis procedure with a porous medium approach. In order to increase the brush seal performance and use at more severe operating conditions, the complex flow in the bristle pack has become the major concern affecting seal features such as blow-down, hang-up, hysteresis, and bristle flutter. In this study, an axisymmetric CFD model is employed to calibrate anisotropic permeability coefficients for the bristle pack based on available experimental data: leakage, axial pressure on the rotor surface, and radial pressure on the backing plate. A simplified form of the force balance equation is introduced for the flow in the porous bristle pack. Different sets of permeability coefficients are defined for the fence height region below the seal backing plate and the upper region of the seal to correlate the different physical structures and behavior of these regions during operation. The upper region is subject to more stiffening due to backing plate support while the fence height region is free to spread and bend in the axial direction. It is found that flow resistance for the upper region should be 20% higher than the fence height region in order to match the experimental pressure within the bristle pack. Analysis results prove that the brush seal is well represented as a porous medium with this approach. Based on the model developed, characteristic flow and pressure fields in the entire bristle pack have been explored. [DOI: 10.1115/1.1808425]

Introduction

A brush seal is a circular seal used for fluid sealing in rotating machinery especially in gas turbines between rotating and stationary parts. It is made of three main components: bristle pack, front plate, and backing plate (Fig. 1). The bristle pack containing flexible-fine wires is clamped at a lay angle between front and backing plates and circumferentially welded at the outer periphery. The seal is mounted to the stator over the rotor surface between two cavities to prevent leakage flow from the high to low pressure side. The backing plate supports the bristle pack to carry the pressure load and prevents the small diameter bristles from blowing outwards. It is convenient to divide the bristle pack into two regions: the fence height and the upper portion. The radial height between bristle tips and backing plate inner diameter is called the fence height. The rest of bristle height out to the bristle pinch point is called the upper region. The total bristle height is the bristle free height.

Brush seals have been successfully applied in rotating machinery since the 1980s. Ferguson and Gorelev et al. [1,2] first reported the better sealing performance of brush seals compared to labyrinth seals. Brush and labyrinth seals were tested at the same operating conditions and brush seals were found to leak considerably less (ranging from 3 to 20 times) than labyrinth seals [1–7]. In addition to significant leakage reduction, the flexible brush seals maintain stable leakage performance for longer service while labyrinth seals suffer permanent performance degradation due to transient rotor excursions.

One of the main advantages of a brush seal arises from the achieved minimum clearance between the rotor surface and bristle tips. The brush seal ring fits on the rotor surface with a very small clearance mostly in interference; therefore it is referred as the contact seal. The only flow path for a line-to-line or interference position is the flow path through randomly formed voids among bristles in the fence height region.

Another characteristic advantage of a brush seal is a result of the lay angle of bristles in the direction of rotor rotation. The flexible bristle bundle tolerates rotor excursions due to operation conditions, such as vibration, centrifugal and thermal growth, with less wear compared to other sealing applications. The flexible bristles also close the clearance as they wear out or after transient rotor excursion by changing their lay angle due to inward radial flow in the bristle pack from the radial pressure gradient. This dynamic behavior of a brush seal, called as blow-down, makes the brush seal dynamic and maintains a minimum leakage performance. On the contrary, once a labyrinth seal is worn by rotor excursion, it is not possible to close the clearance.

The behavior of bristle pack under pressure load characterizes the performance of the brush seal, which is mainly in terms of leakage and life. Both performance criteria depend on the clearance between bristle tips and rotor surface. These two criteria contradict each other. The decreasing clearance, beyond a line-to-line position, minimizes the leakage while shortening the seal life as a result of increasing wear between bristle tips and the rotor surface.

The dynamic sealing performance of brush seals has led to extensive studies to explain the seal behavior and to widen the limits of operating conditions for more severe environments such as higher pressure load, surface speed, temperature, and rotor excursion. A comprehensive brush seal bibliography is given in the literature [6]. There are many involved parameters in a robust brush seal design, as addressed by Dinc et al. [7], and a design procedure has been developed. Extensive experimental data has been reported in the literature [1–7]. Using theoretical knowledge and experimental data, structural and flow models have been developed over the years to increase the seal performance. Flow analysis of the brush seal, which is of interest in this study, has become one of the major steps in the seal design.

The flow and pressure fields in close vicinity of the bristle pack and within the bristle matrix affect the seal dynamics and perfor-

Contributed by the International Gas Turbine Institute (IGTI) of THE AMERICAN SOCIETY OF MECHANICAL ENGINEERS for publication in the ASME JOURNAL OF ENGINEERING FOR GAS TURBINES AND POWER. Paper presented at the International Gas Turbine and Aeroengine Congress and Exhibition, Atlanta, GA, June 16–19, 2003, Paper No. 2003-GT-38970. Manuscript received by IGTI, October 2002, final revision, March 2003. Associate Editor: H. R. Simmons.

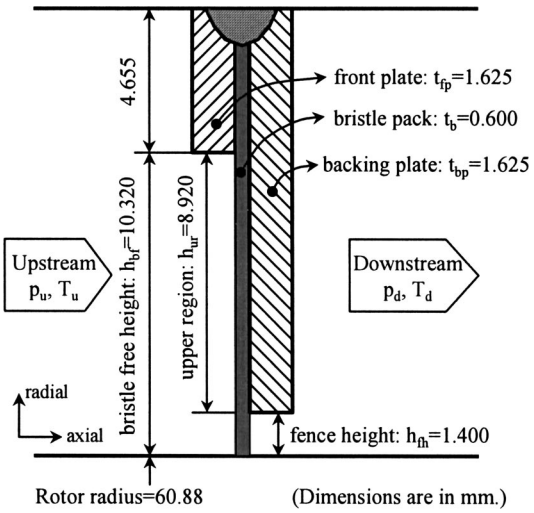

Fig. 1 Brush seal geometry and boundary conditions

mance. In their multiple brush seals tests, O'Neill et al. [8] reported bristle instability caused by the momentum of the leakage flow hitting the bristle pack. The bristle pack forms a complex porous structure blocking the flow path. As the flow diffuses into voids among bristles, the bristles move depending on balance of elastic forces, aerodynamic forces and frictional forces among bristles, and between the bristles and backing plate. There are two main issues arising from the balance of these forces. One is that the bristles get tighter as pressure load pushes them against the backing plate while the inward radial flow pulls them to change the lay angle towards the rotor surface, i.e., blow-down. Blow-down tends to close the clearance with the rotor surface, yet it increases the bristle tip wear for excessive pull down, interference. The other issue is the bristle stiffening effects when the aerodynamic forces cannot overcome the internal friction within the bristle pack. This is called bristle hang-up. After transient rotor excursions or bristle wear, the clearance should close to maintain the minimum leakage. There is also a hysteresis issue for increasing versus decreasing pressure loading during operation. In addition to effects of the force balance, the flow attack angle and aerodynamic forces on the upstream face bring into consideration bristle flutter that causes fatigue failure.

The flow within the bristle pack is the driving mechanism of the seal dynamics; therefore, a clear flow representation has become an unavoidable need in design stages. In order to control the dynamic behaviors affecting seal performance, and to develop certain design tools, the porous medium approach has been successfully used for the flow modeling in the bristle pack. Many flow models have been developed using different approaches to estimate leakage and pressure load. It would be appropriate to categorize the flow modeling studies for the bristle pack into three groups, cross flow analysis through voids among bristles, bulk flow models, and porous medium models. The latter model is the one of interest in this study.

Cross Flow Through Bristles. The first category for flow analysis of brush seals is to analyze the flow through voids among bristles. The bristles under pressure load compact and form a complex structure. It is a challenge to estimate the flow paths among randomly distributed bristles as they dynamically move, bend, flex, and twist during operation. Flow visualization studies show that there is no uniformity of flow paths among bristles [9–12]. Bristles closely touch, at some points fully closing the flow path while there might be a through opening at other circumferential sections. Nonuniform fabrication of bristle pack is the source of these flow paths in addition to dynamic loading effects. It is observed that the void formation is totally spatial and temporal. Many flow patterns, rivering, jetting, lateral, and vorticial, may form among bristles. Axial pressure distribution over bristle pack is also measured as almost linear in the flow visualization studies.

However, the flow analysis through a uniformly positioned column of bristles gives the insight for flow and pressure fields in the bristle pack only in the axial direction. This flow type is very common, especially for heat exchangers and filters, therefore, large numbers of published works are available in the open literature. Staggered and in-line positions of cylindrical bristles are two types of common configurations studied for brush seal. Mullen et al. [13] used in-line position, while Braun and Kudriavtsev [14–16] solved Navier–Stokes equations for flow among a set of staggered multi-row and multi-column cylinders by applying a finite difference method, and compared the flow field with experiments. Sharatchandra and Rhode [17] included the effect of rotor rotation into their numerical analysis and reported the leakage reduction due to rotation for staggered configuration. Demiroglu et al. [18] also used the staggered configuration and estimated the linear axial pressure distribution and leakage rate.

In addition to observing flow patterns, these analyses estimated leakage and pressure drop through the packing thickness. All of these analyses are two-dimensional neglecting the radial direction that is the most important direction for seal dynamics issues: blow-down, hang-up, hysteresis, flutter, etc.

Bulk Flow Models. In the second category, semi-empirical relations are developed based on flow-driven nondimensional parameters and geometrical configurations. These relations are successfully applied to many experimental cases. The definitions of flow-driven parameters are based on analysis results of cross flow through bristles.

One of the first proposed bulk flow models [19–22] uses the friction factor for cross flow in packed fibers [23]. These bulk flow models captured the experimental leakage trend as a function of pressure load.

Another leakage flow model was proposed by Chupp et al. [24]. In addition to the effective brush thickness, which is defined as a measure of the compactness of the bristle pack, the pressure drop in flow across staggered tube bundles [25] was applied in the model. A brush seal flow parameter was used to plot the results. Holle et al. [26] revised the model by assuming the bristle distribution to have hexagonal packing. They pointed out that the use of a single parameter of effective thickness in the flow model is adequate for a bulk flow model. Dowler et al. [27] extended this model to different brush seal sizes. Chupp and Holle [28] used the flow through randomly distributed bristles [29] in their effective-thickness bulk flow model.

Overall, bulk flow models only estimate the leakage mainly as a function of seal geometry and operation parameters, and are useful for the initial design iteration.

Porous Medium Models. The third category in brush seal flow analysis is to treat the entire bristle pack as a single porous medium with defined resistances to flow. The porous medium approach is basically solving the Navier–Stokes equation with the additional flow resistances due to friction between flow and bristles. For the highly resistive porous media, this equation is simplified by neglecting the inertial and viscous terms, which yields a balance equation between pressure gradient and flow resistance terms. This approach has been successfully applied for brush seals.

Apart from the first two flow modeling approaches discussed above, the porous flow model calculates the pressure distribution in the bristle pack in addition to leakage and axial pressure estimations. This pressure distribution can be used in structural models as aerodynamic forces acting on the bristles for seal dynamics issues. The flow field in the entire brush seal regions is also visualized in the porous medium model.

The first leading study on porous medium modeling of brush seals was presented by Bayley and Long [30]. The boundary-layer

equations in the bristle pack were simplified by neglecting the inertial terms that yielded a balance equation between pressure and viscous forces. The resulting linear Darcian porous medium equation was numerically solved by describing the overall porosity of the bristle pack and yielded the pressure distribution in the bristle pack. Valuable experimental work was carried out for 0.25 mm radial interference, and axial pressure on rotor surface and radial pressure on backing plate surface as well as leakage estimate were reported. Their results have widely been referenced in many studies including this one.

Hendricks et al. [31] predicted brush seal leakage using Ergun's porous flow model [32], which is a non-Darcian transport equation for porous media, with modifications for brush seals. Carlile et al.'s experimental data [5] were compared with the model.

Then, there have been increasing numbers of studies on flow modeling of brush seal as a porous medium. Chew and Hogg [33] presented a one-dimensional porosity model for the brush seal. A simplified balance equation between pressure gradient and flow resistance terms was solved. Leakage data from different literature were compared, and the extension of their one-dimensional model into two dimensions was discussed.

A two-dimensional porous medium approach for bristle pack was further studied by Chew et al. [34]. They treated the bristle pack as an axisymmetric and anisotropic porous region with nonlinear flow resistance coefficients. The full Navier–Stokes equations were solved with added resistance forces for the bristle pack. Both viscous and inertial forces were included in the resistance term. The direction of resistance coefficients was defined on a local coordinate system aligned with the bristle lay-angle. The correlation agreed with Bayley and Long's [30] experiments with some overestimations for pressure on the backing plate. This porous medium approach became the originating study for follow on studies [35–37].

Turner et al. [35] extended Bayley and Long's [30] experiments to investigate the effect of clearance. They employed Chew et al.'s [34] CFD model with adjusted resistance coefficients for clearance cases. The mesh density in these CFD models [34,35] was relatively coarse to capture the flow details, and the mesh independent solution was not strongly stated.

Chen et al. [36] iteratively coupled a CFD model [34] with a structural model for the first time. They calculated torque as a function of rotor speed. They defined two different sets of resistance coefficients depending on the level of pressure ratio to match the experiments. They pointed out that the bristles were more closely packed at higher pressure ratios. Consequently, higher flow resistance coefficients were prescribed to match the experimental leakage.

Chen et al. [37] carried out an experimental and numerical study on a five-times large-scale brush seal with geometrical and physical similarities. The large-scale model enabled measurement of the pressure distribution within the bristle pack using hollow bristles. They measured the pressure on the backing plate and at the bristle tips using pressure tappings. Their CFD model is based on Chew et al.'s [34] approach. They divided the bristle pack into several regions to match the linear axial pressure distribution on rotor surface over bristle pack thickness for their large-scale brush seal model.

In the present study, a CFD analysis has been carried out to determine an outline for calibrating the anisotropic permeability coefficients for the porous bristle pack using available experimental data and the flow behavior of a brush seal. Three different experimental criteria have been employed in determining the permeability coefficients: leakage, axial pressure distribution on rotor surface, and radial pressure distribution on backing plate. In order to match these experimental data, it has been concluded that bristle pack is well represented by two distinct regions of permeability coefficients. These regions are the fence height region and the upper region that have different structural behavior during operation. The details of mathematical modeling and permeability calibration are explained below. Based on the calibrated resistances, flow characteristics in bristle pack are investigated and some explored observations are discussed.

Mathematical Formulation

A brush seal is located on the rotor between upstream and downstream cavities as seen in Fig. 1. The up/downstream cavities are extended in the axial direction to ensure the fully developed flow conditions approaching and leaving the seal. The analysis geometry consists of two regions: the cavities (up/downstream) and the bristle pack. The Navier–Stokes equations for a Newtonian fluid defining the steady state mass and momentum transfer in the entire analysis region except bristle pack are written below in Cartesian tensor notations:

$$\frac{\partial \rho u_i}{\partial x_i} = 0 \tag{1}$$

$$u_j \frac{\partial \rho u_i}{\partial x_j} = -\frac{\partial P}{\partial x_i} + \mu \frac{\partial^2 u_i}{\partial x_j \partial x_j} \tag{2}$$

The flow in the entire cavity is modeled as turbulent and compressible. The k-ε model is used for the turbulent flow. The ideal gas law is applied for the compressible air flow. Pressure and temperature boundary conditions are defined at up/downstream boundaries. Constant air properties are taken at cavity temperature and atmospheric pressure conditions. The bristle pack is considered to be a porous medium with defined flow resistance coefficients. The bristle pack porous medium approach and calibration of permeability coefficients are discussed below.

Calibration of Brush Seal Permeability Coefficients

The bristle pack in a brush seal forms a porous medium. The flexible bristles change their shape by bending and moving during operation depending on pressure load and flow conditions. They compact on the backing plate and spread/bloom/bend at the fence height region. Flow visualization studies showed the dynamic nature of the spatial and temporal void formation and flow patterns [9–12]. The porous medium approach for the entire bristle pack overcomes the issues of this dynamic movement and complex structure of bristle pack, yet it needs precisely calibrated permeability coefficients from matching the experimental measurements. The flow and pressure fields in the bristle pack with calibrated permeability should match all available experimental measurements, i.e., mainly leakages and pressure fields.

The flow in a porous medium is subject to additional resistance forces compared to flow in a nonporous medium, that is, the fluid friction with solid bristle surfaces. The permeability of a porous medium is the ability to conduct the fluid. The bulk resistance to a Newtonian fluid flow through a porous solid matrix was first measured by Darcy (1856) and is characterized by applying a volumetric force balance as

$$-\frac{dP}{dx_i} = \frac{\mu}{K_i} u_i \tag{3}$$

where x_i represents the orthotropic flow directions, K_i and u_i are the permeability of the porous media and superficial velocity in the direction of x_i, respectively. The superficial velocity is the velocity that would exist for the same volumetric rate of flow in the absence of porous medium. It is, then, stated as $u_i = u/\varepsilon$, where porosity, ε, is defined as the volumetric fraction of the medium occupied by the fluid in the entire medium.

Equation (3) is a linear Darcian porosity model. There is only a viscous resistance term setting the pressure gradient. Other than Darcy's porosity model, various resistance models have been developed and applied to porous materials. For brush seals, the following resistance relationship has been used and validated experimentally by many researchers [31–37]:

$$-\frac{dP}{dx_i} = a_i \mu u_i + b_i \rho |u_i| u_i \tag{4}$$

where a is the viscous resistance coefficient and b is inertial resistance coefficient. These coefficients can be combined with their multipliers:

$$-\frac{dP}{dx_i} = (\alpha_i |u_i| + \beta_i) u_i \tag{5}$$

where α is inertial resistance and β is viscous resistance. This equation defines one non-Darcian porosity model with added inertial resistance term. The two coefficients, α and β, will be called permeability coefficients while the inverse of a, in Eq. (4), gives the permeability, K, defined by Darcy law in Eq. (3). The resistance coefficients, combined with their multipliers in Eq. (5), result in a single term for inertial and viscous resistances. In this representation, the porous medium is defined as a fluid medium having an effective inertial resistance and an effective viscous resistance to flow. This yields a balance equation between pressure gradient and effective resistance terms. Nevertheless, this representation has included the dependency of the coefficients to working fluid and conditions.

As seen in Eq. (5), there are two permeability coefficients, α and β, for each spatial direction for an anisotropic porous medium. Considering three coordinate directions for a brush seal, it yields six permeability coefficients. These coefficients are to be determined through a calibration procedure using experimental data.

In previous porous brush seal studies [34–37], Eq. (5) was added to the right-hand side of the momentum equation, Eq. (2), as an additional flow resistance force. Chew et al. [34] first solved the resulting equation for completeness of their model and programming convenience. However, the definition of effective viscosity for the bristle pack led to improper modeling of the viscous shear terms, ending with a simple order-of-magnitude estimate.

On the other hand, when the porous medium is highly resistive, the inertial and viscous shear terms in the momentum equation become negligibly small compared to flow resistance terms. Thus, the momentum equation reduces to a balance equation between pressure gradient and flow resistance forces (viscous and inertial forces), which is stated as Eq. (5). The bristles under pressure load move, and get firmly packed against the backing plate forming a highly resistive medium to the flow diffusion. In reality, the aim in the porous medium treatment is to match the measured leakage and pressure distribution in the medium. Instead of dealing with many terms in the momentum equation, Eq. (5) is a simplified form to investigate the flow and pressure fields in the bristle pack. In this study, Eq. (5) is solved for the porous bristle pack. The flow resistance coefficients used in this equation are calibrated to match the experimental data. This is one of the main differences with previous porous medium studies for brush seals [34–37].

Another difference is the definition of directions for resistance coefficients. Previous studies used a local coordinate system along the bristle lay-angle and normal to bristles [30,33–37]. A tensor operation [34] was used to map resistance coefficients to the natural cylindrical coordinate system. In this case, the coefficients in the axial direction and normal to bristles became equal to each other. In the present study, the directions of resistance coefficients are defined in the natural cylindrical coordinate system. There are axial and radial resistance coefficients. The resistance coefficients in the tangential direction are not employed since the rotor rotation is not included in the model. The use of a natural cylindrical coordinate system for defining the directions of resistance terms gives only two spatial directions for a two-dimensional axisymmetric treatment. This reduces the number of directions for resistance terms compared to previous studies and simplifies the permeability calibration procedure.

In order to represent the real flow and pressure behavior in the bristle pack, the porous medium treatment of a brush seal requires a precise definition of permeability coefficients in each direction to satisfy all available experimental data. Leakage and pressures are the two physical quantities measured experimentally. The measured pressures are basically on the rotor surface and the backing plate. Throughout the permeability calibration procedure, three major measurements are matched: leakage, axial pressure distribution on the rotor surface along the bristle packing thickness, and radial pressure distribution on the backing plate. These are the three physical quantities measured so far by using available instrumentation for the brush seal geometrical configuration and operating conditions. Chen et al. [37] used a large-scale brush seal to measure the pressure field in the bristle pack via hollow bristles. These three comparison criteria are further discussed in the results and discussion section.

As addressed above, important facts about the dynamic flow behavior and physical structures of the brush seal should be reflected in the permeability calibration. From the geometry of the brush seal, it is obvious that the fence height region of the bristles has a looser structure compared to the upper region supported by backing plate. The upper region becomes very tight as the pressure load pushes and packs the bristles against the backing plate. In the fence height region, the bristles are free to move downstream as the fluid flows and drags them. As a result, the upper region does not conduct the fluid as much as the fence height region. In other words, the resistivity of the upper region to flow diffusion is higher than the fence height region. The fence height and upper regions form two different physical structures. Consequently, to correlate this effect, the bristle pack is divided into two permeable regions, and two different permeability sets are defined for these two regions. During calibration, two-region treatment of the brush seal was also concluded in order to fit CFD results with experimental data.

The current model could be extended by noting that the bristle region around the edge of the backing plate is the tightest because of the bending effect and relatively higher axial pressure load at this corner region. Thus, it might be more appropriate to divide bristle height into three regions in terms of permeability definition. Some difficulties arise during calibration as the number of divisions increases due to the increasing number of permeability coefficients. Each set has a total of six permeability numbers in three spatial directions. Three regions give 18 permeability numbers to calibrate. Only two regions, fence height and upper portion, are found to be adequate to represent the bristle pack as a permeable medium satisfying three experimental calibration criteria. Chen et al. [37] used five different regions in their large-scale model by dividing the fence height region into four regions in the axial direction. They made these divisions in order to match the measured axial pressure distribution.

It is also evident that the brush seal geometry directly alters the bristle behavior. The bristle diameter sets the porosity. The permeability is a direct function of porosity and brush seal geometry. The positions of bristles change depending on operating conditions like pressure load and rotor excursion. In terms of permeability coefficients, there are two main issues arising from increasing pressure load: structural response of bristle pack and leakage performance change.

The first issue is that, as a result of increased pressure load, the bristles move, compact, and form a complex structure lying on the backing plate. Bristle pack thickness decreases down to a certain point where the bristles touch each other. The bristle pack would have a minimum packing thickness. Beyond this minimum packing thickness point, bristle pack thickness and porosity can be assumed as constant for steady state conditions if there are no dynamic issues like bristle flutter. Tighter bristle pack with narrower voids would have relatively higher resistances to flow diffusion. Based on constant porosity, the permeability coefficients can be assumed constant for higher pressure loads. For lower pressure loads, due to nonsettled bristle thickness, permeability coefficients would change more with respect to porosity variation.

On the other hand, this discussion about the compactness of bristle pack is not truly valid for the fence height region where bristles are free to axially deflect.

The second issue is that the increased pressure load increases the leakage while tightening the bristle pack. The leakage is a function of pressure load. The nonlinear transport equations used for porous bristle pack need to follow the same function in order to reflect the increment in leakage with respect to pressure load.

The dependency of permeability coefficients on the level of pressure load needs further investigation.

Results and Discussion

A CFD model has been developed for the entire seal cavity as shown in Fig. 1. Geometrical dimensions are taken from Bayley and Long's paper [30] to compare the results. There are many experimental leakage data in the literature. However, only a few papers have experimental pressure data within the bristles pack [30,35,37]. Unfortunately, most papers with experimental data do not have all the information for geometry and boundary conditions to be able to model and reproduce. Bayley and Long's paper [30] is one of a few papers with all the information. Other researchers have justified the accuracy of their experimental data, as well. Therefore, their work has been chosen as a basis for the present investigation.

The seal is assembled with a 0.25 mm radial interference. The rotor radius is 60.88 mm. The bristle diameter is 0.0762 mm with a pack thickness of 0.6 mm. The bristle lay angle is 45°. The number of bristles per cm of circumference is 945. The fence height and bristle free height are 1.4 and 10.32 mm, respectively.

The model is built in an axisymmetric coordinate system. Rotor rotation is not included in both the experiment and the model. In reality, the rotor speed and the upstream swirl have significant effect on brush seal flow behavior. Therefore, they should be included in the CFD models as supported with measurements. On the other hand, bristle lay angle will direct the flow towards this angle, even in the absence of rotor rotation. The circumferential velocity component of this flow would be very weak compared to axial and radial velocities since the main pressure load acts in these two directions. The circumferential effects are not included in the present 2-D, axisymmetric model due to the absence of rotor rotation and relatively weak flow.

Only line-to-line working conditions are investigated in the analyses, that is, the bristles touch the rotor surface. The interference and line-to-line assembly have the same geometrical topology in the CFD model domain. The Navier–Stokes equations are solved using a finite volume method. The analysis is run with a specified geometrical configuration under specified boundary conditions. The temperature at the upstream boundary is prescribed as 20°C. The downstream pressure is kept constant at atmospheric pressure for all cases. A certain range of pressure ratios is studied: $R_p = p_u / p_d = 1.01-4$. To capture flow details, the mesh is highly refined around critical regions closer to the bristle pack and fence height region. The mesh density is also tested for a mesh independent solution. The previous CFD studies have not reported a strong statement for a totally mesh independent solution. In a typical mesh topology, the minimum cell size is on the order of 0.03 mm around the fence height region.

After intensive solution iterations for calibration, the best values of anisotropic permeability coefficients were determined. The axial permeability defines how much flow diffuses into the bristle pack, and dominates the axial pressure gradient as well as leakage. The radial permeability is dominant on controlling the flow velocity and pressure in the radial direction. The brush seal is divided into two permeable regions, fence height and upper regions, as explained previously. It is found that flow resistance for the upper region is 20% higher than the fence height region to match the experimental data. The calibrated permeability coefficients for the fence height region are inertial resistances: $\alpha_i = 1\times10^5$ kg/m^4, $\alpha_k = 7.5\times10^6$ kg/m^4 and viscous resistances: $\beta_i = 1\times10^5$ kg/m^3-s, $\beta_k = 4.5\times10^7$ kg/m^3-s. The subscripts, i and k, denote the radial and axial directions, respectively. There are two spatial directions, radial and axial, since the rotor rotation is not included. The resistance coefficients are highly nonuniform in the spatial directions. The same set of permeability coefficients is used for the present analyses over the range of pressure ratios, $R_p = 1.01-4$.

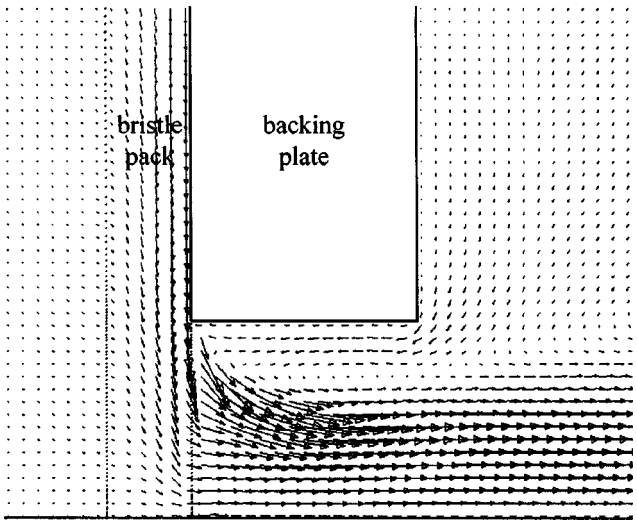

Fig. 2 Velocity vectors

The analyses results and comparison with experiments are presented below. The typical case with a pressure ratio of $R_p = 2.5$ is chosen to plot the results. All plots are produced for this condition unless otherwise stated. Some results are plotted by introducing nondimensional parameters. All analysis cases gave similar results when plotted with respect to the nondimensional parameters.

The velocity vectors in close vicinity of the bristle pack near the fence height region are shown in Fig. 2. The flow smoothly approaches the seal from the upstream cavity. As the flow gets closer to front face, it slightly directs through the fence height region that is the opening region for leakage. The bristle pack in the fence height region blocks the flow, and the filtering flow through the bristles discharges to the downstream cavity. In the upper region of the brush seal, the fluid diffuses into the bristle pack and flows towards the rotor over the backing plate. The accumulated flow diffusion into the bristle pack governs a strong inward radial flow at the upstream face of the backing plate. The flow reaches its maximum velocity around the backing plate corner. This flow affects the axial flow in the fence height region. The inward radial flow from the upper region joins with the axial flow in the fence height region and escapes to the downstream cavity along the rotor surface. This flow behavior was also observed by Chew et al. [34]. The downstream face of the bristle pack in the fence height region is subject to relatively higher axial velocities. This velocity field is pointing out and exerts a pulling force on the last columns of bristles. These bristles have a high tendency to flutter depending on the balance of forces. This characteristic flow is observed for all pressure ratios analyzed, $R_p = 1.01-4$.

Leakage. The leakage, the main performance parameter, is the first experimental data to match. Leakage is plotted as a function of pressure ratio in Fig. 3. It increases almost linearly for the pressure ratios considered, $R_p = 1.01-4$. The present CFD model nicely follows the experimental data. Bayley and Long's prediction [30] underestimates the leakage for smaller pressure ratios.

It is noted that the same set of permeability coefficients is used for all R_p's. As discussed above, as the pressure load increases, the bristle pack becomes tighter and the leakage increases. The permeability coefficients would be higher for tighter bristle pack while they should be lower to accompany the increased leakage.

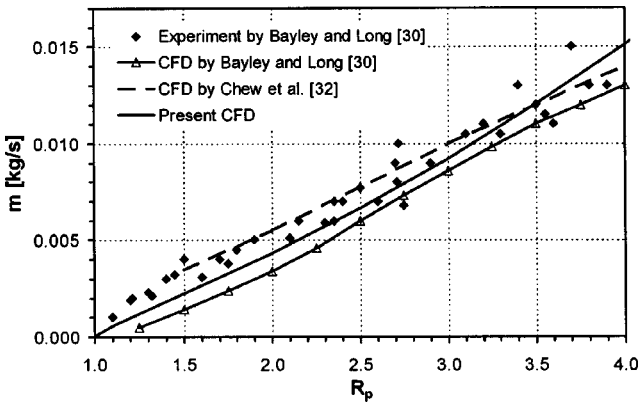

Fig. 3 Comparison of experimental leakage with CFD results

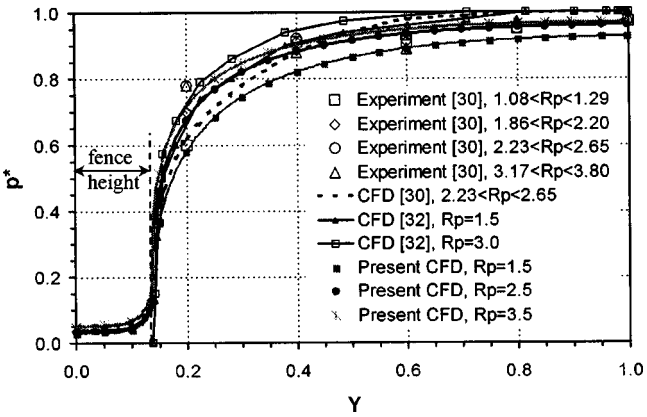

Fig. 5 Comparison of radial pressure distribution on backing plate

In the present analyses, the use of the same set of permeability coefficients within the considered range of R_p gives a very good leakage agreement with the experiments. In order to match the experimental leakage in their CFD model, Chen et al. [36] incorporated the dependency of permeability coefficients to pressure ratio. They defined higher and lower resistance coefficients for higher and lower pressure ratios, respectively.

Axial Pressure on Rotor Surface. The second comparison is made for axial pressure distribution on the rotor surface as plotted in Fig. 4. The brush seal is subject to a certain axial pressure load. There is a pressure drop over the bristle pack thickness from upstream to downstream. The axial pressure distribution on the rotor surface corresponds to the bristle tip pressures measured using pressure tappings located at different circumferential positions. It was reported that there is a roughly linear pressure gradient from upstream to downstream over the bristle packing thickness [30,37]. This nearly linear axial pressure distribution is also reported in flow visualization studies [9–12] and flow analyses of cross flow [13–18]. Figure 4 shows many experimental data points for a range of pressure ratios [30]. The dimensionless pressure, $p^*=(p-p_d)/(p_u-p_d)$, is plotted against axial coordinate, z. The origin of the axial coordinate is located at the upstream face of bristle pack.

Bayley and Long [30] plotted the axial pressure data in three separate graphs. Each graph was plotted for a range of pressure ratios with data from multiple tests. The experimental data was scattered in a wide range. This scatter was attributed to the nonuniform axial bristle deflection in the circumferential direction. On the other hand, the axial pressure has a tendency to follow a linear trend. The measurements for a large-scale brush seal [37] show a linear pressure drop in the first one-third of the bristle thickness on the upstream side. The pressure is likely to stay constant in the middle region before it drops linearly over the last one-third of the bristle thickness on the downstream side. Chen et al. [36] predicted that most of the pressure drop occurred close to the downstream face of the bristle pack. Turner et al. [35] measured the pressure on the rotor surface for clearance cases. Their experimental data also have a wide range of scatter and it is not possible to draw any conclusions about a linear trend.

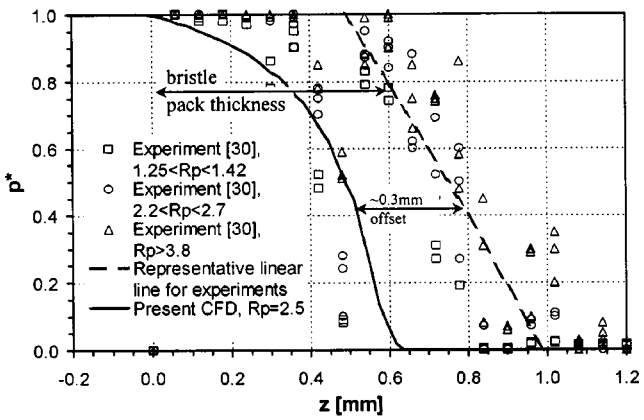

Fig. 4 Comparison of axial pressure distribution on rotor surface

The dotted line in Fig. 4 represents a liner fit versus axial pressure of all experimental data. The present analysis gives almost identical curves for all R_p's. The axial pressure distribution line obtained from the CFD analyses has a nearly parabolic shape closer to the upstream face. Then it approaches a linear variation. It is about 0.3 mm off from the representative experimental line. In the CFD model, the bristle pack is assumed to remain at its original position without any axial deflection during operation. However, in the practical applications, bristles in the fence height region are free to bend in the axial direction depending on balance of aerodynamic, elastic, and frictional forces. The difference of 0.3 mm between experiments and CFD analysis is due to axial bristle deflection for the range of operating conditions [30].

Radial Pressure on Backing Plate. The radial pressure distribution on the backing plate is plotted in Fig. 5. The Y axis, abscissa, shows the normalized radial location from rotor surface defined as $Y=y/h_{bf}$, where y is the distance from rotor surface and h_{bf} is bristle free height between the bristle tip and the bristle pinch point. The bristles under distributed pressure load form a very tight structure. The main leakage flow goes through the fence height region. Meanwhile, a strong inward radial flow develops in the upper region of the seal as the flow diffuses into voids among bristles. Bayley and Long [30] also measured the pressure on the backing plate at five radial locations for four different ranges of pressure ratios. It is observed that there are a certain pressure gradient and an inward radial flow forming on the backing plate. The present CFD results are in good agreement with Bayley and Long's [30] experiments and predictions. Chew et al.'s [34] predictions slightly overestimate the radial pressure on backing plate. The line for the lowest pressure ratio of 1.5 underestimates the measurements. As it is discussed above, the permeability coefficients are sensitive to level of pressure load for especially lower pressure loads. In the present analyses, the same set of permeability coefficients is used over the considered range of pressure ratios: 1.01–4. The observed discrepancy is meaningful from dependency of permeability to lower pressure loads.

Both experimental and present CFD results show that the pressure on the backing plate for upper half of the upper region is constant and nearly equal to the upstream pressure. The pressure gradually drops to the downstream pressure level near the backing

plate corner. Most of the pressure drop occurs near the backing plate edge. This distribution shows that there is a pressure gradient from the upper to fence height regions directing the flow radially inward. This flow pulls the bristles forming a lay angle of typically 45° toward the rotor surface resulting in a ''blow-down effect.''

The results show that the set of permeability coefficients in the analyses has adequately represented the experimental leakage and pressure data over the considered range.

Contour plots for pressure, radial and axial velocities, and turbulent kinetic energy around the fence height region are presented in Fig. 6. Pressure contours are plotted at intervals of 15 kPa. The pressure is constant outside of the bristle pack. It gradually drops from the upstream to downstream pressures over the pack thickness. The densely plotted contour lines closer to downstream face indicate the sudden pressure drop. The velocity contours are plotted at intervals of 3 m/s. For radial velocity, the negative values are for the inward radial flow direction. For axial velocity, the positive flow direction is from upstream to downstream. The flow in the entire bristle pack is radially inward for the presented conditions. The velocity has the maximum magnitude at backing plate tip since the flow is accumulated up to this point as it diffuses into the bristle pack [36]. A recirculation region forms underneath the backing plate as seen in the axial velocity contour plot. The turbulent kinetic energy is plotted at 2 m^2/s^2 intervals. It has the maximum value under the backing plate.

The axial pressure field in the bristle pack at different radial heights from the rotor surface to the seal pinch point is presented in Fig. 7. The data are plotted against the normalized axial location, $Z=z/t_b$, where z is the axial location from the upstream face of bristle pack and t_b is the bristle pack thickness. The first line marked in the legend is the line on the rotor surface. The increasing legend numbers are for increasing distances from rotor surface. The locations of axial lines are shown on the same figure. In the fence height region, up to line 5 at the backing plate tip, there is some deviation from the linear pressure line. The inertial momentum of flow hitting to bristle face diffuses into the bristle pack in the fence height region without any accumulation, unlike the upper region. In the upper region, the flow accumulates on the backing plate. The axial pressure changes linearly for the upper region and becomes almost constant equal to the upstream value for the upper half of the upper region. This pressure field has the same trend as Chen et al.'s [37] measurements for the large-scale brush seal. The axial pressure load over bristle thickness reduces as the radial height increases. It is smaller in the upper region compared to fence height region. The flow resistance coefficients are also dependent on pressure load. The resistance for the upper region is increased by 20% in the CFD model. This increment might seem small at the first look. Although the bristles in the upper region get packed against the backing plate, they are subject to smaller pressure loads. If the upper region were subject to same level of pressure load with fence height region, its resistances would be much higher than the fence height region.

The radial distributions for some flow properties are presented in Fig. 8. Radial lines are numbered from upstream to downstream side on this figure. Line numbers 5 and 9 are located at the upstream and downstream faces of the bristle pack, respectively. Figure 8(*a*) shows the radial pressure field between up/downstream pressures. Within the bristle pack, the radial pressure is almost uniform at the fence height region, then rapidly reaches the upstream pressure close to the backing plate tip. This field was also measured in the large-scale brush seal test [37], with the same trends as the present CFD results. The magnitudes of the radial and axial velocities for the same line numbering convention are presented in Figs. 8(*b*) and 8(*c*), respectively. The radial velocity increases from the pinch point to the backing plate tip. Then it reduces due to the discharging flow through downstream in the

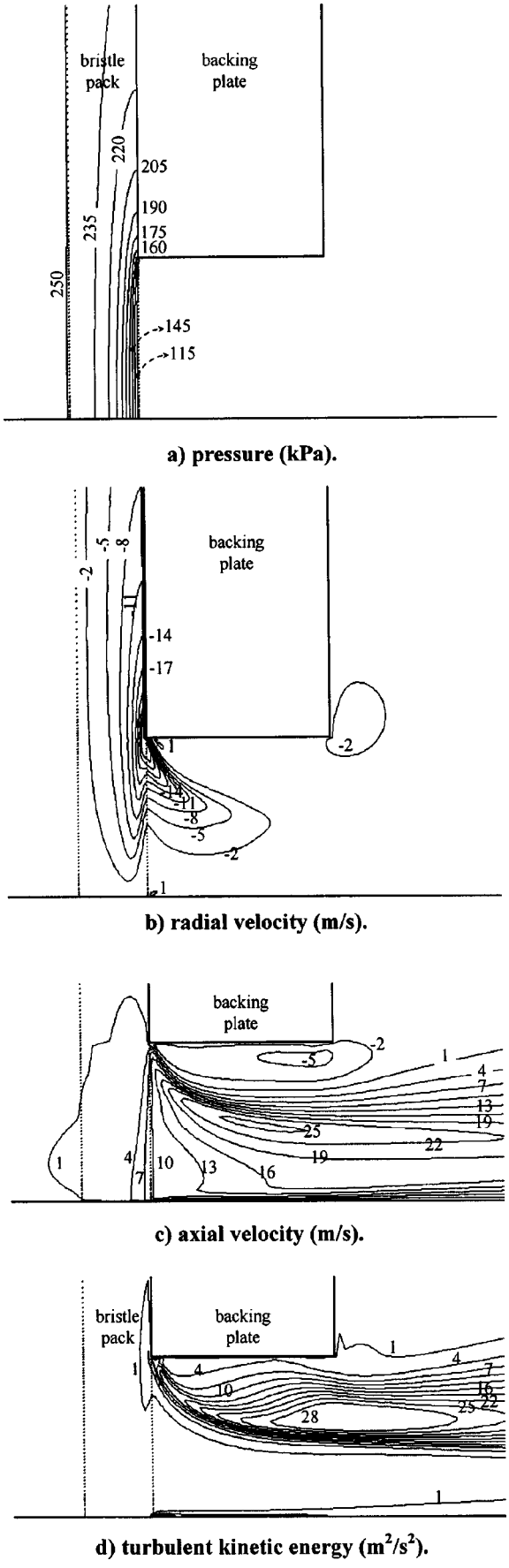

Fig. 6 Contour plots around fence height region

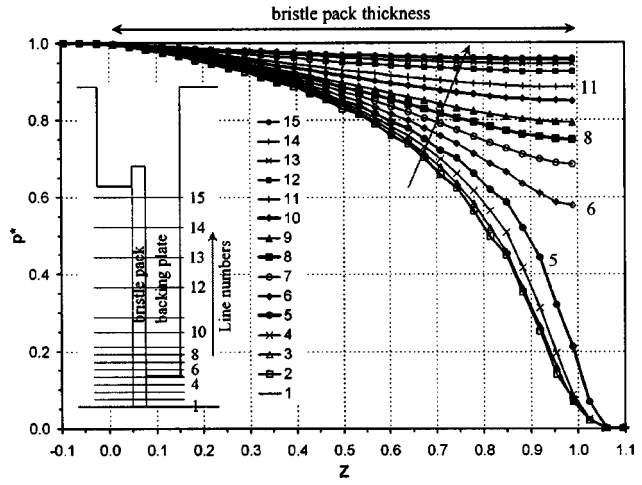

Fig. 7 Axial pressure distribution over bristle pack at different radial heights

fence height region. The axial velocity increases under the backing plate as a result of the merging flow from the fence height region and over the backing plate.

Conclusions

It is shown that the flow analysis in the bristle pack is represented very well by a bulk porous medium approach with calibrated permeability coefficients. The simplified resistance law is adequate to capture the flow nature in the bristle pack.

The permeability calibration can be done using three types of available experimental data, i.e., the leakage, axial pressure along the rotor surface, and the radial pressure along the backing plate. The bristle pack has been divided into two regions to define the permeability coefficients to match the two different structural behaviors during operation. The fence height region has a looser structure while a smaller pressure load is acting on the upper region. It is found that the flow resistance for upper region should be 20% higher than the fence height region to match experimental data.

The flow and pressure fields in the bristle pack have been modeled with the aid of the porous medium approach. The analysis results show a strong inward radial flow that causes bristle "blowdown."

The numerical visualization of flow and pressure fields helps in understanding of the brush seal flow, and can be incorporated in structural analysis. There is a direct interaction between flow field and bristles' dynamics. In order to control the bristles, the flow configuration has to be controlled in close vicinity of the bristles as well as the bristle pack. Further investigation is needed to determine seal design for a prescribed operating environment. More experiments are required to estimate the optimum seal design or the seal failure depending on the operating conditions. Once the seal failure mechanisms are determined through experiments, the presented flow analysis can be used to identify the flow conditions leading the failure. This flow analysis is applicable at the beginning of the design so that the seal can be operated away from the critical flow conditions. This study, which introduces an approach for permeability calibration, quantifies the flow and pressure fields for the brush seal.

An important issue to consider in permeability calibration is that the permeability is a function of pressure gradient over the porous medium. The tightness of the bristle pack depends on how much of the pressure load is acting on the bristle pack. One set of permeability coefficients calibrated for a certain range of pressure

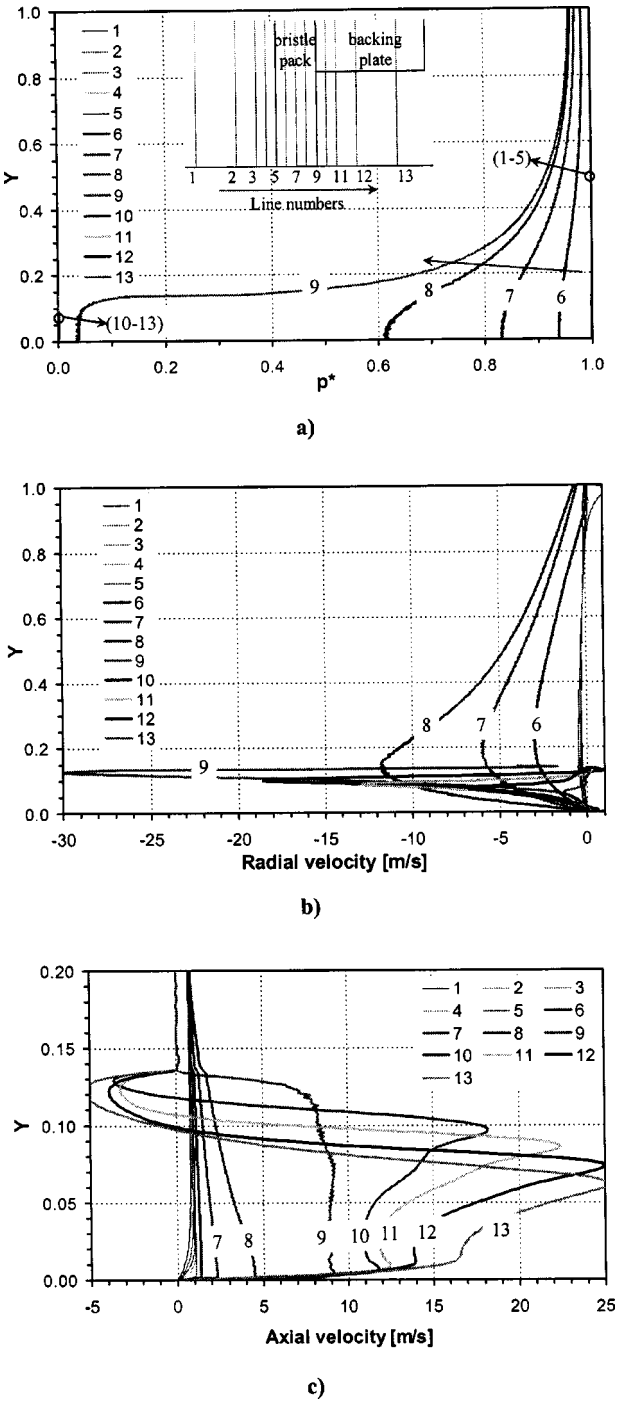

Fig. 8 Radial distribution of flow properties: (*a*) pressure, (*b*) radial velocity, and (*c*) axial velocity

loads would not be applicable for totally different pressure loads. Dependence of permeability coefficients on the pressure load needs to be investigated.

Rotor rotation is another parameter to be investigated. It must be included in the experiments as well as the models.

The case with a clearance between the bristle tips and the rotor surface is not included in this study. Even though it is desired that the brush seal operates at line-to-line or interference position with the rotor surface, the clearance case happens after excessive wear, transiently during start-up and shut-down, and when bristle hang-up occurs depending on the force balance. The clearance

case should also be studied since the flow nature for this situation is considerably different than the line-to-line case.

It should be noted that if the flow path can be specified among thousands of flexible bristles under an uneven load, the flow in the defined paths could be determined using the full Navier–Stokes equations. However, currently available data are insufficient to define the flow path in the bristle pack. Once the position of bristles is determined, the solution of the Navier–Stokes equations around thousands of bristles in 3-D would require a considerable amount of time and computing resources.

Acknowledgments

The author would like to thank Saim Dinc and Raymond Chupp of General Electric Global Research and Mahmut Aksit of Gebze Institute of Technology in Turkey for their support, technical discussion, interest, and encouragement for this work.

Nomenclature

a, b = viscous and inertial resistance coefficient
h_{bf} = bristle free height
h_{fh} = fence height
h_{ur} = upper region height
K = permeability
p = static pressure
p^* = dimensionless pressure$=(p-p_d)/(p_u-p_d)$
R_p = pressure ratio$=p_u/p_d$
t_{bp} = thickness of backing plate
t_{fp} = thickness of front plate
t_b = thickness of bristle pack
u = velocity component
u_i = mean velocity
x = spatial coordinate direction
y = radial distance from rotor surface
Y = normalized radial coordinate$=y/h_{bf}$
z = axial coordinate direction
Z = normalized axial coordinate$=z/t_b$
μ = dynamic viscosity
ρ = density
ε = porosity
α, β = inertial and viscous permeability coefficient

Subscripts

d = downstream
i = spatial coordinate and radial direction
j = spatial coordinate direction
k = axial direction
u = upstream

References

[1] Ferguson, J. G., 1988, "Brushes as High Performance Gas Turbine Seals," ASME paper no. 88-GT-182.
[2] Gorelov, G. M., Reznik, V. E., and Tsibizov, V. I., 1988, "Experimental Study of Brush Seal Flow Characteristics and Comparison With a Labyrinth Seal," Izv. VUZ. Aviatsionnaya Tekhnika, **31**, No. 4, pp. 43–46 (Allerton Press).
[3] Chupp, R. E., and Nelson, P., 1993, "Evaluation of Brush Seals for Limited-Life Engines," J. Propul. Power, **9**, No. 1, pp. 113–118.
[4] Chupp, R. E., and Dowler, C. A., 1993, "Performance Characteristics of Brush Seals for Limited-Life Engines," ASME J. Eng. Gas Turbines Power, **115**, pp. 390–396.
[5] Carlile, J. A., Hendricks, R. C., and Yoder, D. A., 1993, "Brush Seal Leakage Performance With Gaseous Working Fluids at Static and Low Rotor Speed Conditions," ASME J. Eng. Gas Turbines Power, **115**, pp. 397–403.
[6] Chupp, R. E., Aksit, M. F., Ghasripoor, F., Turnquist, N. A., and Demiroglu, M., 2001, "Advanced Seals for Industrial Turbine Applications," AIAA paper no. 2001-3626.
[7] Dinc, S., Demiroglu, M., Turnquist, N., Mortzheim, J., Goetze, G., Maupin, J., Hopkins, J., Wolfe, C., and Florin, M., 2002, "Fundamental Design Issues of Brush Seals for Industrial Applications," ASME J. Turbomach., **124**, pp. 293–300.
[8] O'Neil, A. T., Hogg, S. I., Withers, P. A., Turner, M. T., and Jones, T. V., 1997, "Multiple Brush Seals in Series," ASME paper no. 97-GT-194.
[9] Braun, M., Hendricks, R., and Canacci, V., 1990, "Flow Visualization in a Simulated Brush Seal," ASME paper no. 90-GT-217.
[10] Braun, M. J., Canacci, V. A., and Hendricks, R. C., 1991, "Flow Visualization and Quantitative Velocity and Pressure Measurements in Simulated Single and Double Brush Seals," Tribol. Trans., **34**, pp. 70–80.
[11] Braun, M., Canacci, V., and Hendricks, R., 1990, "Flow Visualization and Motion Analysis for a Series of Four Sequential Brush Seals," AIAA paper no. 90-2482.
[12] Braun, M., Hendricks, R., and Yang, Y., 1991, "Effects of Brush Seal Morphology on Leakage and Pressure Drops," AIAA paper no. 91-2106.
[13] Mullen, R., Braun, M., and Hendricks, R., 1990, "Numerical Modeling of Flows in Simulated Brush Seal Configurations," AIAA paper no. 90-2141.
[14] Braun, M. J., and Kudriavtsev, V. V., 1993, "A Numerical Simulation of a Brush Seal Section and Some Experimental Results," ASME paper no. 93-GT-398.
[15] Kudriavtsev, V. V., and Braun, M. J., 1993, "A Reynolds Number Parametric Numerical Investigation of Flow Structures and Pressure Distribution in a System of Cylinder Arrays," Proc. of ASME Int. Fluid Eng. Conf. FED-Vol. 149, Washington D.C., pp. 83–93.
[16] Braun, M. J., and Kudriavtsev, V. V., 1993, "Numerical Visualization of Flow Structures in Dense Banks of Cylinders Located in a Channel," Proc. of ASME Int. Fluid Eng. Conf. FED-Vol. 172, Washington D.C., pp. 253–260
[17] Sharatchandra, M. C., and Rhode, D. L., 1996, "Computed Effects of Rotor-Induced Swirl on Brush Seal Performance—Part 1: Leakage Analysis," ASME J. Turbomach., **118**, pp. 912–919.
[18] Demiroglu, M., Aksit, M. F., and Tichy, J. A., 1998, "A Numerical Study of Brush Seal Leakage Flow," AIAA paper no. 98-3173.
[19] Braun, M. J., Hendricks, R. C., and Canacci, V. A., 1990, "Non-Intrusive Qualitative and Quantitative Flow Characterization and Bulk Flow Model for Brush Seals," Proceedings of the Japan International Tribology Conference, Nagoya, pp. 1611–1616.
[20] Hendricks, R. C., Braun, M. J., Canacci, V., and Mullen, R. L., 1990, "Brush Seals in Vehicle Tribology," presented at 1990 Leeds/Lyon Symposium, Leeds, England, pp. 231–242.
[21] Hendricks, R. C., Schlumberger, S., Braun, M. J., Choy, F., and Mullen, R. L., 1991, "A Bulk Flow Model of a Brush Seal System," ASME paper no. 91-GT-325.
[22] Hendricks, R., Proctor, M., Schlumberger, J., Braun, M., and Mullen, R., 1991, "Some Preliminary Results of Brush Seal/Rotor Interference Effects on Leakage at Zero and Low RPM Using a Tapered-Plug Rotor," AIAA paper no. 91-3390.
[23] Gunter, A. Y., and Shaw, W. A., 1945, "A General Correlation of Friction Factors for Various Types of Surfaces in Crossflow," Trans. ASME, **67**, pp. 643–660.
[24] Chupp, R. E., Holle, G. F., and Dowler, C. A., 1991, "Simple Leakage Flow Model for Brush Seals," AIAA paper no. 91-1913.
[25] Knudsen, J. G., and Katz, D. L., 1958, *Fluid Dynamics and Heat Transfer*, McGraw-Hill, New York, NY, Chap. 11.
[26] Holle, G. F., Chupp, R. E., and Dowler, C. A., 1992, "Brush Seal Leakage Correlations Based on Effective Thickness," Proceedings of the Fourth International Symposium on Transport Phenomena and Dynamics of Rotating Machinery (ISROMAC-4) Honolulu, HI, pp. 253–261.
[27] Dowler, C. A., Chupp, R. E., and Holle, G. F., 1992, "Simple Effective Thickness Model for Circular Brush Seals," AIAA paper no. 92-3192.
[28] Chupp, R. E., and Holle, G. F., 1996, "Generalizing Circular Brush Seal Leakage Through a Randomly Distributed Bristle Bed," ASME J. Turbomach., **118**, pp. 153–161.
[29] Modi, M., 1992, "Modelling Bristle Lift-Off in Idealized Brush Seal Configurations," Proceedings of the Fourth International Symposium on Transport Phenomena and Dynamics of Rotating Machinery (ISROMAC-4), Honolulu, HI, pp. 623–632.
[30] Bayley, F. J., and Long, C. A., 1993, "A Combined Experimental and Theoretical Study of Flow and Pressure Distributions in a Brush Seal," ASME J. Eng. Gas Turbines Power, **115**, No. 2, pp. 404–410.
[31] Hendricks, R. C., Flower, R., and Howe, H., 1996, "A Brush Seal Program Modeling and Developments," NASA Technical Memorandum 107158.
[32] Ergun, S., 1952, "Fluid Flow Through Packed Columns," Chem. Eng. Prog., **19**, pp. 89–94.
[33] Chew, J. W., and Hogg, S. I., 1997, "Porosity Modeling of Brush Seals," ASME J. Tribol., **119**, pp. 769–775.
[34] Chew, J. W., Lapworth, B. L., and Millener, P. J., 1995, "Mathematical Modeling of Brush Seals," Int. J. Heat Fluid Flow, **16**, No. 6, pp. 494–500.
[35] Turner, M. T., Chew, J. W., and Long, C. A., 1997, "Experimental Investigation and Mathematical Modeling of Clearance Brush Seals," ASME paper no. 97-GT-282.
[36] Chen, L. H., Wood, P. E., Jones, T. V., and Chew, J. W., 1998, "An Iterative CFD and Mechanical Brush Seal Model and Comparison With Experimental Results," ASME paper no. 98-GT-372.
[37] Chen, L. H., Wood, P. E., Jones, T. V., and Chew, J. W., 2000, "Detailed Experimental Studies of Flow in Large Scale Brush Seal Model and a Comparison With CFD Predictions," ASME J. Eng. Gas Turbines Power, **122**, pp. 672–679.

Parametric Analysis of Existing Gas Turbines With Inlet Evaporative and Overspray Fogging

R. Bhargava
Universal Ensco, Inc.,
1811 Bering Drive,
Houston, TX 77057-3100

C. B. Meher-Homji
Bechtel Corporation,
3000 Post Oak Blvd.
Houston, TX 77056

With deregulation in the power generation market and a need for flexibility in terms of power augmentation during the periods of high electricity demand, power plant operators all over the world are exploring means to augment power from both the existing and new gas turbines. An approach becoming increasingly popular is that of the high pressure inlet fogging. In this paper, the results of a comprehensive parametric analysis on the effects of inlet fogging on a wide range of existing gas turbines are presented. Both evaporative and overspray fogging conditions have been analyzed. The results show that the performance parameters indicative of inlet fogging effects have a definitive correlation with the key gas turbine design parameters. In addition, this study indicates that the aeroderivative gas turbines, in comparison to the heavy-duty industrial machines, have higher performance improvement due to inlet fogging effects. Plausible reasons for the observed trends are discussed. This paper represents the first systematic study on the effects of inlet fogging for a large number (a total of 67) of gas turbines available from the major gas turbine manufacturers. [DOI: 10.1115/1.1712980]

Introduction

With the worldwide deregulation of power generation markets, the marketplace for electric power has become highly dynamic and competitive. In such an environment, having the flexibility to augment gas turbine power output during periods when there is a high tariff rate becomes of paramount importance to the profitability of the utilities and the other power producers. Gas turbine power output is a strong function of the ambient air temperature with power output dropping by 0.5% to 0.9% for every 1°C rise in ambient temperature (0.3% to 0.5% per 1°F). On several heavy frame gas turbines, power output drop of approximately 20% can be experienced when ambient temperature reaches 35°C (95°F), coupled with a heat rate increase of about 5%. Aeroderivative gas turbines exhibit even a greater sensitivity to ambient conditions. The effects of ambient temperature on the power output and heat rate for two types of gas turbine are shown in Fig. 1.

The loss in power output presents a significant problem to utilities, cogenerators, merchant power plants and independent power producers when electric power demands are high during the hot summer months. This loss in power output for a power producer with 100 MW capacity (assuming high ambient temperature conditions existed for 6 hours in a day and an electric sale price of 5 cents/kW-hr, and excluding effects of increased fuel consumption) equates into $6,000 per day loss in revenues. One way to counter this drop in power output is to cool the inlet air. While there are several inlet air cooling technologies available, high pressure inlet fogging has seen an increasing level of implementation because of its relatively low first- and operating-cost compared to the other techniques including the media evaporative cooling and refrigeration technologies.[1]

A detailed study conducted by Tawney et al. [1] evaluated several options for power augmentation for combined cycle power plants. It may be noted that their study only considered inlet evaporative fogging. The results indicated that the inlet fogging option had minimal impact on EPC (engineering, procurement and construction) cost. Also, inlet fogging was the only option that provided a small improvement in heat rate,[2] while the other options all worsened heat rate value. The combination of inlet fogging and supplemental firing of the HRSG (heat recovery steam generator) obtained the highest return on investment. In recent years, several combined cycle power plants (CCPPs) have adopted fogging as a power augmentation strategy. Jones and Jacobs [2] have also studied various power enhancement techniques for CCPPs.

In spite of inlet fogging systems having been applied to an estimated 600 gas turbines worldwide, no detailed study is available addressing the following questions: what parametric factors in the *design of a gas turbine* inherently affect the impact of inlet fogging?; what are the general effects of inlet fogging on a *wide range* of gas turbines? Such questions have prompted this parametric study, the results of which are reported in this paper. To the knowledge of authors, there has been no published study available where a detailed in-depth parametric analysis of a large set of gas turbines of different manufacturers and designs has been undertaken. It will be helpful to the gas turbine users if parameters indicative of performance improvement can be correlated to the easily available gas turbine design parameters.

Kitchen and Ebeling [3] analyzed a limited number (15 in total) of machines in an effort to identify gas turbines most suitable for inlet cooling. Their analysis considered the thermal energy storage technique for cooling the inlet air. One of the possible reasons, for identifying no correlation between an inlet air cooling parameter (a nondimensional compressor temperature rise) and the ISO performance parameters (such as heat rate, pressure ratio, exhaust temperature, and specific air consumption) in their study might be that their selection of gas turbines covered a limited range of design and performance parameters.

Contributed by the International Gas Turbine Institute (IGTI) of THE AMERICAN SOCIETY OF MECHANICAL ENGINEERS for publication in the ASME JOURNAL OF ENGINEERING FOR GAS TURBINES AND POWER. Paper presented at the International Gas Turbine and Aeroengine Congress and Exhibition, Amsterdam, The Netherlands, June 3–6, 2002; Paper No. 2002-GT-30560. Manuscript received by IGTI, December 2001, final revision, March 2002. Associate Editor: E. Benvenuti.

[1]Cost ratios are about 5:1 but can vary based on the project specifics.

[2]While this study showed a small improvement in heat rate for CCPPs, the change is very small and can be considered negligible. The heat rate improvements for simple cycles are, however, significant.

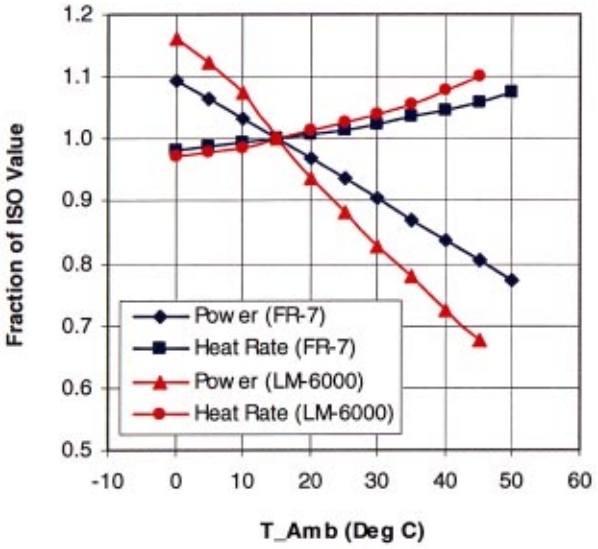

Fig. 1 Effects of ambient temperature on gas turbine power output and heat rate

Inlet Fogging of Gas Turbines. Gas turbine inlet fogging is a method of cooling the intake air where demineralized water is converted into fog droplets by means of special atomizing nozzles operating at approximately 138 bar (2000 psi). The evaporation of small size (5–20 microns) droplets in the intake duct cools the air and consequently increases the mass flow rate. The details pertaining to the thermodynamics and practical aspects of inlet fogging have been described by Meher-Homji and Mee [4,5]. This technique allows close to 100% evaporation effectiveness in terms of attaining saturation conditions and wet-bulb temperature at the gas turbine inlet.

Overspray or Fog Intercooling. High pressure inlet fogging can also be used to create a compressor intercooling effect by allowing excess fog into the compressor (also known as overspray or wet compression) thus, obtaining an additional power boost. The power boost is attained by a reduction in compressor work input. Typically, the amount of excess fog injected into the compressor inlet is between 0.5 to 2% of the inlet air mass flow of the gas turbine. Fog intercooling of gas turbines has been under discussion since 1940 (Kleinschmidt[3] [6] and Wilcox and Trout [7]). Nolan and Twombly [8] described an implementation of overspray on Frame 5 gas turbines in a cogeneration plant. Hill [9] and Arsen'ev and Berkovich [10] have conducted an analysis of water injection into compressor inlets. An application of fog intercooling on heavy-duty gas turbines is described by Ingistov [11].

Table 1 provides results of performance analysis for a 50 Hz heavy-duty gas turbine (GE 9171E) undergoing evaporative and overspray fogging. This tabulated data provides a feel for variation of key gas turbine parameters influenced by inlet fogging. Furthermore, it will be helpful in understanding discussion of the results of a comprehensive study of the effects of inlet fogging on gas turbine performance presented in this paper. In this tabulation, it is interesting to note that the compressor work increases with evaporative fogging because of the increase in air mass flow rate caused by the 13°C temperature drop to the wet-bulb temperature. The turbine section work output increase is, however, proportionately higher resulting in a gas turbine net output increase of about 10 MW. With overspray fogging, the compressor work input is seen to *decrease* as a greater amount of overspray is used due to

[3]This reference includes the term wet compression.

Table 1 Gas Turbine Performance Analysis Results under Base and Inlet Fogging Conditions

PARAMETER	Base Case	Fog to Saturation	Overspray OS = 1%	Overspray OS = 2%
Ambient Temperature, ^{0}C	43	43	43	43
Compressor Inlet Temperature, ^{0}C	43	30	30	30
Compressor Discharge Temperature, ^{0}C	386	371	330	293
Compressor Discharge Pressure, bar	10.93	11.53	11.69	11.84
Overall Pressure Ratio	10.90	11.53	11.60	11.80
Turbine Inlet Temperature, ^{0}C	1122	1121	1120	1118
Exhaust Gas Temperature, ^{0}C	567	557	555	553
Air Mass Flow Rate at Compressor Inlet, kg/sec	357.63	374.59	374.59	374.59
Total Mass Flow Rate at Compressor Inlet, kg/sec	357.63	376.61	380.37	384.14
Fuel Flow Rate, kg/sec	6.304	6.784	6.234	7.677
Compressor Work Input , kW	128,027	134,678	129,305	125,073
Total Turbine Work Output, kW	230,599	247,877	253,003	258,061
Gas Turbine Cycle Efficiency, %	28.67	29.43	30.14	30.58
Turbine Net Work Output Ratio (W_N)	0.45	0.46	0.49	0.52
Compressor Work Input Ratio (W_C)	0.56	0.54	0.51	0.48
Fog Water Flow Rate, kg/sec	0	2.023	5.789	9.555
Gas Turbine Net Output, kW	**100,381**	**110,868**	**121,216**	**130,363**
Heat Rate, kJ/kW-hr	**11,315**	**11,024**	**10,766**	**10,609**

Plant Configuration for Table 1: Simple Cycle Gas Turbine (GE 9171E)
TIT = 1122 ^{0}C (Note: For performance data at the ISO conditions, see Appendix A)
Fuel = Natural Gas, supplied @ 25 ^{0}C, LHV = 50,047 kJ/kg
GT @ 100 % rating, inferred TIT control model, Control curve limit
Site ambient conditions: 1.013 bar, 43 ^{0}C, 40% RH
Total inlet loss = 10 millibars H_2O; Exhaust loss = 12.45 millibars H_2O; Duct & stack loss = 12.45 millibars H_2O

the fog intercooling effect (see Table 1). While the heat rate value improves, the absolute value of fuel flow increases with the use of inlet fogging (both evaporative and overspray fogging) mainly due to increased air mass flow rate and decrease in compressor discharge temperature.

Gas Turbine Selection

Gas turbines were selected for this study such that they represented most of the major gas turbine manufacturers and encompassed a wide range of power outputs, firing temperatures, pressure ratios and design types (industrial and aeroderivative). A total of 67 gas turbines, both for 50 Hz and 60 Hz applications, were selected for the parametric analysis and their performance and design data have been provided in the Appendix. A review of the data for the selected gas turbines as given in the Appendix shows that the values of turbine inlet temperature (TIT) range from 888°C (≈1630°F) to 1427°C (≈2600°F) with values of overall cycle pressure ratio (PR) ranging from 6.6 to 35. The minimum and maximum values of cycle efficiency (η_{th}) are 22.2% and 41.3%, respectively. The values of net power output (P) range from 486 kW to 334,000 kW. Whereas, the values of ISO specific work (W) range from approximately 162 to 483 kW-s/kg.

Analysis Methodology

To study the effects of inlet evaporative and overspray fogging on the selected gas turbines, a uniform ''base condition'' was first defined from which the changes in performance parameters could be evaluated. Base ambient conditions assumed throughout the study were 43°C (≈109°F) at 40% relative humidity[4] and this has been referred to as the ''base case.'' A commercial program (GT-PRO, Tflow6, Release 2) was used to evaluate the thermodynamic performance, at different operating conditions (such as changes in ambient temperature, ambient relative humidity, inlet evaporative fogging and overspray fogging), for the selected gas turbines. This program utilizes a gas turbine model consisting of a compressor map model that relates pressure ratio, corrected airflow, and polytropic efficiency. The compressor map represents the overall compressor performance characteristics. In analyzing the compressor performance, at a given operating condition, the overall compressor pressure ratio range is divided into a large number of computational stages (larger than the number of physical stages). For each computational stage, exit flow conditions are evaluated from the respective inlet flow conditions. Furthermore, an evaporation model for each computational stage, taking into account the effect of water droplet size, is used during an overspray condition. The amount of water in the airstream influences the temperature distribution and air composition through the compressor that changes the compressor work requirement.

The calculations were made for both the evaporative cooling (saturation at the inlet of the gas turbine) and overspray conditions. For overspray fogging, results were obtained at levels of overspray from 0.25% up to 2% of the air mass flow of the gas turbine. While, overspray calculations were made at increments of 0.25%, only results of the three fogging conditions (saturation, 1% and 2% overspray) have been presented and discussed in this paper. The saturation case (i.e., attaining 100% RH value at the compressor inlet) is identified by OS=0% in various figures presented here.

A sensitivity study on the effects of fogging at different values of ambient temperatures and relative humidity was also undertaken. For this sensitivity study, two gas turbines (an industrial and aeroderivative model) were analyzed.

Finally, the selected gas turbines were categorized into the three types: traditional machines (TIT<1200°C), advanced gas turbines (TIT>1200°C), and aeroderivative engines, to identify the parametric response to the inlet fogging effects. It may be noted that the classification based on the TIT value of 1200°C is of a general nature and in some cases a traditional machine with TIT value greater than 1200°C may not be categorized into an advanced industrial type machine.

Thermodynamic Analyses Results

In gas turbine design, the net gas turbine work output ratio (W_N) and compressor work input ratio (W_C) are important design parameters in addition to the turbine inlet temperature (TIT, also known as firing temperature) and the overall cycle pressure ratio (PR). The emphasis of a gas turbine designer is to increase the value of W_N and decrease the value of W_C within the limits of available technologies. As it is commonly understood that inlet evaporative and overspray fogging affects values of W_N and W_C, their correlation with the other key gas turbine design parameters have been examined. The design parameters selected are: specific work (W), turbine inlet temperature (TIT) and overall cycle pressure ratio (PR). The variations of W_N due to fogging effect as a function of W, TIT, and PR are shown in Figs. 2(a), 2(b), and 2(c), respectively. The values of W_N for the base case are also included in Figs. 2(a)–2(c) to show changes in the values of W_N with and without fogging effects.

A comparison of the 2% overspray case with the base case reveals an increase of approximately 8–10% in the value of W_N, across the range of gas turbines, is achievable as shown in Figs. 2(a) and 2(b). Also, there exists a correlation between W_N with W (Fig. 2(a) and TIT (Fig. 2(b)), whereas a weak correlation exists with PR (Fig. 2(c)). The trend lines, shown in Figs. 2(a) and 2(b), are included to show a qualitative relation between the plotted parameters. It must be noted that the trend lines, in various figures presented in this paper, are obtained by a curve fit utilizing a regression analysis. The order of curve fit (linear, polynomial, etc.,) used is included in the legend in each figure. In comparison to the base case, a larger change in the values of W_N takes place, during the overspray condition than due to inlet evaporative fogging. This is expected, as during inlet evaporative fogging there is an increase in compressor work while overspray causes compressor intercooling resulting in lower compressor work (For example, see Table 1).

The values of W_C decrease due to fogging effects in comparison to the base case as shown in Figs. 3(a)–3(c). The variation of W_C indicates a weak correlation with the values of PR as was observed with the variation of W_N. It is evident from Figs. 2 and 3, that a gas turbine with high values of W and TIT has high and low values of W_N and W_C, respectively, with and without the fogging effects. This can be attributed to improvements in gas turbine technologies that have led to increase in the net gas turbine work output and decrease in the compressor work input ratio.

The two design parameters, W_N and W_C, discussed above are, however, not easily available to the gas turbine users as deriving them requires that the gas turbine modeling calculations would have to be made for the compressor and turbine sections. Typically, such a modeling tool and expertise for its effective use are not available with the gas turbine users. The two performance parameters easily accessible to gas turbine users which also directly relate to the gas turbine user's profitability (return on investment) are, net power output (P), and heat rate (HR) or cycle thermal efficiency (η_{th}). Other parameters of interest that contribute to the operating costs are fuel consumption (m_f) and fog water consumption (m_fw).

Another parameter critical but not obvious in evaluating the effects of fogging, is the temperature rise across the compressor section of the gas turbine. It is known from the basics of thermodynamics of a gas turbine cycle, that the specific compressor power input is directly proportional to the temperature rise across the compressor and inversely proportional to the compressor inlet temperature. Therefore, a decrease in the value of temperature rise across the compressor results in less compressor specific work and

[4]Inlet fogging is typically applied at conditions when high ambient temperatures exist which results in gas turbine power output drop. The coincident relative humidity is typically low at high ambient temperature. For this reason, 43°C/40% RH condition was selected as a meaningful baseline.

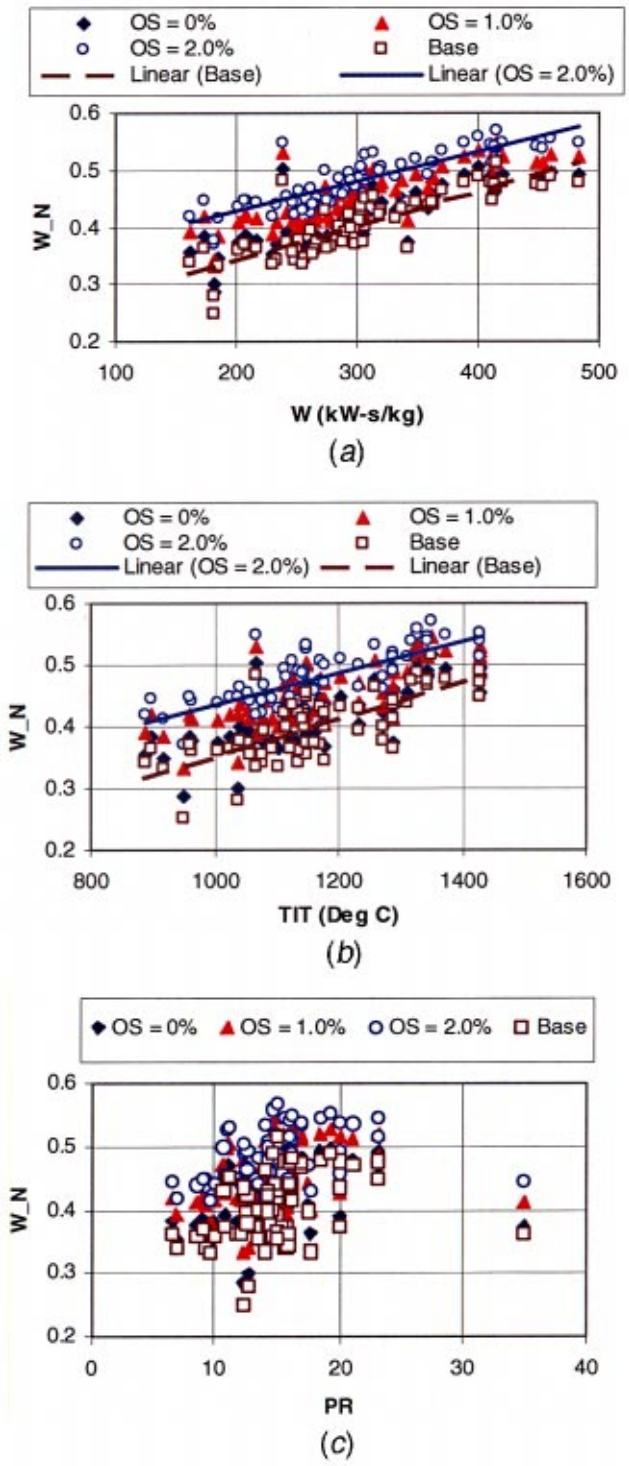

Fig. 2 Effects of inlet evaporative and overspray fogging on turbine net work output ratio (W_N) as a function of (*a*) ISO specific work (W), (*b*) turbine inlet temperature (TIT), (*c*) overall cycle pressure ratio (PR).

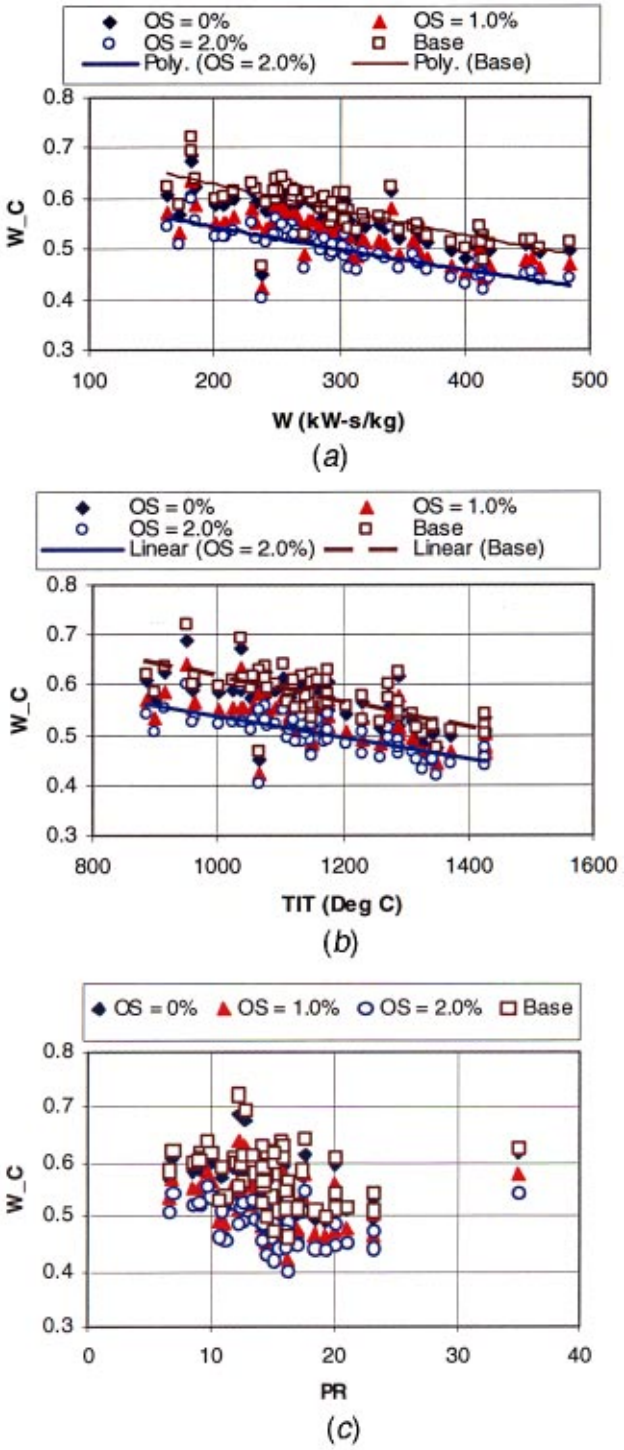

Fig. 3 Effects of inlet evaporative and overspray fogging on compressor work input ratio (W_C) as a function of (*a*) ISO specific work (W), (*b*) turbine inlet temperature (TIT), (*c*) overall cycle pressure ratio (PR).

increased net gas turbine work output. Also as compressor discharge temperature is usually measured, the value of temperature rise across the compressor is field determinable.

The amount of change in power (ΔP_N), expressed in percent with respect to the base case, against the ISO specific work (W) for the three fogging conditions is shown in Fig. 4(*a*). Values of power change for the base case with respect to the ISO values for each gas turbine is also included in Fig. 4(*a*). The examination of Fig. 4(*a*) shows that a larger amount of power boost is obtained due to inlet evaporative fogging compared to the case when overspray fogging is added to the evaporative fogging. For example, considering a typical gas turbine with the ISO specific work of 200 kW-s/kg, going from the ISO condition ambient temperature (15°C) to the base case ambient condition of 43°C results in a power output drop of approximately 26%. By evaporative fogging

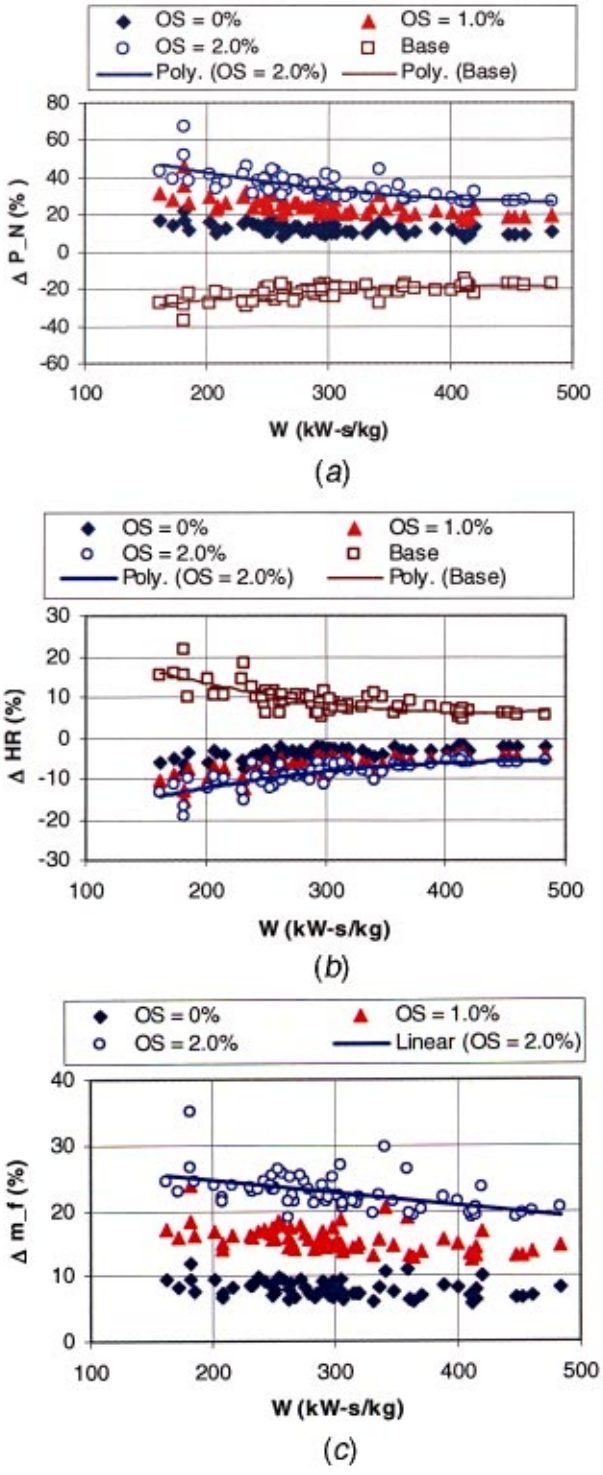

Fig. 4 Effects of inlet evaporative and overspray fogging as a function of ISO specific work (W) on (*a*) power output change (ΔP_N), (*b*) heat rate change (ΔHR) (*c*) fuel flow rate change (Δm_f)

to the wet bulb temperature, approximately a 44% boost in power is attained in comparison to the base case. Thereafter, overspray of 1% and 2% yields power boost of approximately 10% for each step.[5] This demonstrates, what users have intuitively known, that when high ambient temperatures exist (typically with coincident low humidity values), the benefits of direct evaporation are greater than those derived by overspray.

A definitive correlation can be seen in Fig. 4(*a*) between the values of ΔP_N and *W*, where the power boost is higher for gas turbines with low power density (or low specific work). Interestingly, the trends in the variation of ΔP_N versus *W* are opposite for the fogging cases and the ''no fogging'' case (i.e., base case) indicating that lower specific work gas turbines seem to benefit more from fogging, in particular, overspray fogging. As can be seen in Fig. 4(*a*), on the average, the power boost varies from 10–20%, in comparison to the ISO case, for inlet evaporative fogging. The power boost, in comparison to the ISO case, can be 30–40% with a two percent overspray fogging effect for the gas turbines modeled in the present study.

The variation of heat rate change (ΔHR) exhibits a strong correlation with the values of *W* as shown in Fig. 4(*b*). With inlet evaporative fogging, heat rate improvement ranges from 2–7% with respect to the ISO condition. As expected and seen in Fig. 4(*b*), heat rate values further decrease (additional heat rate enhancement) as the amount of overspray fogging increases. For two percent overspray fogging, the amount of heat rate enhancement varies approximately between 5–15% with respect to the ISO condition for the gas turbines considered. An opposite trend in the variation of ΔHR with and without the effects of fogging can also be seen in Fig. 4(*b*). It can also be noted that the heat rate enhancement is higher, as was the case with power boost, for gas turbines with lower values of *W*.

Figure 4(*c*) shows variations of change in fuel consumption, expressed as percent with respect to the base case value, versus ISO values of *W*. The fuel consumption increased, in comparison to the base case, for all the cases of fogging (see Fig. 4(*c*)). This is as expected because for the saturation case, the mass flow of air is increased requiring an increase in fuel flow. Whereas, with overspray, the compressor discharge temperature is reduced in addition to the increase in air flow rate, and more fuel is needed to achieve the design value of TIT. Also, a trend is observed whereby, fuel consumption is higher in presence of fogging for gas turbines with lower values of *W*.

Figure 5(*a*) shows a plot of the fog water consumed per unit power boost (m_fw) versus the ISO values of *W*. The value of m_fw increases with the decrease in the value of *W* for all the fogging conditions.

For evaporative fogging, a slight increase in the value of compressor temperature rise per unit specific power boost (ΔT_C), with the decrease in the value of *W* can be seen in Fig. 5(*b*). The value of ΔT_C appears to be a weak function of *W* for overspray fogging conditions and decreases with increasing levels of fogging.

The variations of performance parameters (ΔP_N, ΔHR, Δm_f, m_fw, and ΔT_C) discussed above were also examined against design parameters such as TIT, PR, and W_N. The resulting trends were similar to those observed with the values of *W*. To conserve space, only few selected plots are shown in Figs. 5(*c*)–5(*g*). Figure 5(*h*) shows that changes in the values of W_N and W_C are proportional with the implementation of fogging as was seen earlier (see Figs. 2(*a*) and 3(*a*)).

Effects of Ambient Temperature and Relative Humidity

The preceding parametric study was conducted with base case ambient conditions of 43°C and a relative humidity of 40%. In order to comprehensively understand the effects of fogging, a sensitivity study by varying the ambient temperature and relative humidity was conducted for two gas turbine models. The two gas turbines chosen were the heavy duty GE Model 7121EA and the aeroderivative Pratt & Whitney FT-8. While it is recognized that these two gas turbines may not be representatives of all the gas turbines used in the study, the basic trends and sensitivities can be evaluated in a qualitative manner. Detailed climatic analyses of

[5]The power boost from overspray or fog intercooling comes from a reduction in compressor work.

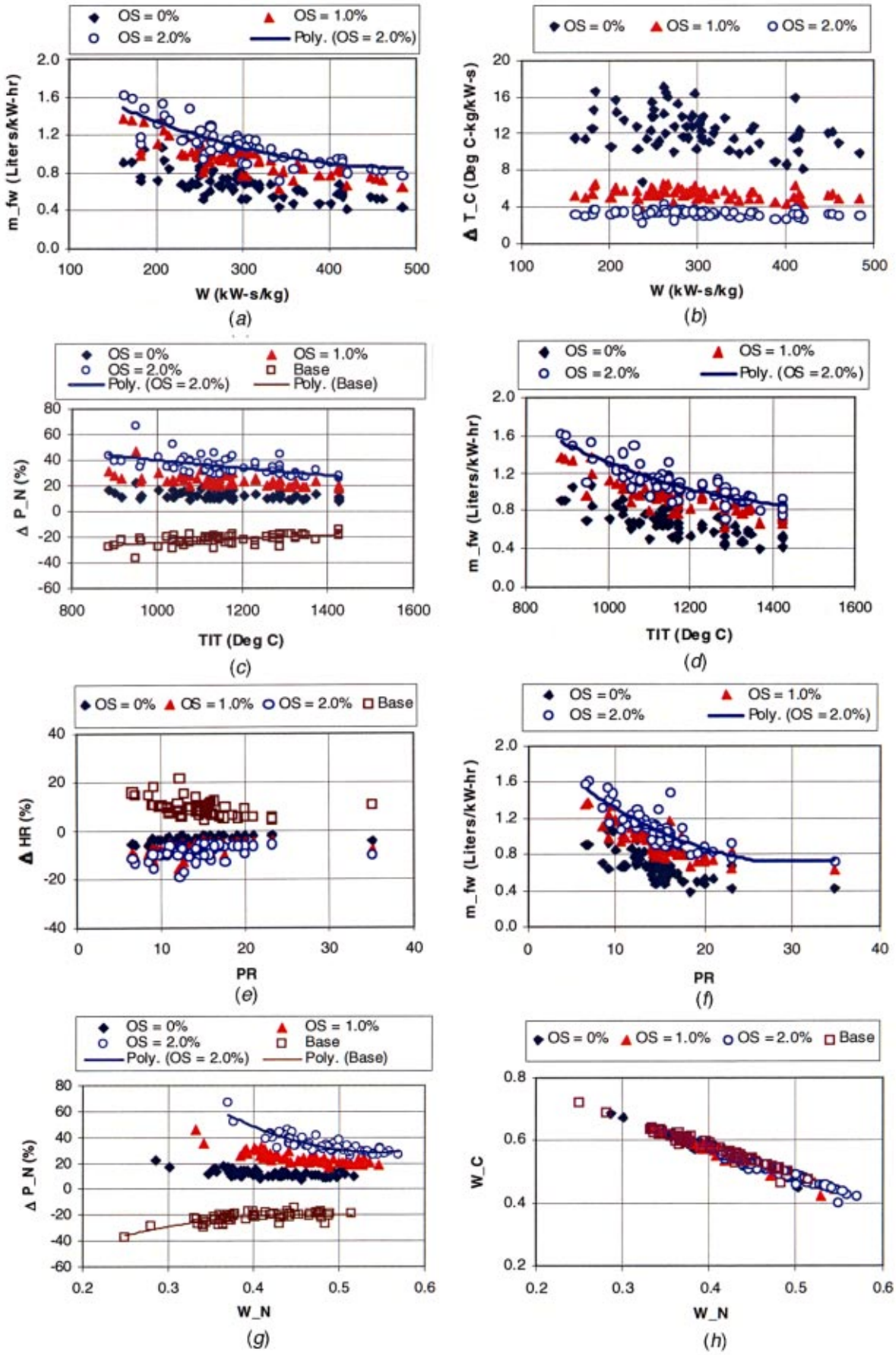

Fig. 5 Effects of inlet evaporative and overspray fogging (*a*) m_FW versus W, (*b*) ΔT_C versus W, (*c*) ΔP_N versus TIT, (*d*) m_fw versus TIT, (*e*) ΔHR versus PR, (*f*) m_fw versus PR, (*g*) ΔP_N versus W_N, (*h*) W_C versus W_N

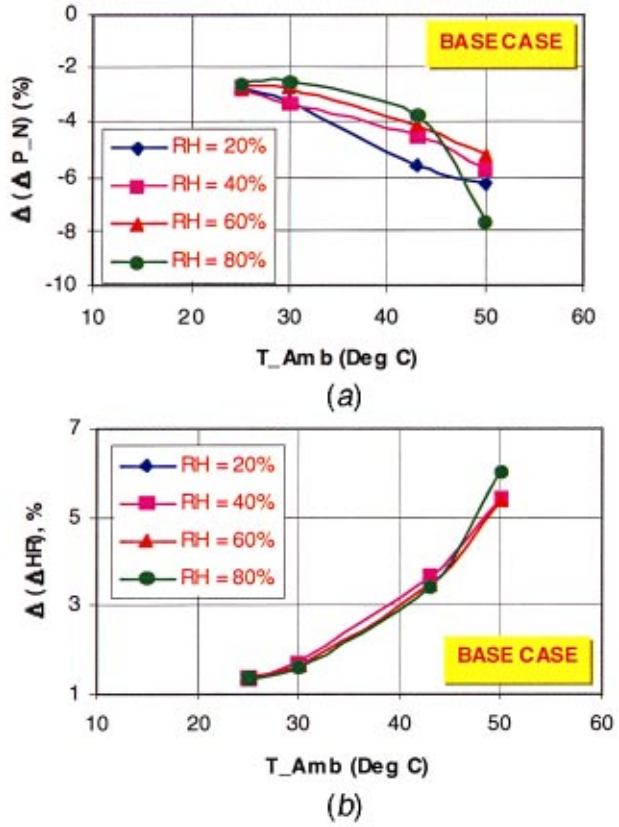

Fig. 6 Effects of ambient temperature and relative humidity–base case (*a*) power output change and (*b*) heat rate change. (Change shown with respect to the industrial gas turbine.)

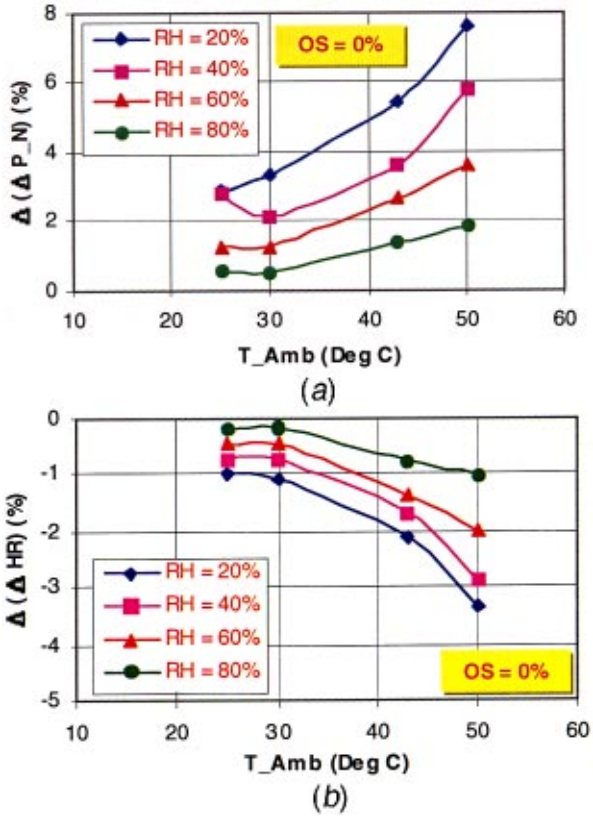

Fig. 7 Effects of ambient temperature and relative humidity–inlet evaporative fogging (*a*) power boost and (*b*) heat rate change. (Change shown with respect to the industrial gas turbine.)

several sites within the U.S. were recently presented by Chaker et al. [12] using the concept of equivalent cooling degree hours that showed considerable amount of evaporative cooling potential, even in very humid climates that would not traditionally be considered as sites for evaporative cooling.

For each gas turbine, four values of ambient temperature (25°C, 30°C, 43°C, and 50°C) and relative humidity (20%, 40%, 60%, and 80%) were examined for the three fogging conditions (OS = 0%, 1%, and 2%). Thus, a total of 48 cases were analyzed for each gas turbine. Results are summarized with only few selected plots. Data is presented, as a change expressed in percent, with respect to the corresponding value of the industrial gas turbine (GE 712IEA). Thus, a given plot directly shows how an aeroderivative gas turbine (P&W FT8) performs in comparison to an industrial gas turbine (GE 712IEA) under different ambient and fogging conditions.

It is well known that, in absence of fogging (i.e., for the base case) the value of ΔP_N is not significantly affected by the change in ambient humidity for a gas turbine.[6] However, the value of ΔP_N decreases with the increase in ambient temperature at a given value of RH. For a given value of relative humidity, a decrease in the value of ΔP_N for the aeroderivative machine is greater at higher values of ambient temperature as shown in Fig. 6(*a*). Changes in heat rate values due to ambient relative humidity for the base case, for both machines, are small (approximately 1%, plot not included). For the base case and at all the ambient conditions investigated, the increment in heat rate values are higher (by approximately 6% maximum), implying more performance degradation, for the aeroderivative than for the industrial gas turbine as shown in Fig. 6(*b*).

[6]Typically the effect of relative humidity on gas turbine output is no more than 1% from 0–100% relative humidity.

With inlet evaporative fogging (OS=0%), an increase in power output can be achieved at all the ambient conditions considered in the study for both gas turbines (plot not included). In addition, the amount of power boost (with respect to the base case) decreases with increase in the value of ambient relative humidity at a given value of ambient temperature (plot not included). This is expected as the evaporative cooling potential depends on the available wet-bulb depression which is lower when high relative humidity conditions exist. Further, a decrease in the amount of power boost with increase in ambient relative humidity increases with the increase in ambient temperature. A comparison of the two machines shows that, for all the values of ambient temperatures and relative humidity examined, power boost is higher for aeroderivative compared to the industrial gas turbine for inlet evaporative fogging as shown in Fig. 7(*a*).

With inlet evaporative fogging and under all the ambient conditions considered, values of ΔHR decreased for both gas turbines (plot not included). Maximum heat rate improvement is achieved for high ambient temperatures and low values of relative humidity, respectively (plot not included). Inlet evaporative fogging reduces the performance degradation due to an increase in the ambient temperature. A comparison of two gas turbines under various ambient conditions shows that heat rate improvements due to inlet evaporative fogging is higher for the aeroderivative than the industrial gas turbine as can be seen in Fig. 7(*b*).

For 2% overspray fogging, the trends in the effect of variation of ambient conditions on the values of ΔP_N were found to be the same as for the inlet evaporative fogging for the industrial gas turbine (plot not included). However, for the aeroderivative gas turbine, effects of relative humidity on power output change were negligible (within 1%) at low values of ambient temperatures as shown in Fig. 8. At low values of ambient temperature, power

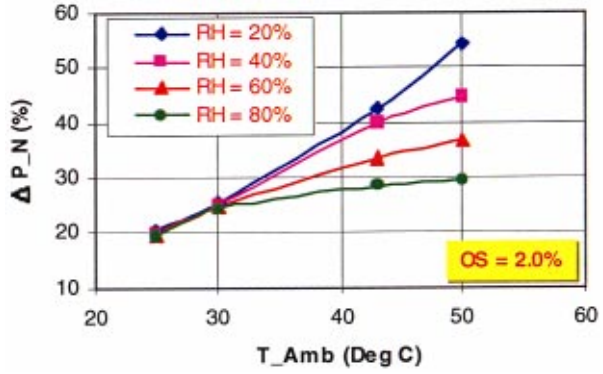

Fig. 8 Effects of ambient temperature and relative humidity on power boost—2% overspray fogging (aeroderivative gas turbines)

boost is higher for industrial than the aeroderivative gas turbine as shown in Fig. 9(*a*). Further, this trend changes at high values of ambient temperature, where aeroderivative gas turbine shows higher power boost in comparison to the industrial gas turbine (see Fig. 9(*a*)). This observed trend probably occurs because the aeroderivative machine displays a greater drop off in power at the higher ambient temperature compared to the industrial gas turbine (for example, see Fig. 1). The variation in heat rate change, with two percent overspray fogging and different ambient conditions resulted in a higher improvement in heat rate values for aeroderivative gas turbines than industrial gas turbine as shown in Fig. 9(*b*). The results show that at low values of ambient temperature,

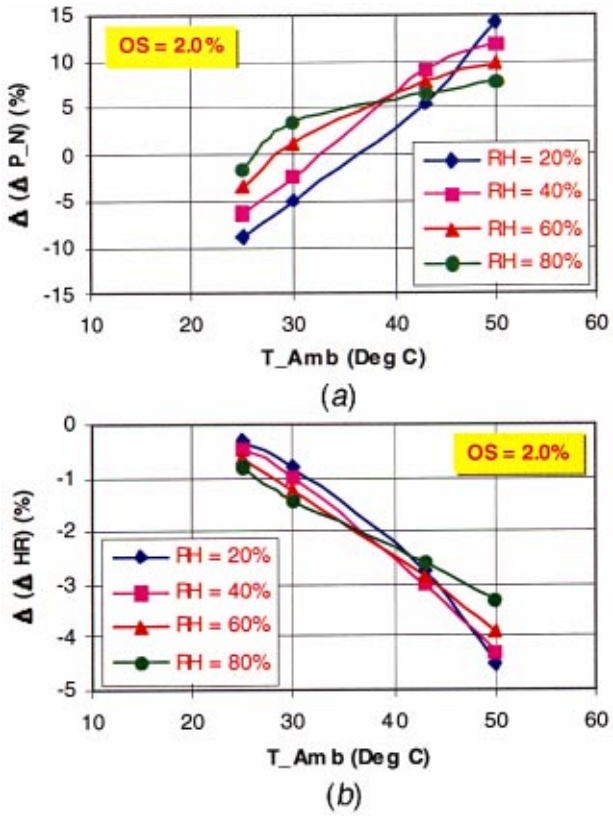

Fig. 9 Effects of ambient temperature and relative humidity with 2% overspray fogging on (*a*) power boost and (*b*) heat rate change. (Change shown with respect to the industrial gas turbine.)

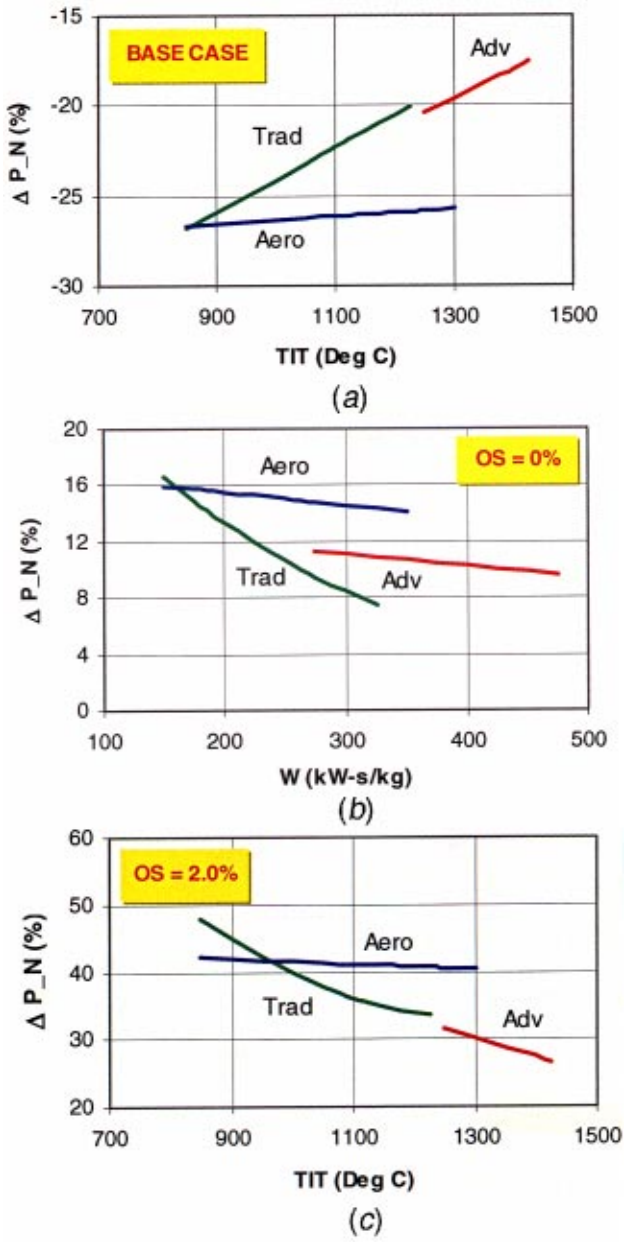

Fig. 10 Power output change (*a*) base case, (*b*) inlet evaporative fogging, and (*c*) 2% overspray. A comparison of three classes of gas turbines.

the heat rate improvement increases by a small amount with an increase in the ambient relative humidity. At 50°C, the trend in the effect of ambient relative humidity is the same as was observed for the inlet evaporative fogging case (see Figs. 9(*a*) and 9(*b*)).

A Comparison of the Three Classes of Gas Turbines Undergoing Inlet Evaporative and Overspray Fogging

There are differences in the design, operational characteristics, response to the ambient temperature etc., among gas turbines currently available in the market. For example, aeroderivative gas turbines have different operational characteristics including a greater sensitivity to ambient temperature compared to the industrial gas turbines. Gas turbines developed in the last decade or so have better cooling technologies and improved aerodynamic design than machines developed earlier (say, three decades ago). As shown in the previous section by comparing performance of two

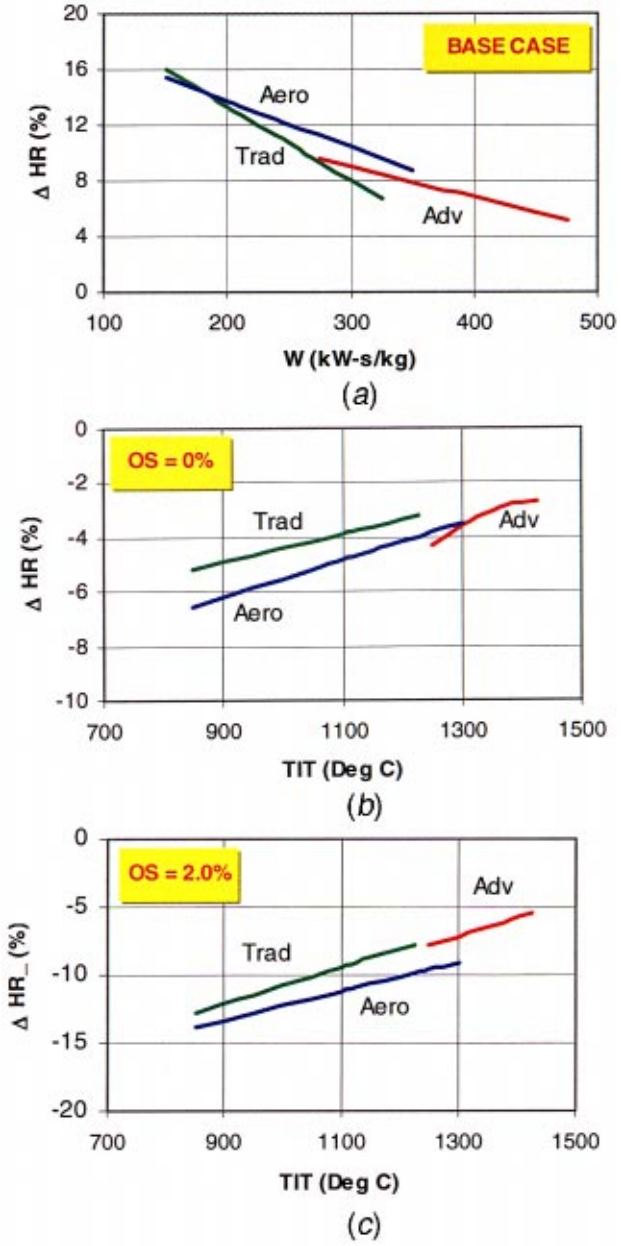

Fig. 11 Heat rate change (*a*) base case, (*b*) inlet evaporative fogging, and (*c*) 2% overspray. A comparison of three classes of gas turbines.

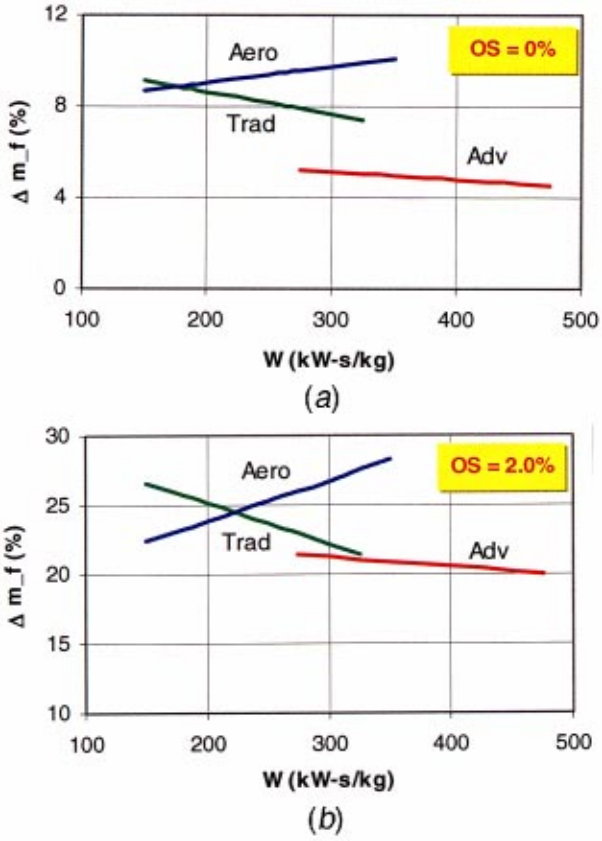

Fig. 12 Effect of fuel flow rate (*a*) inlet evaporative fogging and (*b*) 2% overspray. A comparison of three classes of gas turbines.

machines, that an aeroderivative machine has higher performance improvement (higher power boost and heat rate improvement) compared to the industrial gas turbine in presence of inlet fogging. These results led to a detailed examination of the performance of selected gas turbines. In order to examine the response of different classes of gas turbine to inlet fogging, the selected gas turbines were divided into the following three categories based on the design criteria and the firing temperature: (1) traditional industrial gas turbines (TIT$<$1200°C); (2) advance industrial gas turbines (TIT$>$1200°C); and (3) aeroderivative gas turbines. An examination of the parametric study revealed that there exist some subtle differences with respect to fogging performance among the different classes of gas turbines. These differences could not be seen when the entire set of selected gas turbines were analyzed collectively.

A comparison of various performance parameters based on the three gas turbine classes showed some interesting results. Because of the space limitations, only a few selected plots and the main observations are summarized here. A cautionary note should be made that the curve fits could create false visual impressions. However, we have examined the data scatter and feel that they are at least approximately representatives of the three classes of gas turbines.

A higher drop in power output, under the base condition compared to the ISO condition, was observed for aeroderivatives than for the other two types of gas turbines (see Fig. 10(*a*)). In addition, for the base case, the power output loss for advanced gas turbines is comparatively lower than aeroderivatives and traditional gas turbines. For the base case and all the three classes of gas turbines, the loss in power output reduces with increase in the values of TIT (see Fig. 10(*a*)) and W (plot not included).

With inlet evaporative fogging (to saturation conditions) power boost is higher for the aeroderivative than the traditional and advanced classes of gas turbines over the range of specific work (see Fig. 10(*b*)) and turbine inlet temperatures (plot not shown) considered. Also, the power boost decreases with the increase in the values of W as shown in Fig. 10(*b*) and TIT (plot not included) for all the three classes of gas turbines.

The trend in the variation of power boost with overspray is the same as with inlet evaporative fogging except at values of TIT $<$950°C (see Fig. 10(*c*)) or $W<200$ kW-s/kg (plot not included), where traditional gas turbines show a higher power boost compared to the aeroderivative gas turbines. Also, power boost with overspray fogging was found to be the lowest for advanced gas turbines among the three types of gas turbines as shown in Fig. 10(*c*). However, a higher power boost for advanced class compared to the traditional class of gas turbines occurred with inlet evaporative fogging as shown in Fig. 10(*b*).

The heat rate increase (i.e., loss in performance) is found

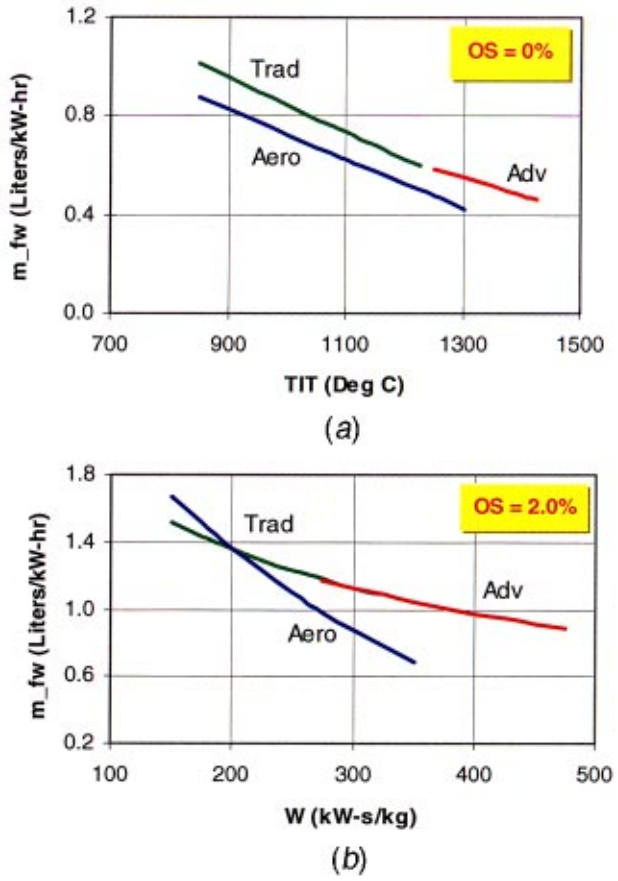

Fig. 13 Effect of fog water flow rate per unit power boost (*a*) inlet evaporation fogging and (*b*) 2% overspray. A comparison of three classes of gas turbines.

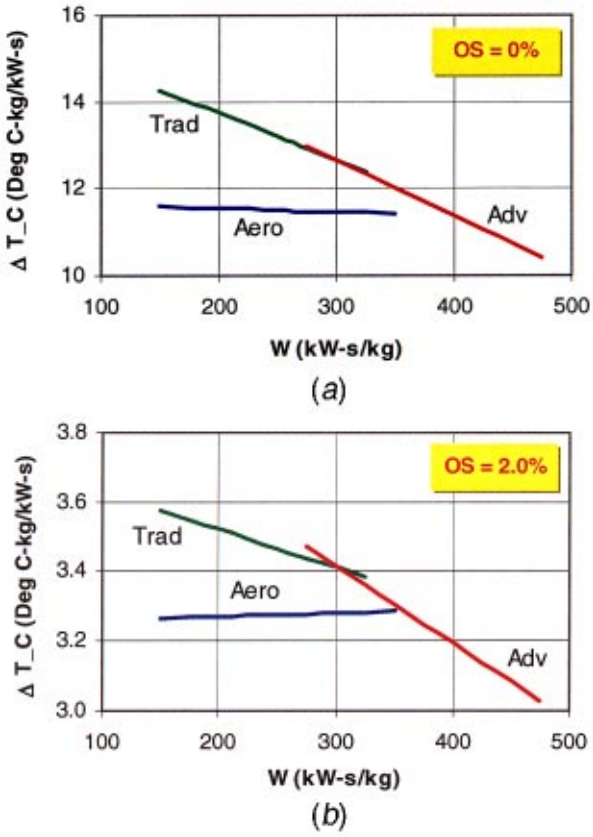

Fig. 14 Effect on compressor temperature rise per unit specific power boost (*a*) inlet evaporative fogging and (*b*) 2% overspray. A comparison of three classes of gas turbines.

greater for aeroderivative engines compared to the other two classes of gas turbines for the base case (see Fig. 11(*a*). This trend was found consistent when considering the variations of heat rate change with *W* and TIT. Advanced industrial gas turbines showed smaller heat rate increases in comparison to the other two gas turbine classes implying a lower performance decrement (see Fig. 11(*a*).

For inlet evaporative fogging (OS=0%), aeroderivative engines exhibited a higher decrease (improvement) in the heat rate values, compared to the base case than the other two classes of gas turbines as shown in Fig. 11(*b*). Also, the heat rate improvement decreases with an increase in TIT (see Fig. 11(*b*)) and *W* (plot not shown) values. In spite of the fact that heat rate improvement for advanced gas turbines is obtained compared to the base case, heat rate improvements are lower than the other two classes of gas turbines (see Fig. 11(*b*)). With overspray fogging (OS =2.0%), the trend in the variation of heat rate change is similar to the case of OS=0% as is evident from Fig. 11(*c*). In comparison to the inlet evaporative fogging case, heat rate improvement increases with 2% overspray, for all classes of gas turbines, mainly because of the increased amount of fogging (see Fig. 11(*c*)).

The amount of fuel flow change, compared to the base case, is observed to be higher for the aeroderivative engine class than the other two classes for inlet evaporative (see Fig. 12(*a*)) and overspray fogging (see Fig. 12(*b*)). The advanced class gas turbines were found to have the lowest increase in fuel flow consumption compared to the other two classes. Also, fuel flow change decreases with increase in the values of *W* for traditional and advanced gas turbines. However, for aeroderivative engines, fuel flow change increases with the increase in the values of *W* (see Figs. 12(*a*) and 12(*b*)).

The amount of fog water flow rate per unit power boost (m_fw) is found lower for aeroderivative engines than for the traditional and advance class of gas turbines for inlet evaporative fogging as shown in Fig. 13(*a*). The value of m_fw decreases with the increase in the values of TIT and *W* (plot not included) and its rate of decrease is higher for the aeroderivative class of gas turbines compared to the other two classes of gas turbines (see Fig. 13(*a*)). The trend in variation of m_fw with overspray fogging is similar to that observed in the case of inlet evaporative fogging except that at low values of *W* (less than 200 kW-s/kg) or low values of TIT (less than 1000°C), traditional machines show lower fog water requirements than the aeroderivative class of gas turbines (see Fig. 13(*b*)). The effects on fuel flow consumption and fog water required for the three classes of gas turbines show that the selection of a gas turbine for fogging application will be determined not only based on the thermodynamic performance benefits but also on the overall economics. It may be noted, however, that economic considerations were not within the scope of this paper.

The variation of compressor temperature rise per unit specific power boost (ΔT_C) with *W* showed lower values for aeroderivatives than the other two classes of gas turbines with inlet evaporative and overspray fogging as shown in Figs. 14(*a*) and 14(*b*), respectively. A considerable decrease in the value of ΔT_C can be seen with overspray fogging compared to the inlet evaporative fogging. This decrease in the value of ΔT_C, which is indicative of improved compressor performance, explains a significant amount of power boost with overspray fogging.

Concluding Remarks

This parametric analysis has attempted to identify correlation between performance and key gas turbine design parameters due to inlet fogging effects. Useful conclusions can be drawn regarding the use of different gas turbines that are subjected to fogging. All performance parameters seem to correlate well with the ISO specific work, net turbine work output ratio and the turbine inlet temperature. A sensitivity study has been done to examine the effects of varying climatic conditions and to see if they modify the general qualitative trends noted. Finally, an attempt has been made to examine the fogging performance parametrically by dividing the selected machines into the three classes of gas turbines.

Some of the main observations include:

- there exists a correlation between performance parameters and main gas turbine design parameters as a result of fogging. The performance parameters included, power boost, heat rate, fuel flow rate, fog water flow rate per unit power boost and compressor temperature rise per unit specific power boost. Design parameters considered were the specific work, turbine inlet temperature, overall cycle pressure ratio, and net gas turbine work output ratio.
- the study consistently showed that gas turbines with low values of specific work and turbine inlet temperature have a higher power boost and heat rate improvement compared to machines with higher corresponding values.
- the analysis of the effects of ambient conditions clearly showed that, as expected, higher performance improvements are achieved using high pressure fogging at higher ambient temperature and lower relative humidity. In addition, the aeroderivative gas turbine, under all ambient conditions and at different fogging conditions, provided, in general, higher performance improvement in comparison to the industrial gas turbine. Exceptions, if any, to the observed trends have been identified.
- a comparison of gas turbines, by classifying them into three categories-traditional, advanced and aeroderivative, showed that aeroderivative machines indicated a higher performance improvement. This observation was consistent with the results obtained by analyzing two specific gas turbines. One of the plausible reasons can be the low value of the compressor temperature rise per unit specific power boost for aeroderivative machines compared to the advanced and traditional gas turbines.

The results are presented in a format that can be useful to the gas turbine users, as all relevant performance parameters have been correlated with the commonly available gas turbine design parameters. These results are relative and any specific application of high pressure inlet fogging would have to be independently evaluated to determine the specific performance behavior. Yet, it can be stated that the study has yielded some important data in understanding the behavior of gas turbine engines to the effects of high pressure inlet fogging.

Acknowledgment

The first author would like to thank the management of Universal Ensco, Inc. for their continued encouragement and financial support for professional growth.

Nomenclature

EGT = exhaust gas temperature (°C)
HR = heat rate (kJ/kWh)
m_a = air mass flow rate at the gas turbine inlet (kg/s)
m_c = total flow at compressor inlet in presence of fogging (kg/s)
m_f = fuel flow rate, (kg/s)
m_fw = fog water flow rate, Liters/hr
m_fw = m_fw/ΔP, fog water flow rate per unit power boost (Liters/kW-hr)
P = net power output (kWe)
P_d = compressor discharge pressure (bar)
PR = cycle pressure ratio
RH = relative humidity (%)
T = temperature (°C)
T_{Amb} = ambient temperature (°C)
T_d = compressor discharge temperature (°C)
TET = exhaust gas temperature (°C)
T_i = compressor inlet temperature (°C)
TIT = inlet temperature to the turbine first stage nozzle (°C)
W = ISO specific work (kW-s/kg)
W_c = compressor work input (kW)
W_n = $(W_t - W_c)$, turbine net work output (kW)
W_t = turbine work output (kW)
W_N = $(W_t - W_c)/W_t$, net turbine work output ratio
W_C = W_c/W_t, compressor work input ratio
ΔHR = percent change in heat rate with respect to the base case (for the base case, this parameter is with respect to the ISO condition)
Δ(ΔHR) = difference, expressed in percent compared to the industrial gas turbine, of percent change in heat rate with respect to the base case (for the base case, this parameter is with respect to the ISO condition)
Δm_f = percent change in fuel flow consumption with respect to the base case
ΔP = power boost due to inlet fogging, kW
ΔP_N = percent change in net power output with respect to the base case (for the base case, this parameter is with respect to the ISO condition)
Δ(ΔP_N) = difference, expressed in percent compared to the industrial gas turbine, of percent change in net power output with respect to the base case (for the base case, this parameter is with respect to the ISO condition)
ΔT_C = $(T_d - T_i)*m_c/\Delta P$, compressor temperature rise per unit specific power boost (°C-kg/kW-s)
η_{th} = LHV cycle efficiency (%)

Acronyms

CCPP = combined cycle power plant
EPC = engineering, procurement and construction
GT = gas turbine
HRSG = heat recovery steam generator
ISO = international standard organization
LHV = lower heating value
OS = overspray
RPM = revolution per minute

Appendix

ISO Performance and Some Design Data for the Selected Gas Turbines

Item #	Model	Shafts	RPM	PR	TIT	TET	Air Flow Rate	Power	HR	η_{th}	Sp. Work ISO
					°C	°C	kg/s	kWe	kJ/kWh	%	kW-s/kg
	TRADITIONAL GAS TURBINES										
1	Alstom Hurricane	1	27245	9.2	1134	602	7	1,630	14,622	24.6	232.86
2	Alstom GT 5	1	14000	12.2	950	446	15	2,726	13,196	27.3	181.73
3	Alstom Typhoon	1	17384	14.8	1149	537	20	5,247	11,948	30.1	262.35
4	Alstom Tornado	1	11085	11.8	1024	478	27	6,726	11,289	31.9	249.11
5	Tempest	1	14045	13.2	1149	553	29	7,726	11,964	30.1	266.41
6	Alstom GT 8C	1	6211	15.7	1172	517	176	52,600	10,526	34.2	298.86
7	Alstom GT 8C2	1	6210	17.4	1177	510	193	57,500	10,387	34.7	297.93
8	Alstom GT 11NM	1	3600	13.5	1146	503	315	89,600	10,592	34.0	284.44
9	Alstom GT 11N2	1	3000	15.1	1146	524	375	113,700	10,460	34.4	303.20
10	Alstom GT 13E2	1	3000	15.0	1171	525	514	164,300	10,086	35.7	319.65
11	GE PGT 2	1	18000	12.7	1038	525	11	2,000	14,628	24.6	181.82
12	GE PGT 5	1	11140	9.1	1038	523	25	5,223	13,396	26.9	208.92
13	GE PGT 5B	1	16630	15.0	1232	571	19	5,500	11,726	30.7	289.47
14	GE PGT 10B	2	7900	15.6	1077	482	47	11,700	11,252	32.0	248.94
15	GE 5731 PA	1	5100	10.0	963	485	123	26,555	12,449	28.9	215.89
16	GE 6581B	1	5160	12.3	1135	542	144	42,170	11,030	32.6	292.85
17	GE 7121EA	1	3600	12.6	1113	534	295	86,650	10,787	33.4	293.73
18	GE 9171E	1	3000	12.3	1124	541	410	124,700	10,603	34.0	304.15
19	GE 9231EC	1	3000	14.2	1204	553	515	172,985	10,144	35.5	335.89
20	KHI M7A-02	1	14000	15.9	1177	521	27	6,930	11,674	30.8	256.67
21	Mitsubishi MF111B	1	9660	14.6	1135	526	56	14,838	11,510	31.3	264.96
22	Siemens / Westinghouse 251 B11/12	1	5400	15.3	1149	514	172	49,500	10,946	32.9	287.79
23	Siemens / Westinghouse 501D5	1	3600	14.2	1141	526	362	109,370	10,508	34.3	302.13
24	Siemens / Westinghouse V84.2	1	3600	11.0	1149	544	354	108,719	10,604	33.9	307.12
25	Siemens / Westinghouse 501D5A	1	3600	14.2	1177	525	378	120,500	10,270	35.1	318.78
26	Siemens / Westinghouse 701D	1	3000	14.2	1116	511	448	132,220	10,529	34.2	295.13
27	Siemens / Westinghouse V94.2	1	3000	11.1	1149	537	500	157,010	10,360	34.7	314.02
28	Solar Saturn	1	22516	6.6	899	512	7	1,210	14,796	24.3	172.86
29	Solar Centaur T-4700	1	14950	9.7	916	444	19	3,515	12,913	27.9	185.00
30	Solar Centaur 50	1	14950	10.7	1054	517	19	4,600	12,270	29.3	242.11
31	Solar Taurus 60	1	14950	12.0	1093	513	22	5,500	11,842	30.4	250.00
32	Solar Taurus 70	1	14950	15.0	1121	490	27	7,520	10,656	33.8	278.52
33	Solar Mars 90	2	8568	16.2	1066	464	39	9,286	11,360	31.7	238.10
34	Solar Mars 100	2	8568	17.6	1104	487	42	10,685	11,136	32.3	254.40
35	Solar Titan 130	1	11220	15.8	1121	493	49	13,500	10,814	33.3	275.51
36	Alstom GT 9D	1	4473	8.9	960	517	158	32,776	13,523	26.6	207.44
37	Alstom GT 11N	1	3600	12.4	1079	515	311	81,600	11,289	31.9	262.38
38	Alstom GT 13D2	1	3000	12.5	1041	490	400	100,500	11,183	32.2	251.25
39	Solar Taurus	2	10400	15	1057	479	26	6,844	10,951	32.9	263.23

Appendix (*Continued*)

Item #	Model	Shafts	RPM	PR	TIT	TET	Air Flow Rate	Power	HR	η_{th}	Sp. Work ISO
					°C	°C	kg/s	kWe	kJ/kWh	%	kW-s/kg
Advanced Gas Turbines											
40	Alstom GTX 100	1	6600	20.0	1288	546	120	43,000	9,722	37.0	358.33
41	GE 6101FA	1	5100	14.8	1288	590	204	70,905	10,481	34.3	347.57
42	GE 7241 FA	1	3600	15.5	1327	599	448	174,000	9,812	36.7	388.39
43	GE 7251 FB	1	3600	18.5	1371	626	445	186,600	9,669	37.2	419.33
44	GE 9351 FA	1	3000	14.6	1327	599	648	259,670	9,643	37.3	400.73
45	GE 9391G	1	3000	23.2	1427	566	685	282,000	9,115	39.5	411.68
46	GE 9001H	1	3000	23.2	1427	621	685	331,000	9,115	39.5	483.21
47	Hitachi H15	1	7280	14.3	1271	556	49	13,860	11,588	31.1	282.86
48	Hitachi H25	1	7280	14.6	1271	556	88	27,010	10,888	33.1	306.93
49	Mitsubishi 501F	1	3600	16.0	1343	607	453	185,400	9,738	37.0	409.27
50	Mitsubishi 501G	1	3600	20.0	1427	596	567	254,000	9,295	38.7	447.97
51	Mitsubishi 701F	1	3000	17.0	1343	586	651	270,300	9,421	38.2	415.21
52	Mitsubishi 701G	1	3000	21.0	1427	587	737	334,000	9,105	39.5	453.19
53	Siemens / Westinghouse V64.3	1	5400	16.1	1288	531	188	62,300	10,233	35.2	331.38
54	Siemens / Westinghouse V64.3A	1	5400	16.2	1310	589	187	68,000	10,186	35.3	363.64
55	Siemens / Westinghouse V84.3	1	3600	16.0	1288	551	425	153,600	9,918	36.3	361.41
56	Siemens / Westinghouse V84.3A	1	3600	16.9	1343	577	440	182,000	9,209	39.1	413.64
57	Siemens / Westinghouse 501F	1	3600	15.0	1349	590	450	186,500	9,532	37.8	414.44
58	Siemens / Westinghouse V94.2A	1	3000	14.0	1260	585	510	189,000	9,933	36.2	370.59
59	Siemens / Westinghouse 501G	1	3600	19.2	1427	594	550	253,000	9,152	39.3	460.00
60	Siemens / Westinghouse V94.3A	1	3000	17.0	1316	584	642	265,540	9,295	38.7	413.61
Aeroderivative Gas Turbines											
61	P+W ST6L-721	2	33000	6.9	888	513	3	486	16,243	22.2	162.00
62	P+W ST6L-813	2	30000	8.5	1004	561	4	808	14,628	24.6	202.00
63	P+W ST18A	2	18910	14.0	1066	532	8	1,845	12,766	28.2	230.63
64	Rolls Royce Trent / 60	3	3600	35.0	1288	448	152	51,930	8,714	41.3	341.64
65	TP+M FT8	3	3600	20.0	1160	456	84	25,600	9,469	38.0	304.76
66	Allied Signal ASE50A	2	16000	10.6	1232	560	14	3,815	11,948	30.1	272.50
67	Rolls Royce 501KB7	1	14600	13.4	1077	536	20	4,942	12,414	29.0	247.10

References

[1] Tawney, R., Pearson, C., and Brown, M., 2001, ''Options to Maximize Power Output for Merchant Plants in Combined Cycle Applications,'' ASME Paper No. 2001-GT-0409.

[2] Jones, C., and Jacobs, J. A., 2000, ''Economics and Technical Considerations for Combined-Cycle Performance-Enhancement Options,'' GE Publication GER-4200.

[3] Kitchen, B. J., and Ebeling, J. A., 1995, ''Qualifying Combustion Turbines for Inlet Air Cooling Capacity Enhancement,'' ASME Paper No. 95-GT-266.

[4] Meher-Homji, C. B., and Mee, T. R., 1999, ''Gas Turbine Power Augmentation by Fogging of Inlet Air,'' *Proceedings of the 28th Turbomachinery Symposium*, Turbomachinery Laboratory, Texas A&M University, Sept., Houston, TX.

[5] Meher-Homji, C. B., and Mee, T. R., 2000, ''Inlet Fogging of Gas Turbine Engines–Part A: Theory, Psychrometrics and Fog Generation and Part B: Practical Considerations, Control and O&M Aspects,'' ASME Paper Nos. 2000-GT-307; 2000-GT-308.

[6] Kleinschmidt, R. V., 1947, ''Value of Wet Compression in Gas Turbine Cycles,'' Mech. Eng. (Am. Soc. Mech. Eng.), **69**, pp. 115–116.

[7] Wilcox, E. C., and Trout, A. M., 1951, ''Analysis of Thrust Augmentation of Turbojet Engines by Water Injection at Compressor Inlet Including Charts for Calculating Compression Processes with Water Injection,'' NACA Report No. 1006.

[8] Nolan, J. P., and Twombly, V. J., 1990, ''Gas Turbine Performance Improvement by Direct Mixing Evaporative Cooling System,'' ASME Paper No. 90-GT-368.

[9] Hill, P. G., 1963, ''Aerodynamic and Thermodynamic Effects of Coolant Injection on Axial Compressors,'' Aeronaut. J., pp. 331–348.

[10] Arsen'ev, L. V., and Berkovich, A. L., 1996, ''The Parameters of Gas-Turbine Units with Water Injected into the Compressor,'' Thermal Engineering, **43**(6), pp. 461–465.

[11] Ingistov, S., 2000, ''Fog System Performance in Power Augmentation of Heavy Duty Power Generating Gas Turbines GE Frame 7EA,'' ASME Paper No. 2000-GT-305.

[12] Chaker, M., Meher-Homji, C. B., Mee, T. R., and Nicolson, A., 2001, ''Inlet Fogging of Gas Turbine Engines-Detailed Climatic Analysis of Gas Turbine Evaporative Cooling Potential,'' ASME J. Eng. Gas Turbines Power, ASME Paper No. 2001-GT-526.

Systematic Assessment of Combustion Turbine Inlet Air-Cooling Techniques

Abdalla M. Al-Amiri
Associate Professor,
Mechanical Engineering Department,
The United Arab Emirates University,
P.O. Box 17555,
Al-Ain, UAE
e-mail: alamiri@uaeu.ac.ae

Montaser M. Zamzam
Senior Mechanical Engineer,
The Engineering and Major Projects Division,
Abu Dhabi Company for Onshore Oil Operations (ADCO),
P.O. Box 270,
Abu Dhabi, UAE
e-mail: mzamzam@adco.ae

The current study is centered on assessing the benefits of incorporating combustion turbine inlet air-cooling systems into a reference combustion turbine plant, which is based on a simple cycle under base load mode. Actual climatic conditions of a selected site were examined thoroughly to identify the different governing weather patterns. The main performance characteristics of both refrigerative and evaporative cooling systems were explored by examining the effect of several parameters including inlet air temperature, airflow-to-turbine output ratio, coefficient of performance (for refrigerative cooling systems), and evaporative degree hours (for evaporative cooling systems). The impact of these parameters was presented against the annual gross energy increase, average heat rate reduction, cooling load requirements and net power increase. Finally, a feasibility design chart was constructed to outline the economic returns of employing a refrigerative cooling unit against different prescribed inlet air temperature values using a wide range of combustion turbine mass flow rates. [DOI: 10.1115/1.1805008]

1 Introduction

The performance of a combustion turbine is inherently tied to ambient air conditions. Gas turbine output suffers significantly at increased temperature levels due to the reduced available combustion air mass flow rate. On the contrary, cooled denser air gives the system a higher mass flow rate and pressure ratio; resulting in an increase in combustion turbine output and usually an overall increase in the system efficiency. In addition, the emission per kWh is reduced as lower exhaust temperatures are attained. This will consequently result in reducing the environmental impact of such units. Recently, combustion turbine inlet air cooling systems have received considerable attention as a viable design option in increasing power output. Such cooling systems bring the combustion turbine units to operate close to manufacturer design condition and in some cases, independently of climatic conditions.

The available technologies today are classified either under evaporative or refrigerative type cooling systems. The aforementioned include water-through-media and fogging options while the latter include continuous cooling, direct expansion, and liquid and absorption chillers. Moreover, absorption chillers can be either driven by waste heat or electricity, which are often coupled with a thermal energy storage system to capitalize from the lower cost of the off-peak generated electricity. In general, evaporative type systems are viewed to be suitable for hot and dry climates since its cooling capability is limited to the ambient wet bulb temperature, which subsequently places a cap on the recovered power. However, it has several advantages such that it requires minor modifications to the inlet house, low capital installation cost (US$50–100 per incremental kW), and it carries a high reliability and a low operating and maintenance (O&M) cost. On the contrary, refrigeration systems are complex and require much higher capital investment (US$200–400 per incremental kW) and O&M cost. However, their applications are not constrained by the wet bulb temperature value and, thus, higher power augmentation can be achieved.

Several investigations, such as Van Der Linden and Searles [1] and Utamura et al. [2], have reported on the current available technologies and their associated economic feasibility studies. Moreover, De Lucia et al. [3], Loud and Staterpryce [4], Jolly et al. [5], and Stewart [6] have all, among others, discussed various techniques that are currently employed for cooling the inlet air. Also, they have highlighted several economic factors relevant to introducing such options into a combustion turbine system. Indeed, the installation and running costs must be weighed against the expected revenues generated from the additional gained output. Furthermore, Daryl et al. [7] presented the effect of thermal energy storage (TES) system on inlet air cooling economics and identified the preferable storage technologies for different applications. Recently, Chaker et al. [8] have reported on the evaporative cooling hours potential using the inlet fogging technique for various cities across the United States.

Our survey of the literature has shown that most of the reported studies have either focused on highlighting available technologies in the market or were tailored to the implementation of a given combustion turbine inlet air cooling (CTIAC) system to a particular station. In principle, the selection of a CTIAC system for an existing station would require studying the behavior of several key design factors. These include detailed climatic conditions, airflow-to-turbine output ratio, turbine performance in terms of power output and heat rate, turbine operation mode, and the expected hours of operation. Definitely, there exists a lack of information on the most suitable CTIAC system in terms of effectiveness and economic feasibility in a broad region. Such a study might ultimately recommend a blend of CTIAC systems to meet the various design conditions.

The main objective of this study is to highlight the associated benefits of employing either an evaporative or a refrigerative CTIAC option under various weather patterns. The choice of the most suitable system(s) will be based on technical and economical considerations. The current study will provide an overview of the potential of CTIAC systems in the Arabian Gulf region as it represents one of the most severe climate conditions around the globe. Furthermore, the United Arab Emirates (UAE) will be considered for performing the details of the investigation as a representative sample of the regional climate. The undertaken assessment measures carried out in this study, however, can be

Contributed by the IGTI Industrial and Cogeneration Committee of THE AMERICAN SOCIETY OF MECHANICAL ENGINEERS for publication in the ASME JOURNAL OF ENGINEERING FOR GAS TURBINES AND POWER. Manuscript received by the I&C Committee November 14, 2003; final revision received by the ASME Headquarters December 8, 2003. Associate Editor: C. Meher-Homji.

systematically extended to other countries even outside the region once detailed weather data are obtained. The objectives sought in the undergoing study are achieved by first identifying the weather information in the chosen area in order to categorize the different existing weather patterns and accordingly propose proper weather design conditions. Next, the performance of a selected number of CTIAC systems are evaluated over a range of prescribed inlet air temperature values by closely examining their impact on the predicted annual gross energy increase, average heat rate reduction, cooling load requirements, and net power increase for a reference plant. The current study is concluded by portraying a ''design chart'' that identifies the economic feasibility of a particular CTIAC option for a broad range of combustion turbine (CT) mass flow rates.

2 Overview of Power Industry in the Arabian Gulf Region

This region, which is located in the southwestern part of the Asian continent, comprises six Arabian countries on the western side of the Gulf (Bahrain, Kuwait, Oman, Qatar, Saudi Arabia, and UAE) and Iran lying on its eastern side. The region is characterized by several common patterns. These include severe summer conditions (hot and humid in the coastal areas becoming hot and dry inland toward the arid areas) and scarce water resources (58% of the world's desalinated water is produced in this region). The UAE alone, for instance, has invested over 1.2 billion dollars last year in the electricity and potable water generation sector. Moreover, the region has shown a great demand for electric power in the past decade due to the rapid growth in both the industrial and commercial sectors. Increased domestic consumption of electricity coupled with volatile swings in peak loads has increased demand for electric power in the region. This phenomenon is further escalated given the relatively low and flat imposed energy tariff (~US$0.04/kWh), which is subsidized by the local governments.

Many of the region states have undertaken measures for deregulating and privatizing the power generation industry to lift the burden associated with the installation expenditures of new units to meet the hike in electric power demand. The total electric power generation in the region is estimated at 49.4 GW (Bahrain 1.1 GW, Kuwait 9.3 GW, Oman 2.1 GW, Qatar 1.9 GW, Saudi Arabia 25 GW, and UAE 10 GW) with an average annual growth exceeding 4%. It is also worth noting that the generating capacity for Saudi Arabia alone is forecasted to double by 2020 at a cost of more than 4.5 billion dollars per year. Our survey has indicated that the power stations in the region are mainly comprised of combustion turbines and combined cycle plants with diesel units as emergency backups. The CT units are widely used for base and peak loads and are heavily favored owing to the relatively cheap input fuel cost, which is abundantly available in the region. It is roughly estimated that at least 65% of the total installed generating units in the region are gas turbine based. This should definitely build an appreciation for the need to tackle the problem of power output deficiency during hot periods.

Although the information at hand is sketchy, several attempts were made to incorporate CTIAC systems into a few of the current stations in place. Despite its growing popularity in the gas turbine plants, CTIAC's have not been implemented on a wide scale in the Arabian Gulf region. One example of such installed units is a refrigeration cooling system that is already in the evaluation phase in Al-Qaseem plant in Saudi Arabia. The cooling unit is based on ice storage with a peak cooling capacity of 19,000 tons of refrigeration (TOR), which is equivalent to 66,500 kW. The system is intended to boost the output of six new GE frame 7EA combustion turbines from 57 MW each in peak summer condition to 77 MW each turbine.

3 Modeling of Climatic Data

Often the weather design conditions are specified in terms of dry bulb temperature (DBT) and relative humidity (RH). Attempts to average these two parameters separately to select the design conditions may lead to improper design of the cooling system, which will impact its economic feasibility. It is commonly perceived that the size of refrigeration equipment is proportional to the increase in the ambient wet bulb temperature (WBT). Indeed, a region identified with ''high humidity'' places a cap on the effectiveness of evaporative cooling systems. However, significant turbine capacity can be recovered in high humidity regions when utilizing refrigerative cooling systems. Designers are also tempted to size a refrigerative cooling system based on the highest recorded DBT and RH values or the highest DBT and lowest RH when incorporating an evaporative cooling system. Since such extreme conditions may never exist in nature, the designed plant may likely end up more expensive due to over predictions.

It is interesting to note that high RH conditions rarely occur with high DBT values as RH has a marked systematic diurnal variation opposite to the temperature. In fact, the moisture-holding capacity of air depends on its temperature and, thus, warmer air can hold more water vapor than cooler air. Accordingly, relative humidity is highest during the cool morning and evening hours and lowest in the hot afternoon hours. In order to properly model the climate conditions for a particular location, it is advisable that the temperature profile in that site be gathered for the past 20 to 30 years based on hourly-recorded data. Then, the average wet and dry bulb coincident temperatures can be sorted out for further analysis to be carried out.

It is a common practice that the design enthalpy (h) value is generally overlooked by the DBT condition. This will subsequently lead to significant flaws in estimating the size of the selected system. In fact, the design condition should be specified in terms of the maximum registered coinciding values for both DBT and WBT that will correspond to the maximum enthalpy value at a given time slot. This will accordingly present the upper bound for the selected cooling system. Also, it is equally important to identify the lower bound to seal the operating envelope of the cooling system. Such a limit can well be the ISO condition, which is defined at DBT=59°F (15°C) and RH=60%. However, a designer might be even tempted to increase the power output above the rated capacity by cooling the inlet air below ISO condition. In particular, attempts to operate below 42°F (5.6°C) would be running the risk of ice formation on the bell-mouth, which might flake off to ultimately damage the compressor blades. Furthermore, the revenues generated from the additional increase in output power upon suppression of inlet air temperature to ISO condition or even lower might not be worth the investment to begin with.

The actual weather data in UAE recorded in the year 2000 were chosen as a basis for performing the analysis in this study. These data were obtained from the Metrological department at the Ministry of Transportation. Upon mapping the weather information obtained for the different geographical areas, three distinct weather patterns were recognized. Moreover, these weather patterns were found to fall under three main cities, namely Al-Ain (pattern I), Abu Dhabi (pattern II), and Fujairah (pattern III). Giving the massive number of data at hand, the daily weather data for each pattern was categorized in one-degree intervals while the subsequent analysis of energy, power and heat rate is based on five-degree intervals.

Figure 1 represents the cumulative hours per year for the recorded DBT and WBT values in the three patterns considered. The qualitative assessment of the data indicates that pattern I is very hot and relatively dry, pattern II is very hot and humid, whereas pattern III is hot and very humid. This is not surprising giving that pattern I represents the inward arid areas while patterns II and III represent the coastal area lying on the Arabian gulf and Oman gulf, respectively. The figure also shows that the margin between

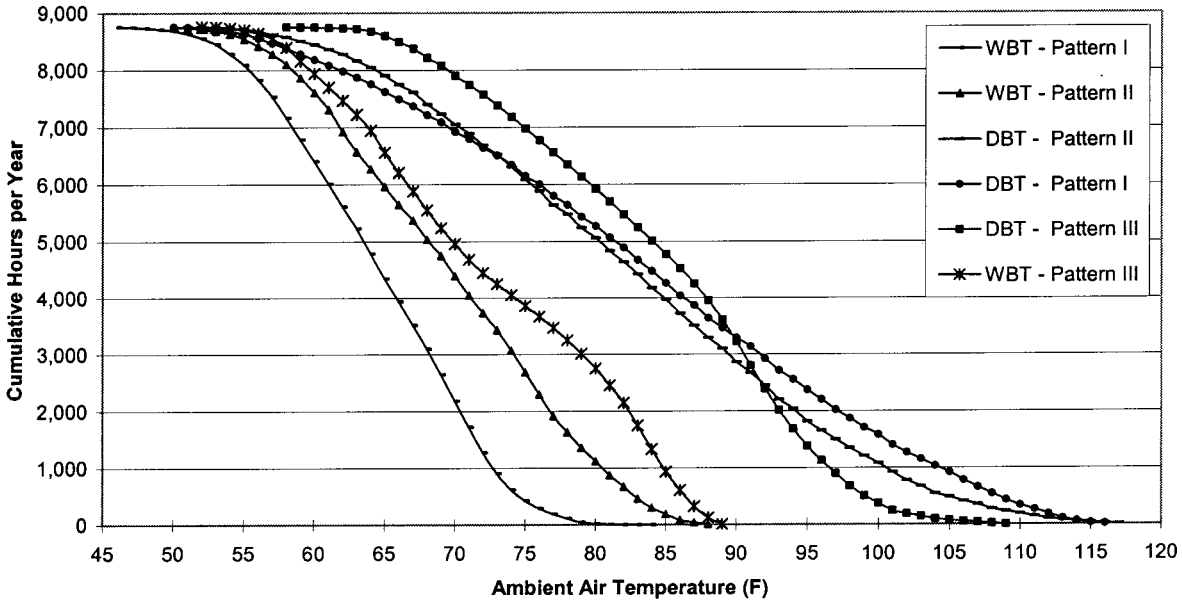

Fig. 1 Annual cumulative hours recorded for DBT and WBT under the three weather patterns

DBT and WBT for pattern I is noted to be the highest. In addition, pattern I tends to enjoy low WBT values which would encourage the application of evaporative cooling over the refrigerated one and the vice versa is true for pattern III. It is interesting to note that although patterns I and II portray higher DBT values, the frequency of registered DBT values between 95 and 110°F (35.0 and 34.3°C) in pattern III is much higher. Another observation is that DBT registered in pattern III was associated with higher WBT than other patterns for approximately 50% of the annual hours, which signals the existence of long periods of high humidity levels.

Pinpointing such observations are crucial in understanding a given weather pattern, which ultimately aids in the selection process of the most suitable CTIAC system. On top of this, Fig. 1 is very beneficial in terms of identifying the number of hours that inlet air cooling will be in operation for a prescribed cooling set point. For instance, if the desired inlet air temperature (IAT) is set to 75°F (23.9°C), the cooling hours for patterns I, II, and III will be 6152, 6152, and 6978 hours, respectively. However, if the prescribed cooling point is further lowered to 65°F (18.3°C), a CTIAC system under patterns I, II, and III will be in operation for over 87%, 90%, and 98%, respectively, of the total annual available hours. These depicted hours clearly indicate that the selected CTIAC system will be required to operate for quite long hours or even continuously year around depending on the prescribed IAT value. It is evident that the longer operation hours will bring about higher energy output increase and, consequently, improve the economic feasibility of the cooling system.

Upon weather data reduction, an operating envelope is constructed, as listed in Table 1, for the three investigated patterns. The mean value is the arithmetic average of the parameter over the summer period May–September (total 3,672 hours). One may deduce from Table 1 that weather pattern I is considered to be the hottest (highest mean value of DBT) while weather pattern III is the wettest (highest mean value of WBT) and are accordingly associated with the highest mean value of enthalpy. The maximum values recorded for DBT, WBT, and h in Table 1 will be considered as the design conditions for each respective pattern. According to the maximum design conditions, weather patterns I, II, and III will lend a dew point temperature (DPT) of 83°F (28.3°C), 90°F (32.2°C), and 91°F (32.8°C), respectively.

Figure 2 demonstrates the cumulative hours of computed ambient enthalpy for the three patterns. It can be seen from the results that pattern III has more than double the accumulated hours of high enthalpy values [over 40 Btu/lb (167.4 kJ/kg)] as compared to the other patterns. This difference is even more pronounced for higher h values. This is attributed to the relatively lower DBT and higher WBT values registered under this pattern. Since inlet air cooling may be attempted to a baseline enthalpy of, for example, 25 Btu/lb (104.7 kJ/kg), the potential for a year round CTIAC operation in the different patterns is vivid.

In order to obtain proper insight into the potential of incorporating an evaporative cooling system, an appraisal of the UAE weather data under pattern II is carried for its hottest months; May through September. This is typically achieved by plotting the cumulative evaporative cooling degree hours (ECDH) for each month against different desired IAT values, as shown in Fig. 3. The parameter ECDH is a measure for the potential of evaporative cooling at a given IAT value. It is typically defined as the summation of the margin between DBT and WBT multiplied by the number of corresponding hours. As can be seen in Fig. 3, the months of July and August carry the largest ECDH values. This is likely to be attributed to the large difference in these two particular months between the registered DBT and WBT at any given

Table 1 Operating weather envelope for UAE

	DBT (°F)			WBT (°F)			h (Btu/lb)		
Pattern	Max	Min	Mean	Max	Min	Mean	Max	Min	Mean
I	120	50	97	83	45	70	47	18	34
II	120	50	94	90	45	77	55	18	40
III	110	58	93	91	50	82	57	18	46

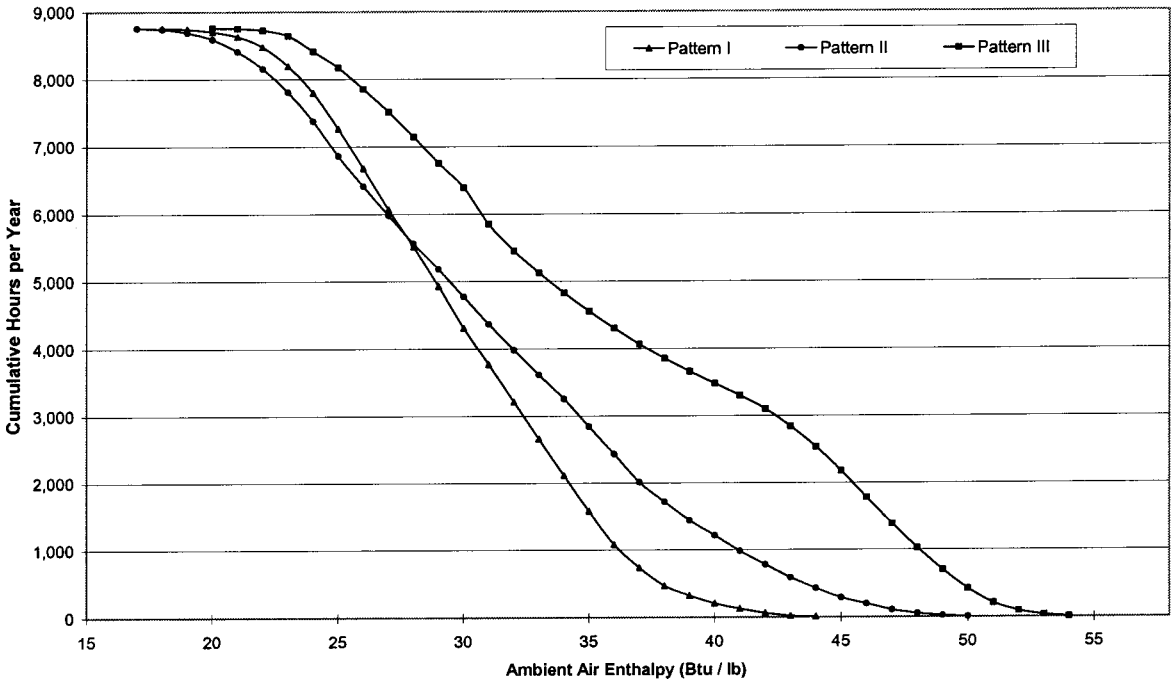

Fig. 2 Annual cumulative hours recorded for enthalpy under the three weather patterns

IAT. The evaporative cooling potential is found to increase with the reduction of achievable IAT up to 65°F (18.3°C), where the curves tend to level implying that further reduction in IAT value can not be achieved. This observation signals that it will not be permissible to obtain further gains as the remainder of the registered WBT is apparently above 65°F (18.3°C). Moreover, it is noted that the ECDH values computed for the month of May surpass those predicted for the months of June and September when IAT is lowered below 74°F (23.3°C). This implies the availability of lower registered WBT than 74°F in May, which consequently makes it more beneficial at such a prescribed IAT value.

4 Technical Feasibility of CTIAC Systems

The analyses associated with power output improvement and the relevant economic returns of employing different CTIAC options will be carried out here using the documented weather data year around for refrigerative cooling systems and for the months of May through September for evaporative cooling systems. Needless to say that implementing a CTIAC option will be even more lucrative in terms of economic returns when extending the analyses to a full year. Although a CT power output is inversely linked with IAT value, the designer must limit the cooling of the inlet air to 42°F (5.6°C) to avoid potential icing problems as stated earlier. Hence, the designer should carefully select the cooling range where maximum power increase can be attained without causing damage to the CT unit.

4.1 Analyses of Output Augmentation Using Refrigerative Cooling. In order to develop an appreciation for the implementation of a refrigerative cooling, a sample case study is examined first under a proposed ambient design conditions of 120°F (48.9°C) DBT and 86°F (30°C) WBT. The corresponding dew point temperature (DPT) in this case would be 75°F (23.9°C). A simple-cycle industrial CT "GE frame 5EA" is considered in this regard with 26.3 MW output and an inlet air mass flow rate of 650.6 lb/s (295 kg/s) at ISO condition, which translates into an inlet specific air mass flow rate (Q) of 35 lb/h/kW (15.9 kg/h/kW). In addition, the variation of power output and heat rate versus IAT

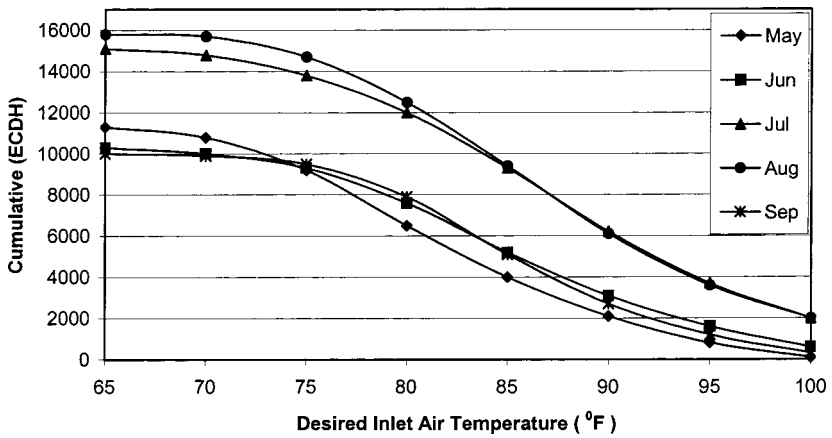

Fig. 3 Cumulative evaporative cooling degree-hour for weather pattern II

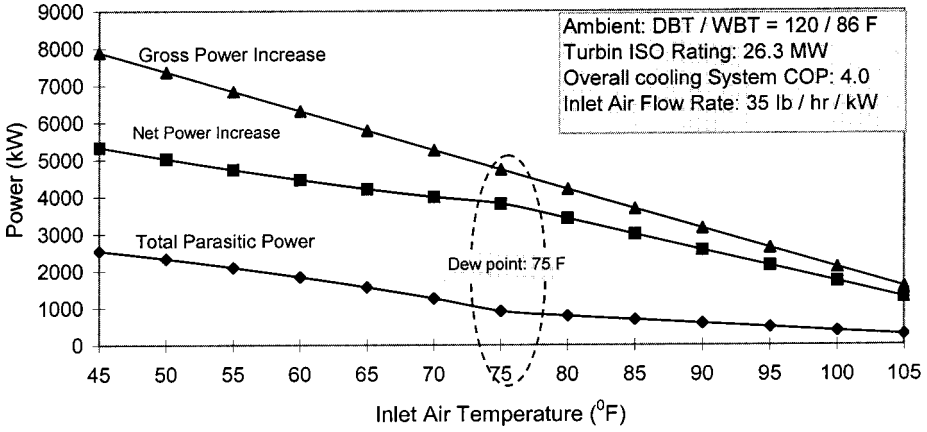

Fig. 4 Typical inlet air temperature impact on the cooling load component

may follow the characteristic of any manufactured combustion turbine. In this study, the characteristics of the power output, heat rate, inlet air mass flow rates and their pertinent correction factors were all accounted for based on the documented report of Brown et al. [9]. The Appendix lists the technical specifications of the turbine used and the associated corrections factors. Moreover, a refrigerative cooling system was incorporated with an assumed average overall coefficient of performance (COP) of 4.0, which is typical for cooling system utilizing water chillers.

4.1.1 Effect of IAT. Upon setting a prescribed inlet air temperature, the obtained data can be used to determine the ''cooling degree hours'' (CDH numbers) for each hour of the year. This subsequently allows a turbine operator to make a very detailed and accurate analysis of potential power gain from inlet air cooling. The results shown in Fig. 4 encompass the main characteristics of a CTIAC system. For a prescribed IAT set above DPT, the incremental increase in the increased power is found to be much higher than the parasitic (consumed) power. This observation is further manifested as the IAT value is lowered closer the design DPT. This is attributed to the fact that cooling is mainly achieved by sensible heat removal mechanism for IAT above DPT value. However, once the prescribed IAT dips below DPT, a drop is noted in the slope of net power increase curve, which reflects that more power has to be consumed to overcome the additional cooling requirement for the moisture (latent heat) removal. In addition, the net power increase curve climbs at a slower pace once IAT is lowered below DPT, which indicates that additional power can still be recovered much below DPT value. In calculating the cooling load and other relevant parameters, 10% of the cooling requirement for CT inlet air is allowed as a provision for cooling the generator and lube oil systems.

Next, the estimated annual gross and consumed energy increase per MW output under ISO rating is plotted against the desired IAT for the three investigated patterns as depicted in Fig. 5. Overall, all three patterns were found to score similar gross energy gains for the given IAT range with pattern I attaining the highest values for IAT greater than 60°F (15.6°C). The annual gross energy increase under pattern III is noted to slightly surpass those predicted in pattern I for IAT values less than 60°F (15.6°C). In addition, pattern III results show almost null increase in annual gross energy for IAT$\geqslant$100°F (37.8°C) while it picks up noticeably for lower IAT values. An increase by 2.3, 2.56, and 2.71 fold can be attained for patterns I, II and III, respectively, if IAT is lowered from 80°F to 65°F (26.7 to 18.3°C). Obviously, the additional gain in annual energy should be weighed against the expenses associated with the consumed energy to overcome cooling load requirements. Thus, the annual consumed energy based on the predicted cooling load was annexed to the figure at hand. The consumed energy predictions follow a similar trend to that of the gross increase. At an IAT of 65°F (18.3°C), the consumed annual energy to the gross increase values for patterns I, II, and III represents 14.6%, 20.5%, and 23.8%, respectively. The relatively

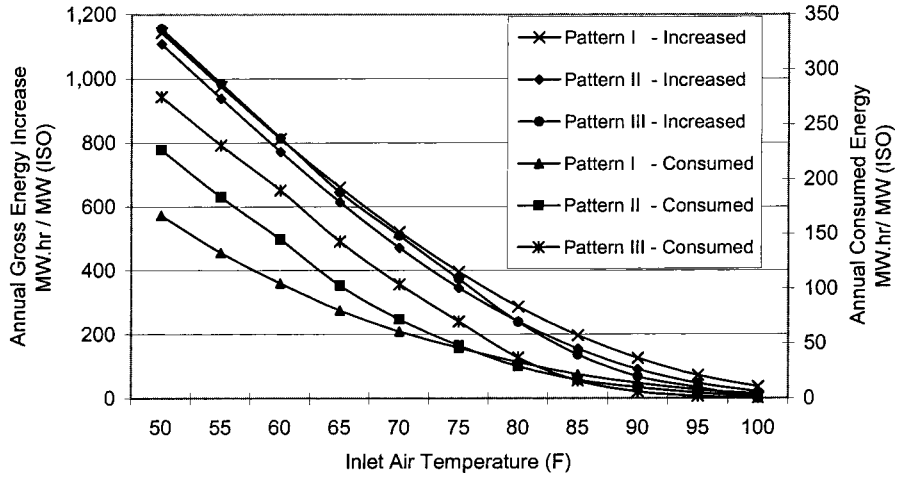

Fig. 5 Variations of the annual gross and consumed energy predictions using refrigerative cooling

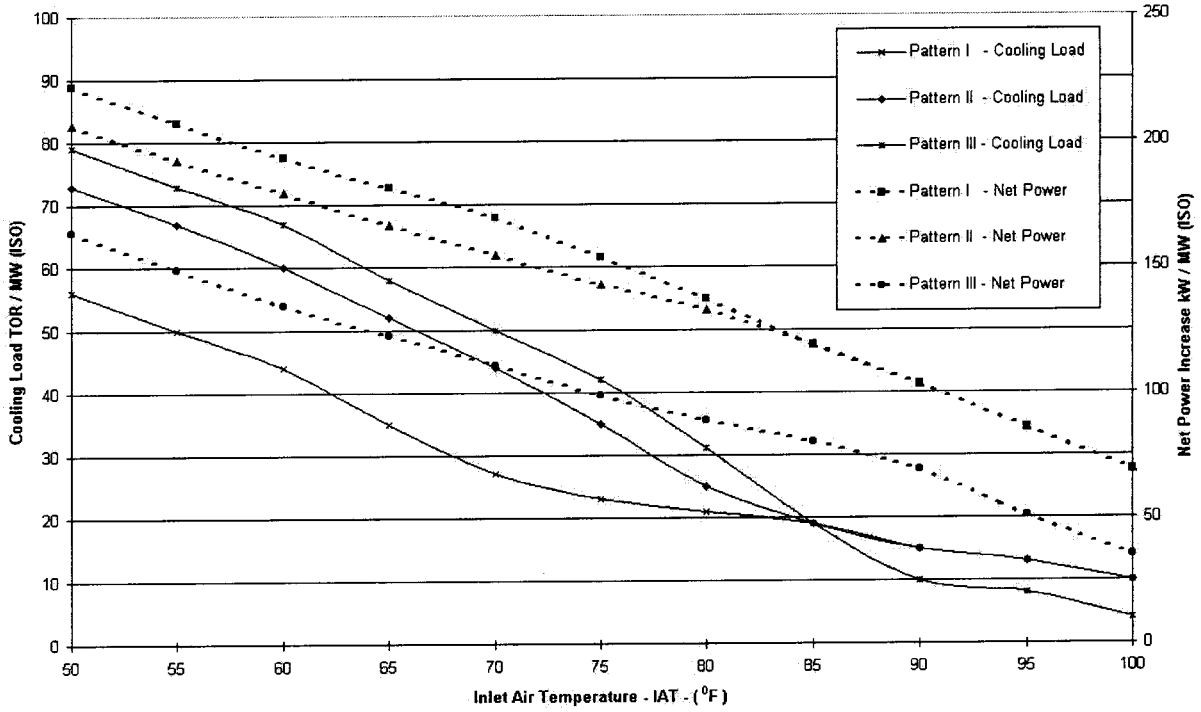

Fig. 6 The cooling load demand and net power variation using refrigerative cooling

higher energy consumption estimated for patterns III is attributed to the frequent recording hours of DBT in the range of 95–110°F (35.0–43.3°C) that coincide with high WBT as noted earlier. This will subsequently prolong the CTIAC operating hours to reach the desired IAT of 65°F (18.3°C).

The above observations prompt us to further examine the implementation of the selected CTIAC under the different weather patterns. The cooling capacity for the chosen CTIAC to achieve a desired IAT for each pattern is shown in Fig. 6. The figure also displays the net power increase in kW per MW (ISO) at the desired IAT. It should be mentioned that the parasitic power is calculated based on 25 lb/h/kW (11.3 kg/h/kW) airflow rate while maintaining the same overall COP of 4.0 for the cooling system. The results show that the different patterns considered to be governed with similar characteristics. As illustrated in Fig. 6, the cooling load is inversely proportional to the desired IAT value. Obviously, cooling load requirements tend to be insignificant up to the DPT value. This is due to the fact that the cooling load requires merely sensible heat removal as pinpointed earlier. Accordingly, the estimated parasitic power in this range tends to increase slightly with the decrease in IAT value. Further reduction in the desired IAT will require moisture removal, which will bring up the contribution of the latent load into effect. The latent load dominates the overall cooling load requirements once IAT dips below the DPT owing to the massive amount of moisture that needs to be carried away. Consequently, the parasitic power consumption increases remarkably, which will negatively impact the net power increase as depicted by the reduction in its slope for IAT less than DPT. It should be pointed out here that appreciated increase in cooling load is not likely to coincide with the maximum stated DPT values for each pattern since very few recorded hours are typically associated with high WBT values, which are close to maximum design conditions. Instead, cooling load depends on the distribution of the majority of WBT recorded. Hence, the inlet air temperature corresponding to significant increase in cooling load per pattern is shown to occur below the maximum design DPT.

Clearly, the DPT value for any pattern plays a detrimental role in the desired IAT value if high net power increase is sought. In this regard, pattern III demonstrates the least increase in the net power output while demand the largest cooling capacity, which is attributed to the onset of latent load at a relatively high IAT of 91°F (32.8°C). By the same token, patterns I and II are found to score an equal net power increase for IAT$\geqslant$82°F (27.8°C). Upon further reduction in IAT, however, the net power increase in pattern II surpasses its counterpart in pattern I. This is likely attributed to the higher DPT registered for pattern II. The net power increase for the different patterns is shown to attain the same proportions for IAT$\leqslant$60°F (15.6°C). It is worth noting that the considered CTIAC operating at IAT equals to 50°F (10.0°C) recovers up to 240 kW/MW (ISO) under pattern I, 210 kW/MW under pattern II, and only 170 kW/MW under pattern III. These values correspond to a net power increase of 24%, 21%, and 17%, respectively.

In a similar manner, the average reduction in the annual heat rate and the corresponding fuel saving are depicted in Fig. 7. The fuel cost for natural gas was taken at a rate of 1.1 US$/10^6 Btu (US$/293kWh), which is common for UAE. The results show a significant reduction in the heat rate for a CT unit located in any of the three patterns once lower IAT values are taken into consideration. For instance, an increase of over three fold is achieved in all patterns for incorporating IAT values up to 65°F (18.3°C) as compared to 85°F (29.4°C).

4.1.2 Effect of Turbine AFTOR and Cooling System COP. In order to further highlight the power augmentation upon incorporating a refrigerative cooling system, two important performance characteristics will be varied to perform a case study. One pertinent characteristic will be selected for the CT units and another for the refrigerative cooling system. These characteristics are the rated airflow-to-turbine output ratio (AFTOR) and the coefficient of performance (COP), respectively. In addition, pattern I will be chosen for conducting this case study. First, the influence of AFTOR on the power enhancement will be examined.

As shown in Fig. 8, the percentage increase in output power against desired IAT is plotted for different AFTOR values. It is apparent from the graph that the CT unit tagged to the lowest AFTOR accomplishes the highest power increase. Attempts to fur-

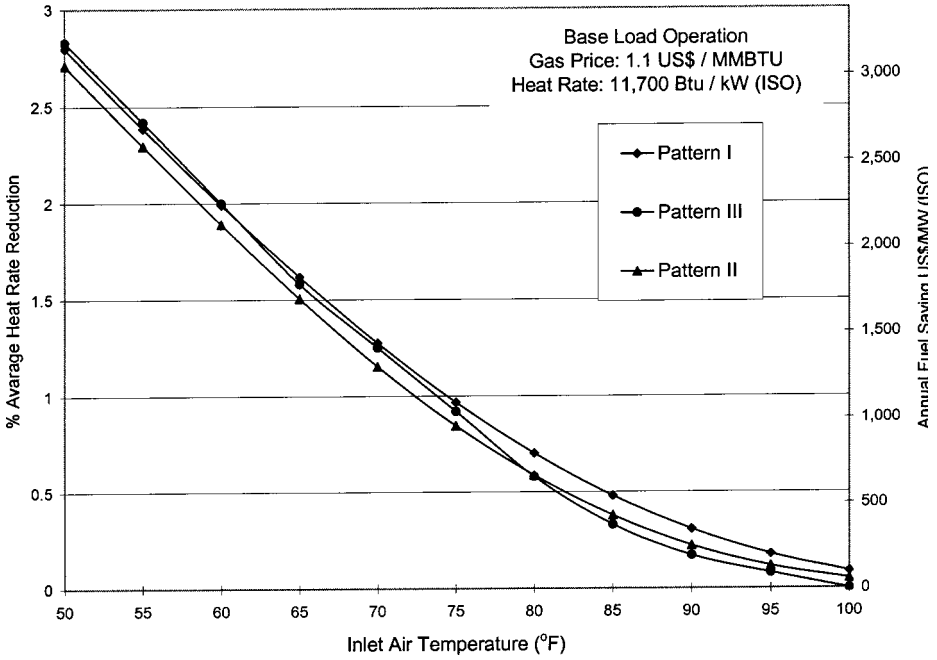

Fig. 7 The percentage average heat rate reduction and the corresponding annual fuel saving for different desired IAT values

ther cool below the registered DPT for this case study will result in the decline of the percentage of power increase. One would need to be cautious though when tempted to cool much below DPT, which might offset the power gains due to substantial increase in cooling system capacity. Next, the impact of incorporating different refrigerative cooling system is examined through employing different COP values, which are typical for the available commercial units in the market. It is evident, as depicted in Fig. 9, that the percentage increase in power is proportional to the COP of the cooling system. It is interesting to note here that cooling systems with COP >6 do not show sensitivity to the reduction in IAT below DPT due to their relatively large cooling capacities.

4.2 Analyses of Output Augmentation Using Evaporative Cooling. The attention will now be shifted towards appraising the impact of incorporating an evaporative cooling system on the reference CT plant. From a theoretical standpoint, a CT unit that is cooled by an evaporative system should receive air at a temperature equivalent to the ambient air WBT. However, the actual IAT is few degrees higher than ambient WBT depending on the cool-

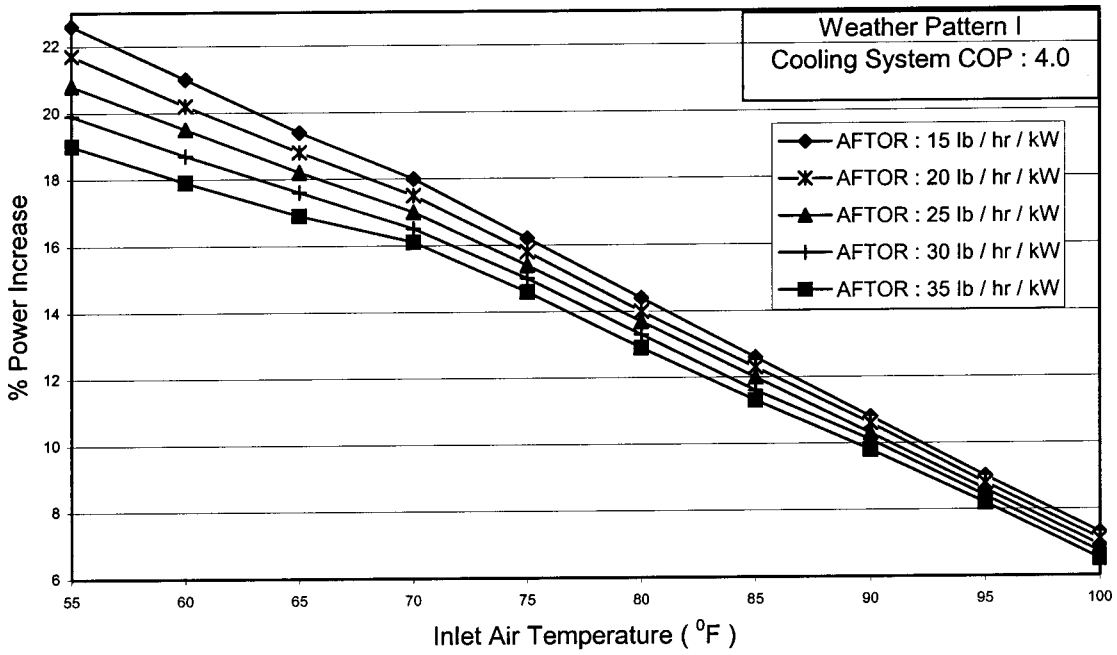

Fig. 8 Effect of AFTOR on the power increase under weather pattern I

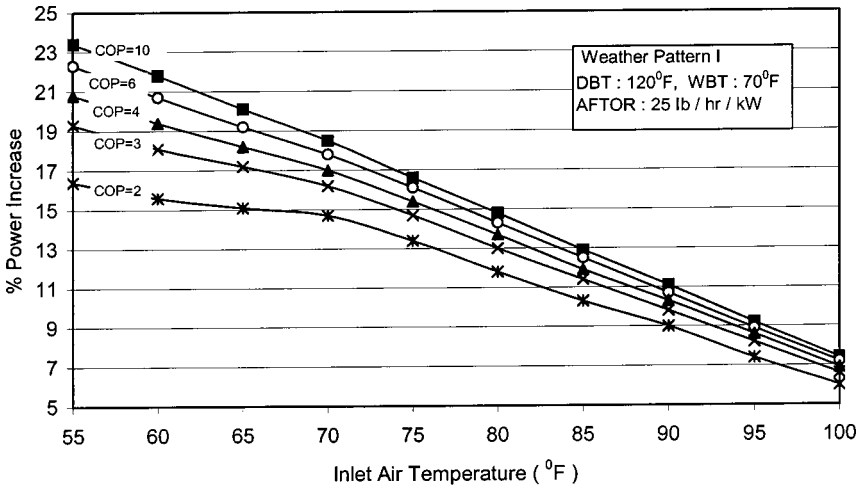

Fig. 9 Effect of cooling system COP on the power increase under weather pattern I

ing system efficiency and cooling effect of air, i.e., the temperature difference between DBT and WBT. As such, CT output uncontrollably varies with the ambient air humidity. From an operational perspective, feasibility of an evaporative cooling system is limited by the lowest IAT that can be achieved and the stability of this temperature during the period considered. For example, under pattern I as presented in Fig. 10, operators can guarantee to run the turbine continuously at IAT≤80°F (26.7°C) around the summer season, while this is only guaranteed for IAT <77°F (25°C). Hence, turbine output will be disturbed for roughly one percent of total summer hours (37 hours). Although 1% less availability is a sound design criterion, this might not be acceptable for some operators. The elliptic symbols depicted on the lines represent the authors' preference for selecting suitable design criteria for evaporative cooling systems. Another conclusion drawn from Fig. 10 is that evaporative cooling can in the worst situation reliably guarantee to cool down IAT to 87°F (30.6°C) or less under pattern III while one can achieve 77°F (25°C) or less under pattern I. This indicates that CT output power can be increased from 8% (pattern III) to 15% (pattern I). Further output enhancement can be achieved but at the cost of operating the CT for longer hours with partial cooling taking place. This further strengthens the argument that an evaporative cooling system would be a more attractive option in dry zones, where a significant number of the recorded hours with low WBT dominate the annual weather data.

Similarly, the increase in the annual gross energy predictions for different desired IAT is demonstrated in Fig. 11. The obtained results reinforce the arguments constructed above. In essence, pattern I is predicted to possess the highest gains due to the fact that is retains the highest number of relatively low WBT year round. This will consequently translate into higher ECDH value and, thus, higher annual energy increase. Apparently, all three patterns tend to become less effective in their potential at lower IAT values as the WBT recorded for the respective patterns are essentially above the desired IAT value.

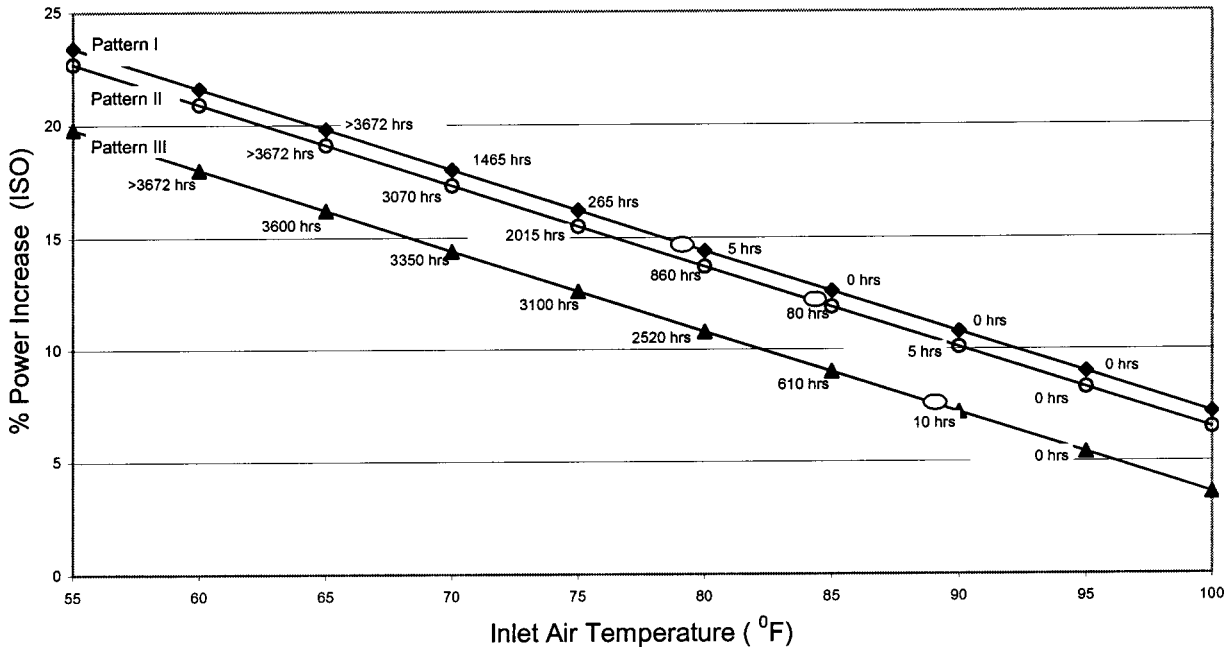

Fig. 10 Variations of the power increase and hours of cooling using evaporative cooling

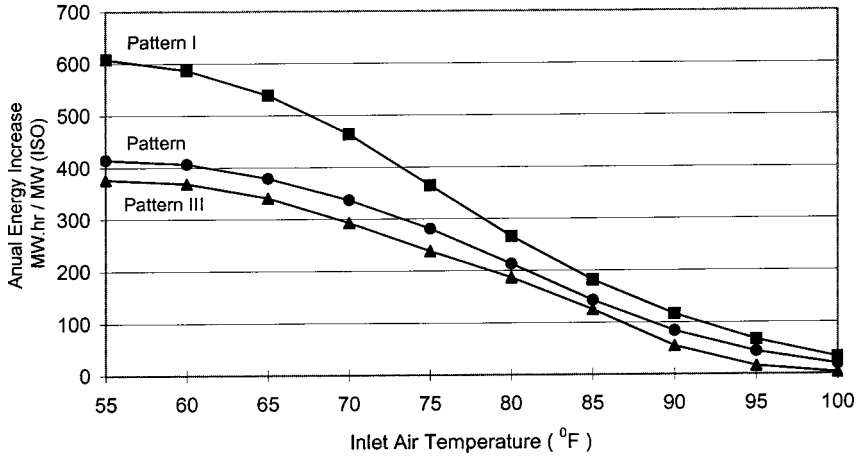

Fig. 11 Variations of the annual gross energy predictions using evaporative cooling

5 Economic Feasibility of CTIAC Systems

The economic evaluation criteria may vary from one power producer to another. However, the major factors that influence the economics of a project are the additional output, installation costs, maintenance, tariff structure, fuel costs, generated revenues, and incentives awarded for meeting or exceeding the required output. All these factors contribute to total revenues and should be properly accounted for in any economic assessment. In addition, the cost of an inlet cooling system is often evaluated in terms of US$ per kW of power increase. This can be misleading when we compare between different options because the output enhancement as a result of inlet air cooling varies with the ambient condition, size of the turbine, AFTOR and other project specific factors such as constructability, generator capacity and lubrication system. Hence, a more appropriate method of evaluating the economic feasibility of a cooling system is through a cost benefit analysis in which the additional revenues are calculated as a result of additional megawatt hours, fuel savings and gain in steam production. In this regard, payback and savings are two important factors to judge the economic feasibility of a project. Savings or net present worth value calculations are another way of determining how much can be saved over the life span of the cooling equipment or the turbine; whichever is shorter, with the proposed option.

The current study is wrapped by examining the feasibility of incorporating a refrigerative cooling system for CT units of different mass flow rates. The capital installation cost of such a cooling system is currently estimated at an average price of US$ 2000/TOR (~US$ 570/kW). A proper cost estimation model should incorporate the additional cost incurred for cooling requirements of the generator and other auxiliaries. With the new installation cost of a CT unit operating under a simple-cycle configuration being currently around US$ 400–600/kW, it is possible to construct a ''feasibility chart'' that outlines the domain where the installation of a CTIAC system can be economically justified. This feasibility chart is illustrated in Fig. 12 for a CT unit located in weather pattern I with different mass flow rate (Q) scenarios. All mass flow rate scenarios are shown to fall below the US$ 400/kW (based on the capital investment) for IAT greater than DPT with the ones with low Q values being the most feasible. This is expected giving that CT units are sensitive to the amount of Q values. Furthermore, attempts to further cool below the DPT show that the CT units with the relatively high Q values to exceed the installation kW cost limit. This becomes even more pronounced if it is intended to reduce IAT below the ISO rating as suggested in several previous studies. It is obvious that the economic return of the net output gain is offset by the escalation in the cooling system capacity, which results in a higher investment cost.

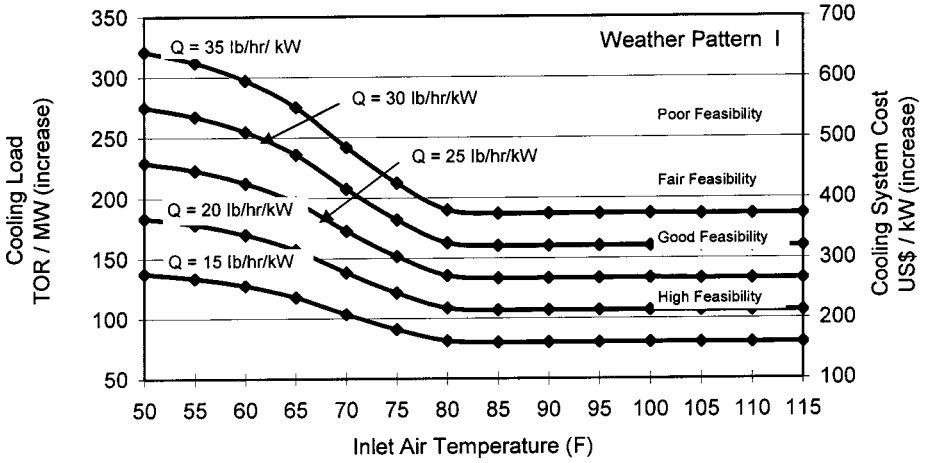

Fig. 12 Economic assessment of a refrigerative cooling system operating under different desired IAT values

6 Conclusion and Recommendations

The current investigation is concerned with the implementation of a combustion turbine inlet air cooling technique in order to improve its performance under elevated temperature conditions. This was achieved by outlining a systematic approach towards assessing the benefits associated with incorporating refrigerative and evaporative cooling systems into a reference combustion turbine unit. The analyses were performed on an industrial CT unit operating on a simple cycle under base load mode. The weather information in United Arab Emirates was chosen for carrying out this investigation. Actual hourly based weather data were used for the sake of establishing weather patterns in different zones and accordingly proposing weather design conditions.

Another objective was to develop an appropriate methodology to explore the impact of different CTIAC options for a desired IAT under different weather patterns. In addition, the impact of IAT setting on the following parameters was closely examined: annual gross energy increase, average heat rate reduction, cooling load requirements and net power increase. The results show high economic feasibility for installing a CTIAC option when operating at a desired IAT value, which is in close proximity to the design DPT for a given weather pattern. Furthermore, it is recommended to set IAT to a constant prescribed value to ensure smooth operation, especially for base load CT units. What is more, a CT unit with a small mass flow rate value was found to be very much economically feasible even upon reducing IAT below the ISO rating. In general, it is recommended to set the desired IAT between 60–75°F (15.6–23.9°C) for a good return on the capital investment of the selected CTIAC system.

The gains in the net power output would be highly appreciated if the current flat rate for energy bills, which is adopted in most Arabian Gulf countries, is altered in favor of scheduled charges as practiced in many other countries. This shall make the savings obtained in output power more beneficial to power plant authorities, which will accordingly bring more attention to considering CTIAC options. Finally, it is highly recommended to extend the current study to cover the rest of the region given the significant number of installed combustion turbines and new installations that are planned. Such a study will be greatly viable once pertinent information related to weather conditions and the performance characteristics of the operating combustion turbines are obtained.

To summarize, the following recommendations are highly advised based on the outcome of the current investigation:

- CTIAC systems to be considered as a standard practice with the new gas turbines installations in UAE, while existing gas turbines installations to be retrofitted to include suitable CTIAC options based on a case by case life cycle analysis.
- Evaporative cooling to be considered whenever the required power increase lies between 8% and 15%. Furthermore, evaporative cooling to be considered as well for peak load turbines or where the turbine is required to work at peak load condition for few hours per day at high temperatures.
- Refrigerative cooling to be employed for sustainable power augmentation in the range of 10–25%, while cooling should be limited to not more than 10–15°F below the design DPT unless power increase ratio is intended to meet a certain target.
- Thermal energy storage (TES) to be considered with the peak load turbines.

Acknowledgment

The first author would like to express his gratitude to Mrs. Mowza Al-Mualla from the Metrological department at the Ministry of Transportation for her efforts in compiling the weather data for the UAE at large.

Nomenclature

AFTOR = air flow to output ratio
CDH = cooling degree hours
COP = coefficient of performance of a refrigerative cooling system
CT = combustion turbine
CTIAC = combustion turbine inlet air cooling
DBT = dry bulb temperature
DPT = dew point temperature
ECDH = equivalent cooling degree hours
h = enthalpy
IAT = inlet air temperature
ISO = International Organization for Standardization
Q = specific mass flow rate per kW output
RH = relative humidity
WBT = wet bulb temperature
TOR = tons of refrigeration based on the standard 12,000 Btu/hr

Appendix

The correction factors for calculating these performance characteristics at non-ISO conditions are presented below for simple-cycle industrial turbine. Up to five adjustment factors (F1 for altitude, F2 for dry-bulb temperature, F3 for humidity, F4 for excess inlet pressure drop, and F5 for excess exhaust pressure drop) are multiplied by the ISO performance to calculate performance at non-ISO conditions. The correction factors are valid in the range 42–120°F (5.5–48.9°C). Beside the correction factors, the following technical specifications were used in the analysis:

ISO power output=100 MW
ISO heat rate=11,700 Btu/kWh based on HHV
ISO inlet air mass flow rate=2,342,346 lb/hr
Power Adjustment Factors:
$F1 = 1.0 - 3.1875 \times 10^{-5} z$; z=altitude, feet
$F2 = 1.23 - 3.875 \times 10^{-3}$ DBT; DBT=inlet air dry bulb temperature, °F
$F3 = 1.0$
$F4 = 1.0 - 4.333 \times 10^{-3} P_i$; P_i=excess inlet air pressure loss, inches H_2O
$F5 = 1.0 - 1.634 \times 10^{-3} P_e$; P_e=excess exhaust air pressure loss, inches H_2O.
Heat Rate Adjustment Factors:
$F1 = 1.0$
$F2 = 0.95 + 8.333 \times 10^{-4}$ DBT if DBT$\leq$60°F; $F2 = 1.0 + 1.666 \times 10^{-3}$ (DBT−60) DBT>60°F
$F3 = 1.0$
$F4 = 1.0 + 1.666 \times 10^{-3} P_i$
$F5 = 1.0 - 1.666 \times 10^{-3} P_e$
Inlet Air Mass Flow Rate Adjustment Factors:
$F1 = 1.0 - 3.1875 \times 10^{-5} z$
$F2 = 1.128 - 2.17 \times 10^{-3}$ DBT
$F3 = 1.0$
$F4 = 1.0 - 2.333 \times 10^{-3} P_i$
$F5 = 1.0$

References

[1] Van Der Linden, S., and Searles, D. E., 1996, "Inlet Conditioning Enhances Performance of Modern Combined Cycle Plants for Cost-Effective Power Generation," ASME Paper No. 96-GT-298.
[2] Utamura, M., Ishikawa, A., Nishimura, Y., and Ando, N., 1996, "Economics of Gas Turbine Inlet Air Cooling System for Power Enhancement," ASME Paper No. 96-GT-515.
[3] De Lucia, M., Bronconi, R., and Carnevale, E., 1993, "Performance and Economic Enhancement of Cogeneration Gas Turbines Through Compressor Inlet Air Cooling," ASME J. Eng. Gas Turbines Power, **116**, pp. 360–365.
[4] Loud, R. L., and Slaterpryce, A. A., 1991, "Gas Turbine Inlet Air Treatment," Technical Report, GE Company, Schenectady, New York, USA, pp. 18–24.
[5] Jolly, S., Nitzken, J., and Shepherd, D., 1998, "Evaluation of Combustion Turbine Inlet Air Cooling Systems," *Presented at the Power-Gen Asia*, New Delhi, India.
[6] Stewart, W. E., 1999, *Design Guide: Combustion Turbine Inlet Air Cooling System*, ASHRAE, Atlanta, GA.

[7] Daryl, R. B., Katipamula, S., and Konynenbelt, H., 1996, ''The Impact of TES on the Economics of Combustion Turbine Inlet Air Cooling,'' Presented at the EPRI Int. Conf. On Sustainable Thermal Energy Storage, Bloomington, Minnesota, USA.
[8] Chaker, M., Meher-Homji, C. B., Mee, III, T., and Nicholson, A., 2003, ''Inlet Fogging of Gas Turbine Engines Detailed Climatic Analysis of Gas Turbine Evaporation Cooling Potential in the USA,'' ASME J. Eng. Gas Turbines Power, **125**, pp. 300–309.
[9] Brown, D. R., Katipamula, S., and Koynenbelt, J. H., 1996, ''A Comparative Assessment of Alternative Combustion Turbine Inlet Air Cooling Systems,'' Pacific Northwest National Lab., Technical Report No. PNNL-10966, Richland, Washington.

R. Bettocchi

M. Pinelli[1]
e-mail: mpinelli@ing.unife.it

Dip. Di Ingegneria,
University of Ferrara,
Via Saragat, 1,
44100 Ferrara, Italy

P. R. Spina
e-mail: pierruggero.spina@unibo.it
DIEM—University of Bologna,
Viale del Risorgimento, 2,
40136 Bologna, Italy

A Multistage Compressor Test Facility: Uncertainty Analysis and Preliminary Test Results

A multistage compressor test facility, fully instrumented with a dedicated data acquisition and processing system, has been developed to conduct experimental research work at the University of Ferrara. This paper provides a systematic description of the uncertainty analysis procedures required for compressor testing, including preliminary performance test results, in addition to a brief description of the test facility and its capabilities.
[DOI: 10.1115/1.1787516]

Introduction

The knowledge of compressor behavior in deteriorated, faulty, and critical working conditions is of great importance in order to evaluate the gas turbine health state. In literature, various mathematical models can be found to simulate different types of compressor deterioration, such as fouling and blade erosion [1–7], and critical working conditions, such as rotating stall and surge, whereas the availability of experimental data on these subjects is quite poor [8]. In particular, information on the correlations between measurement and parameter variations and common faults or malfunction (such as fouling) is difficult to find.

The lack of experimental data is mainly due to the high costs required to perform experimental campaigns on large-size compressors, in particular when critical working conditions and the presence of faults have to be investigated. However, qualitative information on compressor behavior may be obtained by testing small size compressors. The information obtained on these machines may be used to better understand the physical phenomena and to validate mathematical models. These models may be then applied to larger compressors by using adequate scaling rules.

In this context, a multistage compressor test facility, fully instrumented with a dedicated data acquisition and processing system, has been developed to conduct experimental research work at the University of Ferrara. In particular, the facility has been designed to perform different tasks:

- Compressor steady state characterization, such as performance map determination
- Dynamic and acoustic analyses aimed at the investigation of compressor behavior in transient conditions and in the presence of unsteady phenomena, such as stall, flutter, surge, etc.
- Analysis of compressor behavior in the presence of inlet fogging and water ingestion
- Investigation of compressor behavior with implanted faults, such as blade distortion, foreign object damage, tip clearance augmentation, dirty air ingestion, etc.

In this paper, a description of the test facility and its capabilities is first presented. Then a systematic description of the uncertainty analysis procedures required for compressor testing is reported. Finally, the preliminary performance test results on a small size gas turbine compressor with six axial stages and one centrifugal stage are also included.

[1]Author to whom correspondence should be addressed.

Contributed by the International Gas Turbine Institute (IGTI) of THE AMERICAN SOCIETY OF MECHANICAL ENGINEERS for publication in the ASME JOURNAL OF ENGINEERING FOR GAS TURBINES AND POWER. Paper presented at the International Gas Turbine and Aeroengine Congress and Exhibition, Atlanta, GA, June 16–19, 2003, Paper No. 2003-GT-38397. Manuscript received by IGTI, October 2002, final revision, March 2003. Associate Editor: H. R. Simmons.

Experimental Apparatus

Test Rig. The test facility is depicted in Fig. 1. It consists of an asynchronous reversible electric motor/brake bench, operated by an inverter [9]. The motor can give a maximum power of 87 kW at 5000 rpm. The bench can be driven either at constant torque or at constant rotational speed. For the control of the bench, the torque is measured by means of a load cell, while the rotational speed is measured through a 1024-impulse-per-round encoder.

The compressor under test (Fig. 2) is the compressor of the Allison 250-C18 turboshaft engine and is composed of six axial stages and one centrifugal stage. The compressor suction diameter is 0.104 m. At the centrifugal stage exit, two semivolutes (180° wide) are present, which discharge in two circular outlet sections, diametrically opposed to each other, and which have a diameter of 0.05 m.

The compressor operates in an open circuit. The inlet section is an orifice plate, which is used for the measurement of the airflow rate, followed by a 1.1-m-long (equal to 10 diameters of the compressor suction) pipe. The pipe is used to allow the flow to develop fully after the obstruction. Then, after flowing through the axial and centrifugal stages, the air exits through the two circular openings and is fed to a common cylinder in which a butterfly valve is inserted for compressor mass flow rate control. A step-up gearbox with a gear ratio of 5.83:1 (which was part of the original gas turbine) is included in the test setup to analyze an extended range of compressor rotational speeds (up to nearly 30,000 rpm).

Control and Data Acquisition System. In Fig. 1, the system for data acquisition and for the bench remote control is sketched. It relies on two boards [10]:

1. An acquisition board with a 16-bit analog-to-digital (A/D) converter and a maximum sample rate of 1.2 MHz. Three signal conditioning cards are connected to this board [11]: one for pressure transducer, rotational speed, and torque conditioning, one for thermocouple conditioning, and one for accelerometer and microphone acquisition and conditioning. The last card is integrated with variable threshold active low-pass filters.
2. A board for the remote control of the bench, which allows the control of 16 digital signals and of two voltage output and two current output channels. By means of this board it is possible to control the reference signal of the torque and of the rotational speed and the switching of the inverter.

Measurements. In Fig. 3 the measurements used to determine the main compressor performance parameters are outlined. Compressor performance evaluation in steady-state conditions

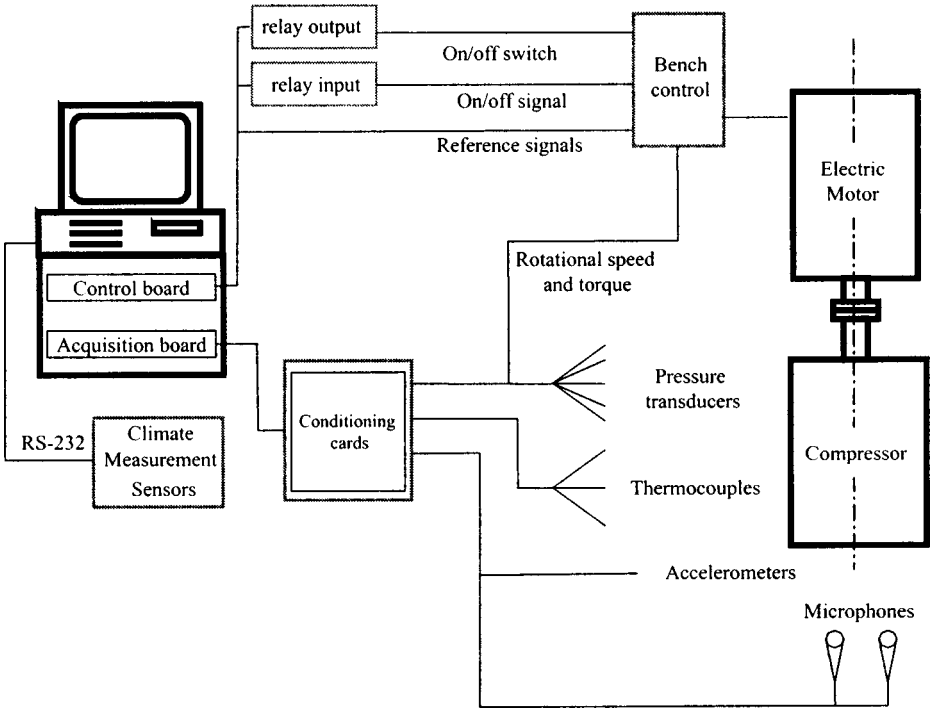

Fig. 1 Acquisition and control system

consists in the determination of compressor performance maps (which link together pressure ratio β_C, efficiency η_C, corrected mass flow μ_C, and corrected rotational speed ν_C) and mechanical power P_C required to drive the compressor.

For the determination of the power required to drive the compressor, the measurements of both torque T_q and rotational speed N_E of the asynchronous electric motor are used:

$$P_E = \frac{2\pi N_E T_q}{60}, \tag{1}$$

$$P_C = P_E - P_G. \tag{2}$$

The gearbox characteristic $P_G = f(N_E)$ as determined by driving the gearbox without compressor and measuring the resisting torque for a number of electric motor rotational speeds.

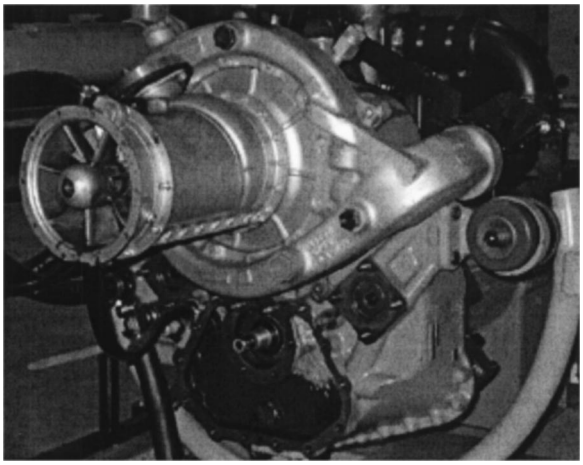

Fig. 2 Compressor of the Allison 250-C18 turboshaft engine

The measured parameters used for the determination of compressor performance maps are as follows:

- The compressor mass flow rate M_C
- The static pressure at section 2 (compressor intake) and total temperature and static pressure at section 3 (compressor discharge) and at section 23 (bleed valve located between the fifth and the sixth axial stage), shown in Fig. 3.

The determination of static temperatures and total pressures is performed by solving the following system of equations [12]:

$$h(T_0) = h(T) + \frac{V^2}{2} = h(T) + \frac{1}{2}\left(\frac{M}{\rho A}\right)^2 = h(T) + \frac{1}{2}\left(\frac{RTM}{pA}\right)^2, \tag{3}$$

$$p_0 = p \; e^{[\Phi(T_0) - \Phi(T)]}, \tag{4}$$

where the operating fluid is considered as a mixture of perfect gases (dry air and water vapor) whose specific heat at constant pressure c_p is a function of temperature and gas composition.

Therefore, for each tested operating point it is possible to determine the corresponding point of the compressor performance maps by using the following equations:

$$\mu_C = \frac{M_C\sqrt{\vartheta}}{\delta}, \tag{5}$$

$$\nu_C = \frac{N_C}{\sqrt{\vartheta}}, \tag{6}$$

$$(\beta_C)_{i-j} = \frac{p_{0j}}{p_{0i}}, \tag{7}$$

$$(\eta_{sC})_{i-j} = \frac{h(T_{0js}) - h(T_{0i})}{h(T_{0j}) - h(T_{0i})}, \tag{8}$$

$$(\eta_{pC})_{i-j} = \frac{\ln(p_{0j}/p_{0i})}{\Phi(T_{0j}) - \Phi(T_{0i})}, \tag{9}$$

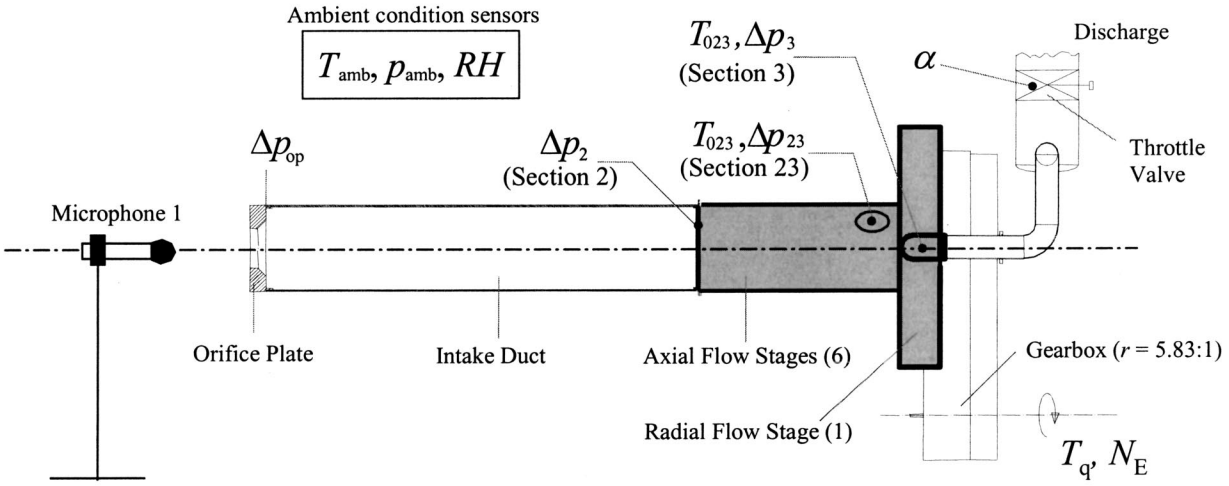

Fig. 3 Compressor test rig and available measured parameters

where i and j are the inlet and outlet sections, respectively, of the compressor part considered (i.e., i may be 2 or 23 while j may be 3 or 23), $\vartheta = T_{0i}/T_{0r}$, $\delta = p_{0i}/p_{0r}$, and $N_C = rN_E$.

The definition of the thermodynamic function ϕ is reported in the Appendix.

Control and Acquisition Software. For the monitoring, the data acquisition and the remote control of the test bench a computer program in LABVIEW language has been developed [13]. The program allows:

- the online monitoring of the compressor through a graphical interface in which the main control measurements are reported.
- the storing of all the measurements performed on the test facility and gathered during every trial. The information is preliminarily stored in a buffer and subsequently can be saved either in a formatted or unformatted file.
- the automatic generation of the performance curves, which can be visualized on the screen by activating a special function on the control panel.
- the control of the bench and of the test procedures.

Measurement Uncertainty

An uncertainty analysis has been performed in order to assess the expected errors in the determination of the performance parameters of the compressor under examination. This analysis, even though referred to the test facility considered in the paper, can easily be extended to other practical situations, since the approach used is general and the obtained results are relative to an instrumentation similar to that used in field testing.

In the past decade, the correct method of evaluating and reporting the uncertainty, and the way in which the uncertainty propagation equation is derived and defined have been thoroughly revised [14, 15]. In particular, the uncertainty propagation equation has received great attention for what concerns its statistical interpretation, its range of validity and its theoretical foundation. An exhaustive discussion of different approaches to this matter can be found in Ref. [16].

If x_i is a single measured parameter, for a given measurement result $y = f(x_1, \ldots, x_n)$ the most general formulation of the law of propagation of uncertainty can be written as

$$u_y = \sqrt{\sum_1^n \vartheta_i^2 u_{x_i}^2}, \tag{10}$$

where u_y is the combined standard uncertainty of the measurement result y, u_{x_i} are the individual standard uncertainties associated with x_i, and ϑ_i are the sensitivity coefficients defined as $\vartheta_i = \partial y/\partial x_i$.

For engineering purposes, a widely accepted evaluation of the individual standard uncertainty u_{x_i} is still performed by distinguishing between uncertainties deriving from systematic effects, B_i, and from random effects, P_i.[1]

If all measurements are considered independent of each other and normally distributed, then

$$u_{x_i} = \sqrt{B_i^2 + P_i^2} = \sqrt{B_i^2 + (k_c S_{x_i})^2}, \tag{11}$$

where B_i and P_i are the root sum square of each individual contribution to systematic and random errors, respectively. In Eq. (11), the term k_c represents the coverage factor that, in the large-sample approximation, is assumed equal to 2 at the 95% level of confidence. The term S_{x_i} is the standard deviation of x_i. In the case for which x_i is obtained by averaging many readings of the ith measurement parameter, in Eq. (11) the standard deviation of the mean $S_{\bar{x}}$ should be used instead of S_{x_i}, where

$$S_{\bar{x}} = \frac{S_{x_i}}{\sqrt{n}}, \tag{12}$$

n being the number of repeated readings of the parameter i.

In the open literature, there are relatively few works that report in detail the actual expected uncertainties in gas turbine and, in particular, in compressor performance determination. Regarding compressor performance determination, some useful information can be found in Ref. [17] (and in its later revision [18]) and in Ref. [19], although they refer to test cases and to examples. One of the best sources of information on this topic is the work of

[1]Regarding this topic, the most recent ISO [14] and NIST [15] publications introduced a new uncertainty categorization: (1) Type A uncertainties, those which are evaluated by statistical methods, and (2) Type B uncertainties, those which are evaluated by other means. In particular, in Ref. [15], it is strongly recommended that this new type of categorization should be used and the usual terminology that categorizes in random/precision and systematic/bias uncertainty should be avoided, in particular concerning (i) the terms precision and bias, which should be referred to instruments rather than measurements; (ii) the use of *uncertainty* in conjunction with systematic and random as adjectives, since systematic and random are appropriate adjectives of *error*. Nevertheless, the usefulness in referring to random and systematic categorization is evident, especially in practical situations such as field or experimental testing in gas turbines.

Table 1 Individual error contribution on total uncertainty

	Errors due to systematic effects					Errors due to random effects	
	Location	Installation	Calibration	Device	Acquisition	Repeatability	u_{x_i}
Δp_{op}	0.30%	0.10%	0.38%	0.10%	0.01%	0.11%	0.52%
Δp_2	1.00%	0.20%	0.30%	0.25%	0.01%	0.57%	1.23%
Δp_{23}	2.00%	0.20%	0.33%	0.15%	0.01%	0.40%	2.08%
Δp_3	1.00%	0.20%	0.10%	0.15%	0.01%	0.25%	1.07%
T_{023}	0.5 K	0.3 K	0.3 K		0.3 K	0.14K	0.7 K
T_{03}	0.3 K	0.6 K	0.7 K		0.3 K	0.14K	1.0 K

Brun and Kurz [20], in which field testing uncertainties on gas-turbine-driven compressors are discussed in detail. In Ref. [20] qualitative and quantitative information on the expected measurement uncertainties and how they affect parameter determination accuracy are reported. Other information on this topic can be found in Ref. [21]. Regarding measurement uncertainty evaluation, Coleman and Steele [16] exhaustively show how to account for various sources of uncertainty and the way in which they can be categorized as systematic or random errors. This kind of information can also be found in Ref. [15] and in Refs. [17,18].

In the following, for each thermodynamic and mechanical measurement a detailed uncertainty analysis has been performed. The most significant features are discussed in detail and finally the parameter uncertainty is evaluated through the use of Eqs. (10) and (11).

If not specified, errors are considered as percent of the measurement sensor full scale (f.s.). In Table 1 the detail of the individual errors on some measurements is reported.

Ambient Condition Measurement. The ambient pressure, temperature, and relative humidity are measured through an integrated sensor for climate measurements. In particular, the ambient pressure is measured through an absolute sensor with 1.050 bar f.s., the ambient temperature through a thermistor and the relative humidity through a capacitive sensor. Manufacturer specifications and repeated observations permitted the estimation of the following total uncertainties: $u_{p_{amb}}=0.6\%$ of full scale, $u_{T_{amb}}=0.2$ K of the reading, $u_{RH}=2.0\%$ of the reading.

Pressure Measurement. Five pressure measurements, all static, are performed. The main sources of errors are the location, installation, calibration, device, and acquisition [18–20]. The pressure taps were checked to ascertain the absence of burrs or slag and, thus, their contribution to total error, which can be remarkable [22], has been neglected. Each sensor has been individually calibrated through a pressure calibrator with an accuracy of 0.01%.

The differential pressure at the orifice plate Δp_{op} is performed through a differential transducer, 0.175 bar gauge f.s. The total systematic error was calculated as equal to 0.50%, with the major contribution due to calibration (0.38%) and to location (0.30%). The latter value was chosen, even if the measurement is performed with a single sensor, since an annular chamber downstream of the orifice plate is used to average the pressure on the section [23] and the flow entering the device is supposed to be symmetrical. The estimated standard deviation was set to 1×10^{-4} bar, based on experience and on some repeated measurements. The standard uncertainty for this measurement was thus calculated as equal to 0.52%.

The compressor intake static pressure Δp_2 is measured with a differential transducer, 0.07 bar gauge f.s. Even if only one sensor is used, the location error was estimated equal to 1.00%, since the pipe downstream of the orifice plate allows the flow to be quite symmetrical. The estimated standard deviation of this measurement was set to 2×10^{-4} bar. The total uncertainty $u_{\Delta p_2}$ was calculated as equal to 1.23%.

The static pressure at the bleed valve Δp_{23} is measured with a transducer with 0.4 bar gauge f.s. Only one sensor was used at the bleed valve of the compressor. Hence, the location error was set as equal to 2.00% [20] and revealed to be much larger than the other errors. The estimated standard deviation was set to 8×10^{-4} bar. Hence, the location error dominates in the total uncertainty, which was calculated as equal to 2.08%.

The compressor discharge static pressure Δp_3 is measured with two transducers with 1.6 bar gauge f.s. located at the centrifugal impeller exit. The estimated standard deviation was set to 2×10^{-3} bar. The total uncertainty $u_{\Delta p_3}$ was calculated as equal to 1.07%. The slight difference with $u_{\Delta p_2}$ was due to the calibration process, which permitted the achievement of a lower calibration error (0.10% versus 0.30%).

Temperature Measurement. Three identical shielded-type K thermocouples (TC_1 for T_{023} measurement, TC_2 and TC_3 for T_{03} measurement) are used for temperature measurements. The thermocouples are inserted within the airstream and, thus, they measure the local total temperature of the air.

The thermocouples were calibrated in a thermostatic bath and a first order (linear) calibration curve was obtained in the range 288–365 K. The systematic error due to calibration was calculated as the result of the individual errors due to the fitting curve, voltage measuring system, ice point reference, and the thermometer used for calibration. In addition, location, installation, and acquisition errors were considered. The total uncertainty u_{TC_1} and u_{TC_2/TC_3} were calculated as equal to 0.7 and 1.0 K, respectively.

The high calibration error for TC_2 and TC_3 is due to the thermostatic bath maximum temperature, which is lower than the maximum temperature expected to be measured by this thermocouple ($\approx$393 K). Hence, over 365 K the voltage–temperature relationship has to be extrapolated.[2] Hence, the calibration error for TC_2 and TC_3 has been considered higher than for TC_1.

Also the installation error for TC_2 and TC_3 is higher than that for TC_1, since the error caused by conduction along the stem becomes more significant due to the higher fluid temperature to be measured by TC_2 and TC_3.

The acquisition error for all the thermocouples (Table 1) is quite large with respect to usual values [20] since tests performed on the complete measurement chain (from sensor to PC) were made and it was noticed that the disturbance originated from the electric motor produced noise in the electronic circuitry. The consequent error was divided into a systematic component (0.3 K) and a random component, which is taken into consideration in the estimation of P_i.

Rotational Speed Measurement. The rotational speed of the electric motor shaft N_E is measured through a 60-tooth wheel and a magnetic pickup sensor. The information available on this sensor allowed the estimation of the total measurement uncertainty (which combines both systematic and random errors) as equal to 5 rpm. In this value the uncertainty associated with the acquisition

[2]This hypothesis can be considered sufficiently accurate only if, as in the present case, a linear (V,T) interpolation curve is used, while it would not be considered correct if a higher order of the interpolation curve is used [24].

(electrical noise) is included. The uncertainty in the electric motor rotational speed measurement leads to an uncertainty of about 30 rpm on the compressor rotational speed N_C, due to the presence of the step-up gearbox with a gear ratio of 5.83:1.

Torque Measurement. The torque was measured with a torsiometer using a four strain gauge transducer, 250 N m f.s., which does not make use of sliding contacts for signal transmission. The main source of error is due, in this case, to the acquisition error, since the torque meter is located near the electric motor. Through a series of analyses on the output signal coming from the torque meter it was possible to estimate the systematic error associated with electrical noise. The systematic uncertainty was set as equal to 0.51%. The random error was estimated to be equal to 0.40%. The total uncertainty in the torque measurement was calculated as equal to 0.65%.

Vibration and Sound Measurement. For the vibration measurement, two miniature accelerometers with an upper frequency limit equal to 16.5 kHz are used. The accelerometers chosen are not current-to-voltage conditioning integrated (ICP) since the casing in which they are mounted can reach a temperature of up to 395 K, which is a limit value for an ICP accelerometer. The accelerometers are connected in series to a charge amplifier, which is excited directly by the conditioning module (see Fig. 1). The uncertainty, derived from the individual calibration chart of the accelerometers, ranges from 1.0% at the lower frequencies up to 2.0% at the upper frequency limit and is related only to the device.

For the sound measurement, two cardioid microphones are used. The microphones are of prepolarized condenser type with a 20 Hz–40 kHz frequency range on axis.

Derived Measurement and Performance Parameter Uncertainty

Once the uncertainties of the measurements performed on the compressor have been estimated, the uncertainties of the derived measurements, which are necessary for the parameter calculation, and, as a consequence, the uncertainties of the parameters themselves, were calculated. To obtain a value of the derived measurement and parameter uncertainty, the uncertainty analysis has been applied to a single working point taken as an example. The test conditions considered refer to a typical working point, namely $N_C=(28{,}948\pm 30)$ rpm and throttle valve at 45 deg. The measurements related to the working point considered are

$$p_{amb}=(1.0287\pm 0.00630)\ \text{bar},$$

$$T_{amb}=(296.5\pm 0.2)\ \text{K},$$

$$\text{RH}=(60.0\pm 1.2)\%,$$

$$T_{02}=(296.5\pm 0.2)\ \text{K},$$

$$T_{03}=(374.3\pm 1.0)\ \text{K},$$

$$\Delta p_{op}=(-0.0830\pm 0.00091)\ \text{barg},$$

$$\Delta p_2=(-0.0451\pm 0.00086)\ \text{barg},$$

$$\Delta p_{23}=(0.2399\pm 0.00832)\ \text{barg},$$

$$\Delta p_3=(0.6296\pm 0.01705)\ \text{barg}.$$

Mass Flow Measurement. The device employed is an orifice plate designed in accordance with the UNI 1590 standard [25]. In Ref. [25] the employment of a particular arrangement in which the flow device is set at an extremity of the pipe rather than being inserted between two elements of the pipe itself, is allowed. This solution has been adopted in the present test rig. The well-known formula for mass flow rate calculation when using an orifice obstruction meter can be written as

$$M=\alpha\varepsilon\frac{\pi d^2}{4}\sqrt{2\rho\Delta p_{op}}, \tag{13}$$

which allows the calculation of a mass flow rate related to the working point considered equal to $M_C=0.526$ kg/s.

The uncertainty in mass flow determination has to be performed through Eq. (10). For simplicity, the uncertainties in α, ϵ, d, Δp_{op}, and ρ are considered independent[3] [23].

The uncertainties associated with α and ϵ are obtained by Ref. [25] and are both equal to 1.5%. The uncertainty of d was estimated to be 0.05% while the uncertainty of Δp_{op} has already been obtained (0.52% f.s.).

The definition of the air density uncertainty u_ρ is also obtained by applying Eq. (10) to the density definition equation $\rho=p/RT$. In the case of humid air, R is a function of gas composition and, thus, of ambient pressure, temperature, and relative humidity, for which the associated uncertainties have been already calculated. The resulting uncertainty $\delta R/R$ was calculated as equal to 0.0154% and was obtained by numerically evaluating the sensitivity coefficients ϑ_i, as explained below. The absolute uncertainty on air density ρ, equal to 1.201 kg/m^3 in the conditions considered, was then calculated as equal to 0.0074 kg/m^3 ($\delta\rho/\rho=0.62\%$). In conclusion, the total uncertainty of the compressor mass flow rate δM_C was calculated as equal to 0.012 kg/s ($\delta M_C/M_C=2.21\%$) and, thus,

$$M_C=(0.526\pm 0.012)\ \text{kg/s}.$$

Absolute Static Pressure Measurement. Since all the pressure measurements are performed through gauge sensors, the absolute values of the pressures that have to be used in the performance calculations must be obtained by adding the measured ambient pressure to the result of the sensor measurement:

$$p_2=p_{amb}+\Delta p_2,\quad p_{23}=p_{amb}+\Delta p_{23},\quad p_3=p_{amb}+\Delta p_3. \tag{14}$$

Hence, the uncertainties of the absolute values have to be computed following Eq. (10). The calculations allowed the estimation of the absolute uncertainties:

$$p_2=(0.98360\pm 0.00636)\ \text{bar},$$

$$p_{23}=(1.2699\pm 0.01037)\ \text{bar},$$

$$p_3=(1.6583\pm 0.01817)\ \text{bar}.$$

It is interesting to note that, when differential transducers are used and when the pressures to be measured are close to ambient pressure, as in the present case, the uncertainty on the latter measurement is dominant with respect to the differential transducer uncertainty. Hence, even if the Δp_2, Δp_{23}, and Δp_3 are measured with a quite high uncertainty, the uncertainties on the absolute values, which are used for the calculation of the performance parameters, are deemed acceptable. For example, in the present case, the result is

$$\delta(\Delta p_2)/\Delta p_2=1.91\%,\quad \text{while}\quad \delta p_2/p_2=0.65\%,$$

$$\delta(\Delta p_{23})/\Delta p_{23}=3.47\%,\quad \text{while}\quad \delta p_{23}/p_{23}=0.82\%,$$

$$\delta(\Delta p_3)/\Delta p_3=2.71\%,\quad \text{while}\quad \delta p_3/p_3=1.10\%.$$

Static Temperature and Absolute Total Pressure Measurement. The static temperatures and the total pressures can be calculated by solving the system of equations constituted by Eqs. (3) and (4). The explicit form of both these equations is quite complicated and, thus, the analytic calculation of the partial derivatives, which are used in the definition of the combined standard uncertainty u_y, Eq. (10), is rather laborious. For this reason, a numerical approximation to the partial derivatives has been

[3]This is not completely correct since, for instance, α depends, among other parameters, on the Reynolds number, which in turn is a function of d and ρ.

calculated by a FORTRAN program which uses a subroutine of the IMSL Library [26]. The functional form of the static temperature and of the total pressure can be written as

$$p_0, T = f(T_{amb}, p_{amb}, \mathrm{RH}, p, M, A, T_0). \tag{15}$$

The results of the uncertainty calculations are as follows:

$$\delta p_{02} = 0.00630 \text{ bar} \quad \text{and} \quad \delta p_{03} = 0.01772 \text{ bar},$$

$$\delta T_2 = 0.2 \text{ K} \quad \text{and} \quad \delta T_3 = 1.0 \text{ K}.$$

It may be noted that the uncertainties of the derived quantities total pressure p_0 and static temperature T are nearly equal to the respective measurements, i.e., the static pressure p and the total temperature T_0.

Performance Parameters. The uncertainties of the mechanical power P_C required to drive the compressor, of the corrected mass flow μ_C, corrected rotational speed ν_C, pressure ratio β_C, and isentropic η_{sC} and small stage η_{pC} efficiencies can at last be calculated. In the case of P_C, ν_C, μ_C, and β_C the analytical solution was derived, while for η_{sC} and η_{pC} the sensitivity coefficients ϑ_i were evaluated numerically.

For both efficiencies, the functional form is

$$\eta_{sC}, \eta_{pC} = f(T_{amb}, p_{amb}, \mathrm{RH}, p_2, T_{02}, p_3, T_{03}, M, A_2, A_3). \tag{16}$$

To obtain a value of the parameter uncertainty, the above considerations were applied to the previously used working point. The calculated values of the performance parameters are $\eta_{sC} = 0.633$, $\eta_{pC} = 0.660$, $\beta = 1.72$, $\mu_C = 0.5404$ kg/s, $\nu_C = 28{,}535$ rpm, $P_C = 53.16$ kW. The results of the uncertainty calculations are as follows:

$$\delta\eta_{sC}/\eta_{sC} = 2.73\%, \quad \delta\eta_{pC}/\eta_{pC} = 2.51\%, \quad \delta\beta_C/\beta_C = 1.23\%,$$

$$\delta\mu_C/\mu_C = 2.30\%, \quad \delta\nu_C/\nu_C = 0.11\%, \quad \delta P_C/P_C = 1.99\%.$$

Preliminary Test Results

Performance Evaluation. The test procedure can be summarized in the following points:

1. Compressor lube oil heating by driving the compressor at $N_C \approx 6000$ rpm with throttle valve fully open, until $T_{oil} \approx 350$ K.
2. Compressor driving at the selected test rotational speed with throttle valve fully open.
3. Once the measurements are steady, the acquisition is started. The acquisition time is set equal to one second, and, for each measured parameter, the stored value is the average value of the measurements acquired in the acquisition time. For steady-state tests the number of the measurements acquired in the acquisition time (1 s) for each measured parameter is usually set to 100.
4. Point 3 is repeated for different positions of the throttle valve.
5. Points 2–4 are repeated for different compressor rotational speeds.

In Fig. 4 the compressor performance maps determined by using the previously described procedure are shown. The working point in which the uncertainty analysis was performed is highlighted together with the uncertainty bands. The curves refer to three values of the corrected rotational speed. It may be noted that the uncertainty on the corrected rotational speed is made up of two terms: one (± 31 rpm for all the curves) was estimated starting from the parameter uncertainty previously calculated ($\delta\nu_C/\nu_C = 0.11\%$), while the other is different for each curve and is due to rotational speed unsteadiness during tests. In the figure, the white symbols refer to steady state conditions, while gray symbols refer to conditions in which unsteady phenomena occur

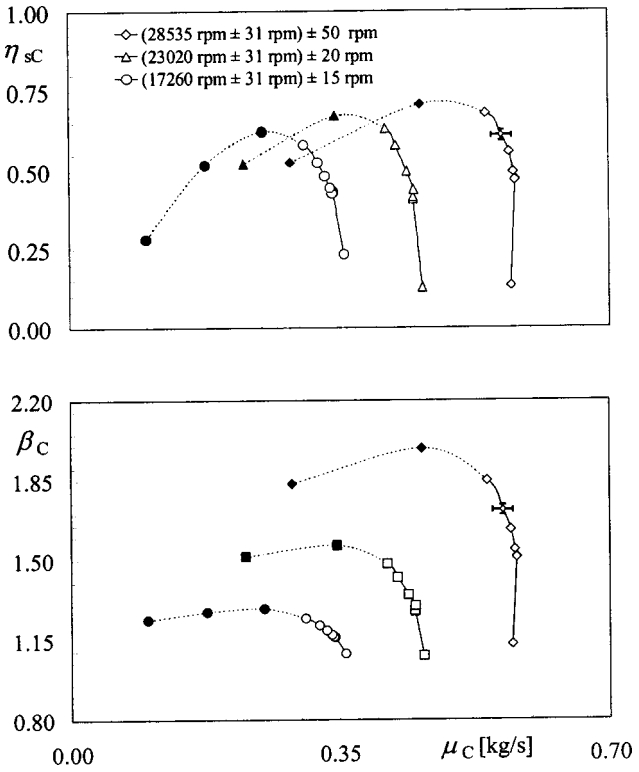

Fig. 4 Compressor performance maps

(surge and/or rotating stall). These phenomena could be detected by analyzing the dynamic trends of flow parameters, such as discharge pressure and suction mass flow rate. As an example, in Fig. 5 the dynamic trends of pressure ratio and corrected mass flow

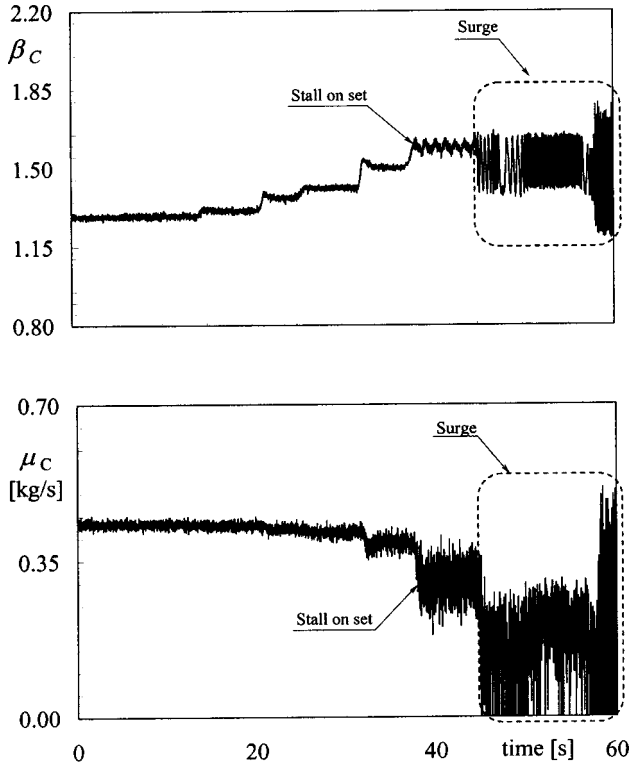

Fig. 5 Dynamic trend of compressor ratio (up) and corrected mass flow rate (down)

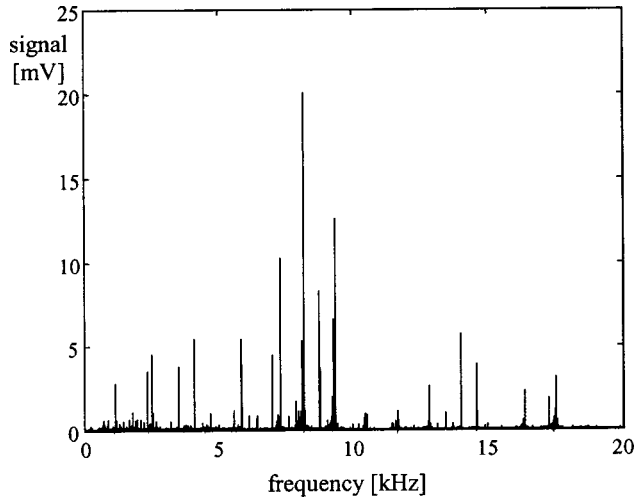

Fig. 6 Power spectrum of the acquired acoustic signal

versus time at constant corrected rotational speed (23,020 rpm±31 rpm)±20 rpm are reported. The trial was performed by gradually closing the throttle valve, thus changing the working point of the compressor. It can be seen how the stall onset point and the compressor operation in surge conditions can be assessed.

Acoustic Measurements. Regarding the acoustic measurements, some preliminary tests were performed to assess instrumentation capability. In order to do this, a microphone was set in front of the inlet duct to measure the blade passing frequencies (BPFs) of the compressor. In fact, the sound signal (indeed this is generally true for every unsteady signal such as pressure or vibration) has its maximum energy in correspondence to these frequencies and their harmonics. Hence, it is expected that signal analysis at these frequencies could contain the most significant information on potential faults occurring in the compressor [27].

If z is the number of rotor blades, the BPF is defined as [28]

$$\mathrm{BPF}=\frac{zN}{60}. \tag{17}$$

In this paper, a power spectrum of the signal was analyzed in order to identify if the BPF of each rotor stage could be recognized by the test instrumentation. In particular, a test was performed at constant compressor rotational speed $N_C=17{,}548$ rpm and with the throttle valve fully open. The power spectrum of the acoustic acquired signal is reported in Fig. 6.

The theoretical BPFs relative to each rotor, which has a different number of blades and, thus, a different BPF, were calculated through Eq. (17) at the rotational speed of the test. The comparison between theoretical and experimental results is reported in Table 2. As can be seen, the agreement is very convincing and the error is negligible, independent of the value of the order of blade passing frequency.

Table 2 Experimental and theoretical BPF

		BPF (Hz) at 17,548 rpm	
Stage	z	Theoretical results	Experimental results
1A	16	4679	4679
2A	20	5849	5849
3A	16	4679	4679
4A	25	7312	7311
5A	28	8189	8188
6A	25	7312	7311
1C	32	9359	9357

Conclusions

The test facility developed at the University of Ferrara has been designed to perform different tasks on small-size compressors, such as steady-state characterization, dynamic and acoustic analyses, analysis of compressor behavior in the presence of inlet fogging, water ingestion or implanted fault, etc. The analysis of the uncertainty of the acquired measurements and of the compressor performance parameters determined from the measurements shows quite a large uncertainty of compressor efficiency (about 2.7% and 2.5% for isentropic and small stage efficiency, respectively) and corrected mass flow rate (about 2.3%). Moreover, even if the uncertainty in electric motor rotational speed measurement is very low (±5 rpm), the determination of performance curves at "constant" corrected rotational speed is affected by an uncertainty on the "constant" value, which can be estimated to be about ±80 rpm. This is mainly due to the presence of the step-up gearbox between motor and compressor and to rotational speed unsteadiness during tests.

Nevertheless, these uncertainties can be considered typical for tests performed on gas turbine compressors.

Finally, the preliminary analysis of the measurement dynamic trends and of acoustic measurements seems to confirm their capability for the study of unsteady phenomena.

Acknowledgments

The work was carried out with the support of the M.U.R.S.T. (Italian Ministry of University and Scientific and Technological Research). The authors gratefully acknowledge Marco Buzzoni for his contribution to the experimental apparatus setup and performance of the tests.

Appendix

Along an isentropic thermodynamic transformation, the relation between pressure and temperature can be derived from the entropy definition in differential form

$$ds=\frac{\delta q}{T}=\frac{c_p dT-(dp/\rho)}{T}. \tag{A1}$$

Hence, since $\rho=p/RT$ and for an isentropic transformation $ds=0$, it results that

$$c_p dT=RT\frac{dp}{p} \tag{A2}$$

$$\frac{dp}{p}=\frac{1}{R}c_p\frac{dT}{T}. \tag{A3}$$

Therefore, by integrating along an isentropic transformation between a reference state "r" and a generic state (p,T), and in the hypothesis that the specific heat at constant pressure c_p is a function of temperature, it results that

$$ln\frac{p}{p_r}=\frac{1}{R}\int_{T_r}^{T}c_p(T)\frac{dT}{T}. \tag{A4}$$

It is then possible to define a thermodynamic function

$$\Phi(T)=\frac{1}{R}\int_{T_r}^{T}c_p(T)\frac{dT}{T}+\Phi(T_r) \tag{A5}$$

so that the relation between pressure and temperature along an isentropic transformation from a state 1 and a state 2 is

$$ln\frac{p_2}{p_1}=\frac{1}{R}\int_{T_1}^{T_2}c_p(T)\frac{dT}{T}=\Phi(T_2)-\phi(T_1). \tag{A6}$$

In particular, if the state 2 is the total physical state and the state 1 is the static physical state, finally it results that

$$p_0=p\cdot e^{[\phi(T_0)-\phi(T)]}. \tag{A7}$$

The compression small stage efficienty is defined as

$$\eta_{pC} = \frac{dh_s}{dh} = \frac{dp/\rho}{c_p dT} = \frac{R(dp/p)}{c_p(dT/T)}. \quad (A8)$$

Therefore, from Eq. (*A*8), it results that, between states 1 and 2 of an adiabatic trasformation for which η_{pC} can be considered constant,

$$ln\frac{p_2}{p_1} = \frac{1}{\eta_{pC}R}\int_{T_1}^{T_2} c_p(T)\frac{dT}{T} = \frac{1}{\eta_{pC}}\Phi(T_2) - \Phi(T_1). \quad (A9)$$

Hence

$$(\eta_{pC})_{1-2} = \frac{ln(p_2/p_1)}{\Phi(T_2) - \Phi(T_1)}. \quad (A10)$$

Nomenclature

A = Area
B_i = Root sum square of each elemental contribution to systematic error
c_p = Specific heat at constant pressure
d = Diameter
h = $\int_{T_r}^{T} c_p(T)dT + h(T_r)$ enthalpy
k_c = Coverage factor
M = Mass flow rate
n = Number of readings
N = Rotational speed
P = Power
P_i = Root sum square of each elemental contribution to random error
p = Absolute pressure
R = Gas constant
RH = relative humidity
r = N_C/N_E, gearbox velocity ratio
S_{x_i} = Standard deviation of x_i
T = Temperature
T_q = Torque
u_{x_i} = Individual standard uncertainty associated with x_i
u_y = Combined standard uncertainty associated with y
V = Flow velocity
x_i = Measured parameter
y = Measurement result
z = Number of blades
α = Throttle valve position, flow coefficient
β = Pressure ratio
Δp = Relative pressure
δ = p_0/p_{0r}, variation
ϵ = Compressibility factor
Φ = $1/R\int_{T_r}^{T} c_p(T)dT/T + \Phi(T_r)$
η = Efficiency
ϑ = T_0/T_{0r}
ϑ_i = $\partial y/\partial x_i$, sensitivity coefficient
μ = $M\sqrt{\vartheta}/\delta$, corrected mass flow rate
ν = $N/\sqrt{\vartheta}$, corrected rotational speed
ρ = Density

Subscripts and Superscripts

0 = Total physical state
2, 23, 3 = Compressor sections
a = Absolute
amb = Ambient
C = Compressor
E = Electric motor
G = Gearbox
o = Outlet section
oil = Lube oil
op = Orifice plate
p = Small stage or polytropic
r = Reference value
s = Isentropic

References

[1] Saravanamuttoo, H. I. H., and Lakshminarasimha, A. N., 1985, "A Preliminary Assessment of Compressor Fouling," ASME Paper No. 85-GT-153.
[2] Aker, G. F., and Saravanamuttoo, H. I. H., 1988, "Predicting Gas Turbine Performance Degradation Due to Compressor Fouling Using Computer Simulation Techniques," ASME Paper No. 88-GT-206.
[3] Seddigh, F., and Saravanamuttoo, H. I. H., 1990, "A Proposed Method for Assessing the Susceptibility of Axial Compressors to Fouling," ASME Paper No. 90-GT-348.
[4] Tabakoff, W., Lakshminarasimha, A. N., and Pasin, M., 1990, "Simulation of Compressor Performance Deterioration Due to Erosion," ASME J. Turbomach., **112**, pp. 78–83.
[5] Massardo, A., 1991, "Simulation of Fouled Axial Multistage Compressors," IMechE Paper No. C423/048.
[6] Cerri, G., Salvini, C., Procacci, R., and Rispoli, F., 1993, "Fouling and Air Bleed Extracted Flow Influence on Compressor Performance," ASME Paper No. 93-GT-366.
[7] Lakshminarasimha, A. N., Boyce, M. P., and Meher-Homji, C. B., 1994, "Modeling and Analysis of Gas Turbine Performance Deterioration," ASME J. Eng. Gas Turbines Power, **116**, pp. 46–52.
[8] Mac Leod, J. D., Taylor, V., and Laflamme, J. C. G., 1992, "Implanted Component Faults and Their Effects on Gas Turbine Engine Performance," ASME J. Eng. Gas Turbines Power, **114**, pp. 174–179.
[9] APIcom, 1997, "Manuale d'uso freno attivo a recupero" (in Italian).
[10] National Instrument Corporation, 2000, "Acquisition Boards User Manual," NI Press, Austin, TX.
[11] National Instrument Corporation, 2000, "SCXI 1531/SCXI 1100/SCXI 1102 B User Manuals," NI Press, Austin, TX.
[12] Spina, P. R., 2002, "Gas Turbine Performance Predictions by Using Generalized Curves of Compressor and Turbine Stages," ASME Paper No. GT-2002-30275.
[13] National Instrument Corporation, 2002, "LabView Manual and LabView Data Acquisition," NI Press, Austin, TX.
[14] ISO, 1993, "Guide to the Expression of Uncertainty in Measurement," ISBN 92-67-10188-9, ISO International Standard, Geneve.
[15] Taylor, B. R., and Kuyatt, C. E., 1994, "Guidelines for Evaluating and Expressing the Uncertainty of NIST Measurement Results," Technical Note No. 1927, NIST, U.S. Gov. Printing Office, Washington, DC.
[16] Coleman, H. W., and Steele, W. G., 1989, Experimentation and uncertainty analysis for engineers, John Wiley & Sons, New York, US.
[17] ANSI/ASME, 1985, "Measurement Uncertainty," PTC 19.1, **1**, ASME, New York.
[18] ANSI/ASME, 1997, "Measurement Uncertainty," PTC 19.1, **1**, ASME, New York.
[19] ISO, 2314, 1989, "Gas Turbines Acceptance Tests," ISO International Standard, Geneve.
[20] Brun, K., and Kurz, R., 2001, "Measurement Uncertainties Encountered During Gas Turbine Driven Compressor Field Testing," ASME J. Eng. Gas Turbines Power, **123**, pp. 62–69.
[21] Brentano, T., "Evaluation of Compressor Field Test Results Using Uncertainty Analysis," ACCT Technical report, http://www.gmrc.org/gmrc/techpapersPDF/2002.
[22] Kurz, R., Brun, K., and Legrand, D. D., 1999, "Field Performance Testing of Gas Turbine Driven Compressor Sets," Proc. 28th Turbomachinery Symposium, A&M University, Houston, TX.
[23] ISO, 5167, 1998, "Orifice Plate Nozzles and Venturi Tubes Inserted in Circular Cross-Section Conduits Running Full," ISO International Standard, Geneve.
[24] von Karman Institute, 1996, "Temperature Measurements," von Karman Institute Lecture Series No. 1996-07 D71996/0238/440, T. Arts, eds., Bruxelles.
[25] UNI 1590 (DIN 1952), 1941, "Regole per le misure di portata mediante boccagli e diaframmi" (in Italian), Italian National Standard, Rome.
[26] Visual Numerics Inc., 1994, "IMSL MATH/LIBRARY: FORTRAN Subroutine for Mathematical Applications," Houston, TX.
[27] Aretakis, N., and Mathioudakis, K., 1996, "Radial Compressor Fault Identification Using Dynamic Measurement Data," ASME Paper No. 96-GT-102.
[28] Wright, T., 1999, Fluid machinery. Performance, analysis and design, CRC, Washington, DC.

Stefan Hurlebaus
e-mail: s.hurlebaus@mecha.uni-stuttgart.de

Lothar Gaul
e-mail: l.gaul@mecha.uni-stuttgart.de

Institute A of Mechanics,
University of Stuttgart,
Allmandring 5b,
70550 Stuttgart, Germany

Calculating the Eigenfrequency of Rotating Acoustic Annulus Inside Labyrinth Seals of Turbomachines

This brief note describes a method for calculating the eigenfrequencies of a rotating acoustic air column inside labyrinth seals in turbomachinery. The method is applied to nonrotating air columns as well as to rotating air columns considering a body fixed and a spatial fixed coordinate system. [DOI: 10.1115/1.1787501]

1 Introduction

High cost pressures and cost savings in our economy have created demands to maximize the efficiency of high performance turbomachinery. However, the continuous trend towards higher power density and better efficiency [1] leads to machines which are more sensitive with respect to failures. Such a failure of turbomachinery is the defect of labyrinth seals which can be caused by excitation of the acoustic annulus between labyrinth seals. In order to guarantee safety and reliability of such labyrinth seals and hence guarantee safety and reliability of turbomachines, it is necessary to calculate the eigenfrequency of such rotating acoustic annulus. Such an eigenfrequency of a rotating labyrinth cavity should not coincide with the rotating frequency of the cavity, the excitation frequency.

Due to static bending, gyroscopic effects, as well as residual unbalances of a shaft, an excentric operation of a rotor of a turbomachine cannot be avoided [2–5]. Therefore pressure differences occur in circumferential direction, which can cause an acoustic oscillation in the annulus between labyrinth seals. This pressure differences can arise due to different gap losses or through the circumferential component of an inlet stream to the seal (Fig. 1). Furthermore, pressure differences occur due to the die gap's dependence of the pressure distribution. The later effect causes a nonconstant static pressure at the circumference of the rotor's surface.

The dependence of the pressure as a function of z is always present, since the pressure has to be changed from p_1 to p_2. At the position, where the gap is narrowest, $\varepsilon_{\min}$, there results a different pressure distribution along z than at the position where the gap is widest, $\varepsilon_{\max}$ (Fig. 2). The pressure difference $p(\varepsilon_{\max}) - p(\varepsilon_{\min})$ produces a restoring force.

Childs and Scharrer [6] derived the basic equations for compressible flow in a labyrinth seal. They assumed the flow to be completely turbulent in circumferential direction. They further assumed that the frequency of the acoustic resonance in the labyrinth cavity is much higher than that of the rotor speed. Their results are compared with the test results of Benckert [7]. The model they derived gives results which are in a range of 25% of the experimental results. However, they state that the discrepancy must be balanced to the known uncertainties in the experimental data. Additional test are performed by Thieleke [8] and the data are compared with the theory derived by Childs and Scharrer [6]. He obtained good agreement. The theory presented in the present paper circumvents the assumption that the acoustic resonance in the labyrinth cavity is much higher than that of the rotor speed. However, for simplicity reasons leakage effects and friction between the gas and the rotor, stator, and labyrinth seals are neglected.

First, the differential equation for the displacement of an acoustic oscillation in a rotating system is derived. The relative kinematics is applied to this differential equation considering a body fixed and a spatial fixed coordinate system. Finally the differential equation are solved for the case of standing waves—and this leads to the calculation of the eigenfrequencies of a rotating acoustic annulus.

2 Derivation of the Equation of Motion

For determining the oscillation of a compressible media, an extensible elastic annulus is considered, which is described in Nackenhorst [9] or Gaul et al. [10]. The deformation is described in polar coordinates and hence the position vector $\mathbf{r}$ can be written as (Fig. 3)

$$\mathbf{r} = R\mathbf{e}_r + u\mathbf{e}_\varphi . \tag{1}$$

The strain in circumferential direction is

$$\epsilon = \frac{1}{R}u', \tag{2}$$

where the expression

$$(\cdots)' = \frac{d(\cdots)}{d\varphi} \tag{3}$$

denotes the derivative with respect to the circumferential coordinate.

The kinetics follows from considering the free-body diagram (Fig. 4). The equation of linear momentum gives

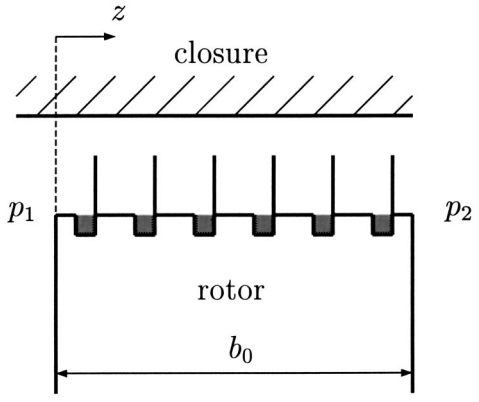

Fig. 1 Labyrinth seals

Contributed by the Stuctures and Dynamics Division of THE AMERICAN SOCIETY OF MECHANICAL ENGINEERS for publication in the ASME JOURNAL OF ENGINEERING FOR GAS TURBINES AND POWER. Manuscript received by the S&D Division October 9, 2002; final revision received November 20, 2003. Associate Editor: N. Arakere.

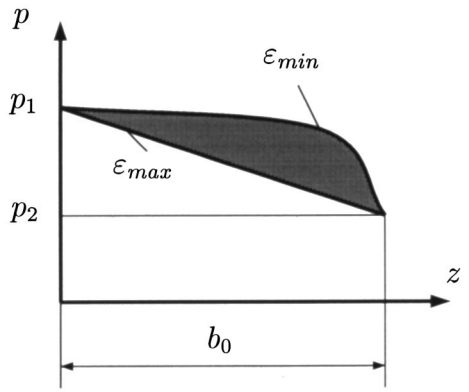

Fig. 2 Pressure distribution

$$\rho A ds \frac{d^2u}{dt^2} = dN. \tag{4}$$

With the relations $ds = Rd\varphi$ and $d(\cdots)/ds = 1/R(\cdots)'$, Eq. (4) leads to

$$\rho A \frac{d^2u}{dt^2} = \frac{1}{R} N'. \tag{5}$$

Hooke's law for linear elastic material properties can be written as $N = EA\epsilon$. Therefore using Eqs. (5) and (2) the equation of motion is obtained as

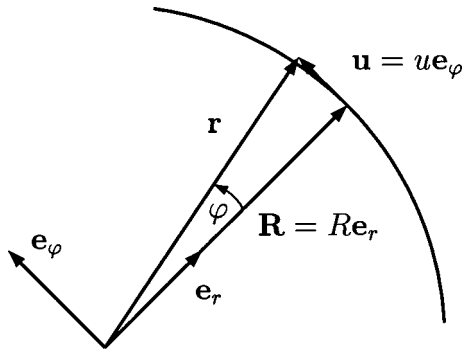

Fig. 3 Kinematical deformation of the extensible elastic annulus

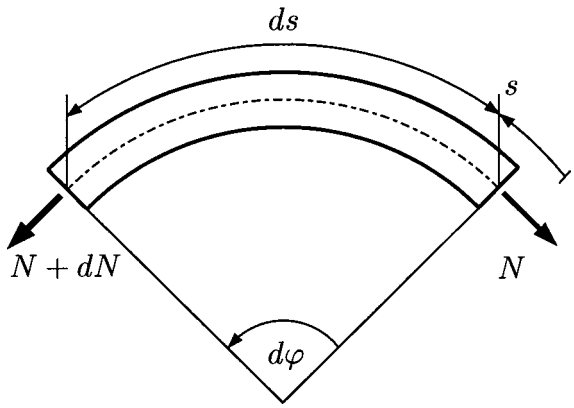

Fig. 4 Forces at the annulus

$$\rho A \frac{d^2u}{dt^2} = \frac{EA}{R^2} u'', \tag{6}$$

which can be simplified to the form

$$\frac{R^2}{c_0^2} \frac{d^2u}{dt^2} - u'' = 0, \tag{7}$$

where c_0 is the velocity of sound of the media ($c_0^2 = E/\rho$).

3 Relative Kinematics

For a body fixed observer ($\mathbf{e}_r - \mathbf{e}_\varphi$ system) the velocity vector is obtained as

$$\mathbf{v} = \frac{dr}{dt} = -\Omega u \mathbf{e}_r + [\dot{u} + R\Omega]\mathbf{e}_\varphi, \tag{8}$$

while the acceleration vector is obtained as

$$\mathbf{a} = \frac{d\mathbf{v}}{dt} = [-2\Omega\dot{u} - \Omega^2 R]\mathbf{e}_r + [\ddot{u} - \Omega^2 u]\mathbf{e}_\varphi \tag{9}$$

using the derivation rule

$$\frac{d(\cdots)}{dt} = \frac{\partial(\cdots)}{\partial t} + \boldsymbol{\Omega} \times (\cdots), \quad \boldsymbol{\Omega} = \Omega \mathbf{e}_z \tag{10}$$

applied to the position vector Eq. (1), where $(\cdots) = \partial(\cdots)/\partial t$.

The derivatives with respect to time for a spatial fixed (ALE =arbitrary Lagrangian-Eulerian) observer ($\hat{\mathbf{e}}_r - \hat{\mathbf{e}}_\varphi$ system) result from [11]

$$\frac{d(\cdots)}{dt} = \frac{\partial(\cdots)}{\partial t} + \mathrm{Grad}(\cdots)\frac{d\boldsymbol{\chi}}{dt}, \tag{11}$$

where the gradient is built with respect to a spatial approach describing the reference configuration of the rigid body motion $\boldsymbol{\chi} = \chi(X)$. Using the operator of the gradient in polar coordinates

$$\mathrm{Grad}(\cdots) = \left(\frac{\partial}{\partial r}\hat{\mathbf{e}}_r + \frac{1}{R}\frac{\partial(\cdots)}{\partial \varphi}\hat{\mathbf{e}}_\varphi \right) \tag{12}$$

it follows for the simple case with $d\boldsymbol{\chi}/dt = R\Omega\hat{\mathbf{e}}_\varphi$,

$$\frac{d(\cdots)}{dt} = \frac{\partial(\cdots)}{\partial t} + \frac{\partial(\cdots)}{\partial \varphi}\Omega. \tag{13}$$

Together with the introduced notation for the relative time derivative and the derivative with respect to φ the spatial presentation of the velocity vector and the acceleration vector is

$$\mathbf{v} = -\Omega u \hat{\mathbf{e}}_r + [\dot{u} + \Omega(R + u')]\hat{\mathbf{e}}_\varphi, \tag{14}$$

$$\mathbf{a} = [-2\Omega\dot{u} - \Omega^2(R + 2u')]\hat{\mathbf{e}}_r + [\ddot{u} + 2\Omega\dot{u}' - \Omega^2(u - u'')]\hat{\mathbf{e}}_\varphi, \tag{15}$$

respectively.

4 Solution of the Equation of Motion

4.1 Nonrotating Air Column. The differential equation for the displacement u for a nonrotating air column is

$$\frac{d^2u}{dt^2} - c_0^2 \frac{\partial^2 u}{\partial s^2} = 0, \tag{16}$$

where c_0 is the velocity of sound of the media. Separation of variables $u(s,t) = U(s)\exp(i\omega t)$ leads to the differential equation

$$\frac{d^2U(s)}{ds^2} + k^2 U(s) = 0, \tag{17}$$

whereby $k = \omega/c_0$ is the wave number. Using the fundamental solution

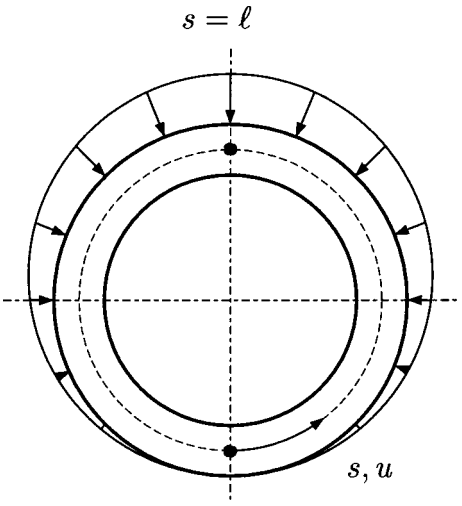

Fig. 5 Fundamental eigenmode of the circular air column

$$U(s)=a\cos ks+b\sin ks \tag{18}$$

and the boundary conditions (Fig. 5) $U(0)=0$ and $U(2\ell)=0$, the wave number can be calculated as $k=n\pi/2\ell$, where $n=1,2,3\ldots$. With the relation $\ell=\pi D_s/2$, where D_s is the shaft diameter, the eigenfrequency can be calculated

$$f=\frac{\omega}{2\pi}=\frac{kc_0}{2\pi}=\frac{nc_0}{4\ell}=\frac{nc_0}{2\pi D_s}. \tag{19}$$

4.2 Rotating Air Column, Body Fixed Observer. If one replaces the acceleration of Eq. (7) with the acceleration of Eq. (9), one obtains the equation of motion for a rotating air column in a body fixed coordinate system,

$$\frac{d^2u}{dt^2}-\Omega^2u-\frac{c_0^2}{R^2}u''=0, \tag{20}$$

where again c_0 denotes the velocity of sound of the media. Separation of variables $u=U\exp(i\omega t)$ yield the differential equation

$$(\omega^2+\Omega^2)U+\frac{c_0^2}{R^2}U''=0, \tag{21}$$

whereby the wave number k is given as $k^2=(\omega^2+\Omega^2)/c_0^2$. Again, using the relations $k=n\pi/2\ell$ and $\ell=\pi D_s/2$ the eigenfrequency can be calculated as

$$f=\frac{\omega}{2\pi}=\frac{1}{2\pi}\sqrt{k^2c_0^2-\Omega^2}=\frac{1}{2\pi}\sqrt{\frac{n^2\pi^2c_0^2}{4\ell^2}-\Omega^2}$$

$$=\frac{1}{2\pi}\sqrt{\frac{n^2c_0^2}{D_s^2}-\Omega^2}. \tag{22}$$

4.3 Rotating Air Column, Spatial Fixed Observer. If one replaces the acceleration of Eq. (7) with the acceleration in circumferential direction of Eq. (15), one obtains the equation of motion for an air column in a spatial fixed coordinate system,

$$\frac{d^2u}{dt^2}+2\Omega\dot{u}'-\Omega^2(u-u'')-\frac{c_0^2}{R^2}u''=0. \tag{23}$$

Again, separation of variables $u=U\exp(i\omega t)$ yield the differential equation

$$\left(\Omega^2-\frac{c_0^2}{R^2}\right)U''+2i\Omega\omega U'-(\Omega^2+\omega^2)U=0. \tag{24}$$

For simplicity reasons a reduced fundamental solution of the form $U=\hat{U}\exp(ikR\phi)$ is given. It is therefore assumed that for generation of a real solution the solution of the conjugate complex system $U=\hat{U}\exp(-ikR\phi)$ has to be superposed with the fundamental solution. Using this fundamental solution one obtains

$$\omega^2+2kR\Omega\omega+\Omega^2+k^2R^2\Omega^2-k^2c_0^2=0. \tag{25}$$

This equation can be solved for the frequency

$$\omega=[\pm\sqrt{k^2c_0^2-\Omega^2}-kR\Omega]. \tag{26}$$

With the relations $k=n\pi/2\ell$ and $\ell=\pi D_s/2$ the eigenfrequency can be calculated as

$$f=\frac{\omega}{2\pi}=\frac{1}{2\pi}[\sqrt{k^2c_0^2-\Omega^2}-kR\Omega]=\frac{1}{2\pi}\left[\sqrt{\frac{n^2\pi^2c_0^2}{4\ell^2}-\Omega^2}-\frac{n\pi R}{2\ell}\Omega\right]=\frac{1}{2\pi}\left[\sqrt{\frac{n^2c_0^2}{D_s^2}-\Omega^2}-\frac{n}{2}\Omega\right] \tag{27}$$

Conclusions

This brief note presents the relations for calculating the eigenfrequencies of a nonrotating and rotating acoustic annulus with a body and a spatial fixed observer. The given relations can be used to check whether or not there exists resonance inside the labyrinth seals of a turbomachine. For damage analysis it is important to note that the critical eigenfrequency is the one which is ''seen'' by a body fixed observer.

Notation

A = Cross sectional area of the annulus
c_0 = Velocity of sound
D_s = Shaft diameter
f = Eigenfrequency
k = Wave number
ℓ = Half circumference
n = Order of vibration mode
N = Normal force
p = Pressure
R = Radius
s = Circumferential coordinate
u = Displacement
z = Coordinate
ϵ = Strain
ε = Die gap
φ = Angle
ω = Circular eigenfrequency
Ω = Circular frequency of rotation
ρ = Mass density
$\mathbf{a}$ = Acceleration vector
$\mathbf{e}_r$, $\mathbf{e}_\varphi$ = Unit vectors
$\mathbf{r}$ = Position vector
$\mathbf{v}$ = Velocity vector
$(\cdots)$ = $\partial(\cdots)/\partial t$

References

[1] Kwanka, K., 1997, ''Improving the Stability of Labyrinth Gas Seals,'' ASME J. Eng. Gas Turbines Power, **123**(2), pp. 383–387.
[2] Childs, D. W., 1993, *Turbomachinery Rotordynamics*, Wiley, New York.
[3] Gasch, R., Nordmann, R., and Pfützner, H., 2002, *Rotordynamik*, Springer, Berlin.
[4] Stetter, H., 1994, *Thermische Strömungsmaschinen, Manuskript zur Vorlesung*, Institut für Thermische Strömungsmaschinen, Universität Stuttgart.
[5] Schuck, G., and Nordmann, R., 2002, ''Investigation of Self-Excited Vibration in Flexible Labyrinth Seals due to Instationary Pressure Fields,'' in *Proceedings IFToMM International Conference on Rotor Dynamics*, pp. 995–1002, Sydney, Australia.
[6] Childs, D. W., and Scharrer, J., 1986, ''An Iwatsubo-Based Solution for Labyrinth Seals—Comparison to Experimental Results,'' ASME J. Eng. Gas Turbines Power, **108**, pp. 325–331.

[7] Benckert, H., 1980, ''Strömungsbedingte Federkennwerte in Labyrinthdichtungen,'' Dissertation, Institut für Strömungsmaschinen und Maschinenlaboratorium, Universität Stuttgart, Stuttgart, Germany.
[8] Thieleke, H., 1991, ''Experimentelle und Theoretische Untersuchungen der Strömungskräfte in Labyrinthdichtungen von Turbomaschinen,'' Dissertation, Institut für Strömungsmaschinen und Maschinenlaboratorium, Universität Stuttgart, Stuttgart, Germany.
[9] Nackenhorst, U., Wiesemann, S., and Lammering, R., 2000, ''Zur Schallabstrahlung Rotierender Strukturen,'' in *Anwendungen der Akustik in der Wehrtechnik*, Deutsche Gesellschaft für Wehrtechnik.
[10] Gaul, L., Nackenhorst, U., and Nolte, B., 2000, ''Numerical Simulation of Noise Radiation From Rolling Tires,'' in W. Wendland, editor, *Multified Problems in Solid and Fluid Mechanics*, Springer, Berlin, pp. 262–269.
[11] Gaul, L., Fischer, M., and Nackenhorst, U., 2002, ''Vibrations and Sound Radiation Generated by Contact Between a Rotating Wheel and a Plane,'' in *Proceedings of ISROMAC-9*, pp. DD-ABS-006:1–6.

The Impact of Oil and Sealing Air Flow, Chamber Pressure, Rotor Speed, and Axial Load on the Power Consumption in an Aeroengine Bearing Chamber

Michael Flouros
MTU Aero Engines,
Air and Oil Systems,
Dachauer Strasse 665,
80995 Murich, Germany
e-mail: Michael.flouros@muc.mtu.de

*Trends in aircraft engines have dictated high speed rolling element bearings up to 3 million DN or more with the consequence of having high amounts of heat rejection in the bearing chambers and high oil scavenge temperatures. A parametric study on the bearing power consumption has been performed with a 124 mm pitch circle diameter (PCD) ball bearing in a bearing chamber that has been adapted from the RB199 turbofan engine (*DN$\sim 2\times10^6$*). The operating parameters such as oil flow, oil temperature, sealing air flow, bearing chamber pressure, and shaft speed have been varied in order to assess the impact on the power consumption. This work is the first part of a survey aiming to reduce power losses in bearing chambers. In the first part, the parameters affecting the power losses are identified and evaluated.* [DOI: 10.1115/1.1805009]

1 Introduction

Highly loaded bearings generate heat in the contact areas between the rolling elements and the races, as well as the rolling elements and the cage and in the annular gaps between the cage and the races. The generated heat is partly caused by friction in the contact areas, partly by churning and windage and partly by Euler work (acceleration to circumferential speed). Additionally the generated heat is considerably affected by the efficiency of the scavenge system, the residence time of the oil in the chamber, and the amount of generated droplets by the bearing.

Oil is usually supplied to roller and ball bearings via the under-race or under-cage method. Only a very small amount of oil is used for lubrication whereas most of the supplied oil is used to remove the heat from the bearing. The bearing design used in the testing is shown in Fig. 1*a*.

A schematic of the test facility is displayed in Fig. 1*b*. The bearing chamber is a vented chamber with the vent being at the top position (12 o'clock) and the scavenge port at the bottom position. The chamber is sealed by a straight labyrinth seal. The bearing has an inner land riding cage and under-race lubrication has been applied. The oil is not directly spread into the rolling elements but is supplied through eighteen 1 mm holes facing the cage from both sides of the bearing. Two oil nozzles supply oil to the forward and rear holes (Fig. 1*a*). The condition of the bearing was monitored by accelerometers, chip detectors, and thermocouples. The latter recorded the temperature of the outer ring at different circumferential locations. The heat rejection of the bearing was monitored by thermocouples, which recorded the temperature of the oil leaving the bearing. Pressure transducers were used to monitor the chamber pressure. Additionally, the torque on the bearing shaft was measured. Torque measurements were used to assess the power consumption of the bearing and therefore enable comparisons among different operating conditions. The oil flow was varied between 15 L/h and 450 L/h, the sealing air flow between 6 kg/h and 100 kg/h, the chamber pressure between 0.9 bar and 4.8 bar, and the temperatures for air and oil were 80°C and 130°C. The shaft speed was varied between 6000 rpm and 19,000 rpm and the axial load between 4 kN and 22 kN. Mobil Jet II was the oil brand.

Contributed by the Structures and Dynamics Division of THE AMERICAN SOCIETY OF MECHANICAL ENGINEERS for publication in the ASME JOURNAL OF ENGINEERING FOR GAS TURBINES AND POWER. Manuscript received by the S&D Division May 30, 2003; final revision received Jan. 15, 2004. Associate Editor: N. Arakere.

2 Results

The bearing power consumption characteristic as a function of oil flow is shown in Fig. 2. Up to 200 L/h the behavior is nonlinear, then becomes linear up to 450 L/h and remains linear above 450 L/h. However, the slope becomes steeper. The hereby selected speed was 10,000 rpm, the oil/air inlet temperature was 130°C, the bearing load 14.7 kN, and the bearing chamber pressure 1.1 bar. Based on the measurements the curve can be approximated between 200 L/h and 450 L/h by a linear function. The parameter P_0 is a value corresponding to 7.0 kW of power consumption and will be used throughout this paper as a value of making power non-dimensional and therefore enable comparisons. P_0 corresponds to a power consumption at 15,000 rpm, 14.7 kN thrust, 350 L/h oil flow, 2.6 bar bearing chamber pressure, and 80°C air and oil inlet temperature.

The bearing power consumption as a function of sealing air flow is shown in Fig. 3. The sealing air flow was varied between 20 kg/h and 100 kg/h, whereas the pressure in the chamber was maintained constant at 2.6 bar. The rotor speed was 15,000 rpm and the axial load on the bearing was 14.7 kN. The test was carried out for oil flows of 175 L/h and 350 L/h, respectively. The measured power consumption at minimum air and oil flow, P_{ref}, was selected as the reference value so that the minimum nondimensional value in Fig. 3 (lower curve) is 1.0. For the oil flow of 175 L/h the power consumption increases between 20 kg/h and 100 kg/h by approximately 4.5% (lower curve). Similarly, for the oil flow of 350 L/h the power consumption increases between 20 kg/h and 100 kg/h by approximately 5.5% (upper curve). It is obvious from Fig. 3 that with decreasing sealing air flow (i.e., below 20 kg/h), maximum benefit in terms of power reduction can be expected. This can be achieved by the use of lower leakage seals (i.e., carbon seals). If the upper and the lower curves are compared (175 L/h vs 350 L/h oil flow) the difference in power consumption is approximately 11% at 20 kg/h and 12% at 100 kg/h sealing air flow.

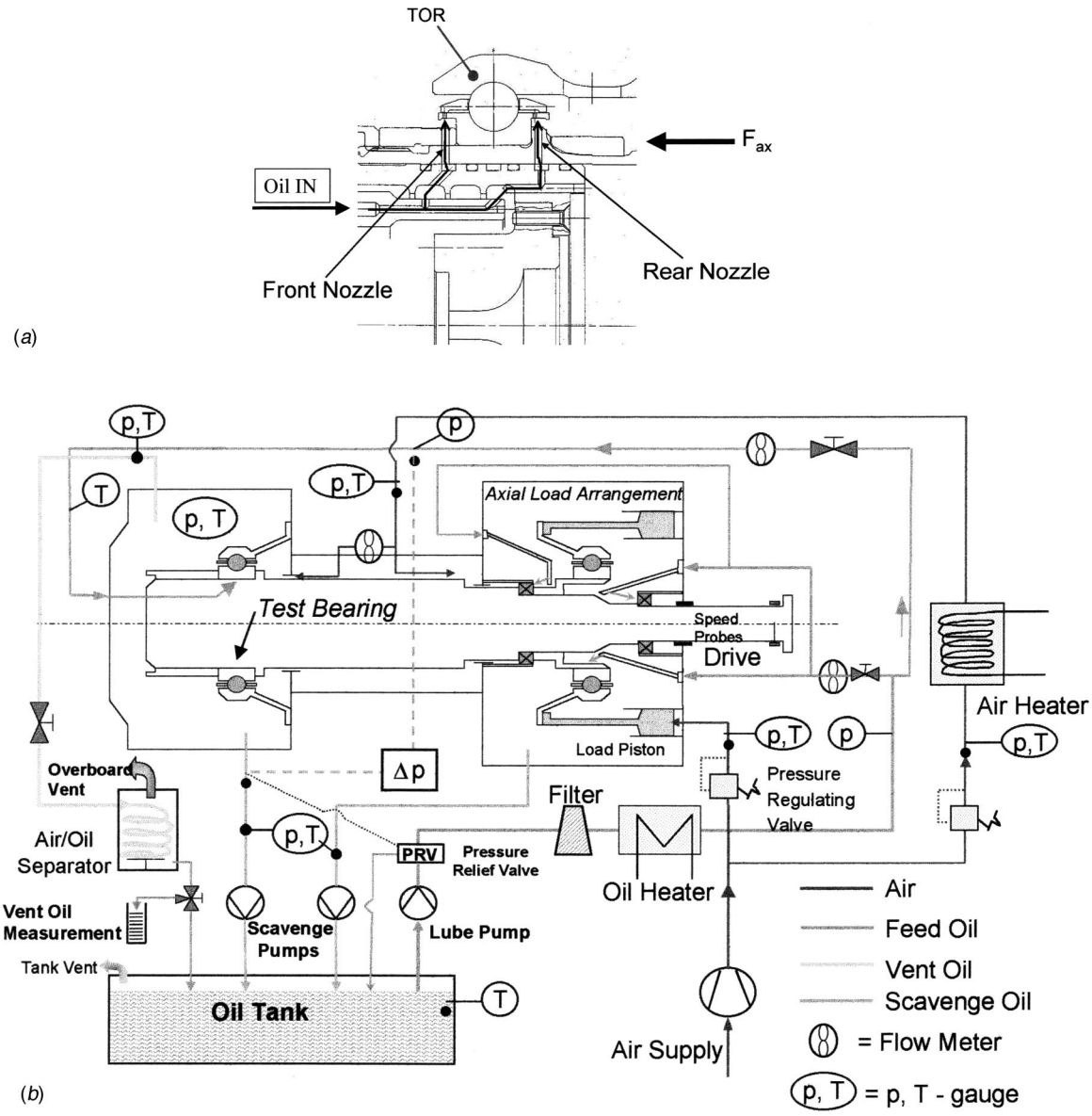

Fig. 1 (*a*) **Schematic of the ball bearing showing the oil supply via front and rear nozzle.** (*b*) **Bearing test facility.**

Figure 4 shows the dependence of bearing power consumption with oil, sealing air flow, and temperature. The five curves have been approximated in the range between 200 L/h and 450 L/h by linear functions as has already been explained above (Fig. 2). The second curve from the top is the one which includes the point P_0. If this curve is selected to be the baseline curve, then all other curves in Fig. 4 show relatively how the power consumption increases or decreases with the air and oil flow. Up to 13.3% less power consumption is between the reference curve and the bottom curve. At a constant temperature the reduction in power consumption between 80 kg/h and 20 kg/h is 6%.

Figure 5 demonstrates the impact of the bearing chamber pressure at temperatures of 80°C and 130°C. A comparison between the top curve (highest pressure, lowest temperature) and the bottom curve (lowest pressure, lowest temperature) yields to a power consumption reduction of 14%. A comparison of the curves at 80°C and pressures of 4.8 bar and 2.6 bar, respectively, yields to a decrease of 2.8% whereas at 130°C the difference is 1.9%.

The benefits of low air flow, low bearing chamber pressure, and low oil flow become more evident with increasing rotor speed. This is depicted in Fig. 6. Comparing the maximum values at 100% rotor speed (19,400 rpm) the difference in power consumption between the top and the bottom curve is 31%. A comparison between the curves at 350 L/h oil flow and 80 kg/h or 6 kg/h sealing air flow shows a reduction in power consumption of 19%.

Figure 7 shows the results of the investigation for the power consumption as a function of the axial load. Again the impact of the sealing air flow and of the chamber pressure is obvious. A comparison between the curves at 80 kg/h and 6 kg/h results to a difference of 18%.

Consequently a bearing at 15,000 rpm, 28 kN axial load, 6 kg/h, and 200 L/h air and oil flow at a chamber pressure of 0.9 bar (bottom curve) would consume the same amount of power like the same bearing at 15,000 rpm, 80 kg/h air flow, 350 L/h oil flow, 2.6 bar chamber pressure, and about 18 kN of axial load.

3 Conclusions

The power consumption in a bearing chamber is considerably affected by the operating conditions such as oil and sealing air

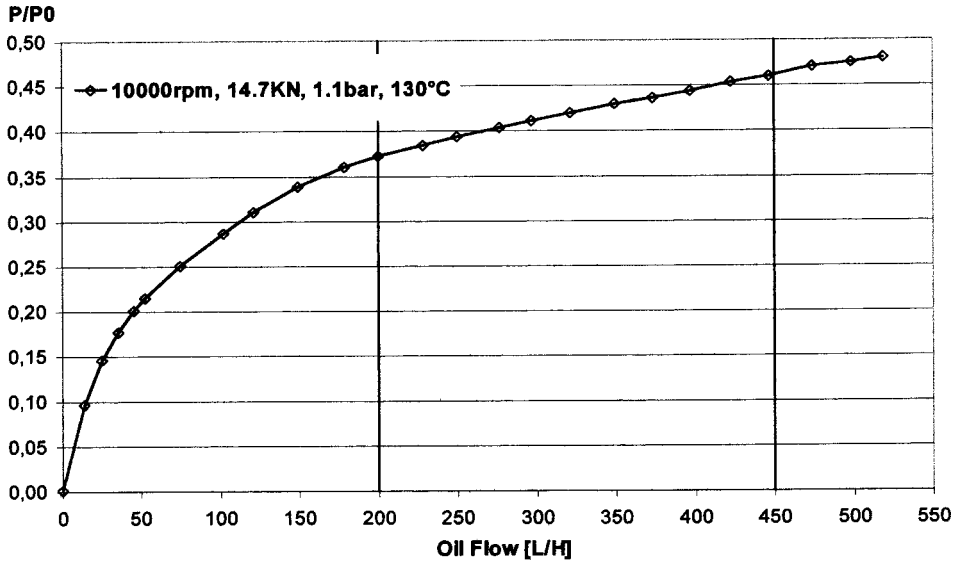

Fig. 2 Bearing power consumption characteristic as a function of the oil flow at 10,000 rpm, 14.7 kN axial load, 1.1 bar chamber pressure, and 130°C oil and air temperature

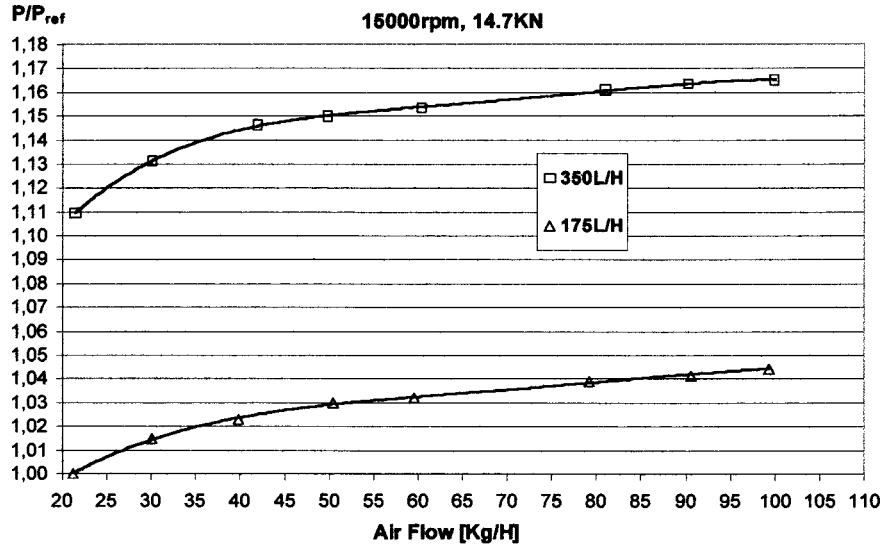

Fig. 3 Power consumption as a function of the air flow for two different oil flows

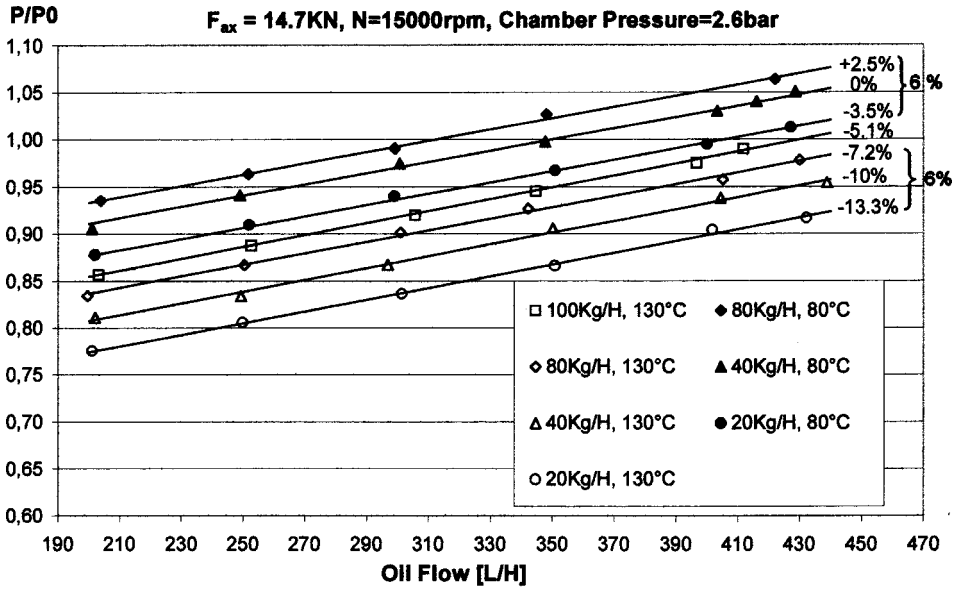

Fig. 4 Power consumption as a function of the air and oil flow at 80°C and 130°C

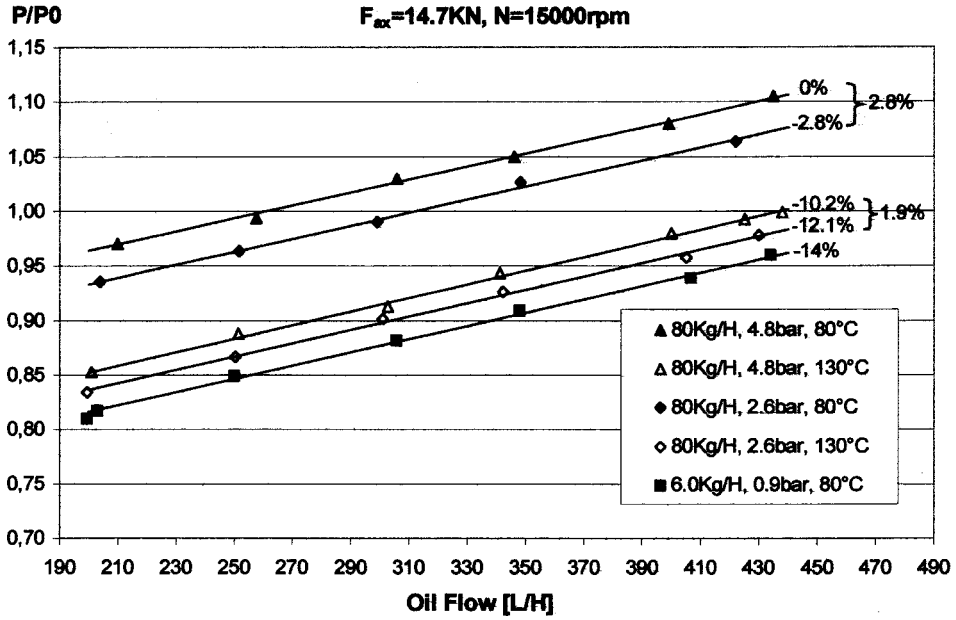

Fig. 5 Power consumption as a function of the bearing chamber pressure

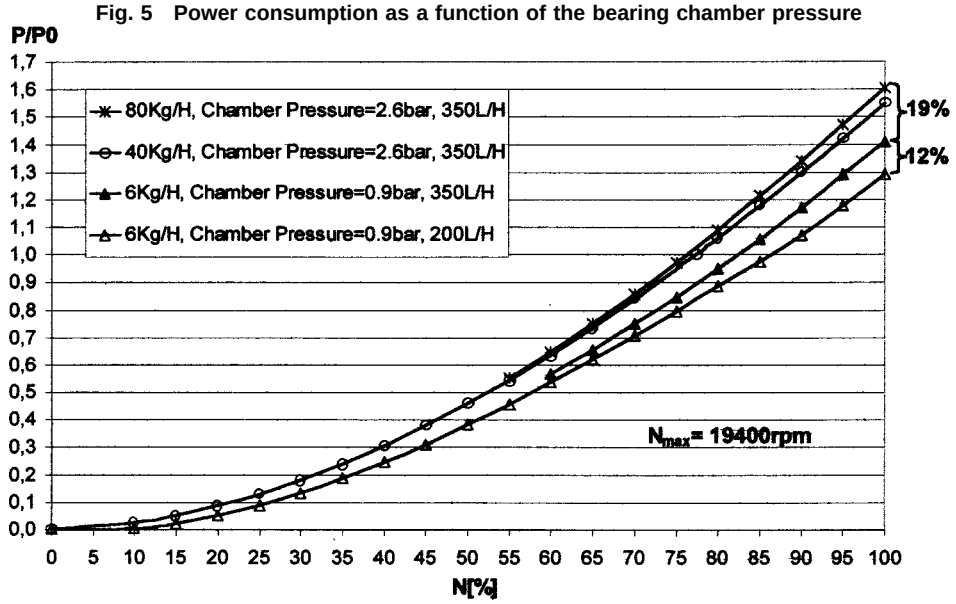

Fig. 6 Power consumption as a function of the rotational speed, air and oil flow, and chamber pressure

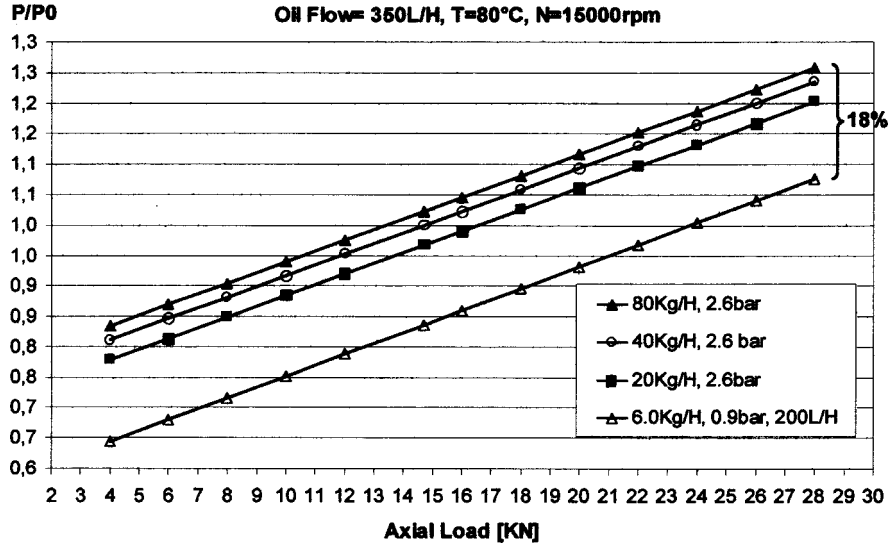

Fig. 7 Impact of axial load on bearing power consumption at different air flows

flow, temperature, chamber pressure, axial load, and rotor speed. However, the trend in modern aeroengines is towards higher rotor speeds. A reduction of the power consumption in bearing chambers can be achieved if the operating conditions are properly selected. The sealing air flow can be reduced, for example, by using carbon or windback seals. This could additionally lead to unvented chambers. The oil flow can be reduced by separating it into cooling and lubricating oil flow. However this demands a more sophisticated lubrication of the bearing which will not be discussed in this paper. Finally the chamber pressure could be maintained low by properly selecting the air source.

The optimization of a bearing chamber would lead to better engine performance since the losses can be considerably reduced leading to reduced mechanical or cost requirements on pumps, coolers, and piping.

Acknowledgment

The author and MTU Aero Engines gratefully acknowledge the support of the European Commission within the GROWTH Research Project ''Advanced Transmission and Oil System Concepts'' (ATOS), contract G4RD-CT-2000-00391.

Nomenclature

D = Bearing bore diameter
F_{ax} = Axial force on the bearing (axial load)
N = Rotor speed
p = Pressure
PCD = Pitch circle diameter
P = Power consumption
P_0 = Value corresponding to 7 kW of bearing power consumption
P_{ref} = Reference value for bearing power consumption at a chamber pressure of 2.6 bar, 15,000 rpm, 14.7 kN axial load, 20 kg/h sealing air flow, and 175 L/h oil flow
T = Temperature
TOR = Outer ring temperature
Δp = Differential pressure

Units for Flow

L/h = Liters per hour
kg/h = Kilograms per hour

Orifice Diameter Effects on Diesel Fuel Jet Flame Structure

Lyle M. Pickett
e-mail: lmpicke@sandia.gov

Dennis L. Siebers

Combustion Research Facility,
Sandia National Laboratories,
P.O. Box 969, MS 9053,
Livermore, CA 94551

The effects of orifice diameter on several aspects of diesel fuel jet flame structure were investigated in a constant-volume combustion vessel under heavy-duty direct-injection (DI) diesel engine conditions using Phillips research grade #2 diesel fuel and orifice diameters ranging from 45 μm to 180 μm. The overall flame structure was visualized with time-averaged OH chemiluminescence and soot luminosity images acquired during the quasi-steady portion of the diesel combustion event that occurs after the transient premixed burn is completed and the flame length is established. The lift-off length, defined as the farthest upstream location of high-temperature combustion, and the flame length were determined from the OH chemiluminescence images. In addition, relative changes in the amount of soot formed for various conditions were determined from the soot incandescence images. Combined with previous investigations of liquid-phase fuel penetration and spray development, the results show that air entrainment upstream of the lift-off length (relative to the amount of fuel injected) is very sensitive to orifice diameter. As orifice diameter decreases, the relative air entrainment upstream of the lift-off length increases significantly. The increased relative air entrainment results in a reduced overall average equivalence ratio in the fuel jet at the lift-off length and reduced soot luminosity downstream of the lift-off length. The reduced soot luminosity indicates that the amount of soot formed relative to the amount of fuel injected decreases with orifice diameter. The flame lengths determined from the images agree well with gas jet theory for momentum-driven nonpremixed turbulent flames. [DOI: 10.1115/1.1760525]

Introduction

The flame structure of spray-driven diesel fuel jets depends on many variables. For typical orifice diameters and injection pressures, a diesel fuel jet becomes a lifted turbulent diffusion flame after the autoignition phase is completed, and remains lifted through to the end of injection. The most upstream location of combustion on the fuel jet during injection is referred to as the lift-off length (or height). There is growing evidence to suggest that flame lift-off length plays a significant role in direct-injection (DI) diesel combustion and emission processes. The lifted flame allows fuel and air to premix prior to reaching the initial combustion zone in a diesel fuel jet (i.e., the lift-off length). Optical measurements by Dec and co-workers, [1], and modeling by Chomiak and Karlsson [2] suggest that this premixed fuel and air react in a fuel-rich reaction zone located in the central region of the fuel jet, just downstream of the lift-off length. This central reaction zone generates a significant local heat release and a high-temperature product gas, rich in unburned and/or partially reacted fuel. The product gas of the central reaction zone becomes the ''fuel'' for all remaining diesel combustion processes further downstream. Moreover, the product gas is ideal for forming soot under typical conditions in current diesel engines.

Recently, experimental investigations of the effects of ambient gas temperature and density, injection pressure, and orifice diameter on the flame lift-off length on a DI diesel fuel jet under quiescent conditions were conducted, [3–5]. The investigations showed that lift-off length decreases with increasing ambient gas temperature or density, and increases with increasing injection pressure or orifice diameter. Air entrainment estimates showed that the amount of fuel-air premixing upstream of the lift-off length was dependent on the magnitude of the lift-off length and/or the effects of the various parameters on the rate of air entrainment relative to the rate of fuel injection. An increase in injection pressure, for example, increased the amount of fuel-air premixing upstream of the lift-off length by increasing the lift-off length, thus allowing more axial distance for air entrainment. However, an increase in ambient gas density had little effect on fuel-air premixing upstream of the lift-off length due to a decrease in the lift-off length that effectively canceled the increase in air entrainment that occurs with an increase in the ambient gas density.

The fuel-air mixture at the lift-off length was shown to have a direct influence on the combustion processes in the reacting diesel jet, [3]. Soot incandescence measurements made with a photodiode, in particular, showed that there was a strong link between the fuel-air mixing upstream of the lift-off length and soot formation. Soot incandescence was observed to decrease as the amount of fuel-air premixing upstream of the lift-off length increased, with no significant soot incandescence (i.e., no significant soot) being observed when enough air was entrained to reduce the average equivalence ratio at the lift-off length to a value less than approximately two.

Furthermore, the recent lift-off length investigation showed that lift-off length was not very sensitive to changes in orifice diameter (d), with lift-off length having only a $d^{-0.3}$ to $d^{-0.4}$ dependence for orifice diameters in the range of 100–363 μm, [3]. However, the amount of air entrained upstream of the lift-off length was found to be strongly affected by orifice diameter due to the strong effect of orifice diameter on air entrainment relative to the amount of fuel being injected. The results suggested that air entrainment upstream of the lift-off length relative to the amount of fuel being injected is 4 to 5 times more sensitive to changes in orifice diameter than to changes in the injection pressure, suggesting that orifice diameter is a critical parameter with respect to diesel combustion.

In this study, several effects of orifice diameter on the diesel fuel jet flame structure were investigated at fixed ambient conditions (i.e., temperature and density). The overall flame structure was visualized through time-averaged OH chemiluminescence and soot incandescence imaging during the quasi-steady portion of the diesel combustion event that occurs after the transient pre-

Contributed by the Internal Combustion Engine Division of THE AMERICAN SOCIETY OF MECHANICAL ENGINEERS for publication in the ASME JOURNAL OF ENGINEERING FOR GAS TURBINES AND POWER. Manuscript received by the ICE Division June 2002; final revision received by the ASME Headquarters Aug. 2003. Associate Editor: D. Assanis.

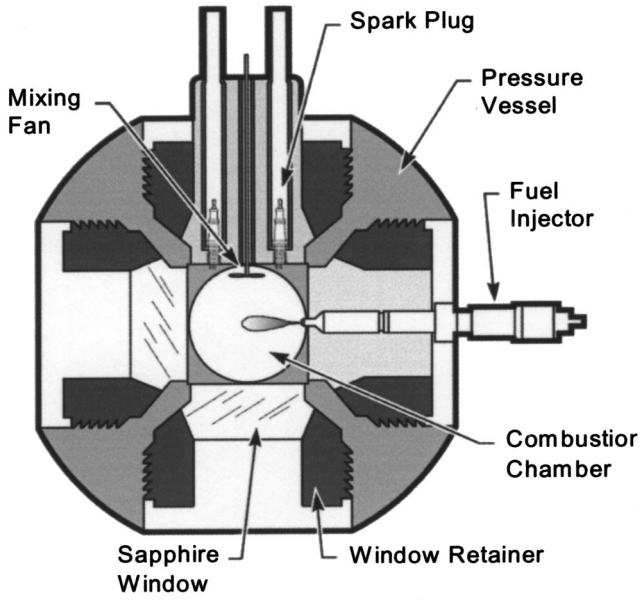

Fig. 1 Schematic cross section of the combustion vessel

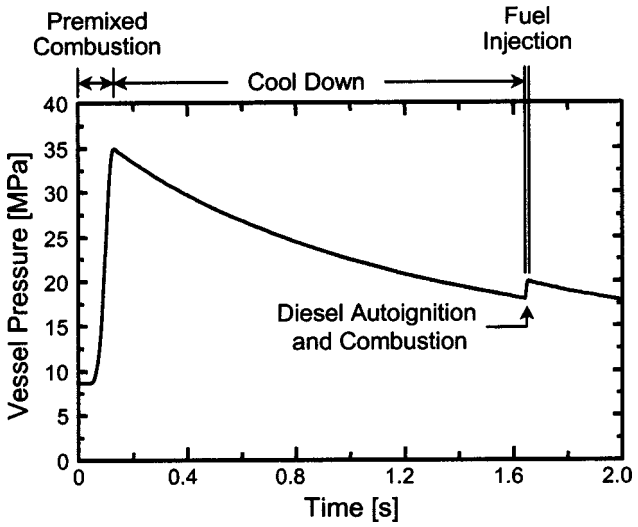

Fig. 2 Pressure history illustrating the diesel combustion simulation procedure in the combustion vessel

mixed burn is completed and the flame length is established. The images were analyzed to determine the lift-off length, total soot incandescence, and flame length (or height), giving a comprehensive overview of orifice diameter effects on DI diesel-type flames. Orifice diameters as small as 45 μm were considered in this investigation.

Experiment Apparatus and Procedure

The experiments were conducted under simulated, quiescent diesel engine conditions in a constant-volume combustion vessel. Figure 1 shows a schematic cross section of the combustion vessel. This combustion vessel is capable of withstanding gas pressures more than double those found in current-technology diesel engines, and can be used to simulate a wide range of in-cylinder thermodynamic conditions.

The combustion vessel has a cubical combustion chamber, 108 mm on a side. Each side of this combustion chamber has a round port with a diameter of 105 mm. The fuel injector is mounted in the right side port in a metal insert. Optical access is provided by sapphire windows located in four of the ports. Two windows are in the left side and the bottom ports of the vessel as shown in the figure. The other two windows form the front and back sides of the combustion chamber in the schematic. The windows permit full optical access into the vessel for optical diagnostics requiring either line-of-sight or orthogonal optical access. The top port in the vessel contains two spark plugs and a mixing fan mounted in a metal insert. The spark plugs and mixing fan are used in establishing the simulated diesel engine environment as discussed later.

The fuel injector used was an electronically controlled common-rail solenoid-activated injector capable of an injection duration from a fraction of a millisecond to several milliseconds. This injector opened and closed rapidly ($<$100 μs) and had a constant injection rate throughout the injection period, resulting in a top-hat injection-rate profile. A more detailed description of the experimental hardware can be found in Refs. [6–8].

The experimental procedure used to simulate diesel-fuel injection and combustion processes in the constant-volume combustion vessel, [6–10], is illustrated by the pressure history in Fig. 2. To summarize, the procedure is started by filling the vessel to a specified density with a premixed, combustible-gas mixture (prior to time zero in Fig. 2). This mixture is then ignited with the spark plugs shown in Fig. 1 and burned, creating a high-temperature high-pressure environment in the vessel (the pressure rise at approximately 0.1 seconds in Fig. 2). As the products of combustion cool over a relatively long time due to heat transfer to the vessel walls, the vessel pressure slowly decreases (between 0.15 and 1.6 seconds for the conditions in Fig. 2). When the desired pressure is reached, the diesel-fuel injector is triggered and the diesel fuel injection, autoignition and combustion processes ensue, as indicated by the pressure rise at a time of 1.65 seconds in Fig. 2.

Throughout an experiment, the mixing fan at the top of the combustion chamber (see Fig. 1) is run. This fan maintains a uniform temperature environment in the combustion vessel up to the time of diesel fuel injection, [6,7]. The gas velocities induced by the fan ($\sim$1 m/s) are insignificant in comparison to the velocity of the dense liquid fuel jet from the injector (typically, in excess of 250 m/s), [6,7]. As a result, the gases in the chamber can be considered quiescent relative to the fuel jet.

The temperature, density, and composition of the ambient gas in the vessel at the time of diesel-fuel injection can be varied widely with this simulation procedure. The ambient gas temperature and density at injection are determined by the ambient gas pressure at the time the fuel injector is triggered and the mass of the gas initially put in the vessel (a constant up to the time of the diesel injection event). The ambient composition is determined by the composition of the combustible-gas mixture burned to generate diesel-like temperatures and pressures. For these experiments, a combustible-gas mixture of 68.1% N_2, 28.4% O_2, 3.0% C_2H_2, and 0.5% H_2 (by volume) was used. The product composition of this combustible mixture simulated air, having a composition of 21.0% O_2, 69.3% N_2, 6.1% CO_2, and 3.6% H_2O (by volume) and a molecular weight of 29.47. Experimental and modeling investigations show that the differences between diesel jet processes (e.g., autoignition and fuel vaporization) in this simulated environment relative to those in air are negligible, [11–13].

A total of nine different orifices were used in the experiments. The orifice diameters and associated length-to-diameter aspect ratios are shown in Table 1. The orifices were oriented so that they were in line with the central axis of the injector. The inlet and outlet of the orifices were sharp edged. The pressure drop across

Table 1 Injector tip orifice diameters (d) and corresponding aspect ratios (l/d)

d (μm)	45	69	71	88	91	100	101	108	180
l/d	20.9	14.4	6.0	11.4	4.3	4.0	9.4	3.6	4.2

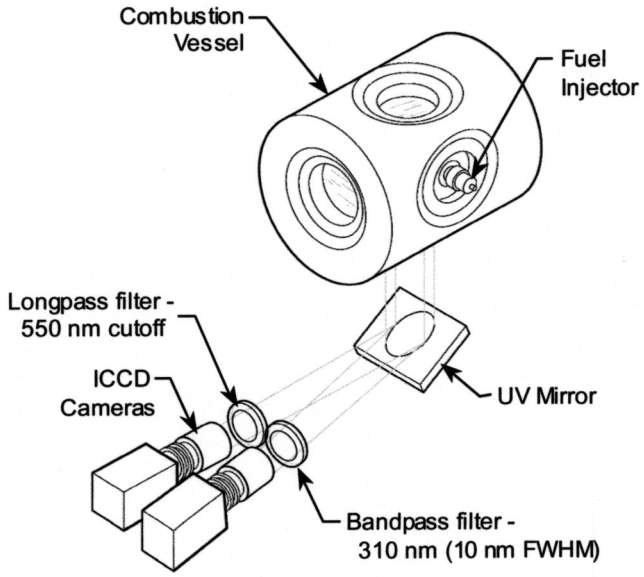

Fig. 3 Optical layout for OH chemiluminescence and soot incandescence imaging

the injector orifice was held constant at 138 MPa for all experiments. At these conditions, the measured discharge coefficient (C_d) and area contraction coefficient (C_a) for the 180-μm orifice are 0.77 and 0.82, respectively, while the same coefficients for the 100-μm orifice are 0.8 and 0.86, respectively, [11]. The coefficient values for the other seven orifices in Table 1 were assumed to be equal to those for the 100-μm orifice for purposes of making estimates of fuel jet air entrainment (to be discussed later). The assumed coefficients are typical of those previously measured for a similar group of sharp edged orifices with diameters ranging from 100 to 498 μm, [11]. The C_d and C_a for previous group of orifices ranged from 0.77 to 0.84 and from 0.79 to 0.88, respectively. This assumption does not significantly effect any interpretations made in this paper based on air entrainment estimates.

The fuel used in the experiments was a Phillips research grade #2 diesel fuel. The initial fuel temperature was 436 K. Relevant fuel properties are given in Ref. [11].

The injection duration depended upon the experiment. It was chosen to allow sufficient time for acquisition of time-averaged images of OH chemiluminescence and soot incandescence, as is discussed in more detail later. For the conditions studied, the ambient conditions (temperature and density) changed very little during the diesel combustion event.

Diagnostics and Measurements

OH chemiluminescence and soot incandescence images of each diesel fuel jet flame were acquired and used to visualize overall spatial features of the flame. In addition, the OH images were analyzed for lift-off length and flame length, and the soot incandescence images were used to determine a relative measure of the total soot incandescence for each diesel combustion event.

Image Acquisition. Simultaneous time-averaged, line-of-sight images of light emission at 310 nm (OH chemiluminescence) and between 550–700 nm (soot incandescence) were acquired with the two cameras shown in the optical setup in Fig. 3. Due to overall geometric constraints in the experimental setup, each camera was required to be two degrees off axis from the image plane. This had a negligible effect on the images. Both cameras used UV-Nikkor 105-mm, f/4.5 lenses with appropriate filtering. The filter in front of the camera used to image the 310-nm light was centered at 310 nm with a 10 nm bandwidth. A long-pass filter with a cutoff wavelength near 550 nm in front of the second camera, coupled with a fall off in the camera sensitivity at 700 nm provided images of light emitted in the 550–700 nm range.

The cameras were electronically gated, intensified CCD video cameras (Xybion ISG-250) with a pixel resolution of 760 by 480. The images were digitized with an 8-bit, 512 by 480 resolution frame grabber. A frame-transfer inhibit on the camera allowed the image acquisition to begin any selected time after the start of injection was detected.

The time-averaging was accomplished by gating the camera intensifier open for 3 ms for all images. The camera gate was started after autoignition was completed and the flame length was established, and ended prior to the end of injection. Use of a 3 ms gate allowed turbulent fluctuations in the fuel jet to be averaged, providing an image of the quasi-steady mean behavior of the jet. Near-instantaneous images (60 μs camera gate) at these conditions have shown that the features of the fuel jet flame fluctuate around the quasi-steady mean locations with fluctuations that are of the scale of fuel jet half-width, [4].

Measurement of Lift-Off Length. Research on lifted, turbulent-diffusion flames shows that stoichiometric or near stoichiometric combustion occurs at the flame stabilization location, [14], i.e., at the lift-off length. The energetic reactions and high temperatures that occur during stoichiometric combustion of typical hydrocarbon fuels form excited state species that include excited state OH (OH*), [15]. The primary kinetic path for forming OH* is the exothermic reaction $CH+O_2 \rightarrow CO+OH^*$, [15]. Once formed, OH* returns rapidly to its ground state, a portion through chemiluminescent emission and a portion through collisional quenching. The time scale for the chemiluminescence process is less than one microsecond, [15]. Since the chemiluminescence process is fast compared with transport processes, OH chemiluminescence provides an excellent marker of the location of high heat release regions, [16], such as the stoichiometric combustion region at the lift-off length.

One of the, strongest bands of OH chemiluminescence occurs near 310 nm [15]. Previous measurements near the flame lift-off region on a diesel fuel jet have shown that light emission at 310 nm is dominated by this band of OH chemiluminescence, [4]. Accordingly, images of light emission at 310 nm were analyzed to determine lift-off lengths in the current investigation in the manner discussed in Ref. [4]. A summary of the procedure is discussed below.

An example image of time-averaged natural light emission at 310 nm is shown in Fig. 4. The injector orifice is located at the left edge of the image. The pressure drop across the orifice and the orifice diameter were 138 MPa and 91 μm while the ambient-gas temperature and density at the time of injection were 1000 K and 30.0 kg/m^3.

The image in Fig. 4 shows that light emission at 310 nm begins at a well defined distance from the injector and extends downstream from there. The light emission at the upstream edge of this region is dominated by OH chemiluminescence with soot incandescence contributing somewhat to the light emission at 310 nm in the downstream direction, [4]. The bright lobes on the upper and lower edges at the upstream end of the fuel jet are caused by line-of-sight averaging of light emission from the ''cylindrical,'' stoichiometric mixing-controlled combustion zone (i.e., the turbulent diffusion flame) that surrounds the periphery of the diesel fuel jet, [1,17].

The semi-logarithmic plot in Fig. 4 of the relative maximum light intensity at 310 nm shows the well-defined rapid rise in light emission resulting in a ''knee'' in the intensity profile as labeled in the figure. As discussed in Ref. [4], a threshold intensity was set at an intensity value approximately equal to a 50% of the intensity at the knee. The lift-off length was then determined by finding the distances between the injector and the first axial locations above and below the fuel jet centerline with an intensity greater than the

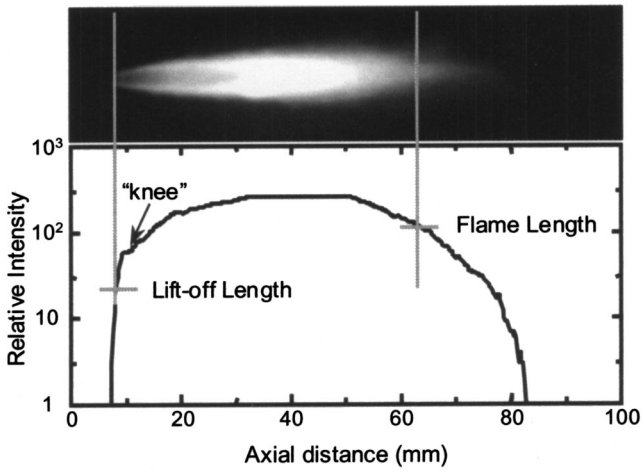

Fig. 4 OH chemiluminescence image (top) and centerline intensity profile (bottom). The image is a time-average of natural light emission at 310 nm from a burning diesel fuel jet injected into an ambient gas with a temperature and density of 1000 K and 30.0 kg/m^3. The pressure drop across the injector orifice and orifice diameter were 138 MPa and 91 μm. Fuel was injected toward the right from an orifice located at the center, left edge of the image.

threshold intensity. The average of these two axial distances is defined as the lift-off length. Due to the steep slope of the curve in the vicinity of the lift-off length, changes in either the camera gain or the threshold intensity had little effect on the measured lift-off length. Discussion in Ref. [4] indicates that the axial intensity at any location upstream of the ''knee'' in the time-averaged images is related to the probability that combustion is occurring at that location, with combustion occurring 100% of the time at the ''knee.'' This indicates that the threshold intensity selected, which falls in the middle of the steep region, occurs at a location where combustion is present approximately 50% of the time. In other words, the location corresponds to the mean upstreammost location of the fluctuating, turbulent, lifted flame.

Measurement of Soot Incandescence. At wavelengths between 550–700 nm it is expected that the light emission will be dominated by soot incandescence. The images of light emission between 550 and 700 nm (simultaneously acquired with the images of OH chemiluminescence) were thus used to assess the spatial locations of hot soot and to give a relative measurement of the amount of soot formed in the fuel jet.

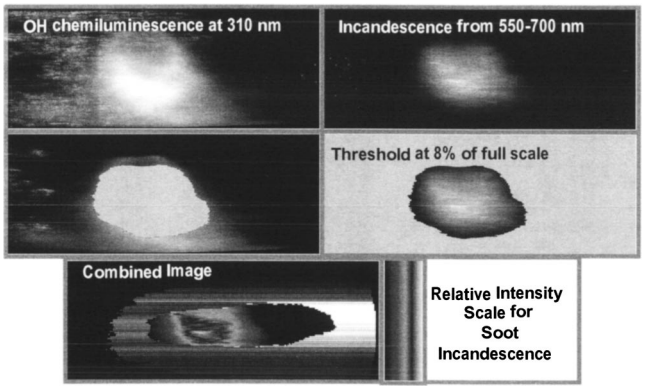

Fig. 5 Procedure for displaying OH chemiluminescence and soot incandescence images

In order to visualize the spatial locations of soot relative to the OH chemiluminescence, the two images were combined as demonstrated in Fig. 5. Shown in the top of Fig. 5 are OH chemiluminescence (top left) and soot incandescence (top right) images for the 101-μm diameter orifice. The other experimental conditions are the same as those given in Fig. 4 except that the ambient density was 14.8 kg/m^3. The soot incandescence image at the top right was thresholded at an intensity equal to 8% of the full-scale intensity and only pixels with intensities above the threshold were kept as shown in the middle image at the right of Fig. 5. The same image area retained in this process was subsequently removed from the OH chemiluminescence image as depicted in the middle left. The two images in the middle of Fig. 5 were then combined as shown at the bottom of Fig. 5. The intensities in the soot incandescence portion of the image are shown in a ''false'' color scale to differentiate them from the OH chemiluminescence portion of the combined image. The OH chemiluminescence was left in a gray scale, but doubled in the combined image in order to show boundary regions more clearly.

A measure of the total soot incandescence was obtained by integrating the soot incandescence image while accounting for the camera gain setting. This total soot incandescence measurement was used to examine the effect of orifice diameter on the amount of soot formed relative to the amount of fuel injected. Typically, soot incandescence cannot be directly related to soot concentration due to soot temperature and optical thickness changes with changing conditions. These issues and their impact on the interpretation of the soot incandescence data will be discussed in detail when the orifice diameter effects on the amount of soot formed are presented later in the paper.

Measurement of Flame Length. The flame length of diesel fuel jets has received little attention, because the actual full flame length is seldom, if ever, established in practical engine situations prior to impingement of the burning fuel jet on in-cylinder walls. However, with the small diameter orifices considered in this study, it was possible to resolve the flame length within the combustion vessel for some of the conditions considered in the current investigation. In typical applications of gas jets at atmospheric conditions, the flame length is an important parameter for air utilization and heat transfer considerations. In gas jets, flame length scales linearly with nozzle diameter, [18,19].

The flame length definition used for gas jets has typically been quite arbitrary. In some instances, the mean value was determined from instantaneous images of flame luminosity, [19], while in other cases the flame length was judged visually by an observer, [18]. In this study, we define the flame length as the location at the tip of the flame with an intensity equal to 50% of the maximum intensity in the time-averaged OH chemiluminescence image (see Fig. 4). The maximum intensity is typically found in the region preceding the tip of the flame (in Fig. 4, this region of maximum intensity is slightly saturated). Other definitions for flame length are clearly possible, but we found that the trends in the results were not very sensitive to the choice. As defined, the flame length determined from OH chemiluminescence approximately corresponds to the location where soot incandescence is no longer detectable in the simultaneously acquired soot incandescence images. As a result, this definition of flame length is believed to be comparable to the traditional visually defined flame length used with sooting, atmospheric pressure, hydrocarbon flames.

Review of Previous Diesel Fuel Jet Lift-Off Length Results

Shown in Fig. 6 are the effects of ambient gas temperature and density on lift-off length as given in Ref. [3]. The figure is a plot of lift-off length versus ambient gas temperature for four ambient

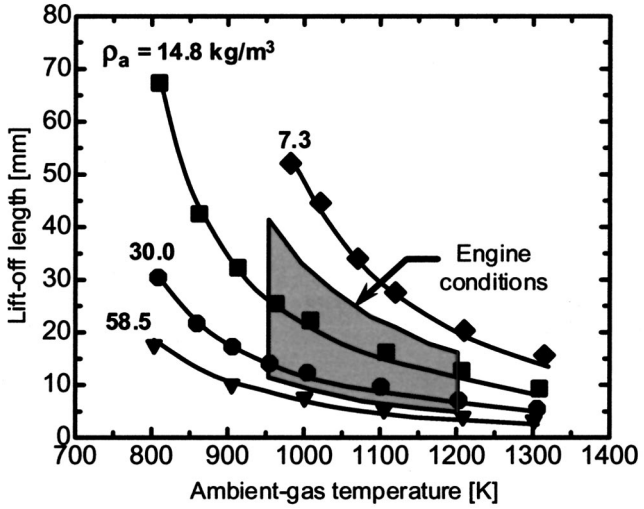

Fig. 6 Lift-off length versus ambient gas temperature for a range of ambient gas densities (ρ_a). The pressure drop across the injector orifice and orifice diameter were 138 MPa and 180 μm. The gray region represents the range of lift-off lengths expected in (quiescent) engines. The curves through the data represent the trends along lines of constant density. (Reproduced from Ref. [3].)

gas densities ranging from 7.3 to 58.5 kg/m^3. The orifice diameter and pressure drop across the orifice were 180 μm and 138 MPa, respectively. The curves through the data are trend lines included to help visualize the effects of temperature at each density. The gray region represents the estimated range of lift-off lengths expected in quiescent-type diesel engines after the premixed burn phase is completed, with a moderate-load, heavy-duty condition falling in the center of the gray region. Figure 6 shows that both ambient gas temperature and density have strong effects on the lift-off length.[1] As either parameter increases, the lift-off length decreases. The effects of both parameters are nonlinear, with the sensitivity of lift-off length to both parameters decreasing as they increase. The temperature and density dependencies noted are proportional to $T^{-3.74}$ and $\rho^{-0.85}$, respectively, based on fits of the data to power-law functions.

Although the trends shown in Fig. 6 indicate a strong effect of temperature and density on the physical dimension of the lift-off length, the data can also be considered in terms of the amount of fuel-air mixing that occurs prior to the initial combustion zone at the lift-off length. The fuel-air mixture at the lift-off length is believed to be important in combustion and pollutant formation processes that occur within the diesel fuel jet, as discussed in the Introduction. The changes in the fuel-air mixture at the lift-off length as a result of changes in operating conditions are therefore of great interest.

The quantity of air entrained prior to the lift-off length can be estimated using the expression for the axial variation of the cross-sectional average equivalence ratio in a fuel jet (ϕ), developed by Naber and Siebers [6]. The reciprocal of that equivalence ratio relationship ($\times 100$), when applied at the lift-off length, gives an expression for the air entrained up to the lift-off location as a percentage of the total air required to burn the fuel being injected. This percentage is defined as the percent of stoichiometric air (ζ_{st}), and is given by Eq. (1) below for ambient gas with an oxygen concentration of 21% (by volume) and diesel fuel that has an air-to-fuel stoichiometric mass ratio of approximately 15.

[1]The two lift-off lengths for the 58.5 kg/m^3 density and temperatures of 800 and 900 K are slightly less than presented in Ref. [3] due to a discrepancy found in the data reduction for lift-off length at those conditions.

$$\zeta_{st}(\%) \equiv \frac{100}{\phi} = \frac{10}{3} \cdot \left(\sqrt{1 + 16 \cdot \left(\frac{H}{x^+} \right)^2} - 1 \right) \tag{1}$$

In Eq. (1), H is lift-off length and x^+ is the characteristic length scale for the fuel jet, [6,11], defined by

$$x^+ = \sqrt{\frac{\rho_f}{\rho_a}} \cdot \frac{\sqrt{C_a} \cdot d}{a \cdot \tan(\theta/2)}. \tag{2}$$

In Eq. (2), the term d is the orifice diameter; C_a is the orifice area contraction coefficient; ρ_f and ρ_a are the injected fuel and ambient-gas densities, respectively; and $\theta/2$ is the measured spreading half-angle of the fuel jet, [11]. The value of the constant a is 0.75. (The value for a is different than the value of 0.66 previously recommended for a, [6]. The new recommendation for a results from new measurements of C_a for the orifices used in Ref. [6]. The new measurements were made with an improved technique for measuring C_a, [11].)

Equation (3) (from Ref. [11]) gives the fuel jet spreading half-angles as a function of the ambient gas to injected fuel density ratio.

$$\tan(\theta/2) = c \cdot \left[\left(\frac{\rho_a}{\rho_f} \right)^{0.19} - 0.0043 \cdot \sqrt{\frac{\rho_f}{\rho_a}} \right] \tag{3}$$

The equation was derived empirically from data for several orifices. The constant c in Eq. (3) is 0.271 and 0.255 for the 180-μm and 100-μm orifices, respectively. For the other seven orifice used in this investigation, the constant c is assumed to be 0.255, the value for the 100-μm orifice. This assumption does not significantly affect the estimation of ζ_{st} for the orifices considered. Equation (3) applies for vaporizing fuel jets, and therefore, applies up to the lift-off length.

The percent of stoichiometric air entrained up to the lift-off length determined with Eqs. (1)–(3) using the lift-off length data in Fig. 6 is plotted in Fig. 7. Figure 7 shows that there is a strong effect of temperature (for a constant density) on ζ_{st}, but little change in ζ_{st} with a change in density (for a constant temperature) indicating that the air-fuel mixture at the lift-off length is more sensitive to changes in temperature than ambient density. This trend is especially true over the range of potential conditions expected in a quiescent diesel after the transient premixed burn phase is completed and the lift-off length becomes established (10 to 45 kg/m^3 and 950 to 1200 K).

Results and Discussion

Lift-Off Length. The effect of orifice diameter on the lift-off length in the size range of 45–180 μm is shown in Fig. 8. Data are shown for ambient temperature and density combinations of 1000 K and 14.8 kg/m^3, 1100 K and 14.8 kg/m^3, and 1000 K and 30.0 kg/m^3.

In agreement with previous results for orifice diameters between 100 and 363 μm, [3], the lift-off length decreases slightly with decreasing orifice diameter. In addition, the lift-off length is shown to decrease with either increasing temperature or density, in agreement with previous results shown in Fig. 6, [3].

Figure 8 also shows the percent of stoichiometric air, ζ_{st}, entrained into the jet up to the lift-off length for the three sets of conditions based on Eqs. (1)–(3). Although the lift-off length decreases with decreasing orifice diameter, ζ_{st} increases quite dramatically as the orifice diameter becomes smaller for all sets of conditions considered. This increase in ζ_{st} is due to the strong dependence of air entrainment (relative to the fuel injection rate) on orifice diameter shown by Eqs. (1)–(2). The trends clearly indicate that although orifice diameter has a relatively weak effect on lift-off length, it has a strong impact on the amount of fuel-air mixing that occurs upstream of the lift-off length.

With respect to temperature and density effects on ζ_{st}, Fig. 8 shows that the amount of air entrained into the fuel jet is signifi-

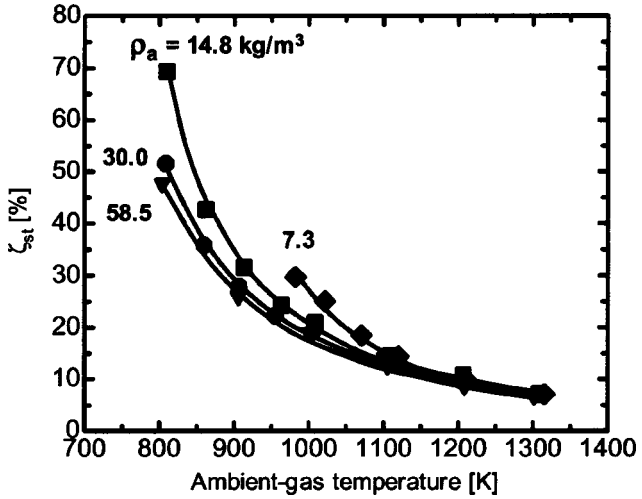

Fig. 7 The percent of stoichiometric air entrained up to the lift-off length versus the ambient gas temperature for a range of gas densities. The pressure drop across the injector orifice and orifice diameter were 138 MPa and 180 μm. (Reproduced from Ref. [3].)

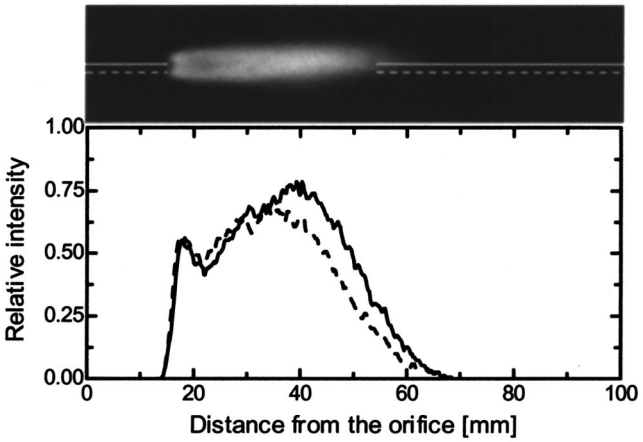

Fig. 9 OH chemiluminescence image and axial intensity profiles for 45 μm orifice with ζ_{st}[%]=58%. The ambient gas temperature, density and pressure drop across the injector orifice of 1000 K, 14.8 kg/m^3 and 138 MPa. The lines drawn on the image correspond to the radial location of the intensity profile shown in the plot below in the same line type.

cantly less for an ambient temperature of 1100 K compared to an ambient temperature of 1000 K. The smaller value for ζ_{st} results in combustion that is more fuel-rich just downstream of the lift-off length for the higher temperature condition. A smaller decrease in ζ_{st} is observed as density increases from 14.8 kg/m^3 to 30.0 kg/m^3 for a temperature of 1000 K. The small reduction in ζ_{st} with the density increase is consistent with the trend shown in Fig. 7 at 1000 K.

Figure 8 indicates that for diameters as small as 45 μm, as much as 60% of the air required for complete combustion can be entrained into the fuel jet prior to the lift-off length for some conditions. Shown in Fig. 9 is a time-averaged OH chemiluminescence image for an orifice diameter of 45 μm and an ambient temperature and density of 1000 K and 14.8 kg/m^3. The percent of stoichiometric air at the lift-off length for this case was ζ_{st} =58%. Two axial intensity profiles for the image are plotted in the lower part of the figure. They are profiles along the line (dashed or solid) through the image on the top of the figure. The intensity profiles show a region of intense combustion occurring very near the lift-off length that results from the high levels of air-entrainment upstream of the lift-off length. The existence of the intense region of combustion just downstream of the lift-off length provides support for the "premixed combustion zone" hypothesized by Dec downstream of the lift-off length, [1], and modeled by Chomiak and Karlsson [2].

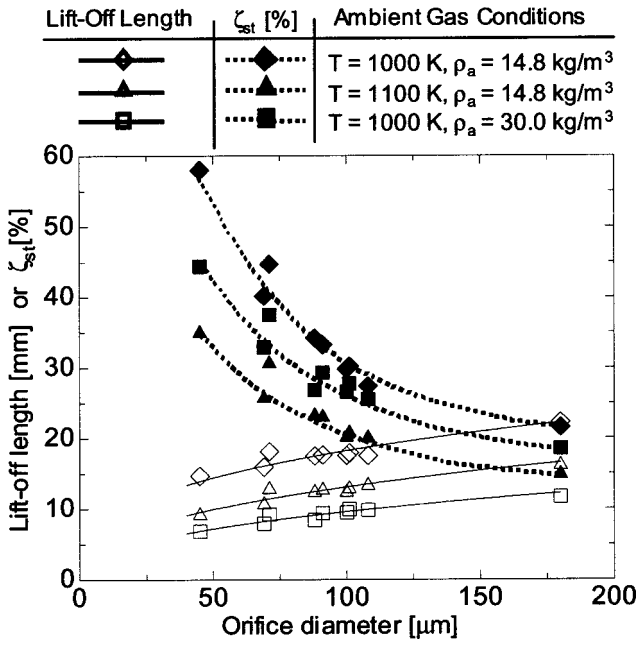

Fig. 8 Effect of orifice diameter on the lift-off length and the percent stoichiometric air entrainment ζ_{st}[%] upstream of the lift-off length. The curves through the data show the trends.

Soot Incandescence. Combined images of OH chemiluminescence and soot incandescence are shown in Fig. 10 for five different orifice diameters at a fixed ambient temperature of 1000 K and ambient density of 14.8 kg/m^3. The procedure for combining the images was illustrated in Fig. 5. The OH chemiluminescence is shown in gray scale while the soot incandescence is presented in a false color scale. Factored into the soot incandescence color scale for each image is the camera gain setting used for acquiring each respective soot incandescence image. The camera gain setting was decreased by more than a factor of 50 between the 45-μm and 180-μm orifices to prevent saturation of the soot incandescence images for the larger orifices.

A clear trend of reduced soot incandescence with decreasing orifice diameter is shown in the images, suggesting reduced soot formation with decreased orifice diameter. A significant fraction of the soot reduction with decreasing orifice diameter is believed to be the result of higher levels of air entrainment (relative to the amount of fuel injected) upstream of the lift-off length that occurs with decreasing orifice diameter, as was shown in Fig. 8. The trends agree with total soot incandescence measurements presented in Ref. [3]. (Note: A portion of the soot reduction is due to less fuel being injected with a smaller orifice diameter. This change in fueling with orifice diameter will be accounted for at the end of this section.)

The combined OH chemiluminescence and soot incandescence images in Fig. 10 also provide insight on the combustion and soot formation regions downstream of the lift-off length. In all of the combined images in Fig. 10 there is a distinct region just downstream of the lift-off length with no luminous soot. In this region it is believed that soot formation and growth are beginning to occur in the hot products immediately downstream of the lift-off length. However, any soot particles formed in this region are still

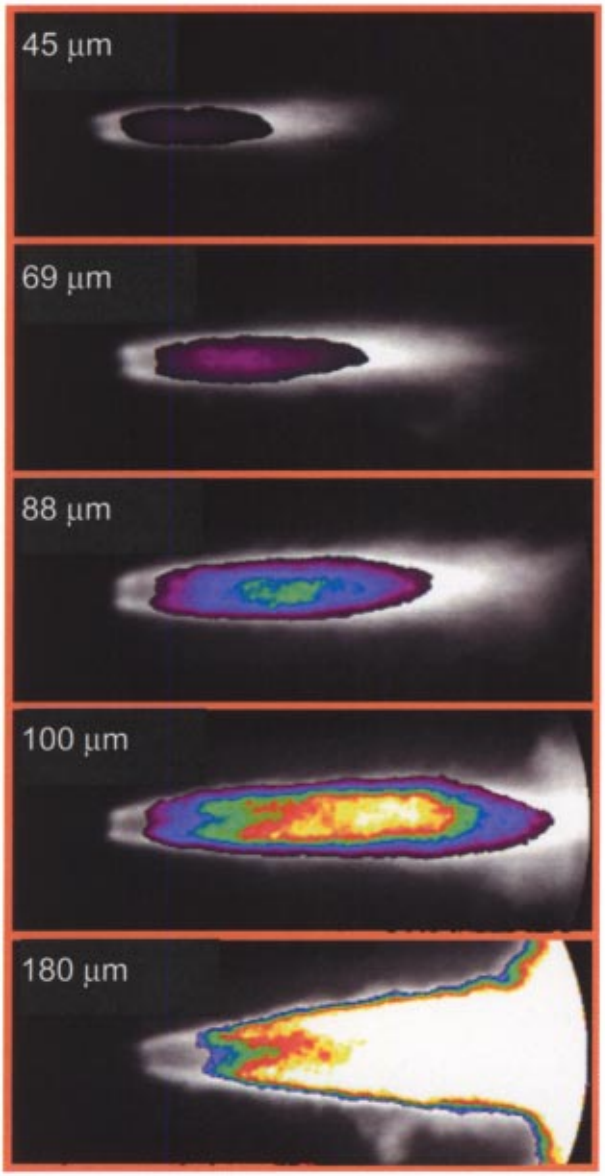

Fig. 10 Combined OH chemiluminescence and soot incandescence images. The OH chemiluminescence is plotted in gray-scale and the soot incandescence is plotted in relative intensity with the color scale given in Fig. 5. The horizontal size of the images is 100 mm and the orifice is located at the left edge of the image. The ambient gas temperature, density and pressure drop across the injector orifice were 1000 K, 14.8 kg/m^3, and 138 MPa. The orifice diameter is given in the upper left corner of the image.

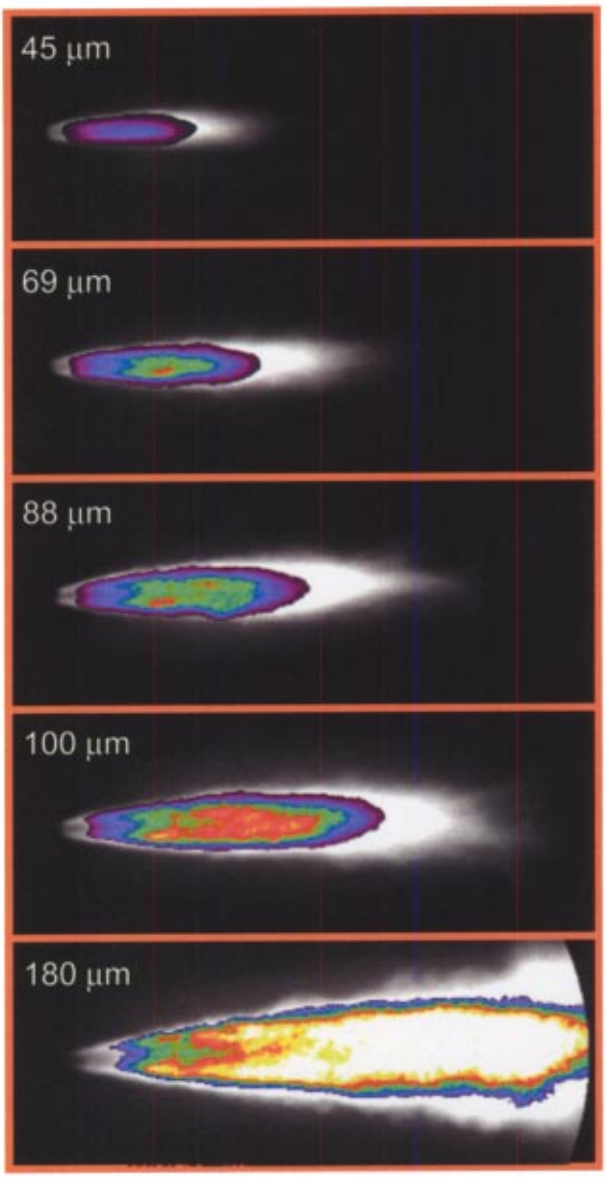

Fig. 11 Combined OH chemiluminescence and soot incandescence images. The OH chemiluminescence is plotted in gray-scale and the soot incandescence is plotted in relative intensity with the color scale equal to 1/2 that given in Fig. 5, i.e., the actual intensities are twice as bright as that shown in the figure. The horizontal size of the images is 100 mm and the orifice is located at the left edge of the image. The ambient gas temperature, density and pressure drop across the injector orifice were 1000 K, 30.0 kg/m^3, and 138 MPa. The orifice diameter is given in the upper left corner of the image.

too small, too low in concentration and/or too cool to emit much soot incandescence. This observation indicates that the images of 310-nm light in the lift-off region are dominated by OH chemiluminescence and are free of any signal due to soot incandescence. An additional observation is that the luminous soot region in the images is contained within the envelope of OH chemiluminescence at the periphery of the jet. This is most visible for the conditions for which the flame length is established prior to wall impingement. Here, the images show no detectable soot incandescence at the tip of the flame indicating that soot-oxidation processes have removed most, if not all, of the soot by the tip of the flame.

The effect of an ambient gas density increase to 30.0 kg/m^3 at an ambient temperature of 1000 K is shown in Fig. 11 for the five orifice diameters shown in Fig. 10. In Fig. 11, the relative soot incandescence intensity represented by the color scale is equal to 1/2 that in Figs. 5 and 10, i.e., the actual intensities are twice as bright as shown in Fig. 11. This modification was necessary because the soot volume-fraction increases in proportion to density (for a similar fuel-air mixture in the soot-forming region of the fuel jet), leading to an increase in local soot incandescence. The trend in reduced light emission from soot incandescence at smaller orifice diameters is again observed in Fig. 11, as would be suggested by the trend of increased relative air entrainment upstream of the lift-off length with reduced orifice diameter for this case (see Fig. 8). When compared with Fig. 10, Fig. 11 also shows

that flame length shortens with increasing density since the flame lengths are shorter for each corresponding orifice diameter in Fig. 11 than in Fig. 10. The flame lengths will be discussed in more detail in the next section.

The total soot incandescence at a given condition was obtained by spatially integrating the soot incandescence images while accounting for the camera gain setting. The integrated soot incandescence value was then normalized by the orifice diameter squared to account for differences in the amount of fuel injected with different orifice diameters. The relative changes in the normalized soot incandescence with orifice diameter for fixed ambient conditions were then used as a relative measure of changes in the amount of soot formed within the fuel jet as a function of orifice diameter. As stated previously, soot incandescence changes typically cannot be easily related to soot concentration changes due to soot temperature and optical thickness changes with changing conditions. However, for a fixed set of ambient gas conditions, the soot temperature and optical thickness changes with changing orifice diameter can be argued to be small and/or result in a conservative interpretation of the data (i.e., greater changes in soot concentration will occur than are indicated by the changes in the soot incandescence), as will be discussed next.

Changes in soot temperature with changing orifice diameter (for fixed ambient conditions) should be small because the adiabatic flame temperature in the stoichiometric, mixing-controlled combustion layer surrounding the burning fuel jet should not change significantly with orifice diameter. An expected increase in the soot temperature in the central region of the fuel jet as a result of a decrease in the equivalence ratio in the rich, central reaction zone with a decrease in orifice diameter should not be a significant factor, since the temperature in this central region should be considerably lower than the temperature near the mixing-controlled combustion layer at the fuel jet periphery. Furthermore, any increase in soot incandescence due to the higher temperatures as orifice diameter decreases would only tend to mask the actual soot reduction with decreasing orifice diameter.

With respect to optical thickness, an increase in the optical thickness of the fuel jet with increasing orifice diameter (for fixed ambient conditions) will occur due to more soot being formed as more fuel is injected. The greater optical thickness will cause the soot incandescence signal to increasingly underrepresent the true amount of soot within the fuel jet as orifice diameter increases.

Two other factors will also contribute to the conservative nature of the interpretation of the soot incandescence signal. First, for larger diameter orifices, the fuel jet passes beyond the window aperture causing some portion of the total incandescence to be uncollected by the camera. This uncollected incandescence will lead to an additional underrepresentation of the actual amount of soot formed for the largest orifice diameters. Second, since soot levels are low for the smaller orifice diameters, chemiluminescence in the 550–700 nm wavelength range (e.g., from C_2) is likely to become a larger fraction of the light collected, again masking actual decreases in soot with decreasing orifice diameter.

Given the above discussion, it is reasonable to expect that the normalized total soot incandescence determined from the images will provide a conservative measure of the soot reduction with decreasing orifice diameter. The normalized total soot incandescence is shown in Fig. 12 as a function of orifice diameter for the three ambient gas temperature and density conditions considered. Consistent with the trends shown in the individual images in Figs. 10 and 11, there is a significant decrease in normalized soot incandescence (i.e., soot) with decreasing orifice diameter for all conditions considered. (Note that direct comparison between the various ambient gas conditions is difficult because significant changes in the soot temperature may occur with these changes, masking any changes in soot concentration.)

When the normalized total soot incandescence is plotted versus the percent of stoichiometric air entrainment, ζ_{st}, as is shown in Fig. 13, the total soot incandescence can be seen to decrease with increasing air entrainment upstream of the lift-off length (relative to the amount of fuel being injected). This trend strongly indicates soot formation per unit of fuel injected is reduced as the relative air entrainment upstream of the lift-off length increases, supporting the concept of a link between soot formation and fuel-air mixing upstream of the lift-off length, [3].

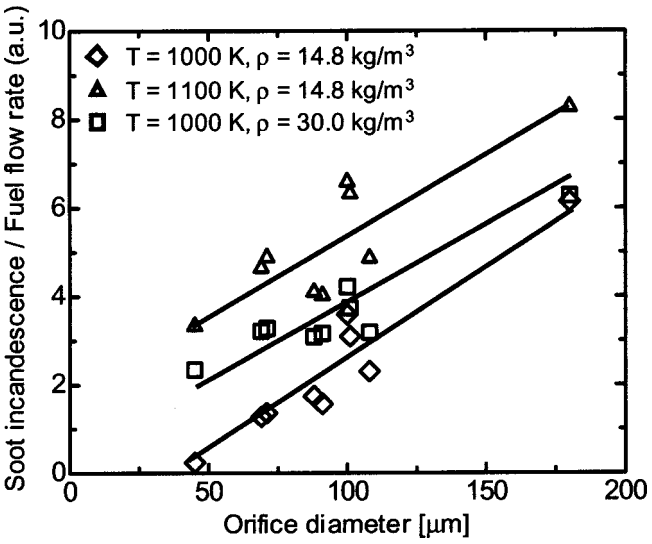

Fig. 12 Total soot incandescence normalized by fuel flow rate at various orifice diameters. The total soot incandescence was obtained by integrating across the entire soot incandescence image. For all cases the pressure drop across the orifice was 138 MPa.

Flame Length. As shown in Fig. 10 and Fig. 11, the tip of the flame is contained within the image area for most of the smaller orifice diameters. The volume that the fuel jet occupies is also small relative to the volume in the combustion chamber, and the ambient environment is considered quiescent relative to the fuel jet. The flame length, H_F, can therefore be analyzed from the images in terms of the orifice diameter and the ambient conditions. As discussed before, the flame length is defined as the location with an intensity equal to 50% of the maximum intensity in the OH chemiluminescence image (see Fig. 4).

Measured flame lengths normalized by orifice diameter are shown in Fig. 14 for a range of operating conditions. The figure shows that the normalized flame length appears to decrease slightly as orifice diameter increases. Also, a trend toward shorter flame lengths with increasing density is visible in the data.

The flame lengths presented in Fig. 14 can be compared to established theories for gas jet flame lengths. Previous research has shown that the flame length on a gas jet is proportional to the source diameter and independent of flow velocity for turbulent conditions, [19]. Buoyancy effects are usually important for typical gas jets. The Richardson number at the flame length determines if the flow is momentum-driven or buoyancy-driven, [18]. The Richardson number is defined as

$$\xi = \left(\frac{g}{U_0^2 \cdot d^2 \cdot (\rho_f / \rho_a)} \right)^{1/3} H_F . \tag{4}$$

The term g in Eq. (4) is the gravitational constant, U_0 is the velocity at the exit of the nozzle, ρ_f is the density of fuel, ρ_a is the density of the ambient, and H_F is the flame length, [18]. The flow becomes more momentum-driven as ξ approaches zero and buoyancy-driven as ξ becomes large. Becker and Liang, [18] proposed the following flame length correlation for the momentum-driven limit (some rearrangement of terms has been performed):

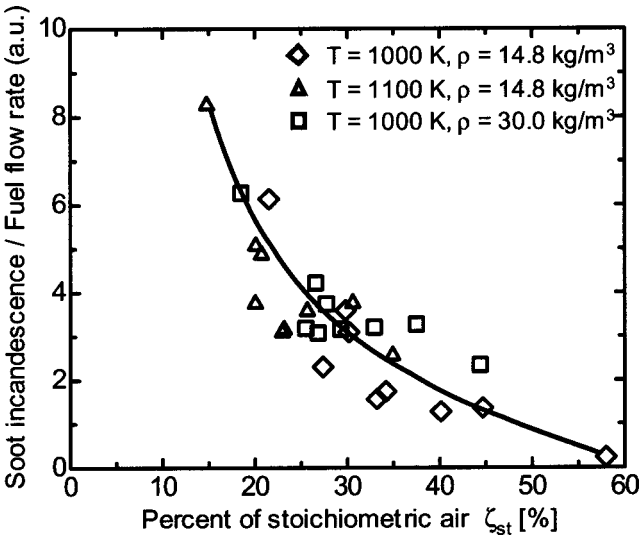

Fig. 13 Total soot incandescence normalized by fuel flow rate as a function of percent stoichiometric air ζ_{st}[%] entrained upstream of the lift-off length. The conditions are the same as given in Fig. 12.

$$H_F/d = C_H \cdot (\rho_f/\rho_a)^{1/2} \cdot \beta \cdot (1 + (A/F)_{st}) \qquad (5)$$

$$\beta = ((M_a \cdot T_{ad})/(M_{\text{prod}} \cdot T_a))^{1/2}.$$

The term C_H in Eq. (5) is the flame length coefficient, $(A/F)_{st}$ is the stoichiometric air-to-fuel mass ratio, M_a and T_a are the ambient gas molecular weight and temperature, M_{prod} and T_{ad} are the product gas molecular weight and adiabatic flame temperature.

Figure 15 shows the flame length coefficient, C_H, calculated with Eq. (5) using the measured flame length data shown in Fig. 14. The figure shows that the C_H falls between 4 and 6 for a wide range of orifice diameters and operating conditions. However, within this range of C_H, trends noted in the actual flame length

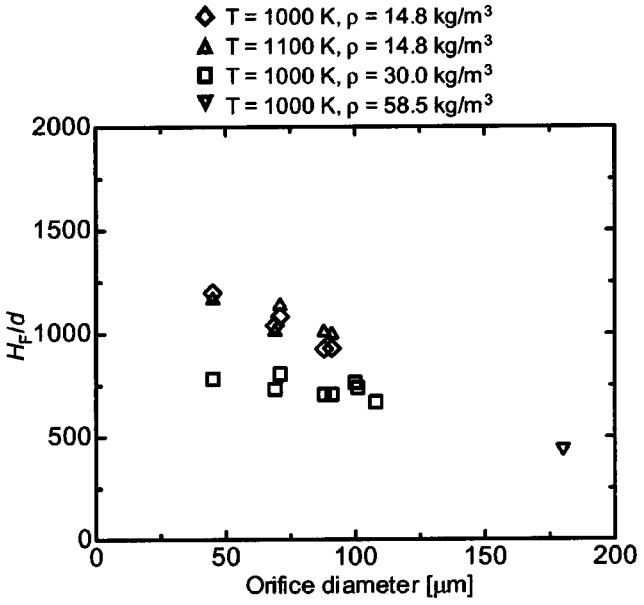

Fig. 14 Normalized flame length as a function of orifice diameter

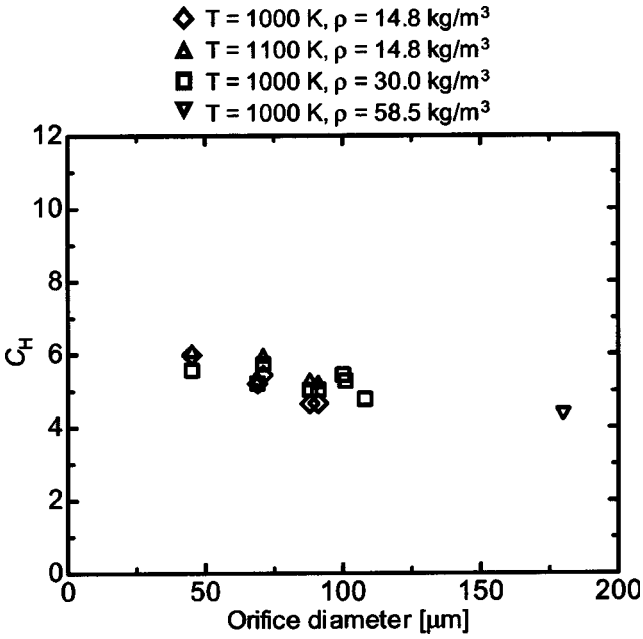

Fig. 15 Flame length coefficient, C_H, at various operating conditions derived from the measured flame lengths and Eq. (5)

data in Fig. 14 are still present. These trends include a slight decrease in C_H with increasing orifice diameter or ambient gas density.

Comparisons can be made to the C_H determined from gas jet experiments, but there is significant scatter in C_H from gas jets, and flame length correlations different than that given in Eq. (5) have been proposed. Becker and Liang [18] suggested a $C_H \approx 11$, while Kalghatgi [19] found $C_H \approx 6$. More recently, Heskestad [20] proposed a form similar to Eq. (5) but used an excess gas temperature in place of T_{ad} in Eq. (5) that was moderately lower than T_{ad}. Accounting for the difference in excess temperatures, Heskestad's results suggest $C_H \approx 8$. An earlier correlation proposed by Delichatsios [21] retained no dependency on flame or ambient temperature (i.e., the term β in Eq. (5)). Accounting for the difference between his recommendation and Eq. (5) suggests $C_H \approx 10$.

Based on the discussion in the previous paragraph, the results presented in Fig. 15 are in closest agreement with the recommendation of Kalghatgi. We note, however, that there is limited data in the momentum limit for gas jets and there remains some question about where the momentum limit begins based on the Richardson number, ξ. The experiments of Becker and Liang were performed at values of ξ as small as 1.2 while Kalghatgi conducted experiments with values of ξ as small as 0.8. For lower values of ξ, Kalghatgi found that C_H decreased significantly as ξ decreased, from approximately 8.5 to 6 as ξ decreased from 1.8 to 0.8. For comparison, a Richardson number estimated using Eq. (4) for typical conditions in our experiments is $\xi \approx 0.4$. This estimated Richardson number supports the agreement noted with Kalghatgi's results for his lowest Richardson number conditions. (Note that Eq. (4) is for a vertical flame but our injector is mounted horizontally. Thus, any effects of buoyancy on our fuel jet should be even less.)

Conclusions

The effects of orifice diameter on the structure of a diesel fuel jet flame were investigated at fixed ambient conditions (i.e., temperature and density) for orifice diameters ranging from 45 μm to 180 μm. The overall flame structure was visualized through time-averaged OH chemiluminescence and soot incandescence imaging

during the quasi-steady portion of the diesel injection. The lift-off length, defined as the farthest upstream location of high-temperature combustion, and the flame length were determined from the OH chemiluminescence images. The simultaneously acquired soot incandescence images were used as a relative measure of the amount of soot formed within the fuel jet and were combined with OH chemiluminescence images to show features of the reacting fuel jet structure. The following conclusions were reached in this study:

1. The lift-off length decreases slightly with decreasing orifice diameter but the estimated amount of air entrained prior to the lift-off length (relative to the amount of fuel injected) increases, resulting in a reduced overall average equivalence ratio in the initial combustion zone of the fuel jet.
2. Even when normalized by the fuel flow rate, the total soot incandescence significantly decreases as orifice diameter decreases for fixed ambient conditions. The soot reduction indicated by the decrease in soot incandescence was attributed to the higher levels of air entrainment prior to the lift-off length (relative to the amount of fuel injected) for smaller orifice diameters.
3. With smaller orifice diameters the flame length could be established within the combustion vessel. The measured flame lengths for these conditions are in general agreement with those suggested by the work of Kalghatgi [19] for momentum-driven gas jets. Only small differences between the two works were noted in the trends with respect to orifice diameter and ambient gas density.

Acknowledgments

Support for this research was provided by the U.S. Department of Energy, Office of Heavy-Duty Vehicle Technologies and Office of Advanced Automotive Technologies. The research was performed at the Combustion Research Facility, Sandia National Laboratories, Livermore, CA.

Nomenclature

$(A/F)_{st}$ = stoichiometric air-to-fuel mass ratio
c = constant in Eq. (3)
C_a = orifice area contraction coefficient
C_d = orifice discharge coefficient
C_H = flame length coefficient
d = orifice diameter
g = acceleration due to gravity
H_F = flame length or height
H = lift-off length or height
l = length of the orifice
M_a = molecular weight of the ambient gas
M_{prod} = molecular weight of the product gas
P = pressure
T = temperature
U_o = fuel velocity at orifice exit
x = axial coordinate of the fuel jet
x^+ = characteristic length scale defined by Eq. (2)
β = temperature parameter of Eq. (5)
ϕ = cross-sectional average equivalence ratio in fuel jet
$\theta/2$ = measured half-cone angle of the fuel jet
ρ = density
ζ_{st} = percent of stoichiometric air entrained into fuel jet (i.e., the air entrained normalized by the air required to burn the injected fuel)
ξ = Richardson number at the flame length

Subscripts

a = ambient gas
f = fuel

References

[1] Dec, J. E., 1997, ''A Conceptual Model of DI Diesel Combustion Based on Laser-Sheet Imaging,'' Trans. SAE, **106**, Sec. 3, pp. 1319–1348 (SAE Technical Paper 970873).
[2] Chomiak, J., and Karlsson, A., 1996, ''Flame Liftoff in Diesel Sprays,'' *Twenty-Sixth Symposium (International) on Combustion*, The Combustion Institute, Pittsburgh, pp. 2557–2504.
[3] Siebers, D. L., and Higgins, B., 2001, ''Flame Lift-Off on Direct-Injection Diesel Sprays Under Quiescent Conditions,'' SAE Technical Paper 2001-01-0530.
[4] Higgins, B. S., and Siebers, D. L., 2001, ''Measurement of the Flame Lift-Off Location on DI Diesel Sprays Using OH Chemiluminescence,'' SAE Technical Paper 2001-01-0918.
[5] Siebers, D. L., and Higgins, B. S., 2000, ''Effects of Injector Conditions on the Flame Lift-Off Length of DI Diesel Sprays,'' Conference on Thermofluidynamic Processes in Diesel Engines, Valencia, Spain, Sept. 14–15.
[6] Naber, J. D., and Siebers, D. L., 1996, ''Effects of Gas Density and Vaporization on Penetration and Dispersion of Diesel Sprays,'' Trans. SAE, **105**, Sec. 3, pp. 82–111 (SAE Technical Paper 960034).
[7] Siebers, D. L., 1998, ''Liquid-Phase Fuel Penetration in Diesel Sprays,'' Trans. SAE, **107**, Sec. 3, pp. 1205–1227 (SAE Technical Paper 980809).
[8] Siebers, D. L., 1985, ''Ignition Delay Characteristics of Alternative Diesel Fuels: Implications on Cetane Number,'' Trans. SAE, **94**, Sec. 7, pp. 673–686 (SAE Technical Paper 852102).
[9] Oren, D. C., Wahiduzzaman, S., and Ferguson, C. R., 1984, ''A Diesel Combustion Bomb: Proof of Concept,'' Trans. SAE, **93**, Sec. 5, pp. 945–960 (SAE Technical Paper 841358).
[10] Durrett, R. P., Oren, D. C., and Ferguson, C. R., 1987, ''A Multidimensional Data Set for Diesel Combustion Model Validation: I—Initial Conditions, Pressure History and Spray Shapes,'' SAE Technical Paper 872087.
[11] Siebers, D. L., 1999, ''Scaling Liquid-Phase Fuel Penetration in Diesel Sprays Based on Mixing-Limited Vaporization,'' SAE Technical Paper 1999-01-0528.
[12] Naber, J. D., Siebers, D. L., Caton, J. A., Westbrook, C. K., and Di Julio, S. S., 1994, ''Natural Gas Autoignition Under Diesel Conditions: Experiments and Chemical Kinetic Modeling,'' Trans. SAE, **103**, Sec. 4, pp. 1735–1753 (SAE Technical Paper 942034).
[13] Naber, J. D., and Siebers, D. L., 1998, ''Hydrogen Combustion Under Diesel Engine Conditions,'' Int. J. Hydrogen Energy, **23**(5), pp. 363–371.
[14] Peters, N., 2000, *Turbulent Combustion*, Cambridge University Press, Cambridge, UK.
[15] Gaydon, A. G., 1974, *The Spectroscopy of Flames*, Chapman and Hall, London.
[16] Crosley, D. R., and Dryer, M. J., 1982, ''Two-Dimensional Imaging of Laser-Induced Fluorescence in OH in a Flame,'' Proceedings of the International Conference on Lasers, Dec.
[17] Kosaka, H., Nishigaki, T., Kamimoto, T., Sano, T., Matsutani, A., and Harada, S., 1996, ''Simultaneous 2-D Imaging of OH Radicals and Soot in a Diesel Flame by Laser Sheet Techniques,'' Trans. SAE, **105**, Sec. 3, pp. 1184–1195 (SAE Technical Paper 960834).
[18] Becker, H. A., and Liang, D., 1978, ''Visible Length of Vertical Free Turbulent Diffusion Flames,'' Combust. Flame, **32**, pp. 115–137.
[19] Kalghatgi, G. T., 1984, ''Lift-Off Heights and Visible Flame Lengths of Vertical Turbulent Jet Diffusion Flames in Still Air,'' Combust. Flame, **41**, pp. 17–19.
[20] Heskestad, G., 1999, ''Turbulent Jet Diffusion Flames: Consolidation of Flame Height Data,'' Combust. Flame, **118**, pp. 51–60.
[21] Delichatsios, M. A., 1993, ''Transition From Momentum to Buoyancy-Controlled Turbulent Jet Diffusion Flames and Flame Height Relationships,'' Combust. Flame, **92**, pp. 349–364.

Main Bearing Friction and Thermal Interaction During the Early Seconds of Cold Engine Operation

Paul J. Shayler
Ford Motor Company,
Dunton Engineering Centre,
Basildon, Essex SS15 6EE, UK

Warren S. Baylis
Mechanical Engineering,
School of MMME,
University of Nottingham,
Nottingham, NG7 2RD United Kingdom

Michael Murphy
Ford Motor Company,
Mariners Whites Hill Stock,
Ingatestone,
Essex, CM4 9QD United Kingdom

Motoring tests have been carried out on an unloaded crankshaft to examine friction levels and the influence of local thermal conditions in and around the main bearings, at speeds covering the range of 200–1000 rev/min and from initial temperatures down to −20°C. The temperatures of the bearing oil film and the adjacent metal are strongly coupled. This directly influences the variation of friction with time during the early seconds of running. The possibility of lowering friction during this period by reducing the strength of the thermal coupling has been investigated. Heat conduction through the bearing shells can be reduced by raising the contact resistance at the rear surface of the shells, raising oil film temperature, and hence, reducing local oil viscosity. Experimental data and model predictions illustrate that a significant reduction in bearing friction can be achieved. [DOI: 10.1115/1.1804538]

1 Introduction

The study reported here is concerned with friction levels in the crankshaft main bearings, and specifically, the interaction between friction and local thermal conditions during the early seconds of cold engine operation. At low ambient temperatures, the initial viscosity of the oil films in the bearings is relatively high giving rise to high friction losses. This contributes to high levels of overall engine friction, which is a key factor controlling start times. When ambient temperature falls to a critical value, usually between −20 and −30°C, automotive diesels exhibit a substantial extension of start time before an unassisted idling condition is achieved. The reason is simply that the engine friction work initially exceeds the indicated work output. The startup cannot be completed until this inequality is reversed by the reduction in friction as the lubricating oil starts to warm up.

Levels of engine frictional resistance immediately after the start of engine cranking, and the subsequent decay of friction levels, have been studied through motoring tests in previous work [1]. Individual tests were carried out at a constant motoring speed. The variations of engine friction mean effective pressure (fmep) and the viscosity of the oil at a reference location, either in the sump or the main gallery, were determined from motoring torque and oil temperature measurements. A typical test result is plotted in Fig. 1 to illustrate that once quasisteady thermal conditions are established, the variation of engine friction follows a power-law dependence on oil viscosity determined at the reference location. The explanation for this relationship, indicated by line ''A'' in Fig. 1, is that after the first minute or so of operation, temperatures rise at similar rates throughout the engine as it warms up. The oil temperature rise determined at the reference point is sufficient to characterize the variation at other points.

During the first tens of seconds of engine operation, the power-law relationship between friction and oil viscosity does not hold. The variation of fmep during this transient decay period is identified by the label ''D'' in Fig. 1. The variation of fmep with time has been described [1] using

$$FR_t = 1 + (FR_I - 1)\exp(-t/\tau) \quad (1)$$

In Eq. (1), FR_t is the ratio of fmep at time t to the corresponding quasisteady value at the same viscosity. FR_I is the initial ratio, at the start of motoring, when the corresponding quasi-steady value is given by point ''C'' in Fig. 1. τ is the time constant for the decay. Friction teardown tests on several engines show qualitatively similar trends. At low temperatures and low motoring speeds, the piston group (which includes big end bearings) contributes most to the total friction. The crankshaft assembly (main bearings, thrust bearings, and oil seals) is generally the second largest contributor. Both the piston group and the crankshaft assembly exhibit similar friction characteristics to those of the complete engine, with an initial transient period during which friction levels fall eventually onto the power-law variation with bulk oil viscosity.

During the early seconds of engine operation, frictional dissipation at the rubbing surfaces raises the temperature of the oil films and the adjacent parts of the engine structure. The increase in film temperature lowers oil viscosity, and hence, reduces friction at the hydrodynamically lubricated surfaces. Hence, friction behavior and changes in local thermal conditions are strongly coupled. In addition, the high oil shear rates can give rise to a temporary shear viscosity loss, although the effect of shear rate is less significant than the film temperature. It follows that if the local oil film temperature is used as the reference temperature to evaluate oil viscosity, rather than the main gallery or sump temperature, the variation of fmep with changing oil viscosity might be characterized by a single power law relationship throughout both the initial transient and quasisteady periods of cold running.

The area around a crankshaft main bearing is reasonably accessible and thermocouples can be inserted relatively easily. The crankshaft assembly is the last remaining in a friction teardown test, making it the least difficult to isolate and motor independently. These features make it the natural choice for the investigation of friction and thermal interaction. The study was structured around three aims. First, to determine by experiment how main bearing friction depends on bearing oil film viscosity during cold running conditions. Second, to develop a computational model of thermal/friction interaction with a view to identifying the heat paths and sinks involved. Third, following from this, to examine the scope to accelerate friction decay rates during the

Contributed by the Internal Combustion Engine Division of THE AMERICAN SOCIETY OF MECHANICAL ENGINEERS for publication in the ASME JOURNAL OF ENGINEERING FOR GAS TURBINES AND POWER. Manuscript received by the ICE Division January 20, 2003; final revision received by the ASME Headquarters March 12, 2004. Associate Editor: D. Assanis.

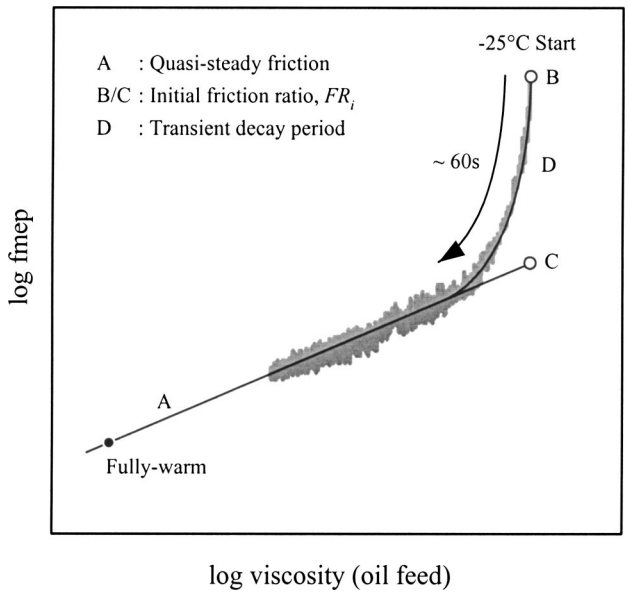

Fig. 1 Initial and quasisteady friction characteristics during engine warm-up phase

early seconds of engine warm-up operation by increasing the contact resistance at the outside surface of the bearing shells.

2 Experimental Investigation

A schematic diagram of the experimental apparatus is shown in Fig. 2. The refrigerated enclosure contained a crankshaft, main bearings and block assembly and could be cold soaked to any initial temperature down to −29°C. Two separate driveshafts were used to drive the crankshaft and the standard oil pump, both of which were driven by a direct current (dc) motor external to the enclosure via two toothed belts. The crankshaft had a torque tube transducer positioned in-line within the drive train. This enabled the crankshaft speed and motoring torque to be recorded as a function of time. The crankshaft was accelerated to the desired test speed within 2 s. The crankshaft was essentially unloaded since there was no gas loading. There is evidence indicating that when averaged over the engine cycle, the main bearing friction torque is effectively independent of engine load [2], and in the current study, the advantage of directly measuring crankshaft friction torque was the key consideration in the design of the test rig. Tests were carried out for crankshaft speeds of 200, 400, 600, 800, and 1000 rev/min. All tests were conducted from an initial cold soak temperature of −20°C. The grade of oil using in the study was SAE 10W-30. The engine components were from a four cylinder, 1.81 diesel. The crankshaft's five main bearings and two seals were retained in the test rig installation. The main bearing journals had a diameter, *D*, of 54 mm and the bearing lengths, *L*, were between 20 and 22 mm. The oil feed to each bearing fed a central oil groove in the upper shell. The groove was 2 mm wide and extended around the full, 180° arc of the shell. Under the low speed, low temperature test conditions investigated, the contribution of the end seals to the frictional torque of the crankshaft assembly was only a few percent of total and has therefore been neglected. Figure 3 shows a comparison of the motoring torques recorded with and without the seals, at 1000 rev/min and an initial temperature of −20°C. Two of the crankshaft bearing caps were instrumented with 0.5 mm diameter "*K*" type thermocouples as illustrated in Figs. 4(*a*) and 4(*b*). The first cap was used to measure the temperature distribution radially through the cap and the second cap was used to record the temperature distribution of the oil film around the lower half of the bearing circumference.

Tests were carried out on three sets of bearing shells. The average radial clearances of each set of bearing shells were determined by measuring the crankshaft journal diameters and the shell diameters separately using a coordinate measuring machine. The

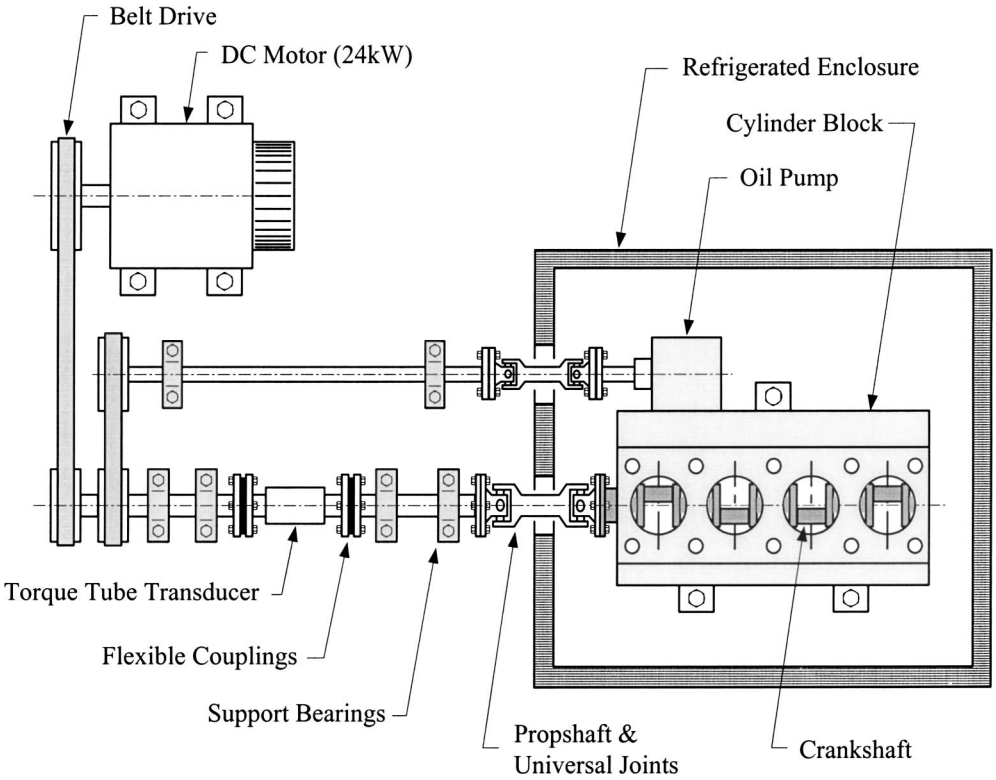

Fig. 2 Experimental apparatus used for crankshaft main bearing study

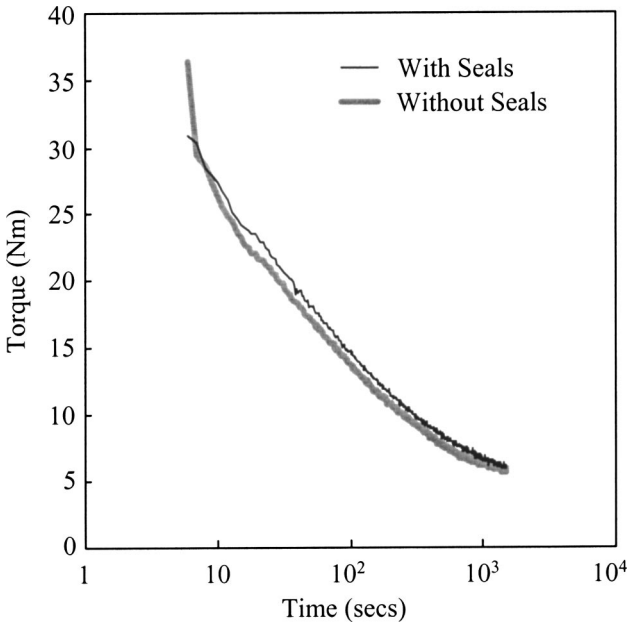

Fig. 3 Comparison of torque required to motor the crankshaft assembly with and without seals, at 1000 rev/min and starting at −20°C

shell diameters were measured after installation into the cylinder block with the bearing cap bolts tightened to the specified torque. The clearance determined by this method includes the increase which occurs when the shells are clamped. This increases the radial clearance by typically 5 μm. Measured values (at $T=20°C$) were 0.0066, 0.0269, and 0.0443 mm; these will be referred to as minimum, mean, and maximum clearances respectively. Changes in the bearing clearance depend upon the average temperatures of the block and crankshaft. The effect of temperature on bearing clearance has been quantified from measurements recorded on an identical block and crankshaft at two temperatures, +20 and +80°C. For this particular crankshaft and block arrangement, the diameter of the bearing journal changes at a rate that is typically 30% higher than the shell diameters located in the cast iron block. Hence, for modeling purposes, the radial bearing clearance at any given temperature is determined from the following equation:

$$c = c_{\text{amb}} - 0.3\frac{D}{2}[\alpha(T - T_{\text{amb}})] \tag{2}$$

where α is the coefficient of linear expansion for the crankshaft material.

The thermal coupling between the oil film and the surrounding metal, due to heat conduction into the bearing shells and the crankshaft journal, is apparent from the film and metal temperature variations shown in Fig. 5. The circumferential variation of oil film temperature taken around the lower half of the bearing cap circumference, is shown in Fig. 6. The data were recorded during a test at 1000 rev/min using shells with maximum clearance. During the first few seconds of the test, a significant temperature peak is observed at the location of thermocouple No. 2, close to the point where oil film thickness is likely to be a minimum. After 10 s into the test, however, the circumferential variation is negligible and film temperature is uniform.

3 Friction and Heat Transfer Model

The thermal coupling of friction and heat transfer reflects the way in which oil film temperature is dictated by the balance between frictional dissipation in and heat removal from the oil film.

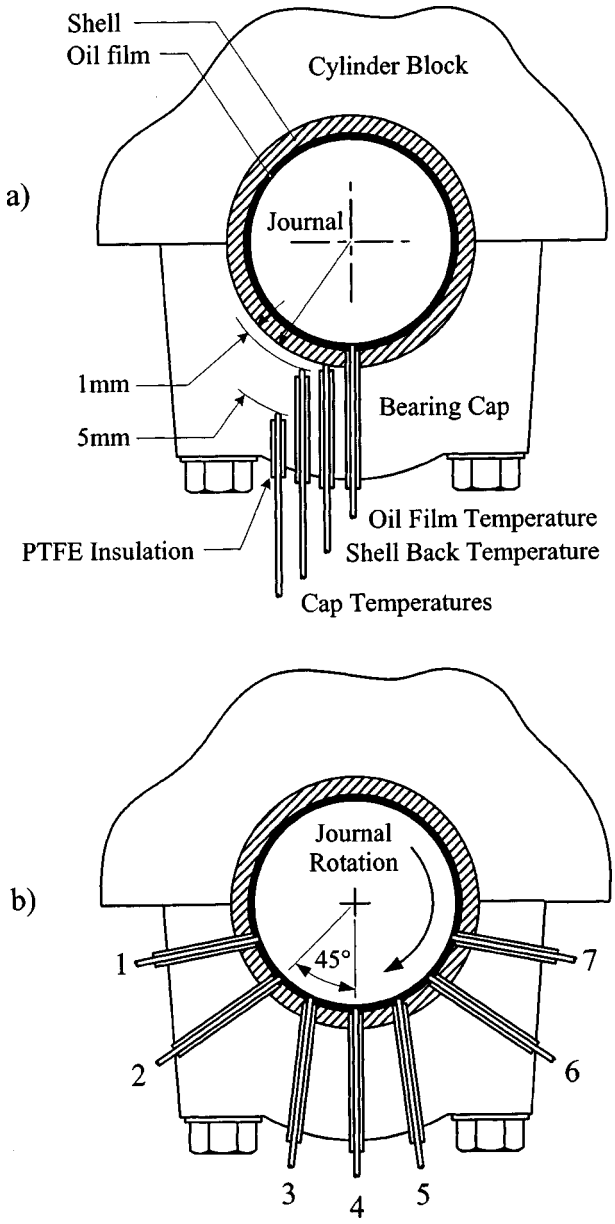

Fig. 4 Instrumentation of bearing caps, (*a*) thermocouple positions to measure temperatures through the shell/cap and (*b*) positions to measure temperature around the oil film circumference

The thermal capacity of the oil film in a journal bearing is sufficiently small to be considered insignificant. Energy conservation then requires

$$\dot{W} = \dot{Q}_{\text{shell,cap}} + \dot{Q}_{\text{shell,block}} + \dot{Q}_{\text{journal}} + \dot{m}C_p\Delta T_{\text{oil}} \tag{3}$$

$\dot{W}$ is the frictional power dissipated in the bearing, given by the product of bearing frictional force and relative surface velocity. The first three terms on the right hand side of Eq. (3) represent the heat flow from the oil film to the block shell, cap shell and journal respectively. The fourth term represents the net enthalpy out flow due to the flow of the oil film. Under cold-start conditions, this last mechanism of heat transfer is small in comparison to heat conduction to the local structure.

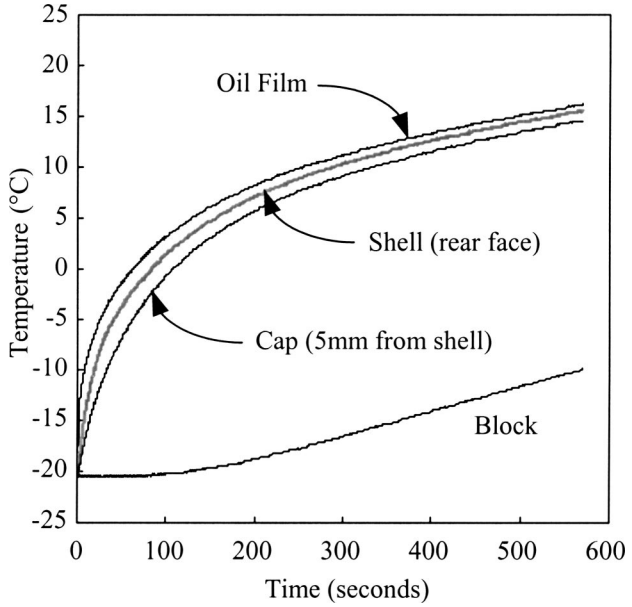

Fig. 5 Temperature variations with time of oil film, shell, cap and block during a typical motored crankshaft friction test from −20°C start

3.1 Friction Force. The description of friction force which follows has been developed by empirically modifying Petroff's equation in the form accounting for the dependence of friction force on eccentricity ratio, ϵ [3]:

$$F_{\text{force}} = \frac{\pi DLU\mu}{c\sqrt{(1-\epsilon^2)}} \tag{4}$$

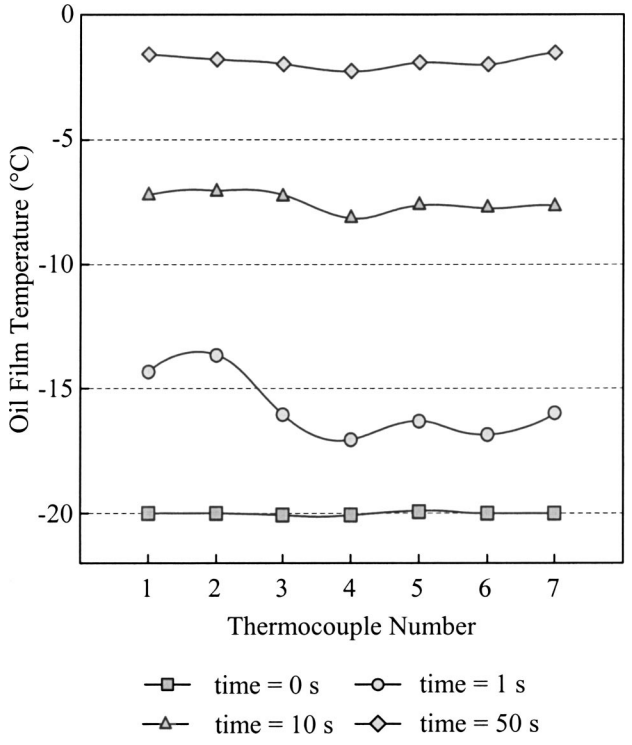

Fig. 6 Temperature variation of the oil film around lower bearing cap circumference, during a motored crankshaft friction test at a speed of 1000 rev/min from a start temperature of −20°C

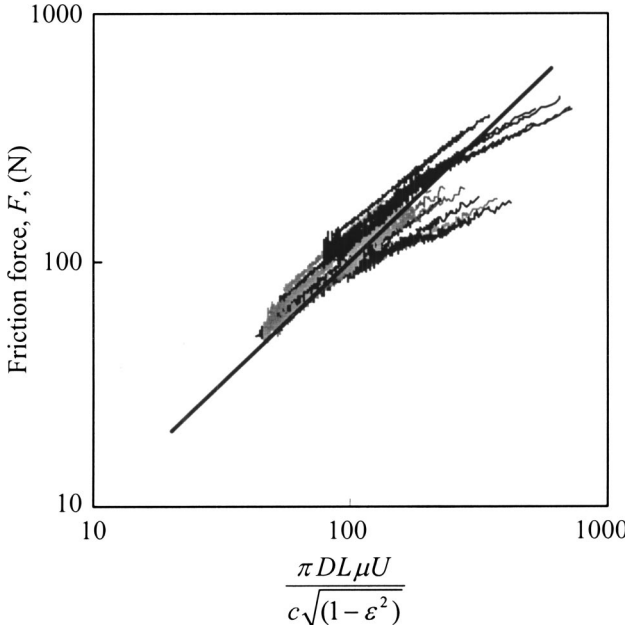

Fig. 7 Measured friction force versus values from Petroff's equation. Constant speed tests starting at −20°C. Data covers 200–1000 rev/min, and three base clearance levels.

The viscosity, μ, is an effective variable with a value which depends upon film temperature and shear rate, if the oil behaves as a non-Newtonian fluid. The value is determined from

$$\mu = \mu_0 \left[s + \frac{(1-s)}{(1+|\gamma/\gamma_c|)^m} \right] \tag{5}$$

This is derived from the Cross equation [4], and used here with constant m taken to be unity. According to Taylor [5], m is between 0.5 and 1.0 for most multigrade oils. The reference viscosity, μ_0, is calculated using the Vogel equation [3]:

$$\mu_0 = \kappa \exp\left(\frac{\theta_1}{\theta_2 + T_{\text{oil}}} \right) \tag{6}$$

which describes the temperature dependence of viscosity more accurately than the Walther equation [3]. For SAE 10W-30, the values of θ_1, θ_2, and κ are 1160, 125°C, and 0.059 (Pa s), respectively [6]. The shear rate, γ_c, at the point when oil viscosity is equal to the mean of zero shear and full shear values, is given by

$$\log_{10}(\gamma_c) = A + BT_{\text{oil}} \tag{7}$$

with $A = 3.5$ and $B = 0.02$ for SAE 10W-30, according to Ref. [5].

Equations (4)–(7) contain a number of approximations and uncertainties which could not be separately quantified in the experimental data. The three independent variables in the test matrix were the bearing surface speed, film temperature, and clearance. After the short, two second period required to accelerate the crankshaft up to the target speed, the crankshaft speed and therefore the bearing surface speed were constant throughout a test. The film temperature and clearance both varied during the test. The results obtained show

$$F_{\text{force}} \propto \frac{U^{0.6}\mu^{0.8}}{c} \tag{8}$$

where the values of the indices of U and μ differ from those in Eq. (4). The measured frictional force is plotted against the value given by Petroff's equation in Fig. 7. The eccentricity ratio, which was not measured here, has been assigned a relatively low constant value of 0.6 to reflect the unloaded test conditions. An ec-

centricity ratio of 0.6 equates to an attitude angle of 45 deg [3], which is consistent with the circumferential location of film peak temperature observed in the studies reported here. The change in clearance during a test has been evaluated from Eq. (2). The data covers tests for each base line clearance and each speed. The effect of clearance is accurately accounted for, but not the effect of relative bearing speed and this gives rise to the spread of the data. The indice of viscosity affects the gradient. After modifying the indices of U and μ, the agreement between predicted and measured values of F_{force} is greatly improved, as shown in Fig. 7, and for a single (unloaded) journal bearing the final result is given by

$$F_{\text{force}} \approx \beta \left(\frac{\pi D L U^{0.6} \mu^{0.8}}{c\sqrt{(1-0.6^2)}} \right) \tag{9}$$

where β is a constant required to maintain the unit of frictional force in Newtons and has a value of 1 $N^{0.2}/s^{0.2}$.

The dependence of friction force on viscosity raised to the power of 0.8 is at odds with the directly proportional relationship expected for journal bearings operating in the hydrodynamic regime. The difference is most probably due to inaccuracies in the modelling of viscosity characteristics. These were not determined for the particular SAE 10W-30 oil used in the test work, and the dependence of viscosity on shear rate and temperature are described using data drawn from the literature. The friction force could be made proportional to viscosity by relatively small adjustments to κ and θ_1 in Eq. (6), to 0.0472 Pa s and 928°C, respectively. Although noted here, the authors elected not to make these more arbitary adjustments.

3.2 Convection. The heat transport which takes place through convection is determined by assuming that the oil temperature rises linearly by dT_{oil}, between entry and exit from the bearing. Hence,

$$\dot{Q}_{\text{conv}} = \dot{V}_{\text{oil}} \rho C_p dT_{\text{oil}} \tag{10}$$

According to Cameron [3], short bearing theory describes the oil volumetric flow rate through the bearing as consisting of two components. The flow rate due to the pressure difference across the bearing is given by

$$\dot{V}_{\text{bearing}} = 0.3\left(2 - \frac{L}{D}\right) UcL \tag{11}$$

and the flow rate due to the feed pressure is given by

$$\dot{V}_{\text{feed}} = \frac{\pi D c^3 P_{\text{pump}}}{6\mu L} \tag{12}$$

Equation (12) is the case for a bearing with a central oil feed groove extending 180 deg around the circumference. P_{pump} is the gauge oil feed pressure. The total given by

$$\dot{V}_{\text{oil}} = \dot{V}_{\text{bearing}} + \dot{V}_{\text{feed}} \tag{13}$$

is in agreement with flow rates measured by collecting the discharge flow from the bearings under similar, steady state motored conditions [7].

3.3 Heat Conduction. Heat conduction through the bearing shells outwards into the bearing cap/cylinder block, and inwards into the journal are the main paths of heat removal from the oil film during the early seconds of operation. This is modeled as a one-dimensional (1D), transient heat conduction problem using cylindrical elements concentric with the bearing as shown in Fig. 8. The outer most bearing cap and cylinder block elements are thermally coupled to lumped elements representing the cap and those parts of the block which act as a heat sink with a temperature which changes relatively slowly. This is shown in Fig. 9. The finite difference formulation for any internal node is given by

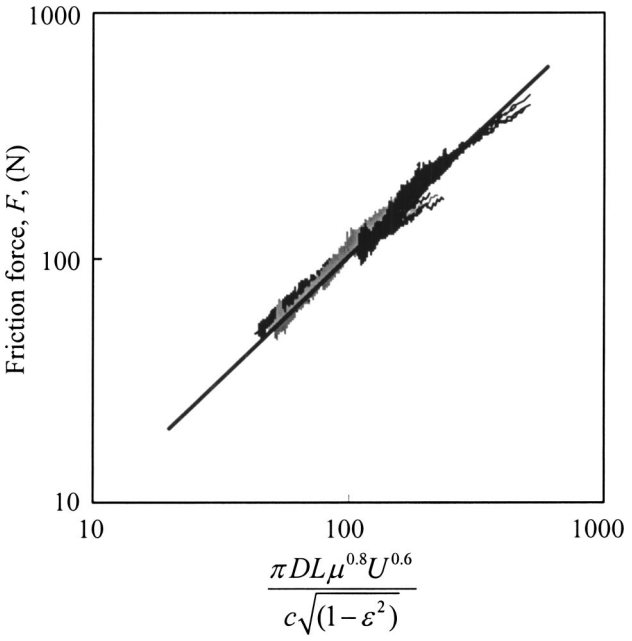

Fig. 8 Measured friction force versus modified prediction, Eq. (9). Data plotted covers the same tests as Fig. 7.

$$T_i' = Fo\left[T_{i+1}\left(1 + \frac{dr}{2r_i}\right) + T_{i-1}\left(1 + \frac{dr}{2r_i}\right) + T_i\left(\frac{1}{Fo} - 2\right)\right] \tag{14}$$

The formulation for any boundary node, in this case for the oil film contact, is given by

$$T_i' = Fo\left\{ T_{i+1}\left(2 - \frac{dr}{r_i}\right) + \frac{2hdrT_{\text{oil}}}{k} + T_i\left[\frac{1}{Fo} - \left(2 - \frac{dr}{r_i} + \frac{2hdr}{k}\right)\right]\right\} \tag{15}$$

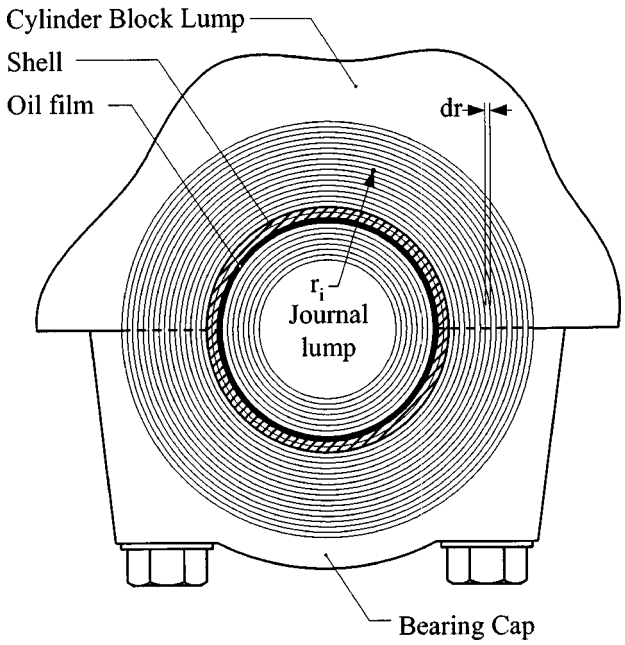

Fig. 9 Distribution of elements used in the one-dimensional finite difference transient heat conduction model

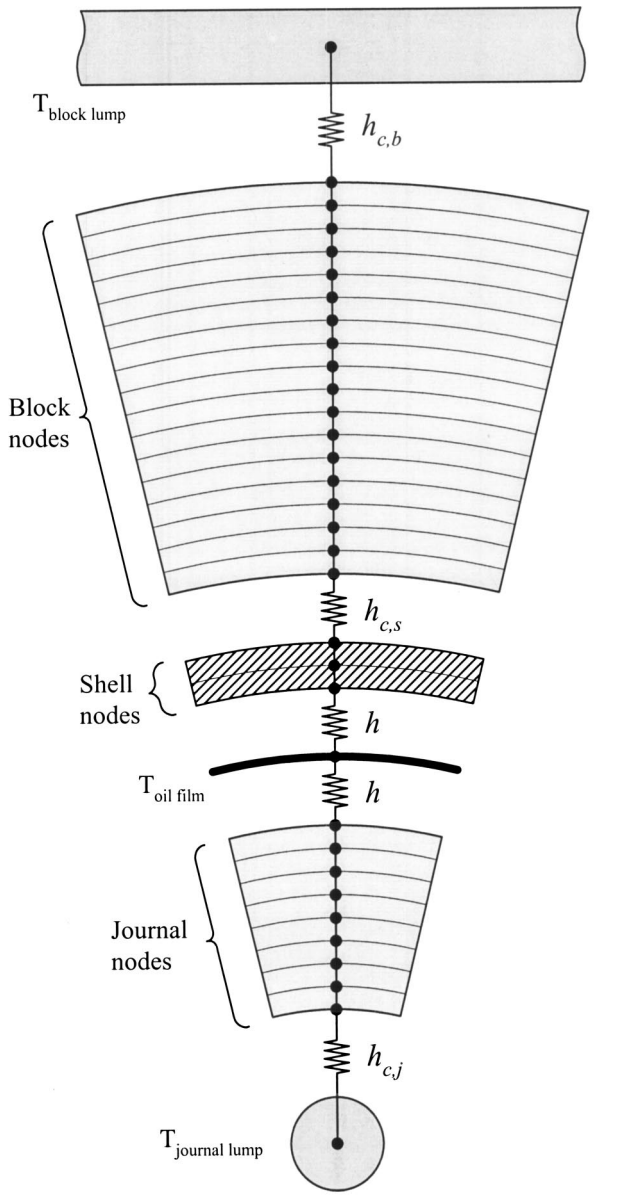

$h_{c,b}$: Cylinder block lump / node contact coefficient
$h_{c,s}$: Cylinder block / shell node contact coefficient
h : Oil film / shell node (journal) heat transfer coefficient
$h_{c,j}$: Journal node / lump contact coefficient

Fig. 10 Finite difference thermal network

The contact coefficient at the interface of the bearing shells and the block or bearing cap shown in Fig. 10 is given by

$$h_{c,s}=\frac{\dot{Q}}{2\pi r_{\text{shell}}L(T_{\text{shell}}-T_{\text{cap/block}})} \tag{16}$$

The two other contact coefficients $h_{c,j}$ and $h_{c,b}$, identified in Fig. 10, are defined in a similar way.

Solutions have been obtained for various cases by time marching from an initially uniform temperature field, with an iteration to find the oil film temperature consistent with the frictional dissipation and heat transfer rate from the film at each time step. The time step used was always less than the maximum for stability of the explicit finite difference scheme

$$dt \leq Fo\,\frac{(dr)^2}{k}\rho C_p \tag{17}$$

where the Fourier number, Fo, is restricted by

$$Fo \leq \frac{1}{\left(2-\frac{dr}{r}+\frac{2hdr}{k}\right)} \tag{18}$$

In practice, the accuracy of the energy balance of the oil film is a greater constraint because of the strong coupling of film temperature and frictional dissipation.

The shell contact coefficient, $h_{c,s}$, and the oil film heat transfer coefficient, h, were treated as empirical constants for the range of conditions examined. The values giving best agreement between measured and predicted temperature fields were 16 000 and 8000 W/m^2 K, respectively. The values for $h_{c,j}$ and $h_{c,b}$, were both assigned a value of 500 W/m^2 K. Comparisons of predictions and experimental data, for three different clearances and for a crankshaft speed of 1000 rev/min, are shown in Fig. 11. The values of frictional force given in the figures are per bearing. Agreement between the predictions and experimental data are excellent throughout the first seconds of crankshaft rotation when thermal conditions are rapidly changing, and subsequently when quasi-steady thermal conditions prevail around the bearing.

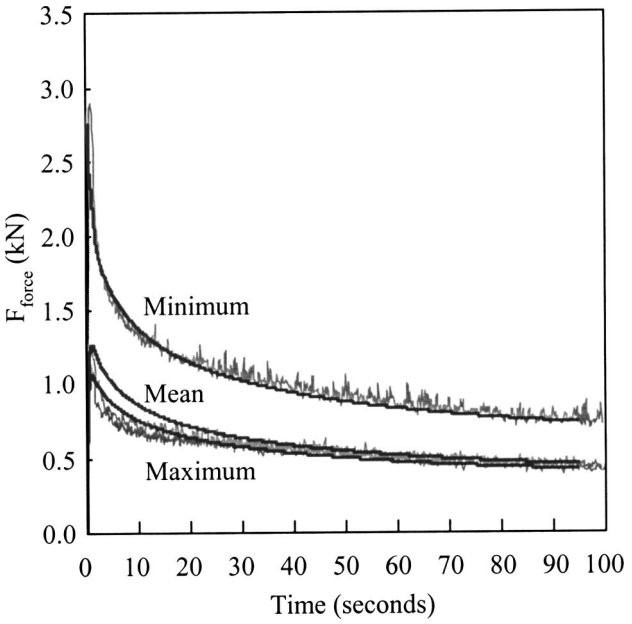

Fig. 11 Comparison of measured and predicted crankshaft main bearing friction force for minimum, mean, and maximum clearance bearing shells at 1000 rev/min

4 Shell Contact Resistance

During the first tens of seconds of cold-running, most of the heat generated by the friction work in the bearings is conducted into the block (and crankshaft) as illustrated by the predictions shown in Fig. 12 for the mean clearance shells at a test speed of 1000 rev/min. It follows that increasing the thermal contact resistance at the shell/block interface should increase the rate of rise of the oil film temperature, reducing oil viscosity, and hence, reducing friction. The increase in thermal resistance was achieved by removing 80% of the contact area on the back of the bearing shells. Figure 13 illustrates a standard plain shell and a shell with

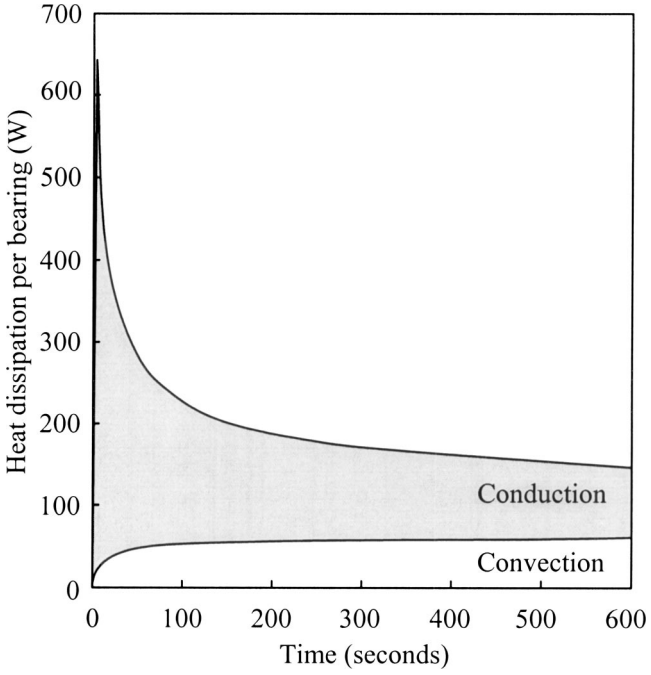

Fig. 12 Comparison of relative conduction and convection heat transfer terms for mean clearance shells, operating at 1000 rev/min

20% of the original contact area. The reduction was achieved through a chemical etching process using a 75:25 mix of water and nitric acid. Areas of the shell not to be etched were masked using printed circuit board track masking tape and etch-resistant ink.

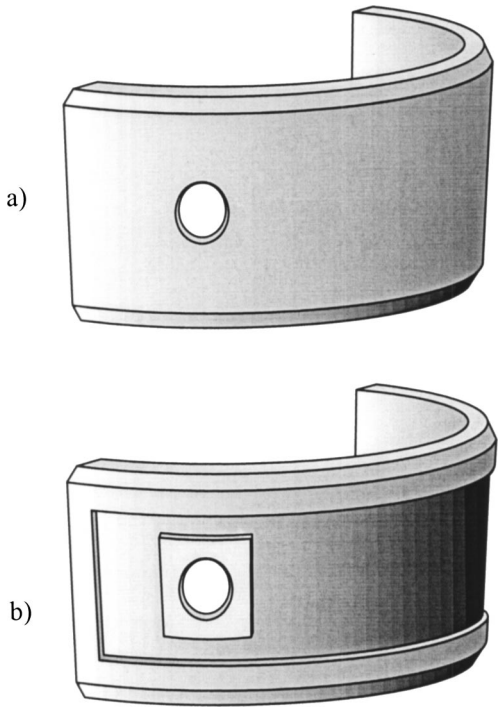

Fig. 13 Illustrations of main bearing shells, (*a*) shows a standard plain shell and (*b*) shows a shell with approximately 20% of the original contact area

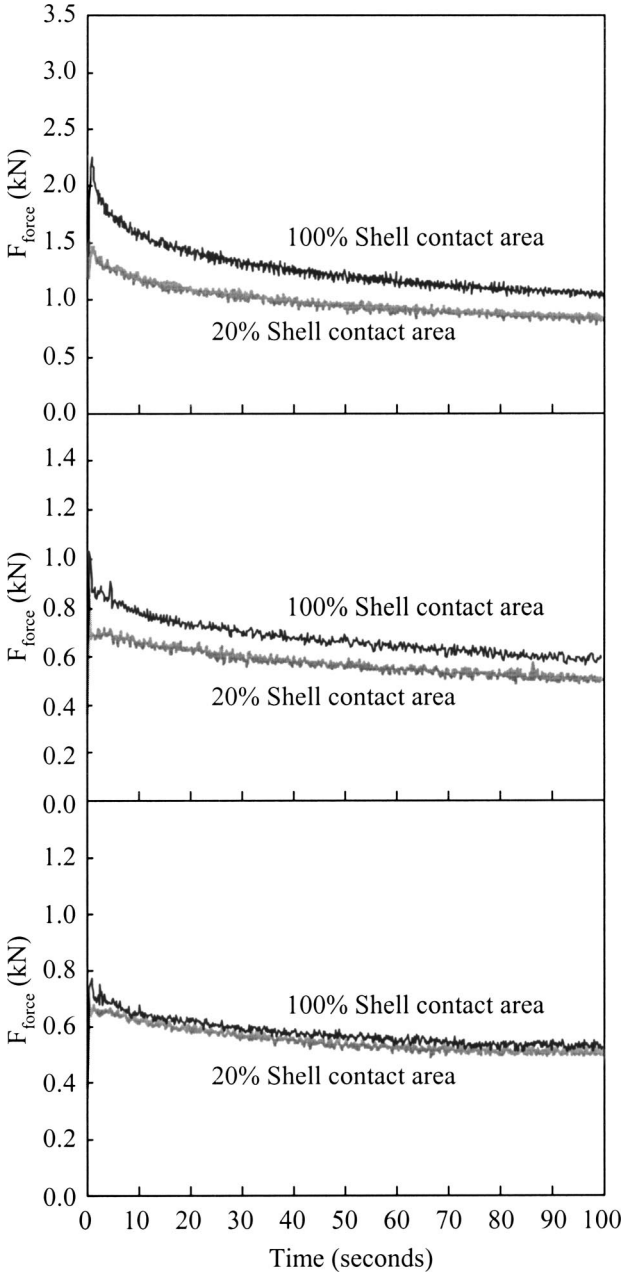

Fig. 14 Main bearing friction force at crankshaft speeds of 200 rev/min for (upper figure) minimum, (middle) mean, and (lower) maximum bearing clearances

The effect of the increase in contact resistance is apparent in comparisons of test results recorded using the original and etched shells. Figure 14 illustrates the differences in bearing friction force for minimum, mean, and maximum clearances, respectively, at a crankshaft speed of 200 rev/min. The corresponding comparisons for a crankshaft speed of 1000 rev/min are shown in Fig. 15. From the data presented increasing the contact resistance had little effect when the maximum clearance shells were used. The increase in contact resistance produced a relatively insignificant reduction of typically 5% in friction during the early seconds of the tests. More encouraging reductions were achieved for the mean and minimum clearance shells. The initial friction level was reduced by typically 22% and 27%, respectively. The greater effect when clearance is smaller is due to the higher rates of frictional heating, and hence, higher heat conduction into the shells. From the results for 1000 rev/min given in Fig. 15 it can also be ob-

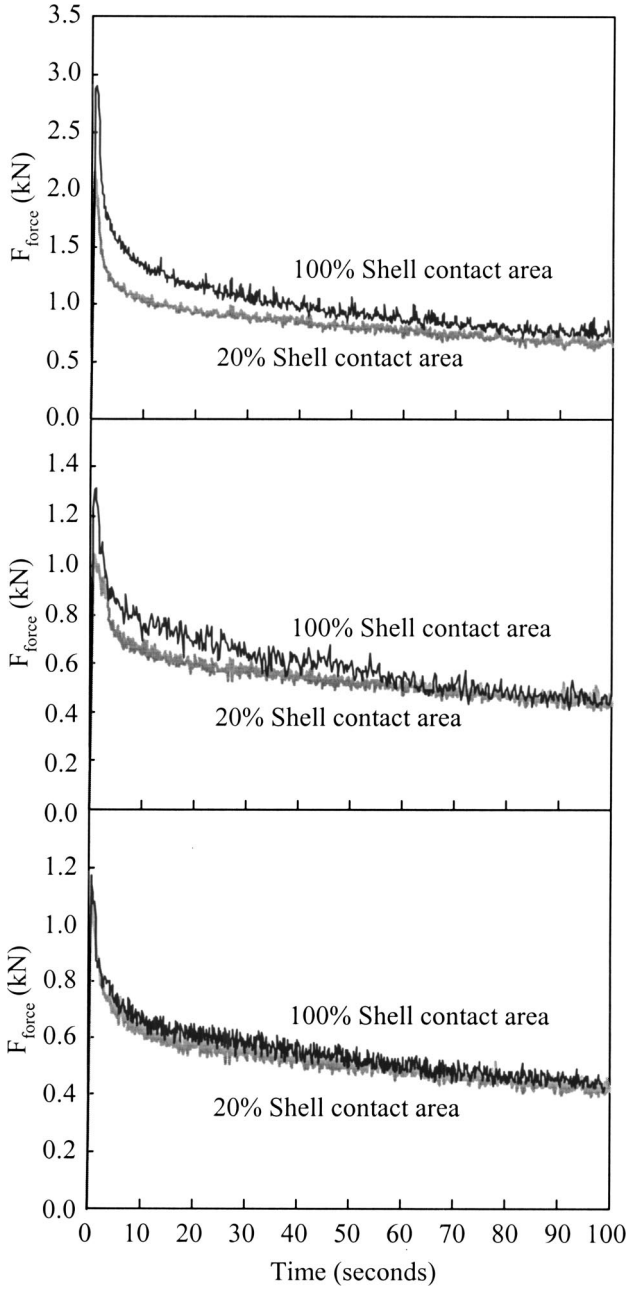

Fig. 15 Main bearing friction force at crankshaft speeds of 1000 rev/min for (upper figure) minimum, (middle) mean, and (lower) maximum bearing clearances

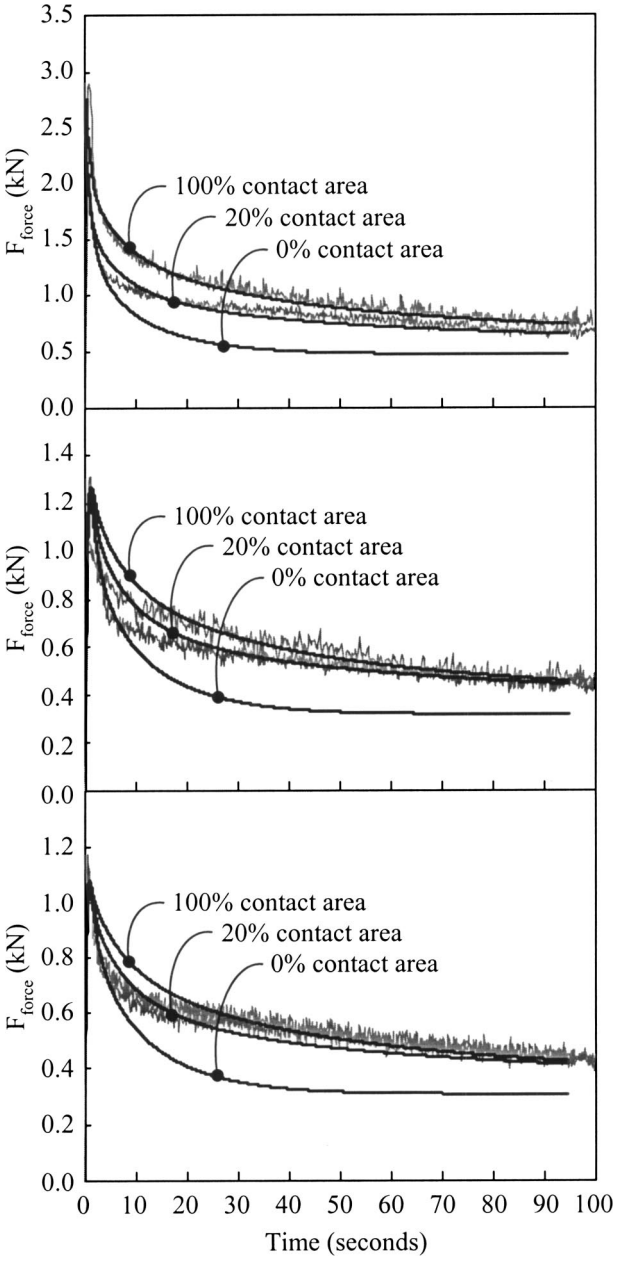

Fig. 16 Measured and predicted effects of shell contact area on friction at 1000 rev/min for (upper figure) minimum, (middle) mean, and (lower) maximum bearing clearances. Predictions for 0% contact are also shown.

served that as time increases, the two friction profiles for each set of clearances converge. This indicates that the shell etching process did not affect the operating clearance of the bearings.

The interface contact coefficient used in the finite difference, transient heat conduction model was reduced from 16 000 to 3200 $W/m^2 K$ to simulate the influence of the 80% reduction in contact area. The predicted variations of friction force agree well with the experimental data. The comparisons of predicted and experimental results presented in Fig. 16 cover the bearing minimum, mean, and maximum clearance cases, respectively. Predictions for a theoretical fully insulated set of bearing shells are also shown, indicating that a further significant reduction in friction force would be achieved by reducing contact area still further, to less than 20% of the original area.

5 Discussion

The results of previous work [1] have shown that engine friction takes some tens of seconds after a cold start to fall onto a power law dependence on viscosity at a reference location. The initial high levels of friction can dictate the start times of diesel engines at ambient temperature around −20°C and below, so there are practical reasons for wanting to understand the behavior in more detail. The study of the crankshaft main bearings shows that thermal conditions local to the bearings influence the oil film temperature and that this, it turn, largely controls the friction force throughout both initial and quasisteady phases of running.

Motoring tests on the crankshaft indicated that main bearing friction was proportional to $\mu^{0.8}$, although the index could be

raised to unity by relatively small changes to the constants in the Vogal equation describing the temperature dependence of viscosity. This is a more likely source of error than the description of viscosity shear loss, which reduces the viscosity by not more than 25%. The power law giving the best fit to the experimental data indicates that friction force was proportional to $U^{0.6}$. A linear fit to the same data, setting friction force proportional to U and consistent with hydrodynamic lubrication, gives a significant offset at zero relative bearing speed. A possible explanation is that the bearings were not fully flooded and/or may have operated in the mixed lubrication regime at lower speeds.

Heat conduction into the shells and journal influences both the initial level of friction and its rate of decay to quasisteady levels. The experimental data and model predictions indicate that these transient characteristics can be influenced by raising the thermal contact resistance between the shell and the bearing cap/cylinder block. The high thermal diffusivity of the shell metal and the strong dependence of oil viscosity on temperature at low temperatures, allows the contact resistance to influence friction within the first second of crankshaft rotation. Opening up the bearing clearance has a similar effect in reducing friction, in this case by reducing oil shear and dissipation rather than by reducing heat transfer and raising film temperature. Generally, for reasons which include noise control, maximum clearances cannot be raised without creating problems. There are no obvious thermodynamic reasons why the contact resistance cannot be raised. This affects heat conduction through the metal surrounding the film, which is important during cold-start-up and the following seconds. When operating fully warm and high rates of heat removal are required, convection is the dominant mode. For mechanical, performance and reliability considerations, which include the possibility of effects on elastohydrodynamic behavior of the bearing, contact resistance would need to be increased by means other than the creation of an air gap, possibly by coating the surface with an insulating material.

6 Conclusions

During the first tens of seconds of cold operation, engine friction is relatively high and rapidly changing. The crankshaft main bearings contribute significantly to the fmep total for an engine. Conditions in and around these main bearings have been investigated to establish what controls the variation of friction with time and how it might be influenced.

The results of motoring tests show that bearing friction force is proportional to $U^{0.6}\mu^{0.8}/c$, where the value of μ is evaluated at the oil film temperature of the bearing. The changes in viscosity produced by changes in film temperature are the most significant influence on bearing friction during cold running at a constant speed. The circumferential variation of film temperature was small.

A computational model was developed and applied to investigate the thermal coupling between bearing friction and the local surroundings of the bearing oil film. The model accurately reproduced measure values of temperature and friction, and showed that heat conduction into the bearing journal and shells is the dominant mechanism of heat removal from the film in the early seconds of cold running.

Increasing the thermal contact resistance at the backsurface of the bearing shells reduces bearing friction during cold running. Increasing contact resistance by reducing the contact area to 20% of the original gave a reduction in friction of just over 20% for clearances at the mean of production tolerances.

Acknowledgment

The authors gratefully acknowledge the support of the Ford Motor Company for the work reported here.

Nomenclature

A = oil shear rate constant
B = oil shear rate constant
c = clearance m
C_p = specific heat at constant pressure J/kg K
D = bearing diameter m
F = friction force N
FR = friction ratio
h = heat transfer coefficient $W/m^2 K$
k = thermal conductivity W/m K, s^{-1}
L = bearing length m
$\dot{m}$ = mass flow rate kg/s
P = pressure Pa
$\dot{Q}$ = heat transfer rate W
r = element radius m
s = full shear to zero shear viscosity ratio
T = temperature K
t = time s
U = relative bearing surface speed m/s
$\dot{V}$ = volume flow rate m^3/s
$\dot{W}$ = power W

Greek Symbols

α = coefficient of linear expansion $°C^{-1}$
β = equation constant $N^{0.2}/s^{0.2}$
γ = shear rate s^{-1}
ϵ = eccentricity ratio
κ = Vogel equation constant mPa s
θ = Vogel equation constant °C
μ = dynamic viscosity Pa s
π = mathematical constant
ρ = density kg/m^3
τ = time constant s

Dimensionless Groups

Fo = Fourier number, $kdt/\rho C_p(dr)^2$

References

[1] Shayler, P. J., Burrows, J. A., Tindle, C. R., and Murphy, M., 2001, ''Engine Friction Characteristics Under Cold Start Conditions,'' Paper No. 2001-ICE-432, ICE Vol. 37-3, 2001 Fall Technical Conference, ASME.
[2] Miura, A., and Shiraishi, K., 1989, ''Investigation of Main Bearing Friction in a Diesel Engine,'' SAE 890140.
[3] Cameron, A., 1981, *Basic Lubrication Theory*, 3rd ed. Ellis Horwood Limited, Chichester, UK.
[4] Cross, M. M., 1965, ''Rheology of Non-Newtonian Fluids: A New Flow Equation for Pseudo Plastic Systems,'' J. Colloid Sci., **20**, p. 417.
[5] Taylor, R. I., 1997, ''Engine Friction: The Influence of Lubricant Rheology,'' Proc. Inst. Mech. Eng., Part J, J. Eng. Tribol., **211**, pp. 233–246.
[6] Sorab, J., Holdeman, H. A., and Chui, G. K., 1993, ''Viscosity Prediction for Multigrade Oils,'' SAE 932833.
[7] Burrows, J. A., 1998, ''An Investigation Into the Cold Start Performance of Automotive Diesel Engines,'' Ph.D. thesis, University of Nottingham.

Experimental Investigation of Oil Accumulation in Second Land of Internal Combustion Engines

T. Icoz[1]

Z. Dursunkaya

Mechanical Engineering Department,
Middle East Technical University,
06531 Ankara, Turkey

Blowback of engine oil suspended in combustion gases, when the gas flows from the piston second land back into the combustion chamber, is believed to contribute to oil consumption and hydrocarbon emissions in internal combustion engines. Oil accumulation in the region between top and second compression rings is a factor that influences this phenomenon. The effects of individual parameters, such as oil film thickness and viscosity, however, have still not been understood. The present study was aimed at constructing an experimental setup to study the effect of oil film thickness on oil accumulation in the second land of internal combustion engines. Due to the inherent difficulties of experimentation on production engines, a modeled piston-cylinder assembly was constructed. Total oil accumulation in the modeled second land after a single piston stroke was measured and compared to oil consumption in operating engines.
[DOI: 10.1115/1.1805011]

Introduction

Oil transport through the cylinder piston route has important implications in the performance of internal combustion engines. The amount of oil available affects power loss due to friction, wear of cylinder components, and piston ring performance. On the other hand, engine oil is also known to contribute to burned and unburned hydrocarbon emissions. Within the last two decades, increasing concerns on the environmental pollution due to emissions from vehicles have brought strict regulations on the emission levels and the contribution of oil loss to emissions has become important. The achievement and maintenance of reduced levels of oil consumption are of prime interest to engine manufacturers for meeting even more stringent future emission standards.

There are two major routes of oil loss in engines, the existence of which have been experimentally verified. These are due to the valve train and the path via the cylinder. In internal combustion engines, oil consumption through the piston-cylinder assembly is the major contributor when compared to oil loss through the valve train. The valve train oil consumption accounts for 15%–25% of total oil loss, whereas the remaining 75%–85% is due to the path via the cylinder [1]. Although the general effects of piston and ring design on oil loss are known to engine and component manufacturers, the underlying physical mechanisms and the effects of individual parameters are still not well understood. Among the three different mechanisms that are perceived to contribute to oil loss through the cylinder path, oil evaporation from the cylinder surface was investigated numerically by Wahiduzzaman et al. [2] and found to account for a relatively small fraction (5%–10%) of total consumption in diesel engines. The second mechanism, oil scraping and pumping by the top compression ring into combustion chamber, has not been experimentally verified. The final mechanism of oil loss due to in-cylinder components is the blowback of oil entrained by the blowby gases into the combustion chamber, which is physically well founded, but modeling and experimentations are still missing.

Oil entrainment into the blowby gases is a complex phenomenon and even though there are several studies in the literature on liquid entrainment into the gas stream, no study exists on oil entrainment into blowby gases in internal combustion engines. Entrainment of oil into blowby gases can be the major oil transport mechanism that effects oil accumulation in the second land, which in turn, is blown back to the combustion chamber early in the exhaust stroke. The amount of oil entrained due to this mechanism is affected by the flow conditions and physical properties of the fluids. Hewitt and Hall-Taylor [3] summarized the entrainment mechanisms based on experimental observations. Droplets can be formed either by breaking up of waves created on the liquid surface during the gas flow or by the emission of a bubble from a liquid surface. Wave undercutting and shearing off of roll wave crests were presented as the main mechanisms encountered in liquid entrainment. They emphasized the strong dependence of droplet entrainment on gas-liquid flow combinations, geometry, and physical properties. Ishii and Grolmes [4] developed inception criteria for droplet entrainment in two-phase flow based on the above-mentioned two mechanisms. They concluded that applicability of mechanisms depends on the flow conditions, and abrupt changes observed in the experiments were attributed to a change in the entrainment mechanism. Ishii and Mishima [5] developed correlations for the entrained fraction of water in the water-air system and used the same two mechanisms in their model. Their results showed that the prevailing entrainment mechanism changes with Reynolds number.

The studies on blowback of oil into combustion chamber, so far, have shown that inter-ring crevice volumes and pressures play an important role in oil blowback [6–11] and the existence of two oil flow paths between the crankcase and piston rings were observed [9,10]. Two routes of oil flow were described. The minor route was the oil flow through the peripheral surface of the piston rings. This route becomes important when thermal and other deformations of the cylinder block render the cylinder bore noncircular and consequently the lubricant finds a path towards the combustion chamber through the top ring. In modern engines due to improved design and production processes, this particular oil

[1]Currently at the Mechanical Engineering Department, Rutgers University, New Brunswick, NJ 08854.

Contributed by the Internal Combustion Division of THE AMERICAN SOCIETY OF MECHANICAL ENGINEERS for publication in the ASME JOURNAL OF ENGINEERING FOR GAS TURBINES AND POWER. Manuscript received by the ICE Division April 24, 2003; final revision received by the ASME Headquarters December 16, 2003. Associate Editor: D. Assanis.

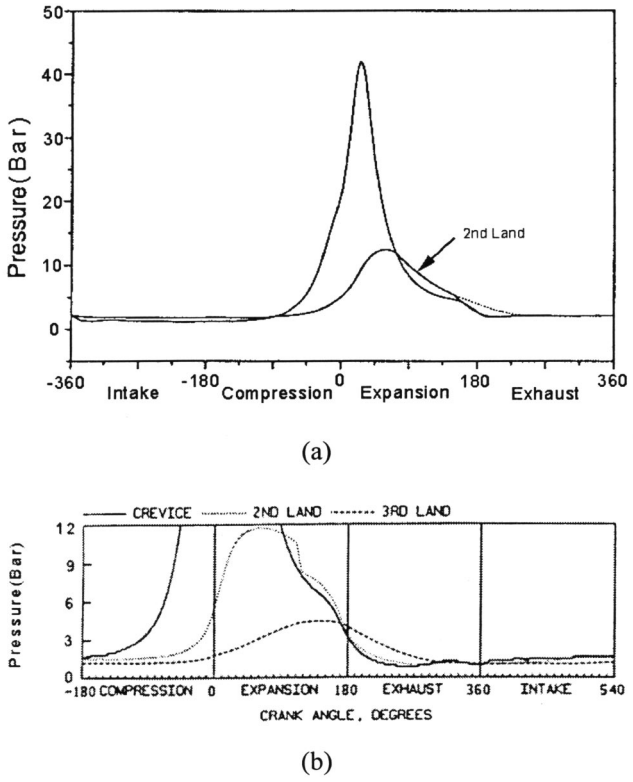

Fig. 1 Cyclic pressure variations given by Dursunkaya et al. [11]: (*a*) cylinder; (*b*) second land

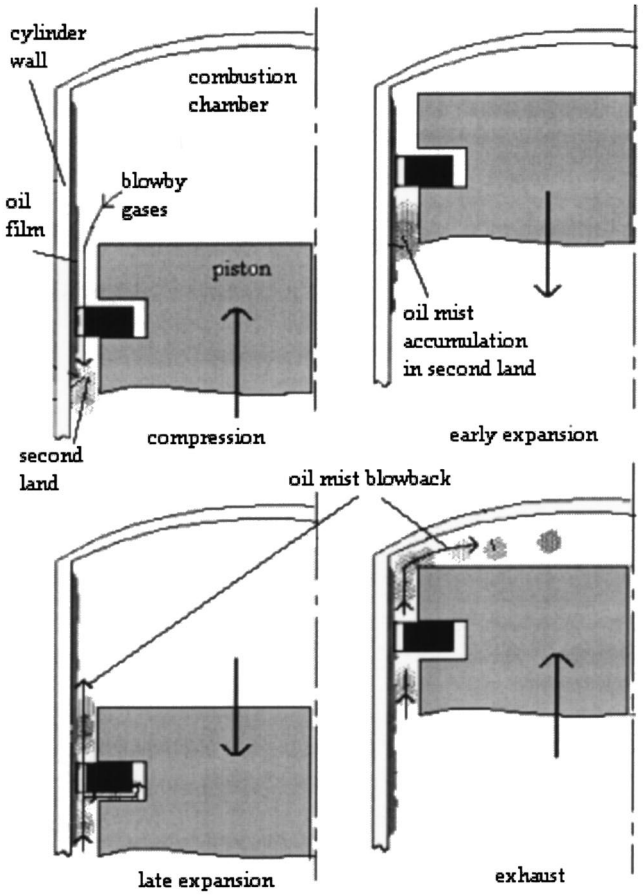

Fig. 2 Mechanism of blowback oil consumption

flow path, however, remains unimportant for blowback oil consumption. The major route was found to be the oil flow through the ring end gaps where the area formed by the ring end gap, the piston crown, and the cylinder liner is considered as the main gas and oil passage area [6,8,9].

It is the inter-ring pressure variation, given in Figs. 1(*a*) and 1(*b*) [11], that is important in understanding the physics of gas flows through the ring end gaps. The cylinder pressure is much higher than the second land pressure (i.e., pressure between the top two compression rings) during compression and early expansion strokes. Until mid-expansion, as a result of this pressure difference, a gas flow at sonic speeds occurs towards the second land. During this process, oil left in the crown land and top ring groove is entrained into the blowby gases and accumulates in the second land as oil mist. Due to rapid expansion and depressurization caused by the opening of the exhaust valve, the cylinder pressure drops below the inter-ring pressure causing a back flow of gas, carrying oil mist into the combustion chamber. This, in turn, is mixed with the combustion products and expelled out of the engine *via* the exhaust valve, appearing as burned and unburned hydrocarbons in the exhaust gases. The schematic representation of the oil blowback mechanism is shown in Fig. 2.

Researchers have so far intended to study the gross effects of some geometric parameters—such as ring end gap positions and piston ring face profiles—on oil consumption. The motion of tracer oil injected into the cylinder was recorded by Saito et al. [12] using a video camera through a transparent glass engine cylinder. They concluded that only a small quantity of oil resided in the third land, the volume between the second compression ring and the oil control ring. They observed that oil did not penetrate the second land or the combustion chamber, and concluded that it did not contribute to oil consumption. Wong and Hoult [13] studied the lubricant film characteristics and oil consumption in a small diesel engine experimentally, using a radioactive tracer for the oil consumption and laser fluorescence diagnostics for the film thickness measurements. The study showed that oil film thickness affected the oil loss in diesel engines. They could not, however, find conclusive evidence that the amount of oil in the second land correlated with the oil consumption. In addition, their results showed that the crown land—the volume between the top compression ring and top surface of the piston—ran dry and therefore could not contribute to oil consumption in any significance. Kim et al. [7] studied the importance of inter-ring crevice volume as a source of unburned hydrocarbon emissions numerically. A physical flow model integrated with a ring dynamics model to predict the gas flows through the inter-ring crevice was constructed. The results showed that late in the expansion stroke some of the inter-ring mixture returned to the combustion chamber. Moreover, they found that the unburned hydrocarbon (HC) emissions caused by the inter-ring mixtures were 10%–30% of the entire unburned HC emissions over an engine speed range of 1250–3500 rpm and the reduction in emissions was closely related to blowby, which was directly related to the volume of the inter-ring crevice.

Although there are numerous related studies, the effect of individual parameters, such as oil film thickness, lubricant type, temperature, and pressure on oil accumulation are unknown. In the present work a model of cylinder piston ring assembly in Cartesian geometry was constructed to investigate the effect of oil film thickness on oil accumulation in the second land volume of a diesel piston cylinder assembly, to assess the contribution to oil consumption in internal combustion engines.

Experimental Setup

Previous experimental studies on oil blowback have been carried out on motored or fired engines equipped with special optical

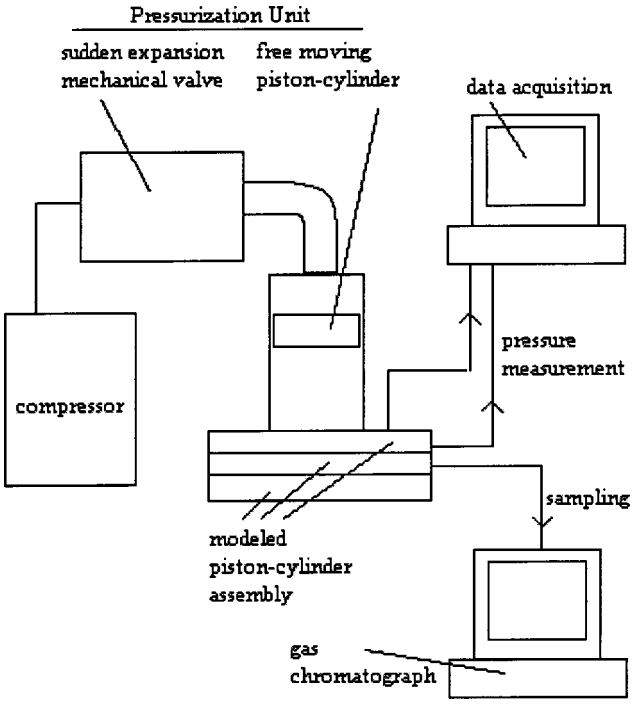

Fig. 3 Schematic of experimental setup

systems to trace the oil flow in the cylinder and were aimed at investigating the gross effects of certain design parameters. The experiments, however, were not designed to assess the effect of individual parameters on oil consumption. In this study, an experimental setup was constructed to investigate the effect of oil film thickness on oil accumulation in the second land in internal combustion engines. Such an investigation on an operating engine is prohibitively difficult to carry out due to the fact that the thickness of the oil film cannot be controlled in an operating engine, since it is affected by the piston axial and lateral motion, ring face profile, ring tilt, and inter-ring pressures.

Therefore, keeping the film thickness constant and uniform at intended values for individual experiments could not be achieved in a real engine. Moreover, sampling must be completed in a short duration, in the order of a few milliseconds, from a narrow but longitudinally distributed inter-ring volume while the piston is in motion, which requires complex experimental designs. To overcome these experimental difficulties and enable a controlled experiment, a representative model of an internal combustion engine piston-cylinder assembly was designed in Cartesian geometry. For the pressurization process a free moving piston-cylinder assembly and a sudden expansion mechanical valve were employed. The pressure data were recorded by a data acquisition system. Oil content in the second land oil-gas mixture was analyzed by a gas chromatograph. The schematic representation of the experimental setup is shown in Fig. 3.

In a heavy-duty diesel engine cylinder pressure can reach 60–160 bars, whereas second land pressures of 6–20 bars are common. Because of the high pressure ratio between the combustion chamber and the second land, the flow between the two volumes occurs under sonic conditions for a long duration of the power stroke. The compressed gas flow is choked during the end of compression and early expansion strokes. Choked flow conditions prevail about 90 deg crank angle of the cycle and most of the oil entrainment and accumulation in the second land occurs during this period, later to be blown back to the combustion chamber as the pressure drops in late power and early exhaust strokes. In other words, depending on the second land and groove volumes, gas that moves to the second land from the top land accumulates a significant amount of entrained oil during this sonic flow, which lasts approximately 10 ms in an engine running at 1500 rpm.

Table 1 Dimensions of the modeled piston cylinder assembly of the heavy-duty diesel engine

Bore diameter	125 mm
Stroke	140 mm
1st Land Diameter	124 mm
2nd Land Diameter	124.44 mm
1st Groove Diameter	112.27 mm
2nd Groove Diameter	112.27 mm
Thickness of Ring Groove 1	3.5 mm
Thickness of Ring Groove 2	3.2 mm
Distance of Groove 1 Top from the Piston Crown	5.7 mm
Distance of Groove 2 Top from the Piston Crown	16 mm
Thickness of 1st Ring	3 mm
Thickness of 2nd Ring	2.8 mm
Width of 1st Ring	5.1 mm
Width of 2nd Ring	5.1 mm
Ring End Gaps	0.5 mm

To have flow conditions similar to operating engines, it was necessary to have choked flow in the setup for a duration of 10 ms. On the other hand, high peak pressures encountered in real engines could not be obtained in the experimental setup, since this would result in a design well beyond the existing equipment and experimental tools. Therefore, a compromise design was sought, where by obtaining a high enough pressure ratio between the simulated combustion chamber and the second land, choked flow conditions were achieved. Simultaneously the pressure rise curve attained in the second land was similar to operating engines. The volumes and passage areas were also similar to those encountered in real engines. However, the peak pressures in the simulated combustion chamber—approximately 8 bars—were substantially less than those seen in real heavy-duty diesel engines, and consequently the mass flow rate of gas through the ring end gaps were less than those of real engines. In order to obtain similar instantaneous mass flow rates, pressurization properties, such as similar pressure ratios, peak pressures, temperatures, and flow durations similar to operating engines had to be obtained. Since the aim of the present study was the investigation of the effects of individual parameters, which were only possible on a representative model of a real engine, in the experiments, the ratio of pressure in the first land to the pressure in the second land was kept above 1.89 so that flow would occur under chocked conditions. For this purpose, a computer code was developed to simulate the slider-crank motion of the piston and the thermodynamic process during a single piston upward stroke to guide the design. The software simulated the pressurization process of the simulated combustion chamber and simulated second land volume, and volumes of the pressurization chamber and simulated combustion chamber that resulted in the desired pressurization characteristics, namely duration and the shape of the pressurization curve were calculated. The software was also used to determine other design parameters such as the activation pressure of the sudden expansion valve and the thickness of piston.

The constructed model was effectively the transformation of piston cylinder, inter-ring crevices in operating engines into a rectangular geometry. The dimensions were kept identical to those of a heavy-duty diesel engine piston-cylinder assembly having the dimensions given in Table 1.

Modeled Piston-Cylinder Assembly. The modeled piston-cylinder assembly was the transformation of engine piston-cylinder volumes and surfaces including the combustion chamber, inter-ring crevice volumes, and ring end gap, into a Cartesian geometry. The stepwise schematic representation of the geometric transformation is shown in Fig. 4. The model consisted of three plates, namely, top, center, and bottom plates, a stopper, a check valve, and a sampling tube as shown in Fig. 5. Each plate represented different locations of piston and cylinder in internal com-

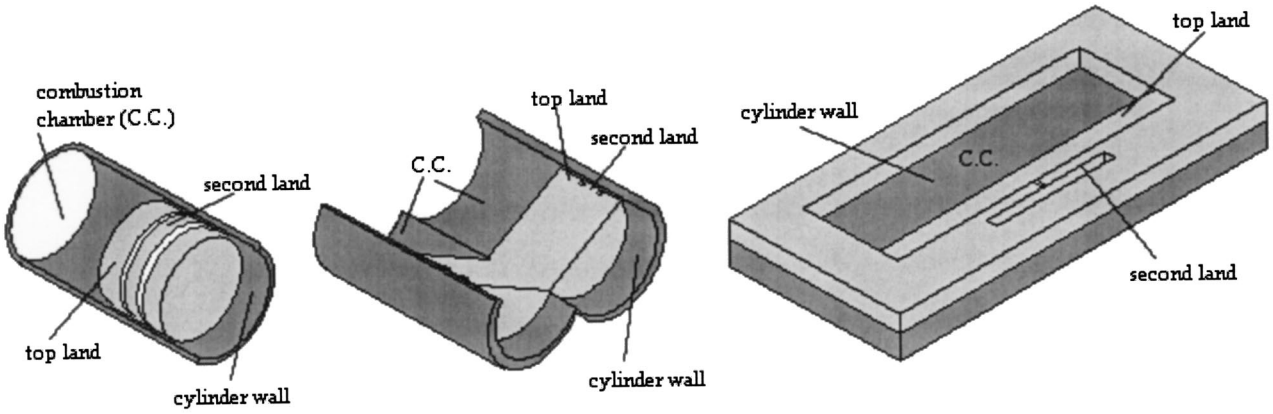

Fig. 4 Schematic of geometric transformation

bustion engines. The function of the top plate was to stop the free-moving piston at the end of pressurization. It also connected the free-moving piston-cylinder assembly to the modeled piston-cylinder assembly and simulated a part of the combustion chamber. The center plate contained the pressurization chamber, sampling chamber, flow passage gap, and flow separator as shown in Fig. 6. The pressurization chamber and the dead volume in the top plate simulated the combustion chamber. The volume of this chamber, about 220 cm^3, corresponded to the average cylinder volume during the expansion stroke, during which the oil blow-back takes place. The sampling chamber was the region where the oil-gas mixture was retrieved. It represented the second land volume in engines. The second land volume was lumped to a narrow rectangular region to obtain a uniform mixture for sampling. The dimensions of the modeled second land was set at $50\times5\times15$ mm. During experiments the pressures in the pressurization chamber and sampling chamber were measured via pressure transducers. The flow passage gap simulated the piston ring end gap, the oil-gas mixture flow passage. The cross sectional dimensions of the flow passage, 0.5×0.5 mm, were similar to real engines and it was the only gas passage area between the pressurization and sampling chambers. The flow separator was designed such that it acted as an obstacle to flow and was used to distribute the pressurized air to both sides so that it would not pass through the flow passage gap directly. This was desired so that the pressurization process would be similar to a polytropic pressurization of real engines. The oil accumulation in the second land volume was measured after a single piston stroke by retrieving and analyzing the gas mixture accumulated in the sampling chamber. For this purpose a measured amount of *n*-hexane was placed in a sampling tube and connected to the sampling chamber. Since engine oil dissolves in *n*-hexane, this was necessary in order to retrieve all the oil collected in the sampling tube, and not leave any in the tube for chromatographic analysis. After the system reached equilibrium, the valve was opened and the oil-gas mixture sampling chamber was admitted in the sampling tube. For the sampling process, the pressures in the pressurization chamber and sampling chamber were kept constant by means of a check valve.

The bottom plate was designed and constructed for simulating the cylinder wall. The upper surface of the plate simulated the cylinder surface and oil was spread on the surface. The oil film

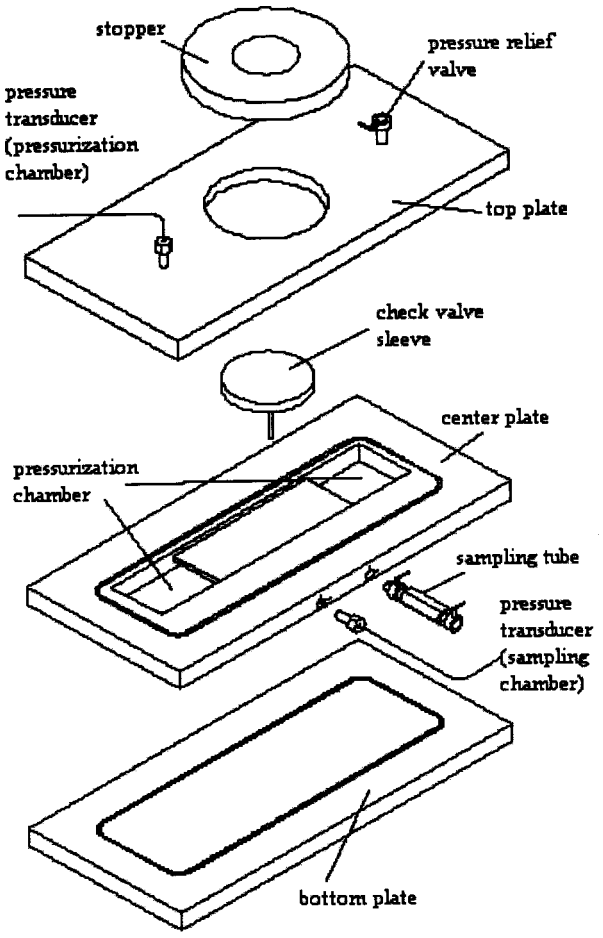

Fig. 5 Modeled piston cylinder assembly

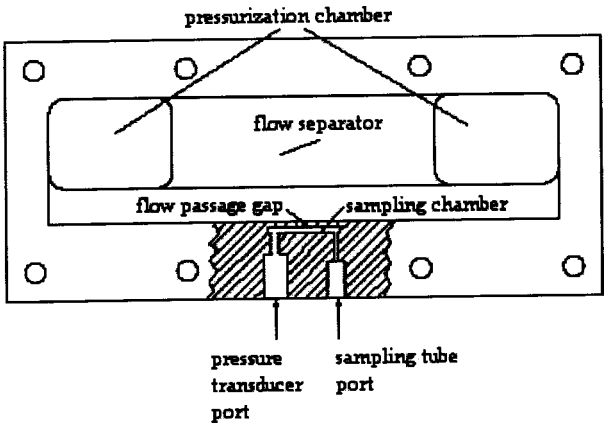

Fig. 6 Center plate

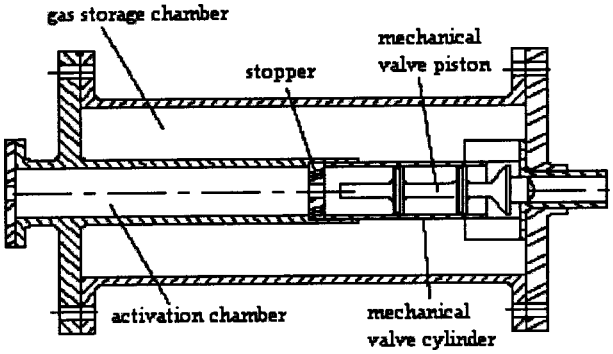

Fig. 7 Sudden expansion mechanical valve

thickness was predicted by means of the total amount of oil spread on the surface prior to every experiment. A measured quantity of oil that corresponded to the desired oil thickness was placed on the surface. The oil was subsequently spread on the surface by a razor blade. This operation initially resulted in ripples, which in time succumbed to surface tension. Experiments were performed once the surface of the spread oil was uniform in appearance. For quantities of oil less than 15 mm, however, the oil surface remained lumpy; therefore, no experiments were performed in this range. The oil accumulated in the sampling chamber was collected for the chromatographic analysis. Sampling tubes having 3.1 cm^3 internal volumes were manufactured for sample collection and two minispherical valves were fitted on both sides of the tubes.

Pressurization Unit

Free Moving Piston-Cylinder Assembly. The pressurization in real engines is a polytropic thermodynamic process. To simulate this, a free-moving piston-cylinder assembly was used for the pressurization of the modeled piston cylinder assembly. A single cylinder of a Ford-OTOSAN Dover engine block together with its piston-ring pack was modified and used later in the experiments. The bore of the cylinder was 104.7 mm. The piston was cut under its first compression ring to increase the compression ratio and the peak pressures in the pressurization chamber and sampling chambers. This modification also reduced the mass of the piston.

During the sampling process, the pressure should remain constant. However, during the preliminary experiments, it was noted that the pressure in pressurization chamber dropped rapidly due to gas flow through the ring end gaps and clearances. To ensure constant pressure after pressurization a check valve was constructed and installed between free moving piston-cylinder and modeled piston-cylinder assemblies.

Sudden Expansion Mechanical Valve. The pressurization of the free-moving piston-cylinder assembly was desired to occur rapidly, similar to the combustion process in internal combustion engines. Several alternatives were conceptualized for this purpose, such as using an explosive charge or a diaphragm. Eventually, a sudden expansion mechanical valve constructed by Kokdemir [14] was used in the experiments. The valve was a combination of a gas storage chamber and an activation chamber with a mechanical valve placed in between. These were two high-pressure chambers separated by the mechanical valve (Fig. 7). The working principle of the mechanical valve was based on a sudden application of a large force on the piston in the direction of the flow orifice. In applying this force, high pressure present in gas storage chamber was utilized. Sudden depressurization of the activation chamber by a solenoid valve causes a high pressure difference on both sides of the piston of the mechanical valve, and the net force pushes the piston towards the activation chamber. During this rapid motion the flow passage area through the free-moving piston-cylinder assembly opens and the gas in gas storage chamber flows through the opening. The opening time depends on the pressure applied on gas storage chamber, and for a pressure difference of 10 bars, the opening time was found as 0.5 ms [14], which was acceptable for the present application.

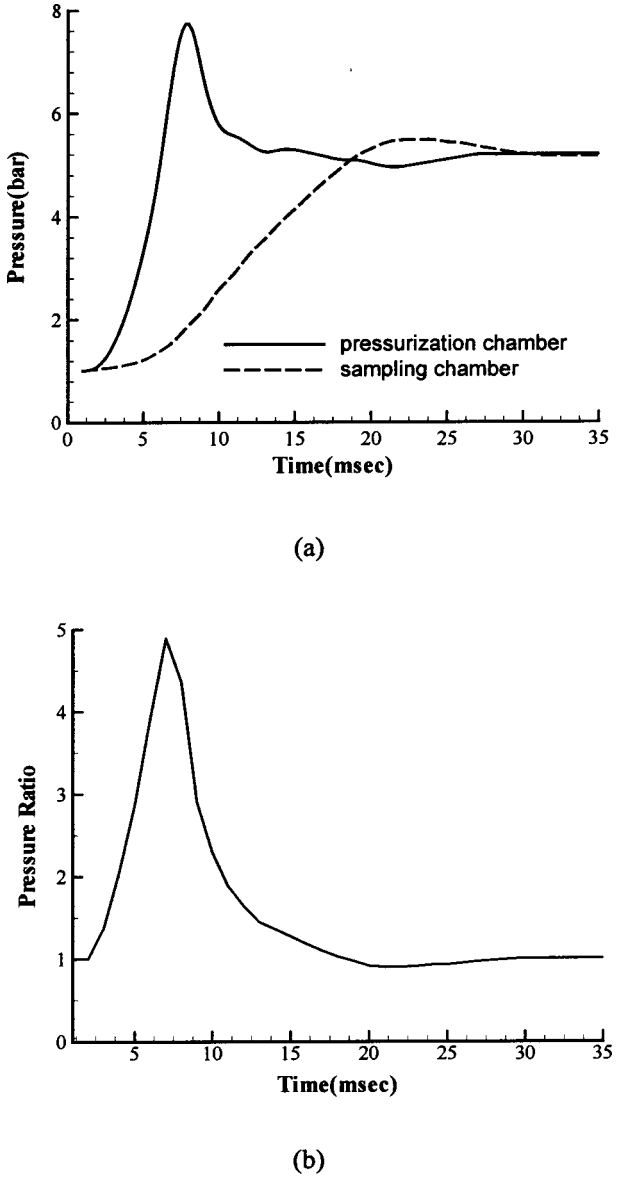

Fig. 8 Experimental pressure variation: (*a*) pressurization chamber and sampling chamber; (*b*) pressure ratio

Data Acquisition and Gas Chromatograph. The pressure data were recorded by means of a data acquisition system through a personal computer. The data frequency was 1 kHz to get sufficient number of data for the pressure curves. For oil content analysis a VARIAN STAR 3400 CX model gas chromatograph with a flame ionization detector was used. Helium and a SUPELCO SPB-1 type column were chosen as carrier gas and capillary gas chromatography column, respectively.

Results

The pressurization curves of the pressurization chamber and sampling chamber shown in Fig. 8 indicate that the gas flow into sampling chamber lasted approximately 12 ms, which, corresponds to an engine operating at around 1400 rpm. The pressure ratio between the two chambers was above 1.89, which indicates that the flow in the passage area was sonic and choked as desired, for almost 10 ms. Even though peak pressures, as well as actual

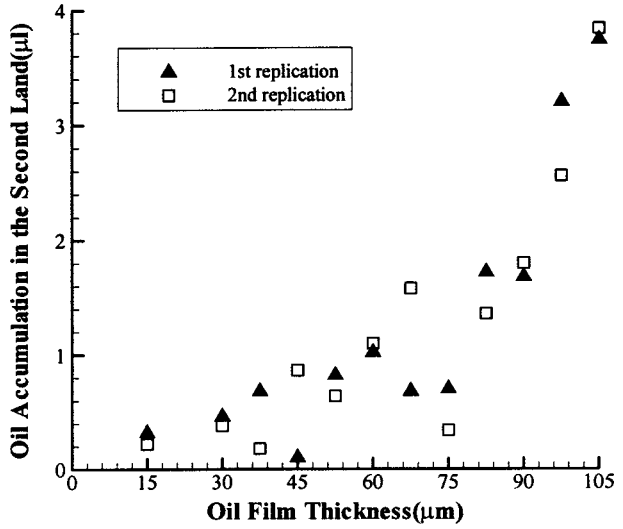

Fig. 9 Oil accumulation into the second land

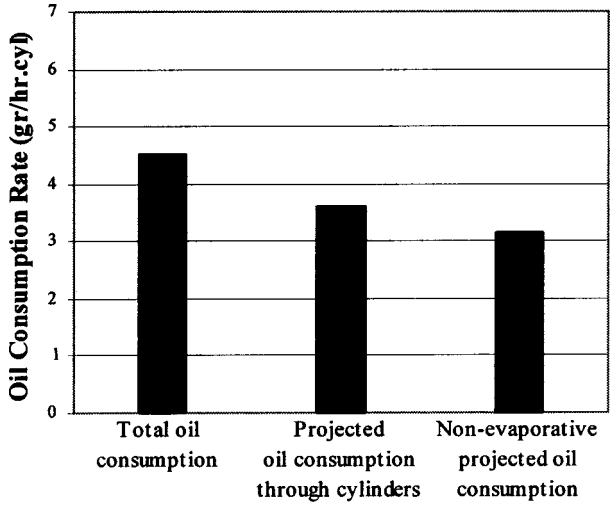

Fig. 10 Oil consumption rates in a diesel engine measured by Iizumi and Koyama [15]

mass flow rates occurring in internal combustion engines, could not be reached, the duration of the process and the prevailing compressible flow conditions were close to actual engine values. The average mass flow rate was estimated to be around 40%–90% of those encountered in internal combustion engine applications. The experimental second land pressure reached 5.2 bar (absolute) within the same time interval, whereas it is in the range of 6–15 bar in a diesel engine. Initially, the experiments were performed between 15 and 105 μm oil film thickness with 15 μm increments and an SAE15-40W type engine oil was used as the lubricating oil. The initial experiments revealed a discontinuity in the data and the experiments were repeated in the 30–105 μm range with 7.5 μm intervals. The samples were retrieved at 5.2 bar pressure. The ambient temperature during the experiments was around 21–24°C; therefore, no considerable effect on physical properties of oil such as viscosity and surface tension were present.

The HC analyses of the oil-gas mixtures were performed on a gas chromatograph. The gas chromatograph separates HC's and evaluates the volume based percentages of different HC's in the mixture. The first analysis was performed on pure *n*-hexane and the results were used as a reference for the samples. In the experiments all HC's originated from *n*-hexane and engine oil only. Therefore, the oil volume percentage in the mixture could be calculated from the difference between total HC's detected in the chromatograph and HC's belonging to *n*-hexane, which have distinct and unique retention times.

After carrying out a set of experiments that spanned the range, a second set of replications were performed. This was deemed necessary due to the unexpected behavior for oil film thicknesses between 47 and 75 μm. The results, given in Fig. 9, indicated that there was a small increase in oil accumulation for oil film thickness up to 45 μm. However, at this thickness an inconsistency between two replications was observed. A similar behavior was seen at around 67.5 μm after which a sudden decrease in oil accumulation was observed up to 75 μm. The difference between two replications at 45 μm and 67.5 μm was attributed to a change in the entrainment mechanisms described in Refs. [4], [5]. However, the underlying phenomena need further investigation. For the rest of the oil film thicknesses (i.e., between 45 μm and 67.5 μm and above 75 μm) an increasing trend in average oil accumulation in the second land was found, which in fact, was expected since the oil available was increased and more oil could be entrained into the air.

The oil consumption of a diesel engine with 135 mm bore and 140 mm stroke running at around 1800 rpm was found to range from 3–6.5 g/h per cylinder [15]. In another research, Ref. [13], the oil consumption of a single cylinder small diesel engine with 75 mm bore and 70 mm stroke was measured to be 1–2 g/h at around 2000 rpm. In order to compare the oil accumulation results with known oil consumption, the following approach was used. A ''projected oil consumption'' value was computed based on the assumption that all oil entrained in gas was transported to the combustion chamber in late power and early exhaust strokes and later consumed. This assumption, however, is not realistic, since only a portion of the entrained oil would be blown back to the combustion chamber, exposing it to consumption. The projected results were compared to known oil losses through different mechanisms as shown in Figs. 10 and 11. The average oil consumption value, obtained from Ref. [15] at 1840 rpm was used to estimate the oil consumption through cylinders and nonevaporative oil consumption by calculating 80% and 70% of the total oil loss value, respectively. These percentages represent the average contribution of these individual mechanisms to total oil consumption and were based on the estimates given in Refs. [1], [2]. The study of Iizumi and Koyama [15] was utilized due to similarities in the dimensions of the diesel engine used. The experimental oil consumption estimates given in Fig. 11 were 9–35 times greater than expected values. This in fact was an expected result since not all the oil accumulated in the second land is lost in real engines. Some portion of oil accumulated flows into the third land,

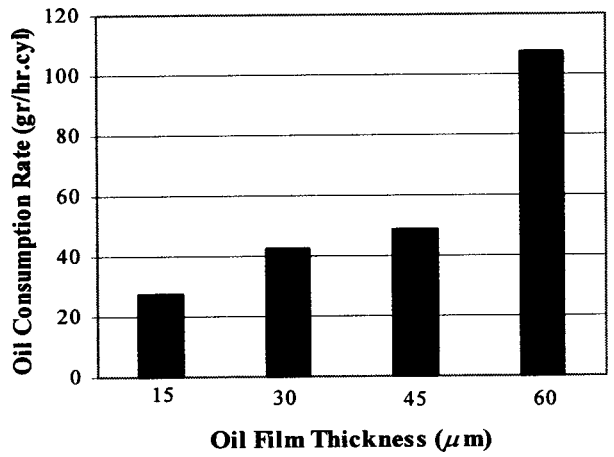

Fig. 11 Effect of oil film thickness on projected non-evaporative oil consumption

whereas some stays in the second land ring grooves. Only 30%–40% of the oil in the second land was expected to flow back into the combustion chamber. Moreover, the oil film thickness on the cylinder wall varies between 1 and 10 μm in an internal combustion engine, but in the experimental setup, a thickness below 15 μm could not be spread. When these effects were taken into consideration, the oil consumption rates evaluated were in the same order of magnitude and showed that the experimental setup could be utilized for investigation of oil accumulation in the second land.

Conclusions

In this study an experimental setup for investigating the effects of individual operating parameters on oil accumulation in the second land of internal combustion engines was constructed. The setup included a modeled piston-cylinder assembly, which simulated the inter-ring crevices and areas in real engines. The effect of oil film thickness on oil accumulation was investigated and compared to known oil consumption in operating engines. The following conclusions were made:

(1) The oil film thickness on the modeled cylinder wall affected oil accumulation in the second land crevice of the modeled piston-cylinder.

(2) Large differences in oil accumulation between two replications of experiments were detected in the neighborhood of oil thickness of 45 μm and 70 μm, in conjunction with sudden increase or decrease of oil accumulation. Although this observation needs further investigation, the prime suspect of this behavior is a shift in the oil entrainment mechanisms at these film thicknesses.

(3) When compared to known oil consumption in a similar real diesel engine, the projected oil consumption rates showed that oil accumulation in the second land could be the major contributor to oil consumption.

The effects of pressurization, different oils, and operating temperatures need to be investigated, for a thorough understanding of the oil consumption due to oil blowback into the combustion chamber. The experimental setup may also be used to study oil accumulation in the third land in internal combustion engines.

Acknowledgment

The authors would like to acknowledge the support of Petroleum Research Laboratory of Middle East Technical University for the gas analyses. This research was supported by the Middle East Technical University under project AFP-2000-03-02-06.

References

[1] Hanaoka, M., Ise, A., Nagasaka, N., Osawa, H., Arakawa, Y., and Obata, T., 1979, ''New Method for Measurement of Engine Oil Consumption (S-Trace Method),'' SAE Paper No. 790936.

[2] Wahiduzzaman, S., Keribar, R., Dursunkaya, Z., and Kelley, F. A., 1992, ''A Model for Evaporative Consumption of Lubricating Oil in Reciprocating Engines,'' SAE Paper No. 922202.

[3] Hewitt, G. F., and Hall-Taylor, N. S., 1970, *Annular Two-Phase Flow*, Pergamon Press, New York, pp. 136–142.

[4] Ishii, M., and Grolmes, M. A., 1975, ''Inception Criteria for Droplet Entrainment in Two-Phase Concurrent Film Flow,'' AIChE J., **21**, pp. 308–318.

[5] Ishii, M., and Mishima, K., 1989, ''Droplet Entrainment Correlation in Annular Two-Phase Flow,'' Int. J. Heat Mass Transfer, **32**, pp. 1835–1846.

[6] Miyachika, M., Hirota, T., and Kashiyama, K., 1984, ''A Consideration on Piston Second Land Pressure and Oil Consumption of Internal Combustion Engines,'' SAE Paper No. 840099.

[7] Kim, C. G., Bae, C. S., and Choi, S. M., 2000, ''Importance of Inter-Ring Crevice Volume as a Source of Unburned Hydrocarbon Emissions-Numerical Considerations,'' J. Automobile Eng., **214**, pp. 395–403.

[8] Kuo, T. W., Sellnau, M. C., Theobald, M. A., and Jones, J. D., 1989, ''Calculation of Flow in the Piston-Cylinder-Ring Crevices of a Homogeneous Charge Engine and Comparison With Experiment,'' SAE Paper No. 890838.

[9] Nakashima, K., Ishihara, S., Urano, K., and Murata, K., 1996, ''Lubricating Oil Flow Into the Combustion Chamber and its Reduction Method in an Automobile Gasoline Engine,'' SAE Paper No. 962034.

[10] Nakashima, K., Ishihara, S., and Urano, K., 1995, ''Influence of Piston Ring Gaps on Lubricating Oil Flow Into the Combustion Chamber,'' SAE Paper No. 952546.

[11] Dursunkaya, Z., Keribar, R., and Richardson, D. E., 1993, ''Experimental and Numerical Investigation of Inter-Ring Gas Pressures and Blowby in a Diesel Engine,'' SAE Paper No. 930792.

[12] Saito, K., Igashira, T., and Nakada, M., 1989, ''Analysis of Oil Consumption by Observing Oil Behavior Around Piston Ring Using a Glass Cylinder Engine,'' SAE Paper No. 892107.

[13] Wong, V. W., and Hoult, D. P., 1991, ''Experimental Survey of Lubricant Film Characteristics and Oil Consumption in a Small Diesel Engine,'' SAE Paper No. 910741.

[14] Kokdemir, H. G., 1970, ''Mechanical Valve Operated Shock Tube,'' M.S. thesis, Mechanical Engineering Department, Middle East Technical University, pp. 25–38; 71–73.

[15] Iizumi, S., and Koyama, T., 1986, ''Measurement of Oil Consumption of Diesel Engine by S-Trace Method,'' SAE Paper No. 860545.

Herbert Kopecek
e-mail: herbert.kopecek@tuwien.ac.at

Soren Charareh

Technische Universität Wien,
Institut für Photonik,
Gusshausstrasse 27/387,
A1040 Wien, Austria

Maximilian Lackner

Christian Forsich

Franz Winter

Vienna University of Technology,
Institute of Chemical Engineering,
Getreidemarkt 9/166,
A1060 Wien, Austria

Johann Klausner

Günther Herdin

GE Jenbacher,
A6200 Jenbach, Austria

Martin Weinrotter

Ernst Wintner

Technische Universität Wien,
Institut für Photonik,
Gusshausstrasse 27/387,
A1040 Wien, Austria

Laser Ignition of Methane-Air Mixtures at High Pressures and Diagnostics

Methane-air mixtures at high fill pressures up to 30 bar and high temperatures up to 200°C were ignited in a high-pressure chamber with automated fill control by a 5 ns pulsed Nd:YAG laser at 1064 nm wavelength. Both, the minimum input laser pulse energy for ignition and the transmitted fraction of energy through the generated plasma were measured as a function of the air/fuel-equivalence ratio (λ). The lean-side ignition limit of methane-air mixtures was found to be λ=2.2. However, only λ<2.1 seems to be practically usable. As a comparison, the limit for conventional spark plug ignition of commercial natural gas engines is λ=1.8. Only with excessive efforts λ=2.0 can be spark ignited. The transmitted pulse shape through the laser-generated plasma was determined temporally as well as its dependence on input laser energy and properties of the specific gases interacting. For a first demonstration of the practical applicability of laser ignition, one cylinder of a 1 MW natural gas engine was ignited by a similar 5 ns pulsed Nd:YAG laser at 1064 nm. The engine worked successfully at λ=1.8 for a first test period of 100 hr without any interruption due to window fouling and other disturbances. Lowest values for NO_x emission were achieved at λ=2.05 (NO_x=0.22 g/KWh). Three parameters obtained from accompanying spectroscopic measurements, namely, water absorbance, flame emission, and the gas inhomogeneity index have proven to be powerful tools to judge laser-induced ignition of methane-air mixtures. The following effects were determined by the absorption spectroscopic technique: formation of water in the vicinity of the laser spark (semi-quantitative); characterization of ignition (ignition delay, incomplete ignition, failed ignition); homogeneity of the gas phase in the vicinity of the ignition; and the progress of combustion. [DOI: 10.1115/1.1805550]

Introduction

For a number of combustion applications, it is interesting to look for alternative ignition sources. Particularly in the case of internal combustion engines, there is a high demand for the potential benefits the laser can provide, such as arbitrary positioning of the ignition location in the cylinder, absence of quenching effects by the spark plug electrodes, precise ignition timing, and easy regulation of the ignition energy deposited in the ignition plasma. Especially for high-power gas engines, it is a primary advantage to minimize service efforts due to the long-lasting performance of a diode-pumped solid-state laser. High-load pressure of the engine for optimum efficiency performance demands for increased spark plug voltage leading to enhanced erosion of the electrodes as well as causing electromagnetic incompatibilities. This is naturally not the case when employing a laser ignition system.

In this work, experiments in a pressure chamber of constant volume were performed to investigate the main characteristics of laser ignition under high pressure and high temperature conditions regarding to the requirements of internal combustion engines. Laser ignition was also implemented to one cylinder of a 1 MW gas engine to demonstrate the feasibility of laser-initiated engine start and reliable operation and to characterize advantageous operation regimes.

Generally, there exist several different approaches how to ignite combustible gas mixtures by a laser [1–4]. In this work, ignition is obtained via nonresonant optical breakdown. Focusing a pulsed laser to a sufficiently small spot size creates high intensities and high electric fields in the focal region, resulting in a well-localized plasma. Consecutively, further energy can be accumulated by the plasma through enhanced absorption, leading to local temperature rise and, if a certain energy threshold is exceeded, to ignition of the gas mixture starting via a self-sustaining flame kernel. Small impurities of the gas mixture, such as aerosols or microparticles, can influence the breakdown probability and, therefore, yield effective ignition [5,6].

Figure 1 shows the processes involved in laser-induced ignition, covering several orders of magnitude in time from the nanosecond domain of the laser pulse to the duration of the combustion lasting several hundreds of milliseconds. As opposed to conventional spark ignition, the laser energy is deposited in a few nanoseconds, leading to shock-wave generation and characteristic asymmetric shapes of the flame kernel [8–11]. Naturally, this difference during the first steps of ignition can influence the whole combustion process significantly. It is, therefore, of serious interest to determine the main characteristics of laser ignition qualitatively and

Contributed by the Internal Combustion Engine Division of THE AMERICAN SOCIETY OF MECHANICAL ENGINEERS for publication in the ASME JOURNAL OF ENGINEERING FOR GAS TURBINES AND POWER. Manuscript received by the ICE Division, July 15, 2003; final revision received March 12, 2004. Associate Editor: D. Assanis.

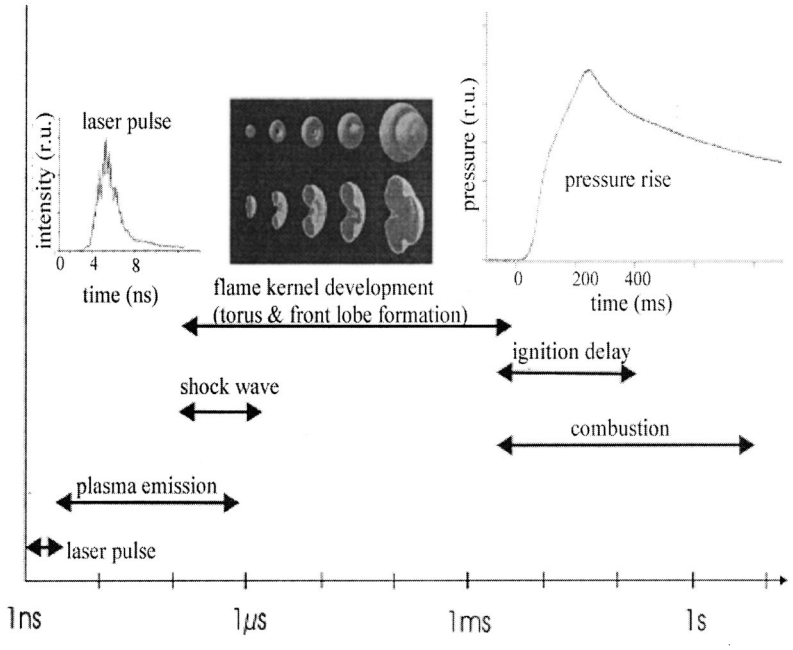

Fig. 1 Scope of timescales of various processes involved in laser-induced ignition. The lengths of the double-arrowed lines indicate the duration ranges of the indicated processes. Inserts: typical laser pulse duration; examples for temporal development of spatially resolved OH concentrations in flame kernels [7]; typical pressure rise in the combustion chamber.

quantitatively by employing diagnostic methods working in different time domains, as it was done within this work.

Linear absorption spectroscopy is used to gather time-resolved information of the entire combustion in the millisecond domain, while fast tracing of transient laser pulses should give an indication of plasma formation during the first nanoseconds [12].

Experiments

a. Setup for Evaluation of Ignition Parameters. Figure 2 depicts the first part of the experiment setup for laser ignition experiments with emphasis on the optical scheme of the igniting laser beam. The beam of a Q-switched Nd:YAG laser with a maximum output energy of 40 mJ per pulse was focused into a high-pressure combustion chamber through a sapphire window of 13 mm clear aperture. Losses due to surface reflections are about 7% per surface and are included in the given results for the minimum pulse energy needed for ignition. The pulse duration was about 5 ns, and the beam quality described by the M^2 factor was less then 2. The laser could be attenuated continuously by using an external wave plate/polarizer setup without affecting any other laser parameters, such as pulse duration or spatial profile of the beam. It has to be said, that a different pulsed Nd:YAG laser was employed for time-resolved transmission measurements, delivering light pulses of different pulse length (10 ns) and temporal and spatial pulse shape ($M^2<1.1$). Both lasers showed a typical temporal multimode behavior. A spherically corrected two-lens system was employed to focus the beam into the chamber achieving well-defined focal diameters for correct calculation of the focal intensity. Parts of the input/transmitted beam (about 4%) were used to measure the energy of each pulse by two pyroelectric detectors (SpectroLas PEM21) and a two-channel pulse energy-measuring unit (LEM2020). Small portions of the input/transmitted beams were used to record the temporal pulse shapes by two fast InGaAs PIN photo detectors (rise/falltime $\tau=250$ ps) and a fast digital storage oscilloscope (1 GHz, 4 GS/s).

For all combustion chamber experiments, methane (99.5% of purity, content of other $C_xH_y<0.3\%$) and air of only technical purity were used in order to yield data relevant for practical applications. Before each ignition event, the combustion chamber was first flushed with air to remove all residual products of the previous combustion. For achieving the intended ratio of the gaseous mixture components, it was necessary to measure the partial pressures of methane and air by using a high-resolution (1 mbar) pressure meter and, of course, thermalization of the filled mixture component was ensured by attending a stationary reading of the pressure meter. To reliably ensure a homogenous mixture, meth-

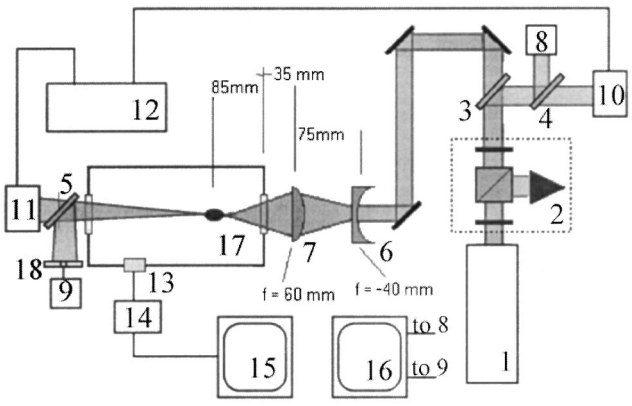

Fig. 2 Experimental setup for evaluation of ignition parameters: 1—Nd:YAG-Laser; 2—beam attenuator; 3,4,5—beam sampler (4%); 6—concave lens f=−40 mm; 7—spherical corrected convex lens f=60 mm; 8,9—InGaAS PIN detector; 10,11—pyroelectric detector; 12—laser energy measuring unit; 13—pressure detector; 14—charge amplifier; 15—digital storage oscilloscope; 16—fast digital storage oscilloscope; 17—combustion chamber; 18—aperture 1 mm

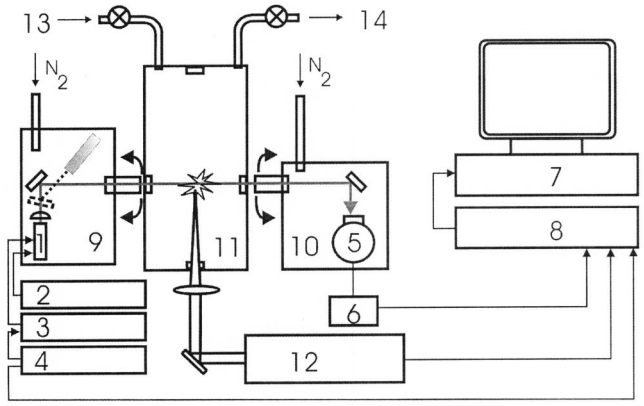

Fig. 3 Experiment setup for ignition diagnostics: 1—diagnostic diode laser at 2.55 μm; 2—temperature controller; 3—laser driver; 4—function generator; 5—detector; 6—amplifier; 7—PC; 8—oscilloscope; 9, 10—boxes purged with N_2; 11—pressurized combustion vessel; 12—Nd:YAG laser; 13—fuel and air inlet; 14—exhaust gas analysis

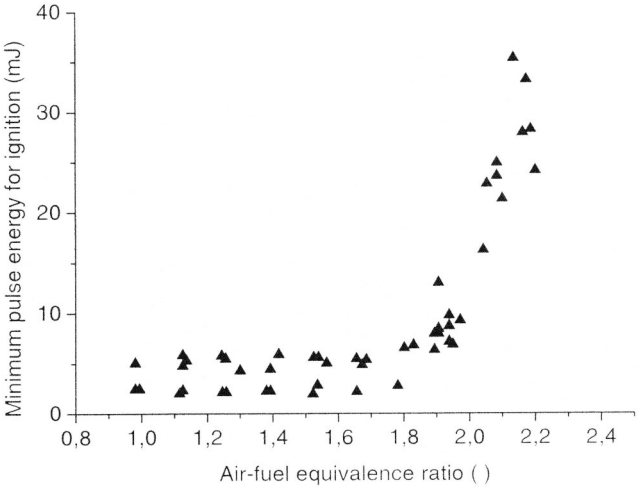

Fig. 4 Minimum pulse energy needed for ignition versus air/fuel-equivalence ratio λ; methane-air mixtures, T=200 °C, fill pressure 30 bar

ane being the species of lower partial pressure should be filled in first. In this way, homogeneity could be easily achieved by the turbulences of the following stream of air.

The interior diameter and length of the chamber were 70 mm and 220 mm, respectively. The maximum fill pressure of each load was 30 bar, and the chamber was heated up to 200 °C constant temperature additionally allowing us to prevent the side effect of water condensation on the chamber windows. After filling, 3 min waiting time was observed before each ignition attempt in order to achieve stabilized mixture conditions. Consecutively, the laser pulse energy was gradually increased with sub-Hertz repetition rates until ignition occurred, thus yielding the data of minimum pulse energy needed for ignition. (No memory effects could be observed at such repetitions rates.) Combustion initiated in this way was monitored on a second storage oscilloscope utilizing a piezoelectric pressure detector in combination with a charge amplifier. The mixture ratio of the filling was measured and calibrated by gas-chromatographic analysis.

b. Setup for Ignition Diagnostics. Laser-induced ignition was investigated with a diagnostic technique based on absorption spectroscopy. A tunable continous-wave diode laser emitting around 2.55 μm was used to track the water formation in the vicinity of the laser spark during the ignition process. Water is one of the combustion products exhibiting strong absorption at this wavelength and, therefore, is qualified as an indicator of the global chemical reaction $CH_4+2O_2\rightarrow CO_2+2H_2O$.

The experiment setup part 2, focusing the absorption measurement, is given in Fig. 3. The collimated diagnostic laser beam of an InGaAsSb/AlGaAsSb quantum well ridge diode laser crosses the combustion chamber perpendicular to the optical path of the ignition laser intersecting at the focal spot of the latter. Correspondingly, the chamber is mounted with four windows of sapphire of 13 mm clear aperture. A laser driver with a transfer function of 44 mA/V was deployed to change the emission wavelength of the laser. A voltage ramp of 0–4 V with a repetition rate of 5 kHz was applied to the laser driver utilizing a function generator. Accordingly, a time resolution of 0.2 ms was achieved. A 15 V current source protected against the line voltage by an overvoltage protector, and an automatic voltage regulator supplied the laser driver and the function generator. A liquid N_2 cooled detector in combination with an amplifier was utilized to detect the transmitted signal. Both, the diagnostic laser and the spectroscopic detector had to be purged with nitrogen to remove the water vapor in the ambient atmosphere along the beam path, which would make it impossible to detect the concentration of water generated during the combustion process. During the experiments, the detector signal was visualized on an oscilloscope, and data collection was performed with a computer equipped data acquisition board having a maximum sampling rate of 125 MS/s, 60 MHz bandwidth, and 12-bit vertical resolution. Further information can be found in Ref. [13].

c. Preliminary Engine Tests. For a first demonstration of the practical applicability of laser ignition, one cylinder of a 1 MW natural gas engine was ignited by a 5 ns pulsed Nd:YAG laser at 1064 nm. The maximum pulse energy of this laser was 150 mJ. The beam was transmitted through the open air to the engine via three mirrors fastened to a solid mechanical construction. The laser pulses were focused into the cylinder by a 200 mm focusing lens through a sapphire window of 5 mm thickness. Losses due to surface reflections are about 7% per surface and are included in the given results for the minimum pulse energy needed for ignition. The generated plasma was located approximately in the middle of the combustion volume to minimize quenching losses due to the cylinder walls. The typical constant engine speed is 1500 rpm; hence, this requires a laser repetition rate of 12.5 Hz easily accessible by the mentioned laser system. The laser was triggered by the engine via custom-made electronics. Cylinder performance data under laser ignition were taken during a test period of approximately 100 hr and will be discussed below. Natural gas was used as a fuel for all engine experiments.

Results and Discussion

For lean gas engine applications, it is very important to know the lean-side ignition limit of the fuel used. Figure 4 depicts this limit measured in case of laser ignition. Mixtures up to $\lambda=1.8$ could be ignited applying only about 4 mJ of laser pulse energy. Applying the maximum available pulse energy of 40 mJ, the lean-side ignition limit was found to be at $\lambda=2.2$. The energy of the transmitted part of the pulse was found to be nearly constant, yielding values from 2 mJ to 6 mJ (Fig. 5).

In the case of very lean mixtures above $\lambda=2.0$, only very low peak pressures were observed as shown in Fig. 6, indicating the unlikeness of practical usability. Employing laser energies above the required minimum yields shorter ignition delays, but the same peak pressure [14]. The dependence of the minimum laser pulse energy needed for ignition on the fill pressure can be found elsewhere [15].

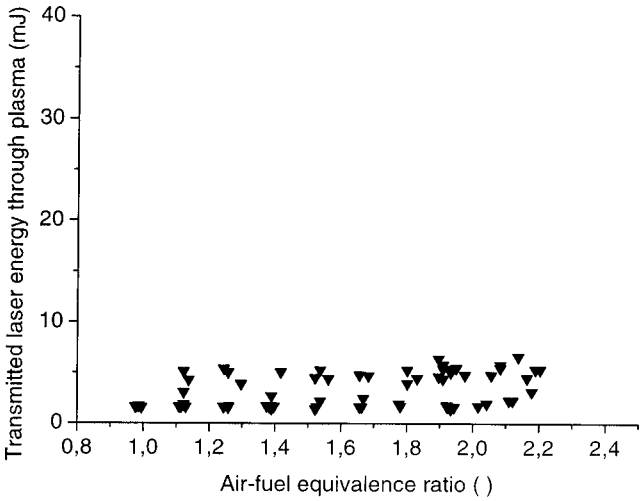

Fig. 5 Transmitted laser energy through plasma versus air/fuel-equivalence ratio λ; methane-air mixtures, T=200 °C, fill pressure 30 bar

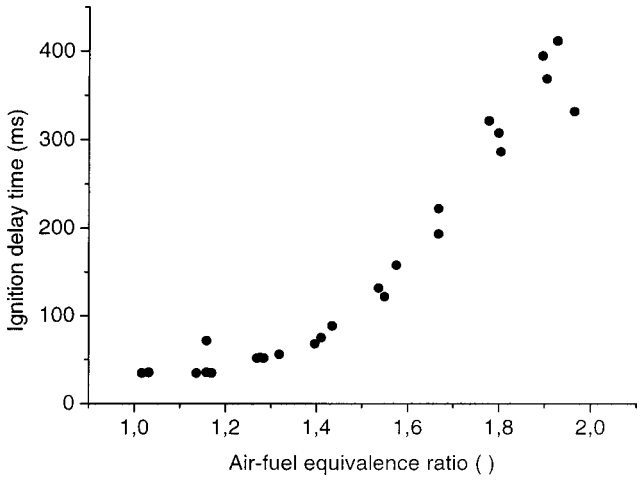

Fig. 7 Ignition delay versus air/fuel-equivalence ratio at minimum laser pulse energy; methane-air mixtures, T=200 °C, fill pressure 30 bar

The measured ignition delay time (defined as temporal interval between the laser pulse and the time when 5% of the peak pressure is reached) versus the air/fuel-equivalence ratio is plotted in Fig. 7.

Time-resolved measurements of the transmitted part of the pulse through the igniting plasma were performed to yield quantitative information about the absorbed fraction of the laser pulse necessary to raise plasma energy and, therefore, sustain ignition. Figure 8 shows averaged shapes of the transmitted pulses depending on their input energy. Up to 0.5 mJ input laser energy corresponding to a focal intensity of 2.5×10^{11} W/cm^2 no plasma is created and hence no shape deformation of the transmitted pulse can be observed. Plasma is generated reliably above 1 mJ absorbing and reflecting the incoming laser light and, therefore, suppressing laser transmission to a large amount. Obviously, the transmitted and smaller reflected parts are lost for ignition implying the necessity of an increase as steep as possible of the laser pulse for a future practical laser ignition system.

Figure 9 reveals the time-resolved intensity plots of the transmitted pulses in different media. All curves were measured at the intensity threshold level for reliable plasma generation. Accordingly, the required intensity for plasma generation in methane is evidently smaller than in air or pure nitrogen. This will lead to slightly higher laser pulse energies needed for successful plasma formation in lean mixtures. The results of Figs. 8 and 9 were achieved by experiments employing different lasers. Thus, the temporal pulse shapes in both figures look quite different.

The diagnostic characterization of laser-induced ignition was judged by three parameters obtained by tunable diode laser spectroscopy, namely, water absorbance, flame emission, and the gas inhomogeneity index.

The first characterization parameter, water absorbance A, was evaluated according to Lambert Beer's law $A=\ln(I_0/I)$, with I being the intensity of the transmitted light and I_0 the incident intensity. Absorption spectroscopy is an inherently integrative technique delivering path-averaged results. When water is formed close to the ignition spot, one will see a signal that stems from both very hot and rather cold regions. The line strength is a func-

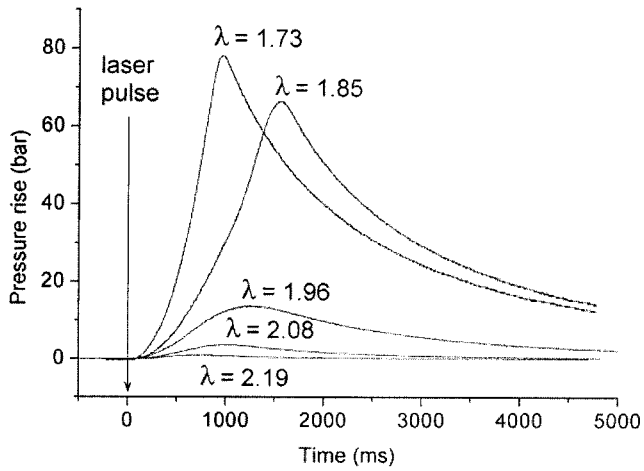

Fig. 6 Pressure rise in the chamber after ignition applying minimum pulse energy; methane-air mixtures, T=200 °C, fill pressure=30 bar, laser pulse energy=25 mJ

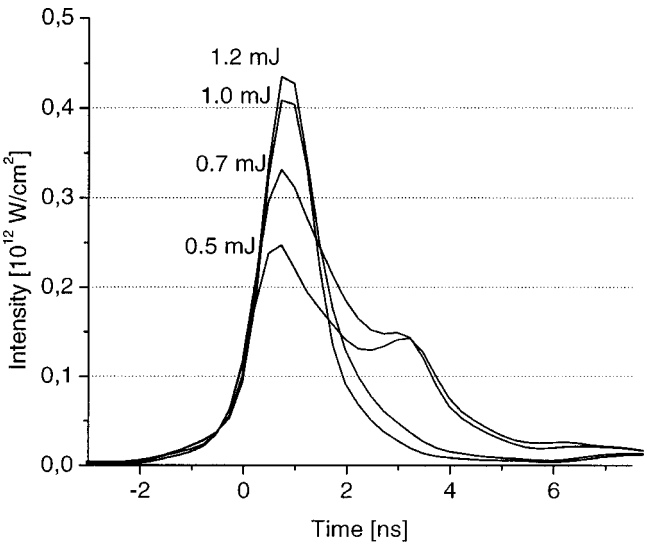

Fig. 8 Temporal shapes of the focal intensity of transmitted pulses through the medium with or without plasma formation. Depending on the input laser pulse energy, plasma is formed if the breakthrough intensity is exceeded, thereby drastically changing the transmitted pulse shape; air of technical purity, T=20 °C, fill pressure 40 bar.

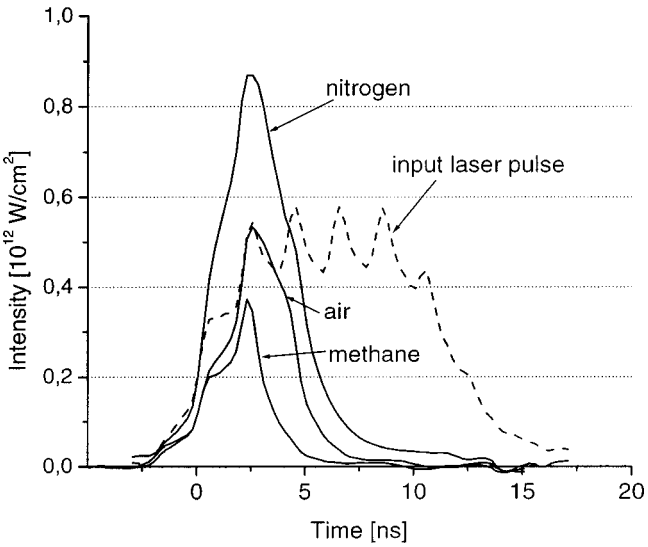

Fig. 9 Temporal shapes of the focal intensity of transmitted pulses under reliable plasma formation condition, depending on different gaseous media (technical purity); T=20 °C, fill pressure 10 bar

tion of temperature, which is neither known exactly nor a constant. In the onset of the combustion process being most interesting, one can assume a homogeneous temperature in the growing flame ball to address and simplify this problem. The pressure inside the combustion reactor rises steeply, so that significant pressure broadening will occur. Pressure broadening limits the use of tunable diode lasers because the wings of the absorption feature cannot be recorded properly any more, due to the limitation of the laser tuning range. In addition, a nonlinear dependence of the concentration on the measured absorbance will be observed if the peak becomes broader than the tuning range. These shortcomings, the obscure temperature and linearity aspects, are relevant for quantitative model purposes. Water that is formed by reactions of different hydrocarbons in the vicinity of the laser spark can therefore be determined merely in a semi-quantitative manner. The absorbance values of water vapor were evaluated up to 4. Without any sophisticated detection schemes, absorbance above 4 becomes difficult to measure because the transmitted intensity approaches zero.

As shown in Fig. 10 for a stoichiometric mixture, the absorbance of water increases sharply with time. After approximately 70 ms, it could not be determined any more because the transmission became too low.

The second parameter characterizing the ignition event is flame emission. Such emissions were captured by the detector as an offset to the voltage caused by the transmitted laser radiation. The photo detector used in these studies has a response wavelength range from 1 to 10 μm. Therefore, most of the infrared radiation contributes to the signal. One can deduct the ignition delay from the time difference between the trigger signal of the laser pulse to the onset of emission. An offset at the beginning of every measurement is caused by the background radiation due to the ambient temperature. The methane flame emissions for the stoichiometric and fuel-rich case resemble each other very much, except for the fact that in the former case the peak value is reached sooner. Comparing to Fig. 11, one can see that the emissions from the flame in the fuel-lean case do not emerge before approximately 150 ms due to the extraordinarily long ignition delay time.

In the experiment setup used, the infrared probe beam traverses the combustion vessel before hitting a photo detector situated in a purged box behind. The transmitted signal fluctuates strongly over time. The nonresonant variation of the transmittance is caused by several effects: The beam may be partially blocked (e.g., by soot particles) or partly deflected from the detector by refractive index gradients inside the vessel (e.g., due to flames). In the experiments the laser beam can also be deflected from the detector by the influence of the plasma and the shock waves, depending on the relative position to the plasma spark. It can also be deflected by refractive index gradients caused by the propagating flame, a fact

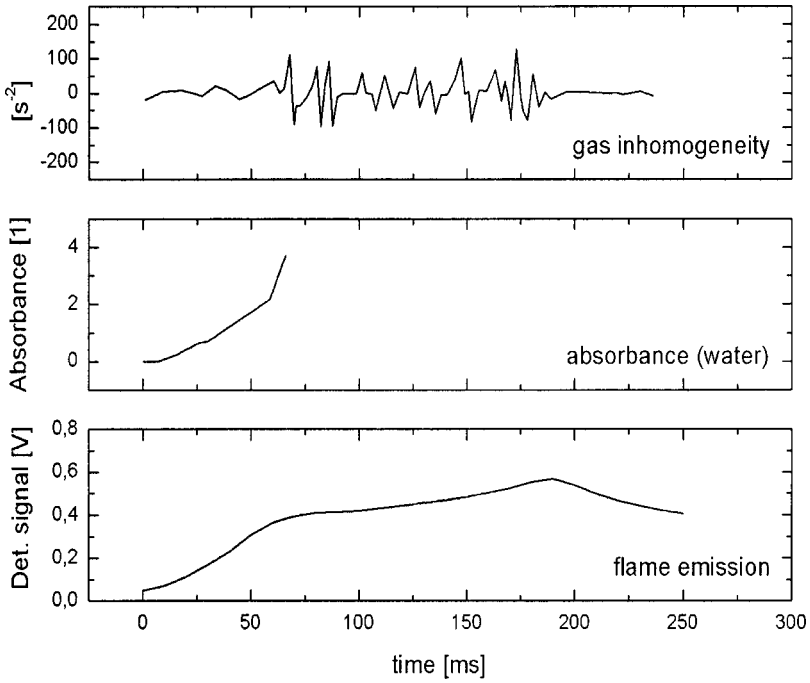

Fig. 10 Evaluated data from the laser-induced ignition of a stoichiometric methane/air mixture, namely, gas inhomogeneity index, water absorbance, and flame emission. T=200 °C, fill pressure 30 bar, air/fuel-equivalence ratio λ=1.0

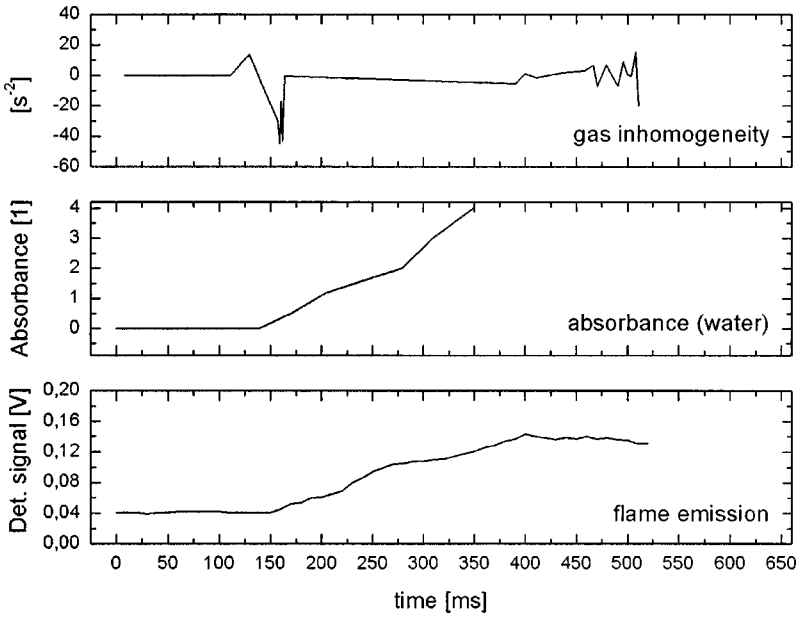

Fig. 11 Evaluated data from the laser-induced ignition of a fuel-lean methane/air mixture, namely, gas inhomogeneity index, water absorbance, and flame emission. T=200 °C, fill pressure 30 bar, air/fuel-equivalence ratio λ=1.7

that was relevant during the entire ignition investigation. The faster the flame develops, the stronger the transmitted signal will fluctuate. The fluctuations can be expressed in terms of a frequency and a derivation thereof. By so doing, it is possible to introduce the third parameter treated in this paper, the so-called *inhomogeneity index* [s^{-2}]. Fuel-rich and stoichiometric methane-air mixtures show a high velocity of flame propagation corresponding to high fluctuations of the gas inhomogeneity. Due to a decelerated combustion process and flame velocity, respectively, slight transmission variations are observed during the ignition process of fuel-lean methane-air mixtures. The index allows one to easily spot the start of combustion, to follow the combustion, and to discern failed or stopped combustion events. Turbulence introduced by the flame into the stagnant air of the constant volume vessel also dominates this inhomogeneity index. Before ignition is launched, the inhomogeneity index can be used to obtain information on the homogeneity of the gas mixture at the location of ignition.

As it was mentioned above, first engine experiments have been carried out. Figure 12 gives an example of typical pressure rises of the laser-ignited cylinder verifying an increase in peak pressure when raising the laser pulse energy.

Figure 13 shows the required ignition energy depending on the mean pressure. In the high-load range, a minimum ignition energy of 15 mJ was sufficient for smooth operation, in the lower-load range, the ignition energy requirement clearly increased. It was easy to set an air/fuel-equivalence ratio of λ=1.8 on the engine

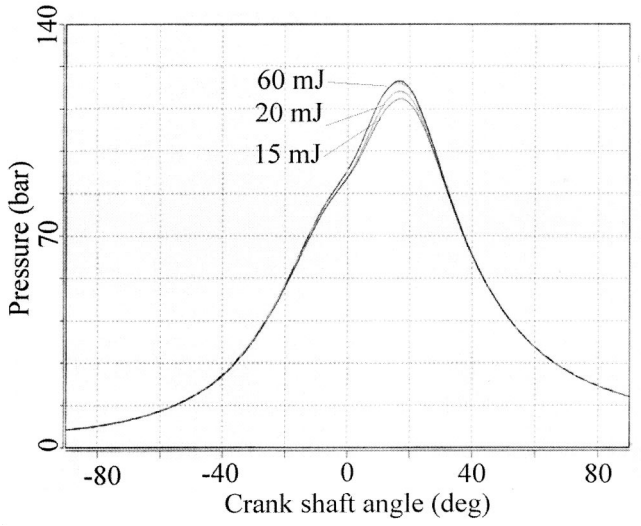

Fig. 12 Pressure rise in a laser-ignited cylinder depending on laser pulse energy; 1 MW natural gas engine, mean pressure 18 bar, time of ignition 20° before DTC, NO_x=500 mg/mN³, averaged over 100 cycles

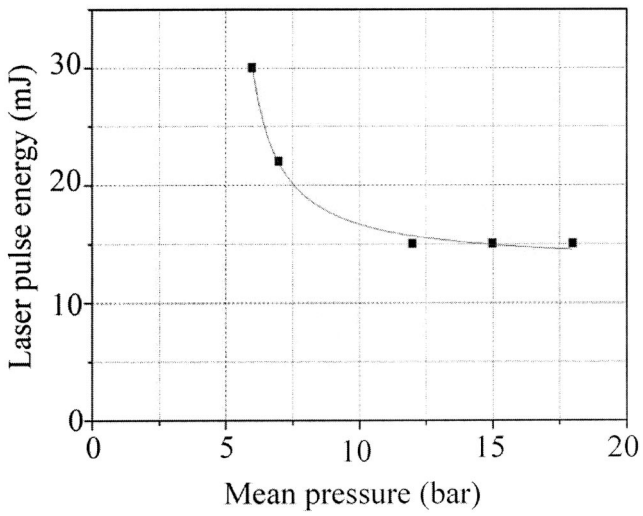

Fig. 13 Required laser pulse energy of a laser-ignited cylinder depending on mean pressure; 1 MW gas engine, air/fuel-equivalence ratio λ=1.8

yielding reliable performance for a first test period of 100 hr, fully equivalent to spark-ignited operation. The lean-burn limit of the tested setup was found to lie close to $\lambda=2.1$. The lowest NO_x emissions were reached at an air/fuel-equivalence ratio of $\lambda=2.05$ with values about 0.22 g/KWh. We claim that this represents the first successful demonstration and measured data of a laser-ignited gas engine. Naturally, the experiment conditions were not optimized so far possessing, however, a large potential for improvement in many respects.

Conclusions

Very lean methane-air mixtures ($\lambda=2.2$) could be ignited successfully at high fill pressures (30 bar) by a Q-switched Nd:YAG laser at 1064 nm, which is significantly leaner compared to the limit for conventional spark plug ignition. The necessary pulse energy for mixtures up to $\lambda=1.8$ was only about 4 mJ to 6 mJ, which could be easily achieved by a compact diode-pumped laser. Temporal measurements of the transmitted pulse through the plasma showed smaller threshold intensity for plasma generation in methane than in air or nitrogen. Time-resolved transmission measurements gave also an indication for the ideal pulse shape of a future laser-ignition system. Such a pulse should have an increase as steep as possible for effective plasma formation, but could have a smooth decrease for sustaining the plasma as long as possible to efficiently heat up the flame kernel.

Three parameters obtained from spectroscopic measurements, namely, water absorbance, flame emission, and the gas inhomogeneity index have proven to be a powerful tool to judge laser-induced ignition of methane-air mixtures. The following effects were determined by the absorption spectroscopic technique: formation of water in the vicinity of the laser spark (semi-quantitative); characterization of ignition (ignition delay, incomplete ignition, failed ignition); homogeneity of the gas phase in the vicinity of the ignition, and the progress of combustion.

To demonstrate the usefulness of laser ignition, one cylinder of a 1 MW natural gas engine was ignited by a 5 ns pulsed Nd:YAG laser at 1064 nm. The engine worked successfully at an air/fuel-equivalence ratio of $\lambda=1.8$ (natural gas) for a test period of 100 hr without any interruption due to window fouling or other disturbances. Lowest values for NO_x emission were achieved at an air/fuel-equivalence ratio of 2.05 ($NO_x=0.22$ g/KWh).

Acknowledgments

Financing by Jenbacher AG, Austria, by the Austrian Industrial Research Promotion Fund under Grant No. FFF 803050, and by the ''Hochschuljubiläumsstiftung der Stadt Wien'' under Grant No. H-1052/2002 is gratefully acknowledged.

References

[1] Ronney, P. D., 1994, ''Laser Versus Conventional Ignition of Flames,'' Opt. Eng., **33**(2), pp. 510–520.

[2] Forch, B. E., and Miziolek, A. W., 1991, ''Laser-Based Ignition of H_2/O_2 and D_2/O_2 Premixed Gases Through Resonant Multiphoton Excitation of H and D Atoms Near 243 nm,'' Combust. Flame, **85**, pp. 254–262.

[3] Morsy, M. H., Ko, Y. S., and Chung, S. H., 1999, ''Laser-Induced Ignition Using a Conical Cavity in CH_4-Air Mixtures,'' Combust. Flame, **119**, pp. 473–482.

[4] Heitzmann, T., and Wolfrum, J., 1995, ''Experimental and Modeling Studies on the Ignition of CH_3OH/O_2-Mixtures With a CO_2-Laser System,'' Z. Phys. Chem. (Munich), **188**, pp. 177–196.

[5] Yablonovich, E., 1974, ''Self Phase Modulation of Light in a Laser Breakdown Plasma,'' Phys. Rev. Lett., **32**, pp. 1101–1104.

[6] Yablonovich, E., 1975, ''Self Phase Modulation and Short Pulse Generation From Laser Breakdown Plasmas,'' Phys. Rev. A, **10**, pp. 1888–1895.

[7] Rüdisser, D., 2002, ''Raum- und zeitaufgelöste optische Diagnostik Laser-gezündeter Gasgemische mit planarer Laser-induzierter Fluoreszenz,'' diploma thesis, Graz University of Technology, Graz.

[8] Spiglanin, T. A., Mcilroy, A., Fournier, E. W., Cohen, R. B., and Syage, J. A., 1995, ''Time-Resolved Imaging of Flame Kernels: Laser Spark Ignition of H2/O2/Ar Mixtures,'' Combust. Flame, **102**, pp. 310–328.

[9] Chen, Y. L., and Lewis, J. W. L., 2001, ''Visualization of Laser-Induced Breakdown and Ignition,'' Opt. Express, **9**, pp. 360–372.

[10] Weinberg, F. J., and Wilson, J. R., 1971, ''A Preliminary Investigation of the use of Focused Beams for Minimum Ignition Energy Studies,'' Proc. R. Soc. London, Ser. A, **321**, pp. 41–52.

[11] Ma, J. X., Ryan, T. W., and Buckingham, J. P., 1998, ''Nd:YAG Laser Ignition of Natural Gas,'' ASME, ICE 30-3, Paper No. 98-ICE–114.

[12] Raffel, B., and Wolfrum, J., 1986, ''Infrared Laser Induced Ignition of Gas Mixtures,'' Ber. Bunsenges. Phys. Chem., **90**, pp. 997–1001.

[13] Lackner, M., Forsich, Ch., Winter, F., Kopecek, H., and Wintner, E., 2003, ''In Situ Investigation of Laser-Induced Ignition and the Early Stages of Methane-Air Combustion at High Pressures Using a Rapidly Tuned Diode Laser at 2.55 μm,'' Spectrochim. Acta, **59**(13), pp. 2997–3018.

[14] Kopecek, H., Wintner, E., Pischinger, H., Herdin, G., Klausner, J., and Jenbacher A. G., 2000, ''Basics for a Future Laser Ignition System for Gas Engines,'' Fall Technical Conference ASME, Preoria, US, ICE-35-2, Paper No. 2000-ICE-316.

[15] Kopecek, H., Maier, H., Reider, G., Winter, F., and Wintner, E., 2003, ''Laser Ignition of Methane-Air Mixtures at High Pressures,'' Exp. Therm. Fluid Sci., **27**, pp. 499–503.